SIMULATIONS OF PULSATILE FLOW THROUGH BILEAFLET MECHANICAL HEART VALVES USING A SUSPENSION FLOW MODEL: TO ASSESS BLOOD DAMAGE

A Thesis
Presented to
The Academic Faculty

By

B. Min Yun

In Partial Fulfillment
Of the Requirements for the Degree
Doctor of Philosophy in Mechanical Engineering

Georgia Institute of Technology

May 2014

Simulations of Pulsatile Flow through Bileaflet Mechanical Heart Valves Using a Suspension Flow Model: To Assess Blood Damage

Approved by:

Dr. Ajit P. Yoganathan, Co-Advisor
Wallace H. Coulter Department of Biomedical Engineering
Georgia Institute of Technology
Emory University

Dr. Cyrus K. Aidun, Co-Advisor
George W. Woodruff Department of Mechanical Engineering
Georgia Institute of Technology

Dr. G. Paul Neitzel
George W. Woodruff Department of Mechanical Engineering
Georgia Institute of Technology

Dr. Don P. Giddens
Wallace H. Coulter Department of Biomedical Engineering
Georgia Institute of Technology
Emory University

Dr. W. Robert Taylor
Wallace H. Coulter Department of Biomedical Engineering
Georgia Institute of Technology
Emory University

Date Approved:
November 13th, 2013

ACKNOWLEDGMENTS

The completion of my thesis would not be possible without great support, guidance, and encouragement. I would like to first acknowledge my co-advisors, Dr. Ajit Yoganathan and Dr. Cyrus Aidun, on providing me with great knowledge and support while navigating this long project. Their insight has been extremely valuable and has helped to shape my work in unexpected, but ultimately productive ways. Dr. Yoganathan has helped to broaden my views and approach to research and has helped keep my focus set on important goals with my work, while bringing me along in my still new exploration of biomedical engineering. Dr. Aidun has provided me with great support and guidance for my entire tenure at Georgia Tech, and has helped me overcome very difficult research obstacles with his long experience and patient approach. I am also grateful to Dr. Neitzel, Dr. Taylor, and Dr. Giddens for serving on my thesis committee and providing their input on my work.

I would like to thank all of my coworkers in both labs as well. Although I did not work side-by-side with anyone, my work would not have been completed without their support and encouragement. From the cardiovascular fluid mechanics lab, I would like to particularly acknowledge (in no particular order) Arvind Santhanakrishnan, Neela Saikrishnan, Lucia Mirabella, Shiva Arjunon, Reza Khiabani, Ikay Okafor, and Elaine Tang for their contributions. I would also like to acknowledge Maria Restrepo, Jean-Pierre Rabbah, Andrew Siefert, Eric Pierce, Brian Jun, Milan Toma, and Joan Fernandez for their time in reading my thesis.

From Dr. Aidun's lab, I'd like to give special thanks to Daniel Reasor and Marmar Mehrabadi for their great help and invaluable discussion about the numerical method and overcoming obstacles in development. I'd also like to acknowledge Jonathan Clausen and Jingshu Wu for their help in bringing me along with the numerical method in my earlier years.

Special thanks go to Dr. Prasad Dasi for his expertise in helping with the validation work of my numerical method, as well as his general fluid dynamics expertise that helped make my work stronger. In addition, I'd like to acknowledge Dr. Minh Do-Quang who worked closely with me to bring our respective numerical methods very far in a limited amount of time.

Although my friends did not provide direct help with my research, their friendship and encouragement was crucial throughout the years and made my life and work much easier. For this, I'd like to thank you all: Aaron, Arnaud, Demijan, Dima, Elaine, Emily, Han, Harrison, Juichia, and Lander.

Finally, I'd like to thank my parents for everything they've done for me throughout the years. The lessons they taught me when I was a 6-year-old are lessons I still carry with me today and find value in as an adult. I'm thankful that they've been so patient with me. I hope to make them very proud with this work.

Thank you all.

TABLE OF CONTENTS

ACKNOWLEDGMENTS ..... **iii**

LIST OF TABLES ..... **xv**

LIST OF FIGURES ..... **xvi**

LIST OF ANIMATIONS ..... **xxxii**

LIST OF SYMBOLS OR ABBREVIATIONS ..... **xxxiv**

SUMMARY ..... **xxxviii**

1. INTRODUCTION **1**

1.1 Heart Valves, Heart Valve Replacement, and Prosthetic Heart Valves 1

1.1.1 Heart Valves 1

1.1.2. Heart valve disease, malfunction, and replacement 3

1.1.3. Prosthetic Heart Valves 4

1.2 Bileaflet Mechanical Heart Valves 7

1.2.1 General design features 7

1.2.2 Popular BMHV designs 9

1.2.3 Complications from BMHV Implantation 13

1.3 Blood and Blood Damage 16

1.3.1 Red Blood Cell Damage 16

1.3.2 Platelet damage 17

1.3.3 Shear Stress in relation to Blood Damage 18

1.3.3.1 Red Blood Cells and Shear Stress 19

1.3.3.2 Platelets and Shear Stress....21
1.3.3.3 Shear Stress on Red Blood Cells vs. Platelets....22
1.4 Previous Investigations....23
1.4.1 Experimental Studies....24
1.4.2 Computational Studies....28
1.5 Importance of Modeling Multiphase Flow....32
1.6 Significance of this Study....33

2. HYPOTHESIS AND SPECIFIC AIMS....37

3. METHODS....42
3.1 LBM-EBF Overview....43
3.2 Numerical Flow Solver....44
3.2.1 Lattice-Boltzmann Method....45
3.2.2 Entropic Lattice-Boltzmann....46
3.3 Fluid-Solid Interaction Methods....47
3.4 Solid modeling....49
3.5 Experimental Setup....51
3.6 Numerical Setup....54
3.6.1 Numerical geometry....55
3.6.2 Suspension flow modeling....61
3.6.3 Inflow and Outflow conditions....65
3.6.4 BMHV Flow Modeling....67

3.6.4.1 Flow initialization 67
3.6.4.2 Pulsatile Flow Modeling 68
3.6.4.3 Leaflet motion modeling 70
3.7 Blood Damage Calculation 75
3.7.1 Note on importance of modeling realistic platelet particles 76
3.8 Validation 77
3.8.1 LBM-EBF Validation 77
3.8.2 Comparison to experiments 80
3.9 Flow visualization 81

4. FLOW SOLVER IMPLEMENTATION AND VALIDATION 84
4.1. LBM-EBF Validation 84
4.1.1 Ellipsoidal Orbit setup 85
4.1.2 Ellipsoidal Orbit Results 88
4.1.2.1 1-way Fluid-Solid Interaction 89
4.1.2.2 2-way Fluid-Solid Interaction 93
4.1.2.3 Subgrid modeling 98
4.1.2.4 Effect of aspect ratio and particle size on particle motion 100
4.1.2.5 Behavior at higher particle Reynolds number 102
4.1.2.6 Subgrid calculation of shear stresses 108
4.2 Parallelization of Numerical Method 111
4.2.1 Parallelization Validation 111
4.2.2 Parallel Scaling Efficiency 114

4.2.2.1 Entropic Lattice-Boltzmann 114

4.2.2.2 External Boundary Force 117

5. SINGLE-PHASE BMHV FLOW SIMULATIONS 121

5.1 Steady Flow Results in Comparison to Experimental Data 122

5.1.1 Re = 750 123

5.1.2 Re = 1250 125

5.1.3 Re = 2400 126

5.1.4 Re = 5000 128

5.1.5 Final comment on matching with steady flow 130

5.2. Mesh Independence 132

5.3 Pulsatile Flow Results in Comparison to Experimental Data 136

5.3.1 Quantitative Comparison 136

5.3.1.1 Final comments on quantitative matching with pulsatile flow 144

5.3.2 Qualitative Comparison for Instantaneous Flow 147

5.4 Pulsatile Flow Visualization 152

5.4.1 Accelerating to Peak Flow 161

5.4.2 Closing phase 166

5.4.3 Diastolic Phase 173

5.5 Turbulent Flow Features 186

5.6 Additional Pulsatile Flow Cases 195

5.6.1 Leaflet Motion Asymmetry - from experiments 196

5.6.2 Leaflet Dysfunction 199

5.6.3 Comments on asymmetric leaflet motion 207
5.7 Leaflet Motion by 2-way FSI.....208
5.7.1 Dynamic Leaflet Motion Results 209

6. BLOOD DAMAGE SIMULATIONS – PHYSIOLOGIC ADULT CASE 213
6.1 Adult conditions and numerical setup.....214
6.2 Systole to early diastole - bulk blood damage 216
6.2.1 Comparison of seeding methodologies 217
6.2.2 Overall platelet damage distribution 219
6.2.3 Bulk blood damage by region 221
6.2.4 Top damage levels 224
6.3 Eulerian tracking of blood damage 225
6.3.1 Eulerian viewpoint 225
6.3.2 Blood damage evolution - Eulerian view.....226
6.4 Lagrangian particle tracking of blood damage 234
6.4.1 Lagrangian viewpoint 235
6.4.2 Highlighted platelet damage paths.....235
6.4.2.1 Leaflet surface path.....236
6.4.2.2 Sinus expansion - near wall 239
6.4.2.3 Sinus expansion - strong recirculation.....245
6.4.2.4 Leaflet closing wake 252
6.5 Blood damage in diastolic flow 257
6.5.1 Diastolic flow setup 257

6.5.2 Platelet distribution and bulk damage values....259
6.5.3 Leakage jet BDI....261
6.6 Platelet rotation and BDI: 1-way and 2-way FSI....267
6.7 Analysis of blood damage in physiologic adult case....271
6.7.1 Comments on flow fields....272
6.7.2 Analysis of systolic flow....274
6.7.3 Analysis of diastolic flow....279
6.7.4 Final notes....281

7. BLOOD DAMAGE SIMULATIONS – PEDIATRIC CASES....282
7.1 Pediatric Case #1 – Child....283
7.1.1 Flow conditions and numerical setup....284
7.1.2 Flow physics....287
7.1.3 Bulk blood damage....289
7.1.4 Eulerian view....292
7.1.5 Lagrangian view....299
7.2 Pediatric Case #1 – Infant....305
7.2.1 Flow conditions and numerical setup....306
7.2.2 Flow physics....309
7.2.3 Bulk blood damage....313
7.2.4 Eulerian view....315
7.2.5 Lagrangian view....318
7.3 Analysis of pediatric valve flows....329

7.3.1 Comments on pediatric flow simulation setup....329
7.3.2 Flow fields....330
7.3.3 Bulk blood damage....337
7.3.4 Eulerian view....341
7.3.5 Lagrangian view....343
7.3.6 Thromboembolic potential....344

8. DISCUSSION....347
8.1 Numerical Methodology....347
8.1.1 Suspension flow solver....347
8.1.2 Parallelization....350
8.2 Single-phase BMHV flows....351
8.2.1 Higher resolution modeling and lattice-Boltzmann advantages....351
8.2.2 Turbulence in BMHV Flows....354
8.3 Blood damage - Physiologic adult conditions....357
8.3.1 Systolic flow....358
8.3.2 Diastolic flow....359
8.4 Pediatric flow cases....360
8.5 Limitations and Recommendations....362
8.5.1 Solid geometry....363
8.5.2 Boundary conditions....364
8.5.3 Leaflet motion....366
8.5.4 Spatiotemporal resolution....368

8.5.5 Blood modeling and suspended particles....369
8.5.6 Other notes....372
8.5.7 Flow analysis – future....373
8.5.8 Future applications....373

9. CONCLUSIONS....375
9.1 Numerical Method....377
9.2 Flow fields....378
9.3 Blood damage....380
9.4 Potential for future....384

APPENDIX A – NUMERICAL METHODS....385
A.1 Lattice-Boltzmann method....385
A.2 Entropic Lattice-Boltzmann....389
A.3 Standard Bounce-Back Method....391
A.4 External Boundary Force Method....393
A.5 Interpolated Bounce-Back Methods....398
A.6 Local Volume Definition....401
A.6.1 Mesh element area calculation....402
A.6.2 Various local volume calculation methods....403
A.6.3 Local volume calculation by conal volume method....405
A.7 Outflow boundary conditions....408
A.7.1 Stress-free outlet and prescribed flow inlet....408

A.7.2 Alternative outflow boundary conditions 411
A.7.2.1 Do Nothing Condition.....411
A.7.2.2 Zero Normal Shear Stress condition 412
A.8 Parallelization of Computational Methodology 413
A.8.1 Lattice-Boltzmann Parallelization.....414
A.8.2 External Boundary Force Parallelization 419
A.8.2.1 Fluid Flow Parallelization 419
A.8.2.2 Particle Force Parallelization 421
A.8.3 Boundary Condition parallelization 422
A.8.4 Leaflet motion parallelization 423
A.8.5 Other notes on parallelization 425

APPENDIX B – NUMERICAL METHODS AND ISSUES 427
B.1 Additional BMHV flow modeling notes 427
B.2 Failed local volume methods for EBF method.....428
B.3 Flow solver issues 431
B.3.1 Entropic Lattice-Boltzmann issues.....432
B.3.2 Additional artificial outflow conditions 434
B.3.3 Interpolated Bounce Back Conditions.....436
B.4 Problems with Dynamic Leaflet Motion 439
B.4.1 Numerical Instabilities 439
B.4.2 Pressure Wave Problems 442

APPENDIX C – ANIMATIONS 444

APPENDIX D – DATA GUIDE 455

REFERENCES.....457

LIST OF TABLES

4-1 List of Jeffery's orbit cases simulated in original methodology paper by Wu and Aidun and in this study 88

4-2 Flow field errors from serial vs. parallel processing 112

4-3 Solid dynamics errors for serial vs. parallel processing when using EBF method for fluid-solid interaction 113

6-1 Platelet and BDI distribution by region – physiologic adult 222

6-2 Platelet and BDI distribution by region and top damaged levels – physiologic adult 224

6-3 Platelet and BDI distribution for diastole 261

6-4 Distribution of platelets by method of leakage to ventricular side with BDI values 266

7-1 Flow conditions for 5-year old child with comparisons to adult conditions 284

7-2 Platelet and BDI distribution by region – 5-year old child 291

7-3 Flow conditions for 6-month old infant with comparisons to adult conditions 306

7-4 Platelet and BDI distribution by region – 6-month old infant 315

7-5 Average BDI values for all platelets, top 10%, and top 1% of damaged platelets for adult, child, and infant flow simulations 340

A-1 List of lattice velocity vectors for 3D, 19-vector Cartesian set 386

A-2 List of weighting coefficients for LBM velocity sets 388

A-3 Comparison of ellipsoid theoretical vs. simulated volumes 407

A-4 Single-phase flow scaling efficiency for 1024^3 LBM domain in shear flow 417

A-5 Multi-phase flow scaling efficiency for 512^3 LBM domain with 13,824 deformable particles in shear flow 418

LIST OF FIGURES

1-1 Diagram of the human heart showing four heart chambers, four heart valves, and connecting arteries and veins 1

1-2 Porcine aortic valve with three leaflets in closed position 2

1-3 Diagram of normal human aortic valve in open and closed positions 3

1-4 Caged-ball (left) and tilting-disk (right) mechanical valves 6

1-5 Bileaflet Mechanical Heart Valve – St. Jude Medical 23mm Regents valve 7

1-6 BMHV schematic for forward flow (perpendicular cross-sectional view) 8

1-7 BMHV schematic for reverse flow (perpendicular cross-sectional view) 9

1-8 CarboMedics (left) and St. Jude Medical (right) 23mm Bileaflet Mechanical Heart Valves 10

1-9 Semicircular leaflet ear fitting into valve housing hinge recess. Gap between leaflet ear and housing referred to as "hinge gap" 11

1-10 Front and side views of SJM and CM hinge regions with leaflet sweep 11

1-11 SJM (top) and CM (bottom) hinge geometries. This view shows closed leaflet position and valves implanted in aortic position 12

1-12 Side view of the SJM and CM valves 12

1-13 Visible clots forming in hinge regions of St. Jude Medical BMHV 15

1-14 Flowchart demonstrating history of CFD studies of blood damage in BMHV flows, including the current study 28

2-1 Flowchart showing major coding steps required to complete Specific Aim 1 39

2-2 Flowchart showing research study progress in specific aims 1 – 4 41

3-1 Numerical method overview for two-way fluid-structure interaction 43

3-2 Example of red blood cell and platelet particles with surface mesh of

triangular elements 49

3-3 *In vitro* experimental PIV setup 52

3-4 Experimental PIV setup showing perpendicular plane where 2D flow fields are determined 53

3-5 Cardiac cycle variation of flowrate (black line), leaflet motion (--•--), aortic pressure (blue dots), and ventricular pressure (red dashed lines) 54

3-6 Cross-sectional view of the $1/6^{th}$ partial cut of the flow chamber (left) and the leaflet geometry (right) used in previous numerical BMHV hinge studies 55

3-7 Cross-sectional view of the full flow chamber (left) and leaflet geometries within the flow chamber (right) created by extension of the partial geometries 56

3-8 Computational recreation of *in vitro* experimental setup. Ventricular side (left) labeled as "inlet", aortic side (right) labeled as "outlet" for systolic flow convention 57

3-9 Transparent viewpoints of SJM valve with fully open leaflets, (top) perpendicular view, (bottom) angled view 58

3-10 Interior view of the fully open leaflets residing in the SJM valve, showing the leaflets fitting into the butterfly hinge recess 59

3-11 Meshed surface of a platelet, 148 nodes and 292 elements 63

3-12 Conversion of Cartesian forces to normal and shear forces on solid surface element 65

3-13 Flowrate and leaflet angle variation for one cardiac cycle taken from experimental data. Zero degrees for leaflet angle is parallel to the axial direction. 69

3-14 Rotational motion of closing leaflets about hinge fulcrum 71

3-15 Example of force on leaflet surfaces causing rotational moments about the hinges 73

3-16 Jeffery's orbit for rotation of a rigid ellipsoid in simple shear flow 78

4-1 Rigid ellipsoid in simple shear flow 85

4-2 Jeffery's orbit for ellipsoid 12x9x9 radius, Re_p = 0.064, G=1/6000, τ = 5. 1-way interaction....89

4-3 Jeffery's orbit for ellipsoid 12x6x6 radius, Re_p = 0.064, G=1/6000, τ = 5. 1-way interaction....90

4-4 Jeffery's orbit for ellipsoid 12x3x3 radius, Re_p = 0.064, G=1/6000, τ = 5. 1-way interaction....91

4-5 Jeffery's orbit for platelet 7x7x3.1 radius, Re_p = 0.0218, G=1/6000, τ = 5. 1-way interaction....92

4-6 Jeffery's orbit for 2-way FSI, 12x9x9 radius, Re_p = 0.064, G=1/6000, τ = 5....95

4-7 Jeffery's orbit for 2-way FSI, sphere radius 10, Re_p = 0.044, G=1/6000, τ = 5....96

4-8 Jeffery's orbit for platelet 7x7x3.1 radius, 2-way FSI, Re_p = 0.0218, G=1/6000, τ = 5....97

4-9 Jeffery's orbit for platelet 0.07x0.07x0.031 radius, 1-way FSI, Re_p = 0.0218, G=1/6000, τ = 5....99

4-10 Effect of aspect ratio on orbital drift from theory for 1-way and 2-way FSI....101

4-11 Effect of particle size on orbital drift from theory for 2-way FSI modeling. Maximum diameter given as major axis diameter in LB units....101

4-12 Nondimensional period of rotation, GT, for increasing particle Reynolds number. Results shown for a 120x120x120 domain, particle aspect ratio of 4, with shear rates G=1/1200 and G=1/600....104

4-13 Nondimensional period of rotation, GT, for increasing particle Reynolds number. Results shown for (left) G=1/1200 and (right) G=1/600 close to the critical Reynolds number....105

4-14 Nondimensional period of rotation, GT, for increasing particle Reynolds number with aspect ratio 4, G=1/600. Results show a comparison of two different LBM-EBF codes....106

4-15 Nondimensional period of rotation, GT, for increasing particle Reynolds number with ellipsoidal particle of aspect ratio 5, G=1/600 and G = 1/1200....107

4-16 Nondimensional period of rotation, GT, for increasing particle Reynolds number for ellipsoidal particles with aspect ratio 4 and 5, at shear rates of G=1/600 and G=1/1200.....108

4-17 Maximum instantaneous particle shear stress (normalized by ambient fluid shear stress μG) variation with respect to angular orientation for isolated platelet-shape ellipsoid in simple shear flow, with decreasing particle diameter *d* from supergrid to subgrid resolution.....109

4-18 Standard BGK vs. Entropic LB for 128 – 4096 cores, performance demonstrated by number of lattice-Boltzmann timesteps per second.....115

4-19 Scaling performance for Standard BGK vs. Entropic LB for 128 – 4096 cores. 116

4-20 Standard Bounce Back vs. External Boundary Force parallelization for 128 - 4096 cores, performance demonstrated as number of lattice-Boltzmann timesteps per second. Multiphase EBF simulation includes 500 platelets suspended in flow field 118

4-21 Scaling performance for Standard Bounce Back vs. External Boundary Force Method for 128 - 4096 cores. Multiphase EBF simulation includes 500 platelets suspended in flow field 119

5-1 Experimental setup showing perpendicular data plane.....122

5-2 Perpendicular lines of comparison for Re = 750.....123

5-3 Axial velocity comparison for Re = 750 at (a) 2.2mm, (b) 10.3mm, (c) 20.1mm, (d) 30.9mm, (e) 40.7mm, (f) 50.6mm downstream of leaflet tips 123

5-4 Axial velocity comparison for Re = 1250 at (a) 2.2mm, (b) 6.7mm, (c) 10.2mm, (d) 20.1mm downstream of leaflet tips 125

5-5 Axial velocity comparison for Re = 2400 at (a) 3.1mm, (b) 5.8mm, (c) 10.3mm, (d) 20.0mm downstream of leaflet tips 127

5-6 Axial velocity comparison for Re = 5000 at (a) 4.0mm, (b) 8.4mm, (c) 10.3mm, (d) 20.1mm downstream of leaflet tips 129

5-7 Comparison of mean flow axial velocity values at peak flow (Re = 5779) between simulations at 80μm and 160μm spatial resolution taken (a) 5.0mm, (b) 10.1mm, and (c) 20.0mm past the leaflet trailing edges.....133

5-8 Comparison of root-mean-square velocity values at peak flow (Re =5779)

between simulations at 80μm and 160μm spatial resolution taken (a) 5.0mm, (b) 10.1mm, and (c) 20.0mm past the leaflet trailing edges 134

5-9 Mean axial velocity computed for 50, 100, and 200 computational ensembles 5.0mm downstream of leaflet tips 137

5-10 Comparison of mean axial flow (left) and root-mean-square (right) velocity values at accelerating flow (Re = 4700) for simulations against experiments for pulsatile flow taken (a) 5.0mm, (b) 10.1mm, and (c) 20.0mm past the leaflet trailing edges 138

5-11 Comparison of mean axial flow (left) and root-mean-square (right) velocity values at peak flow (Re = 5780) for simulations against experiments for pulsatile flow taken (a) 5.0mm, (b) 10.1mm, and (c) 20.0mm past the leaflet trailing edges 139

5-12 Comparison of mean axial flow (left) and root-mean-square (right) velocity values at deceleration flow (Re ~ 1000) for simulations against experiments for pulsatile flow taken (a) 5.0mm, (b) 10.1mm, and (c) 20.0mm past the leaflet trailing edges 141

5-13 Comparison of mean axial velocity values at peak flow (Re = 5780) for simulations at two different cardiac cycles taken (a) 5.0mm, (b) 10.0mm, and (c) 20.0mm, (d) 30.0mm, (e) 50.0mm, (f) 70.0mm past the leaflet trailing edges.....143

5-14 Comparison at leaflet opening phase (Re = 240) between simulations (left) and experiments (right) 148

5-15 Comparison at mid-acceleration phase (Re = 2070) between simulations (left) and experiments (right) 148

5-16 Comparison at peak flow phase (Re = 5779) between simulations (left) and experiments (right).....149

5-17 Comparison at deceleration flow phase (Re = 3600) between simulations (left) and experiments (right) 150

5-18 Comparison at leaflet closing phase (Re = 580 in reverse flow) between simulations (left) and experiments (right).....151

5-19 Transparent view of BMHV and flow chamber showing approximate 3D angled view used in q-criterion visualization of 3D coherent vortical structures 153

5-20 (a) 2D vorticity, (b) 3D q-criterion, and (c) viscous fluid shear stress

(dynes/cm^2) plots of leaflet opening phase (Re = 240) 153

5-21 (a) 2D vorticity, (b) 3D q-criterion, and (c) viscous fluid shear stress (dynes/cm^2) plots of mid-acceleration phase (Re = 2070)* 155

5-22 (a) 2D vorticity, (b) 3D q-criterion, and (c) viscous fluid shear stress (dynes/cm^2) plots of peak flow phase (Re = 5779) 156

5-23 (a) 2D vorticity, (b) 3D q-criterion, and (c) viscous fluid shear stress (dynes/cm^2) plots of closing phase (Re = 580 in reverse flow) 158

5-24 (a) 2D vorticity, (b) 3D q-criterion, and (c) viscous fluid shear stress (dynes/cm^2) plots of mid-diastolic leakage phase (Re = 175 in reverse flow) 159

5-25 (a) High accelerating flow with coherent vortical structures in flow past leaflet tips, with (b) mixing of leaflet vortex wakes and sinus recirculation region.....162

5-26 Peak flow with (a) coherent vortical structures breaking into (b) small-scale eddies.....163

5-27 (a) Small-scale eddies in sinus expansion, (b) interacting with sinus expansion recirculation 164

5-28 Comparison of viscous fluid shear stresses at perpendicular lines downstream of the leaflet tips for accelerating and peak flow.....165

5-29 Vorticity and shear stress field (dynes/cm^2) plots at beginning of closing phase with sudden leaflet motion and initial closing wakes 167

5-30 Vorticity and shear stress field (dynes/cm^2) plots at rapid leaflet closing phase with strong leaflet closing vortex wakes.....168

5-31 Vorticity plots demonstrating (a) leaflet closing impact with valve housing, (b) development and (c) growth of triple leakage jets, and (d) coherent b-datum jet.....169

5-32 Shear stress (dynes/cm^2) plot at leaflet closing with identical time point as figure 5-31d.....171

5-33 Fluid shear stresses (dynes/cm^2) at various leakage jets upon leaflet closing impact 172

5-34 Vorticity contours of mid-diastolic leakage flows directed both (a) centrally upstream and (b) leaning to bottom ventricular half, with (c) representative

mid-diastolic flow time point. 173

5-35 Early-diastolic leakage flows leaning both (a) slightly downwards and (b) slightly upwards, with impending interaction with large vortical structures 175

5-36 Interaction of b-datum jet with leaflet-valve jets causing asymmetry in jet direction. Vorticity magnitude scaling identical in all plots 176

5-37 Asymmetric drift of central b-datum jet in diastolic phase. Vorticity magnitude scaling identical for all plots 178

5-38 Axial velocity at leakage gaps for reverse diastolic flow phase 180

5-39 LDV experimental data of leakage velocities for diastolic flow phase for 27mm SJM valve in aortic position....182

5-40 Fluid shear stresses at leakage gaps for reverse diastolic flow phase 185

5-41 Turbulent kinetic energy rate of dissipation contour plots for 2D perpendicular plane at peak flow using (a) TKE equation, ε, and (b) local isotropy, ε_{iso}, methods 187

5-42 Turbulent kinetic energy rate of dissipation line plots at peak flow, calculated from TKE equation (ε) and local isotropy approximation (ε_{iso})...189

5-43 Instantaneous turbulent energy dissipation rate, ε_{inst}, at peak flow....191

5-44 Contour plot of Kolmogorov spatial scales (η) based on mean dissipation rates, with contour scaling capped at 80μm 192

5-45 1D Energy spectra vs. normalized wavenumber at peak flow 193

5-46 1D Compensated energy spectra vs. normalized wavenumber at peak flow 194

5-47 Vorticity plots with asymmetric leaflet motion comparison showing (a) normal leaflet opening vs. (b) slower opening top leaflet....197

5-48 Vorticity plots of closing phase leaflet motion asymmetry with a faster closing top leaflet 198

5-49 Faster closing top leaflet leading to b-datum leakage vortex that drifts towards the top leaflet 199

5-50 Half-opening bottom leaflet with leading edge vortex shedding 200

5-51 Half-open bottom leaflet in mid-acceleration phase with sharp leading edge causing vortex spilling. 201

5-52 Half-open bottom leaflet in peak flow phase with strong asymmetric vortex shedding caused by sharper leading edge on bottom leaflet 202

5-53 Half-open bottom leaflet in closing phase with stronger vortex wake for closing top leaflet, and delayed vortex washout in sinus region 203

5-54 Fixed closed bottom leaflet with vortex roll from sharper leading edge in early acceleration/opening phase 204

5-55 Fixed closed bottom leaflet in peak flow phase with strong vortex shedding on top half of flow domain 205

5-56 Fixed closed bottom leaflet in closing phase with delayed vortex washout 206

5-57 2D vorticity plot showing leaflet opening from two-way FSI modeling 209

5-58 2D vorticity plot showing leaflet closing from two-way FSI modeling 210

5-59 Comparison of leaflet angle variation for two-way FSI numerical modeling vs. PIV experimental data 211

6-1 300 platelets seeded randomly upstream of BMHV. (a) Side view showing platelets with same axial position, (b) cross-sectional view showing platelets with randomized cross-sectional position 215

6-2 BDI histogram for 4200 platelets after 260ms of systolic flow: (a) positions and angles randomized for every seed, (b) same positions and angles for every seed. Interval: 0.05 dynes•s/cm^2.....217

6-3 BDI histogram for 4200 platelets after 260ms of systolic flow: (a) positions and angles randomized for every seed, (b) same positions and angles for every seed. Interval: 0.025 dynes•s/cm^2.....218

6-4 BDI histogram for 5400 platelets after 460ms of damage accumulation representing full systole and onset of diastole. Interval: 0.05 dynes•s/cm^2 220

6-5 (a) 300 platelets initially seeded upstream of valve; (b) 5400 platelets distributed throughout domain at end of simulation. 221

6-6 Domain split into regions: (1) ventricular side, (2) valve, (3) sinus expansion,

(4) aortic side.....221

6-7 Vorticity plot at peak flow showing strong vortex shedding within sinus region, from flow past leaflets and sinus expansion step.....223

6-8 (a) BDI contour plot, (b) corresponding fluid vorticity plot, and (c) flowrate curve at start of systole (Re ~ 0), 300 platelets.....226

6-9 (a) BDI contour plot, (b) corresponding fluid vorticity plot, and (c) flowrate curve at high acceleration (Re = 5000), 3000 platelets.....227

6-10 (a) BDI contour plot, (b) corresponding fluid vorticity plot, and (c) flowrate curve at peak flow (Re = 5780), 3300 platelets 229

6-11 (a) BDI contour plot, (b) corresponding fluid vorticity plot, and (c) flowrate curve at leaflet closing flow (Re = 650), 5400 platelets 230

6-12 BDI contour plot at leaflet closing flow (Re = 650), 5400 platelets. Contours blanked if damage less than (a) 0.5 dynes•s/cm^2 (b) 0.6 dynes•s/cm^2 231

6-13 (a) BDI contour plot, (b) corresponding fluid vorticity plot, and (c) flowrate curve at early-to-mid diastolic flow (Re = 75 in reverse flow), 5400 released platelets 232

6-14 BDI contour plot at early-to-mid diastolic flow (Re = 75 in reverse flow), 5400 platelets. Contours blanked if damage less than 0.5 dynes•s/cm^2.....233

6-15 (a) Angled view, (b) cross-sectional view, (c) zoomed view of platelet trail, demonstrating high shear stress damage while traversing near bottom leaflet surface 236

6-16 Platelet trail demonstrating high shear stress values while (a) traversing near leaflet surface, (b) corresponding vorticity field, (c) shear stress field.....237

6-17 Platelet damage accumulation versus time for platelet traveling near leaflet surface 239

6-18 Platelet trail close to the sinus expansion wall with high levels of shear stress damage (a) 3D angled view, (b) cross-sectional viewpoint 240

6-19 Platelet trail close to the sinus expansion wall with high levels of shear stress damage (a) perpendicular view, (b) corresponding vorticity field, (c) shear stress field.....241

6-20 Platelet trail in sinus recirculation after additional 100ms with high levels of

shear stress damage (a) 3D view, (b) cross-sectional viewpoint 242

6-21 Platelet trail in sinus recirculation after additional 100ms with high levels of shear stress damage (a) perpendicular view, (b) corresponding vorticity field, (c) shear stress field 243

6-22 Platelet damage accumulation versus time for platelet near sinus expansion wall 244

6-23 Platelet caught in recirculation near sinus expansion (a) 3D angled view, (b) cross-sectional view 245

6-24 Platelet caught in recirculation near sinus expansion (a) perpendicular view, (b) corresponding vorticity field, (c) shear stress field 246

6-25 Platelet in sinus recirculation after additional 90ms with (a) 3D angled view, (b) cross-sectional view, (c) perpendicular view, and corresponding (d) 2D vorticity and (e) shear stress fields 248

6-26 Platelet in sinus recirculation at start of diastole with (a) 3D angled view, (b) cross-sectional view, (c) perpendicular view, and corresponding (d) 2D vorticity and (e) shear stress fields 250

6-27 Platelet damage accumulation versus time for platelet recirculating in sinus expansion 252

6-28 (a) Platelet on aortic side of leaflet during start of leaflet closing motion (b) corresponding vorticity field, (c) shear stress field 252

6-29 (a) Platelet squeezing through valve housing gap during leaflet closing motion (b) corresponding vorticity field, (c) shear stress field 254

6-30 (a) Platelet on ventricular side of leaflet after leaflet closure (b) corresponding vorticity field, (c) shear stress field 255

6-31 Platelet damage accumulation versus time for platelet caught in leaflet closing wake 256

6-32 BMHV flow domain split into four subcategories: (1) Ventricular chamber, (2) Ventricular side within valve, (3) Aortic side within valve, (4) Aortic sinus expansion 259

6-33 2000 platelets seeded on aortic edge of the SJM valve 259

6-34 2000 platelets at end diastole after 320ms of simulation 260

6-35 Cluster of platelets leaking through b-datum gap (a) approaching b-datum line, (b) flowing through gap 2ms later....262

6-36 (a) Cluster of platelets leaking through b-datum gap, (b) corresponding vorticity flow field, (c) shear stress field....263

6-37 Platelet leaking through valve housing gap (a) approaching leaflet, (b) flowing through gap 2ms later, (c) on ventricular side after leakage....264

6-38 Variation of rotation angle and change in BDI over time for low damaged platelet for 1-way and 2-way FSI....268

6-39 Variation of rotation angle and change in BDI over time for higher damaged platelet for 1-way and 2-way FSI....270

6-40 Near peak flow (Re = 5500) showing (a) disorganized vortex shedding past leaflet tips that incur mild damage, (b) corresponding shear stress field, (c) mixing between vortex shedding regions that incur high damage, (d) corresponding shear stress field....272

6-41 2D vorticity flow fields showing high damage regions for (a) near leaflet flow, (b) sinus wall flow....276

7-1 Flowrate and leaflet variation for one cardiac cycle for a 5-year old child case....285

7-2 (a) 300 platelets seeded 1.25 diameter upstream of valve at start of simulations, (b) 5400 platelets at end of simulation of 360ms....286

7-3 2D vorticity magnitude plots of peak flow for (a) adult flow, (b) child flow....288

7-4 Viscous shear stress fields at peak flow for (a) adult flows, (b) child flows....289

7-5 BDI histogram for 5400 platelets after (a) 360ms of damage accumulation for 5-year old child, (b) 460ms of damage accumulation for adult. Interval 0.05 dynes•s/cm^2, with BDI values over 1.0 dynes•s/cm^2 not shown....290

7-6 (a) BDI contour plot, (b) corresponding 2D vorticity plot, and (c) flowrate curve at peak flow (Re = 4418), 3300 platelets....293

7-7 BDI contour plot at peak flow (Re = 4418), 3300 platelets. Contours blanked if damage less than 0.5 dynes•s/cm^2....294

7-8 (a) BDI contour plot, (b) corresponding fluid vorticity plot, and (c) flowrate

curve at leaflet closing flow (Re = 0), 5400 platelets 295

7-9 BDI contour plot at leaflet closing flow (Re = 0), 5400 platelets. Contours blanked if damage less than (a) 0.5 dynes•s/cm^2 (b) 1.0 dynes•s/cm^2 296

7-10 (a) BDI contour plot, (b) corresponding fluid vorticity plot, and (c) flowrate curve at early-to-mid diastolic flow (Re = 75 in reverse flow), 5400 released platelets.....297

7-11 BDI contour plot at end simulation time point (Re = 75 in reverse flow), 5400 platelets. Contours blanked if damage less than (a) 0.5 dynes•s/cm^2 (b) 1.0 dynes•s/cm^2 299

7-12 Platelet trail close to the valve housing wall with high levels of damage (a) 3D angled view, (b) perpendicular viewpoint, (c) corresponding vorticity field, (d) shear stress field (dynes/cm^2).....300

7-13 Platelet trail with high levels of damage while sweeping through sinus region (a) 3D angled view, (b) perpendicular viewpoint, (c) corresponding vorticity field, (d) shear stress field (dynes/cm^2).....302

7-14 Platelet trail with high levels of damage while traveling along aortic downstream wall (a) perpendicular viewpoint, (b) corresponding vorticity field, (c) shear stress field (dynes/cm^2) 304

7-15 Platelet damage accumulation versus time for most damaged platelet for 5-year old child flow case.....305

7-16 Flowrate and leaflet variation for one cardiac cycle for a 6-month old infant.....307

7-17 (a) 300 platelets seeded 1.25 diameters upstream of valve at start of simulations, (b) 3997 remaining platelets at end of simulation of 317ms 308

7-18 2D vorticity magnitude plots of peak flow for (a) adult flow, (b) infant flow 309

7-19 Viscous shear stress fields at peak flow for (a) adult flows, (b) infant flows.....310

7-20 2D vorticity magnitude plots of leaflet closing flow for (a) adult flow, (b) infant flow 311

7-21 Viscous shear stress fields at leaflet closing for (a) adult, (b) infant flows.....313

7-22 BDI histogram for 5400 platelets after (a) 317ms of damage accumulation for 6-month old infant, (b) 460ms of damage accumulation for adult. Interval 0.05 dynes•s/cm^2 314

7-23 (a) BDI contour plot, (b) regions blanked if damage less than 0.5 dynes•s/cm^2, (c) corresponding fluid vorticity plot, and (d) flowrate curve at early-to-mid diastolic flow (Re = 115 in reverse flow), 5400 released platelets 316

7-24 Platelet trail near ventricular wall with high levels of damage (a) 3D view, (b) perpendicular view, (c) cross-sectional view 318

7-25 Platelet trail near valve housing wall with high levels of damage (a) 3D view, (b) perpendicular view, (c) cross-sectional view, (d) corresponding vorticity field, (e) corresponding shear stress field (dynes•s/cm^2) 320

7-26 Platelet trail immediately before impact with closing leaflets (a) perpendicular view, (b) cross-sectional view, (c) corresponding vorticity field, (d) shear stress field.....322

7-27 Platelet trail immediately after impact with closing leaflets (a) perpendicular view, (b) cross-sectional view, (c) corresponding vorticity field, (d) shear stress field.....323

7-28 Platelet trail from motion with leaflet-valve closing leakage jet (a) perpendicular view, (b) cross-sectional view, (c) corresponding vorticity field, (d) shear stress field 325

7-29 Platelet trail near b-datum leakage jet (a) perpendicular view, (b) cross-sectional view, (c) corresponding vorticity field, (d) shear stress field 327

7-30 Platelet damage accumulation versus time for most damaged platelet for 6-month old infant flow case 329

7-31 Peak flow vorticity visualizations for (a) adult – Re = 5780, (b) child – Re = 4418, (c) infant – Re = 2725. 332

7-32 Peak flow shear stress visualizations for (a) adult – Re = 5780, (b) child – Re = 4418, (c) infant – Re = 2725.....334

7-33 BDI distribution for (a) adult, (b) child, (c) infant cases at simulation end time point with interval spacing 0.5 dynes•s/cm^2, with BDI values over 1.0 dynes•s/cm^2 not shown.....338

7-34 BDI contour plot at end simulation time point, 5400 platelets. Contours blanked if damage less than 0.5 dynes•s/cm^2 for (a) adult, (b) child, (c) infant cases 342

8-1 Platelet model with shear stress variation across meshed surface 349

8-2 2D vorticity - pulsatile flow visualization of (a) mid-acceleration and (b) peak flow. 351

8-3 BDI contour plot at early-to-mid diastolic flow (Re = 75 in reverse flow) for angled and cross-sectional viewpoints, 5400 platelets. Contours blanked if damage less than 0.5 dynes•s/cm^2. Cross-sectional slice taken within sinus expansion.....358

A-1 Three-dimensional, 19 lattice velocity diagram for a LBM fluid grid.....385

A-2 General overview of streaming and collision processes 387

A-3 Standard bounce-back (SBB) fluid-solid interaction boundary 393

A-4 Fluid-solid coupling at solid boundary, SBB vs. EBF method 395

A-5 Interpolated bounce-back conditions for determining wall position.....400

A-6 (a) triangular element with 3 nodal points P1, P2, P3, and two vectors **V1**, **V2** formed from nodal points. (b) Mirrored element with equal area. (c) Parallelogram formed by two vectors 402

A-7 Difference in local volumes for a mesh element for: shell particle (left) vs. completely solid particle (right) 404

A-8 Conal local volume method. Determine height value in local volume calculation by dot product of node-to-center distance and the normal vector to surface element.....406

A-9 Flowchart of methodology for imposing prescribed flow inlet, stress-free outlet boundary conditions 408

A-10 Implementation of stress-free outlet boundary condition for lattice-Boltzmann methods.....409

A-11 Implementation of prescribed inlet flow boundary condition for lattice-Boltzmann methods.....410

A-12 Balancing mass of system after imposing prescribed flow inlet, stress-free outlet boundary conditions for lattice-Boltzmann methods 410

A-13 Flowchart demonstrating LBM parallel computing for each timestep 415

A-14 (a) Ghost node fluid data communication across subdomain borders, and (b) Particle data communication to multiple subdomains 416

A-15 Sending of fluid nodal data at fluid subdomain (black squares) to function as double ghost node layer (yellow squares) at neighboring fluid subdomain 420

A-16 Example of two cases of solid nodes (circles with X) lying near fluid subdomain boundaries. Red circles show the radius of influence of the solid node, and the blue shaded areas show the affected area of the current fluid subdomain 421

A-17 Leaflet surface split among multiple subdomains. In this case, the dashed lines mark subdomain boundaries. Leaflets span four subdomains in this 2D view 424

B-1 Pressure wave formation caused by leaflet closing impact with valve housing 427

B-2 Solid domain (gray) imposed within 3D box fluid domain 428

B-3 Jeffery's orbit for sphere radius 10, $Re_p = 0.044$, G=1/6000. Local volume method of equivalent volumes for all mesh elements 429

B-4 Jeffery's orbit for ellipsoid 12x9x9 radius, $Re_p = 0.064$, G=1/6000. Local volume method of equivalent volumes for all mesh elements 430

B-5 Jeffery's orbit for ellipsoid 12x9x9 radius, $Re_p = 0.064$, G=1/6000. Local volume method of proportional volumes based on mesh element area proportion 431

B-6 Poiseuille flow velocity comparison with stress-free (SPP) and zero normal shear stress (ZNS) outlet conditions vs. theoretical Poiseuille flow profile 435

B-7 Poiseuille flow velocity comparison with standard bounce-back and linear interpolated bounce back conditions vs. theoretical values, pipe radius 12 LB units 437

B-8 Poiseuille flow velocity comparison with standard bounce-back and linear interpolated bounce back conditions vs. theoretical values, pipe radius 26 LB units 438

B-9 Shockwaves in flow caused by leaflet "fluttering" from two-way FSI instabilities 440

B-10 Instability in flow field caused by overly rapid leaflet motion in one direction.....441

LIST OF ANIMATIONS

5-1 Out-of-plane vorticity magnitude animation for physiological adult flow, spanning two cardiac cycles and starting from peak flow (5_1_vorticity_adult.avi, 10.8MB) 444

5-2 Viscous fluid shear stress magnitude animation for physiological adult flow, for one cardiac cycle and starting from late diastole (5_2_shearStress_adult.avi, 6.8MB) 445

5-3 Isosurfaces of coherent 3D vortical structures based on the q-criterion for physiological adult flow, for one cardiac cycle and starting from leaflet opening (5_3_q_criterion.avi, 38MB).....446

6-1 Platelet seeding and release of 5400 total platelets, with 300 platelets released 1 diameter upstream of the valve every 20ms during systole (6_1_seeding.avi, 2.4MB).....447

6-2 Eulerian view of blood damage evolution for physiological adult case (6_2_eulerian.avi, 2.6MB) 448

6-3 Lagrangian particle tracking view of highly damaged platelet undergoing near sinus expansion wall recirculation path (6_3_lagrangian.avi, 1.1MB) 449

6-4 Release of 2000 suspended platelets on aortic edge of BMHV for mid-diastole showing platelet leakage (6_4_diastole.avi, 1.9MB).....450

7-1 Out-of-plane vorticity magnitude animation for 5-year old child flow, for one cardiac cycle and starting from late diastole (7_1_vorticity_child.avi, 4.3MB).....451

7-2 Viscous fluid shear stress magnitude animation for 5-year old child flow, for one cardiac cycle and starting from late diastole (7_2_shearStress_child.avi, 6.9MB) 452

7-3 Out-of-plane vorticity magnitude animation for 6-month old infant flow, for one cardiac cycle and starting from late diastole (7_3_vorticity_infant.avi, 2.2MB) 453

7-4 Viscous fluid shear stress magnitude animation for 6-month old infant flow, for one cardiac cycle and starting from late diastole (7_4_shearStress_infant.avi, 5MB).....454

LIST OF SYMBOLS OR ABBREVIATIONS

ATS	Advancing The Standards
AV	Aortic Valve
BDI	Blood Damage Index
BMHV	Bileaflet mechanical heart valve
CFD	Computational fluid dynamics
CM	CarboMedics
DNT	Do Nothing Condition
EBF	External Boundary Force
ELB	Entropic Lattice-Boltzmann
FDA	Food and Drug Administration
FSI	Fluid-structure/solid interaction
LBM	Lattice-Boltzmann method
microCT	micro-computed tomography
MP	Medtronic Parallel
MPI	Message Passing Interface
OpenMP	Open Multi-Processing
PF4	Platelet factor 4
PHV	Prosthetic heart valve
PIV	Particle image velocimetry
RBC	Red blood cell
SBB	Standard bounce-back

SJM	St. Jude Medical
TAT	Thrombin-Antithrombin III
WBC	White blood cell
ZNS	Zero Normal Shear Stress Condition
a	Particle radius
$\boldsymbol{a}$	particle linear acceleration
c_s	Lattice-Boltzmann pseudo sound speed
cSt	centi-stokes (1/1000,000 m^2/s)
d	particle diameter
D	Pipe diameter
$D(\boldsymbol{x})$	Dirac delta function
$\mathbf{e_i}$	Lattice-Boltzmann discrete velocity vectors
$\boldsymbol{F}$	Force
$\boldsymbol{F}^{(b)}$	Bounce-back fluid-solid interaction force
$\boldsymbol{F}^{fsi}$	Fluid-solid interaction force (External Boundary Force method)
f_i	Fluid particle distribution function (lattice-Boltzmann)
$f^{(0)}$	Fluid particle equilibrium distribution function (lattice-Boltzmann)
$\mathbf{g}(\boldsymbol{x},t)$	solid-to-fluid interaction force (lattice-Boltzmann)
G	Shear rate (1/s)
H	Height (wall distance)
$\boldsymbol{I}$	Moment of inertia
L	Length (m)
m	Mass

p	Pressure (mm Hg) (dynes/cm^2 = 0.1 N/m^2)
q	q-criterion
Q	Volume flowrate
r	particle radius
$\mathbf{r}$	3D fluid position
$\vec{\boldsymbol{r}}$	radial arm
R	pipe radius
Re	Bulk flow Reynolds number
$\mathrm{Re_p}$	Particle Reynolds number
$\boldsymbol{s_{ij}}$	rate-of-strain tensor of turbulent velocity field
t	Time (s)
Δt	change in timestep
T	Period of ellipsoidal rotation
$\boldsymbol{T}$	Torque
u	Axial velocity
$\boldsymbol{u_b}$	Boundary velocity
$\mathrm{u_{rms}}$	root-mean-square axial velocity (m/s)
U_{avg}	Average inlet axial velocity (m/s)
$\boldsymbol{U_f}$	Fluid velocity on solid surface (External Boundary Force method)
$\boldsymbol{U_p}$	Solid surface element velocity (External Boundary Force method)
U_w	Wall velocity
w_i	Lattice-Boltzmann weighting coefficients
Wn	Womersley number

x	Axial location of fluid field
$\boldsymbol{x}$	Position vector of particle surface element
$\mathbf{x}^{e}$	Fluid node position vector (External Boundary Force Method)
α	Angular acceleration
ε	rate of dissipation (turbulent energy)
ε_{inst}	instantaneous rate of dissipation (turbulent energy)
ε_{iso}	rate of dissipation with local isotropy approximation (turbulent energy)
η	Kolmogorov length scale
κ	wavenumber
ν	Kinematic viscosity
ρ	Density
ρ_f	Fluid density on solid surface (External Boundary Force method)
τ	Relaxation parameter (lattice-Boltzmann)
τ_{max}	Maximum instantaneous surface shear stress
$\tau_{shear\ stress}$	Fluid viscous shear stress
ϕ	Orientation angle (Jeffery's orbit)
ω	Angular frequency of pulsatile flow

SUMMARY

Native heart valves serve an important function in maintaining unidirectional flow of blood through the heart. Defective or diseased native valves have been replaced by prosthetic heart valves for several decades with improved performance and patient conditions. However, severe complications such as hemolysis and unwanted thrombosis still exist due to the presence of the prostheses. A popular example of a prosthetic device is the bileaflet mechanical heart valve (BMHV). Modern BMHV designs have undergone significant evolution and are frequently chosen due to good hemodynamics performance as well as long durability. However, blood element trauma and thromboembolic events still remain, leading to lifelong dependence on anticoagulants. These problems have been linked to blood damage caused by non-physiological stresses due to complex flow fields that arise due to unnatural prosthetic valve design. In order to reduce the severity of complications, the blood damage that occurs in prosthetic heart valve flows must be well understood.

Most computational methods attempting to quantify blood element damage have limitations in only being able to simulate single-phase fluid flow. Platelets are often assumed to be massless point particles and blood element damage is evaluated from fluid laminar and turbulent stresses. Computational research has not yet been performed for cardiovascular flows with the presence of realistically modeled platelets in order to quantify blood damage. An accurate multiphase flow solver can be used to quantify blood damage and platelet activation by modeling suspended platelets with meshed surfaces for tracking instantaneous surface shear stresses.

The aim of this research is to numerically study platelet damage that occurs in flow through bileaflet mechanical heart valves during the cardiac cycle. The numerical suspension flow simulations use a fluid-solid coupling method that combines lattice-Boltzmann fluid modeling with the novel external boundary force method. The lattice-Boltzmann method (LBM) has been shown to converge to solve the Navier-Stokes equations for fluid flow and extensive literature has been published detailing its accuracy. In addition to being accurate, the LBM employs locally centered calculations, making it optimal for parallel computing. This is especially useful in modeling flows through artificial heart valves, which is computationally expensive due to required high spatiotemporal resolution. The fluid-solid coupling employs the novel external boundary force (EBF) method, which has been validated as 2^{nd} order accurate.

This method is first validated as a general suspension flow solver, then for parallel modeling performance. The flow modeling method is then validated against experimental data of pulsatile, high Reynolds number BMHV flows. Blood damage is then evaluated for a baseline physiologic adult case of BMHV flow and results are analyzed in a variety of viewpoints. This method can also be used as a predictive tool and is employed to assess blood damage performance of BMHVs with pediatric sizing and flow conditions.

The simulations of this study reveal intricate, small-scale BMHV flow features that are resolved due to high spatiotemporal resolution. The presence of turbulence in BMHV flow is also quantified for the first time by demonstrating an inertial range in energy spectra. Blood damage simulations reveal that flow recirculation zones may be of higher importance in causing thromboembolic complications. This suggests a shift from previous evaluations of instantaneous flow and shear stress fields to the determination of

long-term flow recirculation regions when assessing thromboembolic potential of prosthetic devices. In addition, sharp geometries that may induce these recirculation regions should be avoided in device design. Simulations for predictive assessment of pediatric sized valves show increased platelet damage values for potential pediatric valves. However, damage values do not exceed platelet activation thresholds, and highly damaged platelets are found far from the valve where thrombus formation may be unlikely. Thus, the increased damage associated with these resized valves is not such that pediatric valve development should be hindered.

This method can be used as a generic tool for future evaluation of novel prosthetic devices or cardiovascular flow problems. Using accurate blood element damage modeling, the numerical method can help to understand cardiovascular blood flow complications in ways that other experimental and computational methods cannot.

CHAPTER 1

INTRODUCTION

1.1 Heart Valves, Heart Valve Replacement, and Prosthetic Heart Valves

1.1.1 Heart Valves

Heart valves are essential to the cardiovascular circulatory system and function by maintaining unidirectional flow of blood in the four chambers of the heart. The four valves in the heart are split into two subcategories: atrioventricular valves, and semilunar valves. The atrioventricular valves, consisting of the mitral and triscuspid valves, are named due to their position in between the atria and ventricles of the heart. The semilunar valves, consisting of the aortic and pulmonary valves, regulate blood flow leaving the heart from the ventricles.

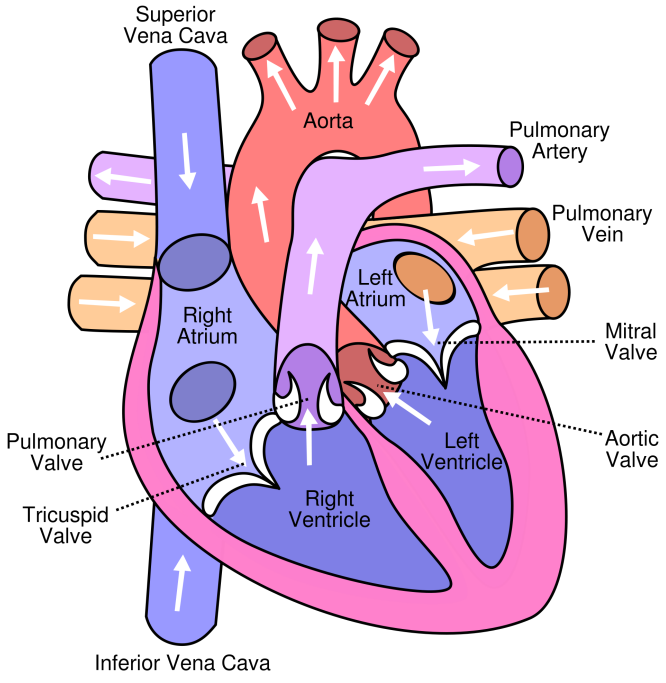

Figure 1-1: Diagram of the human heart showing four heart chambers, four heart valves, and connecting arteries and veins

Heart valves function by opening and closing due to pressure differential across the valves. The atrioventricular and semilunar valves alternate between open and closed positions, with the atrioventricular valves opening during diastole and closing during systole, and the semilunar valves closing during diastole and opening during systole. The normal function of heart valves is to prevent unwanted regurgitation of blood flow in the heart chambers, which may lead to serious complications such as mixing between oxygenated and deoxygenated blood.

The aortic valve (AV), which is of interest to this particular study, is located between the left ventricle and the aorta. The native human aortic valve consists of three flexible leaflets. During systole, the left ventricle contracts, the aortic valve opens, and oxygenated blood flows through the aorta and is directed throughout the body. In the diastolic phase, the AV leaflets coapt and close tightly to prevent regurgitation into the left ventricle.

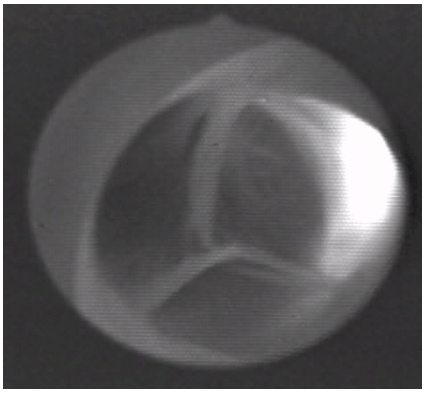

Figure 1-2: Porcine aortic valve with three leaflets in closed position

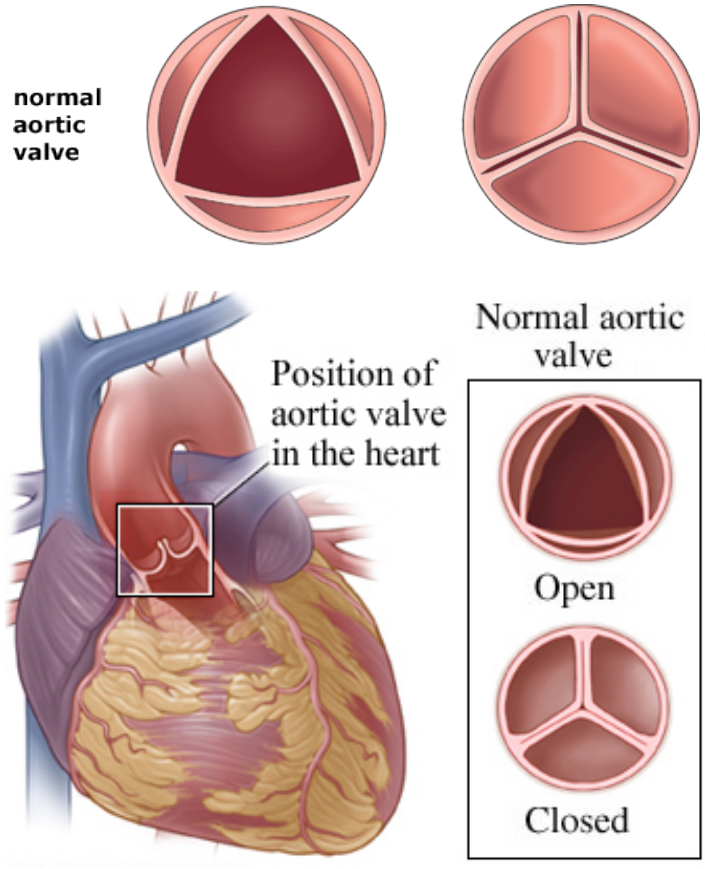

Figure 1-3: Diagram of normal human aortic valve in open and closed positions

1.1.2. Heart valve disease, malfunction, and replacement

Native heart valves may become defective due to congenital birth defects or diseases, such as calcification or bacterial vegetation. As previously mentioned, this malfunction can lead to regurgitation, which can lead to decreased efficiency in left ventricle contraction and insufficient systolic ejection volume. Acute aortic insufficiency, which occurs due to AV regurgitation, leads to sudden increase in left ventricular blood volume. This reduces ventricular efficiency and can cause left ventricular hypertrophy. This may result in sudden death, and thus requires an immediate replacement of the aortic valve. Chronic aortic insufficiency, though not as immediate and severe in complications,

can still result in left ventricle hypertrophy and dilatation. AV replacement is inevitable in these complications.

Since the inception of heart valve replacement in 1960, prosthetic heart valves have evolved in design with considerable improvements and are currently implanted in over 182,000 patients in the world every year, with three million total prosthetic valves implanted [1]. In the United States alone, over 100,000 heart valve procedures were performed in 2005, and device demand grows at over 10% per year [2, 3].

1.1.3. Prosthetic Heart Valves

Although numerous designs exist, prosthetic heart valves can be classified into three broad categories: biological/tissue, polymeric, and mechanical heart valves. Tissue valves, normally made from porcine or pericardial tissues, boast natural and biological form and function as replacement valves. However, they have very limited durability and often require replacement in less than ten years. Due to their biological material properties, tissue valves can undergo rapid structural changes such as leaflet calcification. This requires a secondary or tertiary reoperation of the valve replacement. This reoperation procedure is highly undesirable for patients who have already undergone an initial valve replacement. A study of Chan *et al.* performed follow-up studies on patients who underwent bioprosthetic heart valve replacement with a mean follow-up time of 5.1±4.6 years [4]. Even with this short follow-up time, it was determined that 11% of patients required reoperation. In patients less than 40 years old at the time of initial valve replacement, the 15-year freedom from reoperation was only 34% and 36% following aortic valve replacement and mitral valve replacement, respectively.

Polymeric valves utilize synthetic materials to mimic natural heart valves and their function. These polymeric valves are frequently made of polyurethane, which has the best biocompatibility, thrombogenic resistance, and durability [5]. Though these valve designs are very promising, they are still in early development and clinical testing stages as compared to mechanical and biological prosthetic valves [6].

Mechanical heart valves are currently the most popular prosthetic valve design, with 55% percent of defective native heart valves replaced by mechanical heart valves [7]. Unlike bioprosthetic valves, mechanical valves are completely made of synthetic materials. All mechanical heart valve designs display extraordinary durability due to their material composition, and can last indefinitely without structural breakdown.

Mechanical heart valve designs, in their history, include caged-ball, tilting disc, and bileaflet designs. The caged-ball valve design was the first developed in the 1960s, consisting of a sphere that is housed within a metal cage. However, this preliminary design suffered from high-pressure drops that were required to move the caged-ball, which also led to high turbulent fluid stress levels. As a result, this design was eventually discontinued in 2007. Tilting-disc valves were introduced in the 1960s and feature a circular occlusion (disk) that is held by a metal strut. This disk opens and closes due to pressure differences on either side of the valve (tilting motion). This design significantly improved the pressure drops across the valve and reduced the amount of turbulence in the pulsatile flow. However, despite the durable synthetic material, these early designs also experienced structural fatigue and eventual failure, where the disk could become dislodged from the valve.

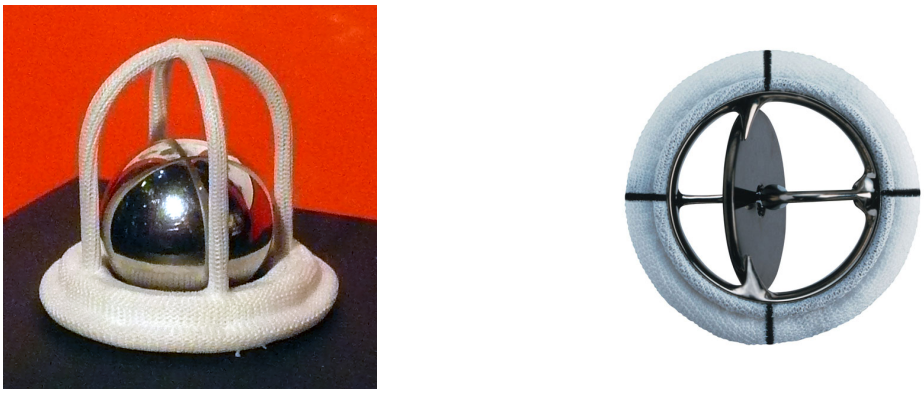

Figure 1-4: Caged-ball (left) and tilting-disk (right) mechanical valves

Among mechanical heart valves, the bileaflet mechanical heart valve (BMHV) is currently the most popular design [7]. Its popularity over other prosthetic heart valves such as caged-ball, tilting disc, and bioprosthetic valves is mainly due to its superior durability, function, and bulk flow hemodynamics. The flow through BMHVs exhibits lower pressure drops and turbulence than prior mechanical valve designs, and also exhibits a larger effective orifice area (EOA). BMHVs have been present since 1979 and have undergone a long period of evolution in order to improve its efficacy. The main disadvantages of BMHVs are the need for lifelong anticoagulation therapy due to risks of hemolysis, platelet aggregation, and thromboembolic events. The impact of BMHVs on cardiovascular flows has been of high interest due to their popularity as heart valve replacements, as well as the severe complications associated with these valves.

Figure 1-5: Bileaflet Mechanical Heart Valve – St. Jude Medical 23mm Regents valve

1.2 Bileaflet Mechanical Heart Valves

Bileaflet mechanical heart valves account for 80% of implanted mechanical valves [7]. For surgical implantation, a sewing cuff is first attached to the annular valve housing. This allows for the suturing of BMHVs to the surrounding heart tissue. Modern BMHVs are often made of pyrolitic carbon, a man-made material that is biocompatible, thromboresistant, and durable, increasing its appeal as a material for a replacement valve. BMHVs have become popular due to low risk of device failure, such as leaflets becoming detached or structural failure. In addition, they have evolved in subtle design features that result in minimal thrombotic complications in comparison to other mechanical valve designs.

1.2.1 General design features

BMHV design consists of two leaflets in the shape of semicircles that are hinged to the valve housing. These leaflets function to regulate blood flow by pivoting from open to closed positions depending on pressure differences on either side of the valve. The pivoting motion is allowed by hinge regions, to which the two leaflets are fixed. The

hinge regions are recesses that are machined into the annular valve housing. The leaflets are fixed to these hinge regions by leaflet ears that slot into the recesses. The differences in BMHV design among various manufacturers are very subtle in nature, and are often related to the design of the leaflet ear and hinge regions.

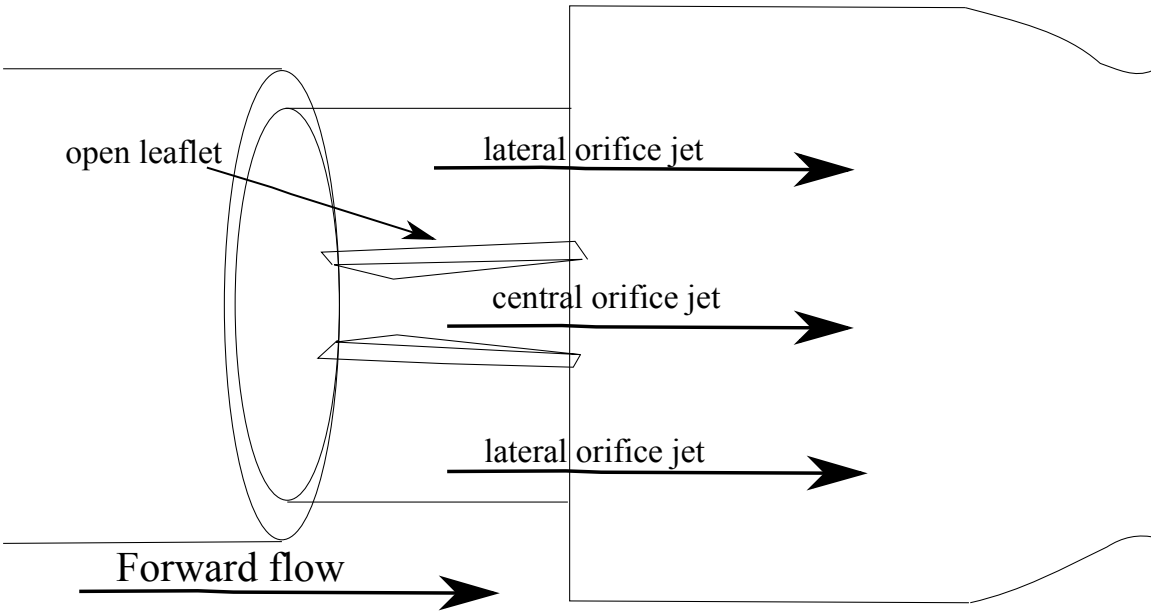

Figure 1-6: BMHV schematic for forward flow (perpendicular cross-sectional view)

Similar to native heart valves, the BMHV leaflets open and close passively based on varying cross-valvular pressures throughout the cardiac cycle. In the open position, the presence of the two leaflets leads to the formation of three orifices for blood flow: two lateral orifices and a central rectangular orifice. In most BMHV designs, the open leaflets form an angle with the axial flow direction, often less than 10 degrees. This angled open position is used to minimize flow disturbances in flow through the valve [8]. Most of the blood flows through the three orifices formed by the open leaflets, although a minimal amount of fluid also flows through the hinge regions.

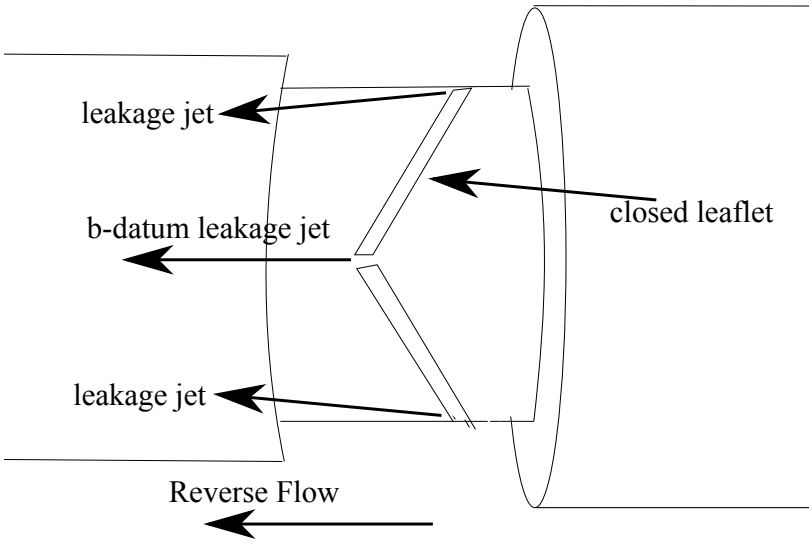

Figure 1-7: BMHV schematic for reverse flow (perpendicular cross-sectional view)

In the closed position, the leaflets come together to occlude the valve and prevent regurgitant flow. The leaflets are not designed to close perpendicular to the flow direction, but rather at an angle of approximately 60 degrees, thus reducing the required leaflet angle sweep from open to closed positions [8]. When closed, the leaflets still allow for minimal leakage flow through small gap regions. The primary gap region is the reduced central orifice region, called the b-datum line. Other gap regions include the hinge recesses and the gaps between the closed leaflets and the annular valve housing. Although these gaps allow minimal regurgitant flow, they are purposefully incorporated to reduce blood element buildup within the valve in order to promote washout regions.

1.2.2 Popular BMHV designs

BMHV design varies by the manufacturer, but after long-term evolution, these variations are minimal, often related to slight differences in the annular housing, leaflet

shape, and leaflet ear / hinge recess design. The popular designs include St. Jude Medical™ (SJM), CarboMedics™ (CM), ATS Open Pivot™, Medtronic™, and Sorin™ valves. These designs are often referenced by the outer cuff diameter (i.e. 23mm SJM valve) for operating surgeons. However, it should be noted that the inner valve diameter is smaller due to the cuff thickness.

Figure 1-8: CarboMedics (left) and St. Jude Medical (right) 23mm Bileaflet Mechanical Heart Valves

The SJM valve is the most popular BMHV design [7]. The valve housing is different from other designs by its inclusion of pivot guards, which are semicircular protrusions. These pivot guards are included to protect the hinge pivoting function from interference from sutures, subvalvular structures, and calcium buildup in the valve. The hinge regions are machined into these two pivot guards, with two hinge recesses for each of the two leaflets. The leaflets of the SJM valve include two 'ears', which are semicircular protrusions designed to slot into the hinge recesses. The leaflet ears of the SJM valve have a smooth semi-circular geometry, designed to promote smooth washout of blood elements caught in the hinge region. The hinge recess, located in the valve housing, is also designed with a circular geometry to match the shape of the leaflet ears. The leaflet ears slot into the hinge recesses and allow for flat surface contact between the

leaflets and the valve housing. This design also includes tolerances in the hinge design, which allows for minimal translational motion for the leaflets.

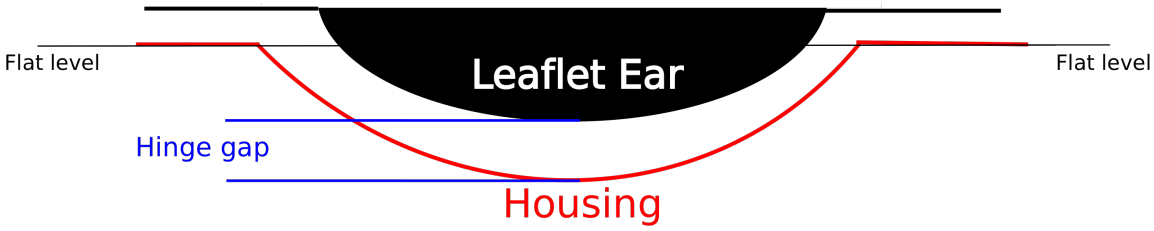

Figure 1-9: Semicircular leaflet ear fitting into valve housing hinge recess. Gap between leaflet ear and housing referred to as "hinge gap"

The circular recess into the valve housing is also swept about the leaflet base axis, allowing for smooth rotational motion of the leaflets during opening and closing. This sweeping recess creates a characteristic 'butterfly hinge' geometry for the SJM valve. The opening and closing angles relative to the axial flow direction are approximately 6° and 61° [8]. This leads to a total sweep angle of 55°. Finally, the SJM valve also includes an expansive 'thumbnail' region, located downstream of the hinge regions, which function by creating a slightly larger orifice area (figure 1-12).

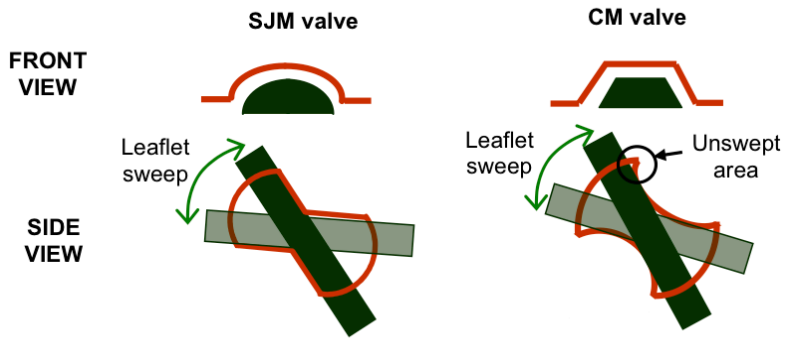

Figure 1-10: Front and side views of SJM and CM hinge regions with leaflet sweep [8]

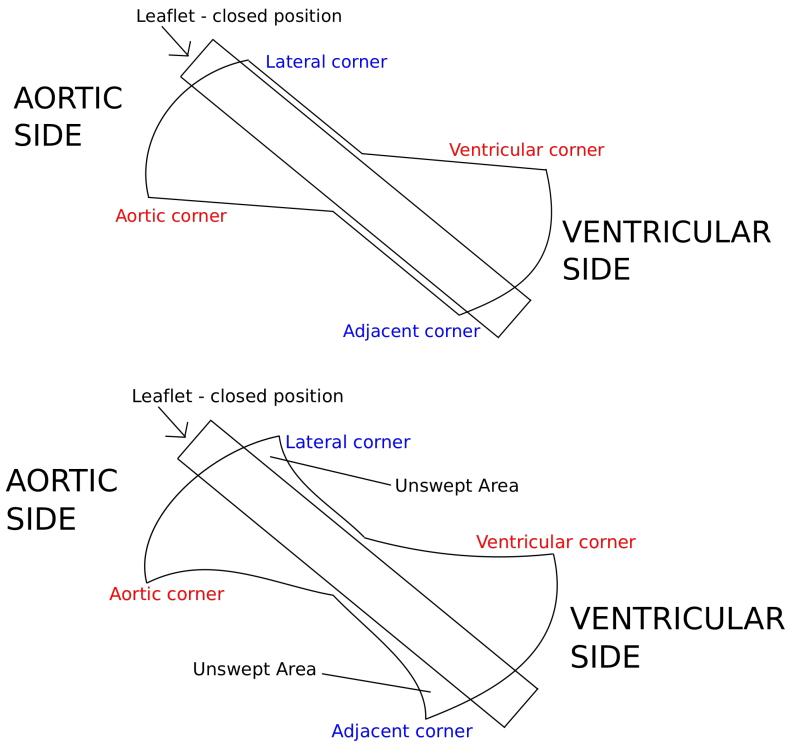

Figure 1-11: SJM (top) and CM (bottom) hinge geometries. This view shows closed leaflet position and valves implanted in aortic position

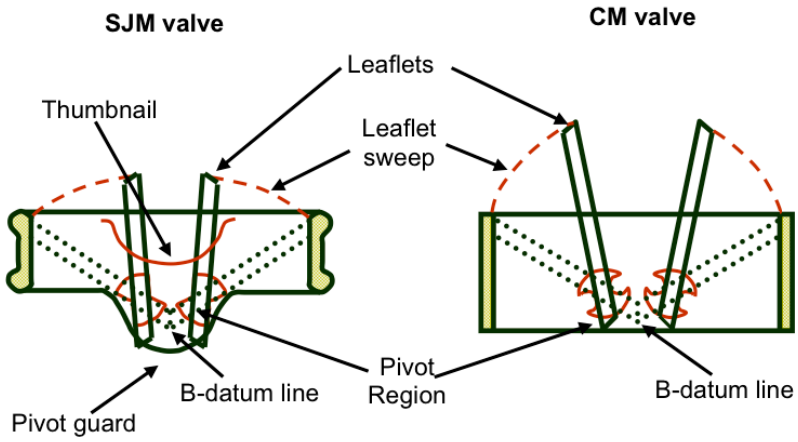

Figure 1-12: Side view of the SJM and CM valves [8]

Another popular design is the CarboMedics (CM) valve design. The CM valve does not include pivot guards or a thumbnail region, but features similar components of the SJM valve such as the leaflet ear - hinge recess fitting. The leaflet ear and hinge recess of the CM valve feature sharper transition geometry, representing a trapezoid instead of a smoother circle like the SJM valve. The pivot recess also contains small, unswept areas at each of the four corners of the hinge. The maximum opening angle of the CM valve is 12°, twice as large as that of the SJM valve [8]. Other BMHV designs are also similar to the SJM and CM valves in leaflet–hinge function, but contain subtle differences in leaflet ear or hinge recess designs as well as valve housing design.

1.2.3 Complications from BMHV Implantation

Despite improvements in design and good hemodynamics performance, BMHVs still cause serious and lifelong complications. The survival rate lowers from 80% five years after surgery, to only 50% after fifteen years. The major complications associated with BMHVs are: valve structural failure, non-structural valve malfunction, thrombosis, embolism, bleeding, and endocarditis [9]. Although long-term design evolution has reduced many of the major complications, there are still serious complications in the form of hemolysis, platelet activation, and thromboembolic events [10, 11]. Thrombus (clot) formation due to platelet damage in BMHV flows has serious consequences, particularly if these clots become detached and become free-floating emboli. These emboli can occlude smaller blood vessels, ultimately resulting in stroke and/or death.

Typical preventative measures for these complications involve the prescription of lifelong anticoagulation therapy. Although this does reduce the chance of clot formation,

anticoagulation therapy itself carries serious complications. These include increased risk of infection, hemorrhaging, autoimmune response, and accelerated calcification [12, 13].

Major complications resulting from blood element damage have been associated with the effect of BMHV design on the pulsatile flow field. As BMHV design is non-physiological and highly different from native heart valves, the complex pulsatile flows through BMHVs could impose abnormal shear stress levels on blood elements. The unnatural flow fields generated by BMHVs are believed to create regions of high shear rates and recirculation, both of which are considered key factors to blood element damage and will be discussed in section 1.3. Both viscous and Reynolds shear stresses have been studied as possible sources of blood damage and clot formation.

Previous studies have shown that flow through BMHVs lead to shear stresses above the acceptable threshold limit of blood element damage [14-16]. High shear rates and shear stresses in these flow fields may cause an undesired activation of platelets, and other coagulation factors that can form a platelet plug. This is known as the coagulation cascade and will be covered in detail in the next section. The recirculation regions caused by BMHV design only exacerbate the problem, as the increased residence time promotes further platelet signaling and activation, ultimately leading to more unwanted thrombus formation. A study by Skoulgaris *et al.* evaluated the hemolysis levels in 80 patients implanted with SJM or Medtronic Hall tilting disk valves. In this study, it was determined that higher levels of hemolysis were related to the design, position, and size of the prosthetic heart valve [17]. This study demonstrated a potential relationship between prosthetic valve design and the severity of associated complications.

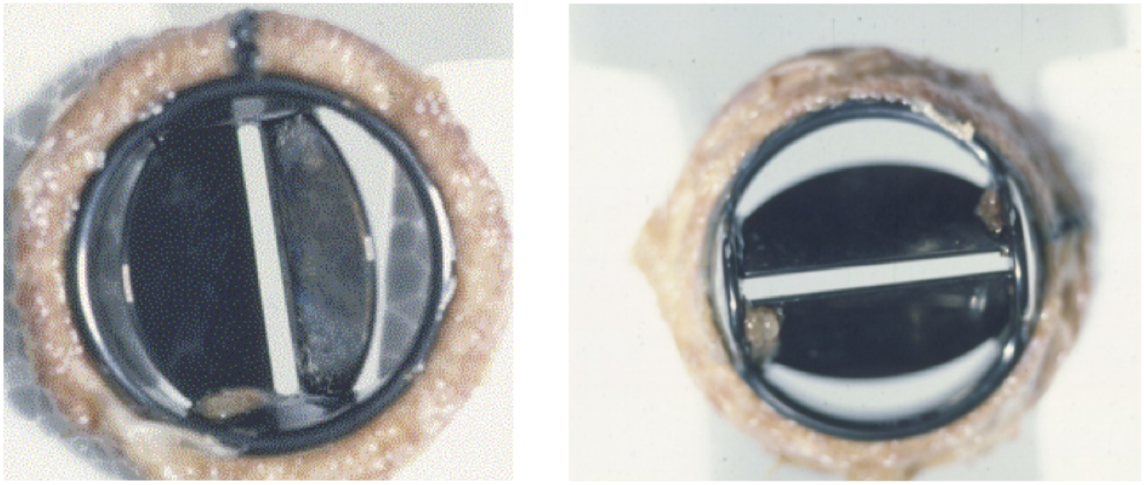

Figure 1-13: Visible clots forming in hinge regions of St. Jude Medical BMHV

Through decades of evolution, modern BMHVs have reduced the severity of hemolysis complications. Design improvements that lead to blood element washout have helped to significantly reduce hemolytic complications, but have not completely eliminated them. Despite improved design and enhanced drug therapies, platelet damage and thromboembolism remain as very serious complications of BMHV implantation. In a clinical study by Vallana *et al.*, the Medtronic Parallel was shown to cause thrombi formation in the hinge regions of BMHVs and was considered unacceptable for implantation [18]. Design related complications, thought to be caused by unnatural flow fields, could be reduced by improvements in design that do not generate flow fields with unnaturally high shear rates or large recirculation regions. First, the pulsatile flow fields and blood element damage incurred in these fields must be well understood, particularly in how they are connected to the valve design.

1.3 Blood and Blood Damage

As most complications with prosthetic heart valves are related to blood damage, it is important to understand the nature and function of blood and its components, the response to damage, and the resultant consequences.

Blood is comprised of formed elements suspended in plasma. Plasma is the base fluid and accounts for approximately 55-60% of blood volume. Although plasma itself has numerous constituents, it behaves as a Newtonian fluid. Formed elements include red blood cells (RBCs), platelets, and white blood cells (WBCs). The most numerous type of blood particle is the red blood cell, which accounts for 95% of the formed elements by volume. The other cellular components of blood, white blood cells and platelets, account for roughly 0.1% and 4.9%, respectively, of the volume fraction of the formed elements. White blood cells function by engulfing and ingesting bacteria and other foreign particles in the blood. Platelets work by forming clots (thrombosis) to repair vascular injuries and stop bleeding. Red blood cells serve by transporting oxygen and waste molecules to and from the heart. The volume fraction of formed elements in blood is referred to as hematocrit, and is approximately 40-45% in normal blood.

1.3.1 Red Blood Cell Damage

Red blood cells (RBCs), also known as erythrocytes, transport oxygen and carbon dioxide throughout the heart, lungs, and tissues. The life span of erythrocytes is approximately 120 days. RBCs have a distinct biconcave discoid shape, with major diameter ranges from 6-8 μm, and a thickness of approximately 2.8μm. The RBC is composed of a flexible phospholipid membrane supported by a cytoskeleton, which

surrounds an aqueous solution of hemoglobin and enzymes. This membrane is non-homogeneous and permeable, allowing for gas diffusion of oxygen and carbon dioxide. Red blood cell membranes can also tolerate large uniaxial strains without tearing. This is due to the excess of RBC membrane in comparison to their volume, allowing for a large amount of deformation. Red blood cell membranes under shear are initially viscoelastic, but under high loads can become viscoplastic [19].

The presence of the RBCs substantially changes the flow characteristics and rheology of suspensions compared to a simple Newtonian fluid. RBCs not only affect the macroscopic rheological properties of blood flow, but also alter the local stress and diffusivity experienced by RBCs themselves and other particles such as platelets and white blood cells [20]. This has ramifications on numerous biological processes.

RBCs can undergo damage in the form of hemolysis, or the rupturing of the RBC membrane. This leads to the release of hemoglobin from within the ruptured RBC membrane to the surrounding plasma. When red blood cell membranes are stretched, holes may form that allow for hemoglobin and protein diffusion into the blood plasma. Although the red blood cell membrane is highly deformable, a large stretch can tear the membrane and spill its contents into the surrounding fluid. Hemolysis can be caused by either instantaneous damage at high levels or cumulative damage to the RBC membrane.

1.3.2 Platelet damage

Platelets are the smallest cellular constituent of blood, with a diameter of approximately 3 μm and an average life span of 10 days. Platelets are produced in bone marrow by megakaryotes, and are colorless particles with no nucleus. Their normal

function is to stop hemorrhage by rapid activation, adhesion and accumulation into blood thrombi at damaged vessel surfaces. Non-activated platelets have a flat discoid shape, but are extremely responsive to the surrounding medium. When activated by stimuli, such as vascular injury, platelets activate typically in three stages: initiation, aggregation and propagation. The platelets ruptured in the initiation phase release tissue factor into blood, which bind to other factors in plasma and eventually activate prothrombin. This compound produces thrombin and other factors that play an important role in platelet aggregation, adhesion and propagation. During this phase, platelets change their cytoskeleton and extend long pseudopods to adhere to the collagen that becomes exposed due to the damaged endothelium. This process is commonly referred to as the coagulation cascade. This cascade converts fibrinogen into fibrin fibers, which aids in the structural formation of blood clots for repairing vascular injuries [21].

Platelets have minimal impact on hemodynamics and flow passively in accordance to fluid and red blood cell forces; however, their transport and the mechanical stresses imposed on them play an important role in the regulation of many biological processes such as platelet deposition, plug formation, and the maintenance of hemostasis. Platelets can also be activated due to long exposure to shear stresses, leading to the formation of unwanted thrombi. These clots can detach and form free-floating emboli that can occlude smaller vessels, ultimately leading to stroke and death.

1.3.3 Shear Stress in relation to Blood Damage

As blood element damage is a serious complication of prosthetic valve devices, it is important to understand how this damage occurs. Specifically, one must understand

blood element damage in relation to flow physics and mechanical stresses and forces imposed on elements. This is particularly important because the implantation of prosthetic devices alters the flow environment, and thus it must be understood how this flow field alteration affects blood elements and their incurred damage.

1.3.3.1 Red Blood Cells and Shear Stress

To examine the effects of mechanical stresses on red blood cells, Nevaril *et al.* applied a nearly uniform stress field on blood using a modified Couette viscometer [22]. The threshold shear stress for red blood cell lysis after two minutes was 1,500 dyn/cm^2, and red blood cells were significantly lysed when shear stress exceeded 3,000 dyn/cm^2. It was also demonstrated that the normal stress was of secondary importance in blood cell lysis in comparison to shear stress. This implied that the primary mechanism of hemolysis and blood element damage was, in fact, the mechanical shear stress imposed on blood elements.

In addition to shear stress imposed on red blood cells, subsequent studies found the importance of exposure time to these mechanical stresses and the resulting hemolysis. Leverett *et al.* determined in 1972 that discrepancies in hemolysis values were due to experiments ignoring the significance of the exposure time, as studies were not taking into account the exposure time-shear stress domain [23].

Blackshear divided shear stress induced hemolysis into three categories: hemolysis induced by surface interaction, by medium stresses occurring in bulk flow (1,000-2,000 dyn/cm^2 for several seconds), and by high stresses occurring in bulk flow (40,000 dyn/cm^2 for milliseconds) [24]. In the case of medium shear stresses, the red

blood cells would become damaged gradually and hemolysis was dependent on exposure time. For high shear stresses, exposure time was not as significant a factor and the instantaneous high shear stresses led to immediate rupture of the RBC membrane.

Hellums *et al.* examined the relationship between hemolysis and shear stress and exposure time more carefully [25]. It was determined that there were two regimes for shear stress and exposure time and the resulting hemolysis damage. In the first regime with low shear stresses and short exposure time, there was little hemolysis damage, and this damage was influenced primarily by surface interaction. In the regime with high shear stress and long exposure time, very high hemolysis was found to occur. In this regime, it was determined that shear stress was the dominant factor of hemolysis. Thus, a new concept was formed of a threshold shear stress that must be surpassed in order to cause significant hemolysis.

The concept of threshold shear stress was further investigated by Sallam and Hwang [26]. In this study, the authors related local shear stress values with red blood cell damage by using a known jet flow field. A threshold shear stress value of 400 N/m^2 was determined corresponding to a 1ms exposure time. Beyond this threshold shear stress, hemolysis increased with increasing shear stress, and below this level no hemolysis was found. Lu *et al.* determined a separate threshold limit for hemolysis in turbulent shear flow of 800 N/m^2 with an exposure time of 1 ms [27]. It was found that the threshold shear stress values by Sallam were an underestimation due to a difference in experimental methodology.

1.3.3.2 Platelets and Shear Stress

Early studies on blood element damage focused on red blood cell damage, as thrombosis and coagulation was not well understood. Eventually, studies were performed to study platelet damage and thrombosis in relation to shear stress. In 1962, Born first developed a method measuring platelet aggregation to find a relation between shear stress and platelet-platelet interaction [28]. However, this early work could not draw clear relations between shear stress and platelet aggregation, as the shear stress applied to platelets was not uniform [29]. Brown *et al.* performed shear stress experiments in which platelet rich plasma was exposed to shear stresses ranging 5 to 900 dyn/cm^2. Even at shear stress values as low as 50 dyn/cm^2, platelets showed biochemical and morphological changes [30]. Platelet function was also altered with shear stresses over 100 dyn/cm^2 applied for five minutes. These experiments first demonstrated that shear stress could alter platelets and their function in addition to causing hemolysis.

Bernstein *et al.* attempted to impose different types of platelet damage and determine their effects. The authors used two devices to separate damage from fluid shear stresses from damage related to surface interaction [31]. The authors showed that high wall impact had no influence on platelet activation or aggregation, but high shear forces applied for a few milliseconds could affect platelet function. A threshold shear stress was determined of 10^5 dyn/cm^2, below which no platelet aggregation or activation was determined. However, at 10^6 dyn/cm^2, structural and functional changes to platelets were observed, albeit without abnormal platelet aggregation.

Hellums expanded upon these studies relating shear stresses and platelet aggregation and found that platelet aggregates could form even at low shear stresses [25].

At higher shear stresses, platelets would not aggregate but could become fragmented. It was determined from these inconsistent results that platelet damage, like hemolysis, could be influenced by factors such as exposure time in addition to shear stress levels.

A study by Anderson *et al.* further explored threshold shear stress levels for platelet damage [32]. Shear stress levels of 50-75 dyn/cm^2 applied for five minutes resulted in reversible swelling and aggregation of platelets. However, at 150 dyn/cm^2 the platelet count dropped significantly, indicating a threshold shear stress level for significant and irreversible platelet activation. It was also shown that the threshold shear stress level increased with decreasing exposure time. This and previous studies indicated that platelet damage is actually related to a combination of exposure time and shear stresses, with varying threshold levels.

A study by Sheriff *et al.* was performed where varying levels of shear stress were imposed on platelets to determine their long-term effect on platelet activation [33]. This study indicated that high shear stress levels on platelets may 'sensitize' platelets to future activation. It was determined that platelets that experienced high shear stress levels but did not activate could later become more easily activated when undergoing lower shear stresses due to their previous exposure. This emphasized the importance of shear stress and exposure time history on the potential of platelets to become activated.

1.3.3.3 Shear Stress on Red Blood Cells vs. Platelets

Previous studies have demonstrated that shear stress is a key factor in both hemolysis and platelet activation and aggregation. However, these studies also indicate that shear stress affects these two blood element types differently. For long exposure

times, platelets are more sensitive to shear stress and incur more damage than red blood cells. In comparison studies by Bernstein [25, 31], results indicated that for two minutes of exposure, the threshold shear stress level for hemolysis was 1500 dyn/cm^2 but ten times lower for platelet lysis. The study by Brown *et al*. also showed hemoglobin leakage levels were not significant compared to ADP leakage from damaged platelets for longer exposure times [30]. It is noted, however, that for very short exposure times, platelets were more resistant to damage at high shear stress levels than red blood cells [32].

The differences observed in these studies between red blood cells and platelets can be attributed to their structural differences. The primary structural difference is in the deformability of their solid surfaces. Red blood cells have a highly deformable membrane surface, and platelets are essentially rigid. Thus, for short exposure times but high shear stress levels, the rigid membrane of the platelet would be more resistant to shear than the deformable membrane of red blood cells. An instantaneous high shear stress level could cause this flexible red blood cell membrane to tear, causing hemolysis. Alternatively, for prolonged exposure to lower shear stresses, red blood cell membranes can deform, allowing an adaptation of shape to minimize tearing. Platelets are unable to deform over time and would become activated under prolonged exposure.

1.4 Previous Investigations

Although the introduction of the prosthetic heart valve greatly improved patient outcome, the serious complications associated with valve implantation warranted studies in an effort to reduce these life-threatening issues. As these complications are related to

blood damage induced by mechanical stresses, these studies were concentrated on characterizing the prosthetic valve flow fields.

1.4.1 Experimental Studies

Early studies on flow through native heart valves were limited but focused primarily in flow dynamics caused by the valve leaflet movement and the effect on vortex formation in the sinus region [34-36]. By characterizing the flow field through heart valves, these studies could identify the regions of high fluid shear stresses and recirculation. These regions are caused by vortex shedding past valve leaflets, as well as recirculation caused by the presence of the sinus expansion. Both could be associated with increased hemolysis or platelet activation. More detailed overviews of flow dynamics in native heart valves are available in select review papers [37, 38]. For prosthetic heart valves (PHVs), the initial research was focused on gross clinical performance of the valve designs and not as much on the specific flow dynamics. A review of these clinical performance studies has been provided by Yoganathan *et al.* [39].

For BMHVs, many studies focused on the hinge region, as visible thrombi were seen to form at these hinges. The hinge region was found to be critical, influencing valve durability, flow dynamics, and thrombus formation [18]. In a comparison study between the ATS and SJM valves, Shipkowtiz *et al.* determined that the hinge location, leaflet position, and outflow orifices influenced the valve pressure distribution [40]. The larger opening angles, allowing for larger orifices of flow, result in improved hemodynamics, less wake turbulence, and less perturbed flow for flow past the open leaflets.

The designs of the hinge region of the SJM and CM valves have been shown to be more favorable in reducing complications, as these two valves both have a lower level of thrombosis and valve related complications compared to the Medtronic Parallel (MP) design [15]. Nonetheless, clinical studies have concluded that the SJM valve performs better than the CM valve [41], thereby suggesting that an optimal valve design may exist. Ellis *et al.* performed studies characterizing flow fields for BMHV hinge regions using Laser Doppler Velocimetry [14, 15, 42]. By characterizing the flow fields of hinge regions, the authors first noted areas of higher fluid shear stresses and flow recirculation. Comparison studies were also performed among different BMHV hinge designs. These experimental studies were continued by Simon *et al.* [43] to associate the different hinge design features of two BMHVs (SJM and CM) with elevated fluid shear stresses and recirculation regions that could cause increased platelet damage. By comparing flow fields, the authors could evaluate the design of the hinge region with blood damage performance and make subsequent recommendations.

Many experimental studies have been performed on flow through prosthetic heart valves to study the complex pulsatile flow dynamics at a larger scale. Lim *et al.* employed Particle Image Velocimetry (PIV) flow measurements at a cutplane of a porcine tissue heart valve in the first use of PIV to study flow through a prosthetic heart valve [44]. These same authors employed PIV to further study PHV flows under steady and pulsatile conditions [45, 46]. These studies showed the complex vortex shedding in the flow through PHVs, which had implications on shear stresses that could cause damage on blood elements caught in these flow regions. A later study by Brucker *et al.* examined pulsatile flow through a trileaflet PHV and showed vortex shedding

downstream of the leaflets [47]. The experiments detailed instantaneous flow fields at horizontal and transverse planes, as well as vorticity fields for leaflet opening.

Diastolic flow through a SJM valve under physiological conditions was also studied, showing a regurgitant flow field caused by the closed leaflets [48]. This study showed the formation of dual vortices in regurgitant flow near the valve leaflets. Another study examined the closing phase and regurgitant diastolic phases experimentally in regards to the potential for the formation of thromboembolic complications [49]. The possible blood damage incurred in backflow past BMHVs has also been studied in detail. An initial study by Lamson et al. showed the blood damage effects of reverse flow are as significant as forward flow during systole [50]. Experimental studies were also expanded to three-dimensions with stereo PIV for flow past polymeric trileaflet PHVs [51].

In vitro experiments were performed by Dasi *et al.* [52] detailing the complex flow features of pulsatile flow past a St. Jude Medical BMHV in the aortic position. These pulsatile flow experiments were performed using a blood analog fluid for visualization purposes that matched the same kinematic viscosity as whole human blood. It was determined that accelerating flow past the valve, though characterized by strong vortex shedding, was still laminar and coherent. More chaotic and disorganized features were observed for peak systolic and decelerating flow. It was also noted that there were strong cycle-to-cycle variations in the flow patterns and leaflet motion, possibly caused by the nature of high Reynolds number pulsatile flow. This naturally occurring flow and leaflet motion asymmetry has not yet been explored in full detail.

Experimental studies have also expanded to quantify blood damage incurred in BMHV flows. Instead of associating potential blood damage with experimental flow

fields, these blood damage experiments subjected actual blood to either BMHV-like flows or through BMHV flows themselves in order to quantify damage. Fallon *et al.* performed experiments of whole human blood flow through stenotic-expansive orifices designed to be similar to the SJM and ATS Open Pivot hinge regions. Blood assays were performed to quantify hemolysis, platelet factor-4 (PF4), and thrombin-antithrombin III (TAT) in steady blood flow through orifices of differing geometries and orifice diameters. Only TAT measurements were statistically different, implying platelet damage is more significant in BMHV hinge flows than red blood cell damage. It was determined in these studies that smoother hinge geometries and larger orifice diameters allowed for less recirculation regions and lower damage, which was quantified in the form of reduced TAT concentration levels. This study confirmed the influence of design parameters on blood damage incurred in BMHV flows.

As BMHV design has been shown to influence blood damage levels, attempts have also been made to reduce blood damage complications by modifying BMHV design. Dasi *et al.* employed passive flow control in order to reduce larger scale vortices during the backflow phase for a SJM valve [53]. These large-scale vortices were thought to be important in inducing blood damage during backflow by increasing the shear stress-exposure time of blood elements caught in these vortical regions. In this study, vortex generators of differing designs (rectangular and circular) were employed in order to break apart the large-scale vortices created in backflow squeezing through the central b-datum orifice formed by the closed leaflets. It was shown that the presence of vortex generators succeeded in breaking up larger vortical structures into smaller scale vortices.

This work was continued by Murphy *et al.* in a study where whole human blood was used in backflow past a SJM valve with the same vortex generator designs [54]. In this study, TAT assays were performed after the experiments of steady backflow in order to quantify platelet damage. It was determined that the vortex generators did reduce TAT concentration levels, thus implying that passive flow control could reduce blood damage in BMHV flows. However, these studies were only performed during the backflow phase and with steady flow, and thus the effect of the vortex generators during the forward flow phase are unknown. These experimental studies only report bulk blood damage values and are limited due to an inability to accurately determine how, when, and where blood damage is incurred in BMHV flows.

1.4.2 Computational Studies

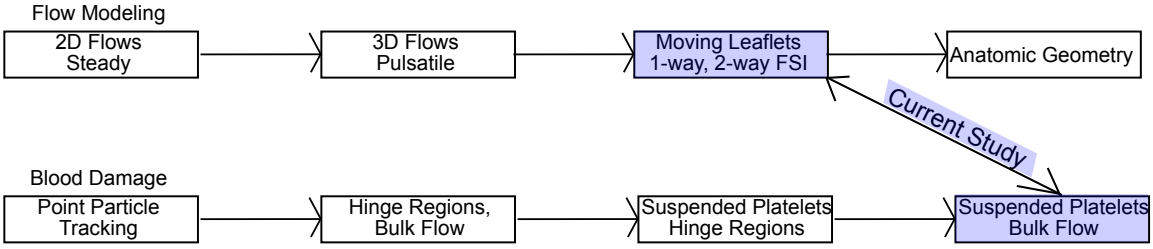

Figure 1-14: Flowchart demonstrating history of CFD studies of blood damage in BMHV flows, including the current study

Computational studies began in the 1970s as an alternative to exploring flows through PHVs [38]. An early example by Peskin employed the immersed boundary method to characterize the 2D flow field past a native mitral valve. A natural advantage of computational fluid dynamics (CFD) to explore flows through PHVs is the ability to model fully three-dimensional flows, whereas experimental studies are mostly limited to

2D planes. Computational simulations began in simple cases of steady flow through fully open leaflets of prosthetic heart valves, and subsequently expanded in complexity. For BMHVs, computational studies first concentrated on characterizing flow fields in an attempt to draw relations with potential blood damage.

In one study by Ge *et al.*, axial velocity values were computed from computational simulations of 3D steady flow through BMHVs for validation with experimental PIV measurements [55]. These simulations were performed at varying Reynolds numbers in both laminar regime and at peak flow where turbulent-like flows were observed. The simulations were able to match these two steady flow regimes at various flow cross sections, thus validating the numerical method. Upon validation, 3D flow fields were detailed, showing complex structures that were previously unavailable from clinical or experimental studies.

These numerical studies were later expanded to pulsatile 3D flows throughout an entire cardiac cycle where qualitative comparisons were made between numerical simulations and PIV measurements [52]. In this study, rich 3D vorticity dynamics were also examined in great detail due to the ability of the numerical method to model and visualize 3D pulsatile flow through a BMHV. Due to cycle-to-cycle variations, comparisons with experiments were made at 2D perpendicular cutplanes using vorticity contours at instantaneous time snapshots. Good qualitative agreement was reached, and the sharp-interface immersed boundary numerical method was able to capture the key flow features of the instantaneous pulsatile flow field. The numerical method was then employed to characterize the 3D pulsatile flow field, showing coherent 3D vortical structures. These simulations highlighted the three-dimensionality of the BMHV flow

field and the need to accurately capture this three-dimensional complexity in order to fully understand BMHV flows and the implications on potential platelet damage. However, the numerical work in this previous study as well as others were limited in only simulating symmetric leaflet motion. In addition, there was no simulation of reverse flow in the cardiac cycle, and zero flowrate was instead substituted for the entire diastolic phase of reverse flow.

Computational simulations of flow through BMHVs have also included dynamic leaflet motion using two-way fluid-structure interaction (FSI). One study employed an immersed boundary method to simulate pulsatile 3D flow through a BMHV for an entire cardiac cycle with dynamic leaflet motion [56]. These simulations matched pulsatile flow measurements from experiments quantitatively, including root-mean-square values for high Reynolds number flows. It was also noted that the two-way leaflet motion was highly dependent on the forward flowrate deceleration as well as the maximum backflow leakage rate. A major limitation of this study was its inability to capture reverse flows, both for leaflet closing impact with the valve (due to singularity problems) and for mid-diastolic leakage flows.

In order to reduce computational costs, parallel computation simulations of flow through PHVs have also been performed with full FSI [57]. Computational methods have also expanded in modeling beyond simplified *in vitro* geometries, focusing on more physiological geometries that include bends in the domain and more anatomical features. Studies by Borazjani *et al.* examined pulsatile 3D flow through a BMHV in an idealized anatomic aorta [58, 59], characterizing the effect of realistic geometries on the BMHV

flow fields. These studies took a step towards creating more anatomically realistic flow domains, although vessel wall motion was not modeled.

As a future direction of computational studies of pulsatile flows through BMHVs, modeled suspended platelets have been used to track potential platelet damage that could lead to thromboembolic complications. These studies have either focused on the bulk flow through BMHVs [11, 60], or through the hinge regions, where thrombi have been clinically observed to form [43, 61-63]. Dumont *et al.* employed point particle tracking to quantify platelet damage that occurs during forward systolic flow for two BMHV designs, using a Lagrangian particle-tracking method in order to assess thromboembolic potential [10]. These particle-tracking methods approximate suspended platelets as massless point particles, with their location and velocity determined by interpolating and integrating local flow velocities. Dumont *et al.* quantified blood damage for these point particles using a linear shear stress-exposure time method, but used local fluid viscous shear stresses as only a single-phase continuum fluid flow was simulated.

Blood damage tracking from a Lagrangian viewpoint was also performed by Shahriari *et al.* using smoothed particle hydrodynamics [64]. In this study, however, cases of severe leaflet dysfunction were modeled to determine the effect on the flow field and on potential platelet damage. Although this numerical method used a form of Lagrangian particle tracking, the damage on suspended blood elements was once again interpolated from fluid viscous shear stress values, and not on accurately modeled suspended particles with finite volume and surface.

Point particle tracking methods were also used in other numerical studies to evaluate various BMHV hinge designs. Damage was computed on modeled suspended

platelets released in flows through the SJM and CM valve hinge regions [61, 62]. These simulations were performed with high spatiotemporal resolution within the hinges with the inclusion of leaflet motion and pulsatile flow fields. These studies also concluded that the SJM valve performs better in reducing thromboembolic complications, and that the leakage phase induced more platelet damage for hinge flows.

1.5 Importance of Modeling Multiphase Flow

Recent computational advancements have allowed for even more complex numerical modeling of BMHV flows. Instead of point-particle tracking, suspended platelets with finite volume and meshed surfaces were released in a numerical study by Wu *et al.* for flows through BMHV hinge-like regions [65]. These simulations computed the shear stress on platelets through realistic fluid-solid interaction forces, and not through interpolating viscous fluid shear stresses. This numerical study was also shown to compare well with whole human blood damage experiments, using a linear shear stress-exposure time damage accumulation method.

This same method was used in another numerical study by Yun *et al.* to quantify platelet damage through various BMHV hinge flows, specifically the SJM and CM hinge designs [63]. These simulations were only performed for mid-diastolic leakage flow, but still modeled thousands of suspended platelets with finite volume and finely meshed surfaces. This numerical method was able to match both the fluid flow in the hinge region with other computational studies, as well as characterize the blood damage performance of each of these hinge regions. In this study, it was also noted that the point particle tracking method was not as accurate for quantifying blood damage. It was shown

in a direct comparison that point particle tracking underestimates the shear stress values on platelet surfaces even in a simple shear flow case. In addition, particle tracking methods are unable to account for the effect of platelet orientation on shear stress values, as platelet that align their major axis with the flow direction experience significantly higher shear stresses than platelets that are oriented normal to the flow.

1.6 Significance of this Study

To date, most studies have been very limited in determining blood damage in flows through bileaflet mechanical heart valves. Experimentally, studies are mostly limited to only capturing two-dimensional flow fields. As numerical studies have shown the highly three-dimensional nature of pulsatile BMHV flows, this 2D characterization is not sufficient for accurately capturing the flow fields or the potential for platelet damage. In addition, these experimental studies are of low spatiotemporal resolution, which can significantly reduce the accuracy of data when capturing high Reynolds number and potentially turbulent flows. These studies are also unable to capture near-valve flows due to optical barriers, thus missing important details from leaflet-valve opening and closing, as well as near-leaflet leakage flows where significant blood damage could occur. Although some experimental studies have examined hinge flows, these flow fields are again limited to two-dimensional views, low spatiotemporal resolution, and optical barriers from the leaflets. Blood damage experiments are able to quantify damage incurred in BMHV flows, but only result in bulk damage values with an inability to pinpoint exactly how damage occurs in valvular flows.

Numerical studies have advantages in modeling three-dimensional flow fields, but are mostly limited due to the expenses of modeling these high spatiotemporal resolution flows. Due to the high Reynolds number at peak flow past BMHVs, very high spatiotemporal resolution is required to capture the chaotic, disorganized, and potentially turbulent flows. In order to save expenses, computational studies include limitations such as: steady flow fields, non-moving leaflets, forward flow only, particle tracking, single-phase flow fields, two-dimensionality, etc. Many of these limitations have been overcome due to improved computational performance. However, studies have yet to be performed to characterize three-dimensional, truly multi-phase, pulsatile BMHV flows with high spatiotemporal resolution, leaflet motion, and accurate platelet damage modeling. An efficient, parallelized, multi-scale, and multiphase flow model is required in order to model these types of BMHV flows.

The objective of this dissertation is to model pulsatile flow through a BMHV with the inclusion of realistically modeled suspended platelets for accurately tracking platelet damage. These simulations will employ heretofore-unseen high spatiotemporal resolution in modeling the entire pulsatile BMHV flow, including high Reynolds number flows and leaflet motion. The released suspended platelets will have finite volume and finely meshed surfaces for accurately tracking surface shear stresses through accurate fluid-solid interaction forces. These simulations will include two-way flow as well as accurately capturing leaflet opening and closing motion, leaflet-valve impact upon closing, and diastolic leakage flow through the b-datum line. Platelet damage can be tracked to determine bulk average damage values as well as highlighting individual

platelets that may incur abnormally high damage. This can be related to flow field visualization to connect BMHV flow with blood damage.

The numerical method is first validated as suitable for modeling suspension flow by comparison to fundamental suspension flow cases. The method is then tested for efficient parallel processing using Message Passing Interface (MPI) protocol. Next, the method is validated as being suitable for modeling BMHV flows by comparing with experimental data for BMHV flows. After validation, simulations are performed to model pulsatile suspension flows through a BMHV. These simulations will employ suspended realistic platelets for accurately tracking damage. As these simulations will track individual platelet paths and damage, it will be possible to draw broad conclusions on the effect of BMHV flow fields on platelet damage, determine specific regions and times of highest damage, and pinpoint specific platelet paths that can incur dangerous levels of damage. Finally, after an in-depth analysis of platelet damage in standard flow through BMHVs, the numerical method will be used in a novel application of determining platelet damage in pediatric flow cases, which are not well understood.

Though these results will greatly aid in understanding blood damage in BMHV flows, this study can also be used as a linking step for future computational evaluation of prosthetic devices. The numerical method employed in this study is generic and can be extended to simulate multiphase particulate pulsatile flow through a variety of other prosthetic valve devices to track shear stress and evaluate blood damage performance. Realistically modeled particles can be used in these future studies to accurately assess blood damage incurred in flows through a wide variety of cardiovascular devices. This numerical method can be used to save expenses in experimental or clinical tests of novel

or existing designs, and ultimately be used to optimize device designs and reduce life-threatening complications.

CHAPTER 2

HYPOTHESIS AND SPECIFIC AIMS

Bileaflet mechanical heart valves (BMHVs) have been used for the past three decades as a suitable replacement for diseased native valves due to better hemodynamics, flow characteristics and blood damage performance than earlier-generation mechanical valves. However, trauma to blood elements and thromboembolic events still remain one of the major complications of BMHV designs. These significant problems have been linked to blood damage caused by non-physiological stresses on blood elements. This damage is also associated with complex flow fields that arise due to BMHV design. In order to reduce the severity of these complications, the blood damage that occurs due to flows through BMHVs must be well understood. Improving design and ultimately reducing the severe complications associated with BMHV flows requires accurate knowledge of the flow dynamics and the quantification of blood damage.

The overall objective of the on-going research is: **Perform computational modeling of flows through prosthetic cardiovascular devices to understand how blood damage occurs in a variety of designs and physiologic and patho-physiologic flow conditions.**

The hypothesis of this study is: **A suspension flow numerical solver can be used to assess blood damage in pulsatile flows through a bileaflet mechanical heart valve for different physiological flow conditions.**

This hypothesis will be evaluated by pursuing the following specific aims:

Aim 1: Develop a high performance, parallel suspension flow method using the lattice-Boltzmann method with external boundary force (LBM-EBF) for the accurate and efficient simulation of suspension flows with sub-grid resolution

Computational simulations can give unprecedented detail on 3D flow dynamics associated with prosthetic heart valves that would not be possible with experimental techniques. The LBM-EBF method was originally developed by Wu and Aidun [66] for shared memory processor modeling of suspension flow. As modeling suspension flows through complete BMHV geometries is computationally expensive, a distributed memory parallel version of the LBM-EBF method is required for use in computational clusters.

This parallelized method, which will be implemented using Message Passing Interface (MPI) parallelization protocol, will allow for efficient and accurate modeling of a wide variety of suspension flows. The parallelized LBM-EBF method will be tested for exactness in matching single-core vs. parallel processor modeling, as well as testing accuracy in modeling fundamental suspension flow cases. Finally, its scaling efficiency in parallel processing will be analyzed. The implementation of a high Reynolds number flow modeler, called Entropic Lattice-Boltzmann (ELB), will also be analyzed. This method can be applied to simulations of pulsatile suspension flows through BMHVs with blood damage quantification using sub-grid resolution. Implementing a parallelized method will allow for the fluid phase to be resolved with high enough spatiotemporal resolution to capture turbulent fluctuations in the pulsatile flow field. In addition, realistically modeled platelets with finite volume and surface meshes can be suspended in the flow to accurately track the shear damage.

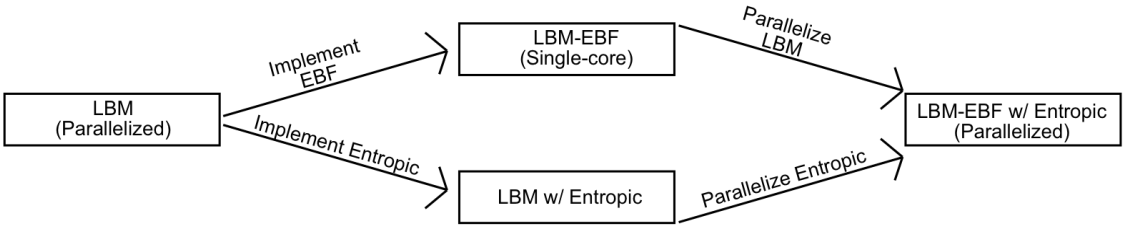

Figure 2-1: Flowchart showing major coding steps required to complete Specific Aim 1

Aim 2: Validate the lattice-Boltzmann method as suitable for modeling pulsatile BMHV flows by comparison against previous experimental data

The LBM-EBF method will be validated for use in this research by comparing against previous studies on BMHV flows. The LBM-EBF method will simulate single-phase flow through a BMHV. The numerical results will be compared quantitatively to steady flow experimental data [55], followed by a comparison to pulsatile experimental flow data [52]. The numerical method has previously been employed to simulate suspension flows through BMHV hinges and hinge-like regions, as in the experimental and numerical studies by Simon *et al.* [43, 62] and Fallon [67]. The LBM-EBF method was validated in a previous study as suitable for quantifying platelet damage through comparison to blood damage experiments.

In order to numerically model BMHV flows, customized coding must be implemented. This includes the implementation of a prescribed flow inlet boundary condition, and an artificial outflow boundary condition. Leaflet motion and pulsatile flow conditions must also be implemented. Finally, two-way fluid-structure interaction (FSI) modeling of leaflet motion will be implemented and simulated using experimental *in vitro* flow conditions. The complicated flow physics will be explored in unprecedented detail from the results of the numerical simulations.

Aim 3: Simulate pulsatile suspension flow through a bileaflet mechanical heart valve with adult flow conditions

Pulsatile suspension flow through BMHVs will be simulated and platelet damage will be quantified for a SJM Regents™ 23mm valve. A baseline case of physiologic adult flow conditions will be simulated. Thousands of suspended platelets will be released to closely examine how, where, and when blood damage occurs.

The simulations will provide data on average platelet damage occurring in various bulk regions of BMHV flow. Eulerian views will also be employed to determine the evolution of platelet damage in small regions over time. The numerical method can track the full temporal history of damage incurred by individual platelets. Lagrangian platelet tracking will be performed to highlight platelet trajectories that incur abnormally high amounts of damage. These quantitative damage results can be associated directly with pulsatile flow field visualization. This will provide better understanding of how complicated BMHV flow fields may lead to increased blood damage and thromboembolic complications.

Aim 4: Assess bileaflet mechanical heart valve fluid mechanic performance for pediatric applications

The LBM-EBF method will be used to predict the blood damage performance of BMHVs in a novel manner. Pediatric sized BMHVs currently do not have FDA approval and have not been studied in detail. Physiologic values will be used to model pediatric flows through BMHVs, with appropriate sizing and flow conditions. These pediatric flow cases

will be simulated to determine how flow fields differ from baseline adult BMHV flows. In addition, blood damage modeling will be performed similar to Specific Aim 3 to highlight the potential complications of pediatric BMHV flows. This can be used to observe similarities in damage patterns between pediatric and adult flow cases, or highlight new dangers associated with pediatric cases that are not present for normal adult patients. These results will assess the potential performance of BMHVs for the pediatric population in a predictive manner, and may help to push for eventual FDA approval for these devices.

This research will be the first use of the LBM-EBF method to evaluate novel scenarios regarding blood damage and prosthetic devices, serving as a linking step to future applications of the numerical tool.

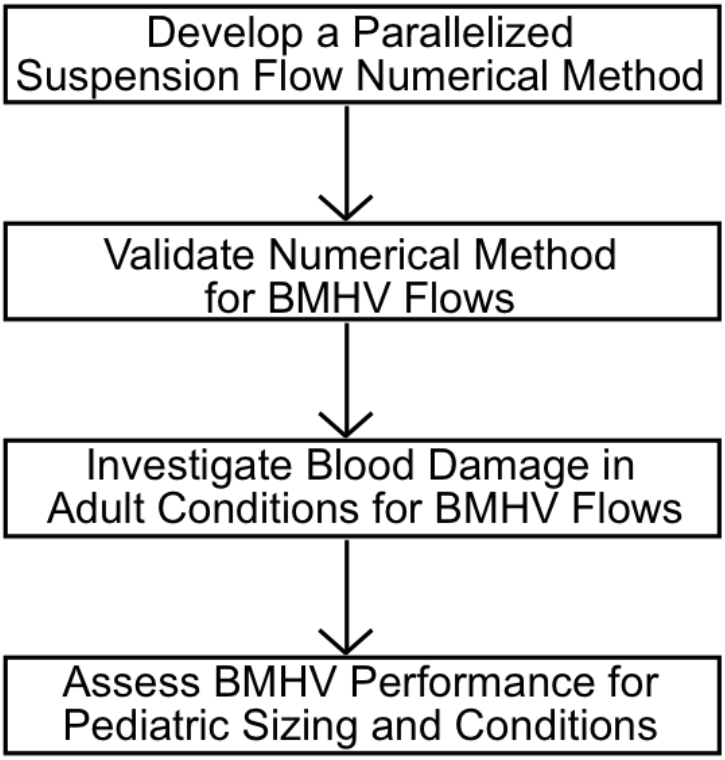

Figure 2-2: Flowchart showing research study progress in specific aims 1 – 4

CHAPTER 3

METHODS

In this chapter, the numerical methods employed in this study are described. This chapter is divided into two primary categories: the numerical methodology is presented as a generic suspension flow modeling method, and a description of the specific problem of this study is given with details of the numerical setup and corresponding experimental setup. The details of the experimental study are brief, as it is not the focus of this research and is used for validation purposes.

The numerical flow methodology is based on the lattice-Boltzmann method (LBM), specifically an extension of the methodology described by Aidun *et al.* [68-70]. The methodology has been expanded in previous research efforts to three-dimensional flow simulations with suspended particles and parallel computing. Fluid-solid interaction with large, stationary surfaces such as pipe walls is derived from the lattice-Boltzmann standard bounce-back (SBB) methodology as described by Aidun *et al.* [68-70] and MacMeccan *et al.* [71]. A more efficient and subgrid resolution External Boundary Force (EBF) fluid-solid interaction method, as first described by Wu and Aidun [66], is added to the numerical methodology for small suspended particles. Finally, a modification to the lattice-Boltzmann method to allow for very high Reynolds number flow simulations is implemented by the entropic lattice-Boltzmann (ELB) method [72]. These numerical methodologies have been extensively validated in the cited previous studies with a variety of single-phase flow simulations as well as suspended particle flow validation simulations.

The *in vitro* experimental methodology that is computationally recreated in this work is described, as well as the validation steps for the numerical methodology and for comparison between simulations and experiments. The methodology for quantifying blood element (specifically, platelet) damage is covered in detail. Modifications to the numerical setup for customization to the problem of this study are also given. Finally, the chapter ends with the parallelization protocol of this full numerical methodology, which is needed to perform the high-resolution simulations of this study.

3.1 LBM-EBF Overview

The lattice-Boltzmann method (LBM) is a fluid flow solver that uses local, linear calculations and is optimal for high performance parallel computing. The motion and orientation of solid particles in suspension flow are determined in this study using simple Newtonian dynamics equations for linear and angular momentum. The interaction between the fluid and wall surfaces is computed using the standard bounce-back (SBB) method. The interaction between the fluid and suspended solid particles is computed using the external boundary force (EBF) method. The lattice-Boltzmann method combined with the external boundary force method is a novel suspension flow modeling methodology.

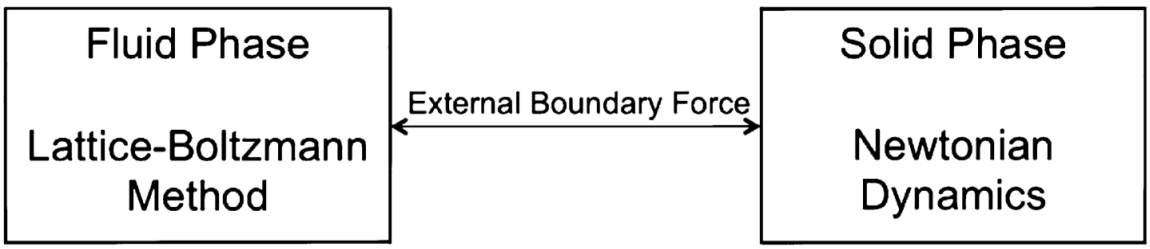

Figure 3-1: Numerical method overview for two-way fluid-structure interaction

The LBM-EBF method provides a significant advantage over other suspension flow modeling methods (such as LBM-SBB) by using separate spatial resolution scales for the fluid and solid phases [66, 71]. This means that LBM-EBF can model very small particles such as platelets without the need for a fluid grid with the same spatial resolution. The LBM-SBB method, in comparison, must have solid and fluid grid resolution of the same relative length scales. This multiscaling ability of LBM-EBF significantly lowers computational cost while still providing highly accurate results. The accuracy of LBM-EBF with multiscaling is demonstrated in sections 4.1.2.3-6 of this study as well as in a previously published study [63].

In addition, the LBM-EBF method models real particles with a meshed surface and volume, allowing for the accurate calculation of shear stress on a particle surface. This ability to calculate shear stress accurately is important in determining particle damage caused by the shear stresses. The ability of the LBM-EBF method to model real particles is a significant advantage over previous computational studies of platelet activation which have assumed the platelets to be point particles with no surface or volume [10, 60, 62, 63]. The more accurate modeling of the platelet particles in the LBM-EBF method allows for a higher accuracy calculation of platelet trajectory and shear damage. Thus, the parallel computing, multiscaling, and real particle modeling abilities of the LBM-EBF method make it optimal for simulations of blood damage and platelet activation.

3.2 Numerical Flow Solver

In this thesis, an initial in-house code for LBM-SBB suspension flow modeling with parallel computation capabilities is used as a starting point in code development.

The numerical methodology features added in the work of this thesis are the inclusion of: the EBF method, the entropic LB method, customized BMHV flow coding, artificial outflow conditions, and interpolated bounce-back conditions. In addition, these added features are all parallelized in the work of this thesis for use in optimal high performance cluster computing.

3.2.1 Lattice-Boltzmann Method

The lattice-Boltzmann method (LBM) is a direct numerical simulation method used for solving fluid flow. It is rooted in kinetic gas theory, derived from the Boltzmann equation for describing statistical behavior of gas particle kinetics. The LBM is based on solving simplified microscopic or mesoscopic kinetic equations, which are derived such that the resulting averaged macroscopic properties obey desired macroscopic equations. In this way, the LBM avoids solving complicated macroscopic continuum equations (the Navier-Stokes equations) and instead models simpler microscopic kinetic equations. The solution of the simpler microscopic kinetic equations converges to the solution of the macroscopic Navier-Stokes equations. Though the LBM is based on gas particle behavior, the end result of using LBM is to obtain averaged macroscopic behavior of the fluid. By modeling kinetic equations, LBM avoids many of the complications and limitations associated with continuum equation discretization and solution.

In addition to its simplicity, LBM has become very popular due to recent advancements in parallel processing and cluster computing. The localized and simple nature of kinetic gas equations that are solved for LBM modeling is straightforward and optimal for parallel computing. The use of lattice-Boltzmann method in modeling particle

suspensions in fluid has been well documented and rigorously validated [68, 69, 73-75]. Although there are several variations to LBM with the number of spatial dimensions and velocity directions, the method described by Aidun *et al*. [69, 70] and employed in this study is a three-dimensional, single-relaxation method that excludes fluid inside solid particles. Details of LBM are given in Appendix A.1.

3.2.2 Entropic Lattice-Boltzmann

The lattice-Boltzmann method described above and by Aidun *et al.* [69, 70] is well-suited for simulations of low to moderate Reynolds number flows. However, when the flow velocity or its spatial gradient becomes too large for the lattice, numerical instabilities arise in the form of negative fluid density values. These instabilities become a significant problem when simulating higher Reynolds number flows. A solution to these instabilities is the use of the entropic lattice-Boltzmann (ELB) method. The ELB method uses a discrete *H*-theorem constraint that enforces positive definiteness on the fluid distribution function values, thus removing the instabilities at higher Reynolds number flows.

The ELB method can be thought of as locally increasing the viscosity at unstable nodes in order to enforce positive definiteness to fluid distribution values. This local increase in viscosity is only performed for unstable nodes at the timestep of instability. The ELB method leads to universally stable explicit algorithms at small viscosities and high Reynolds numbers. Details on the ELB method can be found in the paper by Keating *et al*. [72] and in Appendix A.2.

The LBM is a direct numerical simulation method that recovers Navier-Stokes flows, and thus matching spatial and temporal resolutions to Kolmogorov scales will allow for LBM to model turbulent flows. The entropic LBM employed in this study has been shown to be able to capture turbulence at Reynolds numbers up to 25,000 in free-decaying turbulence simulations by matching the Kolmogorov $k^{-5/3}$ spectrum and comparing to spectral element methods [76-78]. Turbulence was captured using entropic LBM even in cases of under-resolved spatial resolutions. It should also be noted that the Kolmogorov scale calculations are not strict threshold levels, but are rather approximations of the order of magnitude of the turbulent time and length scales. Most importantly, the repeated demonstration of entropic LBM matching the Kolmogorov $k^{-5/3}$ spectrum at very high Reynolds number validates the method as appropriate for capturing turbulent flows.

3.3 Fluid-Solid Interaction Methods

The lattice-Boltzmann method is designed for fluid flow modeling, but differs from other Navier-Stokes solvers by computing microscopic particle kinetic equations. This results in a different treatment for solid surface boundary conditions, specifically no-slip boundaries. The simplest and oldest fluid-solid interaction method is the standard bounce-back (SBB) method. This method is still widely used, however alternative fluid-solid interaction (FSI) methods have been developed for increased accuracy [66, 79, 80]. These new methods are particularly useful for moving surfaces, small particles, and surfaces with irregular boundaries.

The standard boundary condition employed for wall surfaces for LBM is the

standard bounce-back (SBB) condition. This SBB method is employed in this research for fluid-solid interaction with large wall boundaries: valve walls, leaflets, flow domains. Details on the SBB fluid-solid interaction method is given in literature [74, 81, 82] and in Appendix A.3.

For large solid surfaces, such as pipe walls or large obstructions, the standard bounce-back method is suitable for fluid-solid interaction modeling. If the fluid grid resolution is sufficiently high, the SBB method can adequately interpolate the location of the large solid surface. However, for small particles that have irregular and/or deforming shape, the standard bounce-back method is insufficient. The SBB method requires a solid mesh resolution that is equal to or larger than the fluid grid resolution, due to the nature of bounce-back links that must be determined [69-71]. Thus, any sub-grid modeling of solid particles is not possible.

To avoid these problems, a novel method is employed that determines a more accurate fluid-solid interaction boundary. Instead of the traditional standard bounce-back method for fluid-solid coupling, a novel external boundary force (EBF) method developed by Wu and Aidun [66] is used. The small solid particles in the suspension use Lagrangian reference frames that move continuously through the fixed Eulerian fluid domain. The solid particle surface is mapped on the Lagrangian frame by boundary nodes, creating a mesh of surface elements. This Lagrangian frame for the solid is then mapped onto the 3D fluid domain. This method also allows for subgrid modeling, which is crucial to this research for modeling platelets with subgrid resolution.

The external boundary force (EBF) method works by enforcing the no-slip boundary condition at all solid boundary nodes. The external boundary force is the

calculated fluid-solid interaction force required to impose the no-slip boundary condition at each node in the fluid-solid boundary interface. The EBF method has been validated as second-order accurate in space and has been described in detail by Wu and Aidun [66] and in Appendix A.4.

3.4 Solid modeling

For the solid phase, the motion and orientation of small particles are obtained by solving the Newtonian dynamics equations for the total external boundary force for each particle. All solid surfaces are discretized by a mesh network of triangular elements, including both suspended particles and large domain surfaces. The small particles in this study are platelets and are modeled as rigid ellipsoids. Specific details on the platelet modeling of this study will be given in subsection 3.6.2.

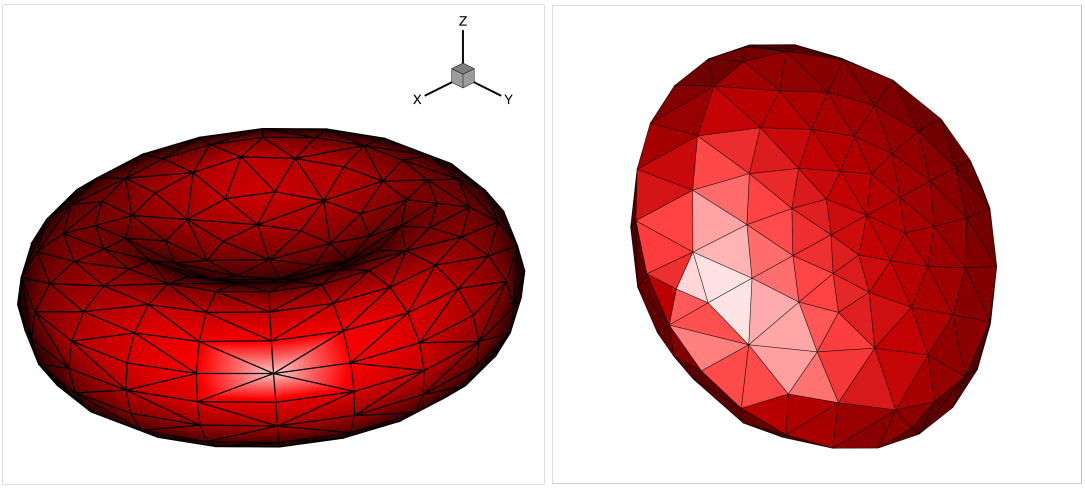

Figure 3-2: Example of red blood cell and platelet particles with surface mesh of triangular elements

The external boundary forces at each solid element are calculated, and these forces are accumulated for the entire particle. Upon determining the total particle forces, the simple Newtonian dynamics equations for linear motion are solved

$$\boldsymbol{F} = \sum_{i=1}^{n} \boldsymbol{F}(\boldsymbol{x}_i) \qquad \text{Equation 3-1}$$

$$\boldsymbol{F} = m\boldsymbol{a} \qquad \text{Equation 3-2}$$

where $\boldsymbol{F}$ is the total particle force, $\boldsymbol{F(x_i)}$ is the individual solid element force, $\boldsymbol{x_i}$ is the position vector of the solid element, m is the mass of the particle, $\boldsymbol{a}$ is the linear acceleration vector, and n is the number of solid particle elements. The 4th order accurate in time Runge-Kutta integration scheme is employed to determine the updated particle velocities and position.

At each solid boundary node, a moment arm $\vec{\boldsymbol{r}}$ is determined from the node to the particle center of mass. Thus, the total particle torque $\boldsymbol{T}$ can be accumulated by

$$\boldsymbol{T} = \sum_{i=1}^{n} \left(\vec{\boldsymbol{r}} \times \boldsymbol{F}(\boldsymbol{x}_i) \right) \qquad \text{Equation 3-3}$$

and the angular acceleration α of the particle can be determined as

$$\boldsymbol{T} = \boldsymbol{I}\,\alpha \qquad \text{Equation 3-4}$$

where $\boldsymbol{I}$ is the moment of inertia tensor of the particle. As with linear momentum, the angular velocities and position are determined using a 4th order accurate in time Runge-Kutta integration scheme.

In cases of pure rotational motion, as employed in leaflet motion modeling,

translational motion is not allowed and only the angular momentum equations are solved. The methodology is otherwise identical in the computation of forces and torques.

It should be noted that deformable particle modeling is possible for the solid phase in combination with the lattice-Boltzmann method. This deformation modeling exists in the form of linear finite element analysis coding [71] or spectrin-link based deformation modeling [83]. This is particularly useful for the inclusion of red blood cells (RBCs) in blood flow simulations. However, since this study assumes rigid platelets, rigid flow chambers, and rigid leaflets, no deformation solid modeling is required.

3.5 Experimental Setup

This computational study employs a recreation of an *in vitro* experimental setup for modeling flows through BMHVs. In addition, validation of the numerical method is performed by comparison against steady and pulsatile *in vitro* flow experiments. Thus, a brief description of the experimental setup and parameters is presented.

In vitro Particle Image Velocimetry (PIV) experiments were performed of steady flow past fully open leaflets of a 23mm SJM valve (Figures 3-3, 3-4) placed in the aortic position using a blood analog fluid [55]. An averaged 2D flow field was determined over 100-200 ensembles for various Reynolds numbers and used for validation with a different numerical method. Data was primarily used with Re=750, representing the laminar mid-acceleration phase of the cardiac cycle, and with Re=5000, representing peak flow.

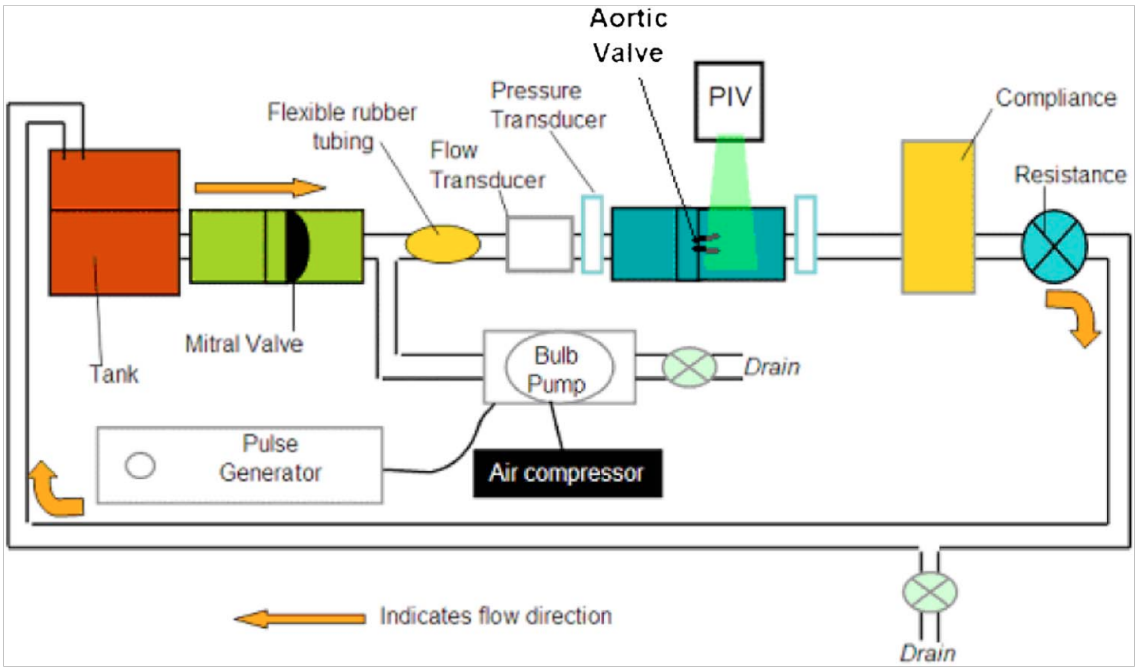

Figure 3-3: *In vitro* experimental PIV setup [52]

The same *in vitro* flow loop was used to recreate pulsatile flow through a SJM valve throughout the cardiac cycle [52]. The cardiac cycle had a period of 860 ms, corresponding to 70 beats/minute. The mean flow rate was adjusted to 4.5 L/min with a peak flow rate of 25.0 L/min and a forward flow duration of approximately 350 ms. A blood analog fluid was used that matched the kinematic viscosity of whole human blood (3.5 cSt), and was composed of 79% saturated aqueous sodium iodide, 20% glycerin, and 1% water by volume. The density of this blood analog was approximately 1620 kg/m^3, as compared to 1060 kg/m^3 for whole human blood. This was necessary to match the refractive index of the fluid to the experimental chamber for optimal visualization. Though the blood analog density does not match that of whole blood, matching kinematic viscosity was determined as most important to modeling pulsatile BMHV flows. The spatial resolution of the PIV flow data used for comparison is approximately 134µm.

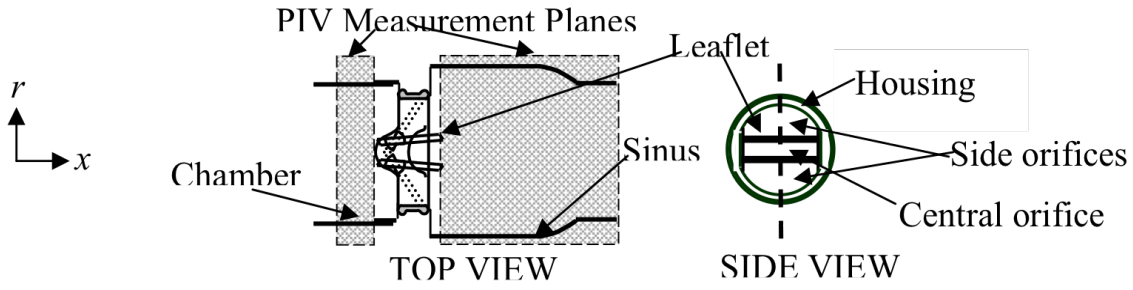

Figure 3-4: Experimental PIV setup showing perpendicular plane where 2D flow fields are determined [52]

Figure 3-4 shows a schematic of the SJM valve in the experimental flow chamber. The chamber was made of rigid straight tubes with a diameter of 25.4mm. The valve itself is a 23mm SJM valve with an inner diameter of 21.4mm. Downstream of the valve on the aortic side is a sudden axisymmetric expansion to a diameter of 31.75mm representing the aortic sinus root immediately downstream of the aortic valve. Figure 3-4 shows the longitudinal cutplanes at which PIV measurements are made, perpendicular to the leaflets and in the center of the valve in the side view. More descriptions of the experimental setup can be found in the work by Dasi *et al*. [52].

Figure 3-5 shows the ensemble-averaged flow rate, leaflet angle, and pressure measurements upstream and downstream as they vary throughout the cardiac cycle for the pulsatile flow experiments.

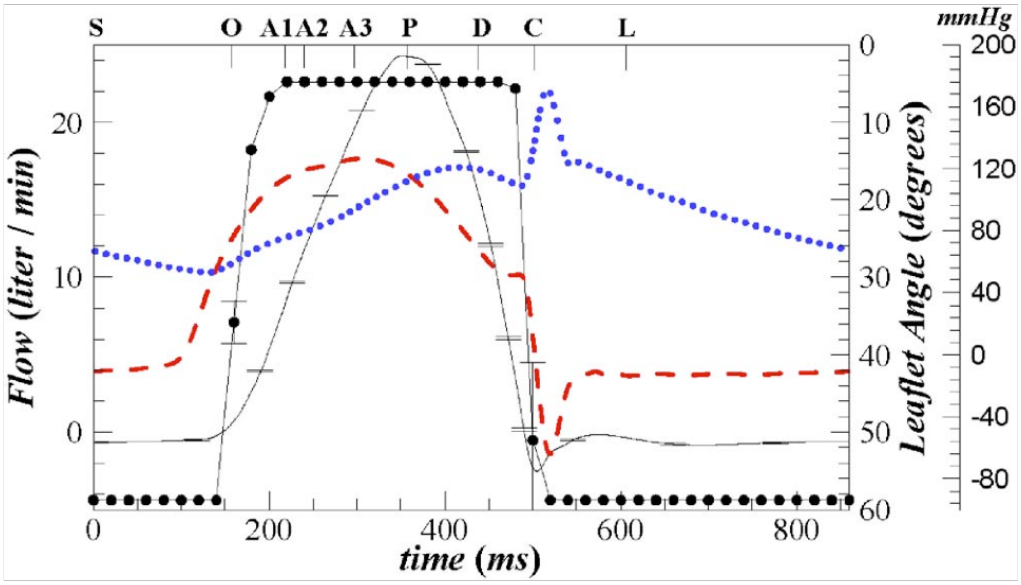

Figure 3-5: Cardiac cycle variation of flowrate (black line), leaflet motion (--•--), aortic pressure (blue dots), and ventricular pressure (red dashed lines) [52]

3.6 Numerical Setup

The simulations of this study are primarily designed around the *in vitro* experimental setup as previously described. This is particularly convenient due to the simplicity of the experimental design, whereas a realistic left ventricle – aorta geometry is difficult to recreate and introduces higher complexities in numerical modeling. For this study, the simpler experimental setup leads an easier numerical design, less expensive simulations, and results that are easier to interpret. The simple design also allows for an easier and more confident validation of the numerical method against the experiments. Though the numerical setup has some limitations compared to the experiments, the computational simulations can provide high-resolution 3D detail in the flow, track particle-based blood damage and visualize individual particle paths, and has no optical barriers in flow visualization.

3.6.1 Numerical geometry

The exact *in vitro* experimental setup is recreated computationally using micro-computed tomography (microCT) and solid modeling/meshing software. The original microCT scan was performed of the 23mm SJM valve hinge regions and leaflets. The large-scale geometry of the flow chamber and leaflets was made for an approximate 1/6th partial cut of the geometry. This partial geometry was employed in numerical hinge flow studies in order to save computational expenses [61-63]. The microCT scans were performed with varying spatial resolution: 18µm for the hinge recess, 15µm for the leaflet ears, and 21µm for the leaflets. It should be noted that the leaflet leading edges (closest to the ventricular side) were slightly cut off due to the limitations of the CURVIB numerical method used in the previous BMHV hinge studies [61, 62]. The flow chamber, being simple in design and axisymmetric, was created in Pro|Engineer using experimental schematics. Details on the microCT scanning and flow chamber geometry reconstruction can be found in the previous hinge studies [8, 61, 62].

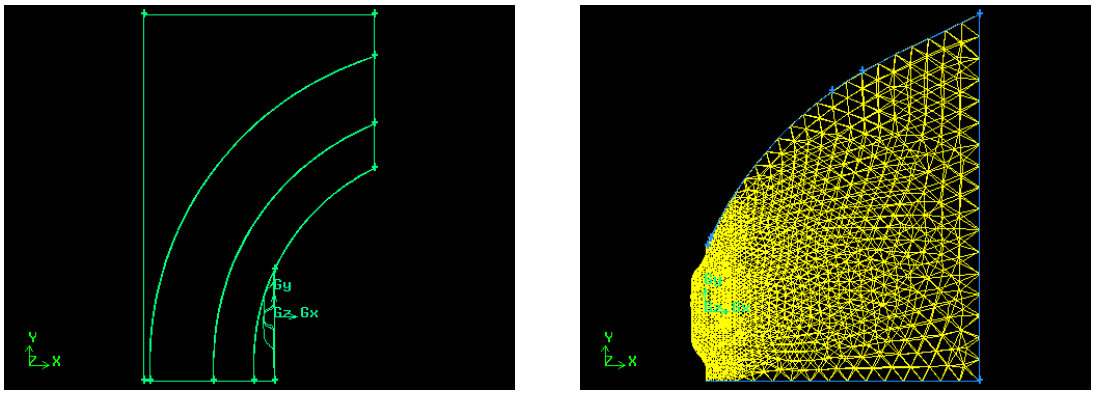

Figure 3-6: Cross-sectional view of the 1/6th partial cut of the flow chamber (left) and the leaflet geometry (right) used in previous numerical BMHV hinge studies

As the research of this dissertation involves flows through the entire BMHV domain, the full experimental setup must be reconstructed. The 1/6th geometry is first extended to a 1/4th cut geometry by extending the geometry of the flow chamber, valve, and leaflets based on their curvature. This is performed in the commercial software Gambit © and ANSYS ©. Upon extending to the 1/4th recreation of the flow chamber, the geometry is reflected across both cross-sectional axes in order to complete the recreation of the full experimental setup.

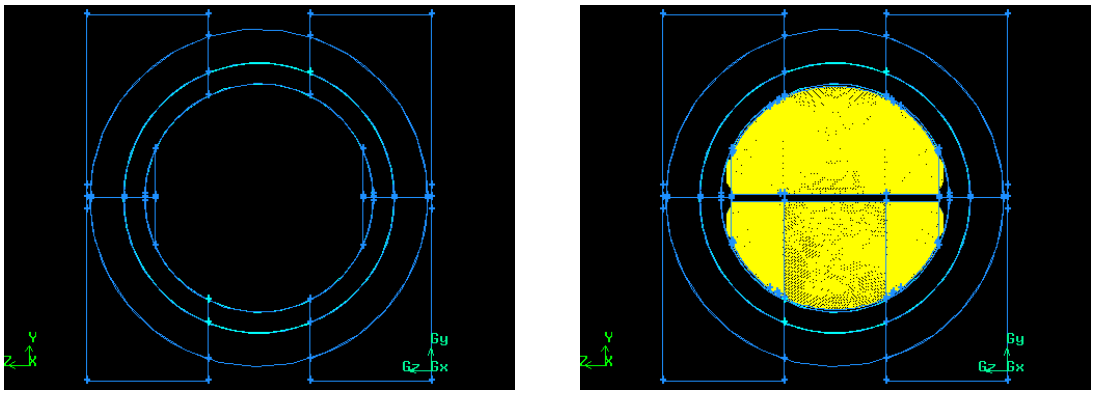

Figure 3-7: Cross-sectional view of the full flow chamber (left) and leaflet geometries within the flow chamber (right) created by extension of the partial geometries

As the geometry is reflected from the 1/4th scan, the numerical setup is perfectly symmetric across both cross-sectional axes. This is different from the real SJM valve, in which certain tolerances exist that lead to slight asymmetries in the experimental design.

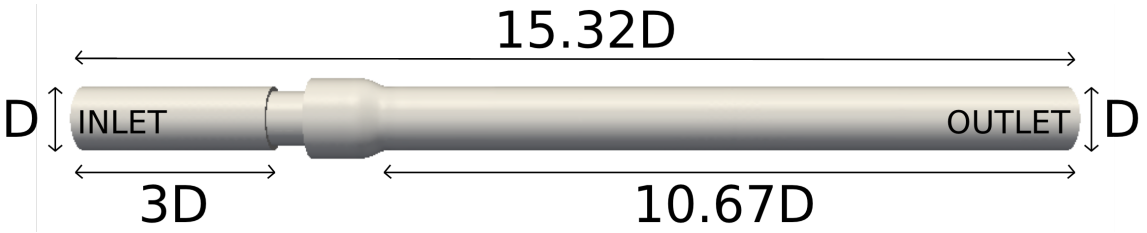

Figure 3-8: Computational recreation of *in vitro* experimental setup. Ventricular side (left) labeled as "inlet", aortic side (right) labeled as "outlet" for systolic flow convention

The fluid domain employs uniform 3D grid spacing, as is necessary with the lattice-Boltzmann method. For comparison with experiments, a spatial resolution of 160μm is employed as well as a temporal resolution of 4.8μs per numerical timestep. Although this spatial resolution is not high enough to resolve flow through the hinge regions or through the gap between the closed leaflets and the valve housing, it is sufficient to resolve the bulk flow through the valve while minimizing computational costs. In addition, the PIV flow data averages the flow features due to cycle-to-cycle variation. Thus the 160μm computational spatial resolution is deemed suitable for capturing the important bulk flow features for experimental comparison with both steady and pulsatile flow past a BMHV. Although the two gap regions are important in a complete study of BMHV flows, only the bulk flow field is of interest for this specific study. The very high temporal resolution allows for accurate direct modeling of unsteady non-periodic and turbulent flow at high Reynolds numbers with small time scales.

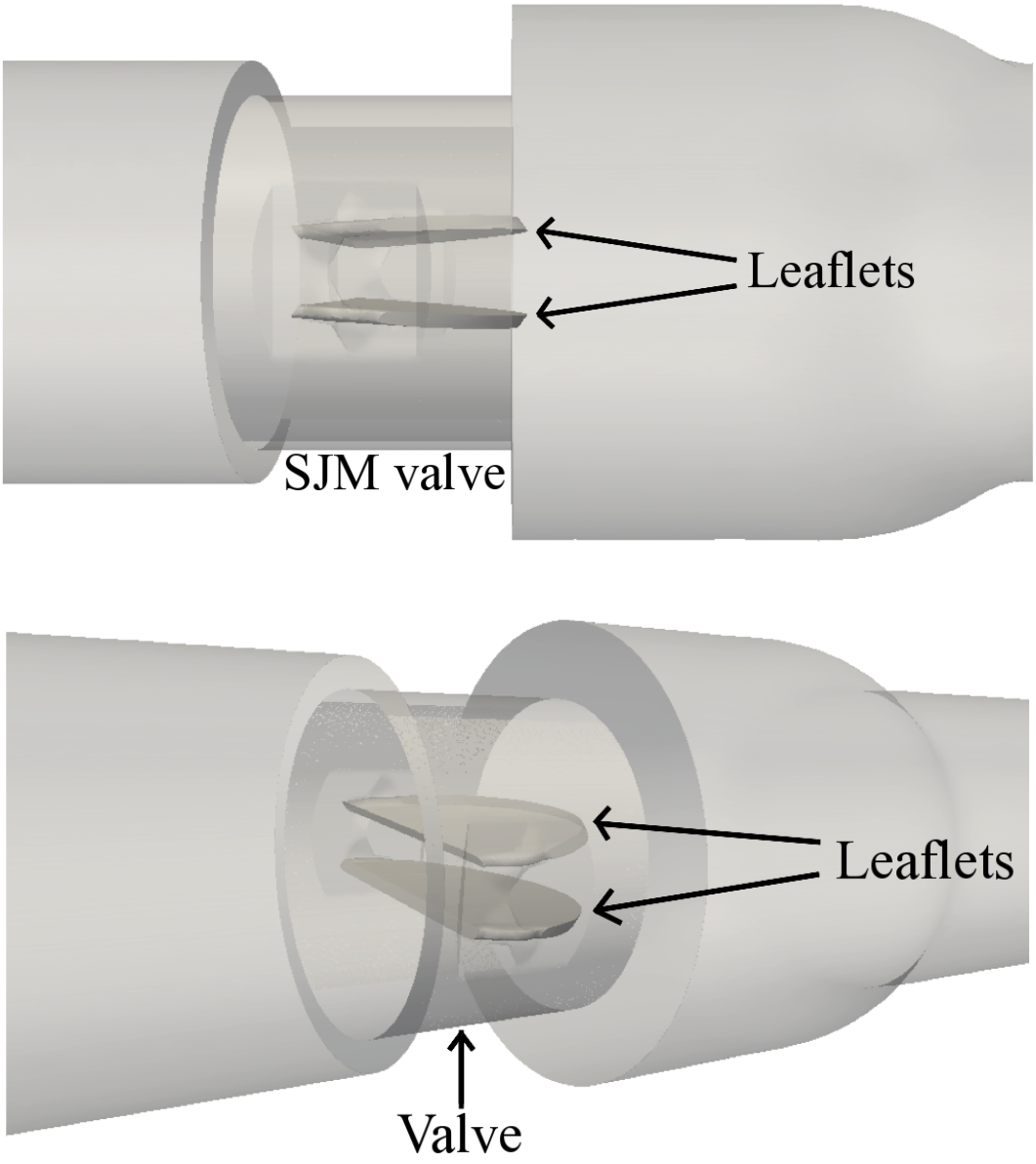

Figure 3-9: Transparent viewpoints of SJM valve with fully open leaflets, (top) perpendicular view, (bottom) angled view

For closer examination of the pulsatile flow fields and for platelet damage modeling, additional simulations are performed with a higher spatiotemporal resolution of 80μm and 2.4μs per numerical timestep. The 80μm spatial resolution is uniform throughout the entire flow domain, and to the knowledge of the author is the highest

spatial resolution for any study modeling whole BMHV flows. An in-depth analysis on whether this spatial resolution captures the smallest Kolmogorov scales in pulsatile BMHV flows is made in the section 5.5.

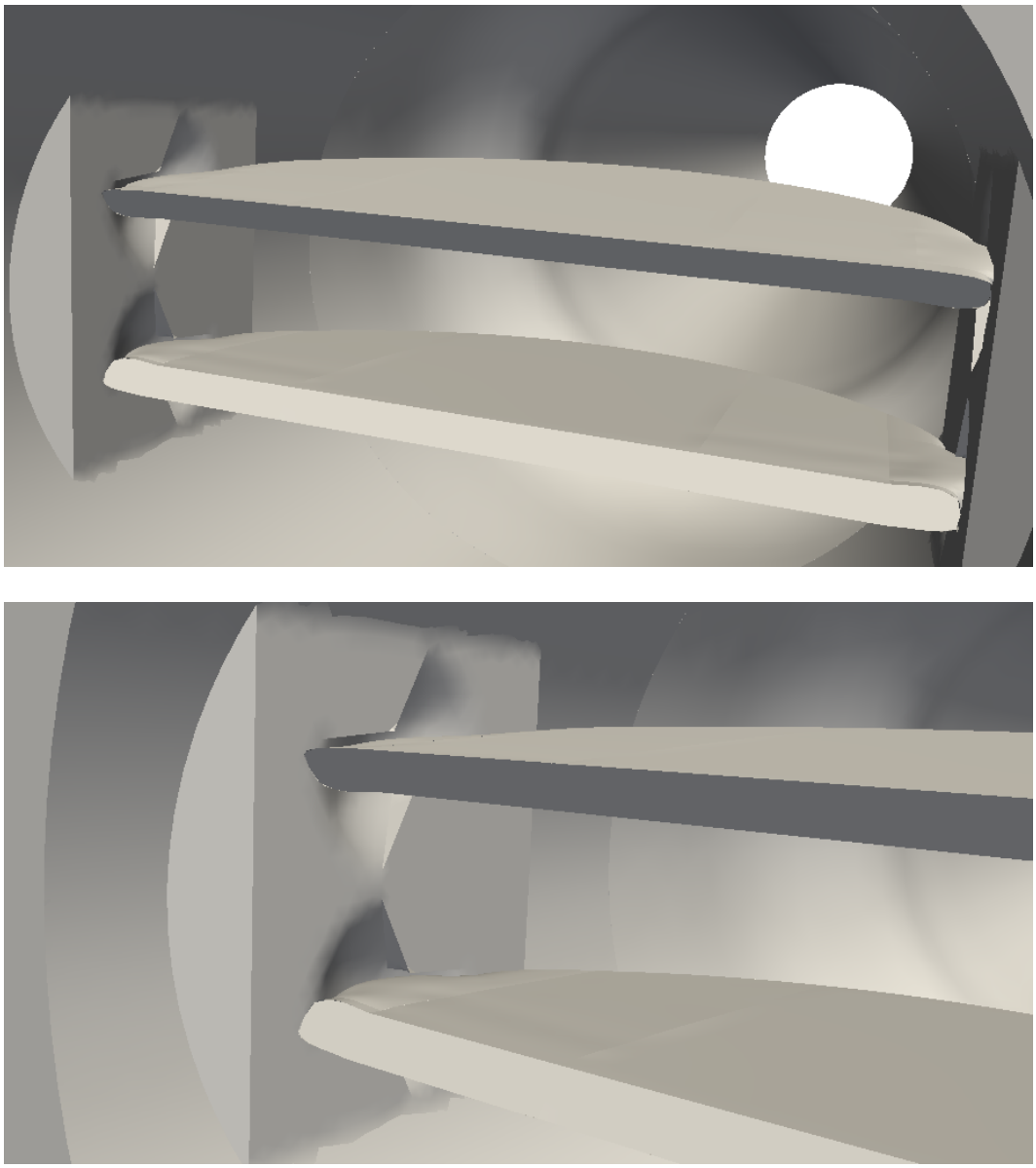

Figure 3-10: Interior view of the fully open leaflets residing in the SJM valve, showing the leaflets fitting into the butterfly hinge recess

The solid domain is meshed using Gambit© software, where the internal surface of the experimental chamber and the leaflet surfaces are discretized using an unstructured triangular mesh. This mesh is immersed into the 3D fluid domain, and only fluid nodes within the experimental chamber boundaries are used in the flow field calculations. The solid domain employs variable spatial resolution meshing, with higher resolution focused on the valve region. Geometries with complex surfaces, such as the leaflet ears or hinge recesses, employ the highest spatial resolution meshing. The ventricular inlet and aortic outlet cylinder lengths employ 320μm length grid spacing for the solid mesh. In the valve region, the grid spacing is variable from 20-40μm, with the highest resolution employed for the hinge recesses. For the leaflets, the grid spacing is variable from 20-50μm, with the highest resolution employed for the leaflet ears.

As the experimental chamber is fixed in time and the leaflets move slowly with respect to the temporal resolution of the simulations, the SBB method is employed for fluid-solid interaction with these "large" surfaces. In this study, "large" surfaces or particles are defined as structures that span across multiple flow subdomains, such as flow chambers or leaflets. This is in comparison to "small" particles such as suspended platelets, which are small compared to flow subdomain sizes. The inaccuracies of the SBB method to determine the fluid-solid interaction boundary are reduced by the large size of these surfaces in comparison to the high spatial resolution of the fluid domain. These surfaces are not irregular and are mostly circular in nature, thus creating a smooth curvature that is sufficiently interpolated by the high fluid domain spatial resolution. Thus, the inaccuracies of the SBB method are reduced for large, smooth curvature surfaces when running high spatial resolution simulations.

Though inaccuracies still exist, there are also advantages for employing the standard bounce-back method for large surfaces. Non-moving surfaces need only to determine bounce-back links once, as these link locations never change for a fixed surface. Only updated fluid distributions at these links need to be determined for fluid-solid interaction. For slow-moving surfaces, solid position may be updated at timestep intervals and not for every timestep. In these cases, the link locations only need to be updated at these timestep intervals, further reducing computational costs. For a higher accuracy FSI method, such as the EBF method, interpolation of fluid distribution values within a radius of two grid nodes must be performed at each solid node for every timestep. This can be very expensive with only a limited increase in FSI accuracy. Thus, for saving significant computational expenses while still maintaining good accuracy of fluid-solid interaction, the SBB method is employed for large solid surfaces.

3.6.2 Suspension flow modeling

For this study, whole human blood is modeled computationally as an incompressible Newtonian fluid, with the same kinematic viscosity as blood (3.5 cSt) and the same density (1060 kg/m^3). For comparison against experiments, the fluid is modeled with the same physical properties of the blood analog solution that was used in experiments. The kinematic viscosity of the blood analog solution is 3.5 cSt, and the density is 1620 kg/m^3. Though blood is a non-Newtonian fluid due to the presence of red blood cells, computational resource limitations do not allow for the modeling of realistic hematocrit levels with red blood cells in such a large flow domain. Thus, blood is

computationally modeled as a Newtonian fluid, which is a common assumption in numerical models of blood flow.

It should be noted that blood kinematic viscosity approaches an asymptotic level of 3.5 cSt at higher shear rates. As pulsatile flow through an aortic valve involves higher shear rates, this approximation of blood as a Newtonian fluid is adequate for this study. The computational matching of blood kinematic viscosity and modeling as a Newtonian fluid was deemed suitable when validating the numerical method of this study against experimental blood damage studies [65].

Though red blood cells are not included in this study, suspended platelets are released in the pulsatile flow. Platelets are modeled as rigid ellipsoids, with a major axis diameter of 3μm and minor axis diameter of 1.33μm. Though this platelet size is significantly smaller than the fluid grid 80μm resolution, the EBF method allows for accurate subgrid modeling for solid particles. The subgrid modeling capabilities of the EBF method were also employed in a previous numerical blood damage study for BMHV hinge flows [63]. This subgrid modeling accuracy with the EBF method will be discussed in the sections 4.1.2.3 and 4.1.2.6.

Modeled platelets were created in the commercial software ANSYS © with a mesh of triangular elements. The platelet surface is meshed with 148 nodes and 292 surface elements. An alternate mesh was generated with 450 nodes and 896 elements, but the computational expenses associated with this mesh were substantially higher and did not significantly alter platelet trajectory or shear stress modeling. Thus, the coarser platelet mesh is used in this study to save computational expense while maintaining

platelet modeling accuracy. The validation cases for platelet modeling shown in section 4.1.2 use this coarser mesh with highly accurate results.

As platelets have approximately the same density as whole blood [84], the suspended platelets are modeled as neutrally buoyant in the base blood fluid. This gives a mass value of 0.0531 nanograms. The moments of inertia were also computed based on mass and radii values of the platelets and used for solid motion and orientation modeling. As platelets were modeled as rigid ellipsoids, forces and torques were computed for each platelet using the EBF method and the Newtonian dynamics equations for rigid particles were solved to determine updated positions, velocities, and orientations.

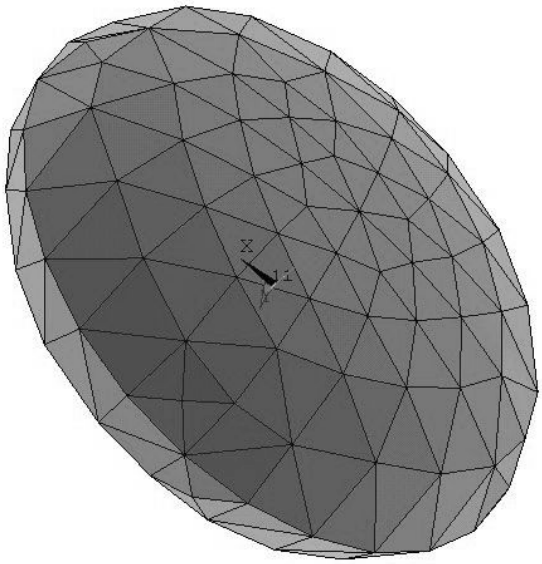

Figure 3-11: Meshed surface of a platelet, 148 nodes and 292 elements

Platelets are released in the pulsatile BMHV flow for tracking paths and damage at various regions and times of the cardiac cycle. Though platelets have less than 0.5% volume fraction in blood flow, the large flow domain of this study prohibits a realistic number of platelets to be simulated. For a fluid grid resolution of 80μm, 409 platelets

would have to be released within just one fluid grid cube to match realistic volume fraction. Though this level of blood modeling cannot be simulated with current available computational resources, the LBM-EBF method can still release thousands of platelets within the pulsatile flow for representative values of platelet paths and damage accumulation.

When releasing the platelets within the flow, a rectangular prism or cylindrical volume is first selected as the region of interest for modeling suspended platelets. The platelets are then "seeded" within this region with randomized positions and orientation angles. Multiple volumes can be selected for platelet release at any point in the cardiac cycle. After seeding, the platelets are initialized with a particle velocity that is interpolated from neighboring fluid node velocities. This is performed so the released platelets are initially advecting with the flow and do not experience high initial fluid-solid interaction forces upon release.

Though the EBF method allows for two-way FSI modeling for suspended particles, the platelets in this study only experience one-way fluid-to-solid interaction forces. This is employed to save significant computational costs for particle modeling. In addition, it is determined through preliminary simulations that employing two-way FSI modeling does not significantly affect the bulk fluid flow. The platelets are found to passively advect in the flow field even using two-way FSI modeling. It is also noted in Biofluids literature that platelets do not significantly affect blood flow hemodynamics [20], and thus this one-way FSI modeling is appropriate.

As shear stresses are important to modeling platelet damage, it is necessary to track shear stresses on the suspended platelets. The platelets are already discretized by a

surface mesh of triangular elements. The center location of each triangular element is the boundary node that is used for fluid-solid interaction modeling with the EBF method. From the EBF method, each solid boundary node experiences an individual FSI force contribution. This force contribution is given in Cartesian vector form and associated with a single mesh element. For each triangular element, normal and tangential vectors to the element can be determined. Thus, the FSI force vector can be translated from Cartesian form into normal and shear force components. As the surface element area is known at each timestep, the shear force can be divided by the element area in order to calculate the shear stress on the element. Thus, from FSI forces on the platelet mesh, one can determine shear stress values across the entire meshed surface.

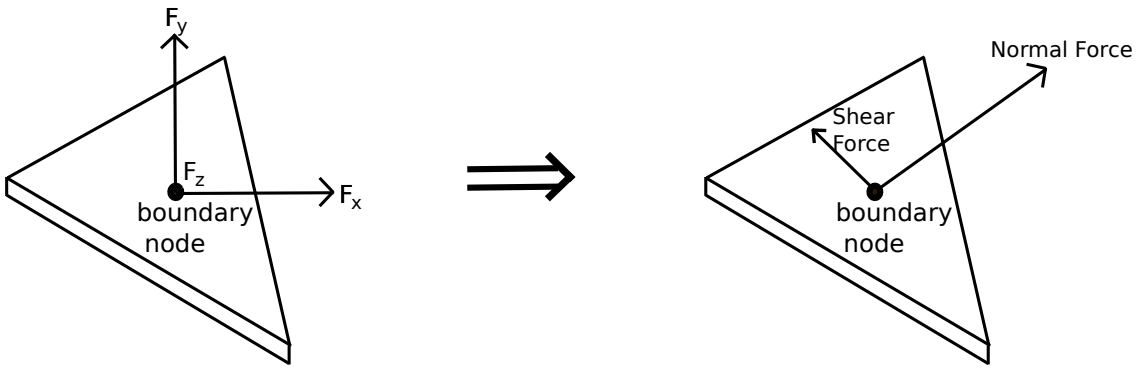

Figure 3-12: Conversion of Cartesian forces to normal and shear forces on solid surface element

3.6.3 Inflow and Outflow conditions

The conventions of this section are for systolic flow through the aortic valve; the ventricular side will be labeled the “inlet” and the aortic side will be called the “outlet”. For these simulations, we define the Womersley number (Wn) as

$$\mathrm{Wn} = \sqrt{\frac{\omega R^2}{\nu}} \qquad \text{Equation 3-5}$$

where ω is the angular frequency of the pulsatile flow, R is the pipe radius, and ν is the kinematic viscosity. The bulk flow Reynolds number (Re) is defined as

$$\mathrm{Re} = \frac{U_{avg} D}{\nu} \qquad \text{Equation 3-6}$$

where U_{avg} is the average velocity at the inlet based on experimental flowrate data, D is the inlet diameter, and ν is the kinematic viscosity. From the flowrate and cardiac cycle data taken from experiments, the Womersley number is Wn = 18. The peak flow Reynolds number is Re = 5779. These values are computed by a cardiac cycle period of 860ms, an inlet diameter of 0.0254m, and a kinematic viscosity of 3.5 cSt.

At the inlet of the domain (ventricular side), an incoming flowrate is prescribed based on the time-varying flowrate curve data from the experimental study (Figure 3-5). The flow field in the valve region is not very sensitive to the inlet flow profile because the inlet is sufficiently far away from the valve. Nonetheless, because the Womersley number is high for the cardiac cycle (Wn = 18), a plug flow inlet profile is prescribed for pulsatile flows. For cases of steady flow validation against experiments, a fully developed Poiseuille flow profile is prescribed at the inlet.

At the outlet of the domain (aortic side), a stress-free boundary condition is applied, as defined by

$$\frac{\partial u_x}{\partial x} = 0 \quad \text{at} \quad x = x_{\max} \qquad \text{Equation 3-7}$$

This boundary condition is artificial when modeling higher Reynolds number flows, as the flow field is not stress-free for high Reynolds number flows, even far downstream of

the valve. However, this outlet condition is necessary due to the finite length domain of the simulations. In order to reduce the effects on the interior fluid flow in the region of interest, the outlet of the domain is extended in length before the stress free boundary condition is applied. The stress-free outlet condition and prescribed flowrate inlet condition are discussed by Aidun *et al.* [69] and in Appendix A.7.1. Other artificial outflow conditions for LBM are discussed in Appendix A.7.2.

3.6.4 BMHV Flow Modeling

The LBM-EBF method, entropic LBM, solid phase modeling, and boundary conditions previously described may be applied to a wide variety of single-phase or suspension flow problems. However, for simulations of flow through BMHVs, some customized coding is required. These are related to the pulsatile nature of BMHV flow, the rotational motion of the leaflets, and the *in vitro* flow chamber domain.

3.6.4.1 Flow initialization

For modeling flow through BMHVs, the flow field is first initialized by steadily increasing the Reynolds number until peak flow is reached. For steady flow, the peak flow is at Re = 5000, and for pulsatile flow the peak flow is at Re = 5779. This slow initialization of the flow to the "worst-case" scenario of peak flow is performed to ensure that all high Reynolds number fluctuations can be modeled without instabilities or numerical errors. Attempts to rapidly initialize from zero Reynolds number to peak flow result in simulation errors in the form of large numerical instabilities.

The Reynolds number is increased in a stepwise manner by maintaining the same inlet flowrate but decreasing the kinematic viscosity. This is performed in LBM by first initializing the flow field for a base relaxation parameter τ value (which is directly related to kinematic viscosity). Then, the relaxation value τ is decreased by a step, thus decreasing viscosity and increasing Reynolds number. After the flow field is sufficiently converged, τ is decreased again and the steps are repeated until peak flow is reached.

For pulsatile flow simulations, after the flow field is initialized to peak Reynolds number, an entire cardiac cycle is simulated in order to remove all initialization effects. After this, multiple cardiac cycles are simulated for pulsatile flow and results are obtained. It is discovered that for each cardiac cycle, the flow washout during diastole is significant enough to make the flow fields qualitatively very similar from cycle to cycle. No discernable flow feature differences are noted from cycle to cycle and thus most results of this study only present flow fields from one cardiac cycle. The cardiac cycle displayed in the results is generally the second cardiac cycle of the simulations.

3.6.4.2 Pulsatile Flow Modeling

For the *in vitro* experiments, the maximum Reynolds number of the cardiac cycle is $Re_f = 5779$. The pulsatile flow simulations also include leakage reverse flow during the diastolic phase. The leaflet motion is either prescribed from experimental data or modeled using two-way FSI. Details on the leaflet motion methodology are described in section 3.6.4.3. Figure 3-13 shows phase-averaged leaflet motion and flowrate variation throughout the cardiac cycle from experimental data. Flowrate data is taken from a flow probe located several diameters upstream of the valve, and leaflet angle variation is

tracked via high-speed cameras. Leaflet angle is defined with zero degrees being parallel to the axial direction.

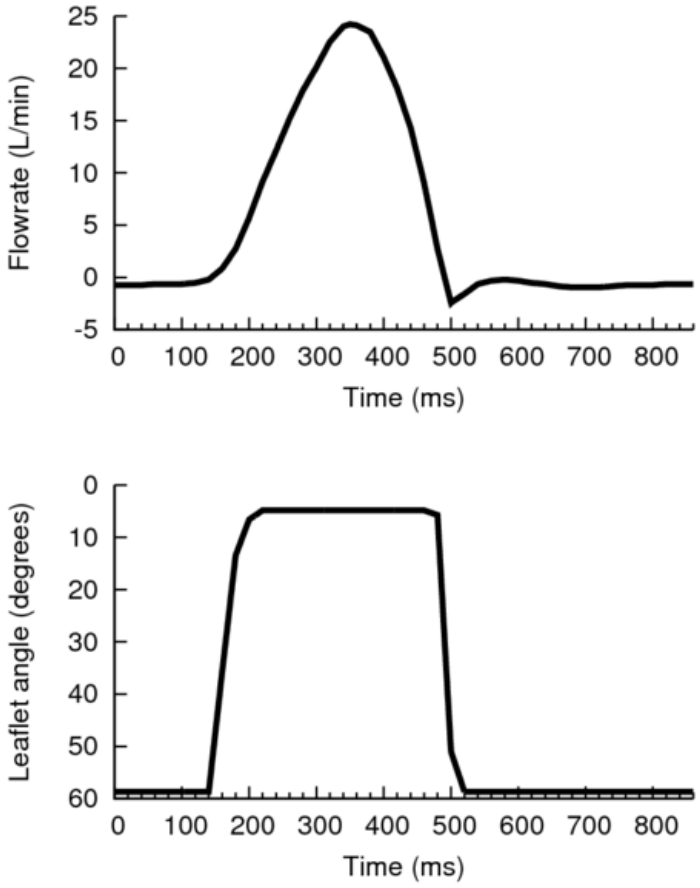

Figure 3-13: Flowrate and leaflet angle variation for one cardiac cycle taken from experimental data [52]. Zero degrees for leaflet angle is parallel to the axial direction

As the LBM is an explicit time-marching computational flow methodology, no sub-iteration loops are used. Though this might be an issue if the temporal resolution is low, the simulations of this study employ very high temporal resolution (2.4 – 4.8 μs per timestep). It is found in the pulsatile flow simulations that even with the explicit time-marching methodology, flowrates at cross-sections throughout the BMHV flow domain

are consistently within 1% of each other. This is found even in cases of high flowrate variation in the cardiac cycle, and thus no additional sub-iteration flow convergence steps are required.

During the diastolic phase when the flowrate becomes negative, the inlet and outlet boundary conditions are switched, allowing two-way pulsatile flow. Thus, the aortic side becomes the prescribed flowrate inlet condition and the ventricular side becomes the stress-free outlet condition for diastolic flow. This allows the numerical method to accurately model the flow field during the leaflet closing phase, leaflet-to-valve closing impact, and diastolic reverse flow with fully closed leaflets.

No flow instabilities are found with this switching of boundary conditions to enable two-way flow. The high temporal resolution of the simulations results in near-zero flowrates when the boundary conditions are switched from forward to reverse flow (or vice-versa), and thus flow fluctuation issues at the inlet and outlet boundaries are minimized. In addition, the LBM employs a pre-conditional operator for the prescribed flow and stress-free boundary conditions that forces 'bounce-back' on fluid distributions exiting the flow domain (described in Appendix A.7.1). This pre-conditional operator automatically handles all fluctuation issues during boundary condition switching and aids in the reversal of flow. Finally, the BMHV flow domain of this study uses extended inlet and outlet lengths, which reduce the effect of boundary condition switching on the interior fluid flow in the region of interest.

3.6.4.3 Leaflet motion modeling

The two leaflets of the bileaflet mechanical heart valve design rotate about a hinge

fulcrum line, with an angular sweep of approximately 55° for the SJM valve. This fulcrum line is located parallel to the leaflet leading edge. The real SJM valve has tolerances with the leaflet ear and hinge recess that allow for minimal translational motion along the parallel fulcrum axis. Though translational motion does occur in real SJM valves, the simulations of this study restrict leaflets to rotational motion only.

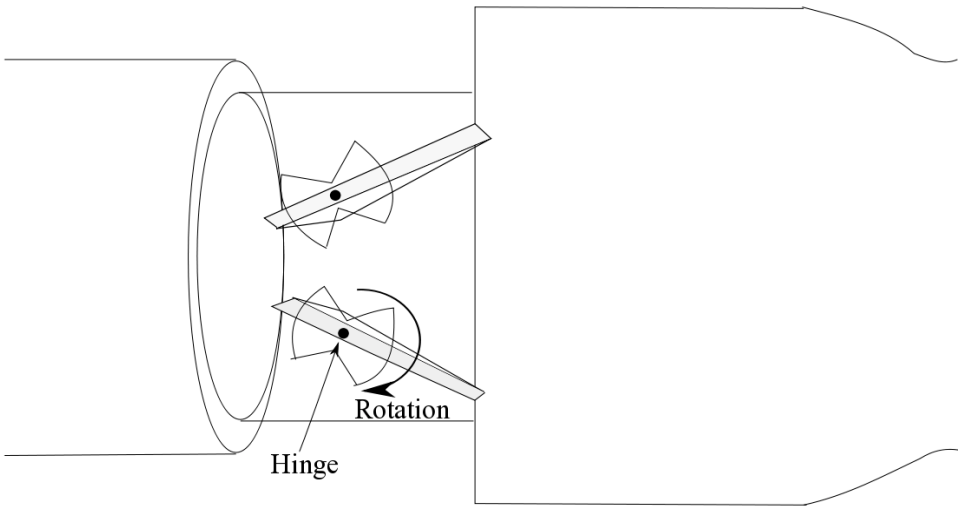

Figure 3-14: Rotational motion of closing leaflets about hinge fulcrum

For all cases, the meshed leaflets are initialized in the flow domain at a default position. For steady flow simulations, the default position is in the fully open position (5° to the axial direction). For pulsatile flow simulations, the default position is in the fully closed position (60° to the axial direction). The location of the hinge fulcrum varies based on the flow domain geometry due to varying inlet lengths. This fulcrum location is determined pre-simulation, by examining the geometry during the solid meshing process.

For prescribed leaflet motion, experimental data of leaflet angle variation with cardiac cycle time is read from an input file. Based on the cardiac cycle time point in the simulation, the required angle for each leaflet is then determined. The angle variation can

be prescribed for each leaflet, thus allowing cases of leaflet motion asymmetry or dysfunction. An "angle change" value is then determined as the difference between the original default leaflet angle and the angle to be prescribed. The entire leaflet mesh is then rotated about the hinge point from its default position to the new position using the angle change value. This new leaflet position is used to subsequently update all fluid-solid interaction bounce-back link locations as required by the SBB method. Thus, updated solid-to-fluid interaction forces can be computed for the new leaflet position.

As the temporal resolution of the pulsatile flow simulations is very high, the leaflet position does not need to be updated at every numerical timestep. The only requirement is that the leaflets do not traverse more than one lattice-Boltzmann grid length per motion. Thus, calculations can be performed to determine the necessary frequency of leaflet motion in order to save computational expenses while satisfying this requirement. For simulations of pulsatile flow at a spatial resolution of 80μm, the leaflet can be moved once every 10 – 15 numerical timesteps. In addition, as the cardiac cycle time periods of leaflet motion are known, the prescribed leaflet motion modeling needs to be performed only for leaflet motion times. For time periods of stationary leaflets (fully closed or fully open leaflets), only the bounce-back fluid distributions need to be updated at the leaflet surfaces. These stationary leaflets are treated identically as pipe walls or flow obstructions at these times.

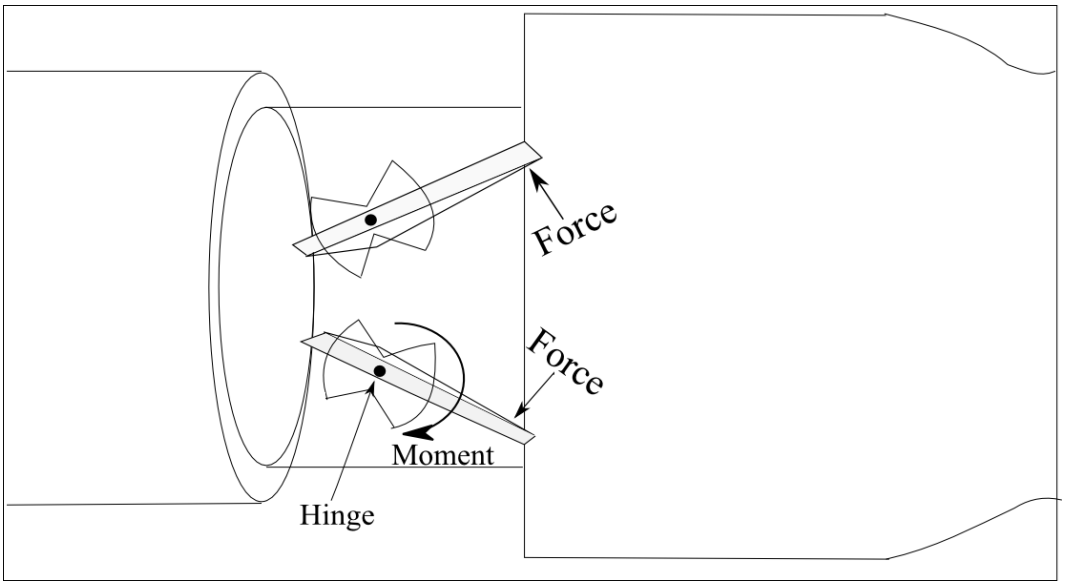

Figure 3-15: Example of force on leaflet surfaces causing rotational moments about the hinges

For dynamic leaflet motion, the leaflets still rotate about their hinge fulcrum, but experimental data is not used to determine leaflet position. Instead, the leaflets move strictly from two-way fluid-solid interaction. As the leaflet motion is purely rotational about the hinge, only the total torque about the hinge fulcrum line is required. The accumulated torque is calculated from individual contributions from each mesh surface element. The fluid-solid interaction forces on the mesh elements are calculated from the standard bounce-back method, as is the case with all "large" particles. The moment arm to the hinge is then determined in order to calculate the individual torque contribution. Upon calculating the total torque, the Newtonian dynamics equation for rotational motion is solved to update the leaflet angle and position. The moving leaflet then exerts forces back onto the fluid field, thus completing two-way fluid-structure interaction.

For dynamic leaflet motion, some further specifications to the methodology are

required in order to obtain accurate leaflet motion from two-way FSI. Details on how these specifications are determined are given in Appendix B.4. Unlike prescribed leaflet motion, the leaflet position and angle must be updated at every numerical timestep for stability reasons. This increases the computational expenses, as prescribed leaflet motion can be calculated with lower frequency and lower number of numerical calculations.

As the forces on the leaflet are determined using the SBB method, torque averaging is performed for stability purposes. In previous studies which employed the LBM with SBB for fluid-solid interaction with small particles, force and torque averaging was employed in order to maintain stability in particle motion and deformation [85, 86]. This was deemed necessary to prevent "odd-even" force fluctuations on small capsule particles. This same concept is employed for the leaflets, which also experience "odd-even" torque fluctuations. The total torque of the current numerical timestep is averaged with the total torque of the previous timestep, and this averaged torque is used to solve the angular Newtonian dynamics equation.

Finally, some cap limits to torque on the leaflets are imposed for stability reasons. These limits are variable depending on the spatiotemporal resolution of the simulation. Without these limits on torque, the leaflet moves too quickly and creates shockwaves in the flow field that crash the simulation. Thus, if the torque grows beyond a threshold limit, it is either reduced or zeroed in order to prevent a rapidly accelerating leaflet from causing unrealistic shockwaves in the flow field. This will be explained in further detail in Appendix B.4.

This torque limitation and averaging is employed for numerical stability reasons, but have a physical basis as well. In real SJM valves, the leaflets experience frictional

forces from the leaflet-hinge contact points that act by dampening the motion of the leaflets. This friction is not modeled in the numerical simulations of this study. The limitations imposed by the numerical method on torque values can be thought of as a mass-spring-damper system to provide stability.

3.7 Blood Damage Calculation

The LBM-EBF method was used to evaluate three different blood damage index (BDI) models in the work by Wu *et al*. [65]. The three BDI models were used to evaluate blood damage in simulations of platelets released in flow through BMHV hinge-like geometries and were identical in study design to the experimental blood study by Fallon *et al*. [67]. The three BDI models, inspired by other blood damage studies, are

- Linear shear stress-exposure time accumulation
    - All shear stress values count towards total damage
- Linear shear stress-exposure time accumulation
    - Shear stress must exceed threshold level to count as damage
- Shear stress-exposure time power law
    - Shear stress more important than exposure time in inducing damage

The linear shear stress-exposure time accumulation method with no threshold value matches best with the experimental blood damage results. The LBM-EBF method has also employed this simple BDI model to determine platelet damage in flows through actual BMHV hinges. This was performed in the work by Yun *et al.* [63] focusing only on the hinge area during mid-diastole. The results of this study in evaluating blood damage performance in various hinge geometries have matched both experimental

(thrombin antithrombin III assays) and other numerical results.

The simple linear shear stress-exposure time damage accumulation blood damage index (BDI) model with no threshold level is thus used for quantifying platelet damage in this study. This blood damage index is defined as

$$BDI = \sum_{t=0}^{t=end} \tau_{\max} \bullet \Delta t \qquad \text{Equation 3-8}$$

where τ_{max} is the maximum instantaneous surface shear stress experienced by the platelet, and Δt is the numerical timestep. Platelet damage is accumulated upon platelet release until the simulation end. The shear stresses are calculated for each mesh surface element, from which the maximum value across the entire platelet surface is determined at each numerical timestep. Damage values are then accumulated for each platelet, and can be averaged across platelets. The flow domain can also be broken down into small subdomain regions, and platelet damage can be averaged for each region. This provides an Eulerian viewpoint of platelet damage in the flow domain. This methodology also allows for the tracking of individual platelet damage with full temporal history of position, orientation, and damage. This allows for Lagrangian tracking of platelet damage, in addition to the aforementioned Eulerian representation of platelet damage.

3.7.1 Note on importance of modeling realistic platelet particles

The work by Yun *et al.* [63] examined the difference between point particle tracking methods and modeling platelets with finite size and meshed surfaces. Even in a simple case of low Reynolds number shear flow, the two suspension modeling methods result in very different shear stress values. The point particle method underestimates the

maximum shear stress on a platelet and also cannot account for shear stress variation based on orientation angle. This is discussed in further detail with an additional test performed in section 4.1.2.6. This re-emphasizes the importance of modeling platelets realistically with finite size and meshed surfaces for tracking platelet trajectories as well as surface shear stresses. This particle path accuracy, damage quantification accuracy, and ability to provide individual platelet damage time history make the numerical method of this study optimal for understanding how platelet damage is incurred in BMHV flows.

3.8 Validation

Validation is required for the numerical method of this study. The LBM-EBF method must be suitable for generally modeling single-phase and suspension flows. The model and numerical method also requires validation as a blood damage quantification methodology. Finally, the numerical method must be able to accurately capture pulsatile BMHV flows. Once validated, the LBM-EBF method is then appropriate for modeling suspensions in pulsatile BMHV flows for the purposes of platelet damage quantification and device evaluation.

3.8.1 LBM-EBF Validation

The lattice-Boltzmann method used in this study has been extensively validated for modeling single-phase and suspension flows [69-71]. The LBM-EBF method has been validated as second-order accurate for modeling 3D suspension flows with deformable particles in the original methodology paper by Wu and Aidun [66]. The EBF method was validated against several fundamental suspension flow cases, including but not limited to:

circular cylinder in simple shear flow, ellipsoid in simple shear flow, sedimentation of a sphere in a square cylinder, red blood cell in capillary pressure-driven flow, and modeling bulk viscosity of blood with dense red blood cell suspensions. All of these validation cases showed excellent agreement between the EBF method and experiments and/or theory.

The EBF method is re-implemented by the author into an in-house LBM code. This EBF implementation is then parallelized for optimal and efficient numerical simulations. Although the EBF method has been extensively validated by Wu and Aidun [66], the newly implemented code must be tested for accuracy. Thus, the case of a rigid ellipsoid in simple shear flow is modeled and compared to theoretical values. This case is also known as Jeffery's orbit and is chosen as platelets are also modeled as rigid ellipsoids.

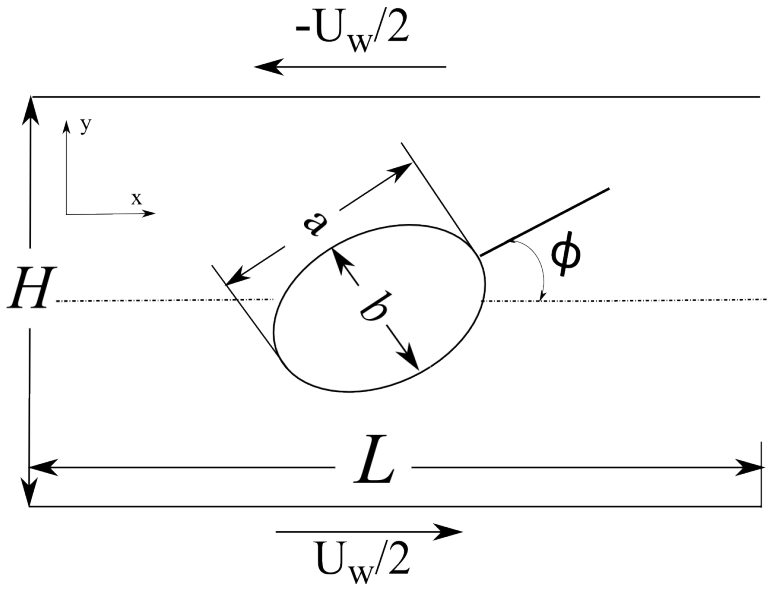

Figure 3-16: Jeffery's orbit for rotation of a rigid ellipsoid in simple shear flow

The motion of a rigid ellipsoid in simple shear flow is calculated analytically at low

Reynolds number by Jeffery [87]. The boundary of this ellipsoid is given by

$$\frac{x^2}{a^2}+\frac{y^2}{b^2}+\frac{z^2}{c^2}=1 \qquad \text{Equation 3-9}$$

When one of the principal axes of the ellipsoid is kept parallel to the vorticity direction, the rotation angle, ϕ, and angular rate of rotation, $\partial\phi/\partial t$, at low Reynolds number are given by

$$\phi=\tan^{-1}\left(\frac{b}{a}\tan\frac{abGt}{a^2+b^2}\right) \qquad \text{Equation 3-10}$$

$$\frac{\partial\phi}{\partial t}=\frac{G}{a^2+b^2}\left(b^2\cos^2\phi+a^2\sin^2\phi\right) \qquad \text{Equation 3-11}$$

where G is the shear rate, defined as $G = U_w/H$. This Jeffery's orbit case is modeled with varying ellipsoid aspect ratios to ensure the accuracy of EBF to model different particle types. Subgrid resolution capabilities are also tested by modeling an ellipsoid with size much smaller than the fluid grid resolution. Finally, parallel coding is tested by comparing numerical results for both serial processing and parallel processing simulations. These validation results are discussed in the section 4.2.1.

Although other validation cases are possible, only the Jeffery's orbit case is performed for the newly implemented EBF method for this study. The EBF method has already been generally tested with a wide variety of validation cases with highly accurate results. Thus, testing the newly implemented and parallelized EBF code of this study with the Jeffery's orbit case is deemed sufficient. Additional validation for the EBF method is pointed to the original methodology paper by Wu and Aidun [66].

3.8.2 Comparison to experiments

The LBM method is next validated as suitable for modeling BMHV flows. This is performed in a series of steps, including the modeling of both steady and pulsatile flows through a BMHV. For quantitative validation of the LBM, axial velocity comparisons are made between the numerical simulations and experimental PIV data [55] of steady flow past the fully open leaflets of a 23mm SJM valve. One comparison is made for Re = 750 representing laminar flow and the other for Re = 5000, representing the higher Reynolds number flows of the cardiac cycle with possible turbulent flow. For the experiments, an average flow field was computed over 100 to 200 ensembles. For Re = 750, due to the steady nature of laminar flow, only one computational time snapshot is needed for comparison with experiments. For Re = 5000, due to the chaotic nature of the high Reynolds number flow, 200 computational ensembles are used to determine an average flow field for comparison with experiments. The comparisons are made for axial velocity at perpendicular cross-section lines past the fully open leaflet trailing edges.

Due to cycle-to-cycle variations, a qualitative comparison between the simulations and experimental data [52] is first performed for the pulsatile flow case. The comparisons are performed at key points of the cardiac cycle, namely: the opening phase (leaflets beginning to open at onset of systole), the acceleration phase (leaflets fully open with increasing flowrate), peak flow (leaflets fully open with maximum flowrate), deceleration phase (leaflets fully open with decreasing flowrate), and closing phase (sudden leaflet closing). Flow features, shown in the form of 2D out-of-plane vorticity contour plots, are compared downstream of the leaflets, using the same contour scaling.

Next, a quantitative comparison is performed for numerical simulations at two different spatial resolutions and against experimental data. The comparison between different numerical spatial resolutions is performed to address grid resolution independence. In addition, the results are analyzed to determine if higher spatial resolution simulations can resolve the turbulent scales of BMHV flow more accurately. Because of computational resource limitations, the numerical simulations are performed for steady flow at Re = 5779, or peak flow Reynolds number. Mean flow fields and root-mean-square (rms) fields are determined over 200 computational ensembles at each spatial resolution. Similar mean flow and rms fields are taken at peak flow from PIV experimental data for pulsatile flow. Though this is not an exact matching of computational to experimental results, it is necessary, as no experimental data exists for steady flow at exact peak Reynolds number. In addition, computational resource limitations prohibit simulations of sufficient pulsatile cardiac cycles to obtain mean flow and rms fields for each spatial resolution case.

3.9 Flow visualization

The pulsatile flow fields in the simulations are visualized in both 2D and 3D representations at key points throughout the cardiac cycle. For 2D visualization, grayscale contour plots of out-of-plane vorticity magnitude are shown at longitudinal cutplanes perpendicular to the open leaflets. The only exception for this color scheme is for the numerical-to-experimental PIV data comparison for pulsatile flow. The experimental data were presented in a previous work using a red-black contour color scheme that was deemed most suitable for comparison with simulations [52], and thus

this same color scheme is employed. All contour plots use the same vorticity magnitude contour scaling for best comparison among cases. Grayscale contour plots are determined as most suitable in depicting important flow features compared to other coloring schemes, particularly in delineating finer flow features such as small eddies.

All perpendicular cutplanes are taken at the center slice of the domain. The perpendicular cutplanes taken at the center slice are chosen as they best represent the flow field for 2D representation. Though parallel cutplanes and off-center slices are possible, these results do not detail features that are novel and interesting enough for inclusion.

As shear stress on suspended blood elements is of interest, plots of instantaneous viscous fluid shear stress magnitude are displayed for the BMHV flows. The viscous fluid stress tensor is defined as

$$\tau_{ij} = \mu\left(\frac{\partial u_i}{\partial x_j} + \frac{\partial u_j}{\partial x_i}\right) \qquad \text{Equation 3-12}$$

For a plane defined by the unit normal vector $\hat{n}$, the magnitude of shear stress $\tau_{shear\ stress}$ projected on the plane is defined as

$$\tau_{shear\ stress} = \left|\hat{t} \bullet \underline{\underline{\tau}} \bullet \hat{n}\right| \qquad \text{Equation 3-13}$$

where $\hat{t}$ is a unit vector tangential to the plane. In this work, shear stresses are projected onto planes perpendicular to the leaflets and are quantified in units of dynes/cm^2.

For 3D flow visualization, the *q*-criterion is employed to determine the presence of coherent 3D vortical structures [88, 89]. The quantity *q* is defined as

$$q = \frac{1}{2}\left(\|\Omega\|^2 - \|S\|^2\right) \qquad \text{Equation 3-14}$$

where Ω and S denote the symmetric (rate-of-rotation) and antisymmetric (rate-of-strain) parts of the velocity gradient tensor, respectively. According to Hunt *et al.*, 3D coherent vortical structures exist where $q > 0$, or where the rotation rate dominates the strain rate [88]. 3D flow visualization is thus performed with uniformly colored isosurfaces shown when $q > 0$, or where a coherent vortical structure exists. In some cases, the large number of vortical structures makes it difficult to pick out important flow features. In these cases, the isosurface threshold is slightly increased to improve 3D visualization and the figures are marked by asterisks (*). The isosurface threshold is variable in each of these cases and is tuned in order to optimize visualization.

The flow visualizations in both 2D and 3D primarily focus on a section of the domain that starts directly upstream of the valve and ends slightly downstream of the sinus aortic expansion region. This is determined as the most interesting region of the flow field to focus on, as the flow far upstream and downstream of the valve involves much less interesting flow features. Thus, only this limited view of the flow field is shown.

CHAPTER 4

FLOW SOLVER IMPLEMENTATION AND VALIDATION

This chapter covers the implementation and validation of the numerical method as a generic suspension flow solver. First, the LBM-EBF method is validated for a fundamental suspension flow case, as well as for subgrid modeling and shear stress quantification. Next, the accuracy of parallel implementation is discussed for the numerical method. Scaling efficiency of the parallelized method is also presented to show the applicability of LBM-EBF to high performance cluster computing.

The legacy code for the LBM-SBB method has been extensively validated in a variety of previous studies [68, 69, 71, 73, 90]. Thus, the fundamental suspension flow case that is modeled in this chapter is sufficient for validation of the LBM-EBF method for this study. Additional validation cases of multiphase flow are also superfluous, as the EBF method has already been validated with a wide variety of suspension flow cases [66, 91]. The validation of the newly implemented parallel EBF method with ellipsoid orbit in shear flow is thus considered sufficient.

4.1 LBM-EBF Validation

The primary validation case of a rigid ellipsoid isolated in the center of simple shear flow is presented. Comments are made on the approach of local volume calculation in combination with the EBF method in Appendix A.6, which was not covered in detail by the methodology paper of Wu and Aidun [66]. Results on a variety of ellipsoid orbit cases are presented with varying ellipsoid aspect ratios. Subgrid modeling cases are also

presented to show the accuracy of the EBF method in simulating multiscale problems and quantifying shear stresses, which is of interest in this study. Accuracy with particle size and aspect ratio are also covered, and higher particle Reynolds number behavior is also detailed. Finally, comments are made about differences between particle tracking and realistic platelet modeling to show the benefits of using the LBM-EBF method for BMHV blood damage studies.

4.1.1 Ellipsoidal Orbit Setup

The case of a rigid ellipsoid in simple shear flow is shown in Figure 4-1 and the theoretical solution for Stokes flow is given by Jeffery [87]. This solution assumes that one of the principal axes is kept parallel to the vorticity vector and that the shear flow is in the Stokes flow regime (Re→0). The top and bottom walls move in opposite directions with magnitude $U_w/2$ and are separated by a wall distance of H.

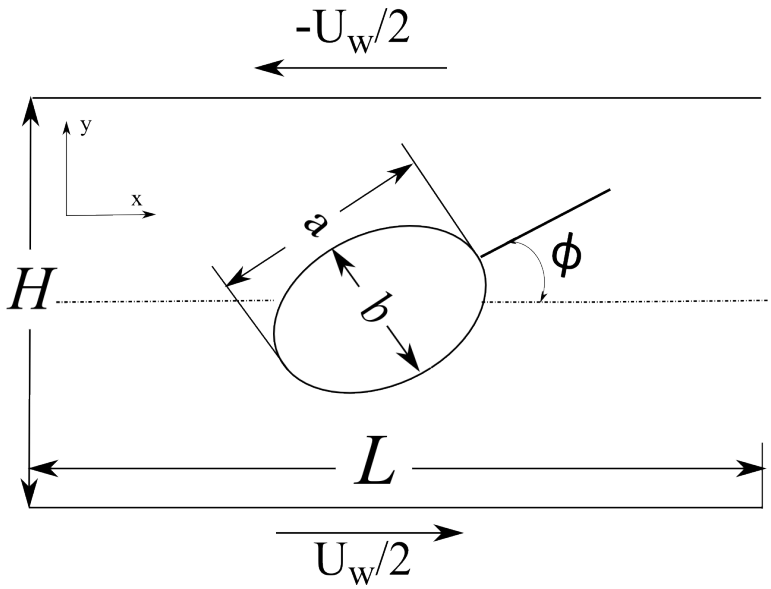

Figure 4-1: Rigid ellipsoid in simple shear flow

The general form of a three-dimensional ellipsoid is given by

$$\frac{x^2}{a^2} + \frac{y^2}{b^2} + \frac{z^2}{c^2} = 1 \qquad \text{Equation 4-1}$$

As the principal axis in the z-direction is kept parallel to the vorticity vector, the radius c in the z-direction does not affect the solution. The particle Reynolds number, Re_p, is defined as

$$\mathrm{Re}_p = \frac{Gd^2}{\upsilon} \qquad \text{Equation 4-2}$$

where G is the shear rate and is calculated as $G = U_w / H$. The particle diameter d is given as twice the major axis radius, or $d = 2a$.

For Stokes flow, the rotation angle, ϕ, and angular rate of rotation, $\partial\phi/\partial t$, are exactly defined as

$$\phi = \tan^{-1}\left(\frac{b}{a}\tan\frac{abGt}{a^2 + b^2}\right) \qquad \text{Equation 4-3}$$

$$\frac{\partial\phi}{\partial t} = \frac{G}{a^2 + b^2}\left(b^2\cos^2\phi + a^2\sin^2\phi\right) \qquad \text{Equation 4-4}$$

Though this solution is theoretically derived for Stokes flow at zero Reynolds number, simulations can still be performed to approximate Jeffery's orbit with Re << 1. Two-dimensional simulations of Jeffery's orbit were also performed for validation of the LBM-SBB method by Aidun *et al.* [69].

In this chapter, accuracy of the EBF method is frequently quantified by determining orbital drift from theory. The orbital drift is defined as

$$\text{Drift} = \frac{\left|T_{sim} - T_{theory}\right|}{T_{theory}} \times 100 \qquad \text{Equation 4-5}$$

$$T_{theory} = \frac{2\pi(a^2 + b^2)}{Gab} \qquad \text{Equation 4-6}$$

where T_{sim} is the time to complete one orbital period for the numerical simulation, T_{theory} is the theoretical time to complete one orbital period from Jeffery's solution, and a and b are the ellipsoid axis radii.

In the EBF methodology paper by Wu and Aidun [69], Jeffery's orbit is performed for a flow domain of 120x120x60 lattice nodes. Two different ellipsoid aspect ratios b/a are modeled, for b/a = 4/3 and b/a = 4. Simulations were performed at Re_p=0.064 with very good matching between simulations and theory. A minor discrepancy is observed for the minimum and maximum values of angular rate of rotation. This imperfect matching is slightly more pronounced for larger aspect ratios. However, noting that the simulations are not exactly performed at zero Reynolds number, the overall matching between simulations and theory is excellent.

The same flow conditions are simulated for the new implementation of the EBF methodology for this study. The flow domain is again 120x120x60 in lattice Boltzmann units, with a channel length and height of 120. The shear rate is given as G = 1/6000, corresponding to a wall velocity of $U_w/2$ = +/- 0.01 in LB units. This higher wall velocity is chosen to reduce the time of simulation, as low particle Reynolds number must be simulated to mimic Stokes flow. The relaxation tau value is given as τ = 5.0, corresponding to a kinematic viscosity of 1.5 in LB units. The particle Reynolds number

varies based on the dimensions of each simulated particle. A list of the Jeffery's orbit cases simulated in the original methodology paper and in this study is given in Table 4-1.

Table 4-1: List of Jeffery's orbit cases simulated in original methodology paper by Wu and Aidun [66] and in this study.

Original cases	Particle dimensions	Flow domain	U_{wall}	Re_p
1-way/2-way FSI	12x9x9	120x120x60	0.02	0.064
1-way/2-way FSI	12x3x3	120x120x60	0.02	0.064
New cases	**Particle dimensions**	**Flow domain**	**U_{wall}**	**Re_p**
1-way FSI	12x9x9	120x120x60	0.02	0.064
1-way FSI	12x6x6	120x120x60	0.02	0.064
1-way FSI	12x3x3	120x120x60	0.02	0.064
1-way FSI	7x7x3.1	120x120x60	0.02	0.0218
2-way FSI	12x9x9	120x120x60	0.02	0.064
2-way FSI	10x10x10	120x120x60	0.02	0.044
2-way FSI	7x7x3.1	120x120x60	0.02	0.0218
1-way FSI	0.07x0.07x0.031	120x120x60	0.02	2.18e-6

4.1.2 Ellipsoidal Orbit Results

The following are results for the ellipsoidal orbit validation case for both 1-way and 2-way fluid-solid interaction using the conal local volume method as described in Appendix A.6.3. 1-way FSI is employed for the suspended platelets of the blood damage simulations of this study. Though 2-way FSI is not employed for suspended platelets, the general performance of the EBF method is important. An important note is also made about the necessity of a damping term when implementing solid-to-fluid forces. This may be crucial to future studies using 2-way FSI with the EBF method. The results include different ellipsoid geometries to show the accuracy of EBF with multiple particle shapes and sizes.

4.1.2.1 1-way Fluid-Solid Interaction

Jeffery's orbit using the conal local volume method matches extremely well for cases of 1-way fluid-solid interaction. The exact case from the original methodology paper by Wu and Aidun [66] is modeled with a 12x9x9 ellipsoid at $Re_p = 0.064$. Plots for orientation angle and rate of rotation are plotted against theory. Orientation angle is normalized by 2π and rate of rotation is normalized against shear rate G. An additional visualization is made by plotting rate of rotation against the cosine of 2ϕ for a more easily compared line plot between theory and simulation.

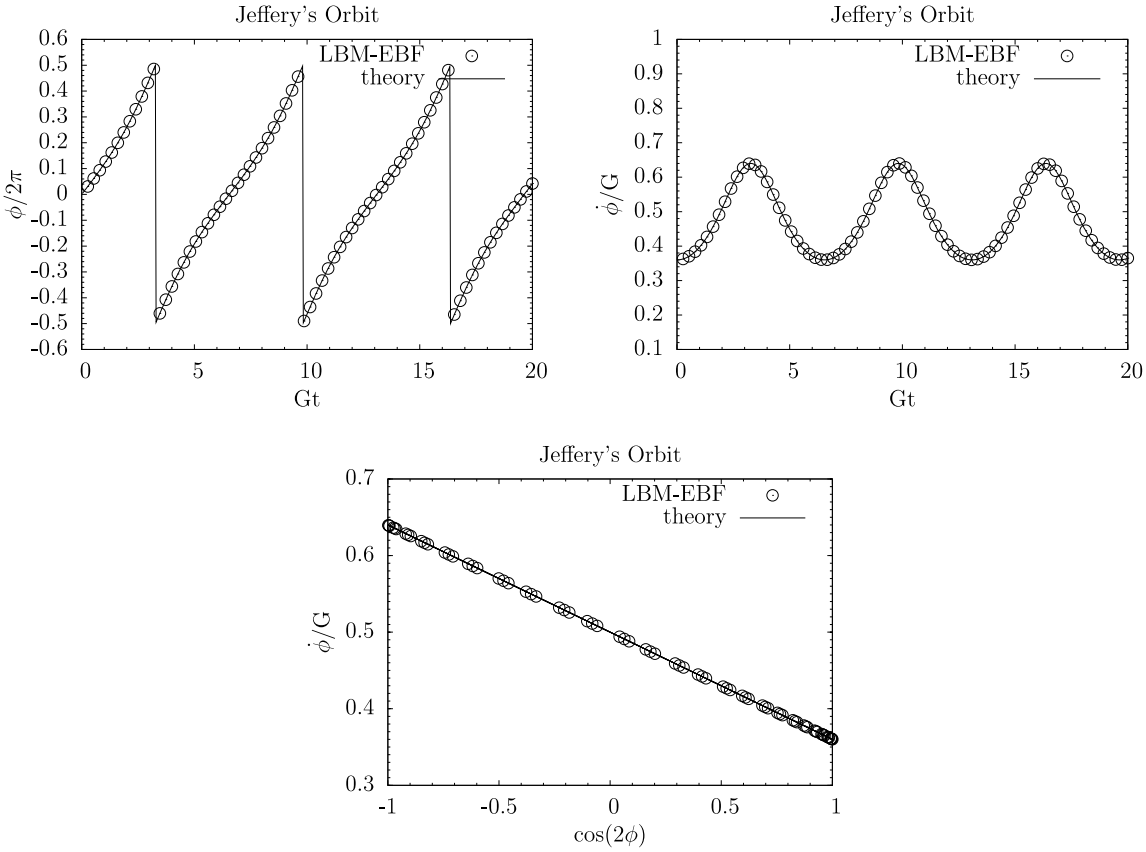

Figure 4-2: Jeffery's orbit for ellipsoid 12x9x9 radius, $Re_p = 0.064$, G=1/6000, $\tau = 5$. 1-way interaction

Only a few rotation periods are displayed in these figures to highlight the excellent matching between the LBM-EBF method and theoretical values. At Gt = 20, after three rotations of the ellipsoid, the difference between simulation and theory is only 0.3% and 0.03% for orientation angle and rate of rotation, respectively. The simulations are performed for up to 10 orbital periods and the same excellent agreement with theory is observed throughout with very minimal orbital drift.

An additional simulation is performed with a 12x6x6 ellipsoid, for larger aspect ratio geometry in the same flow domain. This is performed to demonstrate the ability of LBM-EBF to accurately model FSI for different particle shapes.

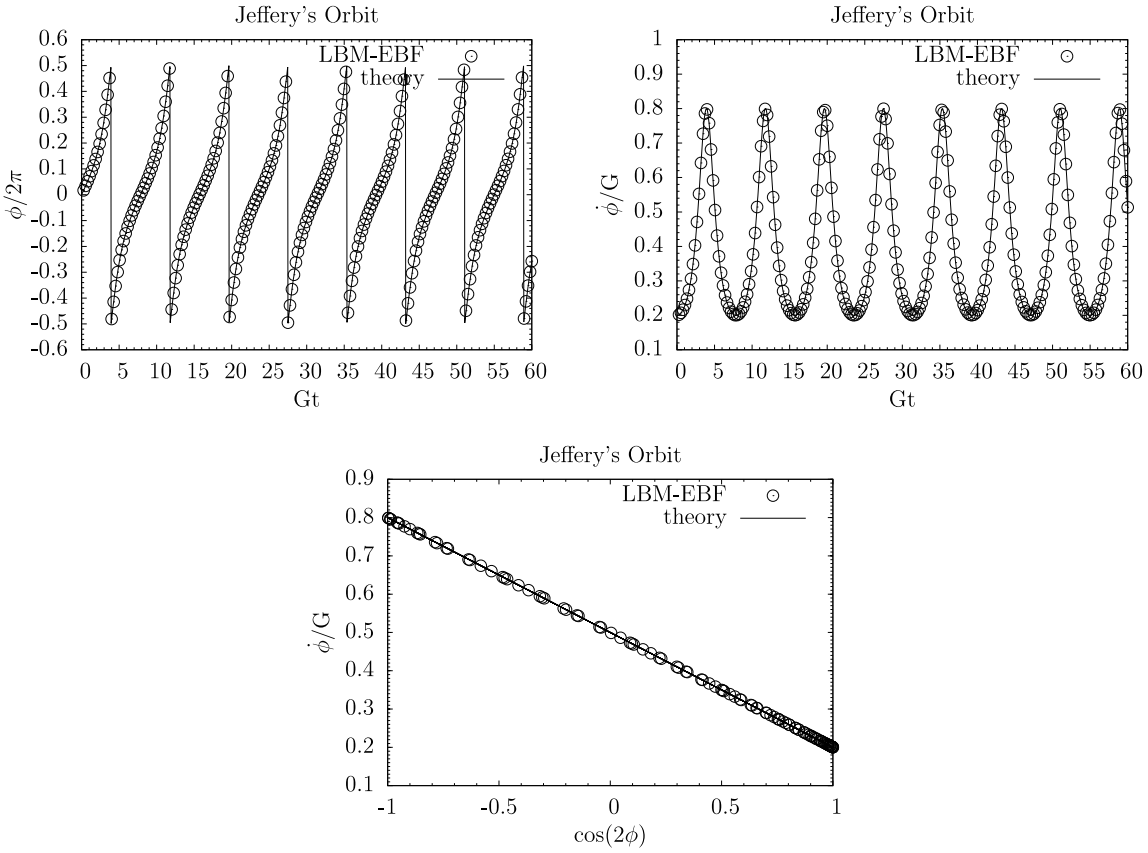

Figure 4-3: Jeffery's orbit for ellipsoid 12x6x6 radius, Re_p = 0.064, G=1/6000, τ = 5. 1-way interaction

These results are shown with a large number of orbital periods simulated. Once again, excellent matching is shown for up to 10 orbital periods with minimal drift observed.

A very large aspect ratio of 4 is simulated with a 12x3x3 ellipsoid in the same flow domain. This corresponds to the second Jeffery's orbit case in the methodology paper by Wu and Aidun [66].

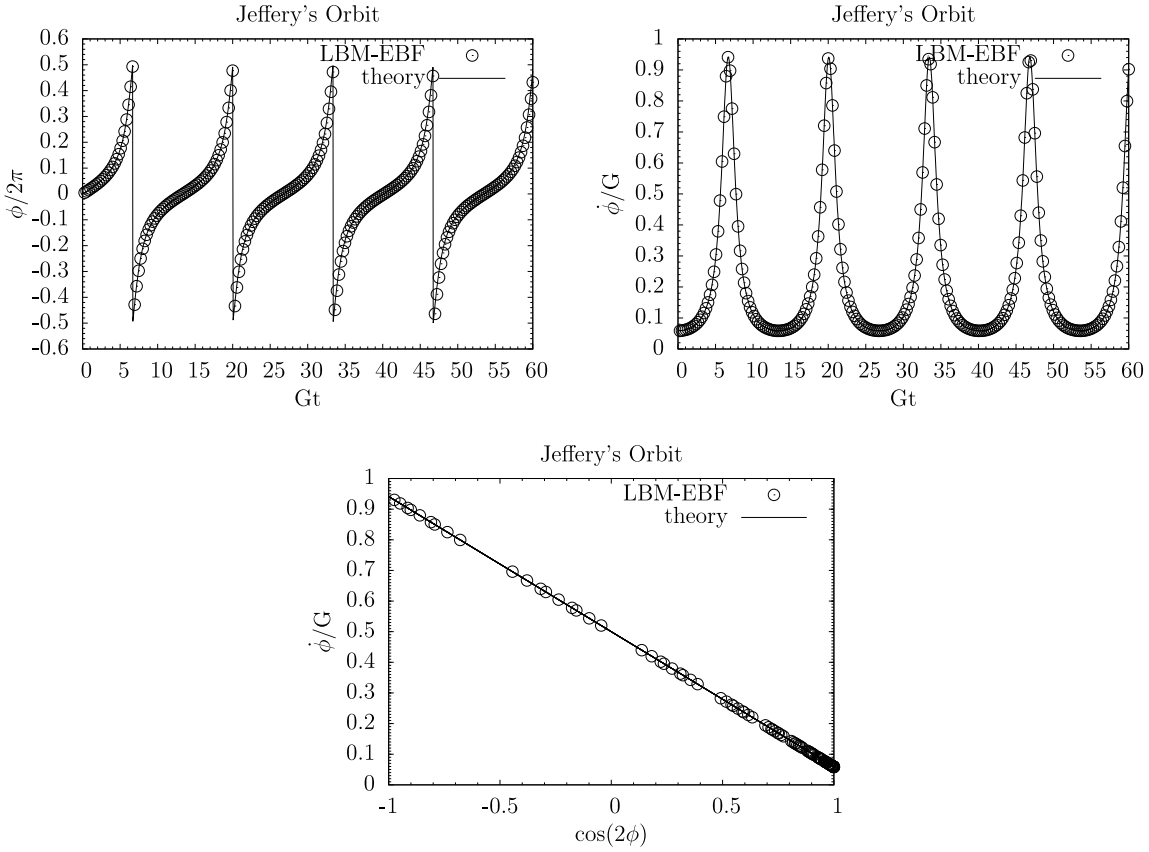

Figure 4-4: Jeffery's orbit for ellipsoid 12x3x3 radius, $Re_p = 0.064$, G=1/6000, $\tau = 5$. 1-way interaction

It is observed that even for this large aspect ratio, excellent matching is observed between simulation and theory. The orbital period is longer for this ellipsoid case, thus only a

limited number of rotations are displayed. However, the LBM-EBF method still shows minimal drift for this large aspect ratio particle. After four rotations of the ellipsoid, the orbital drift compared to theory is only 0.2%.

An oblate spheroid particle that is described as a "flat discoid" is also simulated. This is the general shape of platelets as commonly described in literature. The platelet particle used in the simulations of this study is placed in Jeffery's orbit, with dimensions 7x7x3.1 radii. It is noted that this same platelet is scaled down in size to model realistic platelet size in the BMHV flow simulations of chapters 6 and 7.

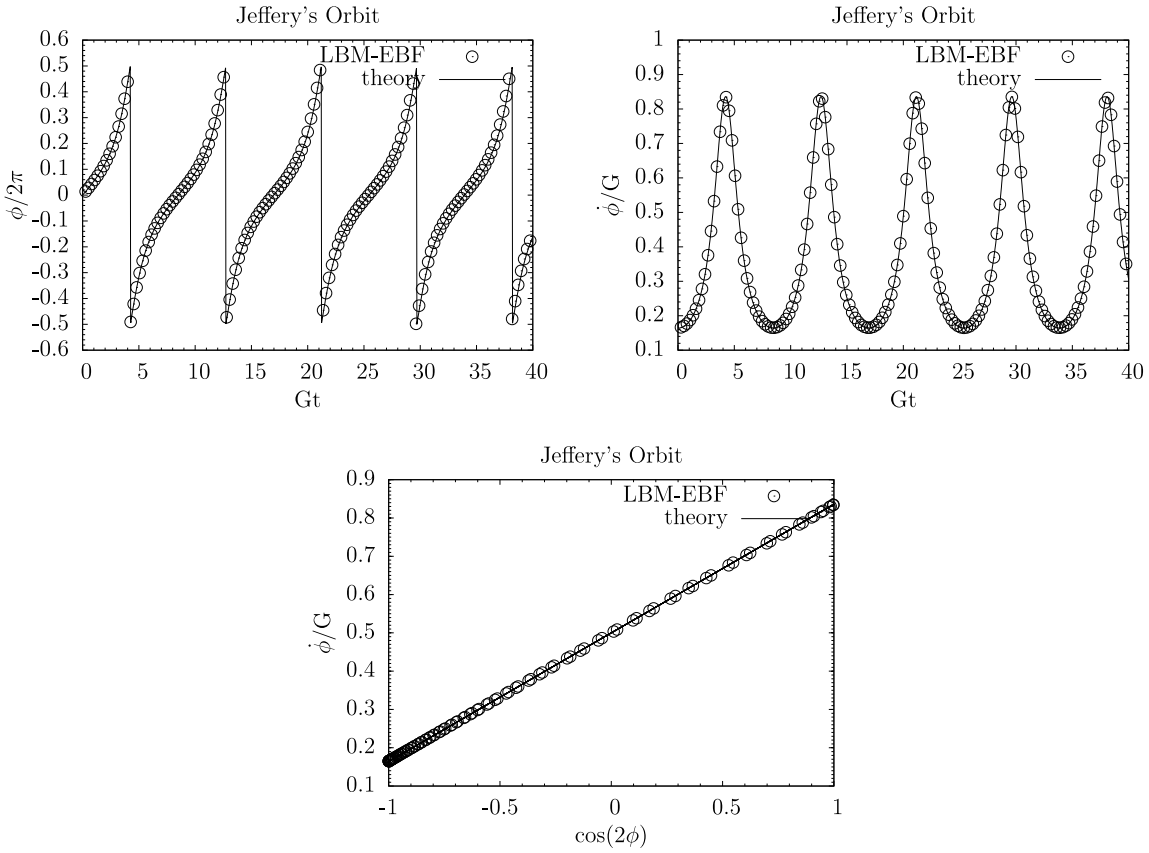

Figure 4-5: Jeffery's orbit for platelet 7x7x3.1 radius, $Re_p = 0.0218$, G=1/6000, $\tau = 5$. 1-way interaction

This oblate spheroid case is slightly different in that there are two major axis diameters ($r_1 = r_2 = 7$), in comparison to the previous cases of two equivalent minor axis diameters for a prolate spheroid. However, even with this modified case, the platelet particle shows excellent matching with theoretical values. Though the full simulation run is not shown, the platelet matches well with theory for 10 orbital periods with no drift.

These results demonstrate the ability of LBM-EBF to model ellipsoids with varying aspect ratios with similar high accuracy, including the realistic platelet shape case, for 1-way FSI.

4.1.2.2 2-way Fluid-Solid Interaction

Though 2-way FSI is not employed for suspended particles in this thesis, tests are still performed to determine the accuracy of this method. In particular, modifications are necessary to the coding to ensure stability of the method. These modifications are crucial to any future studies involving 2-way FSI with the EBF method.

It is observed that for a variety of simulations involving 2-way FSI, instabilities develop in the form of growing interaction forces between the solid and the fluid. These instabilities are consistently observed within the first hundred timesteps of simulation. The general form of these instabilities is:

- Fluid exhibits strong forces onto solid at start of simulation
- Solid is moved rapidly according to strong FSI forces
- Fluid reacts with opposite force onto solid to “correct” for rapid solid motion
- Solid is moved more rapidly in opposite direction

This devolves into a feedback loop where the forces on the particle grow exponentially larger until the simulation crashes.

It is determined that this occurs from the initial transience of the particle motion. Namely, the particle is initially at rest and when suddenly introduced into a flow field, the particle will enter the feedback loop as described above. Attempts by the author to initialize the particle with a starting motion were unsuccessful in removing instabilities. Attempts to bring the flow field from zero velocity flow field to slowly developing simple shear flow were similarly unsuccessful.

The solution to these instabilities is twofold. First, a damping constant is multiplied to the solid-to-fluid force term, $\mathbf{g(x^e,t)}$. The purpose of this damping term is to reduce the overreaction of the solid particle motion to the flow field upon being introduced into the simulation. This damping term can vary with similar results, but values of 0.85 and 0.9 are generally found suitable for the ellipsoidal orbit simulations. A similar damping term was employed in the EBF codes of the original methodology [66], however this term was not mentioned in the original description of the EBF method. It is crucial to introduce this damping term in order to maintain simulation stability. Secondly, the particle should be held in the beginning of the simulation for 3000 to 5000 timesteps. This allows flow streamlines to sufficiently develop around the particle and removes any "shock" from the introduction of the suspended particle into the flow field.

The simulations of this section are performed in a domain of 120x120x60, with walls moving at U = +/- 0.01, in LB units.

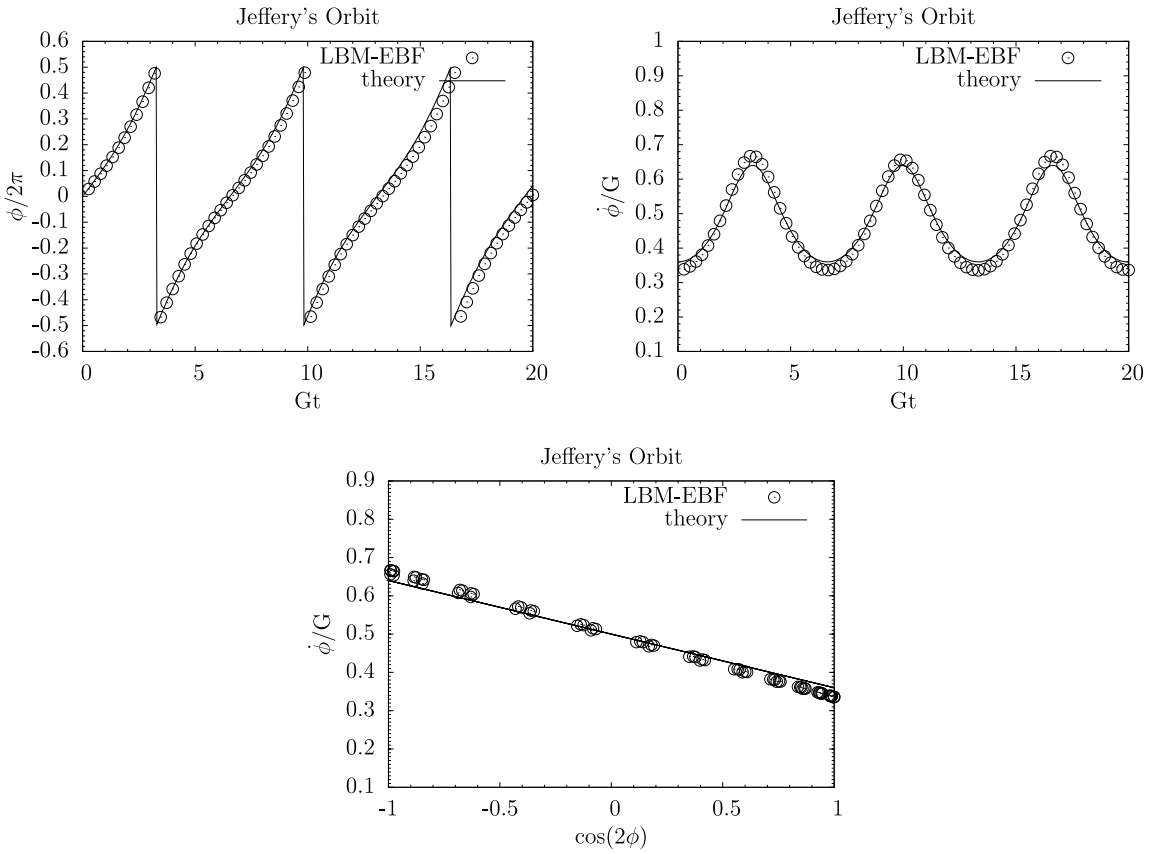

Figure 4-6: Jeffery's orbit for 2-way FSI, 12x9x9 radius, $Re_p = 0.064$, G=1/6000, $\tau = 5$

The simulation for a 12x9x9 radii ellipsoid shows a slight drift from theory within one orbital period, with an imperfect matching of the rate of rotation as well. The slight drift can be explained by the non-zero Reynolds number and the fact that 2-way FSI introduces a perturbation into the flow field, unlike with 1-way FSI. Even with imperfect matching, the drift is only 1.98% from the theoretical value of one orbital period time.

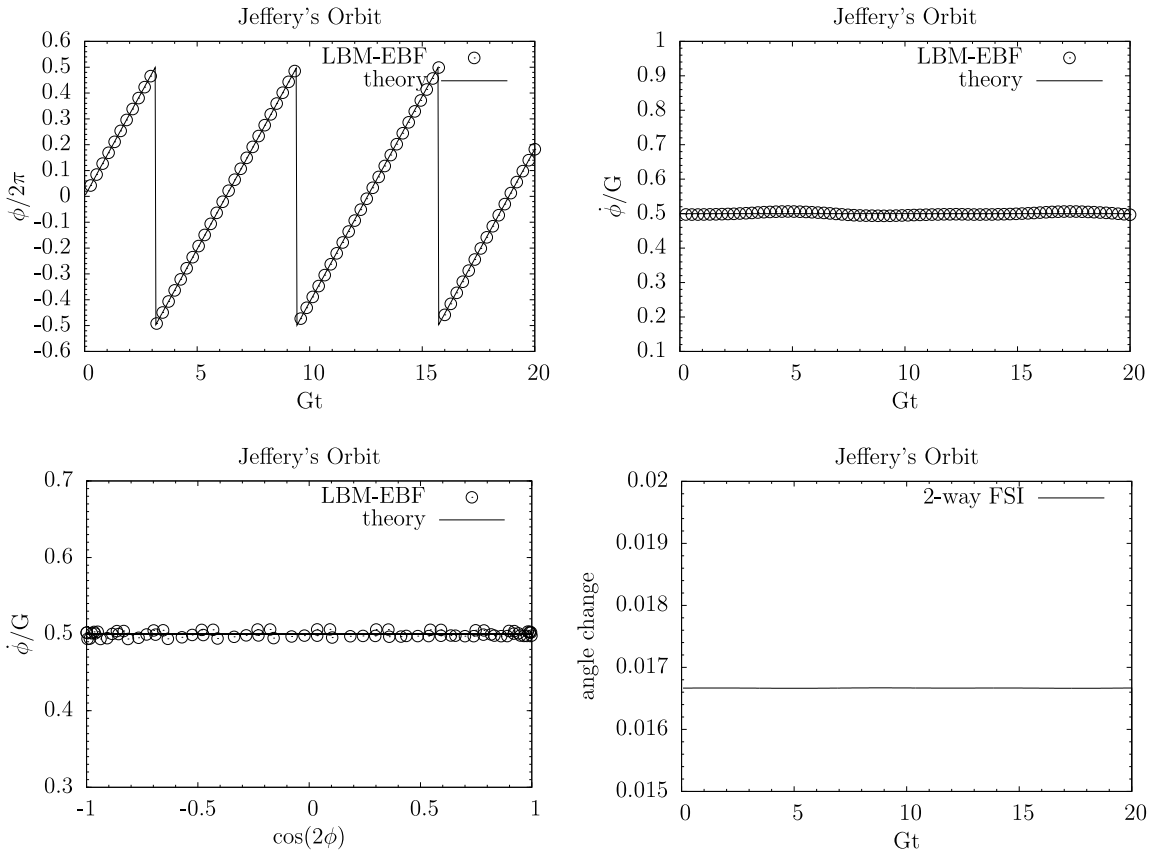

Figure 4-7: Jeffery's orbit for 2-way FSI, sphere radius 10, $Re_p = 0.044$, G=1/6000, $\tau = 5$

A simpler case of a sphere with radius 10 is simulated with 2-way FSI. These results show good matching for normalized angle and rate of rotation with low levels of drift for multiple periods. However, the comparison of rate of rotation as a function of the cosine of orientation angle shows slight imperfection in the results with 2-way FSI. Thus, even with a perfectly symmetric spherical case, slight inaccuracies and fluctuations are observed for angular velocity. This is likely due to the meshed surface of the sphere, as it is not a perfectly smooth sphere surface but meshed with triangular elements. The plot of angle change from numerical timestep to timestep, however, demonstrates that the angular change over time is constant and smooth throughout the rotation.

A case of a platelet particle (7x7x3.1 radii) is simulated with 2-way FSI. In this case, drift is observed again within one orbital period with 6.36% drift from theory after one orbital period due to the larger aspect ratio. The plots of rate of rotation show good matching overall, with some inaccuracies at the extremes of rate of rotation. These 2-way FSI results still demonstrate the general applicability and accuracy of EBF as a 2-way FSI numerical method.

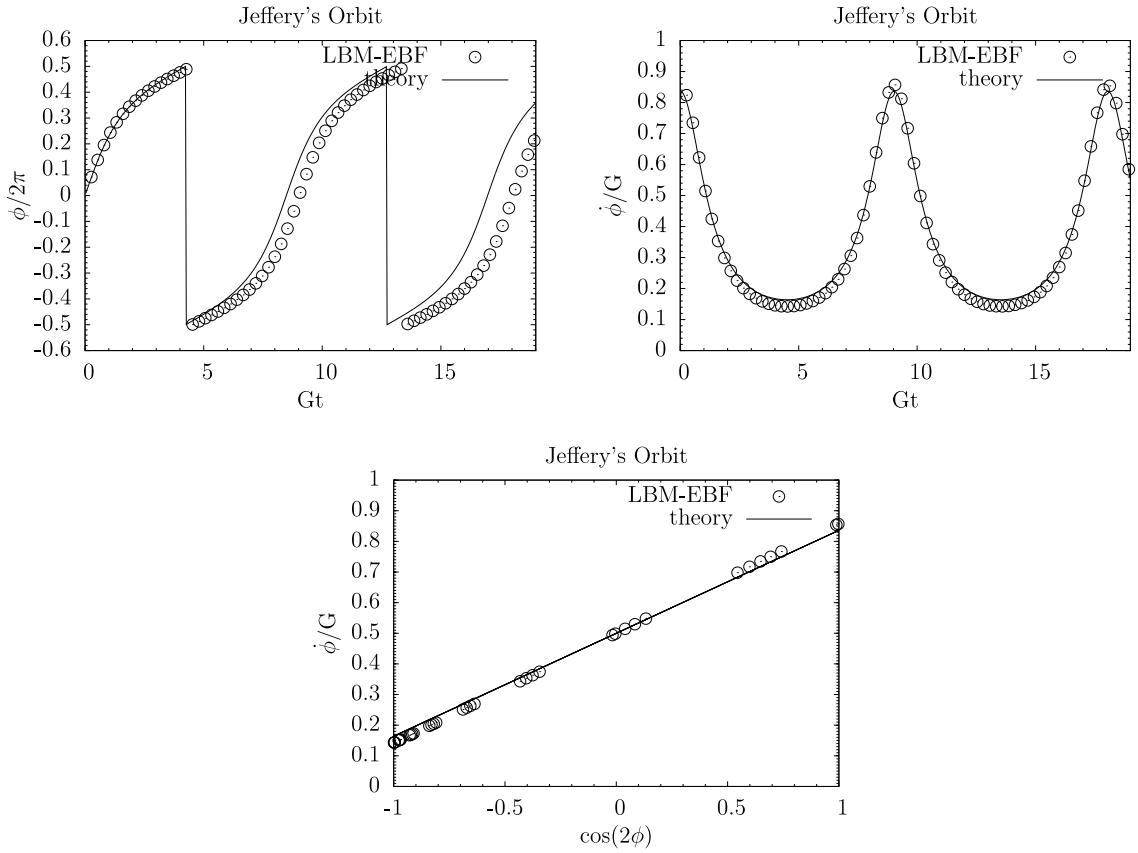

Figure 4-8: Jeffery's orbit for platelet 7x7x3.1 radius, 2-way FSI, $Re_p = 0.0218$, $G=1/6000$, $\tau = 5$

As Jeffery's orbit is derived for zero Reynolds number, some inaccuracies with theoretical values are expected. The previous EBF implementation demonstrated good matching with theoretical results of Jeffery's orbit with 2-way FSI but was not perfect, and also showed some drift with theory. Details on the Jeffery's orbit results of the previous EBF method can be found in the work by Wu and Aidun [66].

It should be noted that the original EBF implementation was performed with lattice-spring methodology, where the total volume is discretized with both inner and outer finite volumes. Thus, forces are exhibited from the solid onto the flow field throughout the entire particle volume for a completely solid particle. In this current implementation, the solid-to-fluid forces are given at the solid surface boundary only, due to the nature of the conal volume methodology (Appendix A.6.3). Thus, the solid-to-fluid forces are implemented as if for a fluid-filled capsule with a shell membrane, with the solid-to-fluid forces exerted at the surface nodes. However, the force magnitudes are still computed as if for a completely solid particle. This inconsistency between the force magnitude calculation and location of the force application may lead to the slight inaccuracies that are observed in the 2-way FSI results. Nevertheless, it is determined that the drift from theoretical values is small and thus this implementation of EBF is sufficient for 2-way FSI modeling.

4.1.2.3 Subgrid Modeling

For 1-way fluid-solid interaction, cases of subgrid scale resolution for modeling of the solid particles are tested. This is particularly relevant as the platelets simulated in this study are 3μm, whereas the fluid resolution is 80μm. Thus, subgrid modeling is a

requirement for any suspension flow modeling method that attempts to model realistic platelet particles.

The platelet originally modeled with radii 7x7x3.1 is scaled by a factor of 1/100. This results in a platelet with maximum diameter of 0.14 times the fluid spatial grid resolution. This particle is released into the identical flow domain of previous 1-way FSI simulations of Jeffery's orbit (120x120x60 domain, walls moving at +/- 0.01 LB units).

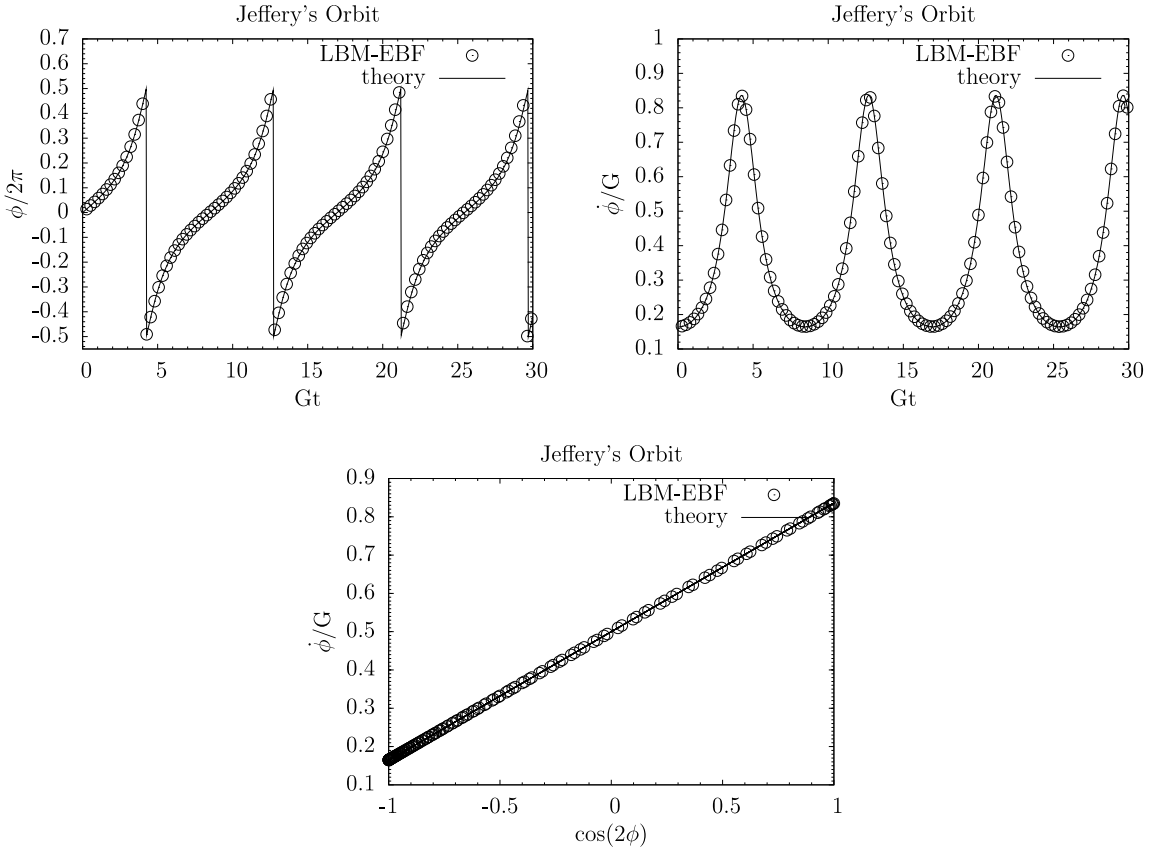

Figure 4-9: Jeffery's orbit for platelet 0.07x0.07x0.031 radius, 1-way FSI, $Re_p = 0.0218$, G=1/6000, $\tau = 5$

These results show excellent matching between theory and simulations for multiple orbital periods, with no drift observed. This is also the case despite the

maximum particle diameter being significantly smaller than the fluid grid spatial resolution. The results of this multiscale Jeffery's orbit simulation again demonstrate that the EBF method is capable of accurately capturing particle dynamics for solid particles much smaller than the fluid grid resolution. The maximum diameter of the particle is 0.14 times the fluid spatial grid, and the solid mesh resolution is at an even finer grid resolution of approximately 0.025 times the fluid spatial grid. For the pulsatile BMHV suspension flow simulations of this study, the maximum diameter of the platelets is approximately 0.04 times the fluid spatial grid. The subgrid resolution modeling capabilities of the EBF method were also demonstrated in the BMHV hinge flow simulations from the study by Yun *et al.* [63]. This combination of results justifies the use of LBM-EBF in this study to accurately capture platelet particle dynamics with subgrid scale modeling.

4.1.2.4 Effect of aspect ratio and particle size on particle motion

The effect of ellipsoid aspect ratio and particle size are explored to determine the limits of the EBF numerical method to accurately capture suspended particle dynamics. The simulations of this section are performed in a domain of 120x120x120, with walls moving at U = +/- 0.01 in LB units, and $\tau = 5$.

Figure 4-10 illustrates the effect of particle aspect ratio on drift from theory for both 1-way and 2-way FSI modeling. The aspect ratio of 1 is a sphere of radius 10, and the other aspect ratio cases all have major axis radius 12, and minor axis radii varying based on the aspect ratio being modeled.

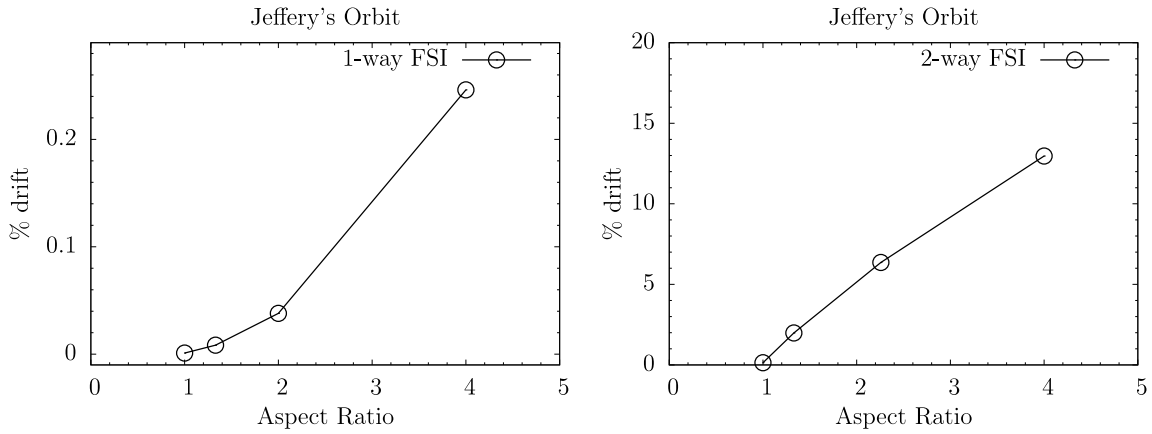

Figure 4-10: Effect of aspect ratio on orbital drift from theory for 1-way and 2-way FSI

It is clearly shown that increased aspect ratio causes a larger drift from theory. However, for 1-way FSI modeling, even a 4:1 aspect ratio results in a drift from theory of only 0.246%. For 2-way FSI, the drift from theory grows from 0.1933% from theory for a perfect sphere to 12.97% for an ellipsoid with aspect ratio of 4:1. The original methodology paper by Wu and Aidun also showed larger drift from Jeffery's orbit theory with a larger aspect ratio particle [66].

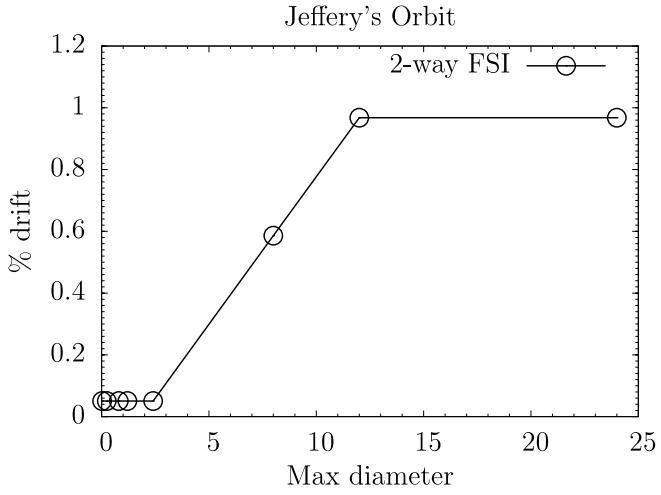

Figure 4-11: Effect of particle size on orbital drift from theory for 2-way FSI modeling. Maximum diameter given as major axis diameter in LB units.

Figure 4-11 demonstrates drift from theory for 2-way FSI based on a particle size that maintains the same aspect ratio, but shrinks in total size. The particle used for these tests is a 12x9x9 radii ellipsoid for the largest case, which is then shrunk in size. It is observed that the shrinking particle leads to closer matching with theory. For a particle with subgrid resolution with 0.012x0.009x0.009 radii, the particle shows only 0.051% drift from Jeffery's orbit theory. This is likely due to the fact that as the particle becomes smaller, the effect it has on the flow field is significantly reduced.

As the particle grows in size, the drift from theory increases to approximately 0.97% for a 12x9x9 ellipsoid. This is likely due to the relative solid mesh resolution at this largest particle size, where the solid surface elements have length greater than the fluid mesh resolution. Thus, as the particle becomes larger, the comparative mesh resolution of the solid surface becomes coarser, leading to higher inaccuracies. Nevertheless, the drift from theory is still less than 1%. These results again demonstrate the high applicability of the numerical method with subgrid resolution capabilities.

4.1.2.5 Behavior at higher particle Reynolds number

Jeffery's orbit is a theoretical solution of an ellipsoid in simple shear flow, but only valid at Stokes flow. However, the behavior of an ellipsoid in shear flow at higher particle Reynolds number can also be investigated to determine the accuracy of the EBF method. Earlier work was performed using lattice-Boltzmann methods with standard bounce-back FSI to determine the effect of inertia on solid particle dynamics. Two studies by Aidun and Ding demonstrated that at higher particle Reynolds number, Re_p,

the orbital period of an ellipsoid in shear flow increases and eventually becomes infinitely large at a critical Reynolds number, Re_c [69, 90]. The nondimensional period of rotation is given as shear rate multiplied by time of one orbital rotation, GT. The work of Ding and Aidun [90] showed that orbital period follows a general scaling law, given as

$$GT = \mathrm{C}\left(\mathrm{Re}_c - \mathrm{Re}_p\right)^{-1/2}$$

Equation 4-7

where C is a constant and Re_c is the critical Reynolds number at which point the ellipsoid stops rotating and becomes stationary in steady-state flow due to saddle-node bifurcation.

To test the ability of the EBF method to capture this behavior, the case of an ellipsoid particle in shear flow is modeled with increasing particle Reynolds number. An ellipsoid with aspect ratio of 4 is modeled (dimensions 12x3x3 radii) in shear flow in a domain of 120x120x120. Two shear rates are tested: G=1/1200 and G=1/600. The nondimensional periods of rotation are determined for these two shear rates at varying particle Reynolds number and are shown in figure 4-12.

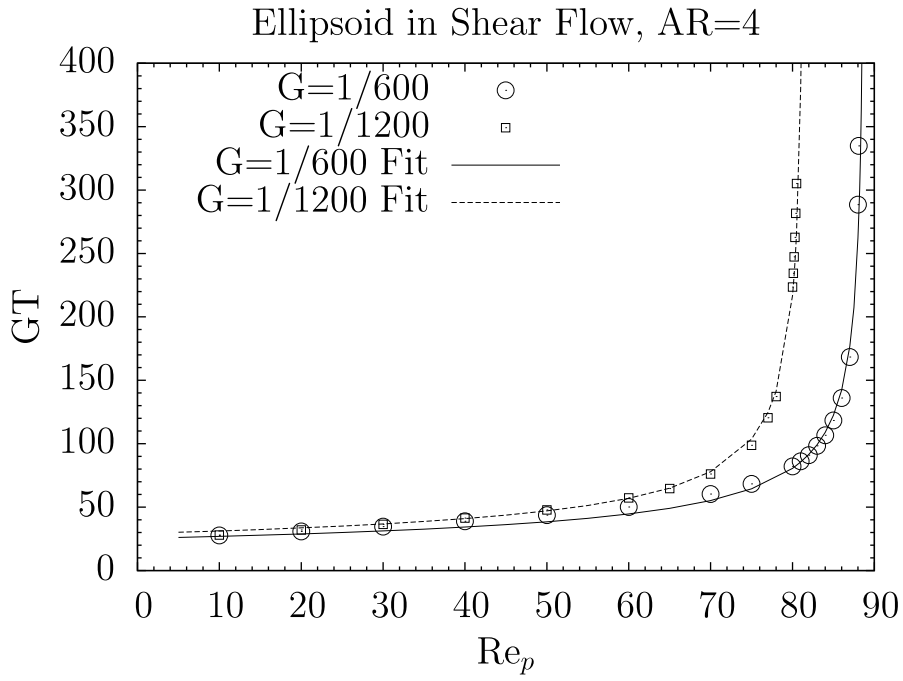

Figure 4-12: Nondimensional period of rotation, GT, for increasing particle Reynolds number. Results shown for a 120x120x120 domain, particle aspect ratio of 4, with shear rates G=1/1200 and G=1/600.

The results demonstrate that for the two shear rates, the orbital periods follow the general scaling law of equation 4-7. For G = 1/1200, the scaling law is fit with C = 263.8, Re_c = 81.48. For the higher shear rate of G = 1/600, the scaling law is fit with C = 240, Re_c = 88.8. The orbital periods follow this general scaling law very well, even at close to the critical Reynolds number (figure 4-12). It is also observed that the lower shear rate of G = 1/1200 results in a lower critical Reynolds number.

A zoomed view of the G = 1/600 and G = 1/1200 cases is also shown (figure 4-13), close to the critical Reynolds number. These plots again show the close matching of the orbital periods with the scaling law fit. These results demonstrate the applicability of

the EBF method to accurately model solid particle dynamics at higher particle Reynolds number, where the effects of inertia cannot be ignored.

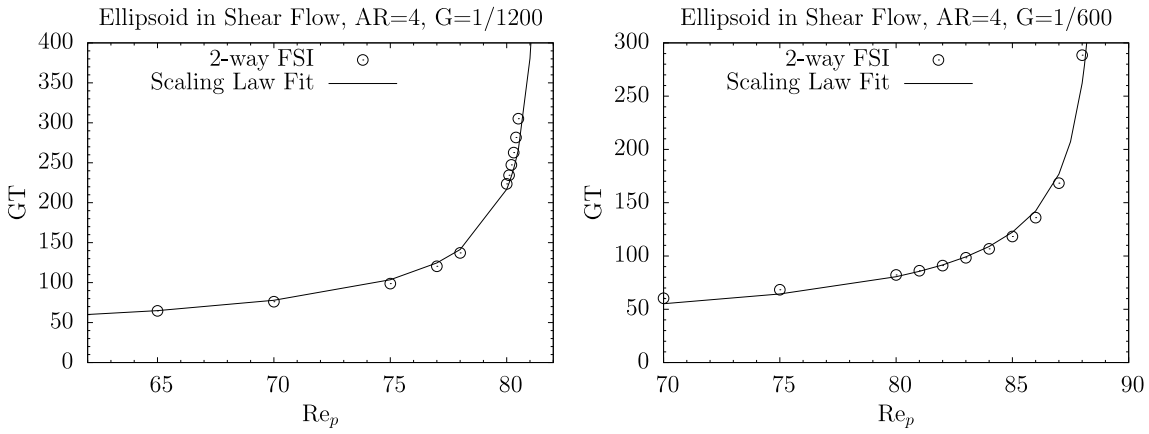

Figure 4-13: Nondimensional period of rotation, GT, for increasing particle Reynolds number. Results shown for (left) G=1/1200 and (right) G=1/600 close to the critical Reynolds number.

The ellipsoid orbit case with G = 1/600 and identical setup and parameters is also modeled by an alternate LBM-EBF code [92]. The results between the two codes are compared in figure 4-14 for both general and near-critical Reynolds number viewpoints. For the alternate LBM-EBF code, the scaling fit yields C = 260, Re_c = 89.3. The results show very good matching for all particle Reynolds numbers. The critical Reynolds number between the two codes differs by less than 0.5 particle Reynolds number.

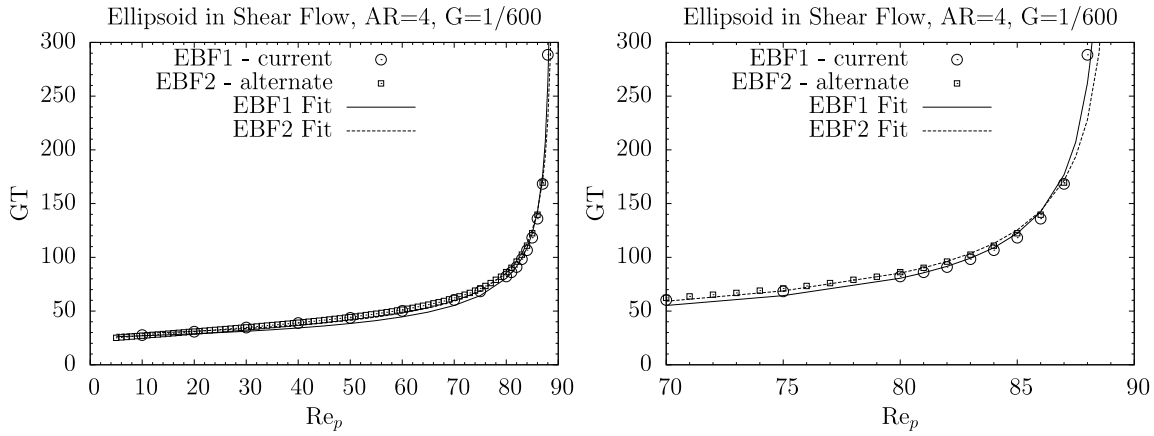

Figure 4-14: Nondimensional period of rotation, GT, for increasing particle Reynolds number with aspect ratio 4, G=1/600. Results show a comparison of two different LBM-EBF codes.

An alternate ellipsoid particle with aspect ratio 5 is also modeled (15x3x3 ellipsoid) in the same shear flow with a 120x120x120 domain. Two shear rates are tested for this particle as well, at G = 1/600 and G = 1/1200, with varying particle Reynolds numbers. The results (figure 4-15) demonstrate that for this larger aspect ratio particle, the orbital periods also follow the general scaling law of equation 4-7. For G = 1/1200, the scaling law is fit with C = 345.5, Re_c = 79.4. For the higher shear rate of G = 1/600, the scaling law is fit with C = 352.5, Re_c = 86.7. The general scaling law fits very well close to the critical Reynolds number, and it is again observed that the lower shear rate of G = 1/1200 results in a lower critical Reynolds number, agreeing with the results of the ellipsoid with aspect ratio 4.

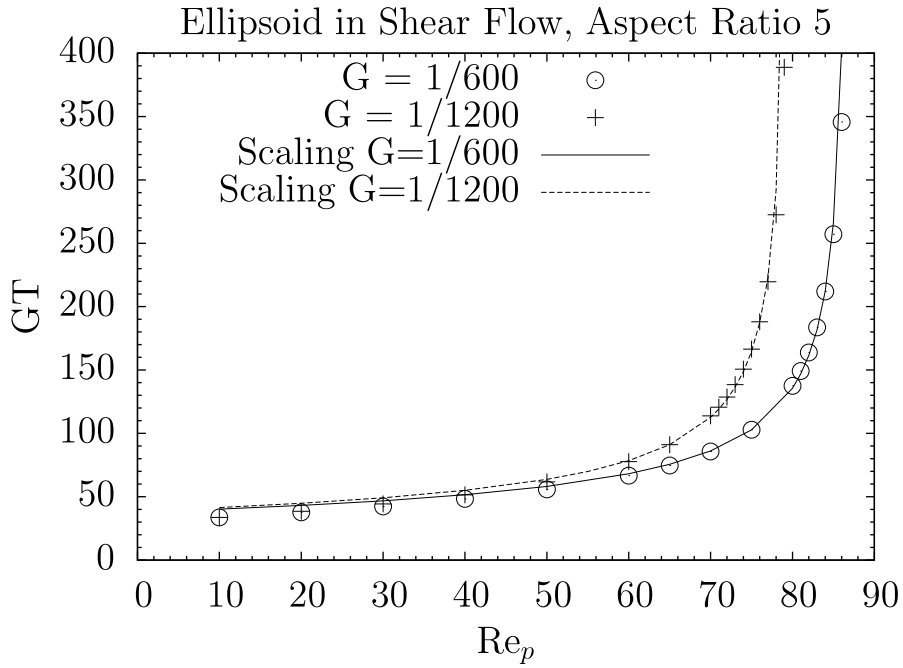

Figure 4-15: Nondimensional period of rotation, GT, for increasing particle Reynolds number with ellipsoidal particle of aspect ratio 5, G = 1/600 and G = 1/1200.

Comparisons are also made between the two ellipsoidal particles of aspect ratio 4 and 5 (figure 4-16). This demonstrates that a larger aspect ratio particle leads to a lower critical Reynolds number, demonstrated for both shear rates of G = 1/1200 and G = 1/600. For both shear rates, the increase in particle aspect ratio from 4 to 5 leads to critical Reynolds number values approximately 2 lower. This decrease in critical Reynolds number for increased particle aspect ratio is also observed by the alternate LBM-EBF code [92].

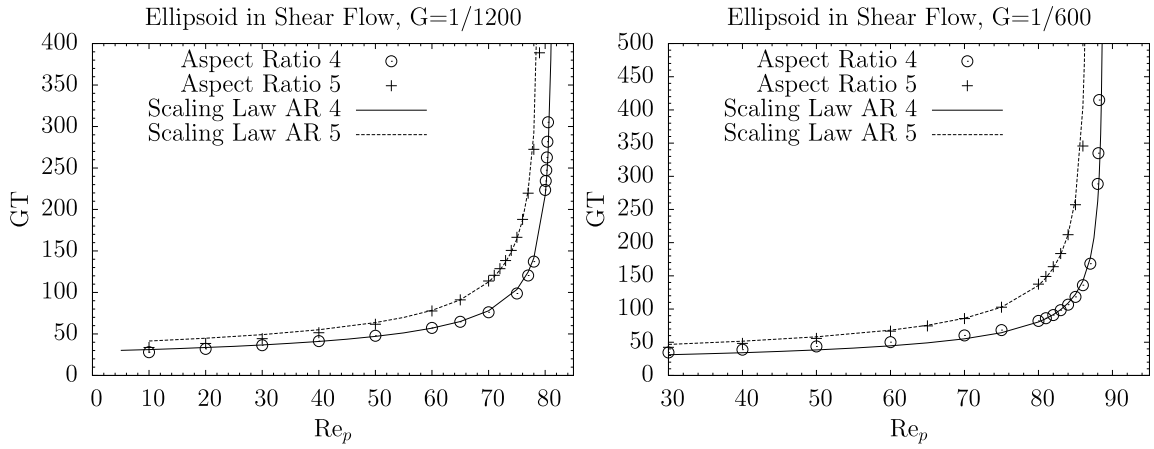

Figure 4-16: Nondimensional period of rotation, GT, for increasing particle Reynolds number for ellipsoidal particles with aspect ratio 4 and 5, at shear rates of G=1/600 and G=1/1200.

4.1.2.6 Subgrid calculation of shear stresses

The accuracy of shear stress quantification for subgrid particles is explored by testing various particle sizes from supergrid (well-resolved particle) to subgrid resolution. This is tested due to the use of shear stress calculations for quantifying blood damage in the simulations of this study. An oblate spheroid particle that is the same shape as the platelet model is used for these tests.

The platelet particle is isolated in simple shear flow in a domain of 120x120x120 LB units, and allowed to rotate with 2-way FSI. The maximum diameter of the largest modeled particle is d = 14.0 LB units. This corresponds to a domain confinement of H/d = 8.6, and thus wall effects are considered minimal. The platelet is tested with shrinking particle sizes while maintaining the same ambient fluid shear field (equal μG in all flow fields) and same particle Reynolds number of Re_p = 2.7e-4. This small particle Reynolds number is within the Stokes flow regime. The smallest particle has d = 0.0375 LB units,

which corresponds to the subgrid resolution size of platelets modeled in chapter 6. Maximum platelet shear stress is determined at every timestep, and then normalized by ambient fluid shear stress μG. Results of normalized platelet maximum shear stress are plotted with $\tau^* = \tau_{\max} / \mu G$.

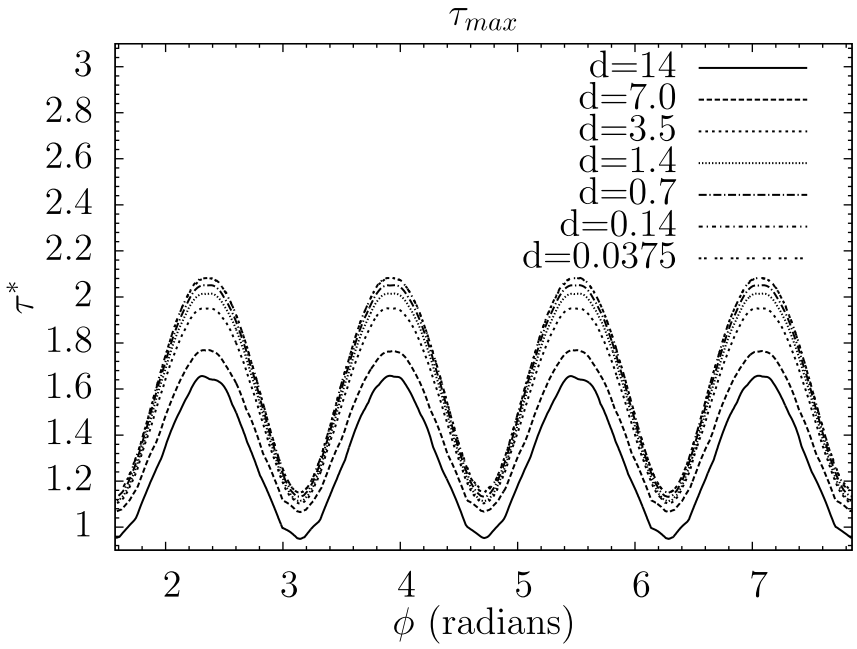

Figure 4-17: Maximum instantaneous particle shear stress (normalized by ambient fluid shear stress μG) variation with respect to angular orientation for isolated platelet-shape ellipsoid in simple shear flow, with decreasing particle diameter *d* from supergrid to subgrid resolution

The variation of normalized maximum shear stress on the particles shows periodic behavior as the particles rotate in shear flow (figure 4-17). The well-resolved supergrid particle (d = 14) shows maximum shear stress variation from 0.95 to 1.65 times the ambient fluid shear stress. As the particles shrink in size, the shear stress calculation is elevated in magnitude but maintains a periodic behavior with respect to variation in

angular orientation. The smallest particle (d = 0.0375) shows shear stress calculations elevated by 20.6% to 25.8% from shear stress calculations of the well-resolved supergrid particle. Although this difference in shear stress calculation is considerable, it is within reasonable accuracy considering the very small subgrid particle size. This shows the general order of accuracy of subgrid modeling of platelet shear stresses.

The particle tracking methods used in alternate numerical methodology studies [10, 62] model platelets as massless point particles with no surface or volume. The particles freely advect with the flow and their velocity is determined by interpolating the fluid flow velocities at the current particle position. The new position is determined from simple time integration of the interpolated velocities. In the particle tracking method, the maximum shear stress on the particle surface is estimated as the interpolated viscous fluid shear stress at the current particle location. This is because the particle tracking method employs massless point particles without an actual surface. Details on point particle tracking and shear stress determination can be found in works by Simon *et al.* [8, 62].

In simple shear flow, this computed shear stress is μG for point particle tracking methods. Using LBM-EBF, the maximum platelet shear stress is shown to vary with angular orientation for well-resolved supergrid particles up to 1.65 times μG. Thus, particle-tracking methods would underestimate the maximum particle shear stress, as well as not account for shear stress variation based on angular orientation of the platelet.

The effects of red blood cells at realistic hematocrit on platelet shear stress calculation using LBM was explored by Reasor [93]. It was shown that RBC presence led to increase in platelet shear stresses by a factor of ~1.7 compared to the case of an isolated platelet. Combined with the results of this study, point particle methods may

underestimate maximum platelet shear stress up to a factor of ~2.8. This further demonstrates the inaccuracy of point particle methods for platelet shear stress calculation.

4.2 Parallelization of Numerical Method

The methodology of parallelization employed in this thesis is discussed in detail in Appendix A.8. The desired outcome for any parallelization of code is to have identical results for parallel processing as with serial processing, and to have good scaling efficiency. For the parallelization results, minor comments are made on the accuracy of the parallelized method. The primary focus of parallelization results is the performance of the code on computational cluster resources.

4.2.1 Parallelization Validation

After parallelization of the numerical method, a wide variety of cases are run with comparison between serial processing and parallel processing simulations. The 3D flow fields are compared by employing a "diff" command on the serial and parallel processing outputs of flow velocity and density. These comparisons are made for the entire 3D flow field with outputs to machine precision level (1e-16 floating point values). The simple shear flow and Poiseuille flow cases are performed for domain sizes of 80x80x60 and 120x120x60 in lattice-Boltzmann units, with outputs generated every 1000 timesteps for 10,000 total timesteps. A wide range of Reynolds numbers are simulated, from Re = 0 to 1000 for each flow case.

For the BMHV flow cases, steady flow through the BMHV domain is performed for both an unexpanded and expanded geometry, representing different spatial

resolutions. For the unexpanded case, the spatial resolution is 1mm and the domain is 388x35x35 in LB units while varying Reynolds number from 5 to 200. For the expanded case, the spatial resolution is 320μm and the domain is 1200x108x108 in LB units with varying Reynolds number from 15 to 600.

Table 4-2: Flow field errors from serial vs. parallel processing

Flow Case	Boundary Conditions	Highest error (floating point)
Shear Flow (Parallel Plates)	Periodic	0.0e-16
Poiseuille Flow (Parallel Plates)	Periodic	0.0e-16
Poiseuille Flow (Parallel Plates)	Stress-Free	0.0e-16
Poiseuille Flow (Circular Pipe)	Periodic	0.0e-16
Poiseuille Flow (Circular Pipe)	Stress-Free	0.0e-16
BMHV Flow (small)	Stress-Free	1.0e-9
BMHV Flow (expanded)	Stress-Free	0.0e-16

The flow field comparison shows perfect matching in the 3D flow fields between serial and parallel processing for a variety of flow cases and boundary conditions. The perfect matching occurs to machine precision level, or 0.0e-16 error for double floating point values. One case of an unexpanded BMHV geometry shows minor differences in parallel processing, with a maximum error of 1.0e-9. However, the cause of this error is the small, unexpanded BMHV geometry having very fine solid grid resolution compared to the fluid resolution. This leads to multiple bounce-back links being formed from the fluid grid to the BMHV surface mesh. These multiple bounce-back links are interpreted differently for parallel processing case, and thus a minor error is observed.

When expanding the BMHV geometry to a larger size that is closer to the size used in the simulations of this study, these multilink issues disappear. The solid grid

resolution is similar to the fluid grid resolution in this case, as is required by the SBB method for fluid-solid interaction. For this more accurate BMHV geometry, the error between serial and parallel processing returns to zero with machine level precision. This perfect matching occurs with a test case spatial resolution of 320μm, which is still four times coarser than the 80μm resolution used in the pulsatile flow simulations of this thesis. Thus we can expect perfect parallelization of results with the BMHV flow simulations of this thesis.

Table 4-3: Solid dynamics errors for serial vs. parallel processing when using EBF method for fluid-solid interaction

Flow Case	Boundary Conditions	Particle Type	Highest error (floating point)
Shear Flow (Parallel Plates)	Periodic	Rigid	0.0e-16
Poiseuille Flow (Parallel Plates)	Periodic	Rigid	0.0e-16
Poiseuille Flow (Parallel Plates)	Stress-Free	Rigid	0.0e-16
Poiseuille Flow (Circular Pipe)	Periodic	Rigid	0.0e-16
Poiseuille Flow (Circular Pipe)	Stress-Free	Rigid	0.0e-16
BMHV Flow (small)	Stress-Free	Rigid	0.0e-16
BMHV Flow (expanded)	Stress-Free	Rigid	0.0e-16
Shear Flow (Parallel Plates)	Periodic	Deformable	0.0e-16
Poiseuille Flow (Parallel Plates)	Periodic	Deformable	0.0e-16
Poiseuille Flow (Parallel Plates)	Stress-Free	Deformable	0.0e-16
Poiseuille Flow (Circular Pipe)	Periodic	Deformable	0.0e-16
Poiseuille Flow (Circular Pipe)	Stress-Free	Deformable	0.0e-16
BMHV Flow (small)	Stress-Free	Deformable	0.0e-16
BMHV Flow (expanded)	Stress-Free	Deformable	0.0e-16

For the EBF method (Table 4-3), the parallelization shows perfect matching with parallel and serial processing. These tests are employed for a wide variety of flow cases, boundary conditions, and for rigid and deformable suspended particles. These tests are also modeled with multiple particles suspended in the same flow field. In all cases, the

solid dynamics (position, angle, velocities, forces and torques on particle) are perfectly identical to machine precision level.

These test results demonstrate that the suspension flow methodology has perfect accuracy for parallel processing for a wide variety of flows and suspensions. These tests are also employed for the BMHV geometries that are used in this study, with perfect flow field and particle dynamics matching. Thus, parallel processing is valid for the simulations of BMHV suspension flow.

4.2.2 Parallel Scaling Efficiency

4.2.2.1 Entropic Lattice-Boltzmann

To test the performance of the Entropic LB (ELB) method, simulations are performed for a case of simple shear with a domain size of 512x512x512 on the Ranger system at the Texas Advanced Computing Center (TACC) at the University of Texas at Austin. The simulations are performed on 128, 256, 512, 1024, 2048, and 4096 cores. Each case is run once with the standard BGK collision operator and once with the ELB method employed at every fluid node. Although the ELB method is typically used only for unstable fluid nodes, the scaling test simulations force the use of the ELB method at every fluid node to demonstrate a worst-case scenario where all fluid nodes are unstable.

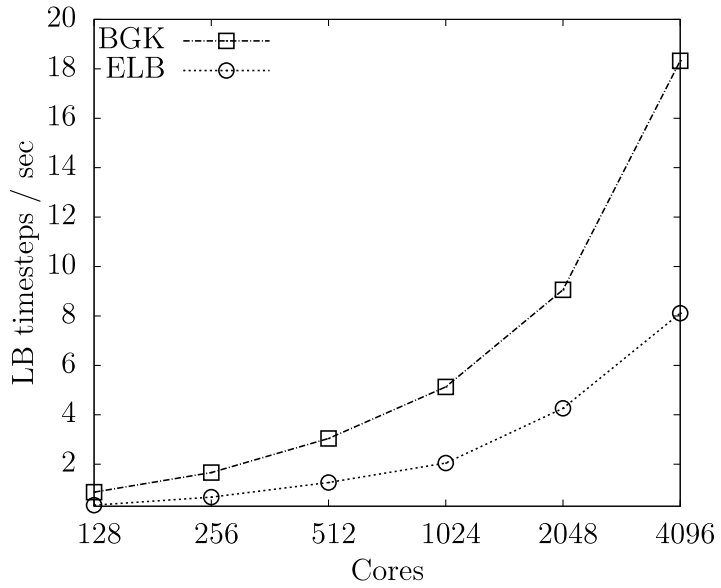

Figure 4-18: Standard BGK vs. Entropic LB for 128 – 4096 cores, performance demonstrated by number of lattice-Boltzmann timesteps per second

Figure 4-18 shows a comparison of the performance for LBM versus ELB methods in number of simulation timesteps per second. This demonstrates the speed of the simulations and clearly shows that the normal LBM is faster than the ELB method. This is expected, as the ELB method requires additional calculations for the modification of the local viscosity.

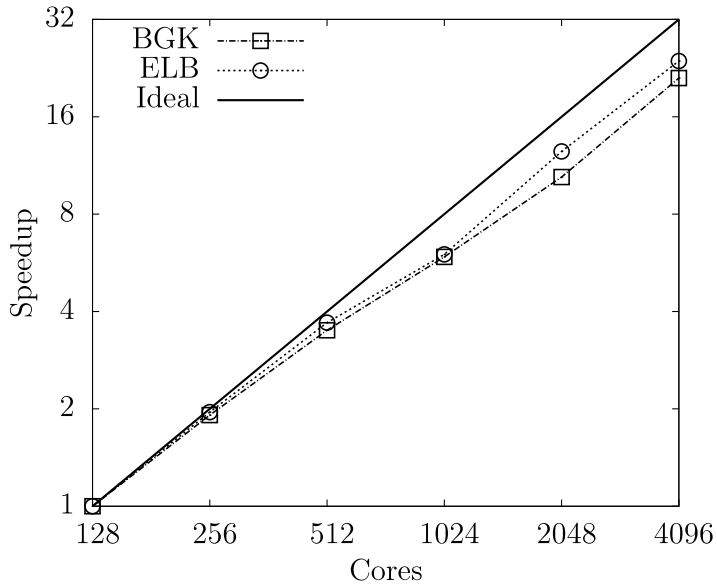

Figure 4-19: Scaling performance for Standard BGK vs. Entropic LB for 128 – 4096 cores.

Figure 4-19 demonstrates scaling efficiency as the number of cores increases from 128 to 4096 by plotting speedup vs. # of cores. For a fixed number of simulation timesteps, speedup is defined as

$$\text{Speedup} = \frac{\text{simulation time}_{\text{base \# of cores}}\ (\text{seconds})}{\text{simulation time}_{\text{increased \# of cores}}\ (\text{seconds})} \qquad \text{Equation 4-8}$$

Ideal performance for a parallelized code is defined as 1:1 speedup, where doubling the number of cores in the simulation would decrease the simulation time in half.

The speedup for the two methods is similar, however the plot shows that the ELB is consistently slightly higher in speedup efficiency than the standard BGK model. The speedup improvement in the ELB method is more pronounced for the 2048 and 4096 core cases. This superior speedup in the ELB method is expected due to the additional calculations required by the ELB method without any extra MPI data communication.

The ratio of number of calculations to MPI data communication is thus consistently higher for the ELB method, leading to better speedup efficiency with an increased number of cores. Particularly for the 4096-core case, the sub-domain size is 32x32x32, and the standard BGK operator does not perform well due to the low computation to communication ratio. The ELB method here shows a consistently better speedup performance as the sub-domain sizes become smaller.

It is determined that the entropic LB is slower than standard LBM due to the increased computations at each fluid node, but the scaling efficiency is even better than standard LBM. Thus, the use of entropic LB for high Reynolds number flows is justified, as there is no reduction in performance for parallel cluster computing. Though the number of calculations required makes entropic LB slower overall, this test is performed for a worst-case scenario where ELB is used at every fluid node. In actual high Reynolds number flow simulations, the entropic LB method is only used on a small percentage of fluid nodes that are unstable.

4.2.2.2 External Boundary Force

To test the scaling efficiency of the EBF method parallelization, simulations are performed for a case of simple shear flow with a domain size of 512x512x512 on the Stampede system at the Texas Advanced Computing Center (TACC) at the University of Texas at Austin. The simulations are performed on 128, 256, 512, 1024, 2048, and 4096 cores. One case is performed with the single ghost-node layer parallelization for the SBB method, with no suspended particles included in the flow field. Another case with the double ghost-node layer parallelization for the EBF method is performed, with no

suspended particles in the flow. Finally, a case with the double ghost-node layer EBF method parallelization and 500 suspended platelets is performed. The moving walls employ the SBB method for fluid-solid interaction in all cases.

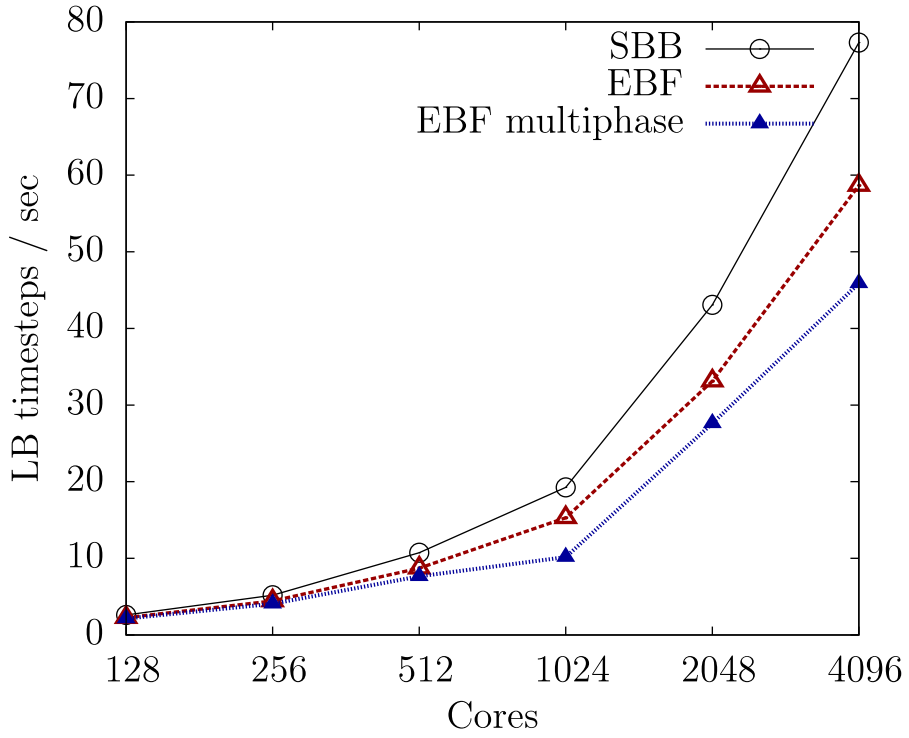

Figure 4-20: Standard Bounce Back vs. External Boundary Force parallelization for 128 - 4096 cores, performance demonstrated as number of lattice-Boltzmann timesteps per second. Multiphase EBF simulation includes 500 platelets suspended in flow field

Figure 4-20 compares the SBB and EBF methods in number of simulation timesteps completed per second. This figure demonstrates that the SBB method is consistently faster than the EBF method. The EBF method with 500 suspended platelets also shows lower number of timesteps simulated per second. This result is expected, as the EBF method requires additional calculations for the double ghost node layer as well as additional MPI data communication. For the suspension flow case, additional

calculations and data communication are required to model the fluid-solid interaction and platelet dynamics, and thus lower simulation performance is observed.

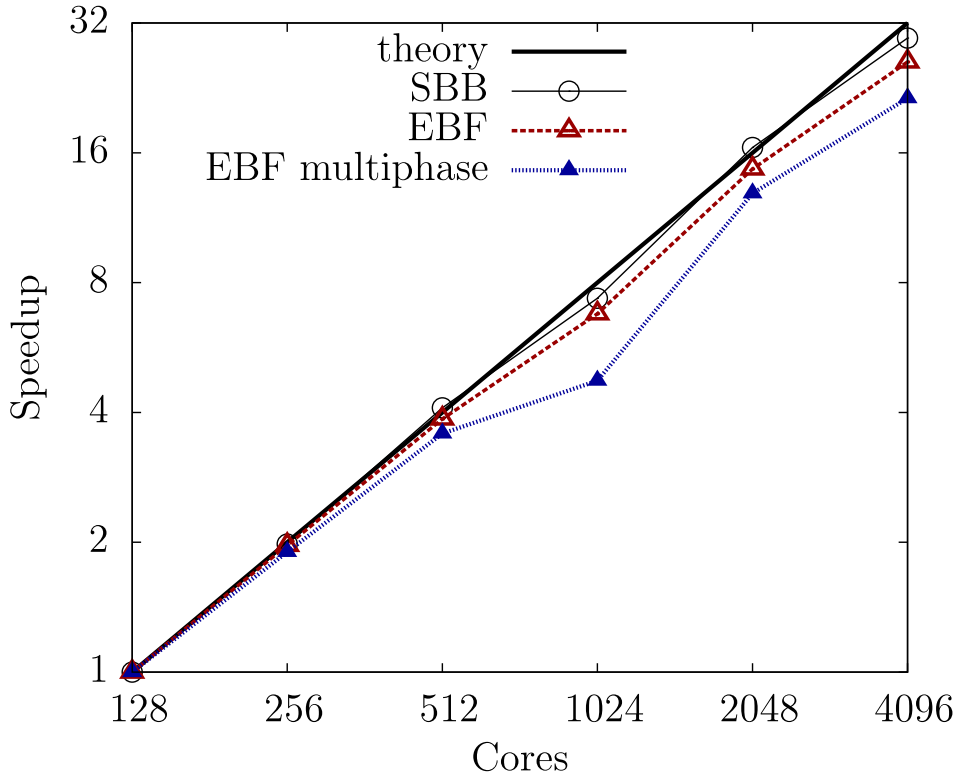

Figure 4-21: Scaling performance for Standard Bounce Back vs. External Boundary Force Method for 128 - 4096 cores. Multiphase EBF simulation includes 500 platelets suspended in flow field

Figure 4-21 demonstrates scaling efficiency as the number of cores increases from 128 to 4096. The speedup efficiencies for the SBB and EBF methods without suspended particles are excellent. In particular, the SBB method shows near perfect scaling efficiency up to 4096 cores, demonstrating again the optimal parallel processing capabilities of LBM. Though the EBF method performs worse, the scaling efficiency is still very good up to 4096 cores. The loss of efficiency compared to the SBB method can

be explained by the increased amount of data communication due to the double ghost node layer required by the EBF method. As the number of cores increases and the subdomain sizes become smaller, the computation-to-communication ratio decreases significantly, and thus lower scaling efficiency is observed.

The scaling efficiency of the EBF method with 500 suspended particles is shown as lower than for both single-phase methods. This is expected, as significant data communication among subdomains is required to compute particle forces and dynamics for a large number of platelets. A similar lower scaling efficiency was observed for multiphase LBM-SBB simulations in the work by Clausen *et al* [94]. This is unavoidable due to the nature of data communication required for any parallel multiphase flow numerical methodology.

The parallel scaling results are still promising for the multiphase flow simulations. The 512-core case corresponds to a 64x64x64 subdomain, which is close to the subdomain sizes of the simulations of BMHV suspension flow in this study. For this subdomain size, the speedup efficiency for the multiphase LBM-EBF simulation is 90% of ideal speedup. Thus, despite modeling 500 suspended particles with fluid-solid interaction, the LBM-EBF method shows excellent scaling performance for cases relevant to this study. The particle concentration level of this test case is similar to the average particle concentration level of the BMHV suspension flow simulations in chapters 6 and 7. This again justifies the LBM-EBF method for parallel processing of the blood damage simulations of this study.

CHAPTER 5

SINGLE-PHASE BMHV FLOW SIMULATIONS

This chapter details simulations of single-phase fluid flows through bileaflet mechanical heart valves. The LBM-EBF method is validated for modeling general suspension flows in chapter 4, thus showing its applicability for the simulations of platelet flow in this study. Previous studies have also employed the LBM-EBF method and validated the numerical method as accurate in quantifying platelet damage in BMHV hinge and hinge-like flows [63, 65]. The lattice-Boltzmann method is now validated in this chapter to model single-phase pulsatile flows through BMHVs. This final step will demonstrate its full applicability as a numerical method to accurately quantify platelet damage in pulsatile suspension flows through BMHVs.

Comparisons are made between simulations and experimental PIV data to validate the numerical method. These comparisons are made for a clinical 23mm SJM valve for both steady flow with fixed open leaflets and pulsatile flow with prescribed leaflet motion and 1-way FSI. Details of the experiments are given in section 3.5 and in the published experimental study [52]. After comparison with experiments, the pulsatile flow is visualized in both 2D and 3D representations to examine the flow fields with detail that is not available from experimental data. Novel flow features are also delineated, focusing on the leaflet closing phase and mid-diastolic leakage jets. Turbulent features of pulsatile BMHV flow are also quantified for the first time with computational simulations. Additional flow cases are simulated prescribing natural leaflet motion asymmetry or severe leaflet dysfunction. Results on 2-way FSI of leaflet motion are also presented.

Understanding the dynamics for BMHV flow is crucial for the connection between the flow fields and blood damage that occurs in these complex flows.

5.1 Steady Flow Results in Comparison to Experimental Data

Quantitative comparisons between simulations and PIV experimental data are made with steady flow past the 23mm SJM bileaflet mechanical heart valve. These comparisons are made for axial velocity at perpendicular lines past the trailing edge of the leaflets. The 2D perpendicular plane of experimental data is taken at the center of the flow chamber cross-section as shown in figure 5-1. Comparisons between simulations and experiments are made at various Reynolds numbers, representing various phases of the cardiac cycle.

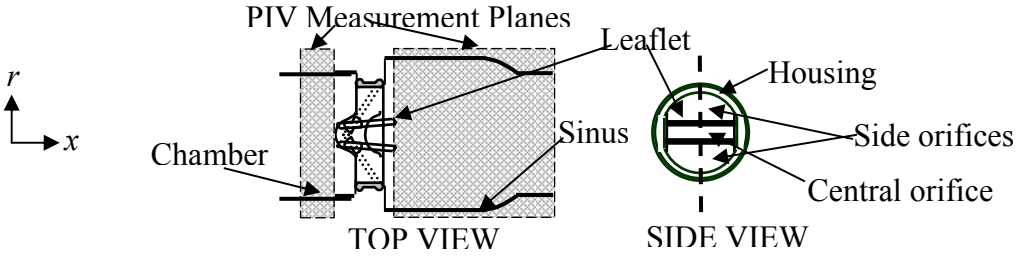

Figure 5-1: Experimental setup showing perpendicular data plane

Reynolds number in this chapter refers to the bulk flow Reynolds number:

$$\mathrm{Re} = \frac{U_{avg} D}{\nu}$$

Equation 5-1

where U_{avg} is the average inlet flow velocity determined by the inlet flowrate, D is the inlet diameter at 25.4mm, and ν is the kinematic viscosity (3.5 cSt).

For all velocity comparisons in this chapter, x = 0 is the axial location of the end leaflet tips, and y = 0 is located at the centerline of the transverse perpendicular direction.

5.1.1 Re = 750

Comparisons at Re = 750 represent the early acceleration phase of the cardiac cycle. For the experiments, an average flow field is computed with 100 time ensembles. For Re = 750, due to the steady nature of laminar flow at this Reynolds number with no oscillations, only one computational time ensemble is needed for comparison with experiments.

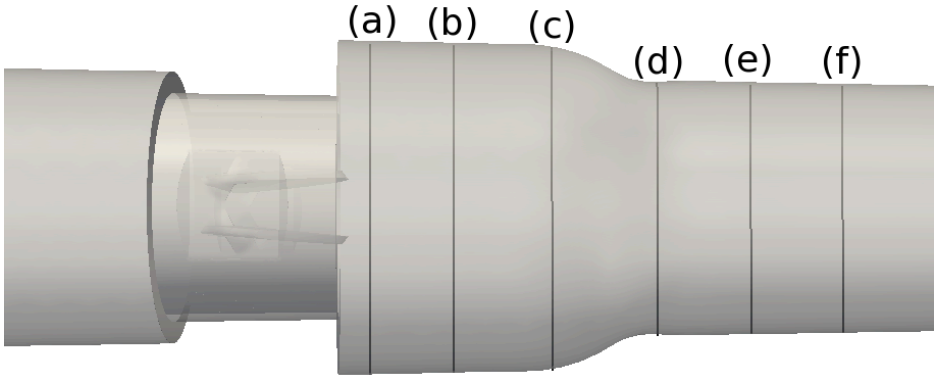

Figure 5-2: Perpendicular lines of comparison for Re = 750

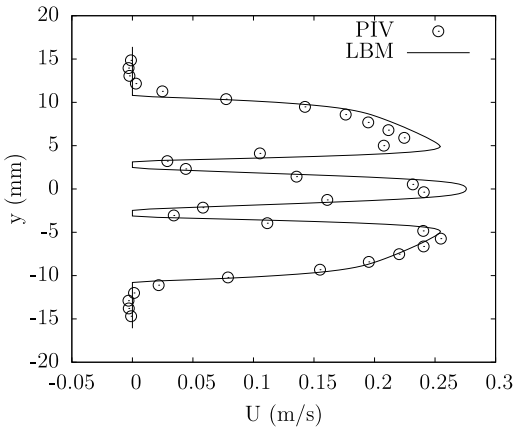

(a) 2.2mm

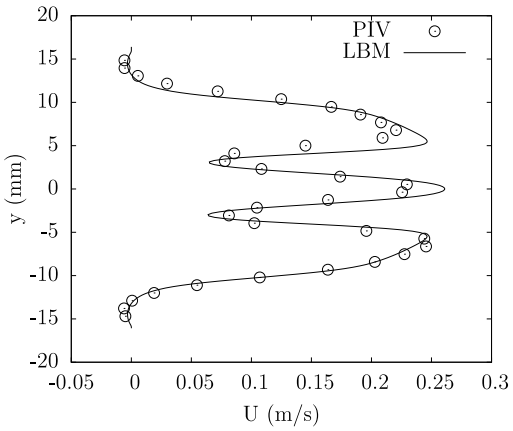

(b) 10.3mm

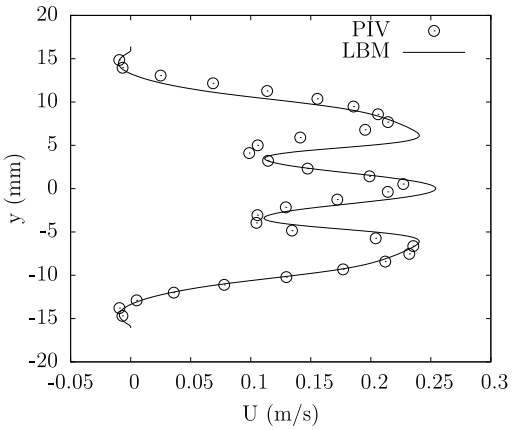

(c) 20.1mm

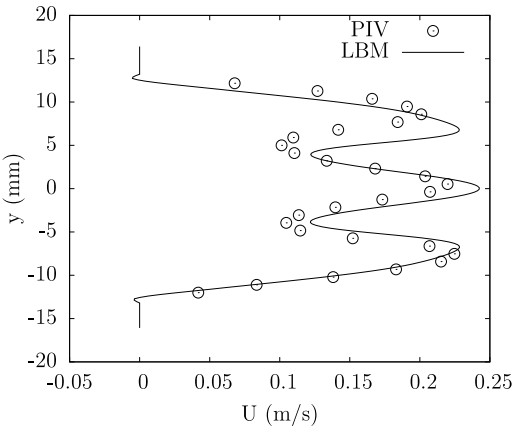

(d) 30.9mm

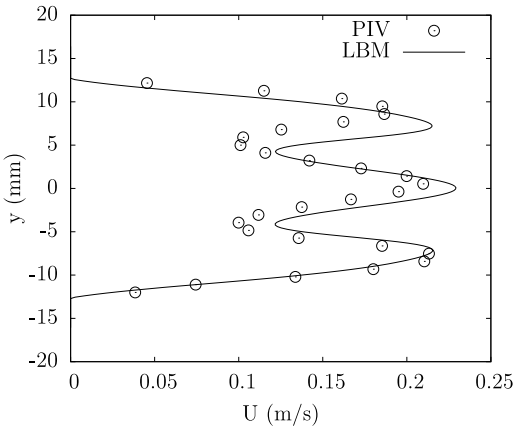

(e) 40.7mm

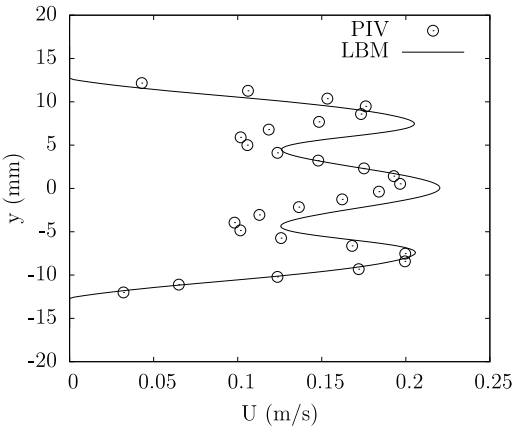

(f) 50.6mm

Figure 5-3: Axial velocity comparison for Re = 750 at (a) 2.2mm, (b) 10.3mm, (c) 20.1mm, (d) 30.9mm, (e) 40.7mm, (f) 50.6mm downstream of leaflet tips

The comparison made immediately downstream of the valve (x = 2.2mm) shows excellent comparison between simulations and PIV data. The slight asymmetry of the experimental results is apparent, as the flow is stronger through the bottom jet than the top jet. The bottom jet shows excellent agreement between the numerical and experimental data.

The remaining five plots, showing comparisons further downstream, indicate good matching between the numerical results and experimental data. The asymmetry of the experimental data is apparent in all of the experimental plots, as the top jet is consistently weaker than the bottom jet. This lack of symmetry in the experimental data was also noted in the previous computational-to-experimental validation work [55]. This may be attributed to imperfections in valve machining. In addition, the two leaflets do not necessarily have the same fully open angle even for steady forward flow, thus leading to some minor asymmetries in the flow field. Nevertheless, the middle jets and particularly the bottom jets show good numerical-to-experimental agreement for all plots.

5.1.2 Re = 1250

Comparisons at Re = 1250 represent the early-to-mid acceleration phase of the cardiac cycle. For the experiments, an average flow field is computed with 100 time ensembles. As flow at Re = 1250 is still laminar in nature, only five computational ensembles are averaged for comparison with experiments. Five ensembles are determined as sufficient to obtain a converged mean flow field at this Reynolds number.

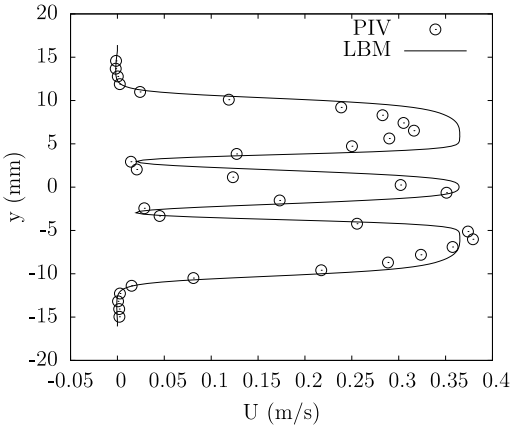

(a) x = 2.2mm

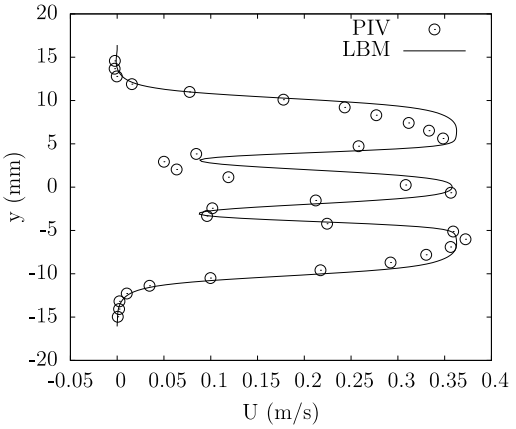

(b) x = 6.7mm

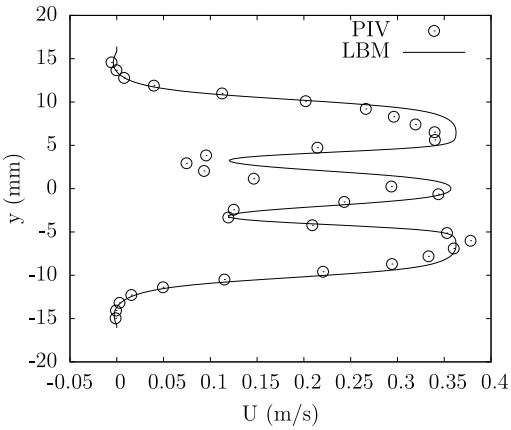

(c) x = 10.2mm

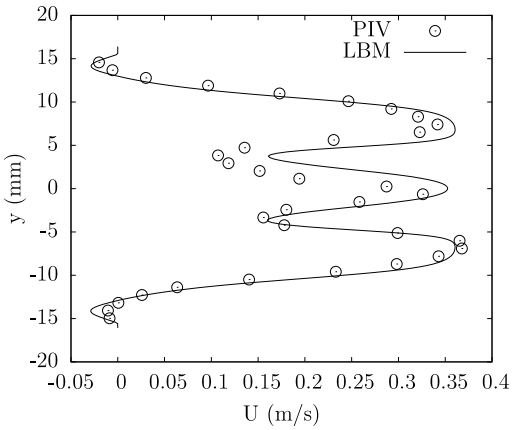

(d) x = 20.1mm

Figure 5-4: Axial velocity comparison for Re = 1250 at (a) 2.2mm, (b) 6.7mm, (c) 10.2mm, (d) 20.1mm downstream of leaflet tips

The comparisons at this second laminar flow regime again show very good matching between simulations and PIV data. Once more, the slight asymmetry of the experimental results is demonstrated, as the bottom jet flow is consistently stronger than the top jet. This asymmetry of experimental data is demonstrated in all plots. The bottom jets show the best numerical-to-experimental agreement, with the middle jets showing good agreement as well. The simulations are also able to capture some negative axial velocities near the housing walls in the sinus expansion, representing recirculating flow.

5.1.3 Re = 2400

Comparisons at Re = 2400 represent the mid-acceleration phase of the cardiac cycle, where some disorganized flow is present. For the experiments, an average flow field is computed with 200 time ensembles. Due to some unsteadiness in vortex shedding at this Reynolds number (as observed for instantaneous flow visualization), 100

computational ensembles are averaged for comparison with experiments. This vortex shedding will be described in section 5.4.

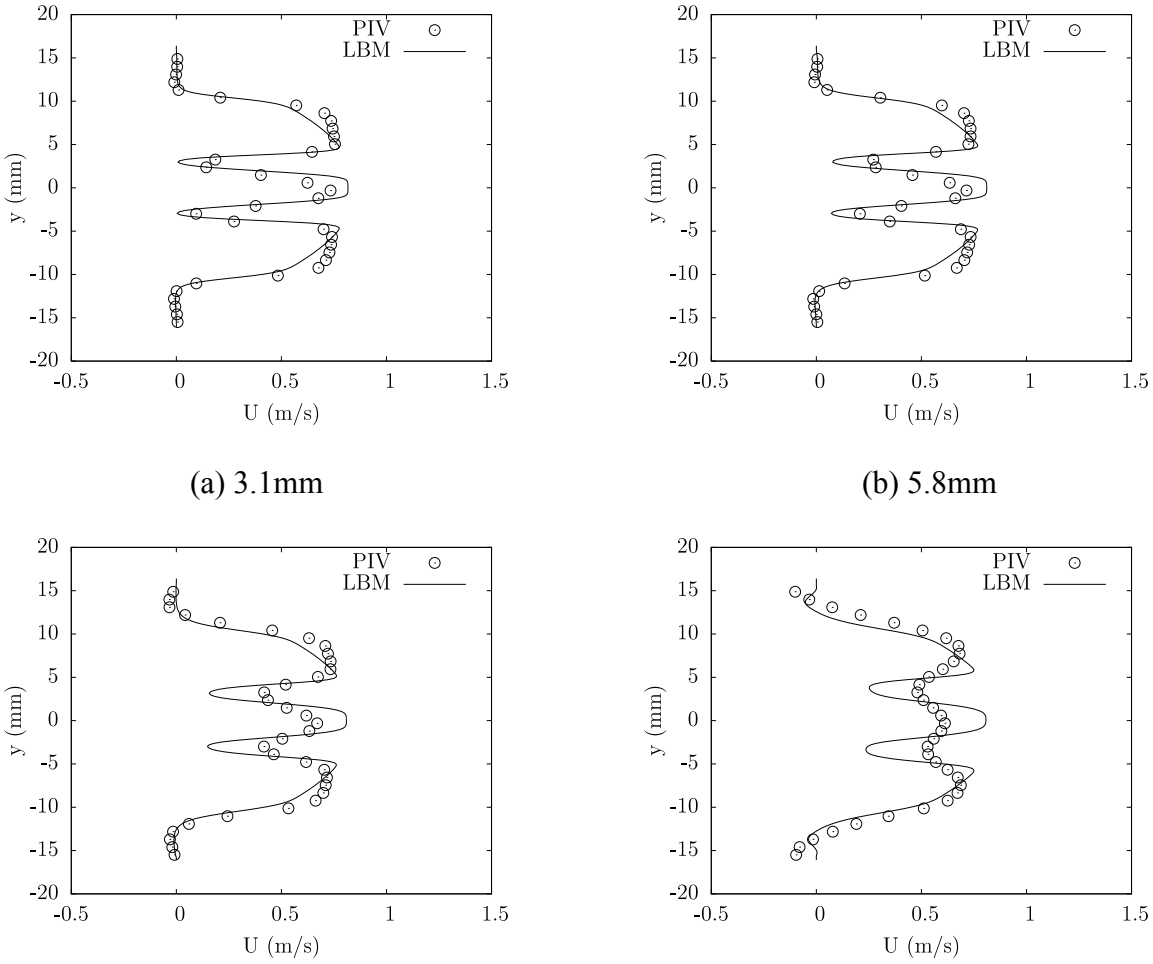

(a) 3.1mm

(b) 5.8mm

(c) 10.3mm

(d) 20.0mm

Figure 5-5: Axial velocity comparison for Re = 2400 at (a) 3.1mm, (b) 5.8mm, (c) 10.3mm, (d) 20.0mm downstream of leaflet tips

The plots show good comparison between the simulations and experiments at this representative mid-acceleration Reynolds number. The experimental results show the triple orifice jets to have more blunted profiles than in the numerical results. Though the

lateral jets match well between simulations and experiments, the blunted profiles near the peak values is not captured by the simulations.

The central jet in the experiments is also consistently weaker than the lateral jets. This is in contrast to the simulations where the central jet is consistently stronger than the lateral jets. This is particularly noted 20.0mm downstream of the leaflets. Nevertheless, all comparisons taken downstream of the leaflet tips show similar good agreement between simulations and experiments for the lateral jets. A comment is made about the central jet matching in section 5.1.5. The negative axial velocities near the valve housing are shown in both the experiments and simulations, representing the recirculation region in the aortic sinus expansion.

5.1.4 Re = 5000

Comparisons at Re = 5000 represent the near peak flow phase of the cardiac cycle, with highly disorganized and chaotic flow structures. For the experiments, an average flow field is computed over 200 time ensembles. Due to the highly disorganized flow at this Reynolds number, 200 computational ensembles are averaged for comparison with experiments. The computational ensembles are spaced 240μs apart with a total sampling time of 48ms, which is within the calculated integral time range for this Reynolds number.

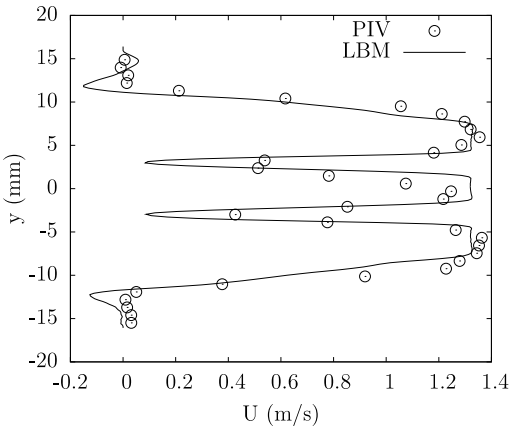

(a) x = 4.0mm

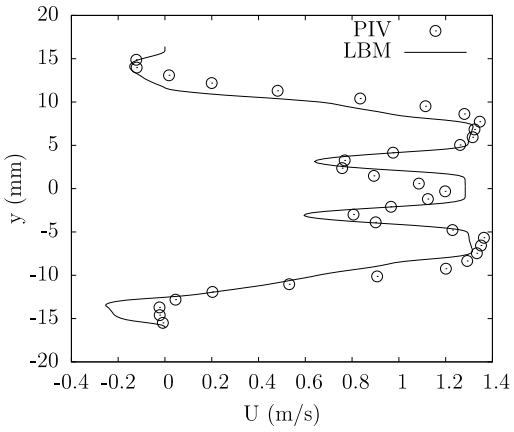

(b) x = 8.4mm

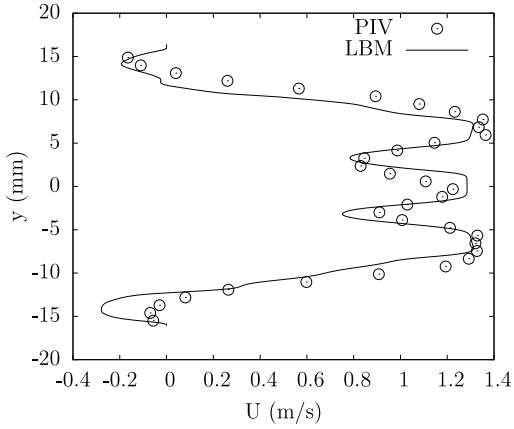

(c) x = 10.3mm

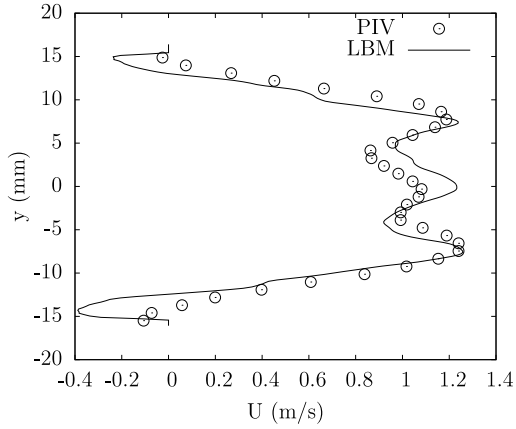

(d) x = 20.1mm

Figure 5-6: Axial velocity comparison for Re = 5000 at (a) 4.0mm, (b) 8.4mm, (c) 10.3mm, (d) 20.1mm downstream of leaflet tips

The plots show very good comparison between simulations and experiments at this representative peak flow Reynolds number. Both the experiments and numerical simulations show blunted profiles for the three orifice jets. For the lateral jets, the simulations slightly overshoot the peak velocities compared to experiments, but still match well. The highly disorganized flow at this Reynolds number is apparent from these comparisons as well. The mean flow fields are converged after 50 computational

ensembles, and the highly converged flow fields using 200 computational and experimental ensembles demonstrate that the mean flow profiles are not symmetric. Lower Reynolds number cases, on the contrary, show symmetric flow profiles for simulations when averaging over sufficient ensembles.

Like the Re = 2400 case, the central jet is consistently weaker than the lateral jets for the experiments. For the simulations at Re = 5000, the central jet is of the same strength when compared to the lateral jets. All comparisons show very good agreement between simulations and experiments for the lateral jets. The negative axial velocities near the valve housing are again highlighted in the simulation results, which show strong reverse velocities in the sinus expansion region.

5.1.5 Final comments on matching with steady flow

When comparing in the laminar regimes of Re = 750 and Re = 1250 (Figures 5-3 and 5-4), it is noted that the LBM compares very well with the experimental PIV data. Even as far downstream as 50.6mm past the leaflet tips, the numerical simulations match the flow profile and velocity magnitudes of the triple jet flow structure well. It is noted in the previous work [55] and from the comparison in this study that a natural asymmetry of the top and bottom orifice flows exists in the experimental data. This again may be due to design imperfections or unequal fully open angles for the two leaflets. Due to the perfect top-bottom symmetry in the computational model, this asymmetry is not present in the numerical results. Despite this, the numerical results show good quantitative agreement with the experiments, particularly in the central and bottom orifice flows.

In all flow comparison cases, the numerical simulations overshoot the peak velocities of the triple orifice flow structure. For the previous study of numerical-to-experimental quantitative comparison at steady flow [55], the simulations of a different numerical method were also shown to consistently overshoot the peak velocities of the triple flow jets as well as show sharper jet profiles. It is possible that the experimental data show a more blunted profile with lower peak velocities due to increased flow mixing in the experiments caused by small experimental design imperfections.

The central jet in the simulations is consistently equal or stronger than the lateral jets at Re = 2400 and Re = 5000, which is opposite of the experimental results. It is noted in the experiments that the maximum flow velocity does occur in the central orifice jet, as expected due to the minimal orifice area. However, in the experiments, this maximum velocity value is found within the valve at the axial location between the leading and trailing leaflet edges. The experimental comparison points, however, are downstream of the trailing leaflet tips, where the lateral jet velocities become stronger than the central orifice jet velocities.

A possible reason for this inconsistency may be due to the computational recreation of the leaflets. The leaflets in the simulations were created in a previous study by scaling up the microCT scan of a leaflet of a 17mm SJM valve [8]. This was performed to create separate scans of the SJM valve housing and leaflets. In addition, the leading edge tips of the leaflet were slightly cut off during microCT scanning. These modifications to the original geometry lead to a slight increase in the central orifice area. However, the central orifice area is only slightly increased and does not affect the bulk flow. Though this modified leaflet geometry and increased b-datum area do not affect the

overall results of this study, it can explain why the simulations show consistently stronger central orifice jets downstream of the trailing leaflet edges.

5.2 Mesh Independence

Mesh independence is detailed for our numerical simulations to determine the appropriateness of 160µm spatial resolution simulations for the purposes of experimental validation. Figures 5-7 and 5-8 show comparison of axial velocities and root-mean-square (rms) values at cross-stream perpendicular lines for numerically simulated flows resolved at 160µm vs. 80µm. The numerical comparisons are performed at steady flow past the open leaflets with Re = 5779, representing the peak flow regime.

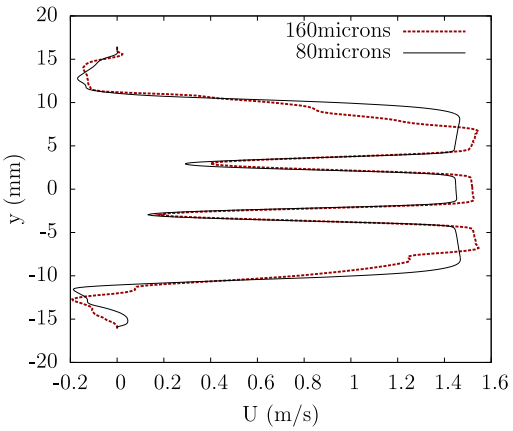

(a) x = 2.2mm

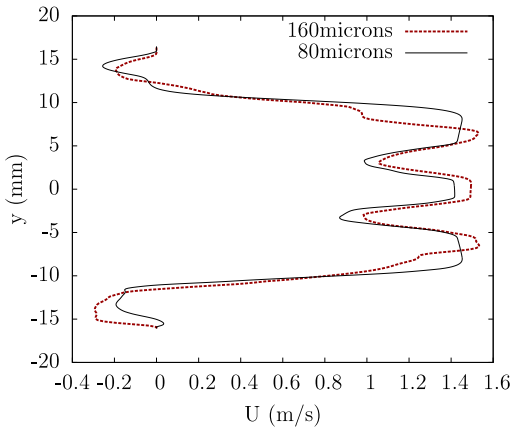

(b) x = 10.1mm

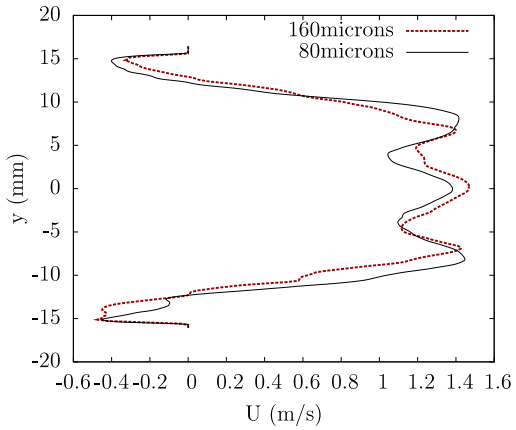

(c) x = 20.0mm

Figure 5-7: Comparison of mean flow axial velocity values at peak flow (Re = 5779) between simulations at 80µm and 160µm spatial resolution taken (a) 5.0mm, (b) 10.1mm, and (c) 20.0mm past the leaflet trailing edges

Mean flow fields are computed by averaging 200 computational ensembles. The mean flow results (figure 5-7) taken downstream of the trailing leaflet tips show that the peak orifice velocities at 160µm resolution are slightly higher with sharper flow profiles when compared to the flow resolved at 80µm. Though the 80µm flow profiles are smoother, the overall flowrate at the perpendicular lines are very similar for both spatial resolution cases. The mean flow fields, though showing some differences at the flow velocity peak values, are still very similar and well captured at the coarser 160µm resolution. The sharper flow profiles at 160µm can be attributed to the 160µm case interpreting slightly smaller flow orifice areas. This occurs due to the coarser resolution of the fluid-solid interaction boundary at the valve and leaflet surfaces.

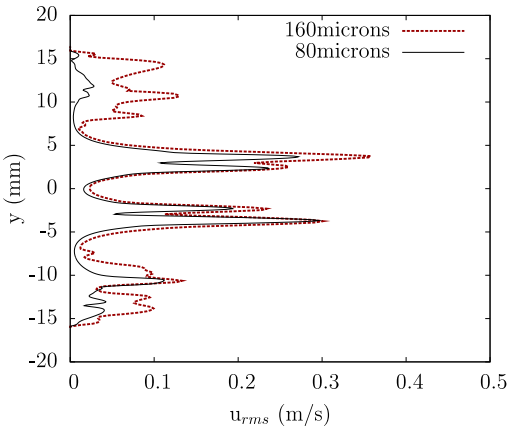

(a) x = 5.0mm

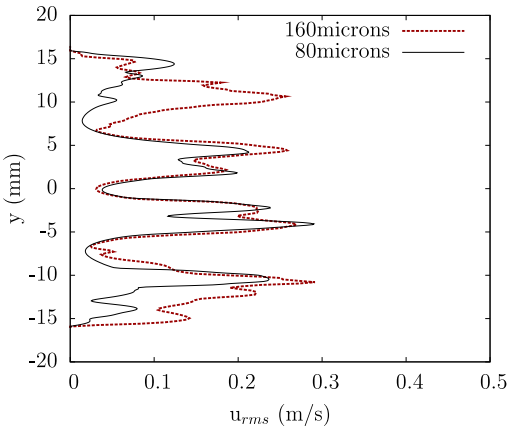

(b) x = 10.mm

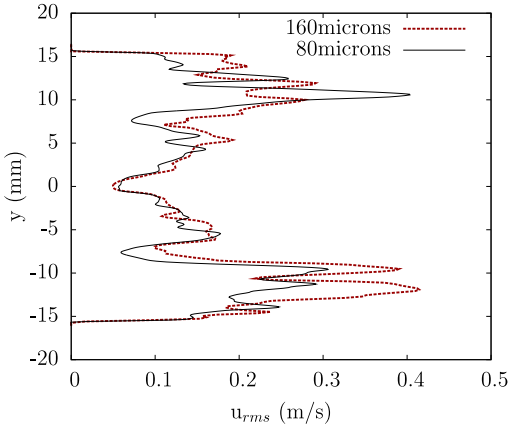

(c) x = 20.0mm

Figure 5-8: Comparison of root-mean-square velocity values at peak flow (Re =5779) between simulations at 80µm and 160µm spatial resolution taken (a) 5.0mm, (b) 10.1mm, and (c) 20.0mm past the leaflet trailing edges

Figure 5-8 shows axial velocity rms values taken at the same perpendicular lines. For the central orifice flow emerging from the valve, the comparison of rms values is excellent from 160µm to 80µm. The largest discrepancies are found outside the central region, representing the sinus expansion region. This difference could be explained by the unstable and disorganized nature of flow within this expansion recirculation region. In

addition, the coarser resolution at 160μm would once again interpret the sudden sinus expansion step differently between 160μm and 80μm, leading to increased differences. Nevertheless, the central orifice rms comparison shows very good agreement.

Despite differences, the mean flow and rms values between the two numerical resolutions show good agreement, and thus validate the 160μm case for use in comparison against experimental data. Bulk flow features are well captured at 160μm, which is key for experimental comparison. However, for the finest details of this pulsatile BMHV flow, simulations should use the higher spatial resolution at 80μm.

A primary concern exists as to whether the lattice-Boltzmann method is appropriate for modeling BMHV flows. For experimental validation, the pulsatile PIV data averaged flow features due cycle-to-cycle variability and lower spatial resolution. Despite these limitations, the experimental data is enough to delineate the key bulk flow features of pulsatile BMHV flow, but would not resolve the turbulent Kolmogorov scales. Thus, for qualitative comparison of bulk flow features with the pulsatile experimental data, the 160μm resolution of the computational simulations is sufficient. For steady flow, comparison at Re = 750 and Re = 1250 does not require a high spatial resolution due to the flow being in the laminar regime. For steady flow at Re = 2400 and Re=5000, the comparison is made for mean flow with an average of 100-200 time ensembles for both the experiments and simulations, making the Kolmogorov turbulent fluctuation scales irrelevant in this steady flow comparison. Thus, the turbulent Kolmogorov scales are not important for all cases of steady flow comparison as well as for qualitative pulsatile flow comparison. The comparison between 80μm and 160μm resolution shown in figure 5-7 shows that the mean flow fields are adequately captured at coarser 160μm

resolution for use in experimental comparison in these cases. However, for the finest details of this pulsatile BMHV flow, future simulations should use the higher resolution at 80μm to capture the smallest flow scales.

5.3 Pulsatile Flow Results in Comparison to Experimental Data

5.3.1 Quantitative Comparison

Quantitative comparisons of pulsatile flow are made for representative flow regimes. The high resolution simulations (80μm and 2.4μs) take 200 samples for each flow regime but only from one cardiac cycle, and are compared to 200 cardiac cycle ensembles from the experiments. The flow regimes are: high accelerating flow (Re = 4700), peak Reynolds number flow (Re = 5780), and decelerating flow (Re ~ 1000), which represent the most chaotic and possibly turbulent flow regimes of the cardiac cycle. Quantitative comparison is performed by computing mean flow fields and rms data. 200 numerical samples are used to match the number of experimental samples taken for averaging flow fields. However, it is determined that even 50 numerical samples are sufficient to determine mean flow fields (figure 5-9). Thus, 200 samples are used to obtain improved rms data.

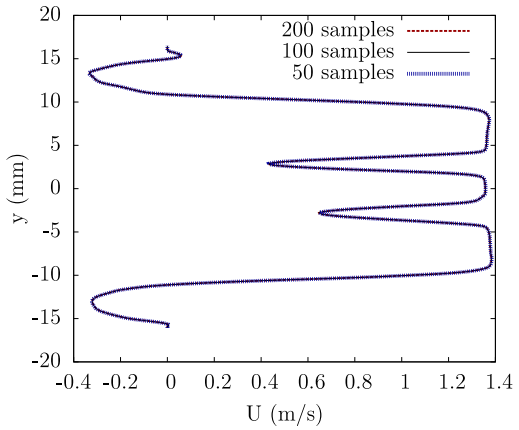

Figure 5-9: Mean axial velocity computed for 50, 100, and 200 computational ensembles 5.0mm downstream of leaflet tips

Comparisons are made at the high accelerating flow phase of Re = 4700 (Figure 5-10). Although the acceleration phase is generally considered a stable and organized flow regime, this high accelerating flow regime is considered transitional flow due to the higher Reynolds number. Mean flow field comparisons at three axial locations show good matching between simulations and experiments. Both simulations and experiments capture negative axial velocities at the sinus expansion regions, though the simulations show larger negative velocities. The simulations show smoother profiles than experiments, which could be due to the higher resolution of numerical data in comparison to experiments. Overall, the simulations and experiments match very well.

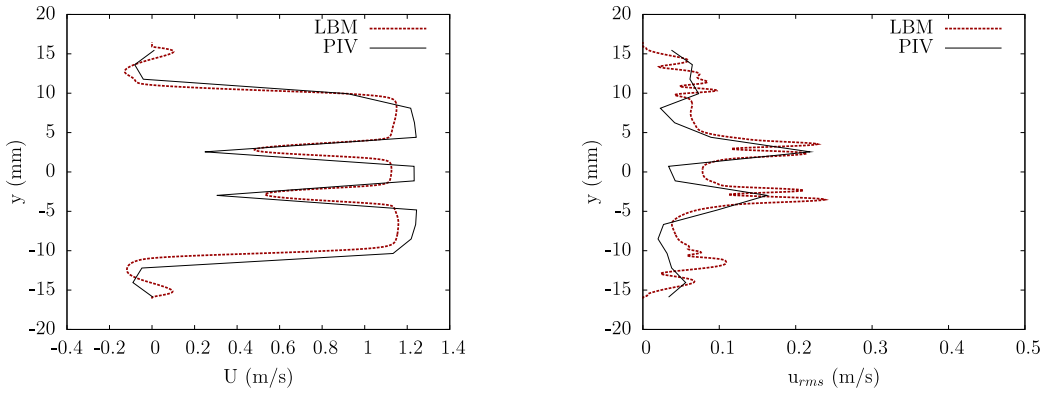

(a) x = 5.0mm

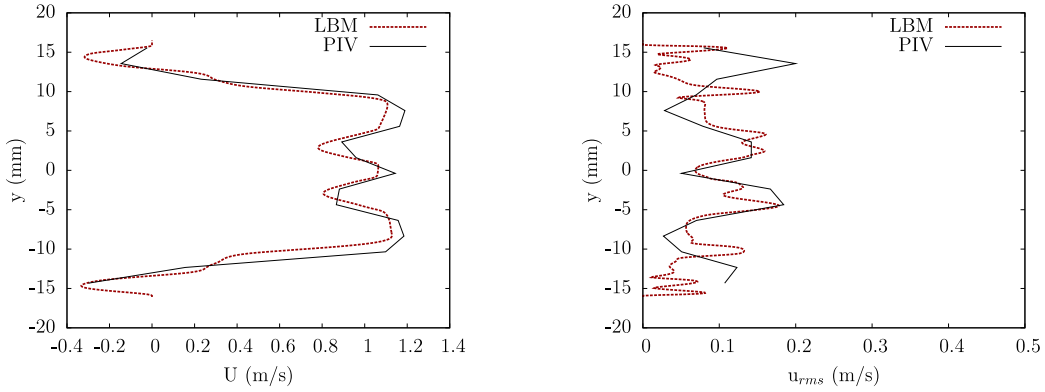

(b) x = 10.1mm

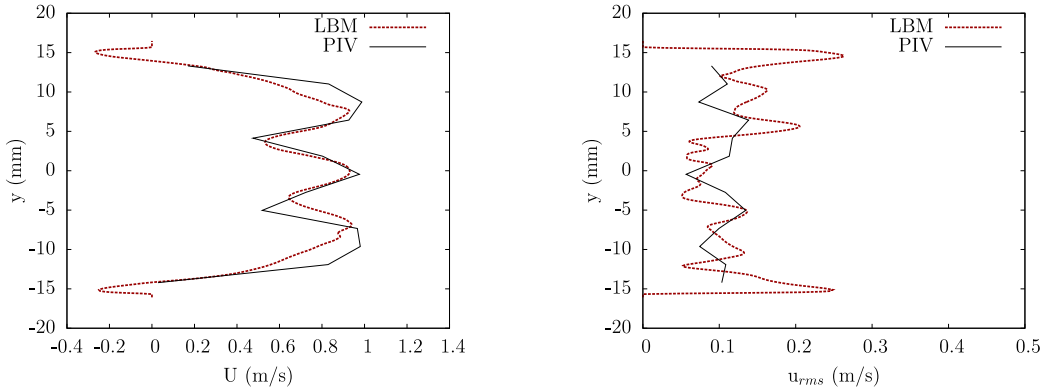

(c) x = 20.0mm

Figure 5-10: Comparison of mean axial flow (left) and root-mean-square (right) velocity values at accelerating flow (Re = 4700) for simulations against experiments for pulsatile flow taken (a) 5.0mm, (b) 10.1mm, and (c) 20.0mm past the leaflet trailing edges

The rms data also show good matching, particularly at 5.0mm downstream of the leaflet tips. The biggest mismatch at all comparison points lies in the sinus expansion regions, which can be explained by the disorganized mixing that occurs in this region. At 20.0mm downstream of the leaflets, this difference is more apparent, but it should be noted that the experimental rms data is cut off near the sinus expansion. Overall, the rms data show good matching between simulations and experiments.

At peak flow (figure 5-11), the numerical simulations and experiments compare very well for mean flow fields at various distances from the leaflet tips. The experimental profiles are slightly lower in magnitude and have sharper orifice flow profiles. The sharper profiles may be attributed to the experimental data resolution being coarser (134μm) than the numerical simulations. Nevertheless, the comparison still shows very good agreement even at peak Reynolds number.

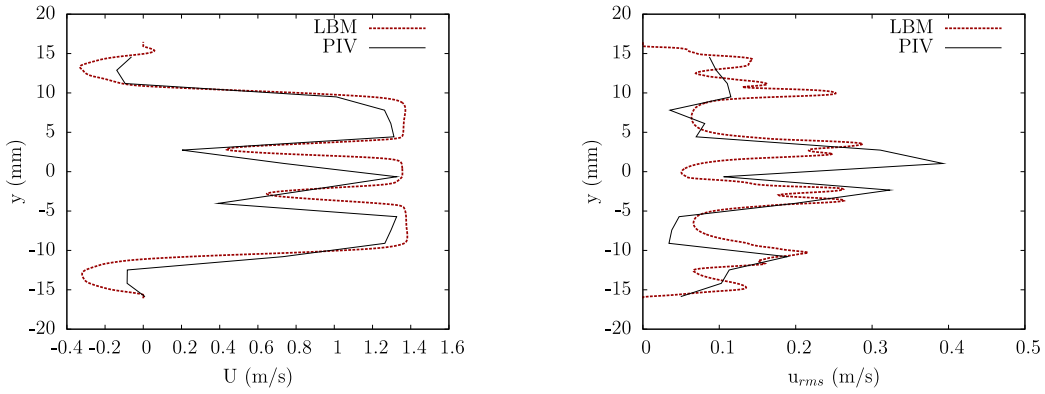

(a) x = 5.0mm

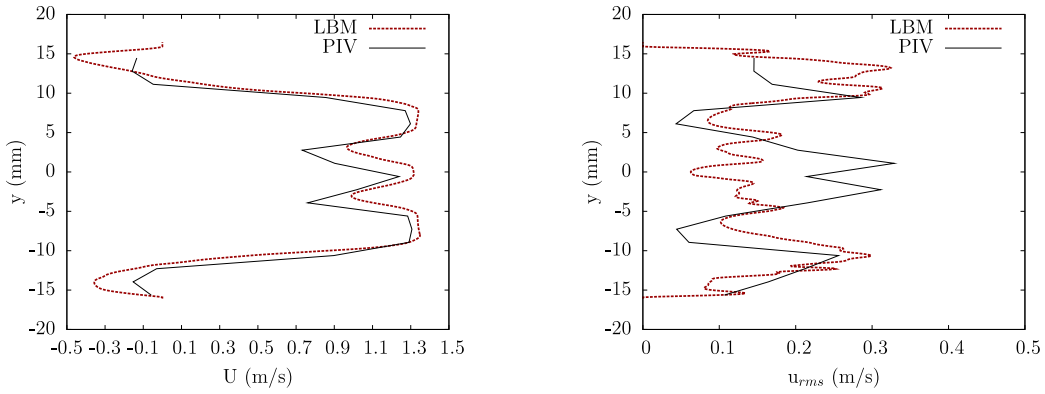

(b) x = 10.1mm

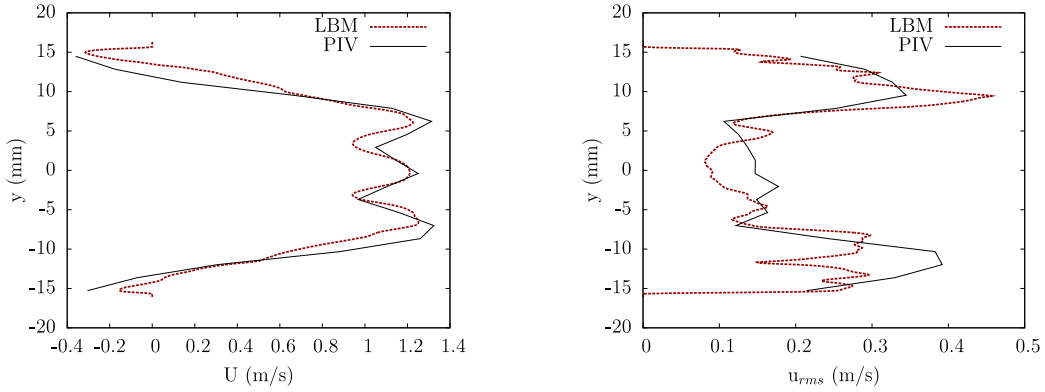

(c) x = 20.0mm

Figure 5-11: Comparison of mean axial flow (left) and root-mean-square (right) velocity values at peak flow (Re = 5780) for simulations against experiments for pulsatile flow taken (a) 5.0mm, (b) 10.1mm, and (c) 20.0mm past the leaflet trailing edges

The experimental rms values are comparable to the numerical simulations in all cases, though slightly higher in some peak values. This can be explained by the pulsatile experimental data including cycle-to-cycle fluctuations in addition to turbulent fluctuations, thus increasing the overall magnitude of rms values.

Quantitative comparisons are also made for the deceleration phase of the cardiac cycle, which is a highly disorganized and unstable flow period. This flow regime is

noted to vary highly from cycle to cycle in experiments [52], and thus matching computational data to experimental data quantitatively for this flow phase may be unreliable. The deceleration phase Reynolds number is approximated at Re ~ 1000, though this may vary highly from cycle to cycle. The comparison of mean flow fields and rms data is shown in figure 5-12.

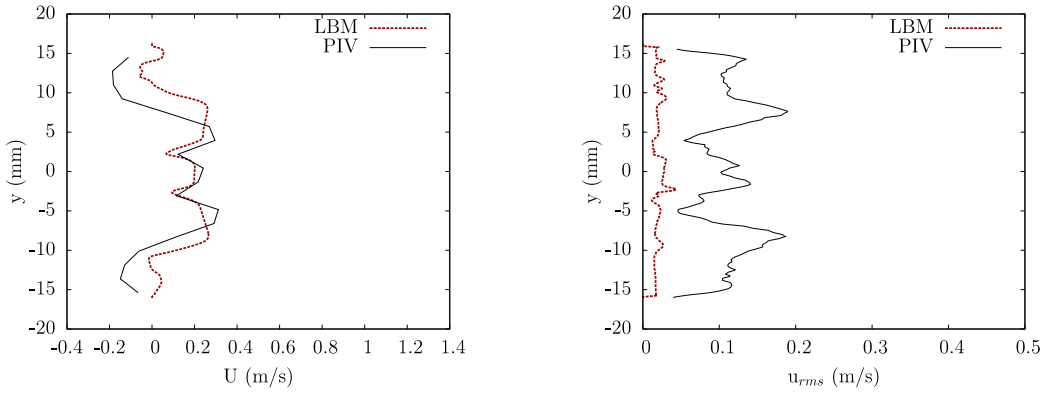

(a) x = 5.0mm

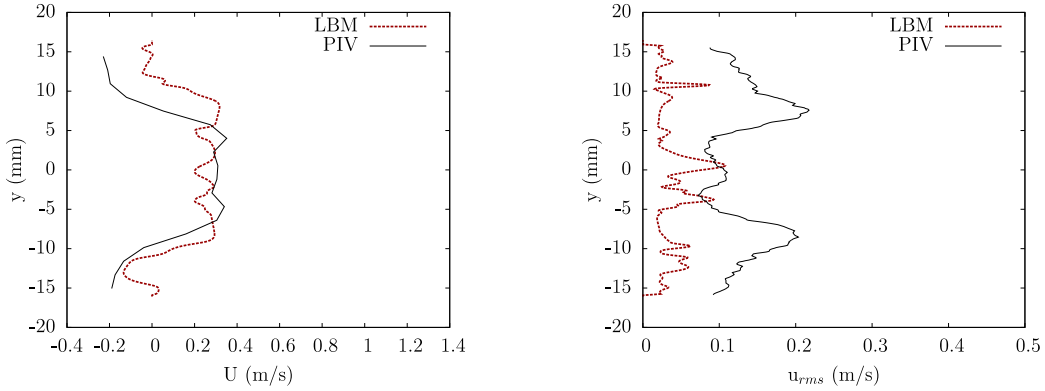

(b) x = 10.1mm

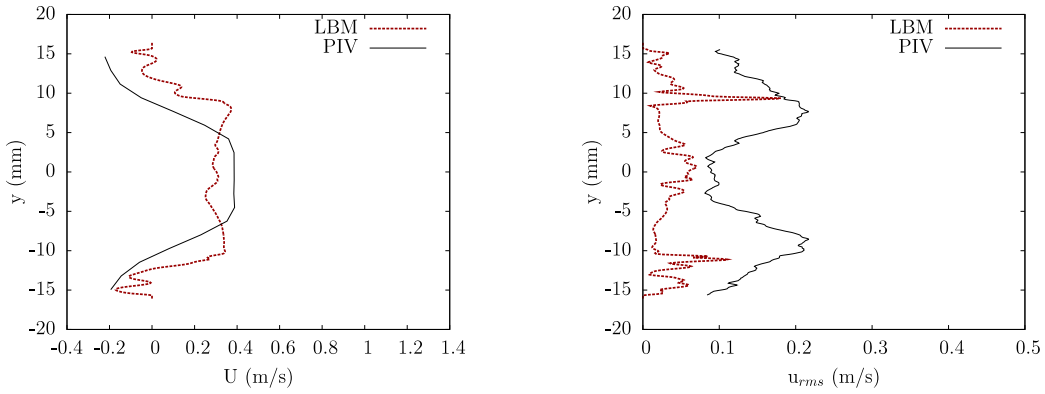

(c) x = 20.0mm

Figure 5-12: Comparison of mean axial flow (left) and root-mean-square (right) velocity values at deceleration flow (Re ~ 1000) for simulations against experiments for pulsatile flow taken (a) 5.0mm, (b) 10.1mm, and (c) 20.0mm past the leaflet trailing edges

The mean flow fields show similar velocity magnitudes and overall flowrates at perpendicular lines past the leaflet tips, but the matching of velocity profile is not very good. The experimental data show more blunted profiles, likely due to coarser resolution and flow averaging across highly varying cardiac cycles. The experimental data also show lower velocity magnitudes further from the center of the cross section, at each perpendicular line. Though the mean flow comparison between simulations and experiments is not particularly good at this deceleration phase, the overall flowrates are similar. It is again emphasized that the deceleration phase is very unstable and varies highly from cycle to cycle, and thus good matching with simulations is not expected.

The rms data comparison shows that experimental rms values are consistently higher than the numerical simulations. For the numerical simulations, velocity fluctuations are primarily due to turbulent fluctuations. For experimental data, however, velocity fluctuations are a combination of turbulent fluctuations and cycle-to-cycle

variations. This rms data demonstrate the high variation in experiments from cycle-to-cycle in the deceleration phase, once again showing the difficulty of comparison between simulations and experiments at this representative flow regime.

The same method of using 200 numerical samples within one cardiac cycle is used for a second cardiac cycle for comparison purposes. The comparison of mean flow fields for these two cardiac cycles is taken at peak flow and given in figure 5-13. Though the mean flow fields are taken from two different cardiac cycles, flowrate and leaflet motion conditions are identically prescribed as "averaged" experimental conditions. The comparison of numerical mean flow fields between the two cardiac cycles is very good, matching well as far as 70mm downstream of the leaflet tips. For 5mm and 10mm downstream of the leaflet, the comparison is excellent. This good matching between two cardiac cycles demonstrates the appropriateness of the numerical ensemble averaging taken from one cardiac cycle. It is noted that the use of average flowrate and leaflet motion data already averages 200 experimental cardiac cycles, thus creating "averaged" experimental flow conditions.

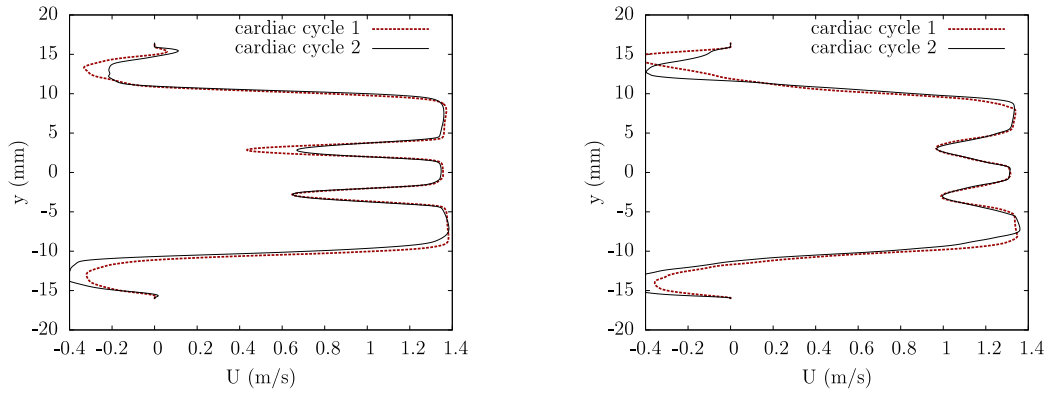

(a) x = 5.0mm (b) x = 10.0mm

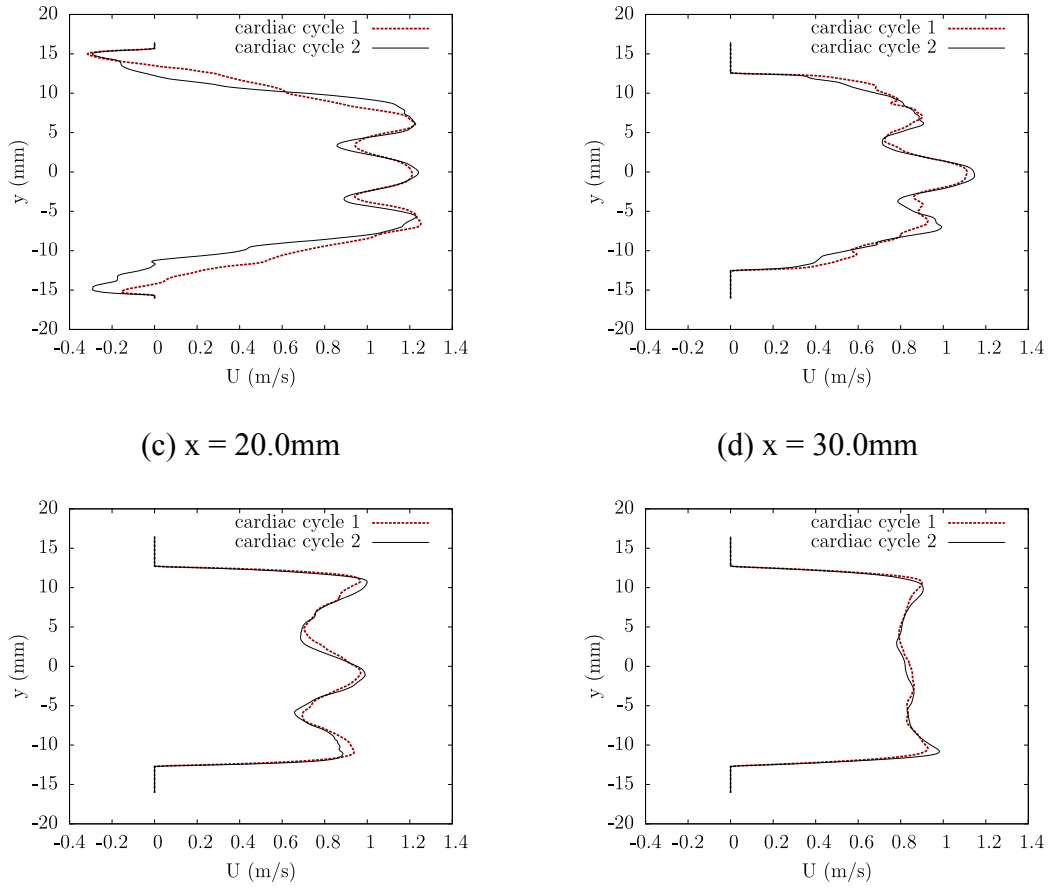

(c) x = 20.0mm (d) x = 30.0mm

(e) x = 50.0mm (f) x = 70.0mm

Figure 5-13: Comparison of mean axial velocity values at peak flow (Re = 5780) for simulations at two different numerical cardiac cycles taken (a) 5.0mm, (b) 10.0mm, and (c) 20.0mm, (d) 30.0mm, (e) 50.0mm, (f) 70.0mm past the leaflet trailing edges

5.3.1.1 Final comments on quantitative matching with pulsatile flow

For the mean flow fields, the experimental data consistently show sharper profiles than the numerical simulations in axial velocities for both flow regimes. The sharper flow profile of the experimental data can be attributed to the lower PIV data resolution (134μm). For peak flow (figure 5-11) the experimental data show slightly lower axial velocity magnitudes in each comparison as well. However, it is noted that the

experimental data is taken from 200 cardiac cycles of pulsatile flow. As there are cycle-to-cycle variations in the experiments, it is likely that the PIV system is unable to capture the exact time points of peak flow for every cardiac cycle ensemble. As peak flow cannot be exactly captured consistently, the overall mean flow fields are expected to be slightly lower in magnitude for experiments. Nonetheless, it is shown that mean flow fields still match well from simulations to experiments for all comparison points at the high accelerating and peak flow regimes. The deceleration flow phase comparison shows poorer matching between simulations and experiments, but this is expected due to the chaotic, disorganized, and highly cycle-to-cycle varying nature of decelerating flow.

For rms values of high accelerating and peak flow (figures 5-10 and 5-11), the comparison between experiments and simulations generally matches well. A primary difference is noted at peak flow (figure 5-11) in the higher magnitude of rms peak values in experiments compared to simulations. These rms values for pulsatile flow in experiments include fluctuations due to high Reynolds number, which are also found in the numerical simulations of pulsatile flow at peak Reynolds number. However, the experimental data also have natural fluctuations due to strong cycle-to-cycle variations in the flow field. These cycle-to-cycle fluctuations are not present in the numerical results for rms values, as only one cardiac cycle of data is sampled. Thus, the overall rms values for experimental data are increased, which can explain the higher peak rms values for experiments as compared to the simulations during the peak flow phase. For decelerating flow, the rms values are much higher for the experiments. This is again due to the high cycle-to-cycle fluctuations that contribute to the rms velocities in experiments that are not present in the numerical simulations.

A limitation of the numerical simulations is that 200 cardiac cycles cannot be simulated due to resource limitations. It is computationally less expensive to sample data from steady flow simulations. However, the nature of steady flow and pulsatile flow are inherently different, and thus a pulsatile flow to pulsatile flow comparison must be performed. Ideally, quantitative comparison for pulsatile flow would include the modeling of many cardiac cycles in order to more accurately compare mean flow fields and rms values, as is performed experimentally. Each cardiac cycle costs approximately 50,000 computational hours to run. As 200 cardiac cycles are required to achieve good statistics, this amounts to approximately 10 million computational hours. Even performing this quantitative comparison at a lower resolution of 160μm would cost approximately 1.5 million computational hours. Thus, modeling 200 cardiac cycles to perform quantitative comparison against experiments for pulsatile flow is not feasible with available computational resources.

Due to computational constraints, the numerical simulations of pulsatile flow sample data from just one cardiac cycle. This is still ensemble averaging, as the numerical data samples are taken within a time range corresponding to the integral time scale for each Reynolds number. This should capture the major flow structures for each flow regime that is compared. The noted cycle-to-cycle variability in experiments could similarly lead to experimental data samples taken within this integral time range for pulsatile flow. In addition, the 200 cardiac cycles are necessary for experiments to average leaflet motion and flowrate cycle-to-cycle variation. Numerically, this variation does not exist as the averaged flowrate and leaflet motion are prescribed exactly in the simulations. Thus, the numerical method of attaining 200 ensembles of pulsatile flow

within one cardiac cycle is a viable alternative for comparison to experiments, and also shows good matching with experiments in figures 5-10 and 5-11. In addition, the comparison of mean flow fields between two cardiac cycles using the same numerical sampling method (figure 5-13) shows very good matching, further demonstrating its applicability.

5.3.2 Qualitative Comparison for Instantaneous Flow

For pulsatile flow, comparisons are made at instantaneous time points throughout the cardiac cycle. Instantaneous time comparisons are performed because ensemble averaging of experimental data removes key flow features that are important for comparison. All comparison plots are made with the same vorticity contour scaling. It should be noted that the instantaneous realizations are taken from the same cardiac cycle for the simulations, but from different cardiac cycles for the experiments, as noted in Dasi *et al.* [52].

Figure 5-14 shows instantaneous out-of-plane vorticity magnitude at the opening phase of the cardiac cycle (Re = 240), which is characterized by two notable features. One shear layer exists from separation of flow at the edge of the valve housing to the sudden sinus expansion region, and another exists from flow separation at the tip of the leaflets as they suddenly open. These are opposite in magnitude and good qualitative comparison is shown with the experiments for both of these features.

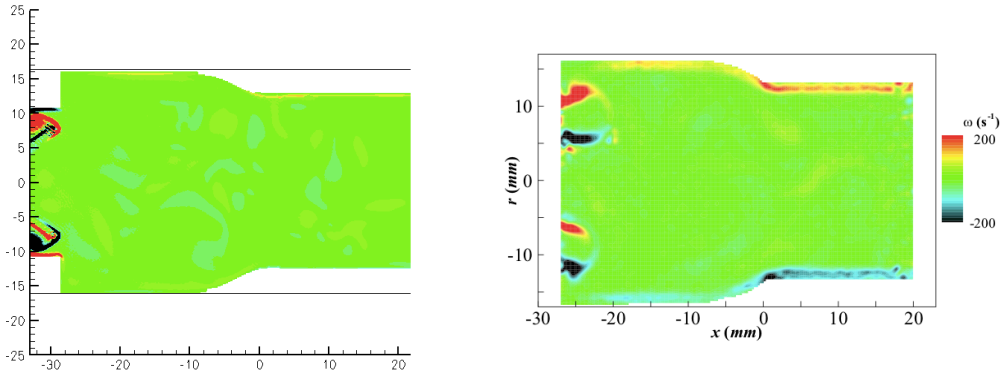

Figure 5-14: Comparison at leaflet opening phase (Re = 240) between simulations (left) and experiments (right)

At the accelerating phase with Re = 2070 (Figure 5-15), the leaflets are fully open and the flow rate past the valve increases. Here the flow past the leaflet tips causes two coherent von Karman vortex wakes. In addition, recirculation vortices are seen in the sinus aortic expansion. The numerical simulations and experiments match very well qualitatively during this phase of the cardiac cycle.

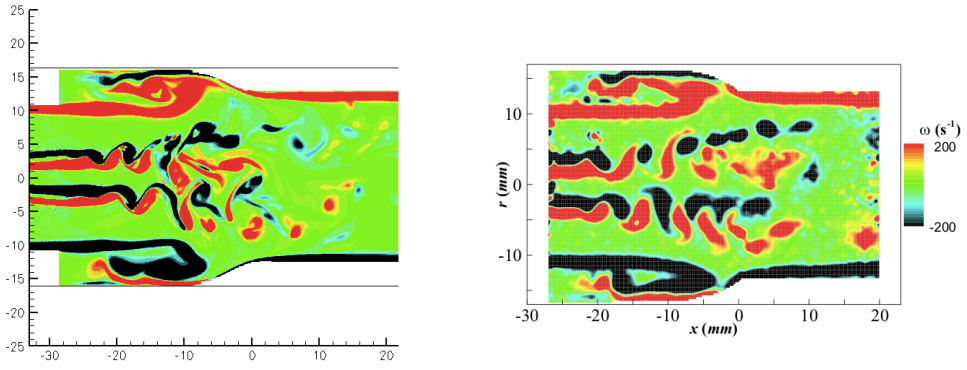

Figure 5-15: Comparison at mid-acceleration phase (Re = 2070) between simulations (left) and experiments (right)

Peak flow, with a Reynolds number of 5779, is shown in figure 5-16. The same qualitative flow features of vortex shedding wakes and recirculation vortices from the acceleration phase are shown in this peak flow phase, however with more unstable motion due to the higher Reynolds number. Though it appears that there are still two von Karman vortex streets from flow past the leaflet tips, this becomes highly disorganized and breaks apart quickly downstream of the valve in the sinus expansion. The shear layer from the sinus step also results in a recirculation region in the sinus expansion, but is broken into smaller scale structures.

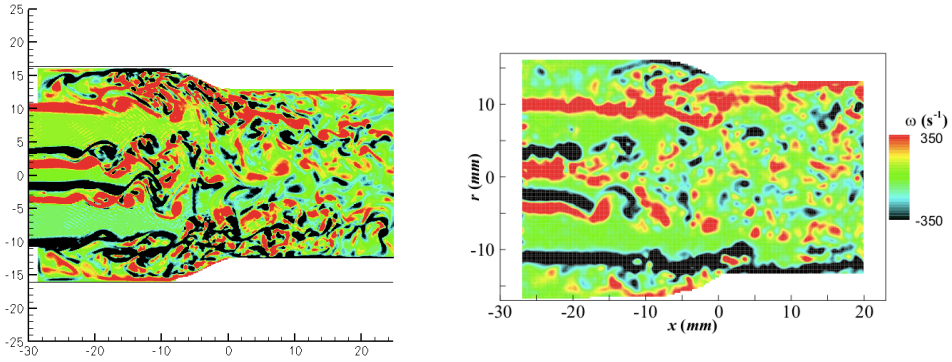

Figure 5-16: Comparison at peak flow phase (Re = 5779) between simulations (left) and experiments (right)

In the deceleration phase (Re = 3600), the leaflets are still fully open but flowrate begins to rapidly decrease (Figure 5-17). It is important to note that this deceleration time point is different from the quantitative comparison of deceleration as shown in section 5.3.1, with different deceleration flow Reynolds number. The same flow features exist in this deceleration phase as with peak flow but the decelerating flow leads to a breakup of the coherent vortical structures downstream of the valve, shown in both the simulations and experiments. The shear layer from the valve housing into the sinus expansion still

exists, but no longer develops into a significant recirculation region. Although the vortex shedding past the leaflet tips still exists, it does not form coherent vortex streets, instead immediately breaking down into smaller eddies. Downstream of the sinus region, only small-scale structures exist due to decreasing flow rate and dissipation. The experimental results show more viscous dissipation than the numerical results downstream of the sinus region but the two still compare well. This may be attributed to smoothing of the vector field in experiments before calculating vorticity in order to remove experimental noise.

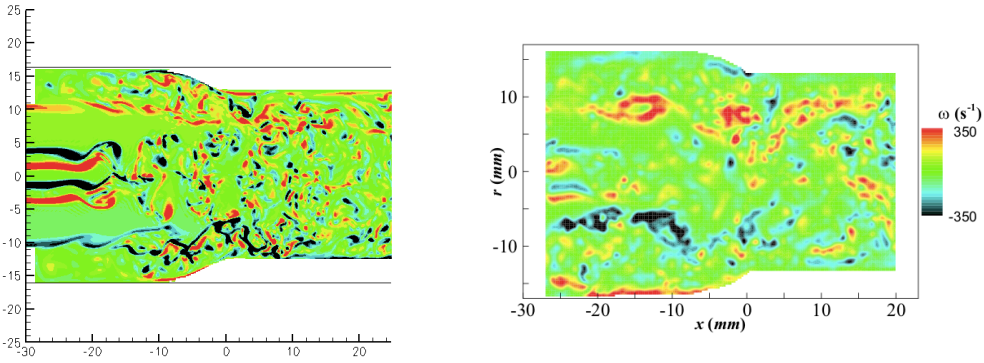

Figure 5-17: Comparison at deceleration flow phase (Re = 3600) between simulations (left) and experiments (right)

The final snapshot at the closing phase (Figure 5-18, Re = 580 in reverse direction flow) shows the leaflets slamming shut due to an adverse pressure gradient. Here, the sudden leaflet closing motion results in vortex wakes that are seen in both the simulations and experiments. The downstream flow is primarily characterized by smaller scale structures that are dissipating rapidly due to the lower flowrate and viscous dissipation.

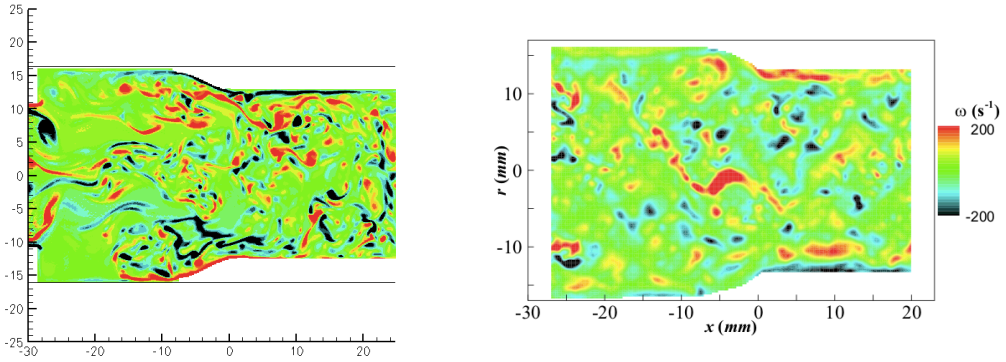

Figure 5-18: Comparison at leaflet closing phase (Re = 580 in reverse flow) between simulations (left) and experiments (right)

Though cycle-to-cycle variations exist in pulsatile flow through the SJM valve, good qualitative agreement is observed when comparing simulations to experiments at multiple instantaneous time points throughout the cardiac cycle. The LBM is able to match key flow features very well, particularly during the opening and acceleration phases of the cardiac cycle. At these time points, the flow is still highly organized and experimental data show clear features such as coherent von Karman vortex streets or sinus recirculation regions, which are also reproduced numerically.

During the unstable peak flow and deceleration flow phases, these features become highly disorganized and it is difficult to pick out clear features in the experimental data. Though the vortex streets and recirculation regions are present, they are not clearly discernible in either the simulations or experiments and thus it becomes difficult to show a clear matching. This is due to the disorganized nature of flow at these phases, where many coherent structures are immediately broken into smaller structures that are not easily matched. The deceleration and closing phases are also characterized by high dissipation of vorticity, which also makes comparison difficult. However, in the

closing phase, the key feature of vortex wakes caused by rapid leaflet closing compares well between simulations and experiments.

The overall good quantitative and qualitative agreement of numerical simulations with experiments validates the use of LBM for modeling various cases of pulsatile flows through BMHVs.

5.4 Pulsatile Flow Visualization

This section details grayscale 2D contour plots of out-of-plane vorticity magnitude at specific time points of the cardiac cycle. These plots, taken from numerical simulations of higher spatiotemporal resolution (80μm and 2.4μs), are shown for improved visualization and depiction of the pulsatile flow features. These 2D contour plots are taken at perpendicular planes of the flow, and all use the same vorticity contour scaling as detailed in the first plot (figure 5-20). In addition, angled 3D plots of q-criterion (section 3.9) are shown to highlight coherent vortical structures in the pulsatile flow field. Plots of viscous fluid shear stresses projected on 2D perpendicular cutplanes (also detailed in section 3.9) are also displayed. Animations of out-of-plane vorticity (animation 5-1), viscous fluid shear stresses (animation 5-2), and 3D q-criterion isosurfaces (animation 5-3) are also given in Appendix C.

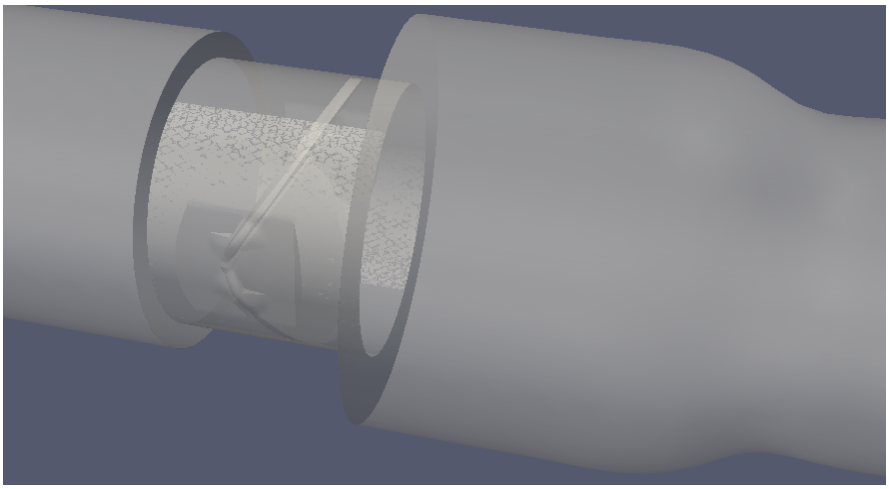

Figure 5-19: Transparent view of BMHV and flow chamber showing approximate 3D angled view used in q-criterion visualization of 3D coherent vortical structures

At leaflet opening, two vortex wakes are shown to form at the points where the leaflet tips separate from the valve housing (figure 5-20). In addition, it is noted that the leaflet opening seems to push fluid upstream in the b-datum line, causing its own wake. This is also apparent from the 3D view, where coherent vortical structures are noted at the leaflet edges as well as at the b-datum rectangular plane. Moderately high instantaneous shear stresses are seen from the leaflet opening wakes as well, with very low shear stress values throughout the rest of the flow field.

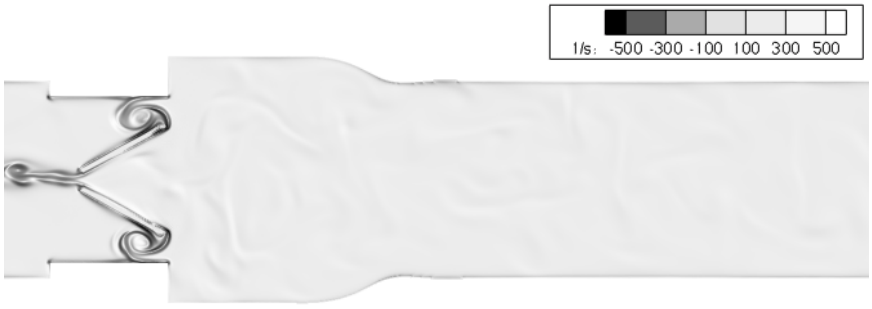

(a) 2D vorticity

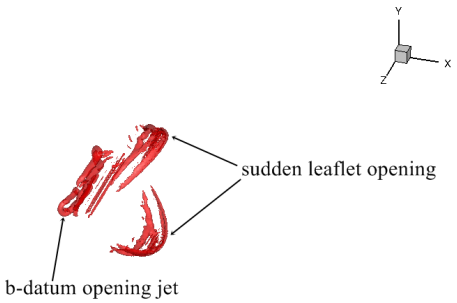

(b) 3D Q-criterion

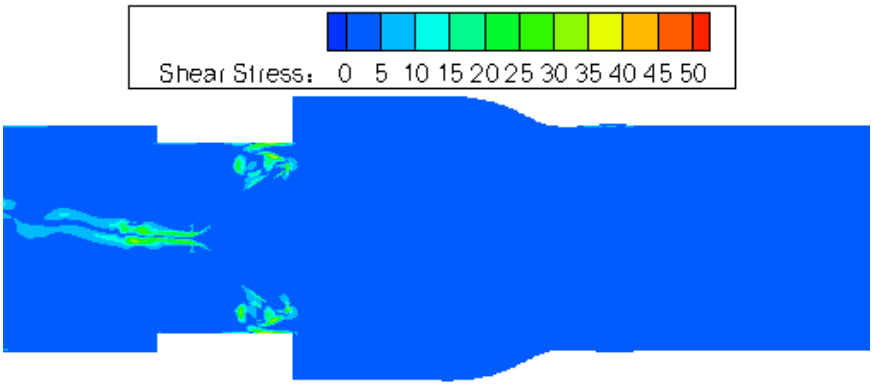

(c) Viscous fluid shear stresses

Figure 5-20: (a) 2D vorticity, (b) 3D q-criterion, and (c) viscous fluid shear stress (dynes/cm^2) plots of leaflet opening phase (Re = 240)

The numerical simulations using higher 80µm spatial resolution detail complex flow features that could not be captured by PIV experiments. During opening (figure 5-20), an interesting feature of a b-datum reverse jet is observed. This seems to form due to the leaflets rapidly opening and pushing back quasi-static fluid on the ventricular side. Though this jet flows immediately towards the ventricular side from leaflet opening, the forward flow pushes this fluid towards the aortic side at the onset of systole. However, it is noted that this feature is not seen in experiments and may be due to slight synchronization issues in simulations between the forward flowrate and leaflet opening.

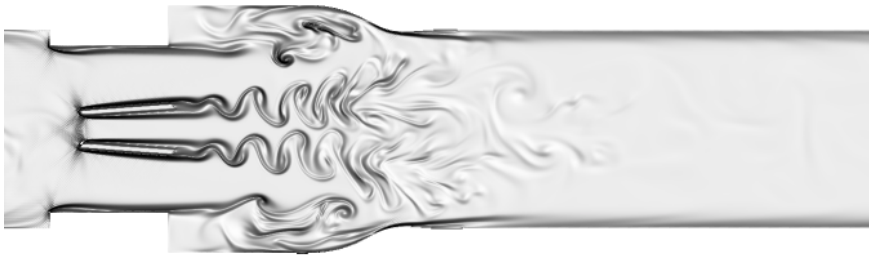

(a) 2D vorticity

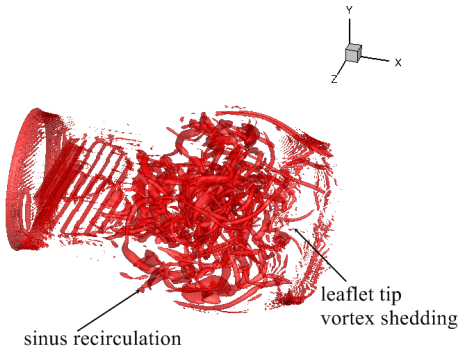

(b) 3D Q-criterion

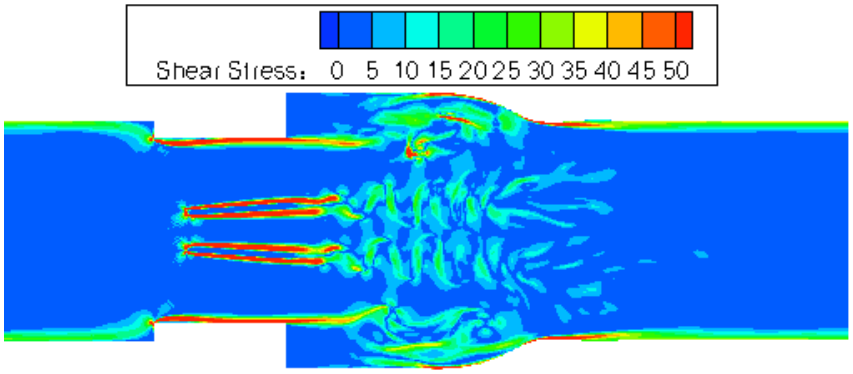

(c) Viscous fluid shear stresses

Figure 5-21: (a) 2D vorticity, (b) 3D q-criterion, and (c) viscous fluid shear stress (dynes/cm^2) plots of mid-acceleration phase (Re = 2070)*

In the acceleration phase (figure 5-21), the flow field is characterized primarily by the two von Karman vortex streets past the two leaflet tips. The sinus expansion region also contains two recirculation zones caused by the increased expansion volume and the vortex shedding caused by the sudden step into the sinus expansion. This flow is still considered laminar during this mid-acceleration phase, with the vortex structures very organized and repeatable in similarity from cycle-to-cycle. The 3D visualization highlights the three-dimensionality of this vortex shedding and recirculation.

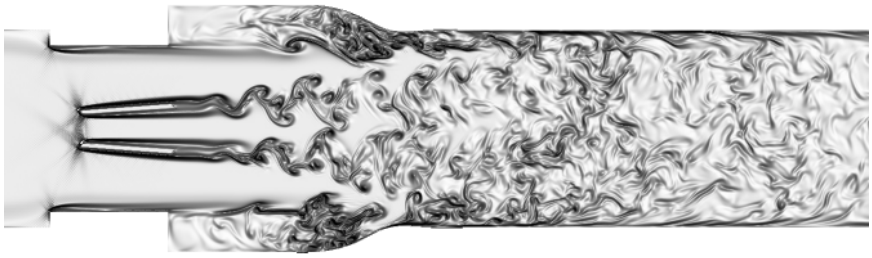

(a) 2D vorticity

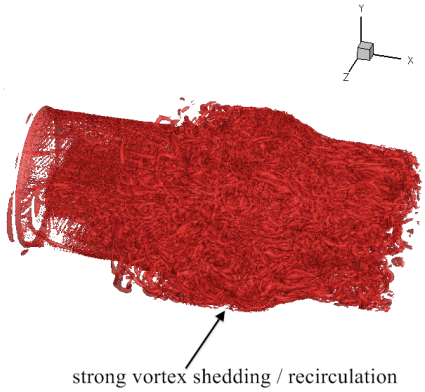

(b) 3D Q-criterion

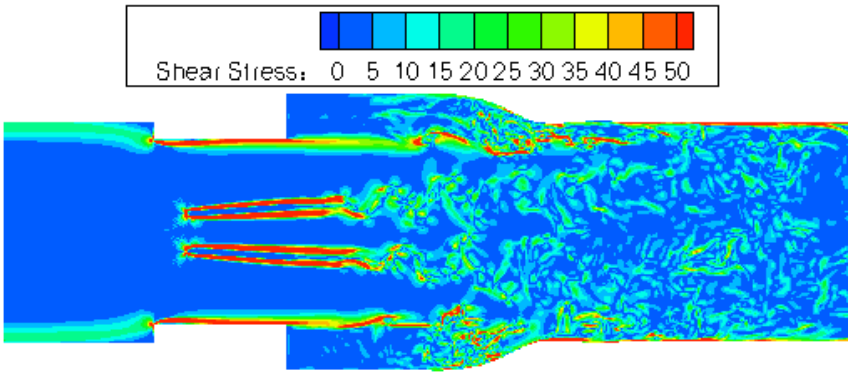

(c) Viscous fluid shear stresses

Figure 5-22: (a) 2D vorticity, (b) 3D q-criterion, and (c) viscous fluid shear stress (dynes/cm^2) plots of peak flow phase (Re = 5779)

At peak flow (figure 5-22) the primary features of vortex shedding past the leaflet tips and sinus step are noted to be similar to accelerating flow. However, the flow field becomes more disorganized and unstable due to the maximum Reynolds number achieved by this flow. The higher resolution simulation shows the breakup of the coherent von Karman vortices into smaller and smaller eddies as the flow becomes more disorganized and unstable. The 3D visualization shows the entire domain to be filled with coherent vortical structures.

At peak flow (figure 5-22), coherent vortical structures that are shed from the leaflet tips quickly break down into smaller eddies. These small-scale vortices are captured at the higher 80μm resolution simulations but appear as a disorganized mix in the 160μm resolution simulations (not shown) and other numerical studies, thus highlighting the capabilities of this numerical method and importance of higher spatial resolution simulations to capture smaller fluctuating vortical scales.

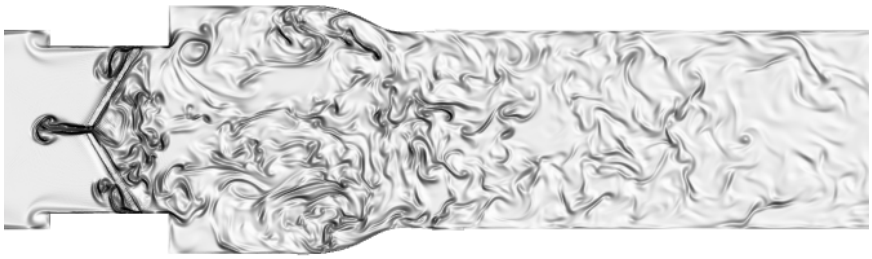

(a) 2D vorticity

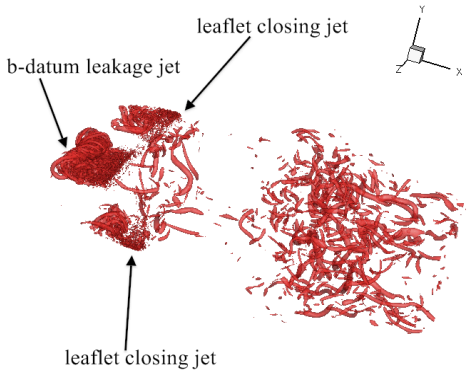

(b) 3D Q-criterion

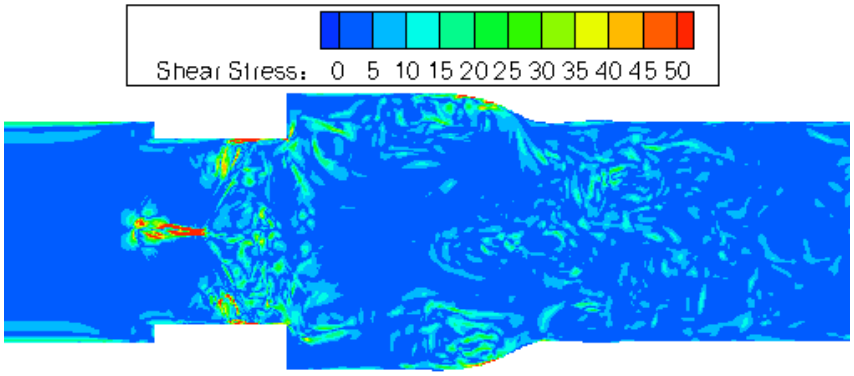

(c) Viscous fluid shear stresses

Figure 5-23: (a) 2D vorticity, (b) 3D q-criterion, and (c) viscous fluid shear stress (dynes/cm^2) plots of closing phase (Re = 580 in reverse flow)

Due to the sudden closing of the leaflets with reverse flow, leaflet closing leakage jets are formed at the instant the leaflet tips touch the valve housing (figure 5-23). In addition, due to the sudden reduction of the central orifice area and the reverse flowrate, a leakage jet squeezes in the upstream direction at the b-datum line. Due to the reduced flowrate and viscous dissipation, vortex washout occurs downstream of the valve, shown by neutral gray contours. This is in comparison to the stronger vorticity in accelerating flow, which is depicted by stronger black and white contours.

During the closing phase (figure 5-23), the leaflets slam shut and result in three strong closing leakage jets. It is possible that blood elements such as platelets could experience high shear stresses if trapped in these leakage jets, and could possibly contact the leaflets as well. The closing leakage jets, though strong, dissipate quickly in the flow on the ventricular side. It should be noted that the b-datum leakage jet upon closing is directed centrally upstream, due to the imposed symmetric closing of the leaflets.

(a) 2D vorticity

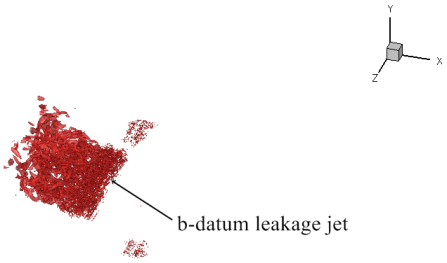

(b) 3D Q-criterion

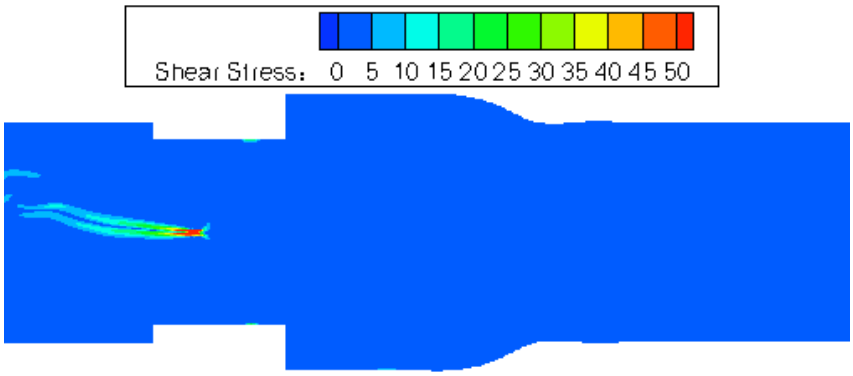

(c) Viscous fluid shear stresses

Figure 5-24: (a) 2D vorticity, (b) 3D q-criterion, and (c) viscous fluid shear stress (dynes/cm^2) plots of mid-diastolic leakage phase (Re = 175 in reverse flow)

Mid-diastole is characterized by vortex washout in the aortic side and reverse leakage flow in the b-datum plane (Figure 5-24). During mid-diastole, the reduced b-datum orifice area results in a strong leakage jet in the upstream direction. This was not captured by previous numerical studies that that cannot capture reverse leakage flows for full cardiac cycle simulations [52, 56]. It is also noted that viscous dissipation has caused a significant vortex washout downstream of the valve. In the 3D visualization, the only coherent structures are from the strong b-datum leakage jet in the upstream direction. The

vortex washout downstream of the valve has dissipated any coherent vortical structures, and thus none are shown.

It is noted that during mid-diastole, the b-datum leakage jet is shown to oscillate preferentially in one direction over time, as illustrated in figure 5-24 with a top-leaning leakage jet. This snapshot is taken in mid diastolic flow, though the b-datum leakage jet does oscillate in direction. This asymmetry of the b-datum leakage jet is observed even under idealized computational conditions where the domain geometry, the leaflet motion, and the inlet flow profile are all symmetric. As we eliminate design or flow condition asymmetries in our computational model, this observed leakage jet asymmetry is most likely due to the disorganized nature of pulsatile high Reynolds number flow through BMHVs, or due to interaction with large scale vortices on the ventricular side. This is explored in more detail in section 5.4.3.

5.4.1 Accelerating to Peak Flow

The simulations are performed at uniform high spatiotemporal resolution, which is able to capture small-scale structures throughout the entire domain. This is particularly observed for the flow past the leaflet tips, where the coherent vortical structures of accelerating flow are broken into small-scale eddies at peak flow. The images in this section use the same vorticity contour scaling for all plots. At high accelerating flow (Re = 4400), coherent vortical structures are still observed past the leaflet tips (figure 5-25a). At a time point only 15ms later, some interaction begins between the leaflet tip vortices and the recirculating region of the sinus expansion (figure 5-25b). It is noted that the

vortex shedding past the leaflet tips is still coherent, but the recirculation region becomes more disorganized and larger, thus causing a mixing with von Karman vortex streets.

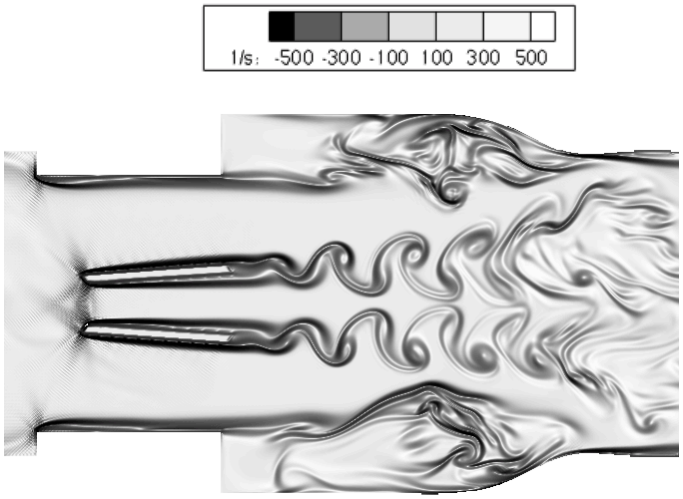

(a) Re = 4400

(b) Time point 15ms later

Figure 5-25: (a) High accelerating flow with coherent vortical structures in flow past leaflet tips, with (b) mixing of leaflet vortex wakes and sinus recirculation region

Near peak flow with Re = 5700, an initial vortex is shed from the leaflet tips (figure 5-26a). Here the vortex is coherent and unmixed with the sinus expansion recirculation region. Just 6ms later at peak flow (figure 5-26b), this vortex is broken into two small-scale eddies. This is captured by the high spatial resolution simulations for the

entire flow domain, whereas other numerical methods concentrate high resolution at only the valve region. This highlights the importance of modeling high resolution throughout the flow domain, as important small-scale features would not be captured otherwise.

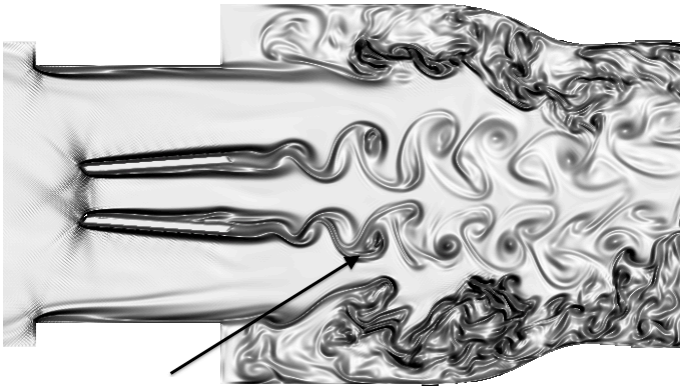

(a) Re = 5700

(b) Time point 6ms later

Figure 5-26: Peak flow with (a) coherent vortical structures breaking into (b) small-scale eddies

When the flowrate decelerates but is still near peak flow (Re = 5600), two small-scale eddies are formed from coherent vortical shedding past the leaflet tips (figure 5-27a). This leaflet tip vortex shedding spreads throughout the sinus expansion further downstream of the valve as smaller eddies are formed. At this higher Reynolds number

flow, the sinus recirculation region is also shown to be very strong and mixes with leaflet tip vortices only 7ms later (figure 5-27b). These figures demonstrate the complex interaction of the vortex shedding past the leaflet tips with the strong recirculation region caused by the sudden sinus expansion step.

(a) Re = 5600, Deceleration phase

(b) Time point 7ms later

Figure 5-27: (a) Small-scale eddies in sinus expansion, (b) interacting with sinus expansion recirculation

The differences in fluid shear stress magnitudes between early accelerating (Re=2070) and peak flow (Re=5780) are detailed in figure 5-28. Immediately downstream of the leaflet tips (figure 5-28a), the fluid stresses at a perpendicular line are

very similar between accelerating and peak flow. This shows maximum peaks representing immediate vortex shedding past the leaflet tips, as well as two additional peaks from flow past the sudden sinus expansion step. At this location, the vortices are immediately shed from the leaflets and have not had a chance to break up into smaller eddies in the case of peak flow, thus resulting in similar shear stress profiles.

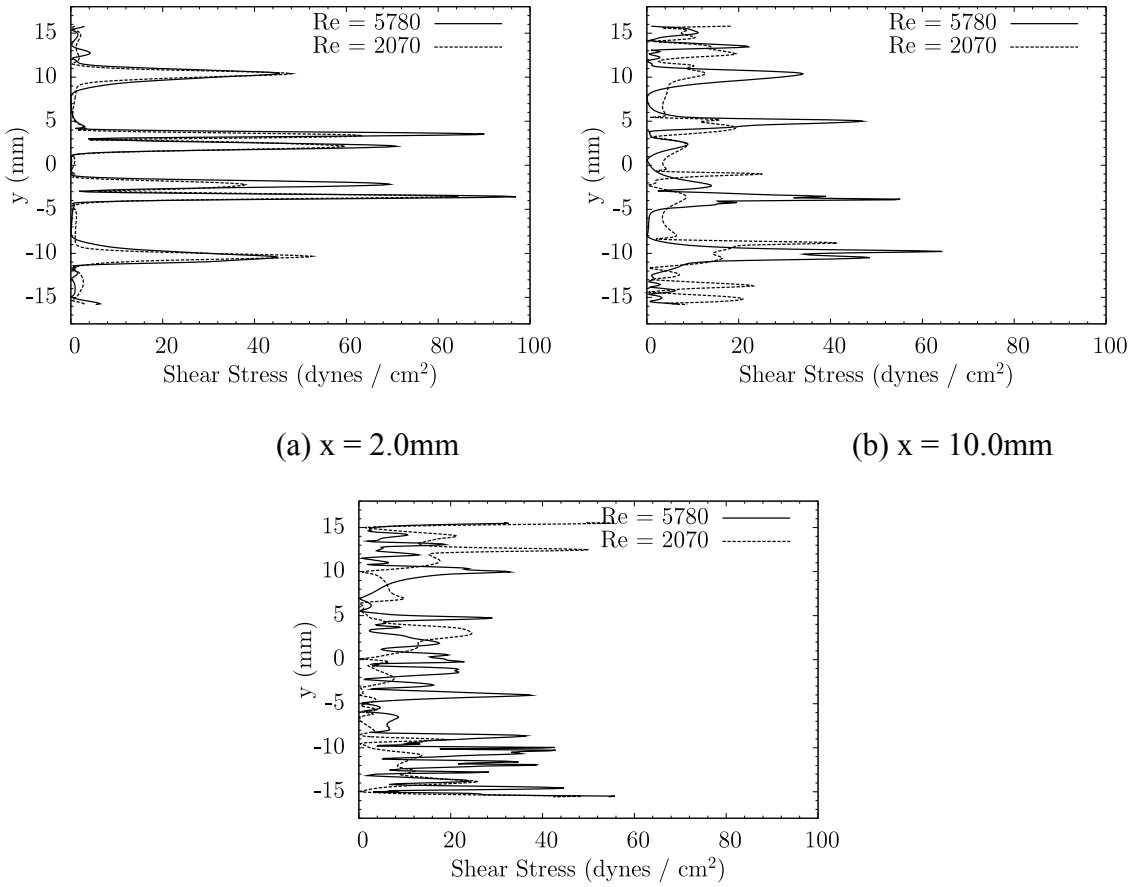

(a) x = 2.0mm (b) x = 10.0mm

(c) x = 20.0mm

Figure 5-28: Comparison of viscous fluid shear stresses at perpendicular lines downstream of the leaflet tips for accelerating and peak flow

10mm downstream of the leaflets (figure 5-28b), the two flow regimes show greater differences in fluid stresses. For peak flow, the shear stresses are higher in peak

magnitudes (at the leaflet vortex shedding and sinus expansion step) and also show high fluctuations. This is likely due to the more chaotic and disorganized flow downstream of the leaflets, where the coherent vortices break into smaller scale eddies for peak flow. Thus, due to presence of smaller scale vortices downstream of the leaflets, the shear stress variation is higher for peak flow.

Finally, 20mm downstream of the leaflets but still within the sinus region (figure 5-28c), the shear stress profiles are drastically different. The peak flow profile shows high fluctuations in shear stresses, particularly in the sinus region where the strong recirculation regions are observed. This high fluctuation is also observed in the center of the domain, again representing the unsteady fluctuation in shear stresses due to the smaller scale eddies that are present at peak flow. It is important to note, however, that the overall magnitudes of the shear stresses decrease further downstream of the leaflets despite the high fluctuations. It is also important to highlight that these fluctuations are observed quantitatively (in addition to previous qualitative observations in the vorticity plots) significantly downstream of the valve region. Thus, high spatial resolution is needed beyond just the valve region, as the important small scale flow features and shear stress fluctuations are found downstream of the valve.

5.4.2 Closing phase

The numerical simulations of this study are able to capture the closing leaflet phase without any contact modeling problems between the leaflet and valve housing. The ventricular upstream is four diameters in length and is sufficient for the interior flow field to not be affected by the outflow boundary condition. Previous studies have not

concentrated on capturing the complex dynamics of sudden leaflet closure, as well as leaflet-valve impact. The vorticity plots in this section all use the same contour scaling, as shown in figure 5-29.

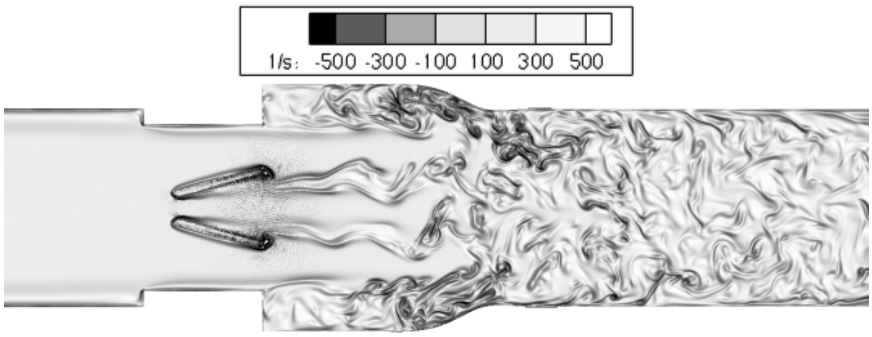

(a) 2D vorticity

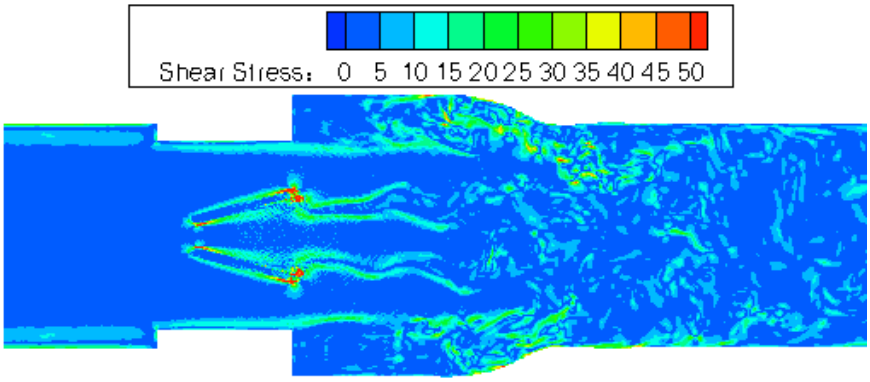

(b) Viscous Shear Stress - dynes/cm^2

Figure 5-29: Vorticity and shear stress field (dynes/cm^2) plots at beginning of closing phase with sudden leaflet motion and initial closing wakes

At the beginning of sudden leaflet closing, many of the vortical structures on the aortic side begin to dissipate and closing leaflet wakes begin to form (figure 5-29). The remnants of forward flow past the leaflet tips are shown as a weak vortex trail in the sinus expansion. The shear stress plot also demonstrates low and moderate instantaneous shear stresses in the aortic downstream region with some higher shear stresses in the sinus

expansion. High instantaneous shear stress values are observed at the leaflet tips caused by the rapid leaflet motion.

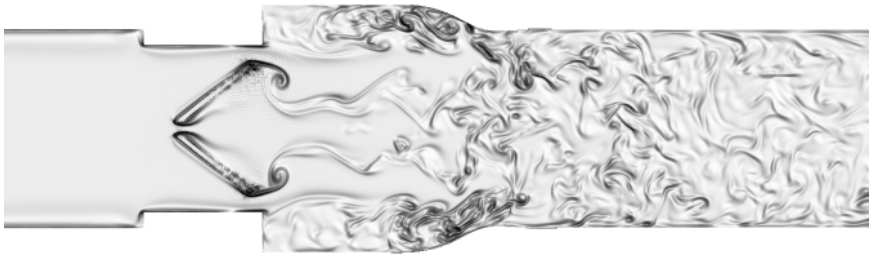

(a) 2D vorticity

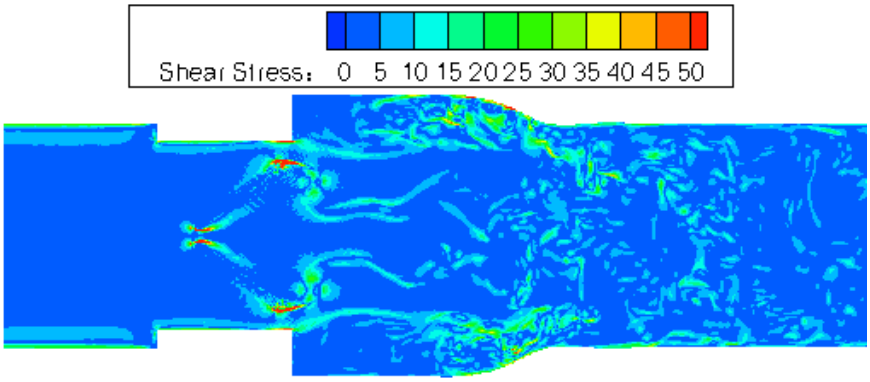

(b) Viscous Shear Stress - dynes/cm^2

Figure 5-30: Vorticity and shear stress field (dynes/cm^2) plots at rapid leaflet closing phase with strong leaflet closing vortex wakes

At a time point 10ms later, the leaflet rapid motion causes vortex shedding in its wake, as shown in figure 5-30. This leaflet wake also shows a trail vortex wake in the sinus expansion caused by the remnants of vortex shedding past the leaflet. These two coherent closing wake vortices are also highlighted by strong instantaneous shear stresses near the leaflet tips. Downstream of the valve, the shear stress field shows very low stress values as caused by viscous dissipation and the low overall flow rate.

Leaflet closing impact with the valve housing shows very interesting flow features as well. The initial impact between the leaflets and valve housing (figure 5-31a) results in leaflet closing wakes along the valve housing surface. In addition, a noticeable squeeze jet is observed due to the reduction of the central orifice area. This squeeze jet is initially directed in the aortic side of the valve. The downstream region is characterized by rapidly dissipating flow structures at the onset of diastole.

10ms afterwards, the initial formation of 3 leakage jets is observed, which are caused by the leaflet-valve housing impact as well as the b-datum central orifice (figure 5-31b). These three jets are formed on the ventricular side of the valve, and fluid is shown to squeeze in these small gaps. The initial impact causes a central jet on both the ventricular and aortic sides as the leaflets have rapidly closed. At this time point, vortical structures are shown to form directly downstream of the valve due to leaflet-valve impact.

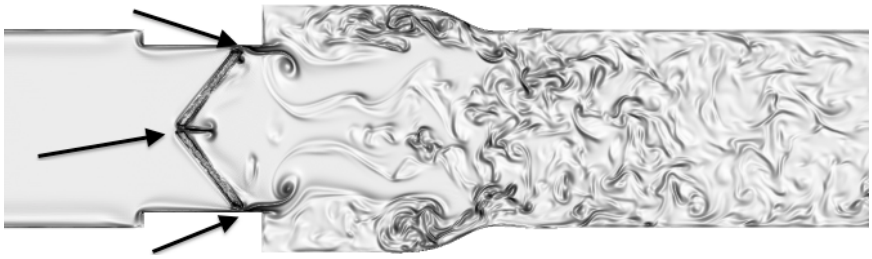

(a) Leaflets - initial closing impact

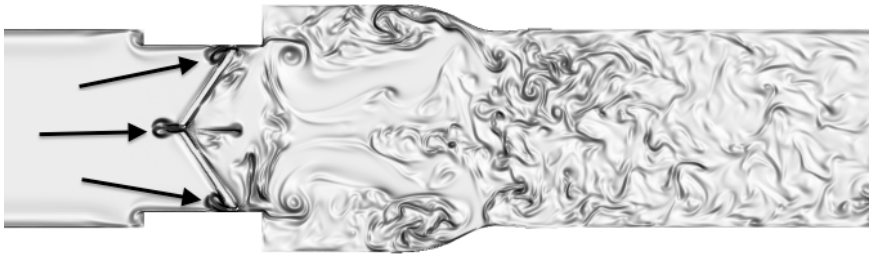

(b) Generation of triple leakage jets

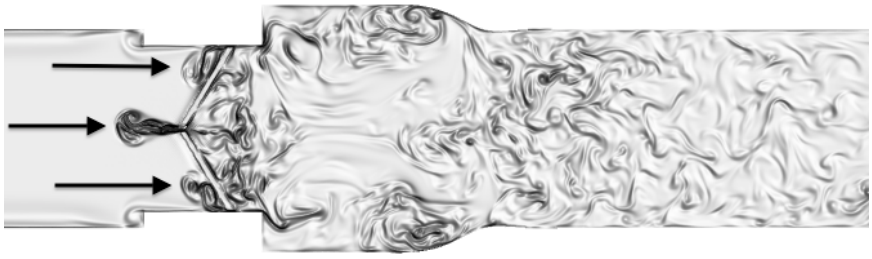

(c) Growth of triple leakage jets

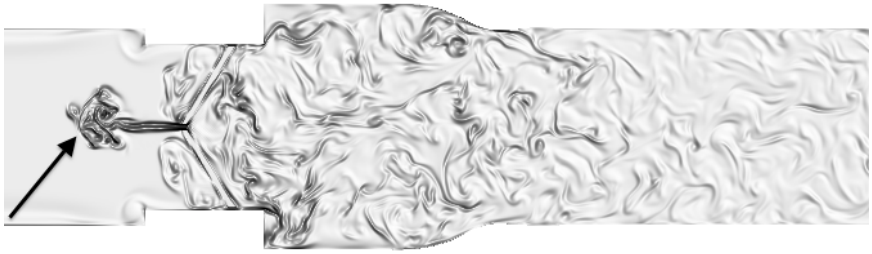

(d) Coherent B-datum jet with vorticity washout in rest of domain

Figure 5-31: Vorticity plots demonstrating (a) leaflet closing impact with valve housing, (b) development and (c) growth of triple leakage jets, and (d) coherent b-datum jet

A stronger b-datum jet advects towards the ventricular side centrally after an additional 10ms (figure 5-31c), although the tip of this structure grows in size. Also noticeable is the growth of vortical structures on the immediate aortic side of the leaflets, caused by the sudden leaflet impact with the valve. Figure 5-31d shows a time point 20ms later, with a washout of vortical structures throughout the flow domain. However, it is noted that the b-datum central jet is still coherent and advects centrally upstream, spreading outwards throughout the ventricular side.

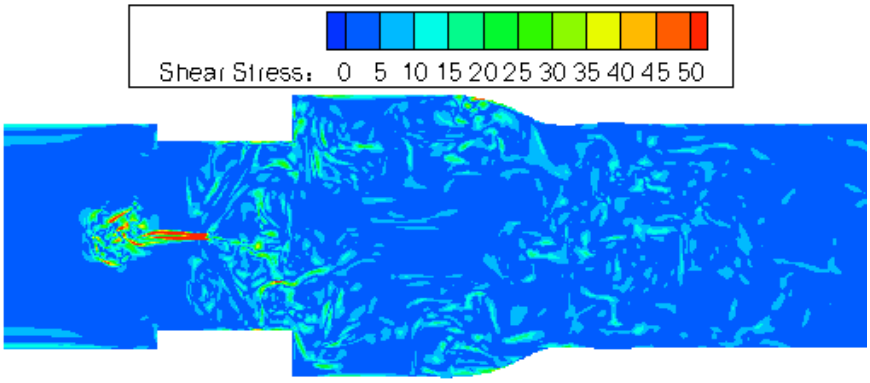

Figure 5-32: Shear stress (dynes/cm^2) plot at leaflet closing with identical time point as figure 5-31d

The viscous shear stress plot at leaflet impact for the flow domain at a 2D slice demonstrates a very high instantaneous shear stress at the b-datum jet but rapid decrease in shear stress values throughout the rest of the domain (figure 5-32).

The simulations from this study are also able to resolve leakage jets for both the central b-datum jet and the circular gap between the leaflets and the valve housing. The b-datum central gap between the two closed leaflets (gap distance in perpendicular transverse direction) is estimated at 0.76mm. The gap between the closed leaflets and the valve housing is estimated at 0.336mm. The instantaneous shear stresses are averaged for fluid nodes across these gap regions and are plotted in figure 5-33.

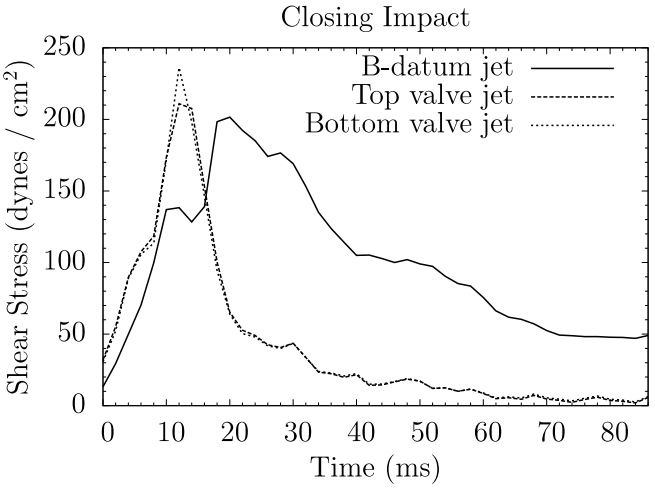

Figure 5-33: Fluid shear stresses (dynes/cm^2) at various leakage jets upon leaflet closing impact

The shear stress variation upon leaflet closing impact is very similar for both the top and bottom leaflet-valve impact jets. In addition, the peak value of shear stress across this gap is comparable to the peak value of shear stress for the central b-datum jet. It is interesting to note that the maximum shear stress occurs for the central jet approximately 10ms after the time point for maximum shear stress for the leaflet-valve jets. The shear stress rise to maximum value is slightly slower for the central leakage jet, despite the gap reduction occurring simultaneously with leaflet-valve impact.

It is also shown that upon initial impact, the shear stress levels rise to a maximum value and then steadily decrease during the early part of the diastolic reverse flow phase. However, the shear stress magnitude for the b-datum jet drops slowly as compared to the rapid decrease in stress values for the valve housing leakage jets. It is shown in the next subsection that this drop in shear stresses precedes a mid-diastolic leakage flow through these same gaps.

5.4.3 Diastolic phase

The results in this section are taken throughout the quasi-steady mid-diastolic time period, after the leaflets have fully closed and the primary closing leakage jets have dissipated. Vorticity contours at various instantaneous time points during mid-diastole are plotted (figure 5-34a/b). These images are taken from multiple cardiac cycles and illustrate that the diastolic leakage jet can vary in direction of flow. These plots are taken from various numerical simulations of different spatiotemporal resolutions (80μm and 160μm). The figures employ the same contour scaling as the previous grayscale contour plots but different background intensities to highlight certain flow features. Figure 5-34c shows a representative time point of mid-diastole which demonstrates a quasi-steady reverse flowrate.

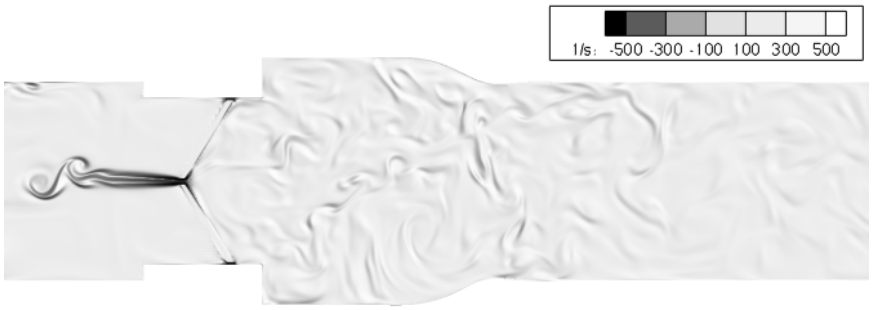

(a) Central b-datum jet

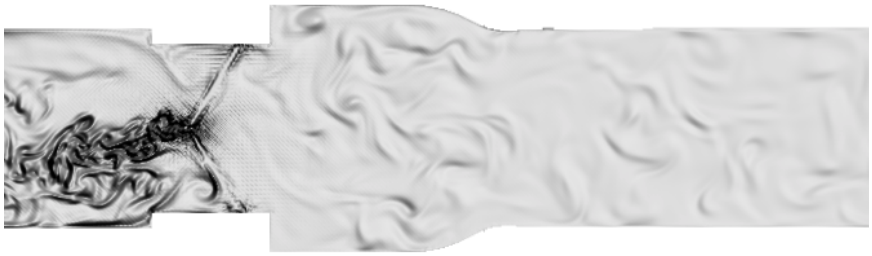

(b) Asymmetry of b-datum jet towards bottom side

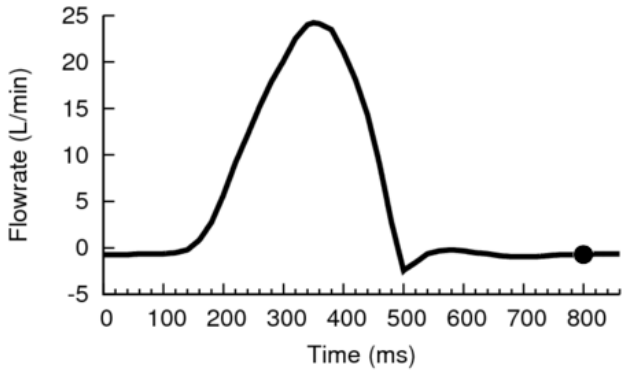

(c) Representative time point of mid-diastole flow

Figure 5-34: Vorticity contours of mid-diastolic leakage flows directed both (a) centrally upstream and (b) leaning to bottom ventricular half, with (c) representative mid-diastolic flow time point.

Figure 5-34a shows a more centrally flowing b-datum jet with no large-scale vortical structures shown besides the b-datum leakage jet, and is taken from an 80μm resolution simulation. Figure 5-34b shows the diastolic leakage jet mixing with large scale vortices on the bottom half of the ventricular side (backlighting slightly modified), taken from a 160μm resolution simulation. This is in contrast to figure 5-24, which demonstrates a top-leaning mid-diastolic leakage jet.

Figure 5-35a/b shows the unorganized flow on the ventricular side during diastole, with an obvious lack of symmetry in the vorticity field. These are taken from 160μm resolution simulations, where multiple cardiac cycles were simulated at lower computational expense. In these two figures, a small b-datum leakage jet shows a slight preferential direction that corresponds with the side that shows stronger large scale

vortical structures. This preferential direction is observed even before interaction between the leakage jet and the large vortical structures.

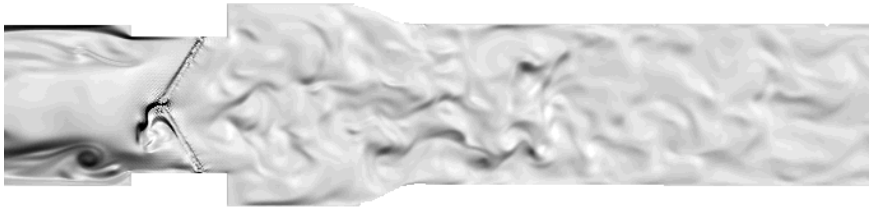

(a) Slight asymmetry towards bottom side

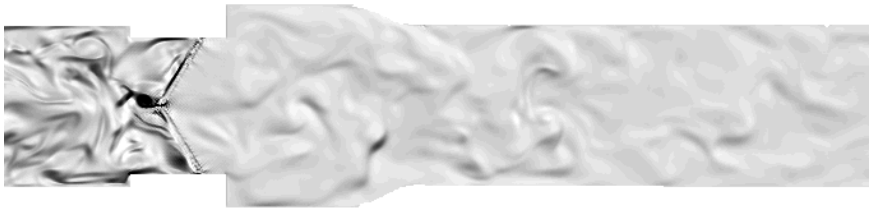

(b) Slight asymmetry towards top side

Figure 5-35: Early-diastolic leakage flows leaning both (a) slightly downwards and (b) slightly upwards, with impending interaction with large vortical structures

It is surmised that leakage jet asymmetry is likely due to interaction with larger scale vortices on the ventricular side that come into contact with the incoming b-datum leakage jet. Figure 5-35a shows a mixing of the leakage jet from the b-datum plane with strong vortical structures on the bottom half of the ventricular side. The flow on the ventricular side is highly disorganized and in turn the large-scale vortices are not symmetric about the b-datum plane. This unorganized and asymmetric vorticity field is again highlighted in Figures 5-35b. In both of these figures, the leakage jet shows a slight drift towards the side with the stronger (black and white contours) vortical structures even before their direct interaction.

Thus, it is postulated that the asymmetry in the large-scale vortices would interact with the b-datum leakage jet and cause an oscillation in direction. However, it can also be surmised that asymmetry of the large-scale vortices would lead to a preferential direction for the b-datum jet over time. It is primarily observed that the section of the ventricular side with stronger vortical structures tends to "pull" the incoming b-datum leakage jet into interaction.

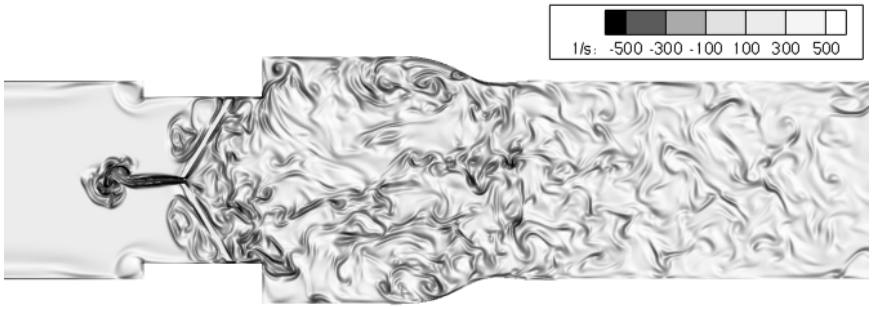

(a) Triple leakage jets with initial formation and growth

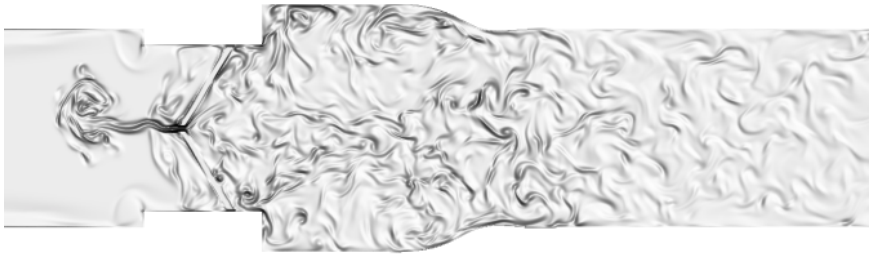

(b) Initial interaction between leaflet-valve housing impact jets with b-datum jet

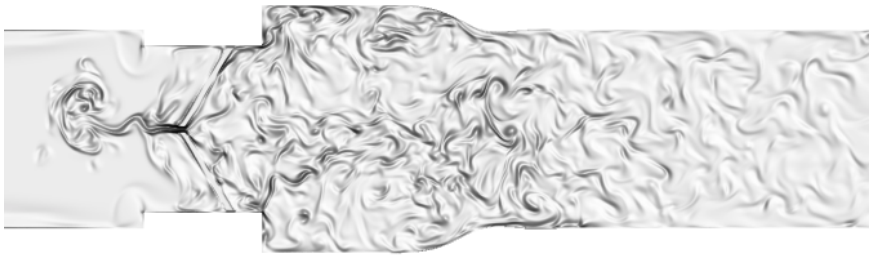

(c) Development of asymmetry in b-datum jet due to leakage jet interaction

Figure 5-36: Interaction of b-datum jet with leaflet-valve jets causing asymmetry in jet direction. Vorticity magnitude scaling identical in all plots

Large vortices that exist on the ventricular side may interact with the incoming b-datum jet to influence its direction, as demonstrated in figure 5-36. These flow fields are from 80μm resolution simulations. Upon initial closing impact, a centrally flowing b-datum jet is formed with two large vortical structures emanating from the valve walls towards the b-datum jet (Figure 5-36a). 20ms later, these two large valve-wall vortices begin to interact with the b-datum jet (figure 5-36b), causing a wave-like instability in the b-datum central leakage jet. After an additional 8ms, in figure 5-36c, the b-datum jet is shown to be oscillating in direction due to further interaction with the large-scale vortices. These snapshots, taken milliseconds apart, show how even in simulations with perfect symmetrical design, the disorganized nature of pulsatile flow in BMHVs and leakage jet vortex interaction cause the b-datum jet to oscillate in direction.

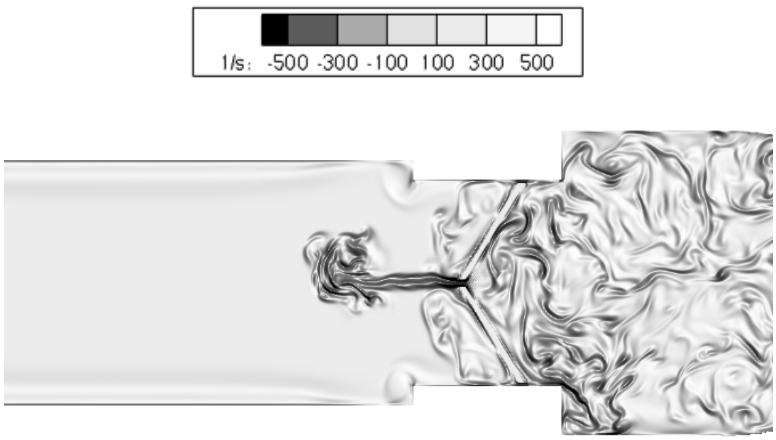

(a) Initial jet flowing centrally upon leaflet closure

(b) Dissipation of first central b-datum jet

(c) Secondary jet forming through b-datum gap

(d) Slight asymmetric pull towards remnants of first jet

Figure 5-37: Asymmetric drift of central b-datum jet in diastolic phase. Vorticity magnitude scaling identical for all plots

This asymmetric drifting motion of the diastolic leakage jet occurs in the mid-diastole phase as well. Upon leaflet closing, the central b-datum jet is shown to spread outwards towards the ventricular side in figure 5-37a. However, it is noted that as the central jet widens, vortical structures are slightly asymmetric with slight bias towards the top side. A time point 40ms later (figure 5-37b) shows that this initial leakage jet has weakened, but has also spread wider throughout the ventricular side. After an additional 80ms (figure 5-37c), a secondary b-datum leakage jet begins to form through the central orifice. However, it is noted that the previous leakage jet structure has spread throughout the ventricular side with dispersed, but weaker vortical structures. These vortices are not symmetric, but rather show a bias towards the top side. The secondary b-datum leakage jet shows slight asymmetry at this time point favoring the top side, with a slight pull from the larger vortical structures but without direct interaction. After an additional 80ms (figure 5-37d), the b-datum leakage jet is shown to interact with the larger vortices, pulling upwards towards the top side where the large-scale vortices are located. This demonstrates that even under idealized conditions, the initial leakage jet spreads

asymmetrically and influences the pull direction of the mid-diastolic secondary b-datum leakage jet.

It is observed in 160μm simulations that for multiple cardiac cycles, the mid-diastolic leakage jet always oscillates in time and prefers one wall direction with larger vortical structures, though the degree of asymmetry and frequency of oscillation in the leakage jet varies from cycle-to-cycle. This further highlights the disorganized nature of pulsatile flow through BMHVs even in the low flowrate diastolic phase. This could have implications of platelet damage incurred in the b-datum leakage jet. The oscillations and preferential jet direction could lead to platelets that do not advect centrally towards the ventricular side where the vortical structures dissipate. Instead, these platelets might become caught in the large-scale vortices, thus increasing their exposure time to higher surface shear stresses. This would increase the chances of thromboembolic complications incurred in diastolic flows, beyond those complications already known to occur in the hinge regions, and is covered in section 6.5.

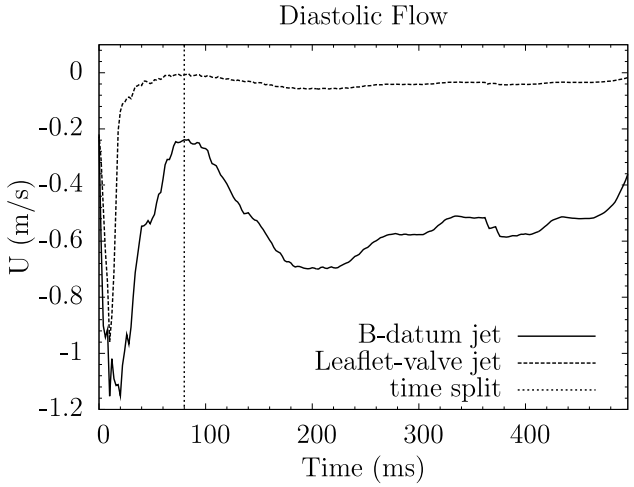

Figure 5-38: Axial velocity at leakage gaps for reverse diastolic flow phase

Axial velocities at the central b-datum jet and valve housing leakage jet are determined for the entire diastolic phase, including closing impact and mid-to-end diastole (figure 5-38). The velocity is averaged across leakage gaps, as similarly performed for shear stresses in figure 5-33.

The axial velocity plot shows strong negative velocities at the leakage gaps upon leaflet impact. It is observed that the maximum negative velocity for the central jet is larger than for the valve housing leakage jets. A slight offset is again observed of 10ms for the time point of maximum velocity, similar to the time point of maximum shear stress in figure 5-33. The rapid decrease in velocity after initial closing impact is observed for both leakage jets. However, it is seen that the decrease in leakage jet velocity is very rapid for the valve housing leakage jet, with a near-zero reverse axial velocity 80ms after initial impact.

The mid-diastolic flow phase is clearly demarcated by a time split line in figure 5-38. After the sudden reduction in reverse axial velocity, the mid-diastolic leakage phase leads to a secondary reverse flow. This reverse flow is not as strong as for initial impact, but lasts for over 400ms during diastole. For the valve housing gaps, the reverse axial velocity is quasi-steady but with magnitudes close to zero.

The central b-datum plane is rectangular and approximately 13.35 mm^2 in area. Thus, the maximum leakage flowrate through the central jet can be approximated (based on area times average velocity) as 15.35 cm^3/s, or 0.92115 L/min. The valve housing gap is circular and approximately 11.17 mm^2 in area. The maximum leakage flowrate through this gap can be approximated as 10.71 cm^3/s, or 0.64266 L/min. The hinge regions are not resolved spatially with an 80μm resolution and thus these leakage gaps cannot be

captured. The total maximum leakage flowrate is thus calculated at 1.56 L/min, though it is noted that the prescribed maximum leakage flowrate from experimental data is 2.4 L/min. It is important to note that these calculations are performed assuming average leakage gap velocity applies throughout the entire gap area, and is thus an approximation.

Qualitative comparisons are made between the simulations and LDV data at the diastolic flow phase. LDV experiments were performed previously to determine leaflet closing and mid-diastolic leakage jet velocities for a 27mm SJM carbon valve in the aortic position for hinge and b-datum leakage flows [95]. As the LDV experimental setup and flow conditions are different from the PIV experimental setup and flow conditions recreated in this computational study [52], only qualitative comparisons are made between simulations and LDV experiments.

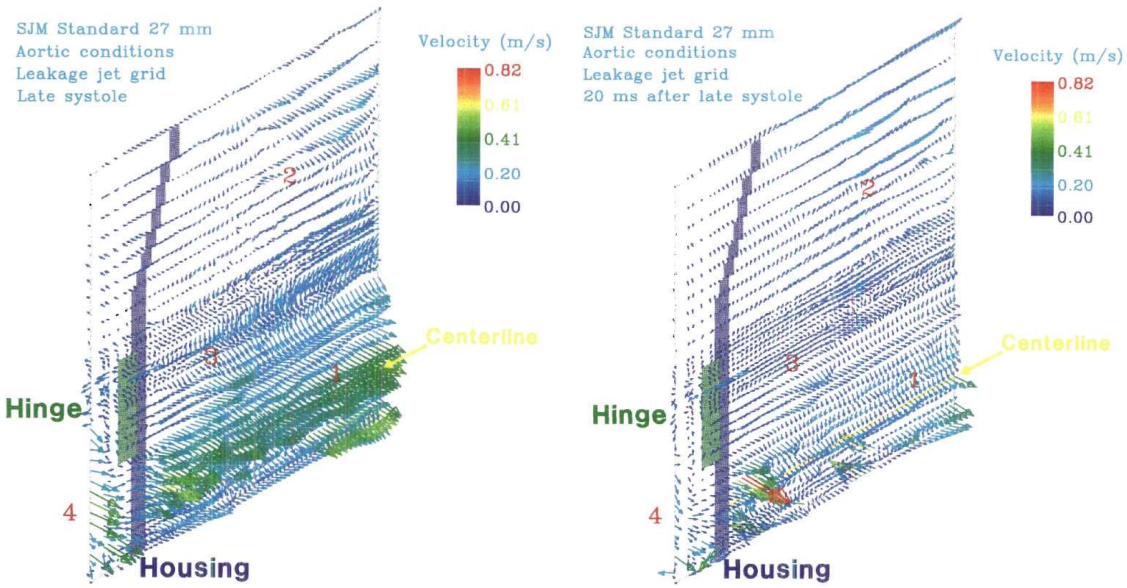

(a) Late systole

(b) 20ms after late systole

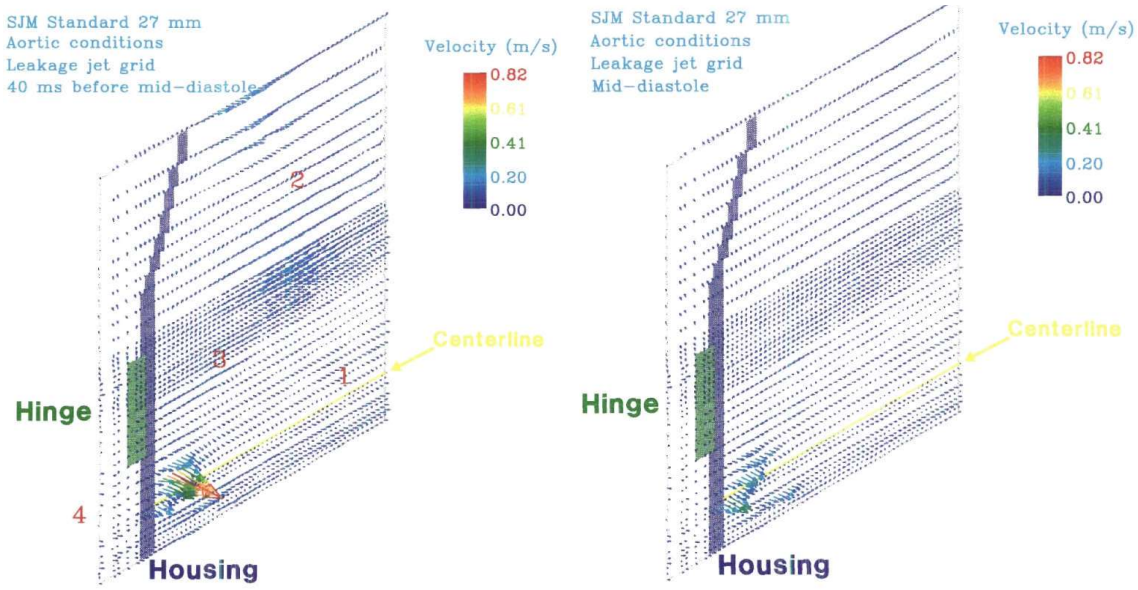

(c) 40ms before mid-diastole (d) Mid-diastole

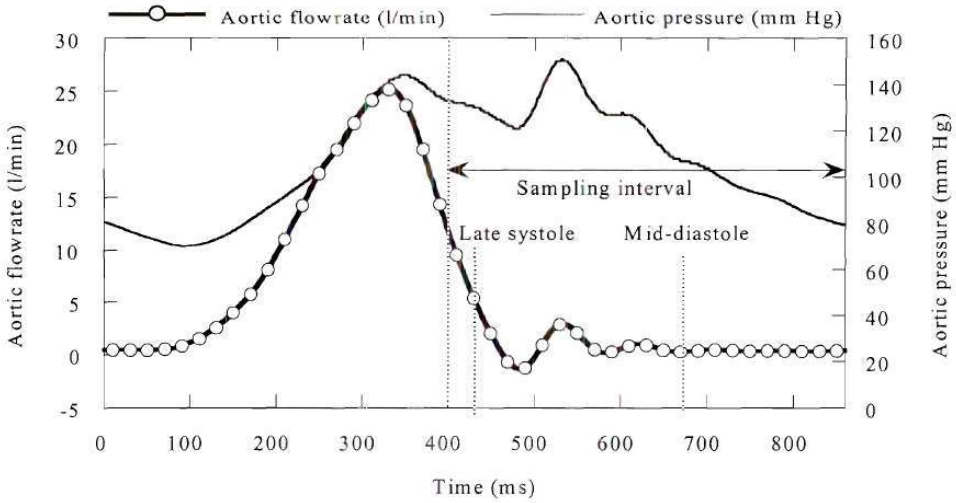

(e) Aortic flow and pressure waveform for LDV experiments

Figure 5-39: LDV experimental data of leakage velocities for diastolic flow phase for 27mm SJM valve in aortic position [95]

At late systole (figure 5-39a), the leaflets approach the fully closed position and cause a large band of squeeze flow. This results in b-datum leakage velocity magnitudes

of approximately 0.50 m/s in the LDV experiments. Similarly in the numerical simulations (figure 5-38), the squeeze jet rapidly increases in velocity magnitude from 0 to 0.8 m/s during leaflet closing. Although the experimental setup is different, the late systole phase corresponds to the numerical simulation phase of rapid leaflet closing, where the velocity magnitudes rapidly increase due to the central squeeze jet.

20ms after late systole (figure 5-39b), the leaflets fully close and a maximum leakage jet velocity of 0.82 m/s is observed at the centerline for the experiments. In the numerical simulations, this corresponds to maximum leakage velocity at the central b-datum gap of 1.1 m/s. At mid-diastole (figure 5-39c/d), the LDV experiments show central jet velocities varying from 0.2 to 0.6 m/s. The simulations show varying mid-diastolic b-datum velocities from 0.4 to 0.7 m/s.

The qualitative comparison shows that the simulations consistently have higher leakage jet velocities at the centerline than the LDV data. Comparisons are not performed at the hinge leakage jets, as the simulations do not resolve hinge leakage. However, the general trend of rising leakage velocity magnitudes due to the squeeze jet, followed by decrease of velocity magnitudes during mid-diastole, is matched in both the LDV experiments and numerical simulations. Although the velocity magnitudes do not compare particularly well, it is emphasized that the LDV experiments were performed for a different valve and experimental setup. It is also unclear what the exact leaflet position is for the "late systole" stages of the LDV data. For these reasons, only good qualitative comparison is expected and achieved between LDV experiments and numerical simulations.

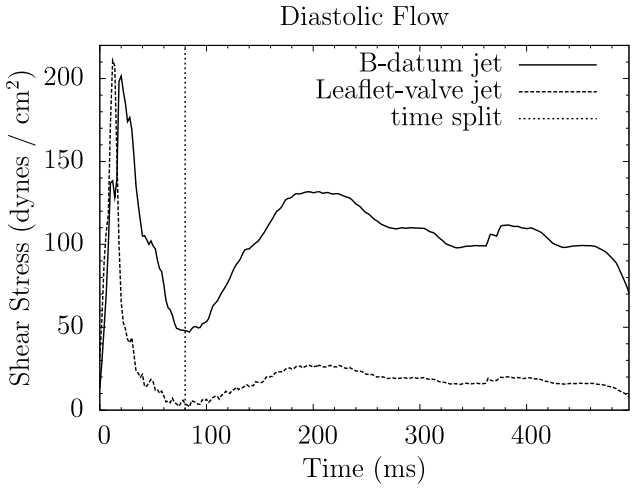

Figure 5-40: Fluid shear stresses at leakage gaps for reverse diastolic flow phase

For shear stress variation for the diastolic flow phase, the initial closing impact leads to high shear stresses across the various leakage gaps that rapidly decrease after 80ms (figure 5-40). Similar to the axial velocity variation (figure 5-38), a clear time demarcation can be made between early diastolic impact and the quasi-steady mid-diastolic flow phase.

Once again, as in the axial velocity variation, the shear stress values for mid-diastole do not reach the maximum levels as in closing impact. However, the moderate levels of shear stress for the b-datum jet are maintained for over 400ms of diastole. It is observed that the b-datum jet shear stresses are significantly larger than for the valve housing gaps. This has implications on potential platelet damage, as platelets caught in leakage flow through this central gap may experience high levels of damage and then recirculate in larger vortices of the ventricular side, as detailed in figure 5-37.

5.5 Turbulent Flow Features

For quantitative validation of pulsatile flow, 200 ensembles are taken within the integral time scale of peak flow when comparing to mean flow data from experiments, as simulating 200 cardiac cycles is not possible due to computational resource constraints. This same methodology of taking samples within the peak flow integral time scale is employed to characterize turbulence in this flow. The estimated integral time scale at peak flow is on the order of 34ms. Thus, 200 ensembles of the flow field are taken in a 25ms time period to detail the turbulent features of peak flow, which is of the same order of the integral time scale. From these ensembles, the mean velocity flow field is first computed and the fluctuating turbulent velocity fields are then computed for each of the 200 ensembles.

The rate of dissipation of turbulent kinetic energy, η, is calculated for the peak flow phase of the cardiac cycle. From turbulent kinetic energy (TKE) equations, this rate is defined as

$$\varepsilon = 2\nu\left\langle \boldsymbol{s}_{ij}\boldsymbol{s}_{ij} \right\rangle \qquad \text{Equation 5-2}$$

where $\boldsymbol{s}_{ij}$ is the rate of strain tensor of the turbulent fluctuating velocity field (u', v', w'), and < > denotes time averaging. As the components of $\boldsymbol{s}_{ij}$ include three-dimensional velocity gradients, a 3D flow field is technically required. Thus, an additional 200 ensembles are taken at the same simulation time points but from a 2D perpendicular flow field plane that is one grid spacing apart in the depth (z) direction. This creates a thin 3D flow field of data, allowing the computation of the full 3D velocity gradient tensor and thus the calculation of the turbulent kinetic energy dissipation rate, ε.

In the case of experiments where only 2D plane data and measurements are possible, the rate of turbulent kinetic energy dissipation is sometimes approximated by assuming local isotopy [96, 97]. This approximation is given by

$$\varepsilon_{iso} = 15\nu\left\langle\left(\frac{\partial u'}{\partial x}\right)^2\right\rangle \qquad \text{Equation 5-3}$$

These two methods are employed and their results are compared, both to determine turbulent energy dissipation rate and to evaluate the validity of the local isotropy approximation ε_{iso} for this specific BMHV flow. 2D contour plots of ε and ε_{iso} are calculated by the two methods for 200 ensembles (figure 5-41). Qualitatively the two fields are similar with high dissipation rates observed in the top sinus region. The local isotropy approximation method also shows a higher peak dissipation rate for vortex shedding past the top leaflet.

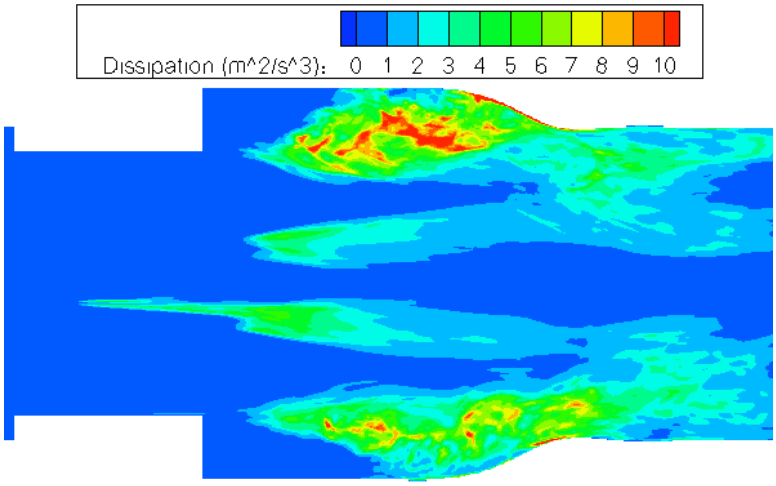

(a) Dissipation rate, ε, from TKE equation

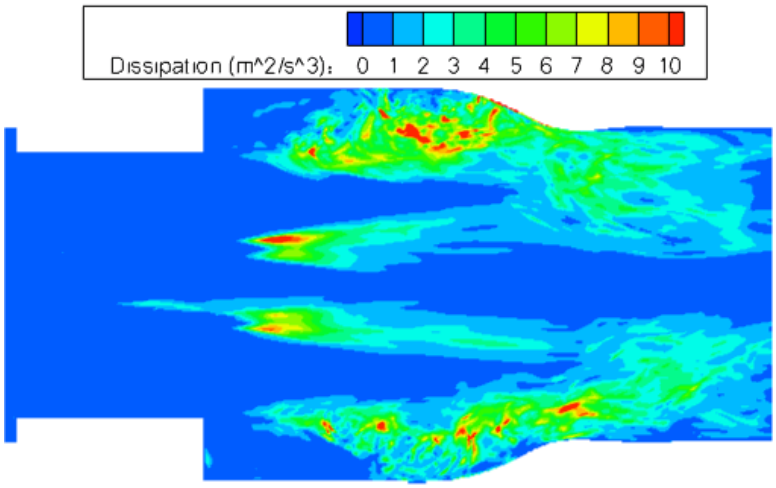

(b) Dissipation rate, ε_{iso}, assuming local isotropy

Figure 5-41: Turbulent kinetic energy rate of dissipation contour plots for 2D perpendicular plane at peak flow using (a) TKE equation, ε, and (b) local isotropy, ε_{iso}, methods

It is observed that the dissipation rate plot is not symmetric about the centerline, despite the use of 200 ensembles. This can be explained by the nature of the time averaging that is employed, in that it is taken for pulsatile flow within a small time period of 25ms. Though this time period is important because it is on the same order of the integral time scale of peak flow, this also means that the natural asymmetries of vortex shedding will not be averaged within this small time range. Thus, some degree of asymmetry in the contour fields of ε and ε_{iso} are expected.

The two dissipation rate calculation methods are also compared at perpendicular lines downstream of the leaflets. 5mm downstream of the leaflets (figure 5-42a), the two methods show similar dissipation rates in the sinus expansion regions. However, the local isotropy approximation method computes a significantly higher maximum dissipation

rate for flow past the leaflets (ε_{iso} = 12.85 m^2/s^3) compared to the 3D TKE equation definition (ε = 5.87 m^2/s^3). 10mm downstream of the leaflets (figure 5-42b), the dissipation rates are similar both in shape and in magnitudes.

The dissipation rate is highest in the sinus expansion region, at 16 - 17mm downstream of the leaflets for both methods (figures 5-42c/d). This occurs at slightly different axial positions, but the magnitudes of maximum dissipation rate are similar (18 m^2/s^3). Further downstream of the leaflets (30mm and 40mm), the two methods show similar profiles both qualitatively and in magnitudes (figures 5-42e/f).

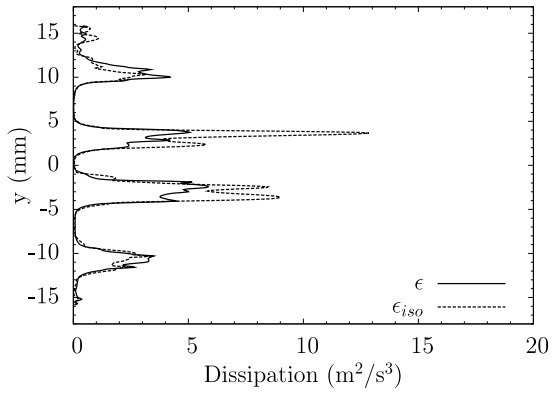

(a) x=5.0mm

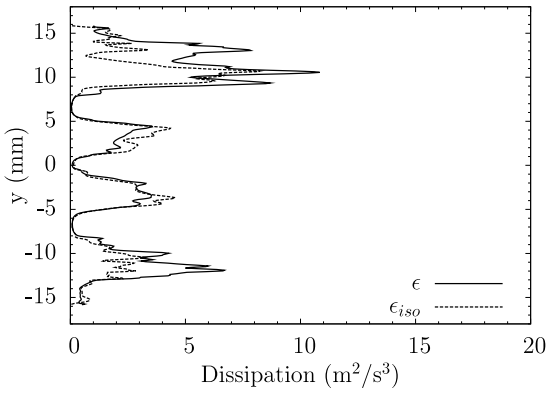

(b) x=10.0mm

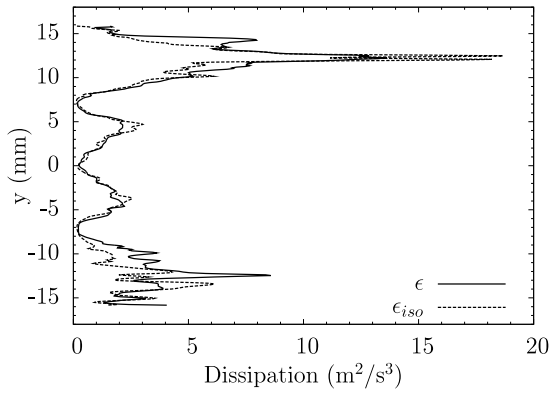

(c) x=16.0mm

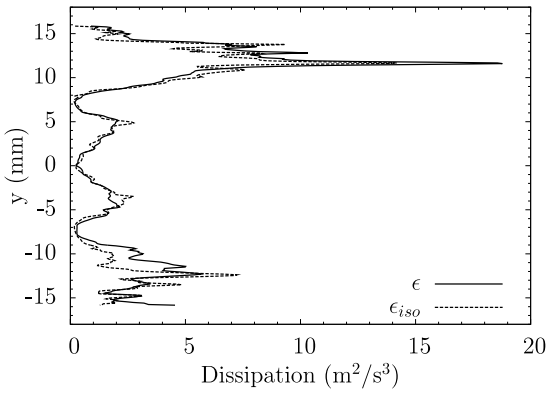

(d) x=17.0mm

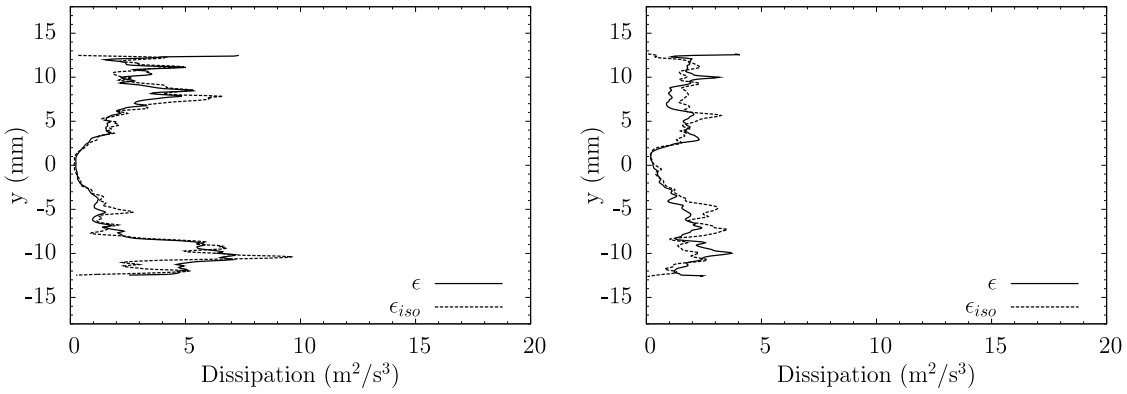

(e) x=30.0mm (f) x=40.0mm

Figure 5-42: Turbulent kinetic energy rate of dissipation line plots at peak flow, calculated from TKE equation (ε) and local isotropy approximation (ε_{iso})

It is determined that for comparisons at perpendicular lines downstream of the leaflets, the two methods are similar in profile and magnitude of dissipation rates for peak flow. The only major difference is observed 5mm downstream of the leaflets (figure 5-42a), where the dissipation rate downstream of the leaflets is significantly higher for the local isotropy approximation ε_{iso} method. Goodness-of-fit R^2 analysis is performed for comparisons of ε and ε_{iso} at these perpendicular lines. This analysis results in R^2 values varying from 0.813 to 0.914 for perpendicular lines, with one notable exception at 5mm downstream of the leaflets where $R^2 = 0.503$. Other than this discrepancy, the assumption of local isotropy in order to calculate turbulent energy dissipation rates is shown to be a good approximation.

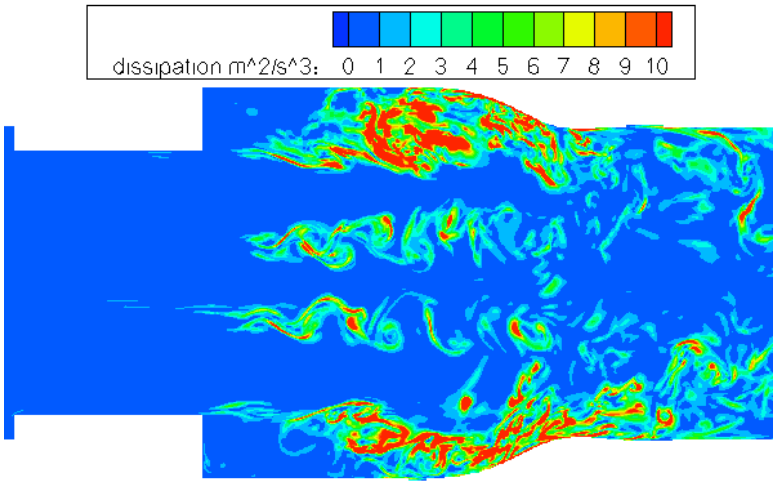

Figure 5-43: Instantaneous turbulent energy dissipation rate, ε_{inst}, at peak flow

The instantaneous turbulent energy dissipation rate can be calculated for peak flow as well (figure 5-43), and is defined as

$$\varepsilon_{inst} = 2\nu\, s_{ij}s_{ij} \qquad \text{Equation 5-4}$$

Compared to the mean dissipation rate contour plots (figure 5-41), high instantaneous dissipation rates are observed throughout the flow field (figure 5-43), particularly for the sinus recirculation and leaflet wake regions. This also demonstrates the high fluctuations present in these regions and the high potential for turbulence in this flow, particularly for the peak flow phase.

The Kolmogorov scale is calculated from the mean dissipation rate as

$$\eta = \left(\frac{\nu^3}{\varepsilon}\right)^{1/4} \qquad \text{Equation 5-5}$$

For the sinus expansion, the peak dissipation rates correspond to Kolmogorov lengths of approximately 40-42μm in the recirculation region. For flow past the leaflet tips, the definition from the TKE equation yields a Kolmogorov length of approximately 52μm.

From the local isotropy approximation, the Kolmogorov length is approximated as 43µm. As the spatial resolution of these simulations is 80µm, the smallest Kolmogorov lengths are not being resolved by the numerical simulations. However, it should be noted that the Kolmogorov scales are not a strict threshold but represent an order of magnitude of the smallest eddy scales.

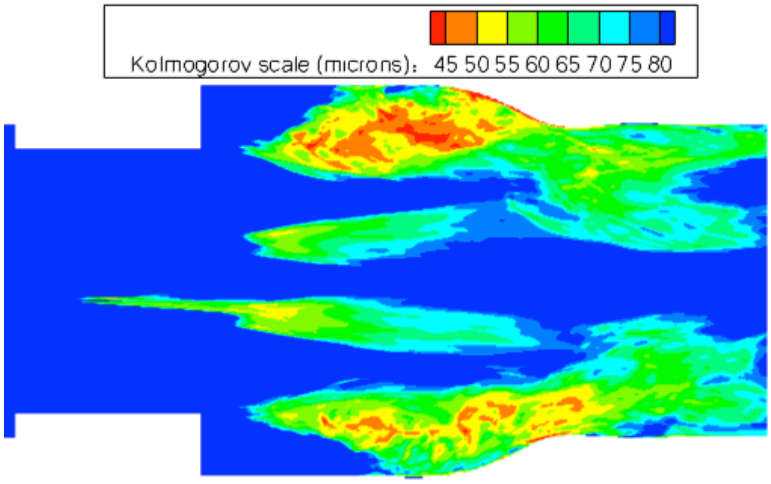

Figure 5-44: Contour plot of Kolmogorov spatial scales (η) based on mean dissipation rates, with contour scaling capped at 80µm

The Kolmogorov spatial scales can be estimated throughout the central plane of the flow (figure 5-44) based on the calculated mean dissipation rates ε at each point and equation 5-5. This demonstrates that most of the flow field is being resolved by the high spatial resolution of these simulations at 80µm. The lowest scale is in the top sinus region, with a Kolmogorov length of approximately 40µm. Although this again means that the simulations technically under-resolve the Kolmogorov scale, the spatial resolution is within two times the lowest Kolmogorov length scale. Thus, the numerical simulations are still able resolve the lower order moments of the turbulent flow [98, 99].

Energy spectra can also be plotted against wavenumber for peak flow to determine the existence of turbulence in this BMHV flow (figure 5-45). This spectra is generated for wavenumber κ_1 corresponding to the streamwise axial direction. Sampling for this spectra is performed for 200 time ensembles spanning 25ms. Sampling is also performed at multiple positions along the transverse (perpendicular to the leaflets) y-axis. This encompasses flow past the leaflets as well as the sinus recirculation region.

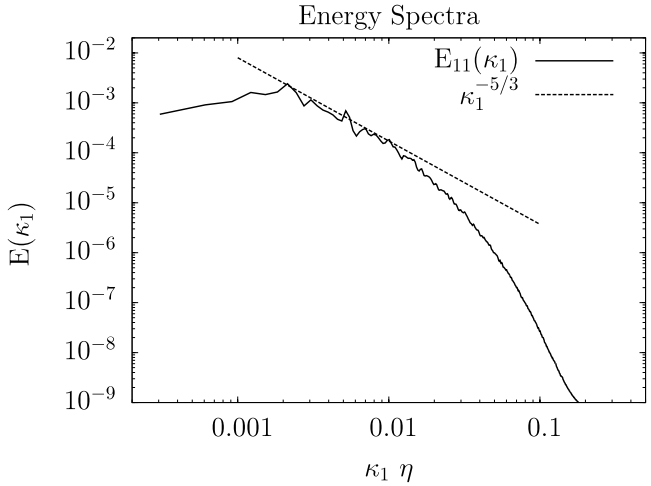

Figure 5-45: 1D Energy spectra vs. normalized wavenumber at peak flow

The spectra is generated for $E_{11}(\kappa_1)$, or energy for the streamwise turbulent velocity component, u'. Although BMHV flow is complex in its pulsatile nature and flow past two leaflets, it most resembles turbulent pipe flow. Thus, the streamwise velocity component and associated energy are chosen as most appropriate for the assumption of homogeneous flow for plotting energy spectra. The flow velocity in the transverse y-direction is strongly affected by the presence of the two leaflets in BMHV flow, and thus energy is not computed for other velocity components. In classic turbulent channel and

pipe flow problems as well, the transverse velocities are considered to not satisfy the condition of homogeneity [100].

The plotted spectra (figure 5-45) also shows the -5/3rd slope to demonstrate the presence of an inertial range and the presence of turbulence at peak flow. Though this inertial range contains some noise, a relatively good fit is shown with the -5/3rd slope for a small range of wavenumber modes. This hints at the presence of turbulence at peak flow, despite the Reynolds number being relatively moderate (Re = 5780 at peak flow).

The compensated energy spectra is also plotted (figure 5-46) along with the zero-slope constant C_1 line corresponding to the inertial range for 1D energy spectra, where $C_1 \cong 0.49$ [98]. Once again, this compensated spectra demonstrates noise in the inertial range but shows matching with the predicted C_1 line. A clear demonstration of turbulence in this pulsatile BMHV flow is not apparent, but these energy spectra show the development of an inertial range.

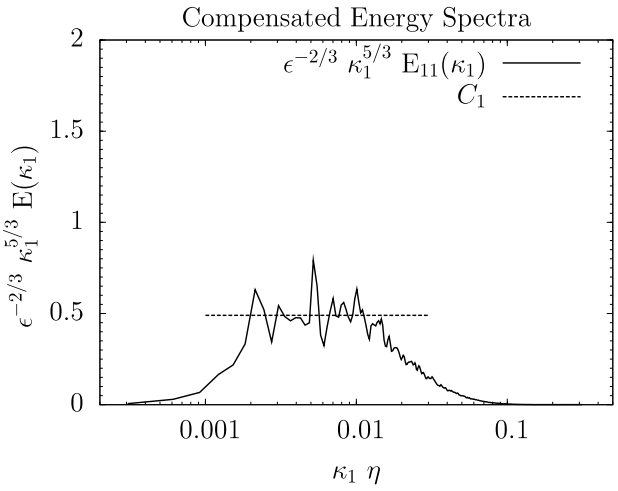

Figure 5-46: 1D Compensated energy spectra vs. normalized wavenumber at peak flow

It is also observed that after the -5/3rd scaling for the inertial range, the dissipation range shows slow energy decay with an approximate -3 scaling law. This slow decay starts at a normalized wavenumber around $\kappa_1 = 0.015$, which is associated with a spatial length scale of approximately 3mm. Thus it is found that the dissipation range exists for spatial scales of smallest lengths at 40-50μm to the length scale of 3mm, which is approximately 60 times the Kolmogorov scale. This is consistent with the definition by Pope [98] where demarcation length scales are approximated at $L_{DI} = 60$.

5.6 Additional Pulsatile Flow Cases

Additional simulations are performed with prescribed asymmetric leaflet motion, representing normal cycle-to-cycle asymmetry and cases of severe leaflet dysfunction. Due to computational resource limitations, these simulations are performed with 160μm and 4.2μs spatiotemporal resolution. These simulations are compared only qualitatively to explore flow field differences, but all employ the same vorticity scaling for 2D plots and Q-criterion thresholds for 3D plots.

The first simulations prescribe the observed asymmetric motion of the leaflets that was documented in the experimental study [52]. Although 100 cardiac cycles of leaflet asymmetry were documented in the experiments, only a representative sample of two of these cardiac cycles is simulated. The cycles were selected qualitatively by choosing extreme cases of leaflet motion asymmetry. One selection is made on opening phase asymmetry, and one for closing phase asymmetry.

The same flow curve data used in the symmetric leaflet motion cases are used as a prescribed inlet condition. The same initial flow field conditions are also used at the

beginning of the cardiac cycle for both leaflet motion cases. This allows for a more accurate comparison between symmetric and asymmetric leaflet motion.

Simulations are also performed with extreme cases of asymmetric leaflet motion. Scenarios in which a thrombus forms at the hinges of BMHVs may result in extreme dysfunction leading to strong leaflet asymmetry or a fixed leaflet throughout the cardiac cycle. These possible cases are simulated to show how important normal leaflet function is on the flow dynamics throughout the cardiac cycle. One case of a leaflet that only opens halfway is simulated, as well as a case of a leaflet fixed closed throughout the cardiac cycle. These dysfunction cases show the effect of thrombus formation, a known complication of BMHVs, on valve performance in maintaining normal hemodynamics.

5.6.1 Leaflet Motion Asymmetry – from experiments

Comparisons are made between the symmetric and natural asymmetric leaflet motion cases at instantaneous time points. In the case of opening phase asymmetry, the top leaflet is prescribed to open slower than the bottom leaflet (Figure 5-47). The slower opening top leaflet results in a smaller top orifice with stronger vorticity magnitude as compared to the bottom orifice. The vortex shedding past the leaflet trailing edges is slightly different for the two leaflets due to asymmetry. In addition, flow separation from the top leaflet on the b-datum side is sharper than for the bottom leaflet. This is caused by the slower opening top leaflet, which creates a sharp leading edge. The vortex shedding from the step expansion from the valve to the sinus is similar for both the top and bottom regions. However, these differences do not result in significant flow differences.

(a) Normal leaflet opening

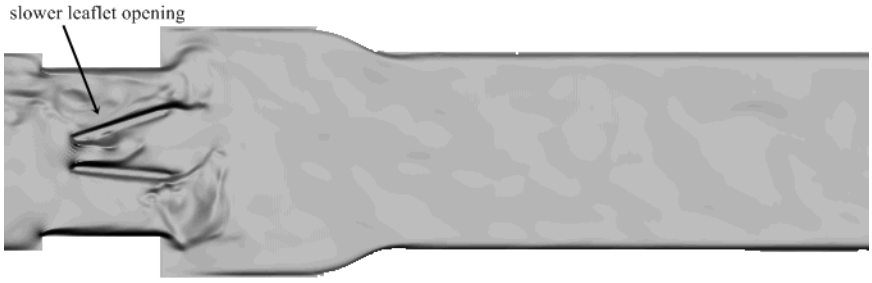

(b) Slower opening top leaflet

Figure 5-47: Vorticity plots with asymmetric leaflet motion comparison showing (a) normal leaflet opening vs. (b) slower opening top leaflet

The case of closing phase asymmetry is also modeled, where the top leaflet closes faster than the bottom leaflet. Figure 5-48a shows the initial closing phase, where the faster top leaflet causes a much stronger vortex wake than the bottom leaflet. When the top leaflet hits the valve housing (figure 5-48b), a leaflet closing leakage jet is formed. The reduced b-datum orifice from the closed top leaflet also causes a b-datum leakage jet.

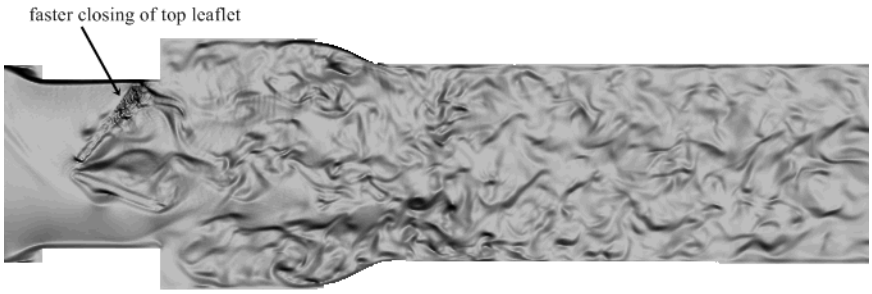

(a) Faster closing top leaflet

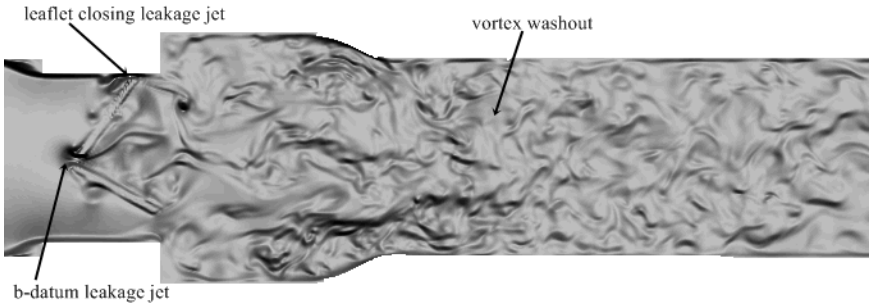

(b) Top leaflet hitting valve housing

Figure 5-48: Vorticity plots of closing phase leaflet motion asymmetry with a faster closing top leaflet

The asymmetric closing of the leaflets results in a b-datum leakage vortex formation that drifts towards the top leaflet (Figure 5-49a). This is a change from symmetric leaflet closing where the instant b-datum leakage flows centrally in the axial upstream direction. A weaker leakage jet is formed when the bottom leaflet hits the valve housing (figure 5-49b). In addition, the b-datum leakage vortex is shown to continue to drift towards the top side of the valve housing.

(a) B-datum leaflet vortex from closing phase

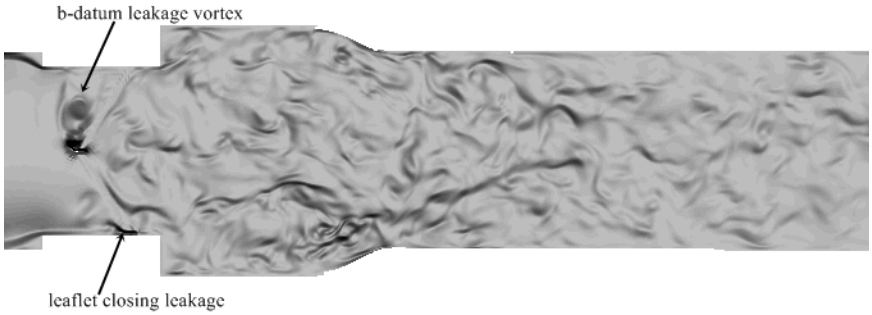

(b) Drifting of b-datum leakage vortex

Figure 5-49: Faster closing top leaflet leading to b-datum leakage vortex that drifts towards the top leaflet

Comparison for the other points of the cardiac cycle not related to leaflet motion asymmetry (forward systolic flow, mid-diastolic leakage flow) did not show any noticeable differences in flow features when compared to the perfectly symmetric case. Thus, these time points are not shown as no qualitative differences are observed.

5.6.2 Leaflet Dysfunction

This section examines the case of a bottom leaflet that only opens halfway during systolic flow. The leaflet motion is otherwise symmetric besides limiting the range of

motion of the bottom leaflet. In the opening phase (figure 5-50), the bottom leaflet has only opened halfway and the top leaflet has just finished opening. Upon leaflet opening, the reduced bottom orifice area due to the half-open leaflet causes a stronger flow past the sinus expansion step. The two flow features of note are the vortex shedding past the bottom leaflet's leading edge, which is sharper due to the leaflet only opening halfway, and the sinus step expansion vortex shedding in the bottom orifice.

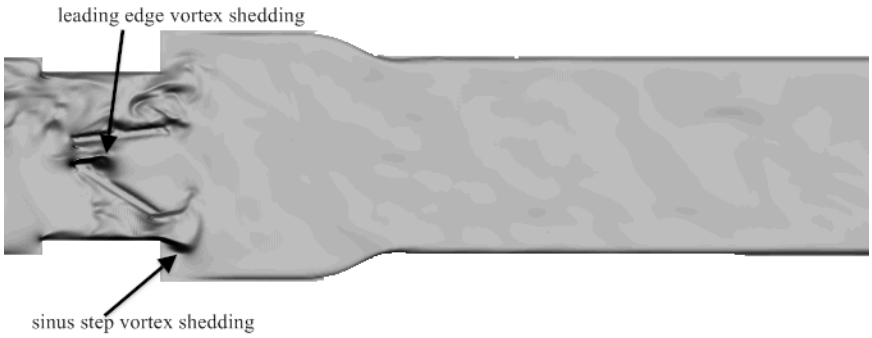

(a) 2D vorticity

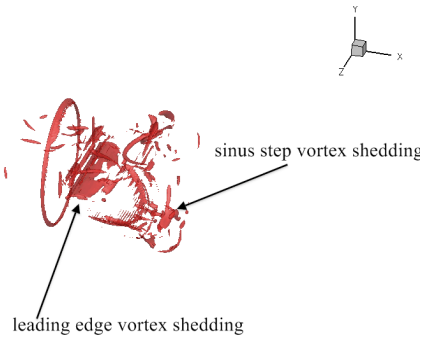

(b) 3D Q-criterion

Figure 5-50: Half-opening bottom leaflet with leading edge vortex shedding

For accelerating flow, large differences between the top and bottom regions of flow past the valve are observed (Figure 5-51). The flow past the fully open top leaflet

results in a von Karman vortex street and sinus recirculation region. These flow features are qualitatively very similar to the normal function case. For the bottom leaflet, the flow past the sharp leading edge leads to vortex shedding into the bottom sinus region that also mixes with the vortex shedding past the sinus expansion step. This leads to a complex recirculation region for the bottom half of the sinus region.

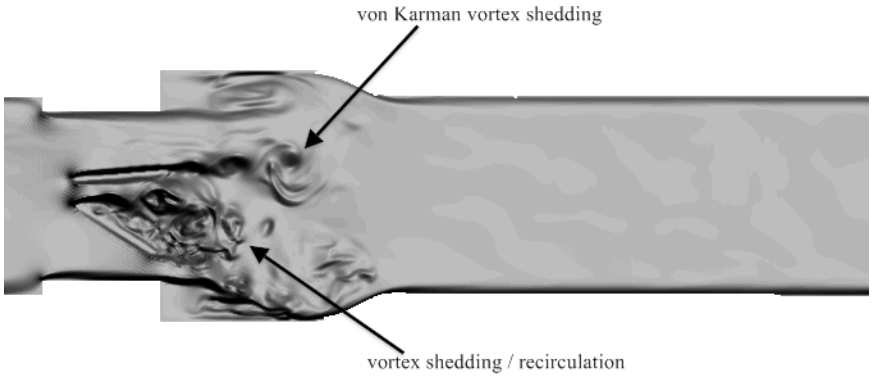

(a) 2D vorticity

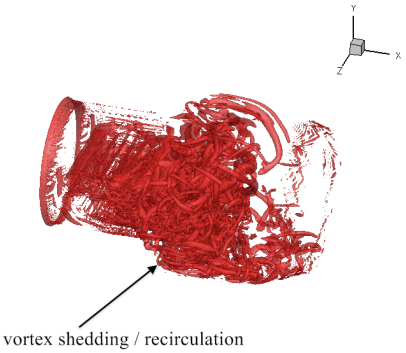

(b) 3D Q-criterion

Figure 5-51: Half-open bottom leaflet in mid-acceleration phase with sharp leading edge causing vortex spilling

Peak flow is shown in figure 5-52, which shows the same features as accelerating flow but with more unstable and disorganized structures. In particular, the bottom half of

the sinus region shows very strong mixing and vortical structures, and there is also weaker recirculation in the top half.

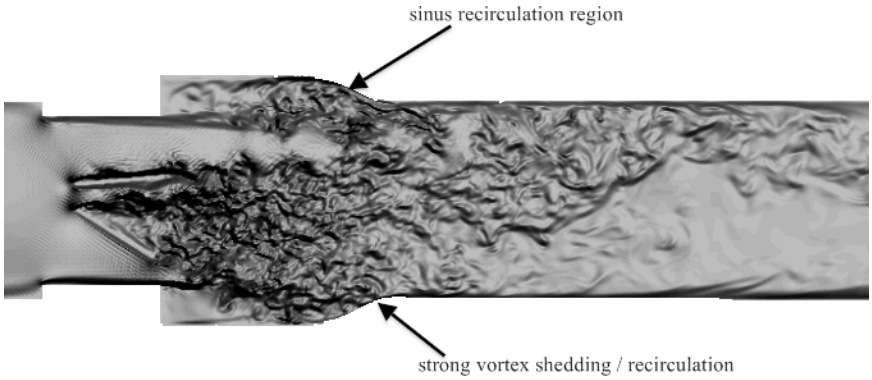

(a) 2D vorticity

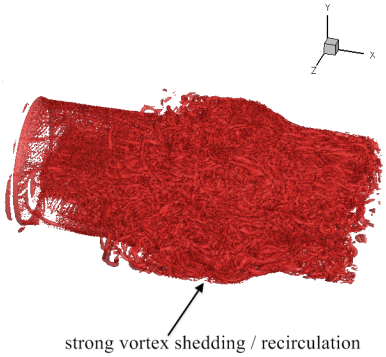

(b) 3D Q-criterion

Figure 5-52: Half-open bottom leaflet in peak flow phase with strong asymmetric vortex shedding caused by sharper leading edge on bottom leaflet

In the closing phase, the full range of motion of the top leaflet leads to a stronger vortex wake than the bottom leaflet, which only closes halfway (Figure 5-53). In addition, the strong vortical structures from peak systolic flow persist even with the low flowrate, causing a delay in the vortex washout. This slow vortex washout is more

evident in the bottom sinus region, where the strongest of the unstable structures were present during peak flow.

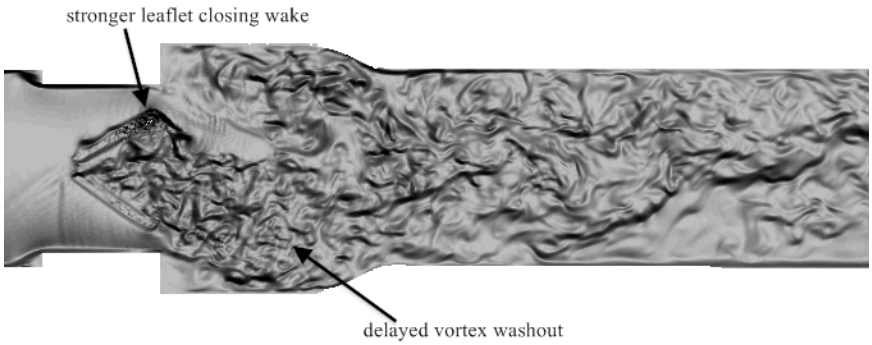

(a) 2D vorticity

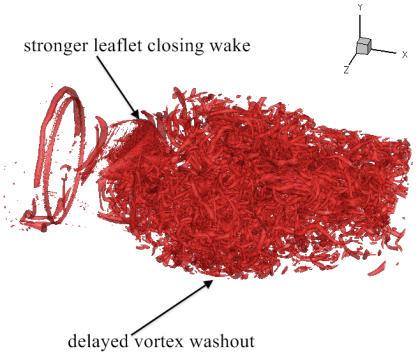

(b) 3D Q-criterion

Figure 5-53: Half-open bottom leaflet in closing phase with stronger vortex wake for closing top leaflet, and delayed vortex washout in sinus region

Figures 5-54, 5-55, and 5-56 shows the case of the bottom leaflet fixed closed throughout the cardiac cycle. Starting with the opening phase (figure 5-54), the top orifice is shown as having strong vorticity due to the reduced total area of forward flow. In addition, the flow through the central orifice results in a vortex that is advected into the low flow region downstream of the fixed bottom leaflet and in the sinus region. This is

most likely due to the fast moving fluid squeezing through the central orifice and mixing with the quasi-static flow region on the "bottom" section of the valve. 3D visualization also shows flow past the open top leaflet as well as a vortical structure seeming to roll from the central orifice and spill into the bottom sinus region, caused by the sharp leading edge of the bottom leaflet.

(a) 2D vorticity

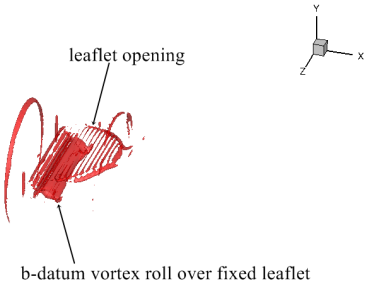

(b) 3D Q-criterion

Figure 5-54: Fixed closed bottom leaflet with vortex roll from sharper leading edge in early acceleration/opening phase

During peak systolic flow, the effects of the closed leaflet are very apparent (Figure 5-55). Here, an extremely strong jet of flow passes through the top and central

orifices resulting in very strong vorticity magnitudes. On the top leaflet side, there is strong recirculation near the sinus expansion wall. Chaotic and disorganized structures also exist on the top half of the valve and extend far downstream of the valve.

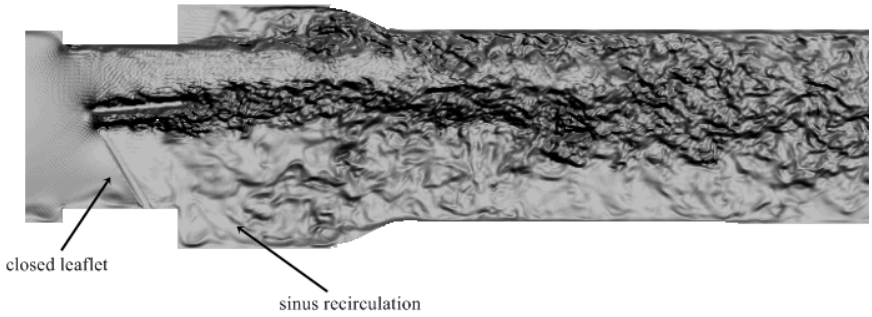

(a) 2D vorticity

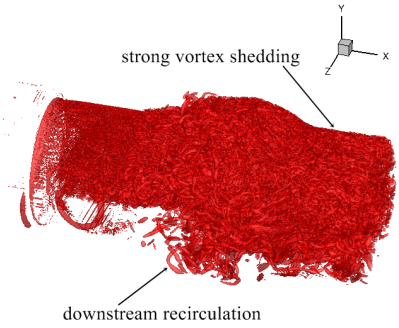

(b) 3D Q-criterion

Figure 5-55: Fixed closed bottom leaflet in peak flow phase with strong vortex shedding on top half of flow domain

Finally, a large recirculation of flow occurs in the bottom part of the valve where there is weaker flow due to the fixed closed bottom leaflet. This recirculation comes from the strong top orifice jet mixing with the quasi-static flow beneath, and recirculation even occurs far downstream of the sinus expansion region. This massive recirculation

region is different from the normal case, where the recirculation zone only exists in the sinus expansion. These features are apparent in the 3D visualization, where the top half of the domain is dominated by strong coherent vortical structures. The bottom half of the domain shows flow recirculation far downstream of the valve returning to the valve.

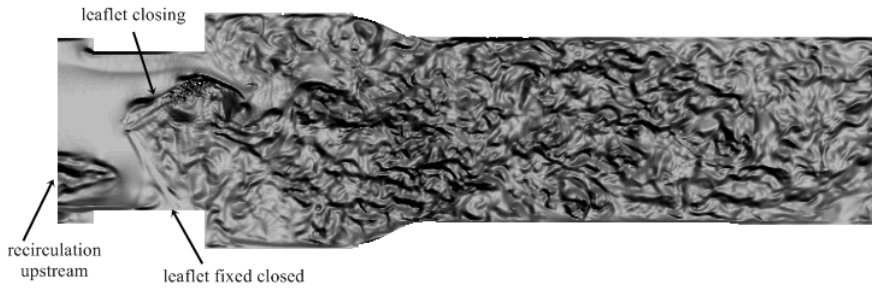

(a) 2D vorticity

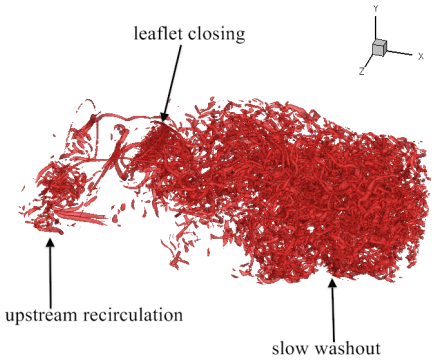

(b) 3D Q-criterion

Figure 5-56: Fixed closed bottom leaflet in closing phase with delayed vortex washout

In the closing phase, the top leaflet closing causes a strong vortex wake as expected (Figure 5-56). It is noted that the remnants of the systolic flow are still very present even during the closing phase, with very little vortex washout at this time point. This is also noted in the 3D visualization where many coherent vortical structures are still present downstream of the valve. This is likely due to the flow through the reduced top

orifice causing strong flow structures that are not easily dissipated, even with the reduced flow rate during the closing phase.

Finally, it is noted that due to the fixed bottom leaflet, there is also some recirculation that occurs upstream of the valve, hitting the bottom leaflet. This could be due to flow upstream not completely diverting towards the top orifice, thus resulting in flow hitting the bottom leaflet and causing a recirculation region. This recirculation upstream of the leaflets is also visible in the 3D plot. Although not shown, the fixed closed leaflet causes a lengthy delay in vortex washout that persists throughout a significant part of diastole before all vortical structures downstream of the valve finally dissipate in mid-diastole.

5.6.3 Comments on asymmetric leaflet motion

In both cases of realistic asymmetric leaflet motion simulations (figures 5-47 to 5-49) there are no lasting effects on flow dynamics once the cardiac cycle moves into the systolic and diastolic phases. The opening phase asymmetry in particular has very minor flow feature differences and does not affect systole at all. This is due to the nature of the opening phase, where the forward flow rate is so low that the asymmetries cannot affect the flow dynamics significantly. In the case of closing phase asymmetry, the b-datum leakage jet is affected in its drift direction and the vortex washout downstream of the valve is shown to be slower. However, by mid-diastole, there are no lingering effects.

The leaflet closing asymmetry may have implications on platelet damage incurred during the closing phase. This leaflet motion asymmetry may lead to stronger leakage jet asymmetry during the diastolic phase and stronger vortical mixing in the ventricular

upstream section. This could cause elevated damage incurred on platelets that are caught in these vortices.

With cases of extreme leaflet dysfunction (figures 5-50 to 5-56), we note strong flow differences throughout the cardiac cycle. Though unlikely, this extreme representation of a complication from thrombus formation is shown to demonstrate a worst-case scenario. Starting from the opening phase, the flow fields are heavily affected by reduced flow orifices, which cause extremely strong flow jets. These could lead to extremely high shear stresses on platelets that could lead to unwanted platelet activation. In addition, a strong flow recirculation occurs from far downstream of the valves to bring fluid back to the sinus expansion region. This only exacerbates the problem by subjecting blood elements to high shear stresses and long exposure times due to the flow recirculation. This combination of shear stress and exposure time has been shown to lead to blood element damage in previous studies. Finally, the strong flow throughout systole causes a long delay in complete vortex washout, extending far into the diastolic phase. These three considerable differences as compared to the normal symmetric motion case highlight the significant effects of extreme leaflet asymmetry on blood flow dynamics.

5.7 Leaflet Motion by 2-way FSI

The simulations of platelet damage in this study employ prescribed leaflet motion in order to save computational expenses. However, single-phase simulations are also performed in which the leaflet motion is dictated by two-way fluid-solid interaction forces. Translational motion is restricted, and rotational motion is only allowed about the hinge fulcrum line. The accuracy of the dynamic leaflet motion modeling is important

for future studies employing this numerical method, where experimental data on valve leaflet motion may not be available and thus dynamic leaflet motion modeling may be required. Some issues with dynamic leaflet modeling are discussed in Appendix B.4.

5.7.1 Dynamic Leaflet Motion Results

A simulation is also performed for leaflet motion using 2-way FSI. Forces across the leaflet surface are determined using the SBB method, and torques are accumulated for each leaflet based on calculated forces and the moment arm to the hinge fulcrum line. Allowing only for rotational motion about the hinge fulcrum line, the rotation of the leaflets is determined by solving Newtonian angular dynamics equations, with a moment of inertia of $4.375 \bullet 10^{-9}$ kg m^2 for each leaflet.

Figure 5-57 demonstrates leaflet opening from two-way FSI modeling of leaflet motion. This shows asymmetric opening of the leaflets, with the bottom leaflet opening much faster than the top leaflet. As flow conditions and geometry are perfectly symmetric, this shows natural asymmetry in leaflet motion in the cardiac cycle due to the disorganized nature of pulsatile BMHV flow. Though this highlights asymmetry in leaflet opening, the leaflets are fully open at relatively close times in the cardiac cycle.

Figure 5-57: 2D vorticity plot showing leaflet opening from two-way FSI modeling

For leaflet closing due to two-way FSI modeling, relatively symmetric closing of the top and bottom leaflets is observed (Figure 5-58). The fast rotational motion of the leaflets leads to some shock-like regions near the leaflet tips. However, these regions remain localized to the leaflet tips and do not affect the rest of the flow field. The simulations remain stable even with the fast rotation of the leaflets.

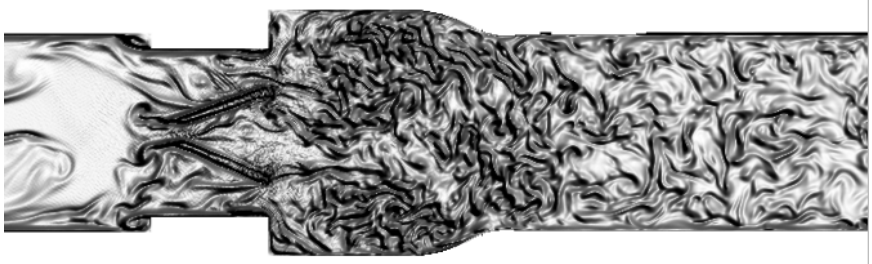

Figure 5-58: 2D vorticity plot showing leaflet closing from two-way FSI modeling

To test the accuracy of the dynamic leaflet motion implementation, the angle variation of both leaflets are compared to the experimental PIV leaflet motion data. This is displayed for a 860ms cardiac cycle, and is shown in figure 5-59.

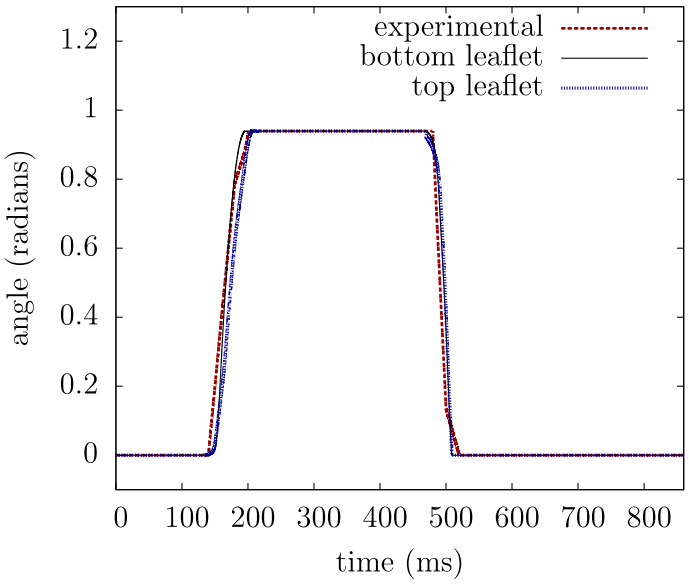

Figure 5-59: Comparison of leaflet angle variation for two-way FSI numerical modeling vs. PIV experimental data

For leaflet opening, the experimental PIV data shows a 66.7ms opening time from the fully closed to fully open leaflet positions. For the numerical simulations, the top leaflet opening time is 81ms, and the bottom leaflet opening time is 64ms. The bottom leaflet matches very well with the experimental data of leaflet opening, for the time of leaflet opening as well as the leaflet angle slope during opening. The top leaflet, as previously shown in figure 5-57, opens slower than the bottom leaflet and demonstrates notable asymmetry. For the simulations, both leaflets open approximately 20ms after the experimental data show the start of leaflet opening. This could be due to the extended ventricular inlet length of 13 diameters, which is necessary for two-way FSI modeling of leaflet motion. This increased inlet length results in a slight offset in leaflet motion time. Nevertheless, the numerical modeling of leaflet opening matches very well with experimental data when the start timing of leaflet motion is matched.

For leaflet closing, the experimental PIV data shows a 40ms closing time from the fully open to fully closed leaflet positions. For the dynamic leaflet modeling, the top leaflet closing time is 39ms, and the bottom leaflet closing time is 38.5ms. Both leaflets match extremely well with the experimental data, for both the time of leaflet closing and the leaflet angle deceleration slope. In order to obtain accurate leaflet closing motion, the deceleration rate of the inlet flowrate curve was doubled. This modification of the flowrate curve results in the leaflet closing motion starting earlier in the cardiac cycle for the simulations when compared to the experimental data. Despite this offset time, the numerical modeling of leaflet closing matches very well with experimental data for the period of leaflet closing. It is noted that this modification of the flowrate curve is made only to the deceleration rate, but does not affect the maximum forward or reverse flowrate values. This flowrate modification was also employed by another numerical study that modeled two-way dynamic leaflet motion for pulsatile BMHV flows [56]. Both the LBM-EBF method of this study and the numerical method of the previous numerical study require faster deceleration rates for the flowrate curve in order to obtain accurate leaflet closing motion.

CHAPTER 6

BLOOD DAMAGE SIMULATIONS – PHYSIOLOGIC ADULT CASE

Simulations are performed of pulsatile flow through a 23mm SJM valve with the presence of suspended platelets for physiologic adult conditions. Though previous simulations and experiments have examined flows and blood damage through BMHVs in adult conditions, the simulations of this study are performed with the highest spatiotemporal resolution to date and with realistic platelet modeling. Previous use of this numerical methodology has demonstrated the importance of modeling realistic suspended platelets for accurately quantifying platelet damage [63]. In addition, this numerical method is shown in section 5.5 to be able to capture the smallest scales of pulsatile, high Reynolds number BMHV flow [101, 102]. Thus, these simulations model blood damage in BMHV flows with very high accuracy in flow modeling, suspension modeling, and blood damage quantification to attempt to better understand thromboembolic potential in these flows.

Platelet position and damage are calculated and tracked through time for individual platelets released in the pulsatile BMHV flow. These data are then analyzed to understand blood damage from both Lagrangian and Eulerian viewpoints. A simulation on mid-diastolic flows is also presented to understand damage throughout the cardiac cycle. Finally, comments are made on the relation between platelet rotation and BDI. The results of these simulations are also used as a baseline for comparison with non-adult

cases as performed with the pediatric flow cases of chapter 7, using this numerical method.

6.1 Adult conditions and numerical setup

The same flow conditions used in the single-phase flow simulations of chapter 5 are employed in the simulations of this chapter. A 860ms cardiac cycle with peak flowrate of 25.0 L/min, average flowrate of 4.5 L/min, and forward systolic flow duration of 350ms is modeled. Due to computational resource limitations, only one cardiac cycle of flow is simulated with the presence of suspended platelets. All platelets are modeled with the same shape (3D ellipsoid) and size (3μm major axis diameter) and with the same surface mesh (292 triangular elements).

To obtain realistic volume fraction of platelets, billions of platelets must be simulated [103]. This type of computational resource is not available, and thus a representative sample is instead used in the simulations. For the forward flow simulations, 300 platelets are released every 20ms during the systolic phase with an initial seed of 300 platelets at the start of systole. This totals 5400 released platelets in the blood damage simulation.

Platelets are released one diameter upstream of the valve as the damage that occurs in flows through BMHVs is of interest for this study. The cardiac cycle flow modeling is first performed without the presence of platelets through the end of diastole. Platelets are released at the start of systole when the leaflets open, and damage is tracked throughout the simulation. The simulations tracking platelet damage cover 460ms of the 860ms cardiac cycle, representing all of systole, leaflet closing, and early diastole.

Each platelet is released from the same axial position upstream of the valve, but with randomized cross-sectional position and angular orientation. Cross-sectional position is chosen using a disk-seeding algorithm [104] and random number generation (figure 6-1). As the platelet suspension is very dilute in the simulations, no contact modeling between platelets is required.

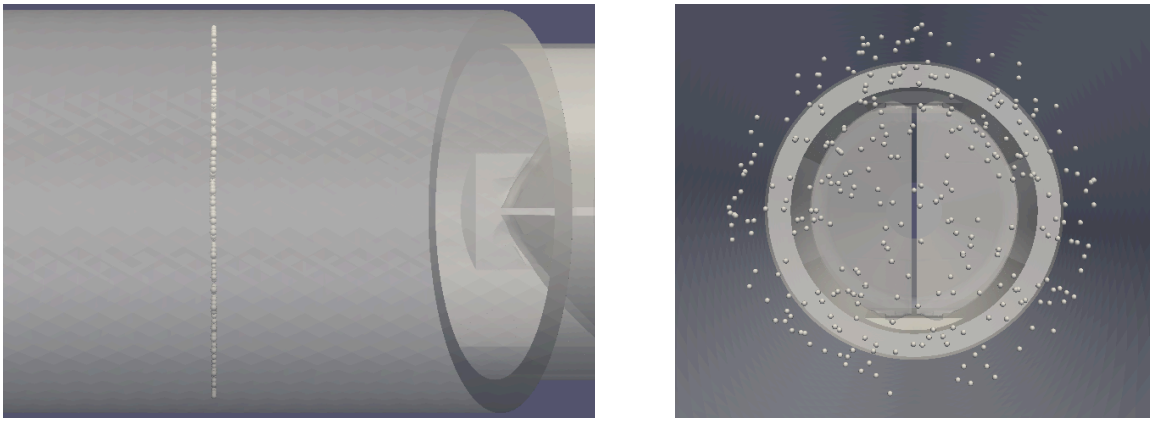

(a) Side view (b) Cross-sectional view

Figure 6-1: 300 platelets seeded randomly upstream of BMHV. (a) Side view showing platelets with same axial position, (b) cross-sectional view showing platelets with randomized cross-sectional position

The platelet suspension does consist of thousands of platelets, which are sufficient to determine a statistical distribution of platelet damage as well as position. 5400 platelets are released in the domain, which are still several orders of magnitude less than the realistic number of platelets ($10^{10} \sim 10^{11}$ platelets) that would exist for *in vivo* conditions [103]. The platelets are randomly seeded at a cross-section upstream of the valve. To test if the random seeding distribution influences blood damage results, two different

random seeding methods are employed and their BDI distributions are compared. One seeding method uses randomized positions and angles for every seed, and the other method uses the same positions and angles for every seed. The comparison is made 260ms after the start of systole, at which point 4200 platelets have been released in each simulation. These results are discussed in section 6.2.1.

6.2 Systole to early diastole - bulk blood damage

The following results are for platelets released during systole, with the simulation ending in early diastole (80ms after the leaflets close). It should be noted that sections 6.2, 6.3, and 6.4 describe results from the same simulation, but post-processed and visualized in different ways. The numerical methodology is capable of tracking individual platelet position and damage history. However, bulk damage values are also of importance, particularly when separated by regions of the domain. This can demonstrate how blood damage is generally distributed.

6.2.1 Comparison of seeding methodologies

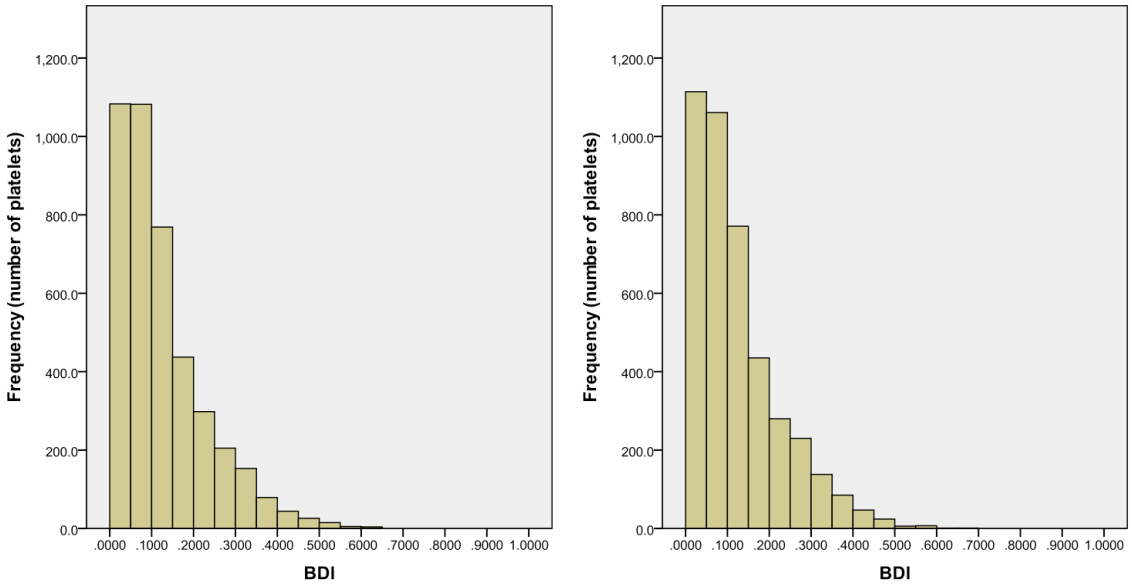

(a) (b)

Figure 6-2: BDI histogram for 4200 platelets after 260ms of systolic flow: (a) positions and angles randomized for every seed, (b) same positions and angles for every seed. Interval: 0.05 dynes•s/cm^2

The two seeding methods are compared by a histogram (Figure 6-2) of blood damage index (BDI). With interval spacing of 0.05 dynes•s/cm^2, the BDI distributions using the two seeding methods compare very well. Most platelets skew towards lesser damage, as expected by the different exposure times of platelets to shear damage due to different release times. For this comparison point, the average BDI is 0.12 dynes•s/cm^2 with a standard deviation of 0.10 dynes•s/cm^2 for both platelet release methods.

Figure 6-3 shows the same data with even finer intervals of 0.025 dynes•s/cm^2, and again shows the good matching between the two platelet seeding methods. Very

slight mismatch occurs at the lower BDI levels, but for higher BDI levels the matching between the two platelet release methods is excellent.

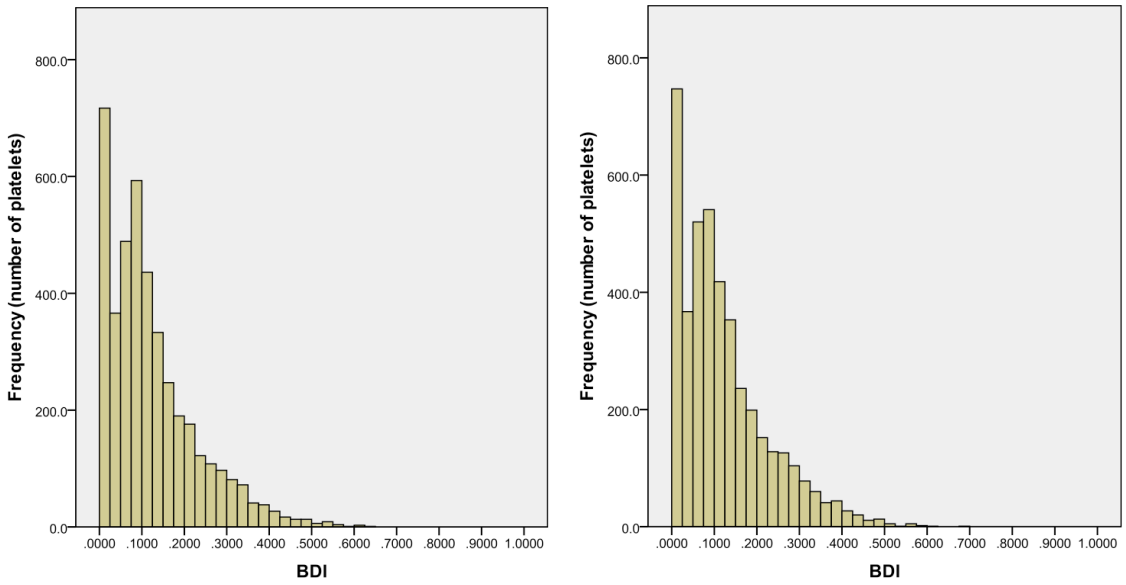

(a) (b)

Figure 6-3: BDI histogram for 4200 platelets after 260ms of systolic flow: (a) positions and angles randomized for every seed, (b) same positions and angles for every seed. Interval: 0.025 dynes•s/cm^2

Although 5400 platelets is several orders of magnitude lower than the realistic number of platelets in this domain, the results showing very similar BDI distribution (figures 6-2 and 6-3) demonstrate that the random seeding methods can be representative of platelets at a cross-section upstream of the valve. This is performed with just 300 platelets for every seed at the cross-section.

Though the release of a higher number of platelets may be more accurate, computational costs become too high. It is postulated that 5400 platelets are enough to obtain good statistical distribution in platelet positions and damage values, but a more

rigorous statistical analysis can be performed in the future with simulations seeding various numbers of platelets. However, the comparison of random seeding methodologies does show that just 300 platelets per seed are representative of platelets that flow through a cross-section at a given time.

6.2.2 Overall platelet damage distribution

A histogram of BDI for all 5400 platelets after 460ms of simulation is plotted (Figure 6-4), representing all of systolic flow and early diastole with an interval spacing of 0.05 dynes•s/cm^2. The average BDI for all 5400 platelets is 0.224 dynes•s/cm^2 with a standard deviation of 0.154 dynes•s/cm^2. Almost 1000 platelets (18.5%) experience an accumulated damage of 0.15 to 0.20 dynes•s/cm^2. It should be noted that platelets are no longer released as leaflet closure begins. However, an additional 80ms is simulated after full leaflet closure, allowing for more damage accumulation for all platelets during leaflet closure and early diastole. The histogram demonstrates that the majority of platelets in the simulation experience low levels of accumulated damage as they pass through the BMHV.

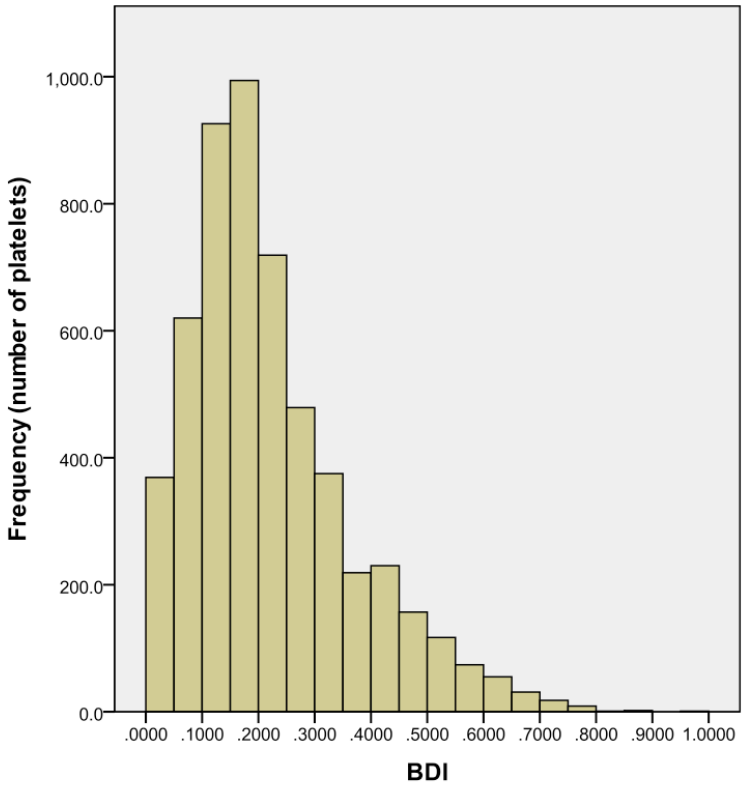

Figure 6-4: BDI histogram for 5400 platelets after 460ms of damage accumulation representing full systole and onset of diastole. Interval: 0.05 dynes•s/cm^2

Only four platelets out of 5400 (0.07%) have damage accumulation larger than 1.0 dynes•s/cm^2, with a maximum platelet damage value of 3.6 dynes•s/cm^2. Additionally, 5084 of 5400 platelets (94.1%) have damage accumulation less than 0.5 dynes•s/cm^2. As the damage accumulation thresholds for platelet activation are commonly given as 35.0 dynes•s/cm^2 or greater, this demonstrates that for one pass through a BMHV, platelets are not in danger of becoming activated. A previous computational study also showed that for one pass of forward flow through a BMHV, platelets do not approach the activation threshold [10]. However, it should be noted that this methodology assumes all platelets begin with zero damage values. In addition, this

simulation stops at the onset of diastole and does not account for prolonged exposure due to recirculation near the valve. These scenarios are discussed with the Lagrangian particle tracking results in section 6.4.2.

6.2.3 Bulk blood damage by region

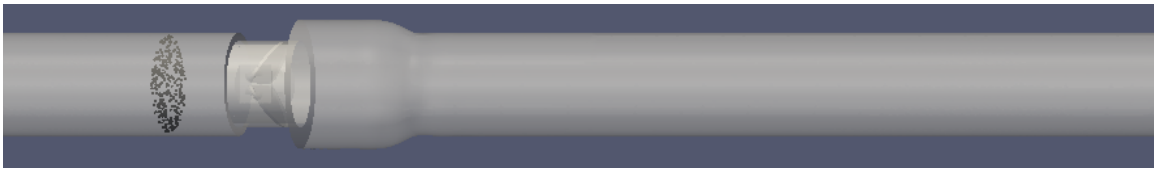

(a) Initial seed of 300 platelets

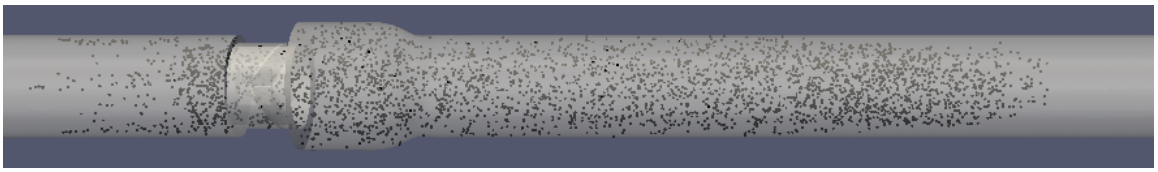

(b) Final distribution of 5400 platelets

Figure 6-5: (a) 300 platelets initially seeded upstream of valve; (b) 5400 platelets distributed throughout domain at end of simulation.

Figure 6-5 shows the initial seed of 300 platelets at the onset of systole and the final distribution of 5400 platelets as the leaflets close for diastole (animation 6-1). After 460ms of simulation, the platelets are well distributed throughout the domain.

Figure 6-6: Domain split into regions: (1) ventricular side, (2) valve, (3) sinus expansion, (4) aortic side.

The platelet damage by region of the domain is given in table 6-1 representing accumulated blood damage index values after 460ms of simulation. The domain is split into four regions (figure 6-6): the ventricular side, the valve, the sinus expansion, and the aortic side.

Table 6-1: Platelet and BDI distribution by region – physiologic adult

Region	# of platelets	BDI average (dynes s / cm^2)
Overall	5400	0.2248
Ventricular side	732	0.0739
Valve	302	0.1988
Sinus expansion	951	0.3227
Aortic side	3415	0.2322

Although flow recirculation regions are known to exist, 63% of platelets advect downstream of the sinus expansion region to the aortic chamber. 17.6% of platelets remain in the sinus expansion region immediately downstream of the valve. The sinus region includes platelets that are caught in recirculation in the sinus expansion, and platelets that have not advected beyond the sinus region before the end of the simulation.

5.6% of platelets are in the valve region itself, though it is found that very few of these platelets have been caught in recirculation. Instead, these platelets have not advected downstream past the valve before the onset of diastole. Finally, 13.6% of platelets remain on the ventricular chamber side of the valve. These platelets are released but have not advected downstream quickly enough before the onset of diastole. It should be noted that the simulation ends at the early part of diastole, before mid-diastolic

leakage jets are formed at the valve. Platelets near the valve in mid-diastolic flows are covered in a separate simulation, covered in section 6.5.

Though only 17.6% of platelets remain in the sinus expansion, the average damage accumulation in this region is highest. This average damage value is 40% higher than the average value for platelets located in the aortic downstream chamber. Platelets in the sinus expansion also have 44% higher damage than the total average, and 62% higher damage than platelets within the valve. The ventricular side chamber has the lowest average BDI, though this can be attributed to platelets released late in the simulation that have not gone through the BMHV.

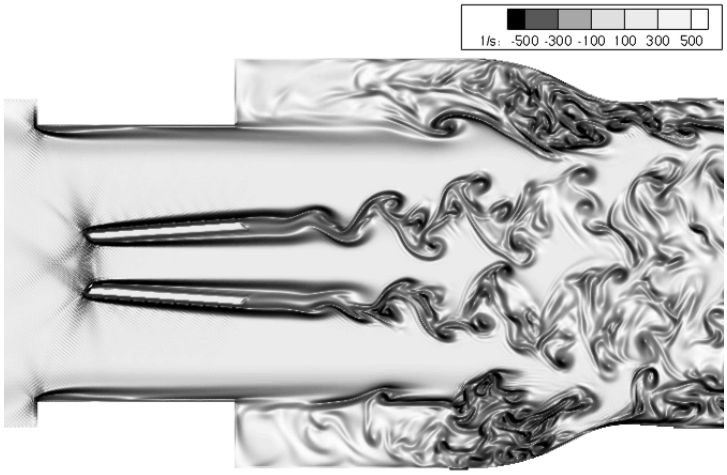

Figure 6-7: Vorticity plot at peak flow showing strong vortex shedding within sinus region, from flow past leaflets and sinus expansion step.

The sinus expansion region is characterized by strong vortical structures such as vortex shedding past the leaflet tips and sinus expansion step (figure 6-7). It has also been shown in chapter 5 that these structures are associated with elevated instantaneous fluid shear stresses. The fact that the sinus expansion is the highest damage region

warrants further investigation. This result implies that platelets that continue to accumulate damage due to recirculation may be of highest danger, highlighting the importance of recirculation zones. This will be explored in further detail in section 6.4.

6.2.4 Top damage levels

Table 6-2: Platelet and BDI distribution by region and top damaged levels – physiologic adult

	Overall		Top 10%		Top 1%	
Region	# platelets	BDI average (dynes s / cm^2)	# platelets	BDI average (dynes s / cm^2)	# platelets	BDI average (dynes s / cm^2)
Overall	5400	0.2248	540	0.5509	54	0.8355
Ventricular side	732	0.0739	10	0.5421	2	0.7325
Valve	302	0.1988	27	0.7173	5	1.586
Sinus expansion	951	0.3227	214	0.5633	29	0.7891
Aortic side	3415	0.2322	289	0.5265	18	0.7131

Table 6-2 shows a breakdown of the overall and top 10% and 1% of damaged platelets for the physiologic adult case. It is interesting to note that for the top 10% damaged platelets, the valve has the highest average damage. This may be due to highly damaged platelets caught in leaflet closing wakes. The ventricular chamber side also has high average damage, comparable to average damage in the sinus expansion. Though platelets in the valve and ventricular side have elevated damage, these account for only 37 platelets out of 540. The sinus region has the second highest damage level in addition to 39.6% of these top 10% highly damaged platelets.

Examining the top 1% of damaged platelets, the valve region shows the highest average damage values. This again highlights potential damage from leaflet closing

wakes, although these account for only 9.3% of the top 1% damaged platelets. The sinus expansion, however, has the second highest average damage and account for 53.7% of these highly damaged platelets. Thus, this analysis reinforces that the sinus expansion is a highlighted danger region for platelet damage.

6.3 Eulerian tracking of blood damage

Blood damage in prosthetic valve flows is often visualized in two manners: bulk blood damage distribution (section 6.2) or Lagrangian particle tracking (section 6.4). These viewpoints are important for understanding blood damage in these flows, but miss the potential of a fine level Eulerian tracking of blood damage. A high-resolution Eulerian tracking of blood damage could highlight specific regions of the domain that are of particular concern in BMHV flows.

6.3.1 Eulerian viewpoint

The flow domain is discretized into cubic regions of size 2.5mm x 2.5mm x 2.5mm. The number of platelets residing in each cubic region is determined, as well as the average accumulated damage across these platelets. The average damage by cubic region is plotted in 3D contours throughout the domain. This is an Eulerian representation of average platelet damage by region and over time.

The cube size of 2.5mm x 2.5mm x 2.5mm is chosen as optimal for discretization of the flow domain. This cube size results in a large number of "subregions" that discretize the domain in a fine resolution, but is also large enough so that multiple

platelets are found in each region. For improved visualization, cubic regions with no platelets are blanked from the 3D contour plot.

6.3.2 Blood damage evolution – Eulerian view

The 3D plots of average BDI values by region are displayed with a maximum contour of 0.5 dynes•s/cm^2 (animation 6-2). This maximum contour value is chosen as optimal for highlighting a significant number of danger regions of the flow in red contours. 300 platelets are initially released upstream of the valve with zero BDI values (Figure 6-8) at the onset of systole, with Re ~ 0.

(a) BDI contour

(b) 2D vorticity

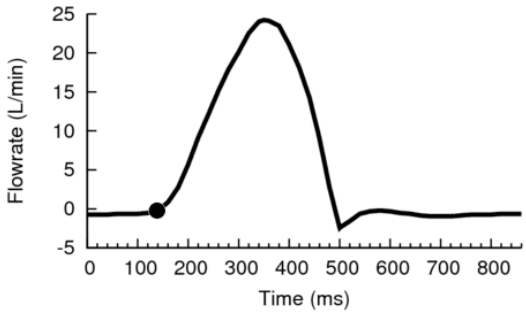

(c) time point of simulation

Figure 6-8: (a) BDI contour plot, (b) corresponding fluid vorticity plot, and (c) flowrate curve at start of systole (Re ~ 0), 300 platelets

At high accelerating flow (Re = 5000), 3000 platelets have been released in the domain (Figure 6-9). Many platelets have traversed through the valve and into the sinus region. Average platelet damage values are very low throughout the flow at this point, with some notable exceptions in the sinus expansion region near the walls.

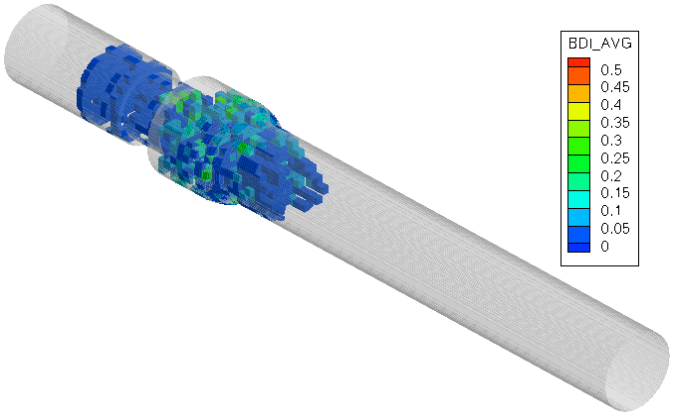

(a) BDI contour plot

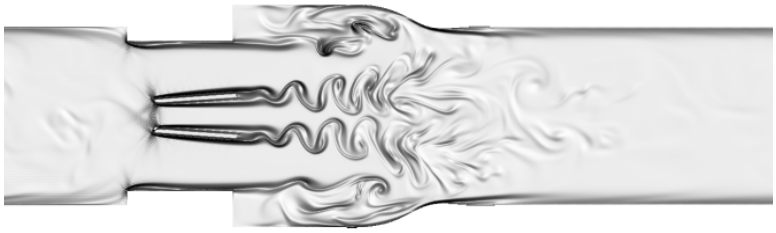

(b) 2D vorticity

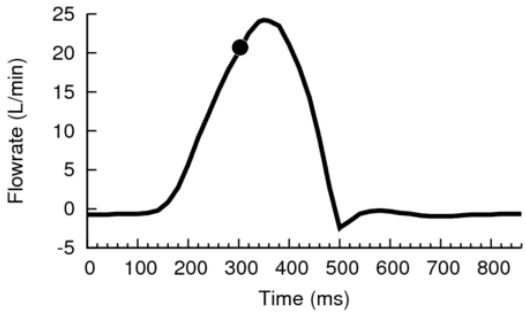

(c) time point of simulation

Figure 6-9: (a) BDI contour plot, (b) corresponding fluid vorticity plot, and (c) flowrate curve at high acceleration (Re = 5000), 3000 platelets

At peak flow (Re = 5780), 3300 platelets have been released in the domain and the forward flowrate is at its strongest point (Figure 6-10). Many platelets advect downstream of the sinus region and are highlighted with higher blood damage values. However, the majority of high damage region still exist within the sinus expansion region.

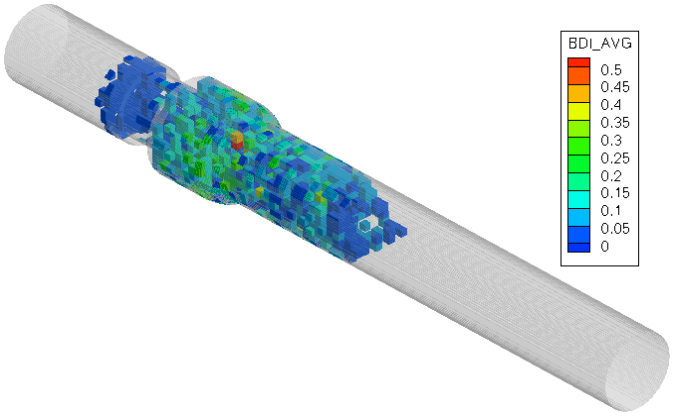

(a) BDI contour

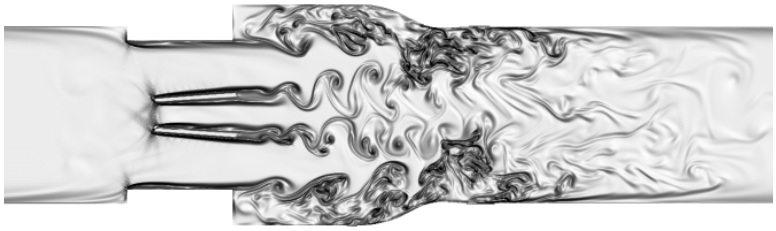

(b) 2D vorticity

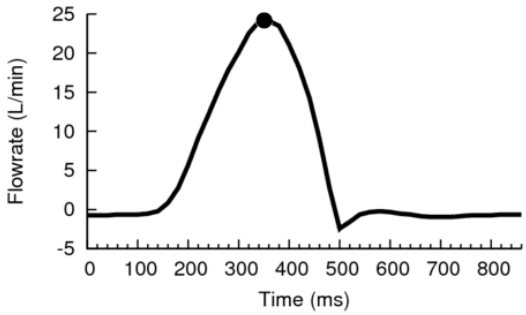

(c) time point of simulation

Figure 6-10: (a) BDI contour plot, (b) corresponding fluid vorticity plot, and (c) flowrate curve at peak flow (Re = 5780), 3300 platelets

The leaflets begin to close with a forward flowrate (Re = 650) at the end of systole but a negative pressure gradient causing leaflet closure. At this point, all 5400 platelets have been released in the domain. The BDI contour plot (figure 6-11) shows

higher damage regions in both the sinus expansion region and the downstream aortic chamber. Very low damage regions are observed in the upstream ventricular side.

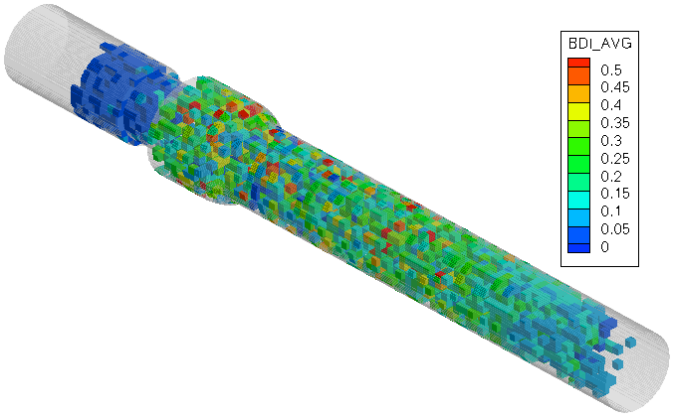

(a) BDI contour

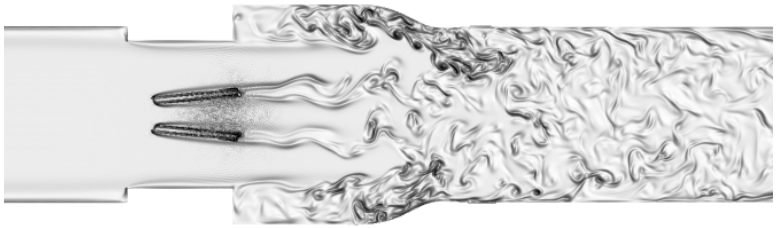

(b) 2D vorticity

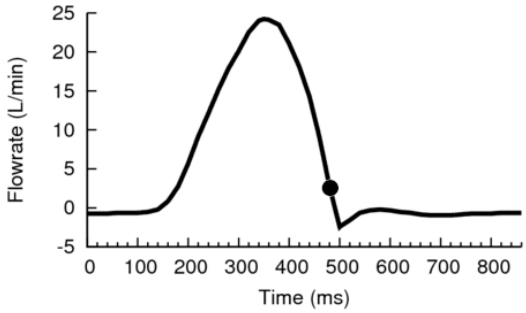

(c) time point of simulation

Figure 6-11: (a) BDI contour plot, (b) corresponding fluid vorticity plot, and (c) flowrate curve at leaflet closing flow (Re = 650), 5400 platelets

Blanking all regions with damage accumulation average lower than 0.5 dynes•s/cm^2 shows potential danger regions as the leaflets begin to close. Figure 6-12a demonstrates that as the leaflets begin to close, the number of high damage regions is relatively similar between the sinus expansion and aortic downstream chamber. With a slightly higher threshold blanking value of 0.6 dynes•s/cm^2, the sinus expansion region shows more high damage regions than the aortic downstream chamber (figure 6-12b).

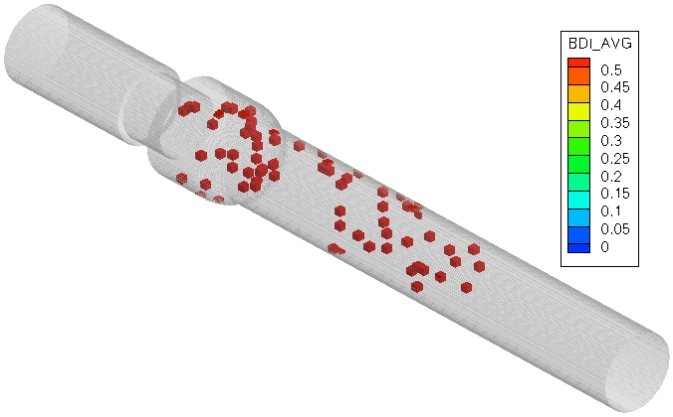

(a) threshold at 0.5 dynes•s/cm^2

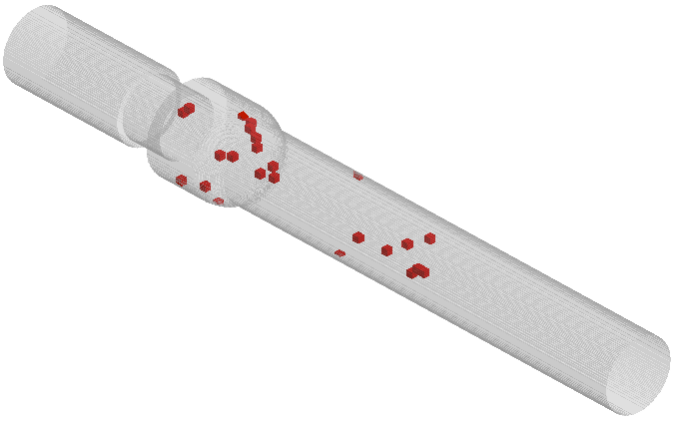

(b) threshold at 0.6 dynes•s/cm^2

Figure 6-12: BDI contour plot at leaflet closing flow (Re = 650), 5400 platelets. Contours blanked if damage less than (a) 0.5 dynes•s/cm^2 (b) 0.6 dynes•s/cm^2

The simulation ends after 460ms of modeling, representing full leaflet closure and the early-to-mid diastolic phase (Re = 75 in reverse flow). Figure 6-13 shows the platelet damage distribution throughout the domain, again demonstrating higher damage regions existing throughout the sinus expansion and downstream aortic chamber.

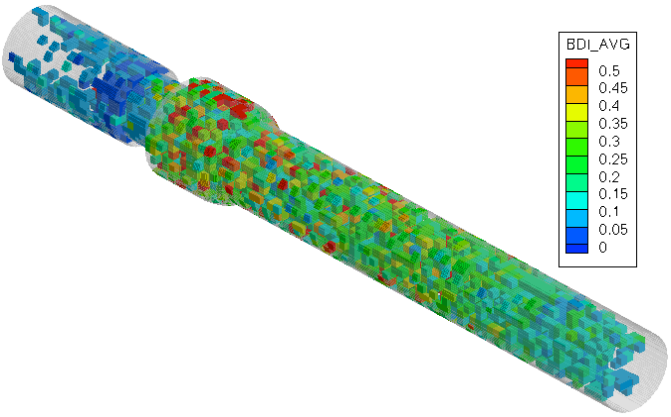

(a) BDI contour

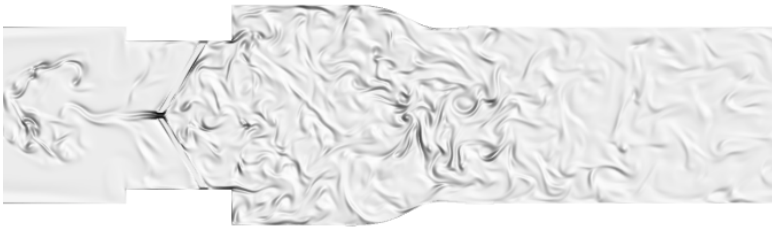

(b) 2D vorticity

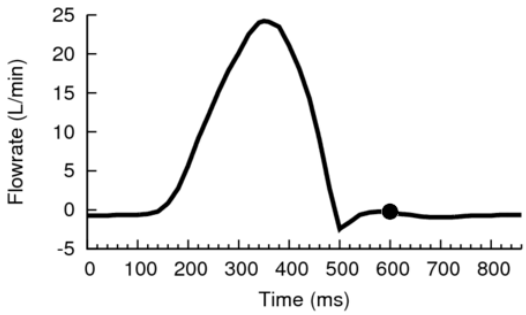

(c) time point of simulation

Figure 6-13: (a) BDI contour plot, (b) corresponding fluid vorticity plot, and (c) flowrate curve at early-to-mid diastolic flow (Re = 75 in reverse flow), 5400 released platelets

A similar blanking procedure is performed for this end time point of the simulation (figure 6-14). This plot demonstrates a larger number of high damage regions due to prolonged exposure time (460ms) of platelets to shear damage. The ventricular upstream chamber also contains some higher damage regions in this BDI threshold plot.

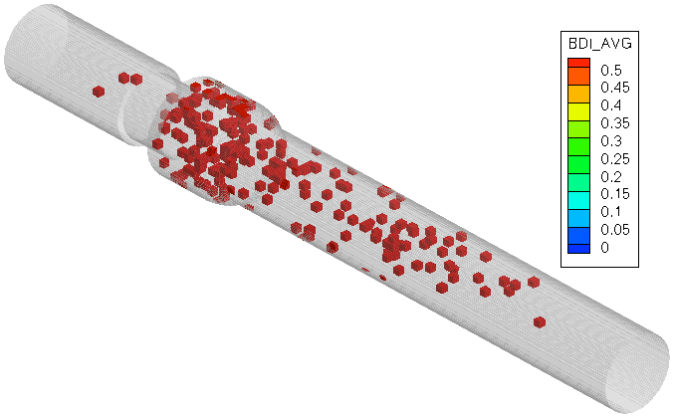

Figure 6-14: BDI contour plot at early-to-mid diastolic flow (Re = 75 in reverse flow), 5400 platelets. Contours blanked if damage less than 0.5 dynes•s/cm^2

An immediate difference between the final simulation time point and the time point at beginning of leaflet closing is the existence of high damage regions in the ventricular upstream chamber. It is not apparent whether these regions occur due to leakage jets or due to the leaflet closing wakes. However, the sudden existence of these high damage regions demonstrates that the leaflet closing and the early diastolic phase can contribute to platelet damage significantly.

Though high damage regions exist in the sinus expansion and aortic downstream chamber, there is a larger clustering of high damage regions in the sinus expansion at the end time point. This larger number of high damage regions, in addition to the fact that

the sinus expansion volume is smaller than the aortic downstream chamber, again highlights platelet damage dangers of the sinus expansion as a whole.

Finally, it is noted that very few high damage regions exist within the valve itself. This could be due to the fact that very few platelets (302 platelets, 5.6%) reside in the valve region at this time. From the analysis of top 10% and 1% damaged platelets, the ventricular side is known to contain highly damaged individual platelets. It is possible that cluster regions of highly damaged platelets are not observed due to the low number of total platelets in the valve.

The aortic chamber contains platelets that have a longer exposure time, which may explain the high damage. However, these regions are also widely scattered throughout a large volume. Platelets in these regions are also at low risk of being caught in diastolic leakage jet flows, as they are far downstream of the valve and simply recirculate during diastole. At the onset of the next systolic phase, these platelets would simply advect through the aorta. Thus, although platelets in the aortic chamber section have high accumulated damage, they are not of serious concern in these BMHV flows.

6.4 Lagrangian particle tracking of blood damage

Platelets are released in the simulations and the full temporal history of position, instantaneous damage, and accumulated damage are tracked. This Lagrangian viewpoint is important for precisely determining blood damage to individual platelets in these flows, and to directly connect instantaneous damage to the instantaneous flow fields. This may help to understand how the flow fields through prosthetic valves directly influence damage to platelets caught in these flows.

6.4.1 Lagrangian viewpoint

Platelet damage data is processed to determine which platelet pathlines incur the highest levels of damage. It is important to emphasize that the platelets are modeled in the simulations with rigid 3D ellipsoidal shape. However, for visualization purposes, platelets are displayed in the following figures as spheres multiplied in size and colored by contour scaling of their maximum instantaneous surface shear stress. These platelets are visualized within the large domain as spheres of diameter 320μm, as they would not be visible if represented by their actual size (3μm).

The platelet visual representation is colored uniformly by maximum surface shear stress to clearly demonstrate the amount of instantaneous shear damage that is incurred by the platelet. A platelet trail is created to better visualize the pathlines of individual platelets, with each trail particle spaced apart by 2.5ms. In zoomed viewpoints focusing on individual platelets, the realistic 3D ellipsoidal shape is apparent with shear stress distribution across the surface. All viscous shear stress plots for the flow field are given with a contour scaling in units of dynes/cm^2.

6.4.2 Highlighted platelet damage paths

It is determined that the platelets with the 10 highest accumulated damage values all reside within the valve or sinus expansion at the end simulation time point. These platelets are divided into three categories: platelets traversing very close to the leaflet surface, platelets caught in sinus expansion recirculation, and platelets caught in the sudden leaflet closing wake.

6.4.2.1 Leaflet surface path

A platelet that is close to the leaflet surface is highlighted as it incurs high levels of damage (Figure 6-15). The clustering of the particle trail during this time period shows the relatively low velocity of the platelet near the leaflet surface, despite the flow being near peak flow (Re = 5000). The zoomed viewpoint (figure 6-15c) focusing on the platelet shows the realistic 3D ellipsoidal shape is apparent with shear stress distribution across the surface. While the platelet is close to the leaflet surface, it experiences continuously high shear stress levels (10 – 25 dynes/cm^2 maximum shear stress), which corresponds to higher accumulation of damage over time.

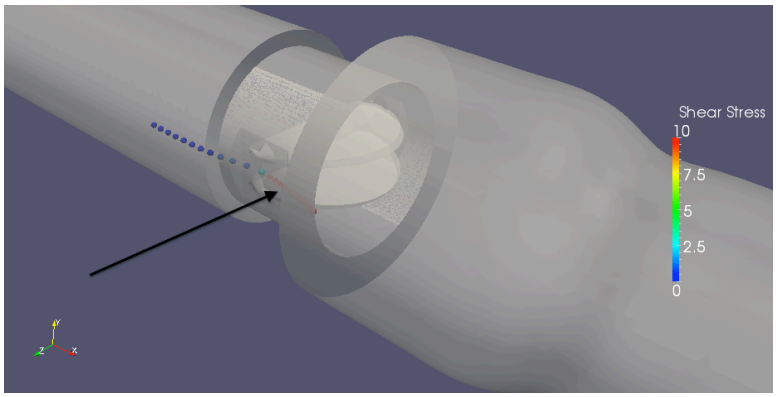

(a) Angled view

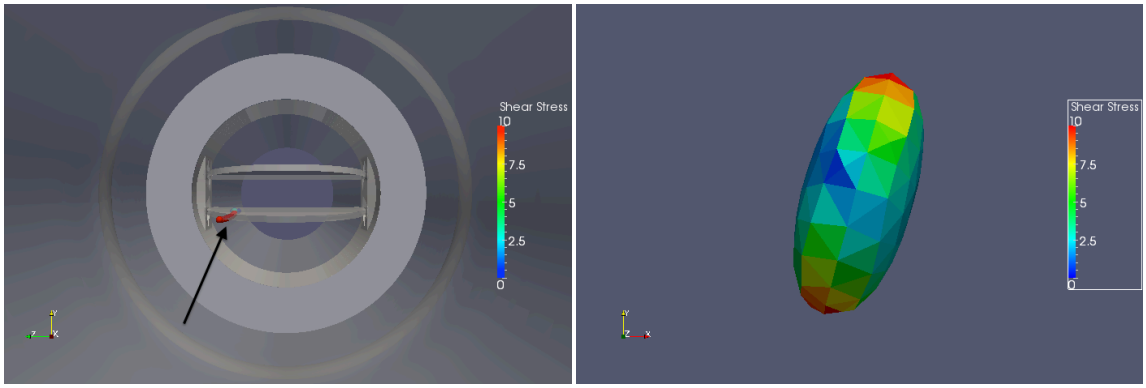

(b) Cross-sectional view (c) zoomed view of platelet

Figure 6-15: (a) Angled view, (b) cross-sectional view, (c) zoomed view of platelet trail, demonstrating high shear stress damage while traversing near bottom leaflet surface.

The perpendicular viewpoint (figure 6-16) shows the slow motion of the platelet near the leaflet surface with corresponding vorticity and shear stress fields. It is shown that there is no flow separation along the leaflet surface (figure 6-16b), which causes the slow velocity of the platelet. Fluid shear stresses near the leaflet are very high (figure 6-16c) due to a thin shear layer, explaining the high levels of damage incurred by the platelet traveling near the leaflet surface.

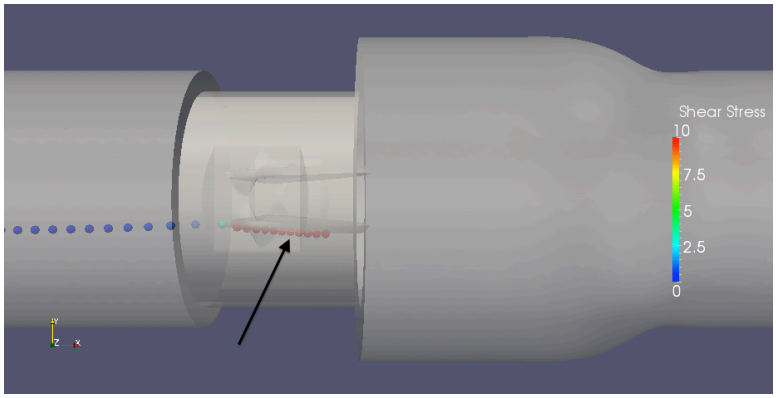

(a) Perpendicular view of platelet trail

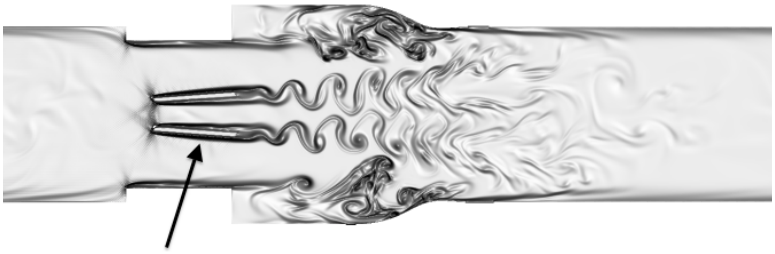

(b) 2D vorticity

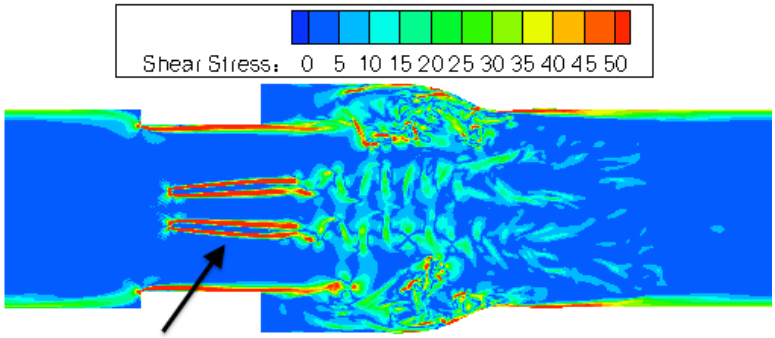

(c) 2D viscous shear stresses

Figure 6-16: Platelet trail demonstrating high shear stress values while (a) traversing near leaflet surface, (b) corresponding vorticity field, (c) shear stress field

The time history of damage accumulation for the platelet caught near the leaflet surface is also determined (Figure 6-17). This demonstrates that after very little damage accumulation upon initial release, the platelet incurs continuously high levels of shear stress damage while traveling close to the leaflet surface.

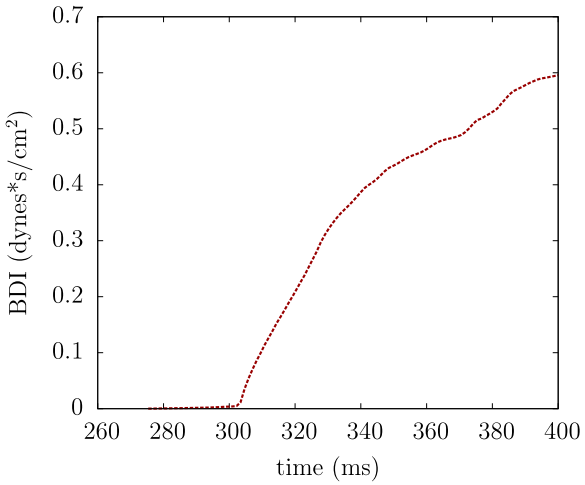

Figure 6-17: Platelet damage accumulation versus time for platelet traveling near leaflet surface

6.4.2.2 Sinus expansion – near wall

Several of the most damaged platelets incur high levels of damage due to the sinus expansion recirculation region. One way in which this damage can occur is from near wall positions, where the motion is slow but damage levels are high. A platelet path near the sinus expansion wall is shown, where the cluster trail of particles shows the high level of damage incurred while the platelet velocity is relatively low (Figure 6-18). The cross-sectional view also demonstrates the proximity of the platelet to the sinus expansion wall. This platelet damage pathline is also displayed in a rotating view in animation 6-3.

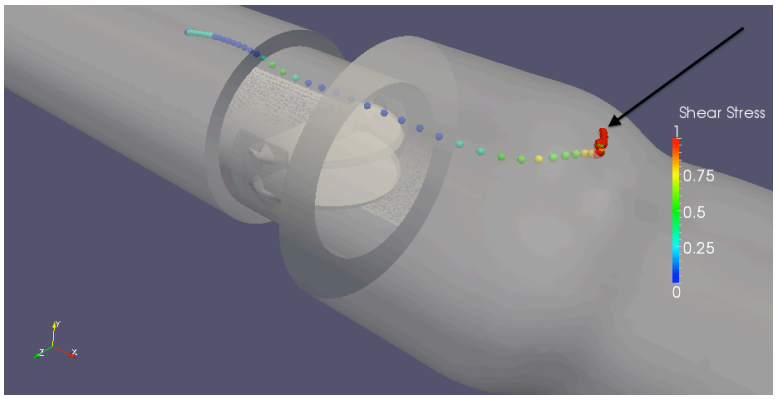

(a) Angled view

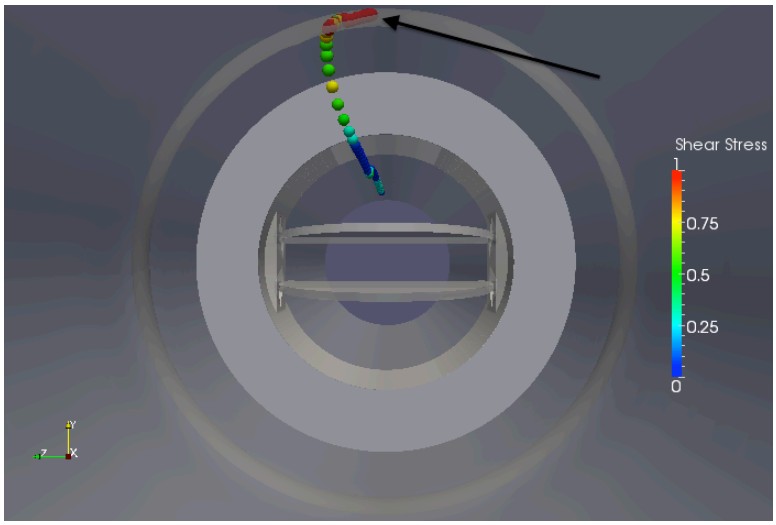

(b) cross-sectional view

Figure 6-18: Platelet trail close to the sinus expansion wall with high levels of shear stress damage (a) 3D angled view, (b) cross-sectional viewpoint

A perpendicular viewpoint (Figure 6-19) again demonstrates how close the platelet is to the expansion wall during this period of high shear stress (15 – 50 dynes/cm^2 maximum shear stress). For a period of 30ms, the platelet slowly moves near the sinus expansion wall. The corresponding vorticity and shear stress fields show the strong

recirculation shear region where the platelet is located, explaining the high level of incurred damage.

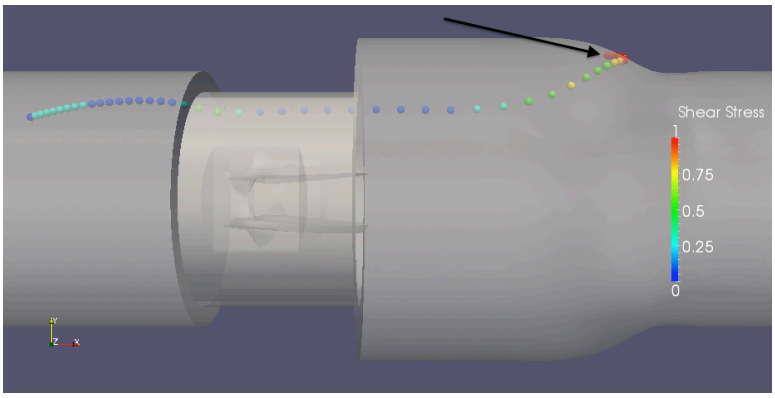

(a) Perpendicular view of platelet trail

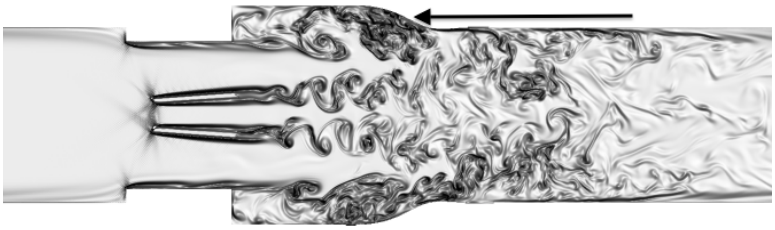

(b) 2D vorticity

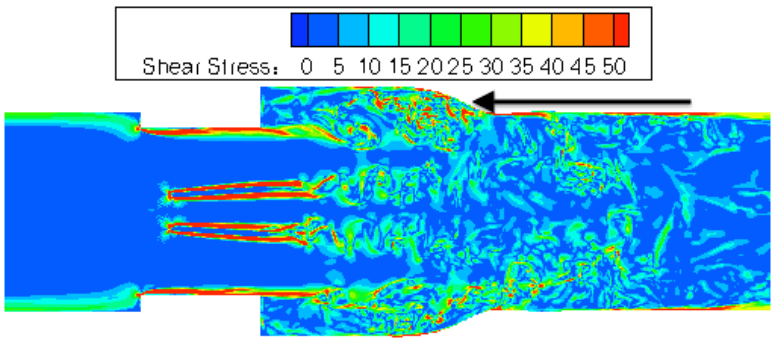

(c) Viscous shear stresses

Figure 6-19: Platelet trail close to the sinus expansion wall with high levels of shear stress damage (a) perpendicular view, (b) corresponding vorticity field, (c) shear stress field

Approximately 100ms later during the deceleration phase, the platelet is still moving slowly within the sinus expansion recirculation region. With the platelet close to the expansion walls, the platelet experiences consistently high levels of shear stress (Figure 6-20). This platelet is eventually swept out of the recirculation region, but still experiences moderately high levels of shear stress (10 – 20 dynes/cm^2 maximum shear stress) even away from the walls.

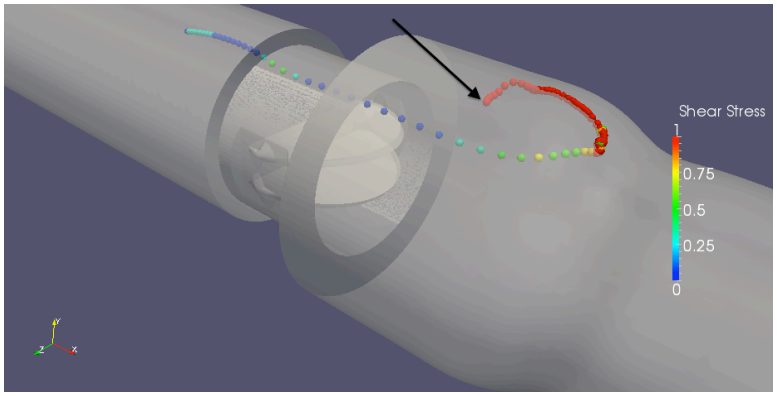

(a) Angled view

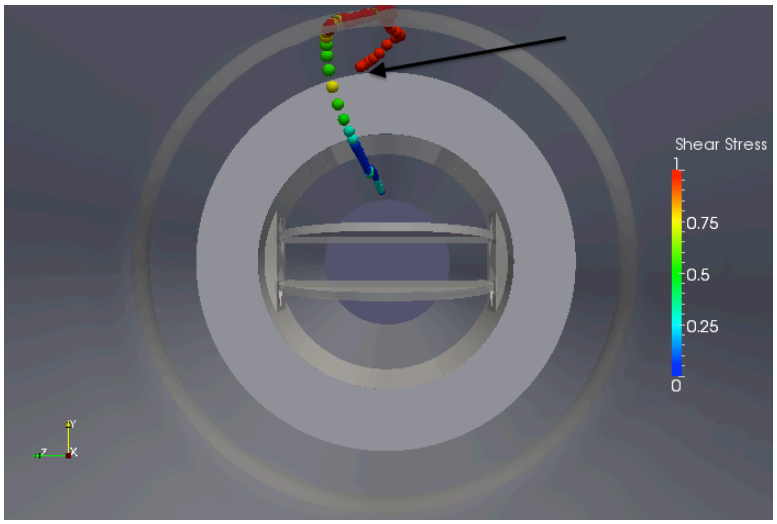

(b) cross-sectional view

Figure 6-20: Platelet trail in sinus recirculation after additional 100ms with high levels of shear stress damage (a) 3D view, (b) cross-sectional viewpoint

Although the platelet is no longer very close to the walls, it still resides in the sinus recirculation region. This is demonstrated again from a different viewpoint (figure 6-21), where the platelet is still seen to experience high shear stress due to the strong recirculation region in the sinus expansion. This highlights the danger of platelets in the sinus region and close to the expansion walls, where low velocity – high shear stress time periods can occur for an extended amount of time before platelets are eventually swept out of the recirculation region.

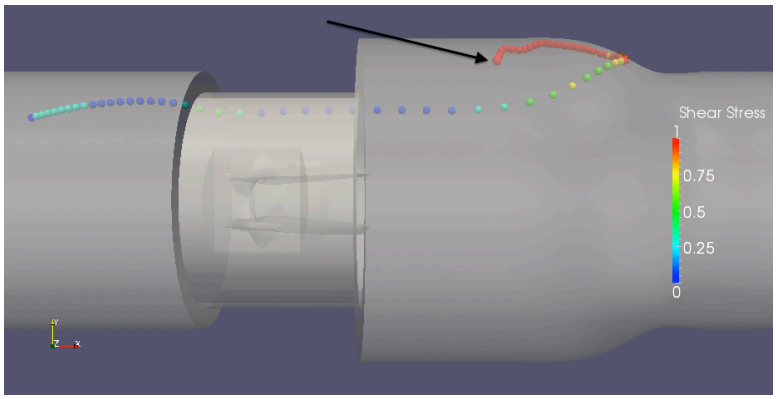

(a) Perpendicular view of platelet trail

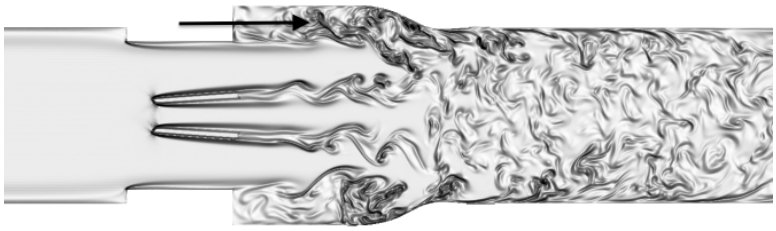

(b) 2D vorticity

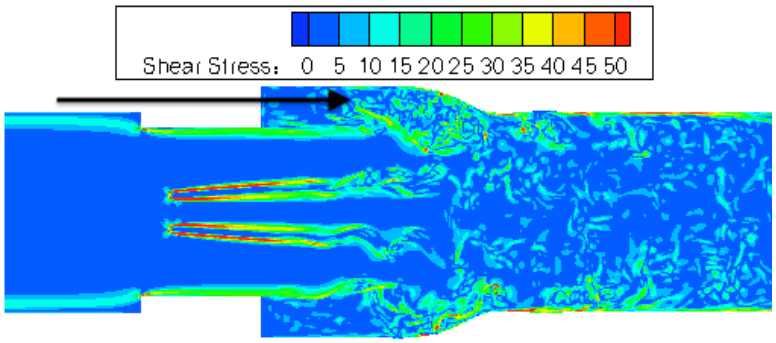

(c) Viscous shear stresses

Figure 6-21: Platelet trail in sinus recirculation after additional 100ms with high levels of shear stress damage (a) perpendicular view, (b) corresponding vorticity field, (c) shear stress field

The time history of damage accumulation for the platelet close to the sinus expansion wall is determined (Figure 6-22). This demonstrates a sharp increase in damage accumulation representing the time period where the platelet travels slowly along the sinus wall, experiencing high levels of instantaneous shear stress.

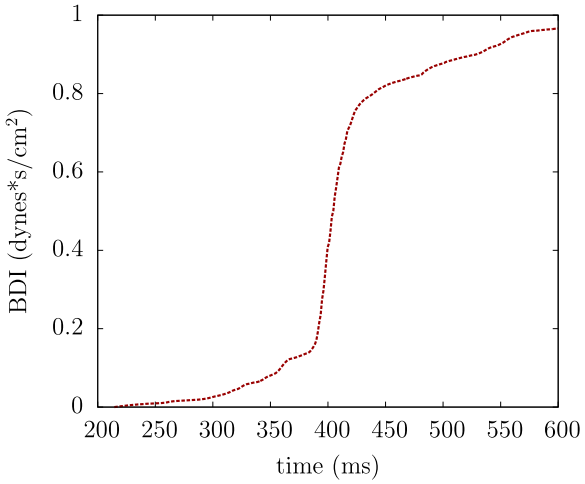

Figure 6-22: Platelet damage accumulation versus time for platelet near sinus expansion wall

6.4.2.3 Sinus expansion – strong recirculation

An additional way in which sinus recirculation regions can cause platelet damage is strong recirculation of a platelet over an extended period of time. These platelets do not experience very high instantaneous levels of shear stress, but moderate levels (5 – 12 dynes/cm^2 maximum shear stress) over a long time, leading to high accumulated damage. One example is given of a platelet caught in the sinus recirculation region for 225ms of systole. 45ms after being caught in recirculation (Figure 6-23), the platelet experiences moderate levels of damage. The circular cluster of platelets shows how the platelet is recirculating, but with only moderate levels of instantaneous damage.

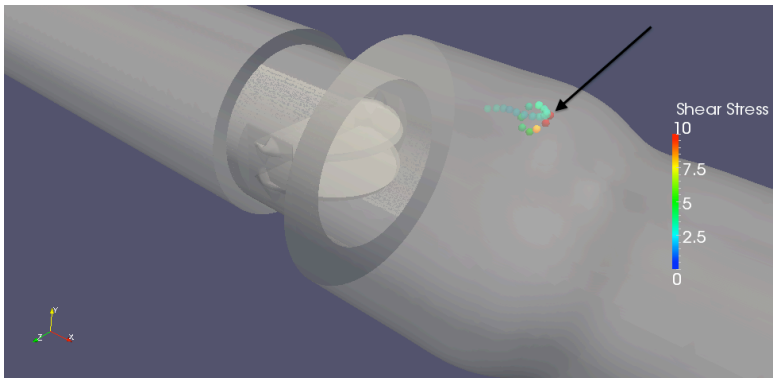

(a) Angled view

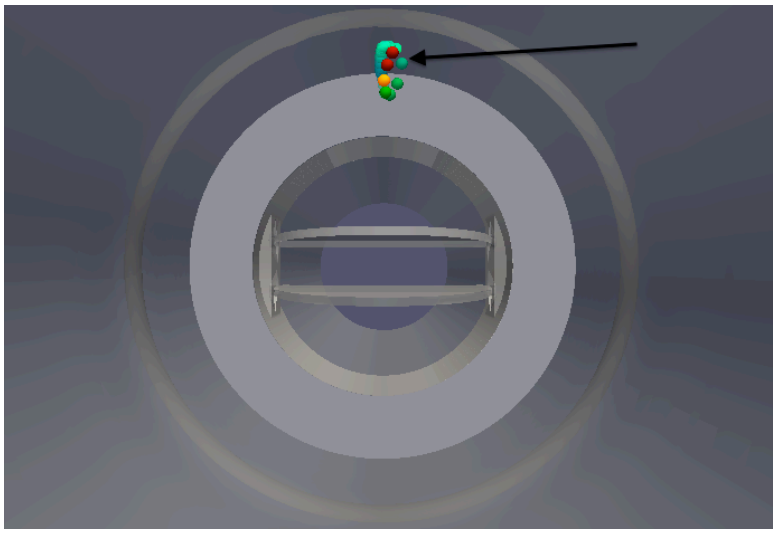

(b) cross-sectional view

Figure 6-23: Platelet caught in recirculation near sinus expansion (a) 3D angled view, (b) cross-sectional view

This recirculation of platelets is demonstrated again (figure 6-24), where the corresponding vorticity and shear stress fields show the wide sinus expansion recirculation zone that the platelet is trapped within.

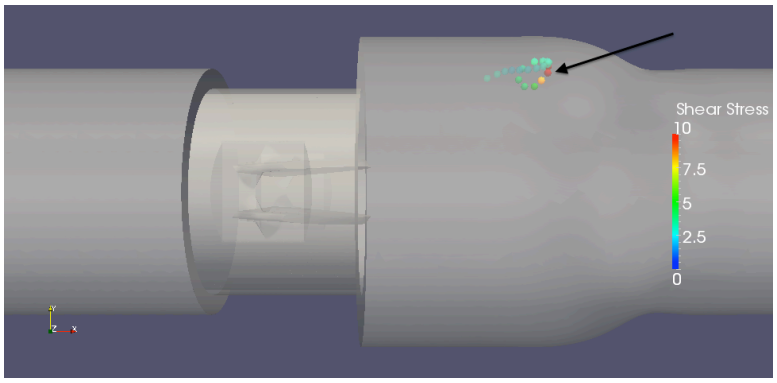

(a) Perpendicular view of platelet trail

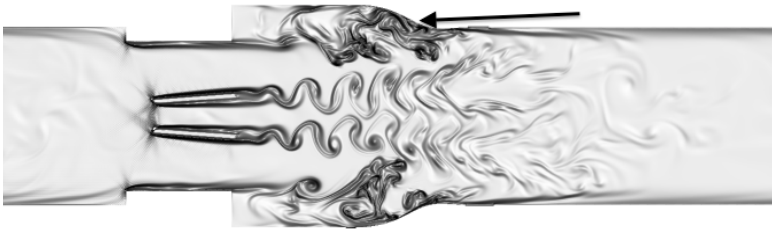

(b) 2D vorticity

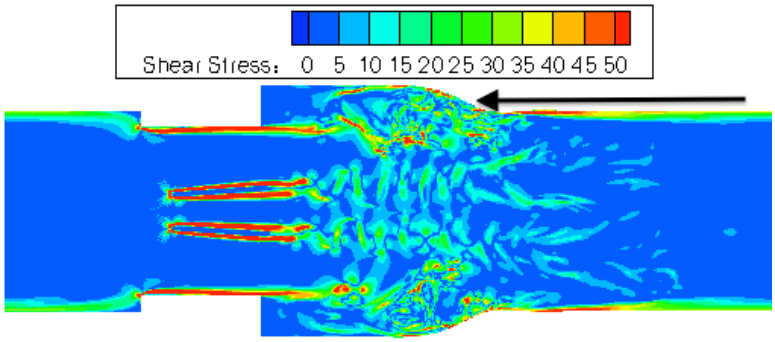

(c) Viscous shear stresses

Figure 6-24: Platelet caught in recirculation near sinus expansion (a) perpendicular view, (b) corresponding vorticity field, (c) shear stress field

At a time point 90ms later, the platelet undergoes the same recirculation with moderate levels of platelet shear stress (Figure 6-25). Similar to the previous figure, the vorticity field shows a recirculation zone near the sinus expansion that causes a circular path for the platelet.

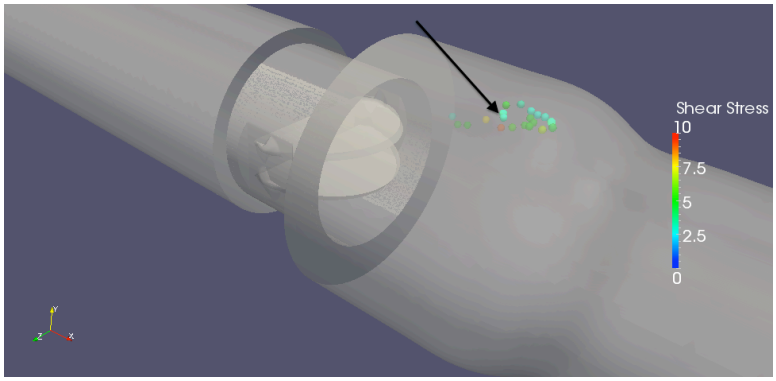

(a) Angled view

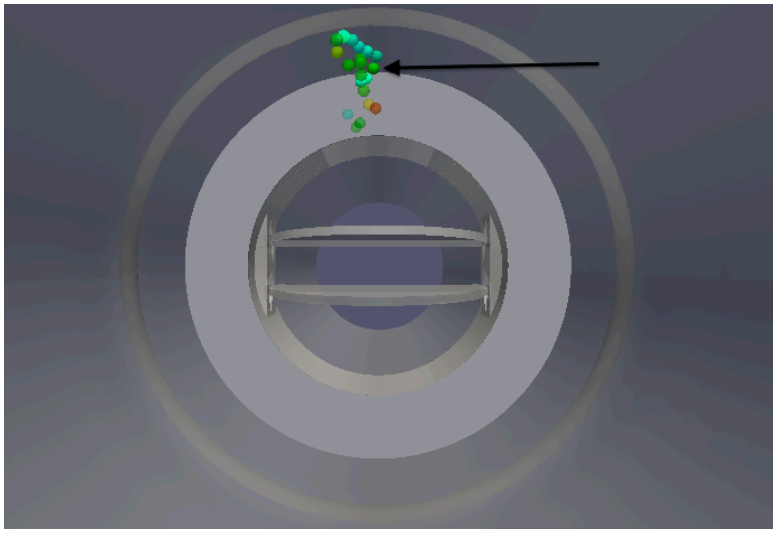

(b) Cross-sectional view

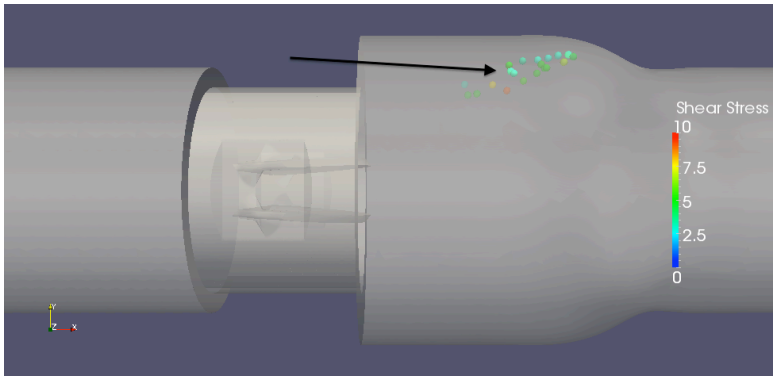

(c) Perpendicular view

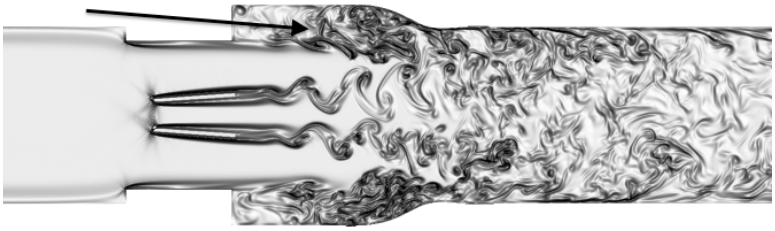

(d) 2D vorticity

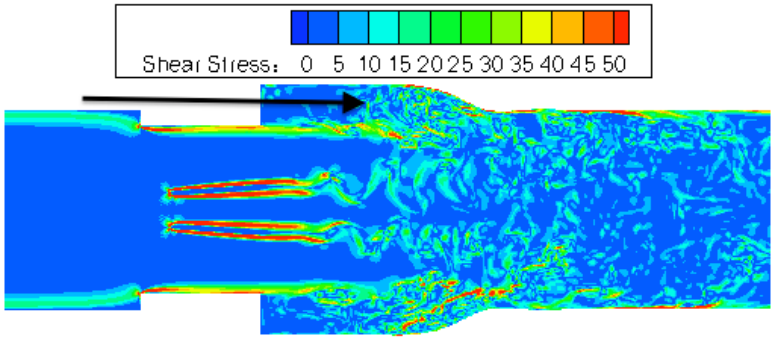

(e) Viscous shear stresses

Figure 6-25: Platelet in sinus recirculation after additional 90ms with (a) 3D angled view, (b) cross-sectional view, (c) perpendicular view, and corresponding (d) 2D vorticity and (e) shear stress fields

After an additional 90ms, the leaflets close and the diastolic flow phase begins (figure 6-26). However, we note that the platelet is still within the sinus expansion region, continuously recirculating and incurring damage. Although this platelet experiences only moderate levels of instantaneous shear stress (5 – 10 dynes/cm^2 maximum shear stress), the long recirculation time contributes to an overall high accumulated platelet damage. This underlines the danger of continual recirculation zones in BMHV flows.

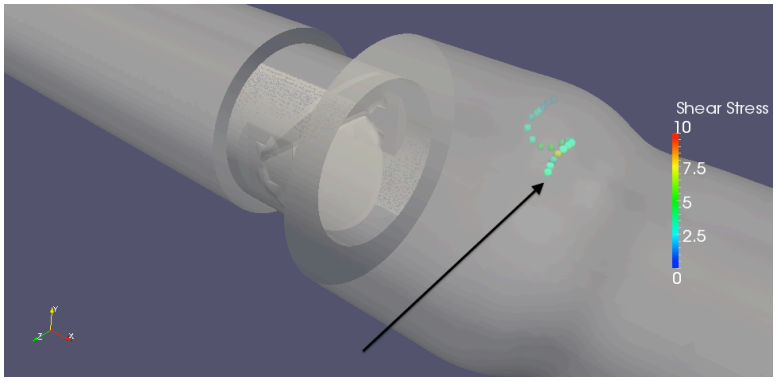

(a) Angled view

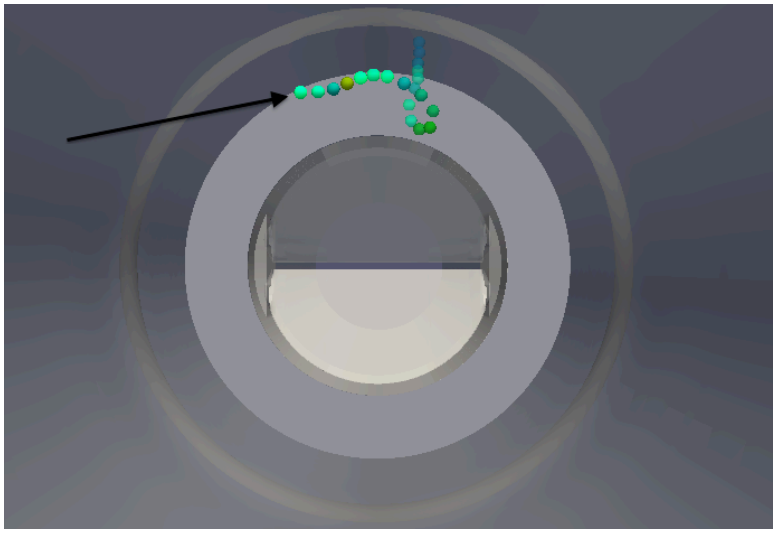

(b) Cross-sectional view

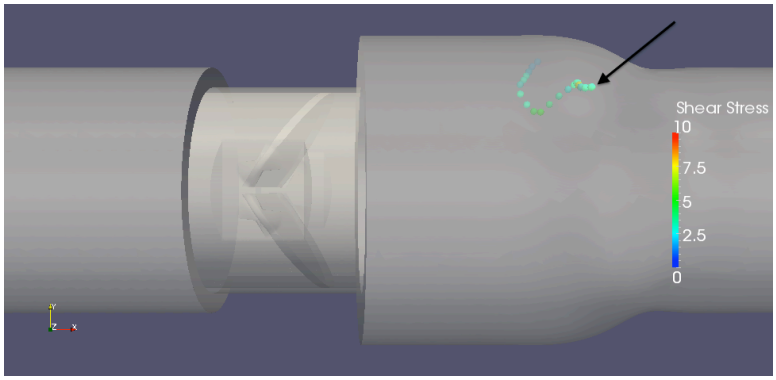

(c) Perpendicular view

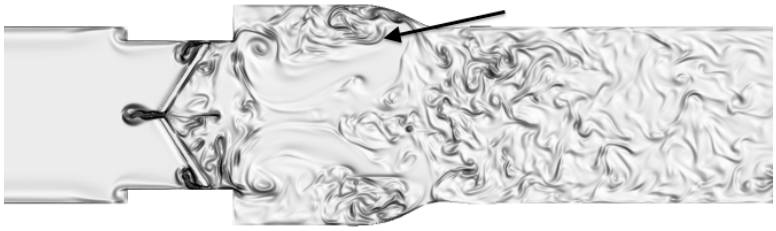

(d) 2D vorticity

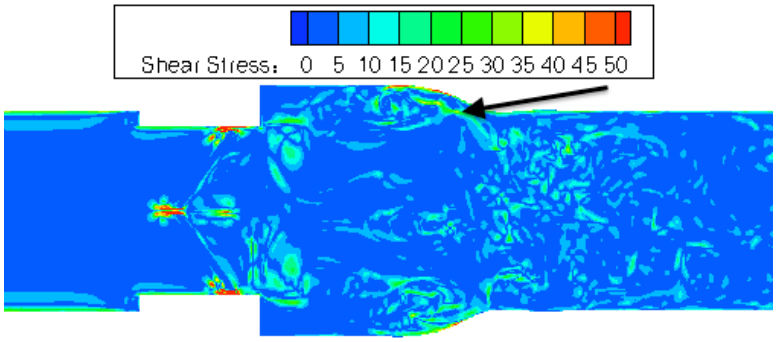

(e) Viscous shear stresses

Figure 6-26: Platelet in sinus recirculation at start of diastole with (a) 3D angled view, (b) cross-sectional view, (c) perpendicular view, and corresponding (d) 2D vorticity and (e) shear stress fields

The time history of damage accumulation for the platelet recirculating in the sinus region shows a gradual, but continuous increase in damage accumulation for the platelet for a long period of time (Figure 6-27). This represents the time period of moderate shear stress experienced by the platelet as it continuously recirculates in the sinus expansion.

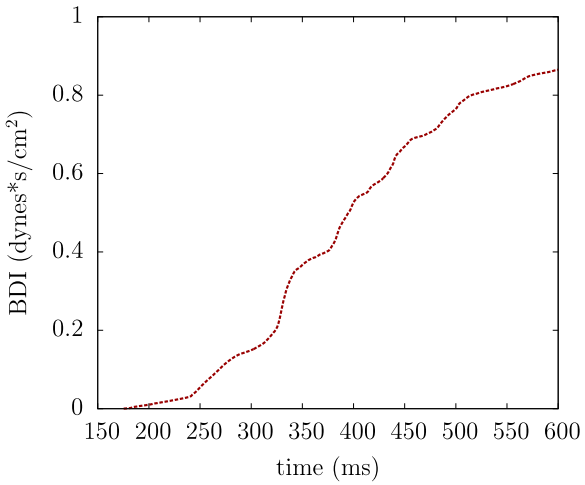

Figure 6-27: Platelet damage accumulation versus time for platelet recirculating in sinus expansion

6.4.2.4 Leaflet closing wake

The two most damaged platelets (and four of the top 8) in the simulation experience very high levels of shear stress when caught in the vortex wakes caused by rapid leaflet closing motion. As the leaflets begin to close, a platelet very close to the leaflet but still on the aortic side is observed (Figure 6-28).

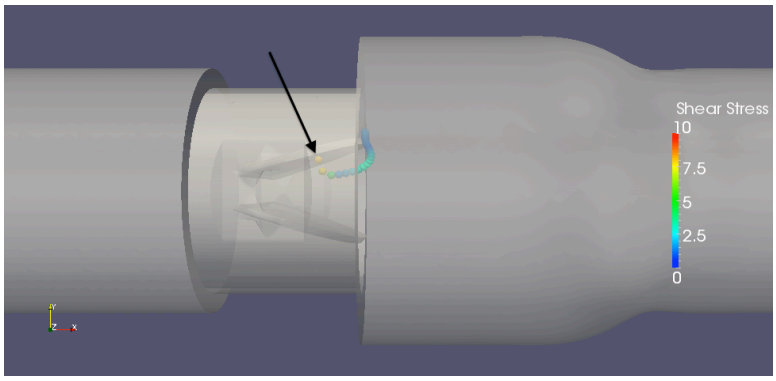

(a) Perpendicular view of platelet trail

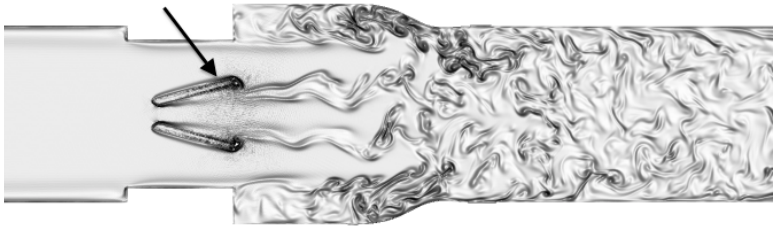

(b) 2D vorticity

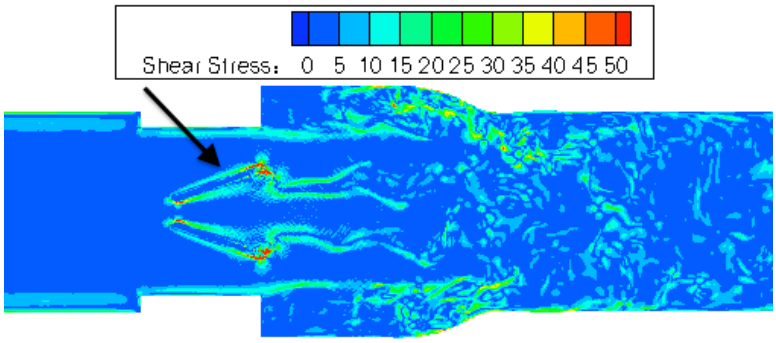

(c) Viscous shear stresses

Figure 6-28: (a) Platelet on aortic side of leaflet during start of leaflet closing motion (b) corresponding vorticity field, (c) shear stress field

As the leaflet closing wake becomes stronger, the platelet squeezes through the gap between the leaflet and the valve housing. At this gap, the platelet experiences a high level of shear stress (40 – 50 dynes/cm^2 maximum shear stress) from both the leakage jet and the leaflet closing wake (figure 6-29).

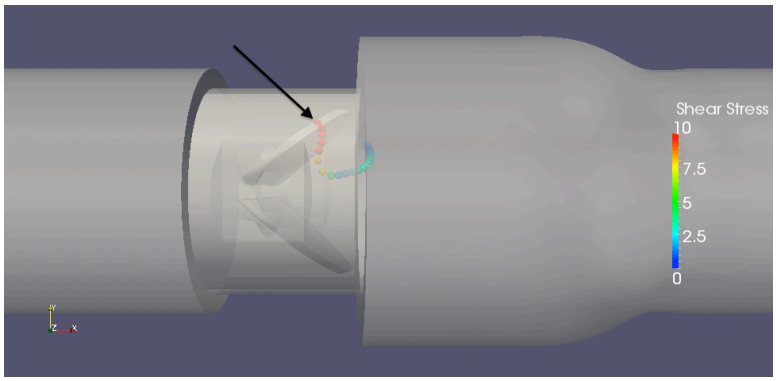

(a) Perpendicular view of platelet trail

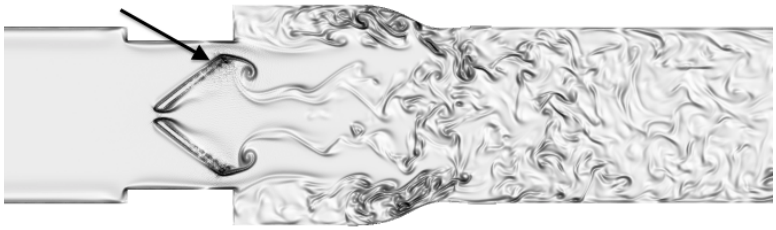

(b) 2D vorticity

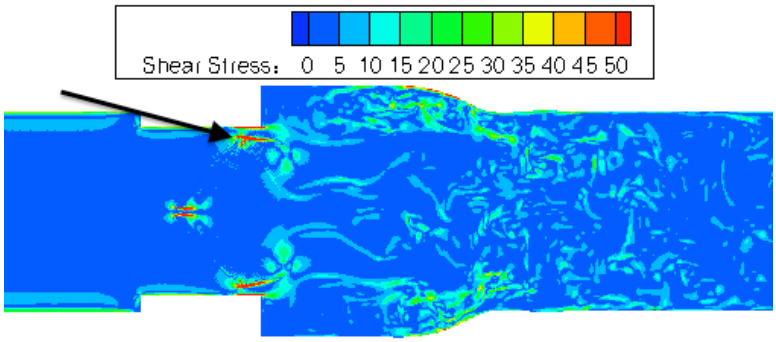

(c) Viscous shear stresses

Figure 6-29: (a) Platelet squeezing through valve housing gap during leaflet closing motion (b) corresponding vorticity field, (c) shear stress field

As the leaflets close, leakage jets form in the b-datum line as well as from leaflet-valve housing contact. The platelet is now on the ventricular side of the leaflet and incurs a high amount of shear stress (20 – 30 dynes/cm^2 maximum shear stress) due to the

leaflet-valve closure jets that come from the valve housing (figure 6-30). This platelet experiences very high shear stresses in a relatively short amount of time during leaflet closure, and begins recirculation on the ventricular side. This platelet, which has squeezed through to the ventricular side, can incur even more damage in the systolic phase of the next cardiac cycle.

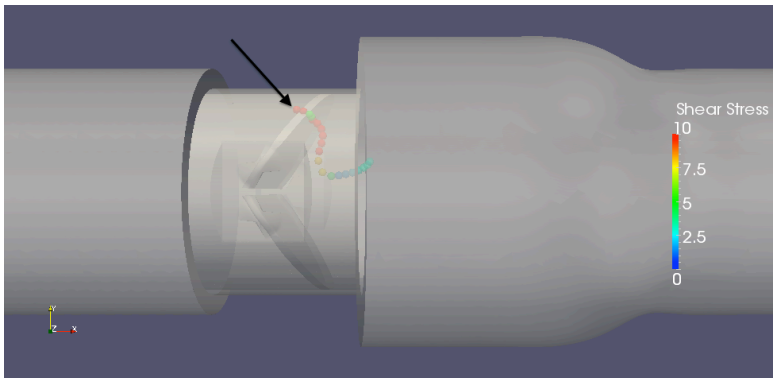

(a) Perpendicular view of platelet trail

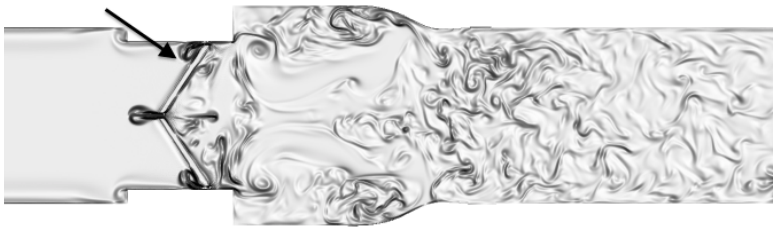

(b) 2D vorticity

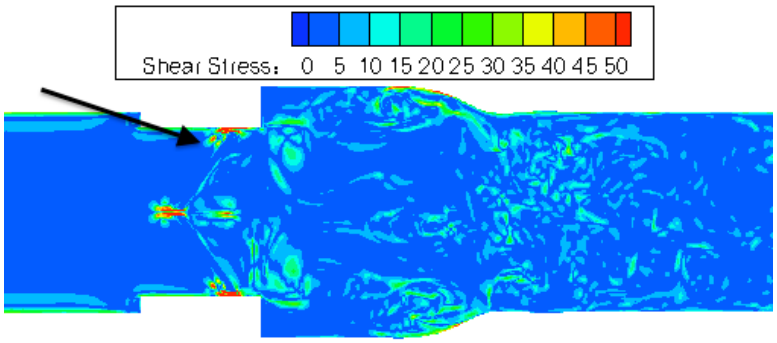

(c) Viscous shear stresses

Figure 6-30: (a) Platelet on ventricular side of leaflet after leaflet closure (b) corresponding vorticity field, (c) shear stress field

The time history of damage accumulation for the platelet caught in the leaflet closing wake shows a sharp and sudden increase in damage accumulation for the platelet when the leaflets suddenly close (Figure 6-31). This shows that platelets near the leaflet have low levels of damage accumulation but can experience very high levels of shear stress for a short amount of time when caught in the leaflet closing wake.

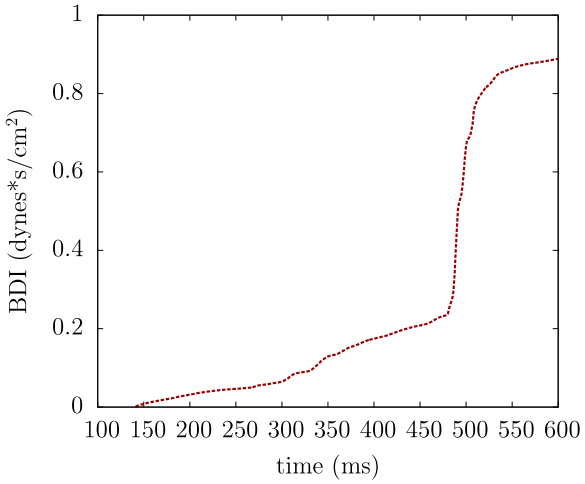

Figure 6-31: Platelet damage accumulation versus time for platelet caught in leaflet closing wake

Platelets caught in the leaflet closing wake experience the highest levels of instantaneous shear stress, with maximum shear stresses recorded as high as 400 – 700 dynes/cm^2. However, this high instantaneous shear stress occurs for a very brief period of time. Only 4 of 5400 platelets (0.07%) are caught in these leaflet closing wakes, but with high enough instantaneous shear stress to be among the top 20 most damaged platelets.

6.5 Blood damage in diastolic flow

A separate simulation on the effects of diastolic leakage flow on platelet damage is also performed. During mid-diastole, most flow throughout the domain shows low vorticity and slow recirculation [102]. Of interest is flow near the valve, where leakage flow past the closed leaflets in the valve may cause high platelet damage. Although this study does not include hinge gap leakage, the effects of diastolic leakage flow through the b-datum line and valve housing gaps can be explored.

6.5.1 Diastolic flow setup

To determine platelet damage in diastolic flow, 2000 platelets are randomly seeded at the aortic edge of the BMHV at the start of mid-diastole. These platelets are seeded at the edge of the valve on the aortic side. This simulation is performed for a pulsatile flow cardiac cycle during mid-diastole, at a time point almost 150ms after leaflet closure. However, mid-diastolic flow at this point has a quasi-steady reverse flowrate and most of the flow structures from systole and leaflet closing have dissipated.

2000 platelets for the diastolic flow simulation are technically less than the 5400 total platelets simulated for systolic forward flow. However, the 300 platelets per seed for the systolic flow simulation represent a cross-sectional seed density of 1 platelet per 1.7mm^2. For diastolic flow, the 2000 released platelets represent a much higher seed density of 1 platelet per 0.18mm^2. In addition, the systolic phase results in forward flow rates up to 25 L/min, which is much higher than reverse flow rates of mid-diastole (< 1 L/min). Finally, the continuous seeding of platelets is necessary for systole as there is a coherent forward flow through the valve during this phase. For diastole, the flow field is more recirculating in nature and there is no coherent reverse flow, thus eliminating the need for continuous seeding of platelets.

At the mid-diastolic time point of the cardiac cycle, the leaflets are closed and leakage jets exist in the b-datum line and the valve housing gaps. The diastolic flow time period that is simulated is 320ms, representing all of mid-diastolic quasi-steady flow up to end diastole right before the leaflets re-open. Platelet damage is quantified and damage values are determined in four primary regions (figure 6-32): 1) ventricular chamber section, 2) ventricular side within the valve, 3) aortic side within the valve, and 4) aortic sinus expansion.

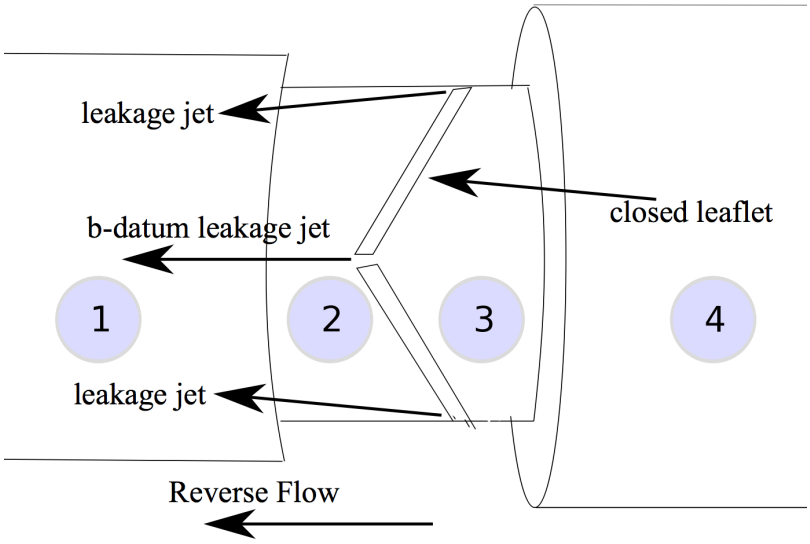

Figure 6-32: BMHV flow domain split into four subcategories: (1) Ventricular chamber, (2) Ventricular side within valve, (3) Aortic side within valve, (4) Aortic sinus expansion

6.5.2 Platelet distribution and bulk damage values

The initial seed of 2000 platelets is randomly distributed at the aortic edge of the BMHV (Figure 6-33). This platelet seeding is performed with the same disk point method as with the systolic flow simulations.

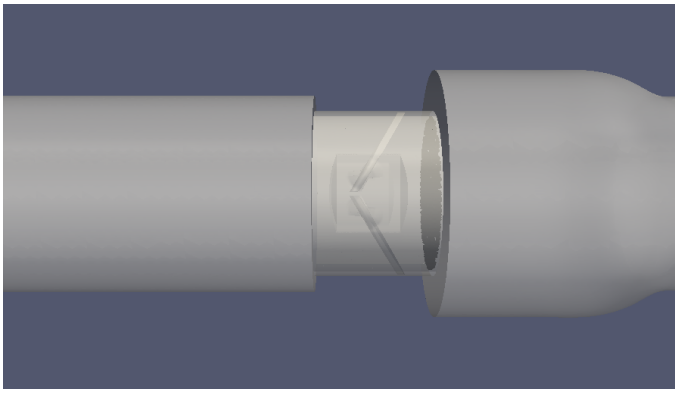

Figure 6-33: 2000 platelets seeded on aortic edge of the SJM valve

After simulation of the mid-diastolic phase (320ms), platelets are distributed on either side of the valve and are shown in figure 6-34. Platelets that have leaked to the ventricular side have mostly traversed to the ventricular chamber section and do not remain in the valve. This is due to the strong b-datum jet advecting leaked platelets centrally towards the ventricular side. Alternatively, some platelets leak through the small valve housing gaps. These two different leakage cases will be discussed in section 6.5.3. On the aortic side, platelets are well distributed both within the valve and in the aortic sinus expansion. The mid-diastolic leakage of platelets is shown in animation 6-4.

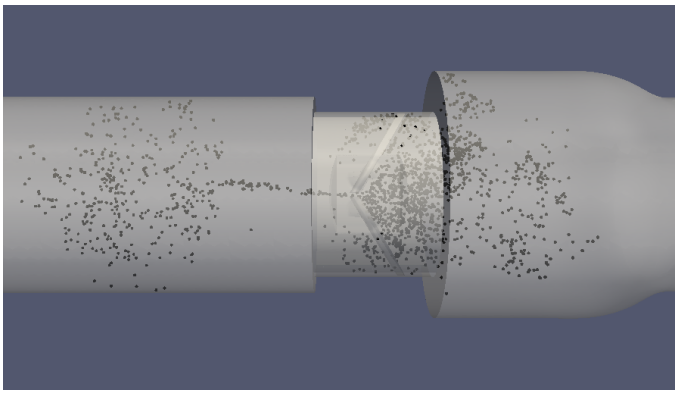

Figure 6-34: 2000 platelets at end diastole after 320ms of simulation

Damage in leaked platelets is compared to damage in platelets that remain on the aortic side (table 6-3). The majority of platelets (68.9%) remain on the aortic side of the leaflets, with 54.1% of the total platelets in the aortic sinus expansion and 14.8% of the total remaining within the valve on the aortic side. Platelets that have leaked to the ventricular side of the leaflets (31.1% of total platelets) are mostly advected to the ventricular chamber (23.1% of total platelets) with a small number within the valve (8% of total platelets) on the ventricular side.

Table 6-3: Platelet and BDI distribution for diastole

Region	# of platelets	% of total platelets	BDI average (dynes s / cm^2)
Overall	2000	100	0.0646
Ventricular side	623	31.1	0.1137
Aortic side	1377	68.9	0.0425

Although most platelets do not leak to the ventricular side, the platelets that do experience 2.68 times more damage than those that remain on the aortic side. The average damage for platelets on the ventricular side is still low, at 0.1137 dynes•s/cm^2, but only represent 320ms of exposure time. In addition to incurring higher levels of damage, platelets on the ventricular side will likely flow through the valve again at the systolic phase of the next cardiac cycle.

This underlines the potential dangers of sinus expansion recirculation, as platelets caught in these regions can potentially incur high levels of damage during systole, additional damage during diastolic leakage flow, and more damage during the next phase of systolic flow. Although only a small percentage of platelets would be caught in this recirculation flow scenario, this still highlights the danger of recirculation in BMHVs.

6.5.3 Leakage jet BDI

Though the spatial resolution of the simulations is not high enough to resolve hinge leakage, two primary leakage jets can be resolved: b-datum central leakage and valve housing leakage. The difference in damage in these leakage jets is compared.

It is found that all platelets caught in the b-datum central leakage jet are advected into the ventricular chamber and do not reside within the valve. All platelets that leak through the valve housing gaps, however, remain within the valve upon traversing to the ventricular side. Figure 6-35 demonstrates a small cluster of platelets approaching the b-datum gap. Only 2ms later, this cluster of platelets leaks through the b-datum gap onto the ventricular side.

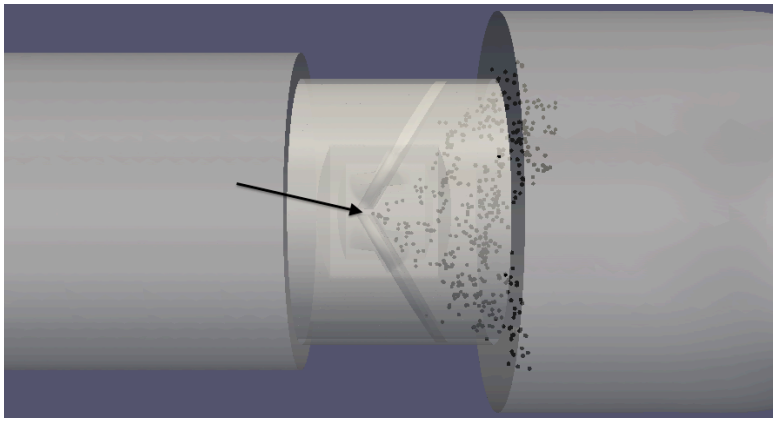

(a) Platelets approaching b-datum gap

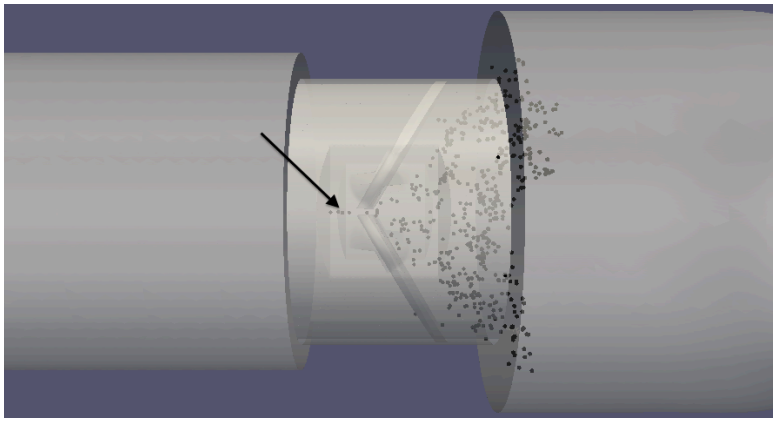

(b) Platelets flowing through gap

Figure 6-35: Cluster of platelets leaking through b-datum gap (a) approaching b-datum line, (b) flowing through gap 2ms later

At a time point 25ms later (Figure 6-36), this cluster of platelets has advected well into the ventricular chamber due to the strength of the b-datum leakage jet. The vorticity and shear stress fields are also shown in this figure, demonstrating the strong b-datum jet that causes the platelets to quickly traverse into the ventricular chamber, and the high shear stresses associated with this leakage.

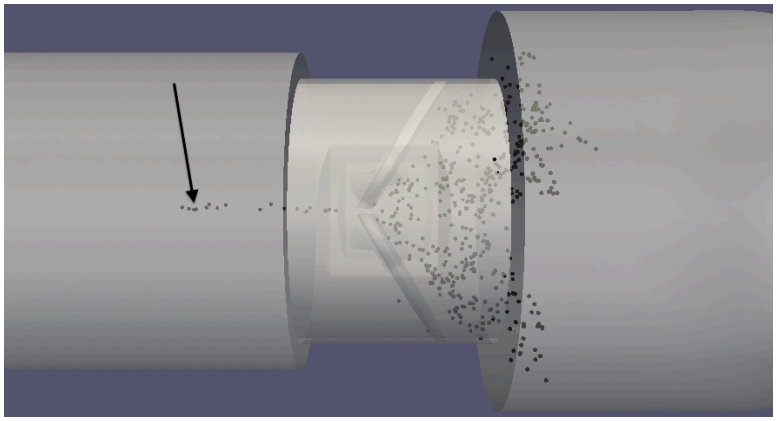

(a) Platelets advecting to ventricular chamber through b-datum gap

(b) 2D vorticity

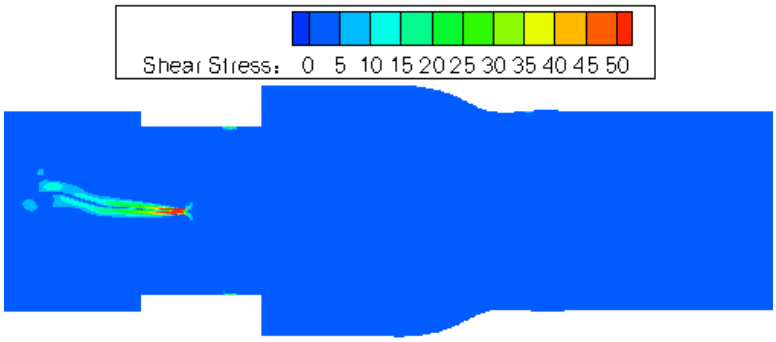

(c) Viscous shear stresses

Figure 6-36: (a) Cluster of platelets leaking through b-datum gap, (b) corresponding vorticity flow field, (c) shear stress field

Platelets that leak through valve housing gaps traverse quickly through the gap but reside within the valve afterwards. Figure 6-37 shows an example of a platelet approaching the valve housing gap. After 2ms, the platelet is in the valve housing leakage gap. The platelet appears to come out of the domain due to the visualization of the platelet as an enlarged sphere. After an additional 2ms, the platelet is through the valve housing gap and on the ventricular side of the valve.

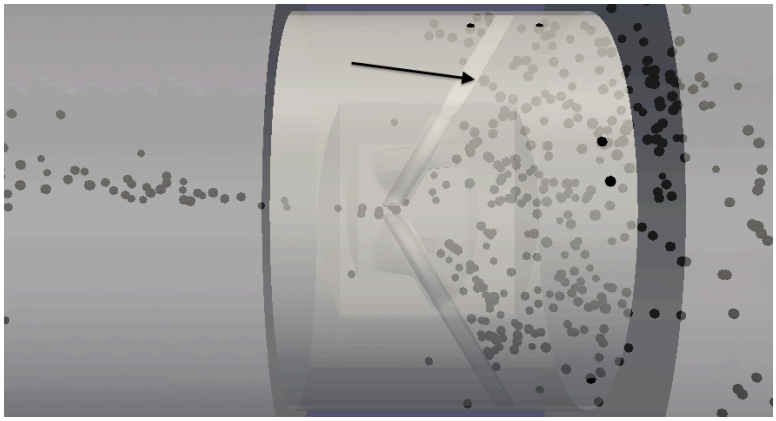

(a) Platelet approaching valve housing gap

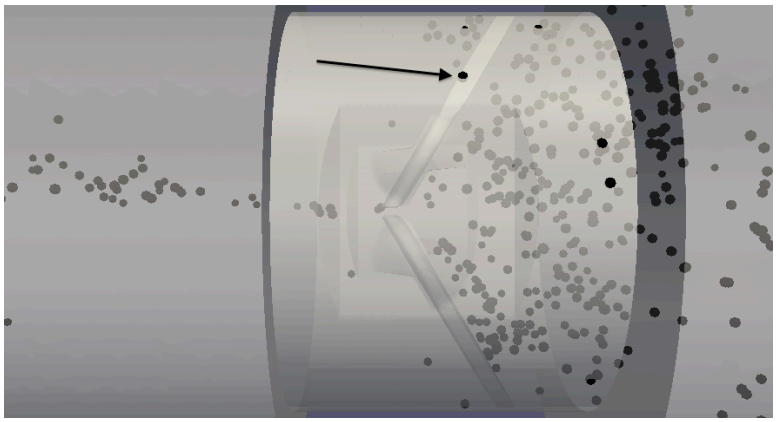

(b) Platelet squeezing through gap

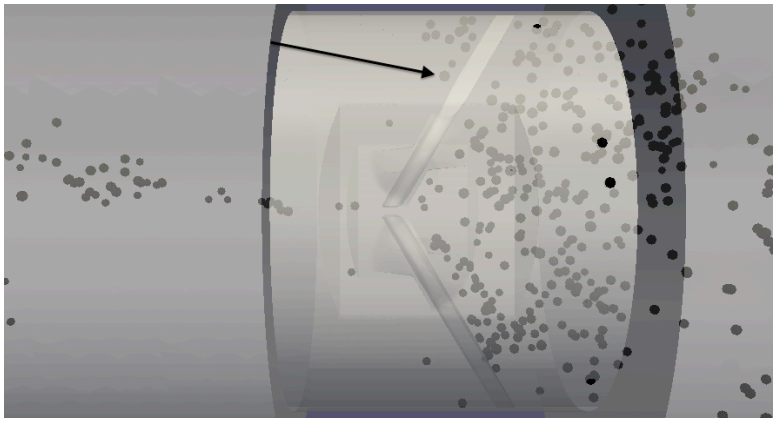

(c) Platelet on ventricular side of leafleet

Figure 6-37: Platelet leaking through valve housing gap (a) approaching leaflet, (b) flowing through gap 2ms later, (c) on ventricular side after leakage

It is observed that all platelets that leak through the valve housing gaps remain within the valve at the end of the simulation. These platelets flow quickly through the gap to the ventricular side, but have slow recirculating motion within the valve region afterwards. Thus, none of the platelets from valve housing leakage traverse into the ventricular chamber. This is contrary to platelets that leak through the b-datum orifice, in which all platelets are immediately swept into the ventricular chamber.

Platelets that leak to the ventricular side through the central b-datum gap versus the valve housing gap are differentiated as well (Table 6-4). 31.1% of the total platelets leak through to the ventricular side after 320ms of simulation. Most of these platelets (74.3%) leaking to the ventricular side go through the b-datum gap, and experience 3.0 times more damage than platelets that remain on the aortic side. Platelets that leak through valve housing gaps still experience 1.71 times more damage than platelets that remain on the aortic side.

Table 6-4: Distribution of platelets by method of leakage to ventricular side with BDI values

Leakage gap	# of platelets	% of leaked platelets	BDI average (dynes s / cm^2)
Total	623	100	0.1137
B-datum gap	463	74.3	0.1278
Valve housing gap	160	25.7	0.0727

This lesser damage from valve housing leakage flow is likely due to the fact that after leaking through the valve housing gaps, platelets simply recirculate within the valve, similar to platelets that recirculate on the aortic side of the valve. Platelets that flow through the b-datum gap are instead caught in a strong leakage jet and are afterwards caught in continuous recirculation vortices in the ventricular chamber. This b-datum leakage jet is also associated with high fluid shear stresses (figure 6-36c), explaining why these platelets experience 1.76 times more accumulated damage than platelets flowing through valve housing gaps. From the variation of shear stresses at these two leakage gaps over the diastolic phase (figure 5-39), it is also apparent that the b-datum jet is

associated with much higher shear stress values than valve housing leakage for the entire diastolic phase. More comments on the diastolic flow phase are made in section 6.7.3.

6.6 Platelet rotation and BDI: 1-way and 2-way FSI

The correlation between platelet angular rotation and platelet damage is determined through Lagrangian tracking of selected platelets. In addition, the difference between 1-way and 2-way FSI modeling of suspended subgrid platelets is tested for this BMHV flow. 300 platelets are seeded at peak flow at an axial location immediately downstream of the leaflet tips. These platelets are randomly distributed over a cross-section encompassing the sinus expansion. The platelets are released from peak flow to late systole. Two simulations are performed with identical setups, but one simulation employs 1-way FSI of platelets and the other uses 2-way FSI. Two representative platelets are chosen: a platelet with low overall damage and a platelet with higher accumulated damage.

The angular orientation of a platelet is defined by three angles: θ, ϕ, and ψ. As the platelets are modeled as oblate spheroids, θ and ϕ represent rotation about the two major axes (3μm diameter), and ψ represents rotation about the minor axis (1.3μm diameter). The angular rotation is defined as the absolute value of the difference in an angle of orientation over a timestep, Δt. For example, the angular rotation of θ at time t is defined as

$$\theta_{rotation} = \left| \theta_t - \theta_{t-\Delta t} \right| \qquad \text{Equation 6-1}$$

where t is the current numerical timestep, and Δt corresponds to the frequency of data output of 200 numerical timesteps (0.5ms).

Change of platelet damage is determined over time as well, quantified as change in BDI value for a platelet over a timestep, Δt. This is defined as

$$\Delta BDI = BDI_t - BDI_{t-\Delta t} \qquad \text{Equation 6-2}$$

with BDI quantified in units of dynes•s/cm^2.

Platelet 1 (figure 6-38) incurs a low accumulated damage of 0.22 dynes•s/cm^2. This platelet is released near the center of the cross-section, and simply advects downstream into the aortic chamber. The results for 2-way FSI modeling are very close with only 0.59% difference in final BDI value. The rotation angle over time (figure 6-38a/b) shows little angular orientation change throughout the simulation with scattered spikes of instantaneous angle change, and the results for 1-way and 2-way FSI are very similar. The corresponding plot of blood damage change over time (figure 6-38c/d) shows spikes of instantaneous angle change are associated with spikes of BDI increase, and also shows very similar results for 1-way and 2-way FSI.

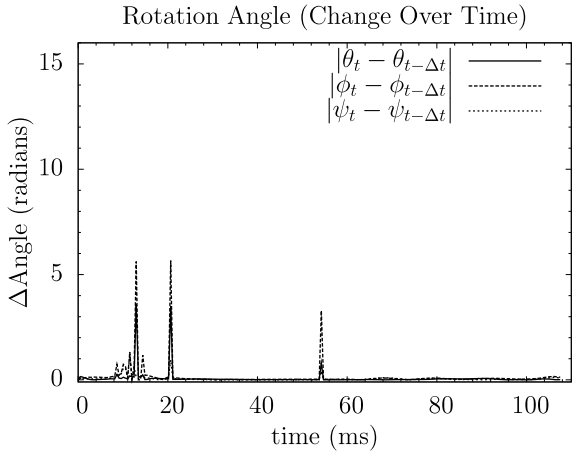

(a) Platelet 1: 1-way FSI - rotation angle

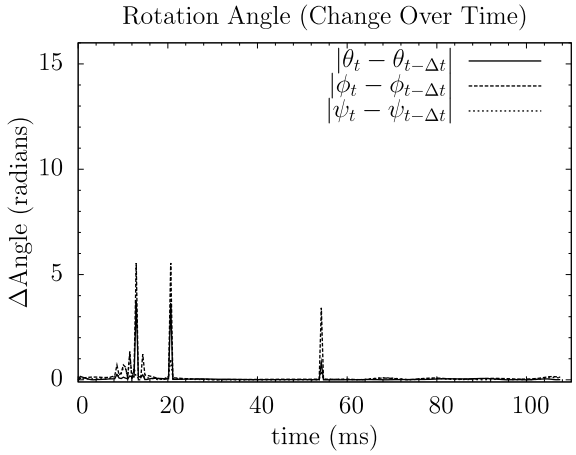

(b) Platelet 1: 2-way FSI – rotation angle

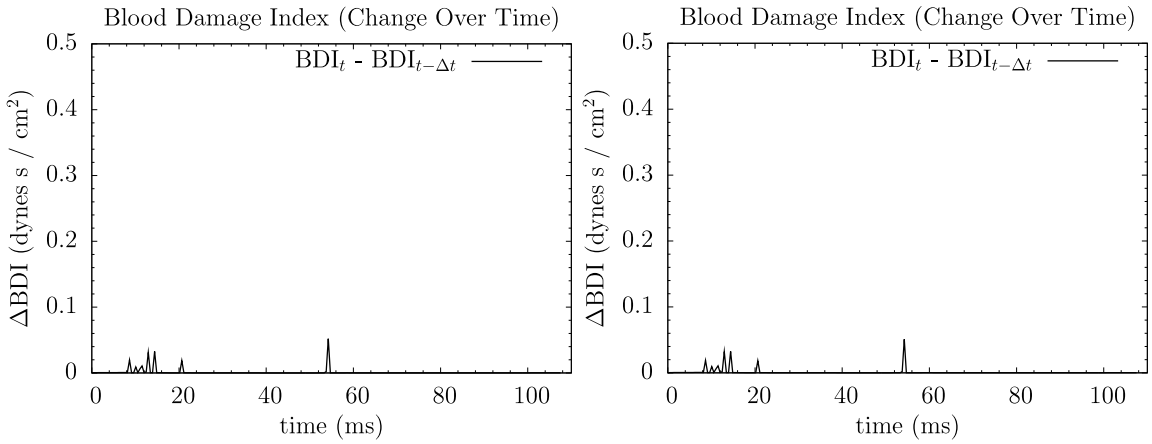

(c) Platelet 1: 1-way FSI - BDI change (d) Platelet 1: 2-way FSI – BDI change

Figure 6-38: Variation of rotation angle and change in BDI over time for low damaged platelet for 1-way and 2-way FSI.

A second example platelet is released closer to the sinus expansion walls, and recirculates within the sinus expansion. Platelet 2 (figure 6-39) incurs 1.6 dynes•s/cm^2 of damage. The rotation angle over time (figure 6-39a/b) shows more spikes in changes in angular orientation, with close matching of 1-way and 2-way FSI. The corresponding plot of blood damage change (figure 6-39c/d) also shows correlating increases in BDI for the changes of angular orientation, with good matching of 1-way and 2-way FSI. The results of 2-way FSI show just 1.1% difference in final BDI value compared to 1-way FSI.

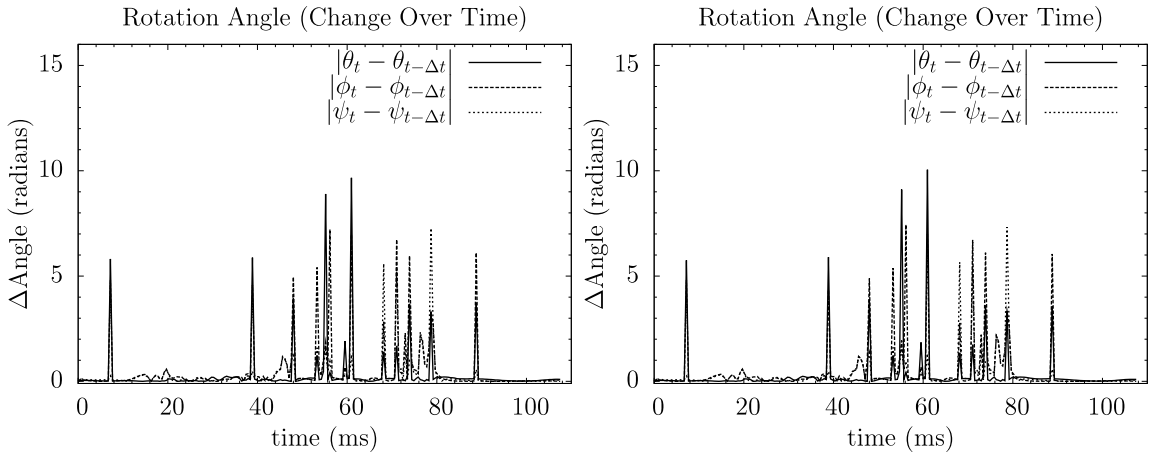

(a) Platelet 2: 1-way FSI - rotation angle

(b) Platelet 2: 2-way FSI – rotation angle

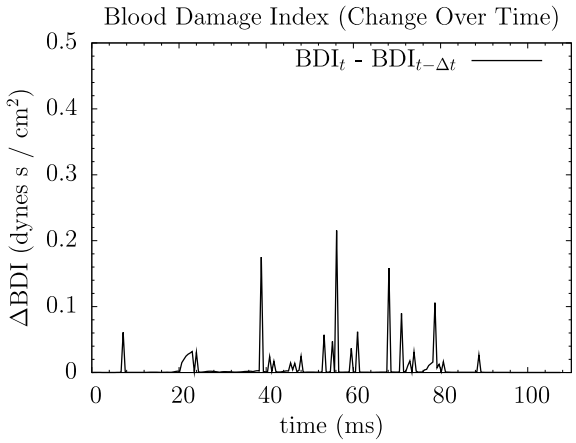

(c) Platelet 2: 1-way FSI - BDI change

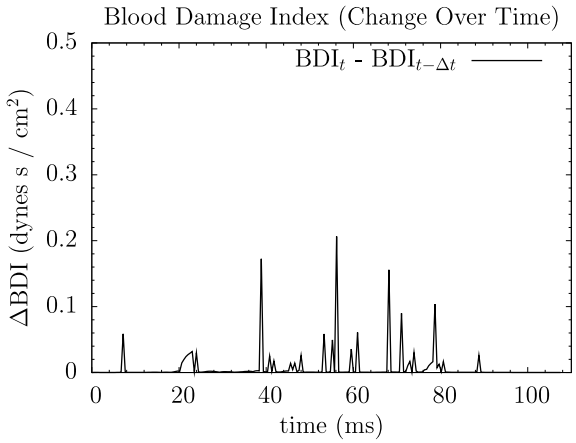

(d) Platelet 2: 2-way FSI – BDI change

Figure 6-39: Variation of rotation angle and change in BDI over time for higher damaged platelet for 1-way and 2-way FSI.

For all 300 released platelets in this test, the 1-way and 2-way FSI simulations give very similar results for platelet motion and BDI values. This demonstrates that the 1-way FSI approximation for platelets of the BMHV blood damage studies closely matches what would be modeled for 2-way FSI, when performing at subgrid resolution. As shown in section 4.1.2.6, calculated shear stress values are elevated for subgrid particles but within 30% of calculated values for well-resolved supergrid particles. Thus,

the subgrid 1-way FSI modeling of platelets is a reasonable approximation for determining platelet motion, shear stress calculation, and BDI calculation.

6.7 Analysis of blood damage in physiologic adult case

Simulations performed with physiologic adult conditions can highlight aspects of the BMHV flow field that could lead to thromboembolic complications. This data can only be viewed as a "one-pass" model, as platelets that pass through the valve and through the aorta may not return back to the heart for some time. In addition, platelets that do return to the heart will likely not undergo the same platelet path for each pass through the BMHV. Although none of the BDI data can be extrapolated over multiple flows through the valve, the results of this research can still infer insight to highlight regions of the domain, aspects of the flow field, and platelet pathlines that may be of interest for thromboembolic complications. No strong conclusions can be made on thromboembolic potential of valves based on one-pass simulations. However, these and future simulations can be used in combination with experimental studies to better assess valve hemodynamics and blood damage performance. This can be performed with blood damage experiments, for example, to correlate BDI values from computational simulations to blood damage experimental data.

The effects of red blood cells and more anatomic geometries on the flow and platelet damage are unknown for these simulations. These simulations only model dilute platelet suspensions due to computational limitations, but still represent a significant step in BMHV flow modeling compared to previous studies.

6.7.1 Comments on flow fields

Upon analysis of the platelet damage paths, it is surprisingly found that relatively low instantaneous damage occurs for platelets caught in the leaflet vortex wakes. Only moderate levels of instantaneous shear stress (5 – 15 dynes/cm^2 maximum shear stress) occur in near-peak flow when these vortex wakes break into small eddies (figure 6-40a/b). However, larger amounts of instantaneous shear stress (20 – 50 dynes/cm^2 maximum shear stress) occur in platelets caught in mixing vortical regions where the sinus expansion vortex shedding and the leaflet tip vortex shedding interact (figure 6-40c/d).

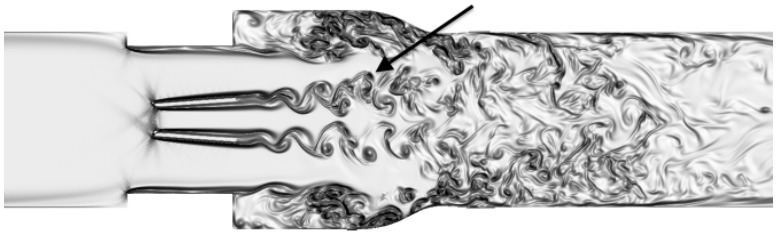

(a) Small scale eddies – 2D vorticity

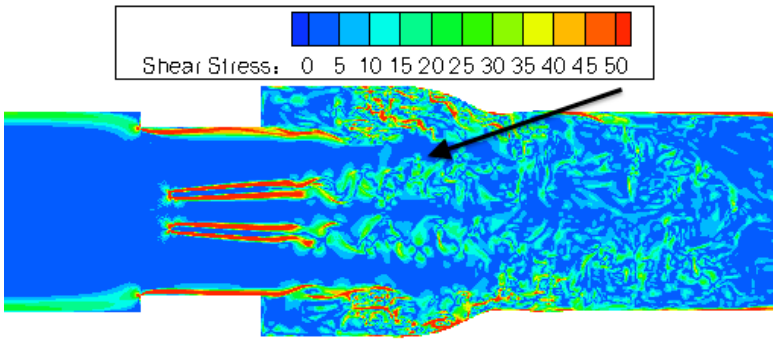

(b) Shear stresses in region of small eddies

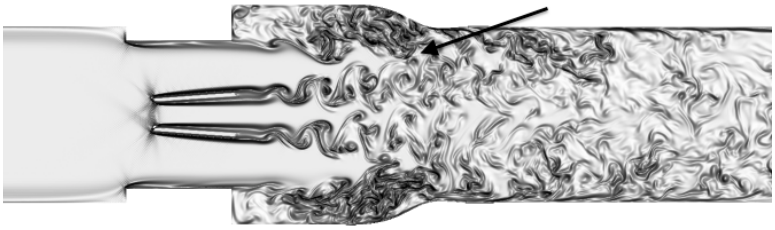

(c) Sinus recirculation region – 2D vorticity

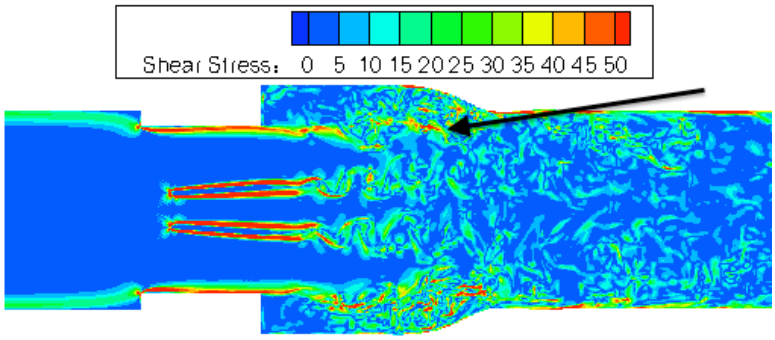

(d) Shear stress regions in sinus recirculation

Figure 6-40: Near peak flow (Re = 5500) showing (a) disorganized vortex shedding past leaflet tips that incur mild damage, (b) corresponding shear stress field, (c) mixing between vortex shedding regions that incur high damage, (d) corresponding shear stress field

Generally, platelets caught in the leaflet tip vortex wakes that do not mix with the sinus expansion recirculation vortices experience mild platelet shear stress (5 – 15 dynes/cm^2 maximum shear stress). This also results in only moderate levels of accumulated platelet damage at the end simulation time point (< 0.5 dynes•s/cm^2) as these platelets quickly advect downstream, where vortical structures dissipate and damage levels are low.

This demonstrates that leaflet tip vortex shedding itself does not induce high levels of damage, but mixing with the sinus recirculation region could lead to high platelet damage. The sinus recirculation regions of these simulations cause both higher levels of instantaneous shear stress (20 – 50 dynes/cm^2 maximum shear stress) on platelets and have longer exposure times that lead to high accumulated damage values.

6.7.2 Analysis of systolic flow

The Lagrangian viewpoint tracks platelet position and instantaneous and accumulated damage over time, which can be connected to the instantaneous flow fields. The four highlighted platelet damage paths in section 6.4.2 are representative of the 10 most damaged platelets. Although high damage regions are noted in the aortic downstream and ventricular chamber in the Eulerian viewpoint, none of the most damaged platelets reside in these regions.

The highlighted platelet damage paths of interest can be categorized as follows: near surface paths, constant recirculation, and leaflet closing wakes. The damage for a platelet traveling near the leaflet surface is not common, as only two of the top 20 most damaged platelets follow this path. These platelets travel very close to the leaflet surface and incur high levels of damage as they slowly travel along the leaflet. It is interesting to note that these platelets do not get swept away from this near leaflet layer. Contact modeling is not employed for the platelets in these simulations, but platelets are very small and in this case do not actually touch the leaflets. Instead, the platelets simply travel very close to the leaflet and experience near-wall shear. The lack of flow separation for flow along the leaflet surface leads to this highly damaged platelet. It

should be noted that this is for an idealized geometry. In real flow conditions, flow separation along the leaflet surface may occur due to design imperfections.

The platelets along the leaflet surface in the simulation eventually traverse to the ending leaflet tips, where they advect to the aortic downstream region quickly due to the vortex shedding past the leaflet tips. Although the platelets incur a high level of damage, they are not of particular danger once they advect downstream. In addition, as BMHV leaflets are made of thromboresistant pyrolitic carbon, it is unlikely that damaged platelets would activate and aggregate on leaflet surfaces. A potential danger of this platelet path is a scenario in which the leaflets close before the platelet moves to the ending tips. This would result in high additional damage due to the leaflet closing wakes.

It has previously been shown that vortex generators on leaflet surfaces can reduce blood damage potential during diastolic flows [53, 54]. These vortex generators are primarily designed for reduction of blood damage in diastolic flows through the breakup of coherent vortices in the b-datum jet. However, their effects on systolic flow are unknown. It is also noted (figure 6-40) that damage from the vortices shedding from the leaflet tips are not connected with high levels of accumulated damage. Thus, it is possible that vortex generators may help reduce damage in systolic flows as well. These may cause flow separation from the leaflet surfaces, thus preventing near-leaflet shear regions that cause platelet damage. The vortex shedding wakes from these vortex generators could cause minimal damage to platelets, similar to the vortices shed from leaflet tips. However, this should be investigated in detail in the future, as the possibility of recirculation caused by these vortex generators is unknown. In addition, the flow separation from the leaflet surface may cause increased mixing with the sinus

recirculation region, which is also dangerous. Thus, further investigation in numerical simulations is warranted.

The platelet damage path for leaflet closing wake causes the two highest damaged platelets at 3.6 and 2.0 dynes•s/cm^2. However, only four platelets of the top 20 most damaged platelets to experience this pathline. Though unlikely, this platelet damage path is characterized by generally low damage for most of the simulation and a sudden increase in accumulated damage during leaflet closing. These platelets are positioned very close to the trailing leaflet tips just as the leaflets close. Upon leaflet closure, the platelets near the leaflet tips become trapped in the strong closing wake, incurring high levels of shear stress up to 700 dynes/cm^2. Although this platelet damage path is of interest, it is both rare in occurrence and difficult to recommend any solution, as the leaflets must close to prevent regurgitation. Strong closing wakes are an unavoidable feature of BMHVs due to the nature of the closing phase.

The platelet damage paths of highest interest are sinus recirculation paths. This accounts for 14 of the top 20 most damaged platelets. Though both occurring in the sinus region, platelets can be damaged by near sinus wall paths or constant recirculation paths. The near wall path incurs high damage for the platelet, similar to the path along the leaflet surface. However, the levels of shear stress for the platelet are higher for the sinus wall (15 – 50 dynes/cm^2) than for the leaflet surface (10 – 25 dynes/cm^2).

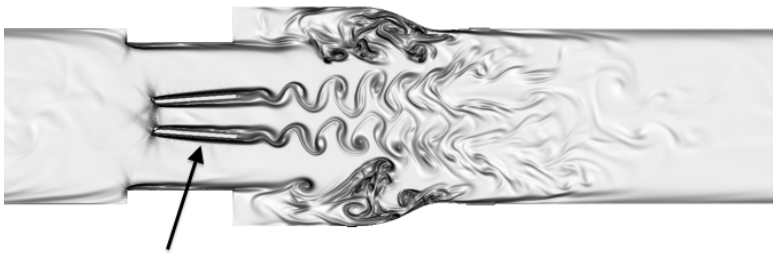

(a) Near leaflet flow

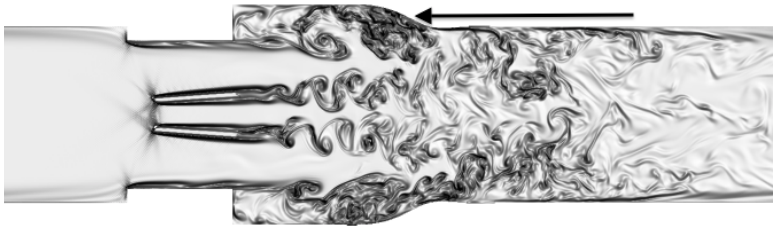

(b) Sinus recirculation regions

Figure 6-41: 2D vorticity flow fields showing high damage regions for (a) near leaflet flow, (b) sinus wall flow

Figure 6-41 shows two flow fields for the time periods of high platelet damage with arrows pointing to the near-wall region that causes high damage. The leaflet surface plot shows the flow layer close to the leaflet surface, which is maintained very close to the surface. For the sinus wall, the recirculation region near the platelet is larger. The nature of the flow in the sinus recirculation region could lead to the higher levels of instantaneous damage, despite both pathlines being near-wall paths.

The most common path for high platelet damage occurs for constant recirculation in the sinus region, which accounts for 10 of the top 20 most damaged platelets for the systolic flow simulation. This path is noted by a moderate level of instantaneous damage but for an extended period of time. This pathline is more common due to the large region of the sinus expansion as compared to the other damage path regions (near wall, near leaflet closing wake). In addition, the sinus recirculation occurs for the entire systolic phase of 350ms, allowing for many platelets to be trapped in this flow.

This recirculation flow and platelet path is of considerable concern, as it is very easy for platelets to be caught in the sinus expansion. Platelets in this sinus region do not advect downstream but continue to recirculate throughout the cycle. Upon platelet

activation, this continuous recirculation could lead to a coagulation cascade from release of activating factor to other nearby platelets that are also recirculating. This is similar to the development of thrombus in the hinge regions, which is also caused by stagnation and recirculation regions.

It is noted that platelets residing in the aortic downstream region at the end of the simulation are not among the most damaged platelets. Platelets in the aortic downstream region are generally caught in the vortex shedding from the leaflet ending tips and experience both low instantaneous shear stress (5 – 15 dynes/cm^2) and low accumulated damage. This low damage occurs even in peak flow when the large vortices break into small scale eddies. Thus, attempting to characterize instantaneous flow fields and attributing high damage to the unstable and disorganized features of peak flow past the leaflet tips is shown to be not accurate in assessing actual platelet damage. This previous method has commonly been used in literature to connect instantaneous flow fields with platelet damage [56, 64, 105]. The results of the simulations of this study demonstrate that recirculation regions cause both higher instantaneous damage and higher accumulated damage, and these regions should be focused on in the future when assessing single-phase flow simulation results. This also demonstrates the need for Lagrangian particle tracking to more accurately assess platelet damage.

Sinus regions are naturally present in the aorta, and recirculation regions are present even in native aortic valve flows. The simulations of this research also are performed for a domain with a sudden sinus step expansion, whereas the physiological sinus has a more gradual expansion. The sudden step expansion in these simulations leads to a stronger recirculation region in the simulations than would actually occur *in*

vivo. Even with a native aortic sinus, however, recirculation regions would occur that could cause high platelet damage. Nonetheless, it is likely that the level of platelet damage for a native sinus region would be lower.

The conclusion of these results is not that the sinus itself is a particular danger, or that anything may be fixed with a native aortic sinus. It is instead determined that strong recirculation regions, such as those present in the sinus expansion of this study, are more dangerous for platelet activation than instantaneous damage levels caused by flows. As the aortic sinus is not something to be fixed, the recommendation for the creation of future prosthetic devices is to avoid designs that cause strong recirculation zones. In the previous work by Wu *et al.* [65] and Yun *et al.* [63], it is determined that sharp geometries lead to stagnation and recirculation regions in BMHV hinges that lead to thromboembolic complications. Similarly, from the results of this research, it is shown that sharp transition geometries may lead to high damage in bulk BMHV flows due to recirculation regions. Thus, it is recommended that future valve design (housing, leaflets, hinges) generally avoid sharp geometries to avoid high damage levels and recirculation regions that cause high accumulated platelet damage.

6.7.3 Analysis of diastolic flow

The diastolic flow simulations are performed with 2000 platelets in mid-diastolic leakage flow. As this flow is quasi-steady, multiple release times of platelets are not necessary. This is a much greater number of seeded platelets than the 300 platelets previously deemed suitable as a representative sample in a cross-section. The valve diameter is also smaller than the ventricular chamber diameter. The flow in mid-diastole

is not a coherent reverse flow as well, as evidenced by the 68.9% of platelets that remain on the aortic side of the valve after 320ms of simulation. Thus, these 2000 platelets can be considered a sufficient sample of platelets near the valve in mid-diastolic flow.

Though the majority of platelets stay on the aortic side during diastole, 31.1% of platelets still leak through to the ventricular side. These platelets that leak through the leaflets experience 2.68 times more damage and also must flow through the valve again during the next systolic phase. It should be noted that platelets that leak through the leaflets do not experience high-accumulated damage (0.1137 dynes•s/cm^2 average) even for 320ms of exposure time. Thus, for one pass in systolic or diastolic flow, platelets are not in danger of becoming activated. It is the continuous recirculation of platelets near the valve that is of particular concern.

It is found that few (8.0%) platelets leak through the valve housing gaps. These platelets also experience lower damage compared to platelets that leak through the b-datum gap. This is primarily due to the slow recirculation of platelets after they have leaked through the valve housing gaps. The platelets that flow through the b-datum leakage jet experience higher instantaneous damage for a longer period of time. This is due to interaction between the b-datum leakage jet and large-scale vortices in the upstream ventricular region, which were previously shown in chapter 5. The continuous interaction of the b-datum jet with larger vortices on the ventricular side may explain the higher damage experienced by platelets in b-datum leakage flows.

This simulation demonstrates that valve housing leakage jets are not highly damaging to platelets, particularly when compared to b-datum leakage or the known dangers of hinge leakage. The design of leakage-valve housing tolerance gaps should

thus be concentrated on reducing regurgitant leakage flows, rather than being cautious of platelet damage. The potential of b-datum leakage jets to incur damage is more troubling, and efforts should be focused on reducing the coherent jets through this region. This can be accomplished by the inclusion of vortex generators, as has been previously proposed [53, 54] and demonstrated.

6.7.4 Final notes

The results of rotation angle and BDI change over time show a strong association between change in platelet orientation angle and increase in BDI value. These results also underline the importance of modeling suspended platelets of realistic shape and size. It is clearly demonstrated that angular rotation of the platelets is related to increase in blood damage. This would not be captured by point particle tracking, as there can be no torque on an infinitesimally small particle. Platelets modeled as idealized spheres also cannot capture the appropriate torques and angular rotation dynamics of the realistic oblate spheroid shape. This again highlights the abilities of the EBF method to model platelets with realistic shape and size for accurate BDI quantification, while employing subgrid modeling and very high spatiotemporal resolution.

Although the simulations of this study have highlighted damage patterns in pulsatile BMHV flow, the numerical method can be applied as a general tool for blood damage assessment. BMHVs are well-evolved and their thromboembolic potential has been studied for many years. The generic suspension flow solver of this study can be used in the future as a predictive tool as well, for novel devices in cardiovascular flows.

CHAPTER 7

BLOOD DAMAGE SIMULATIONS – PEDIATRIC CASES

Congenital heart valve disease is one of the most common abnormalities in children, with limited solutions available for treating children with this malformation. Although prosthetic heart valves are widely used for adults with valve disease and can be implanted in children in some circumstances, there are currently no FDA approved prosthetic heart valves available for use in the pediatric population. Custom-sized valves are available for special patient cases in the form of the Humanitarian Device Exemption (HDE). Despite this exception case scenario, there is a pressing need for FDA approved prosthetic heart valves for use in the pediatric population [106].

In a study by Karamlou *et al.* [107], competing risks analysis was performed for risk factors after aortic valve replacement (AVR) in 160 children. The study, which analyzed the use of mechanical and bioprosthetic valves in children, showed implantation of a bioprosthetic valve as a risk factor for need for second AVR. Another study by Raghuveer *et al.* was performed for children aged < 5 years undergoing mechanical mitral valve replacement [108]. It was demonstrated that overall prosthesis size and valve size mismatch were indicators of shorter prosthesis survival. The most common complication requiring second valve replacement was prosthetic valve stenosis, caused by valve size mismatch. This further demonstrates the need for appropriately sized prosthetic valves designed and approved for use in the pediatric population

The study by Raghuveer *et al.* also showed prosthetic valve thrombosis as the second most common complication for implanted mechanical valves in children. Clinical

studies on the performance of prosthetic valves have been routinely conducted for the adult population, but have typically excluded pediatric patients. The exclusion of the pediatric population in clinical trials for prosthetic valves include: limited patient pool, complex health histories, and limited available valve sizes [106].

As adult sized valves are FDA approved and have a proven design, it has been recommended that pediatric valves take previous adult-sized designs and scale them down to fit a smaller pediatric patient [106]. The hemodynamics and blood damage performance of these potential pediatric valves is not well understood. The numerical method of this study can model appropriately sized pediatric valves that are scaled down from adult sizes, and assess their blood damage performance. This and future modeling efforts may help push for the approval of these devices.

As with the physiologic adult case, suspended platelets are released in these pediatric valve flows. Platelet position and damage are calculated and tracked through time for individual platelets. This data is then analyzed along with flow visualization and compared to the baseline adult flows of chapter 6. Although the assessment of blood damage performance for these pediatric cases is predictive in nature, this preliminary assessment can help to understand the hemodynamics and blood damage profile of potential pediatric-sized mechanical heart valves.

7.1 Pediatric Case #1 – Child

Conditions for a 5-year old child are determined from a sampling of literature [106, 109-113] and close consultation with Dr. Doff McElhinney of NYU Langone Medical Center. Additional input is provided by members of Children's Healthcare of

Atlanta (Dr. Timothy Slesnick, Kathy Spitzer, Dr. Brian Kogon) and Children's Hospital of Boston (Greg Matte, Dr. Pedro del Nido).

7.1.1 Flow conditions and numerical setup

Flow conditions and sizing are chosen for an average 5-year old child. Although children are defined in age as 5 to 12 years of age [106], the younger age of 5 years is chosen to perform simulations of a case that is markedly different than the physiologic adult case. The overall flow conditions are listed in table 7-1. Valve size in table 7-1 refers to the internal diameter of the valve and not the sewing cuff diameter as commonly labeled for BMHVs.

Table 7-1: Flow conditions for 5-year old child with comparisons to adult conditions

Age	Valve Size (mm)	Systolic %	Heart rate (bpm)	Cardiac output (L/min)	Left side MAP (mmHg)	Right side MAP (mmHg)
18+ years	21.4	40%	70	5.0	93	20
5 years	14	40%	90	2.5	80	20

A 666ms cardiac cycle with an average flowrate of 2.5 L/min is modeled to match the heart rate and cardiac output of a 5-year old child. Systolic flow duration of 267ms is modeled to match the 40% systolic duration. The flowrate curve of the adult case is scaled to match the cardiac output, resulting in a peak flowrate of the cardiac cycle for the child at 12.5 L/min. All platelets are modeled exactly as in the physiologic adult case with the same shape (3D ellipsoid) and size (3μm major axis diameter) and with the same surface mesh (292 triangular elements).

The exact geometry is taken from the physiologic adult case, but scaled down to fit the appropriate valve sizing for a 5-year old child. It should be noted that not all valve components would necessarily be scaled linearly for a pediatric valve, as some structural components may be scaled differently to maintain a design and stress envelope consistent with adult valves [106]. However, for this study, the entire geometry is scaled linearly including all flow chambers and valve components. The LBM numerical method scales all physical parameters to lattice-Boltzmann units for modeling, and thus only the adjustment of physical-to-LBM scaling is required to model different size and flow conditions. The spatiotemporal resolution of the child simulation is 51.6μm and 1.52μs per numerical timestep, compared to 80μm and 2.4μs for the physiologic adult case.

As the systolic duration % is the same for the child case as the adult case, the flowrate and leaflet motion variation for the adult case is simply scaled in time to a 666ms cardiac cycle for a child, in contrast to a 860ms cardiac cycle for an adult. The entire flowrate curve (including the diastolic phase) is then scaled in magnitude until the desired cardiac output of 2.5 L/min is reached. These modified curves are shown in figure 7-1. The peak Reynolds number for this modified flow curve is 4418.

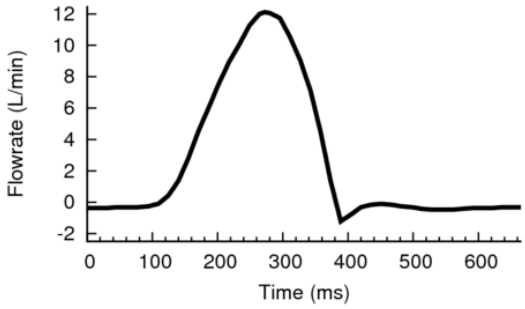

(a) Flowrate variation

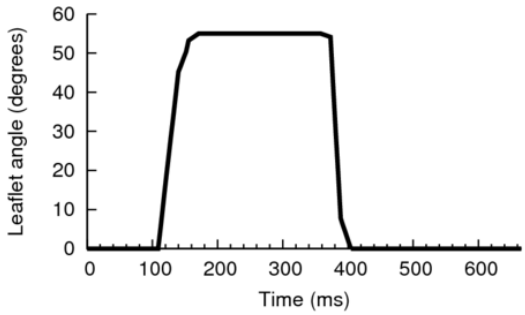

(b) Leaflet angle variation

Figure 7-1: Flowrate and leaflet variation for one cardiac cycle for a 5-year old child case

As with the adult case, 5400 platelets are released during the systolic flow phase. This is performed to match the total number of platelets seeded for the physiologic adult case. 300 platelets are released every 15.5ms in order to reach the same 5400 number of platelets in the suspension as with adult flow modeling. These platelets are seeded 300 at a time with randomized cross-sectional position and angular orientation, with platelet seeding ending as the leaflet closure phase begins. As with the adult flow case, the simulation covers all of systole, leaflet closure, and early diastole with a total simulation time of 360ms out of the 666ms cardiac cycle. This 360ms time period of simulation is the same fraction of the cardiac cycle as modeled in the adult flow case.

The platelets are released slightly further upstream (1.25D compared to 1D for the adult case) of the valve so that they do not exit the domain during the simulation. Figure 7-2 demonstrates the initial seed position of 300 platelets, followed by the final distribution of all 5400 platelets at the end of the simulation.

(a) Initial seed of 300 platelets

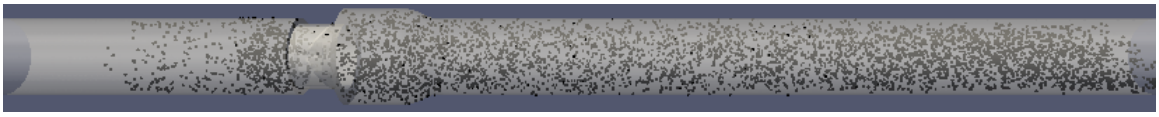

(b) Final distribution of 5400 platelets

Figure 7-2: (a) 300 platelets seeded 1.25 diameter upstream of valve at start of simulations, (b) 5400 platelets at end of simulation of 360ms.

7.1.2 Flow physics

As the peak flow Reynolds number of the child case (Re = 4418) is less than that of the adult flow case (Re = 5780), some flow field differences are expected. It is observed that for leaflet opening and early acceleration, the flow fields are qualitatively similar. This is due to the low Reynolds numbers of leaflet opening in both cases. For peak flow, however, the adult flows show more small-scale eddies and disorganized flow downstream of the valve (figure 7-3a). The vortex shedding past the leaflets breaks into smaller eddies that also interact with the sinus recirculation, as described in detail in chapter 5. The peak flow field for the child case (figure 7-3b) demonstrates vortex wakes past the leaflet tips, but less breakdown of coherent vortices into small-scale eddies. A sinus recirculation region is present in both peak flows, but with stronger and wider recirculation zones in the adult flow case. The leaflet wake vortices in the child case are more coherent, with less mixing with the sinus region, and lower overall recirculation. The vorticity animation of the child flow simulation is given in animation 7-1.

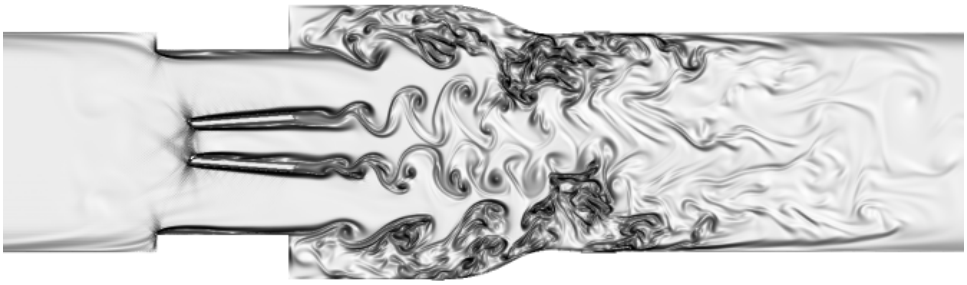

(a) Adult

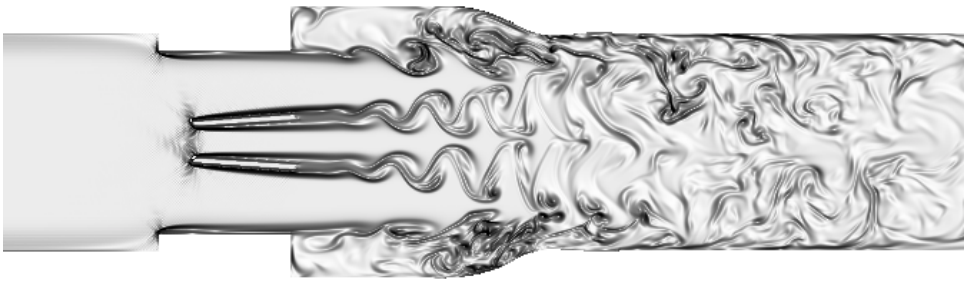

(b) Child

Figure 7-3: 2D vorticity magnitude plots of peak flow for (a) adult flow, (b) child flow

Although the vorticity fields are different at peak flows, these differences are not immediately apparent upon comparison as even the child flow case has some small-scale flow structures. Observing the viscous shear stress fields (animation 7-2), the child case shows higher shear stress magnitudes in the flow field downstream of the valves. This is particularly apparent immediately downstream of the leaflet tips and at the sinus step expansion (figure 7-4). Although the adult case is associated with many small-scale structures and velocity fluctuations, the shear stresses of these small eddies is lower than the shear stresses of the more coherent vortices in the child case. It should be noted that although the peak Reynolds number of the child flow case is lower than the adult case, the peak inlet flow velocity (based on peak flowrate and chamber diameter) is 17% higher for the child case. These flow field differences will be explored in section 7.3.2.

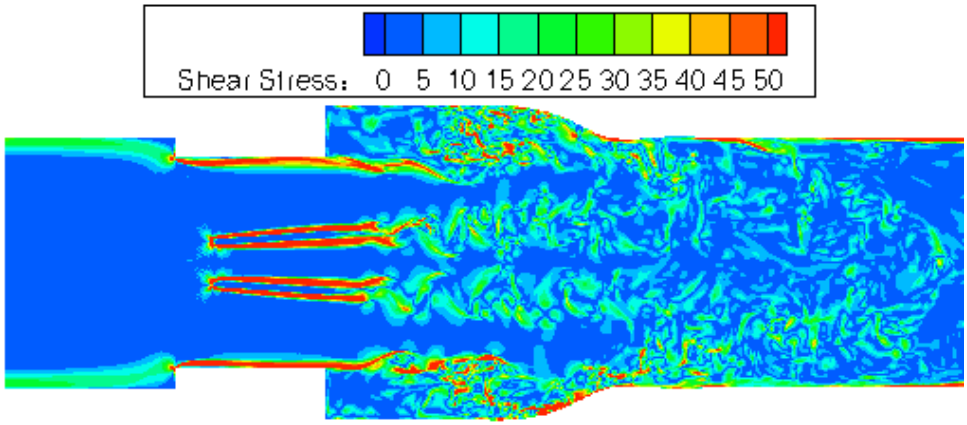

(a) Adult

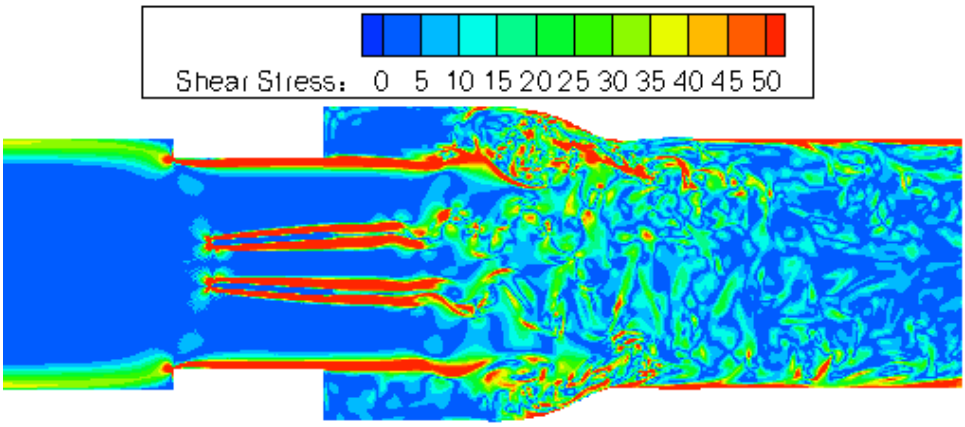

(b) Child

Figure 7-4: Viscous shear stress fields at peak flow for (a) adult flows, (b) child flows

7.1.3 Bulk blood damage

After 360ms of simulation, the released platelets are well distributed throughout the entire flow domain. The average BDI for all 5400 platelets is 0.342 dynes•s/cm^2 with a standard deviation of 0.238 dynes•s/cm^2. Though these blood damage simulations represent one-pass scenarios for BMHV flow, it should be noted that the higher heart rate for the child case results in a shorter exposure time for all platelets. Even with this shorter

overall exposure time for platelets in the child case, the average accumulated damage value is 53% higher than for the adult flow case.

A histogram of BDI for all 5400 platelets after 360ms of simulation is plotted (figure 7-5) representing all of systolic flow and early diastole with interval spacing of 0.05 dynes•s/cm^2, with a comparison to the adult damage distribution. The histogram demonstrates qualitative similarity to the adult case where distribution is skewed to lesser damage. Almost 1400 platelets have damage values between 0.15 and 0.25 dynes•s/cm^2.

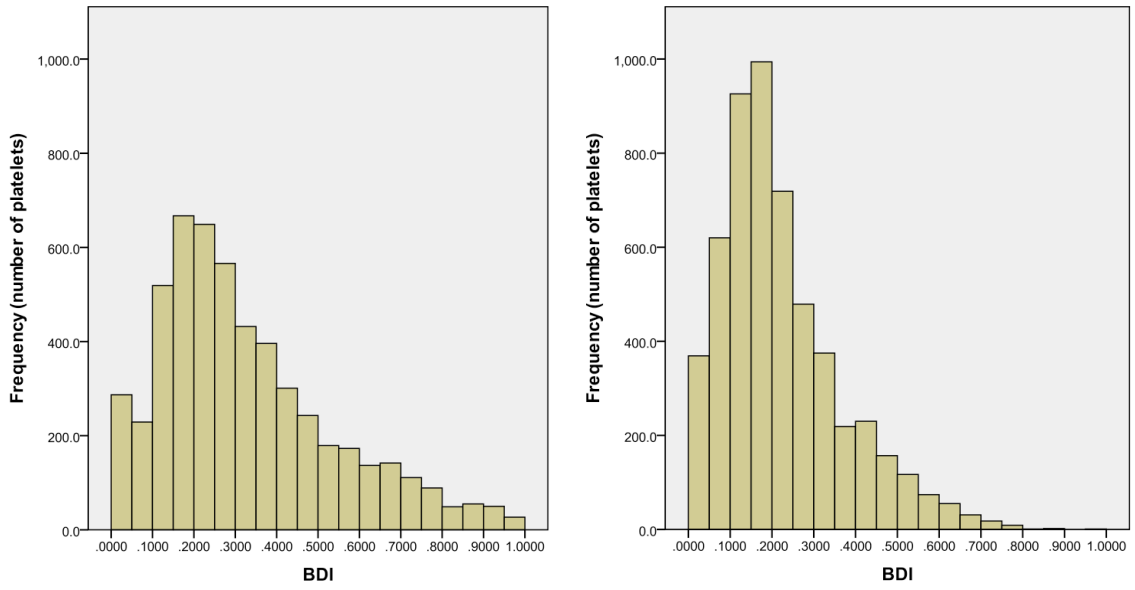

(a) 5-year old child (b) Adult

Figure 7-5: BDI histogram for 5400 platelets after (a) 360ms of damage accumulation for 5-year old child, (b) 460ms of damage accumulation for adult. Interval 0.05 dynes•s/cm^2, with BDI values over 1.0 dynes•s/cm^2 not shown.

For higher levels of accumulated damage, the child flow case shows a larger number of platelets in these ranges as compared to the adult case. The maximum platelet damage for the child case is 1.77 dynes•s/cm^2, which is lower than the maximum for the

adult case at 3.60 dynes•s/cm^2. However, it is noted that only 4 out of 5400 platelets (0.07%) for the adult case have accumulated damage higher than 1.0 dynes•s/cm^2. For the child case, 99 of 5400 platelets (1.83%) have damager higher than this level. Although there is a greater number of platelets with high accumulated damage, these values are still below the minimum platelet activation threshold of 10.0 – 35.0 dynes•s/cm^2 [25] and are thus not in danger of activation for one flow through a BMHV.

For the platelet distribution by region, 3879 of the 5400 platelets (71.8%) advect downstream of the sinus expansion to the aortic side. 697 platelets (12.9%) remain in the sinus expansion region, and only 114 platelets (2.1%) are in the valve region. 710 platelets (13.1%) are on the ventricular side, similar to the number of platelets (732) for the adult flow case. Compared to the adult flow distribution, more platelets (71.8% vs. 63%) advect downstream of the sinus expansion for the child flow, and less platelets remain in the valve or sinus expansion regions. In the adult flow case, the sinus region has average damage 62% higher than in the valve. However for the child flow case, the average damage in the sinus expansion is only 1.5% higher than for the valve region.

Table 7-2: Platelet and BDI distribution by region – 5-year old child

	Overall		Top 10%		Top 1%	
Region	# platelets	BDI average (dynes s / cm^2)	# platelets	BDI average (dynes s / cm^2)	# platelets	BDI average (dynes s / cm^2)
Overall	5400	0.3416	540	0.8662	54	1.286
Ventricular side	710	0.1066	13	0.9259	3	1.197
Valve	114	0.4441	22	0.8727	2	1.315
Sinus expansion	697	0.4512	128	0.9056	18	1.343
Aortic side	3879	0.3619	376	0.8526	31	1.260

The top 1% and 10% of damaged platelets in the child flow simulation by region is also shown in table 7-2. For the top 10% damaged platelets, the ventricular region interestingly has the highest average damage. For the top 1%, the sinus region has the highest average damage. Although high damage averages are found throughout the domain, the large majority of the top damaged platelets are located in the aortic chamber. This demonstrates that although the damage values are higher for the child flow case as compared to adult flow cases, most of the damaged platelets are swept into the aortic chamber.

7.1.4 Eulerian view

As with the adult flow case, the flow domain is discretized into small cubic regions. For the child case, these regions are of size 1.64mm x 1.64mm x 1.64mm. The same methodology for creating the BDI contour plot is employed for the child case, with a 3D contour maximum of 0.5 dynes•s/cm^2.

For blood damage at peak flow (Re = 4418), 3300 platelets have been released in the domain (figure 7-6). Many platelets have advected downstream at this peak flowrate, and high damage regions are highlighted within the sinus expansion region and the beginning of the aortic chamber region. The corresponding flow visualization shows vortex shedding past the leaflet tips with few small eddies. However, there is mixing in the sinus expansion region, similar to the adult flow case.

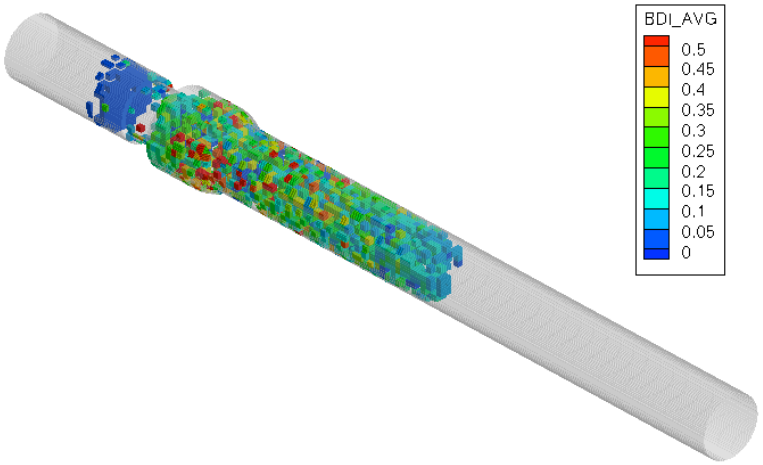

(a) BDI contour plot

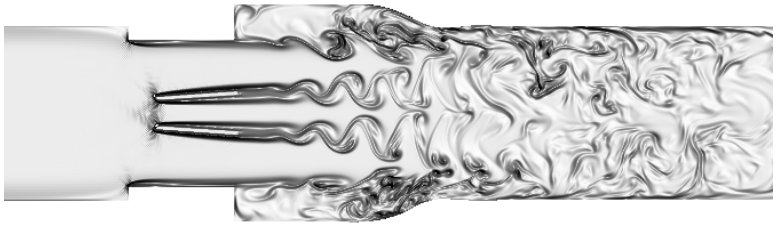

(b) 2D vorticity

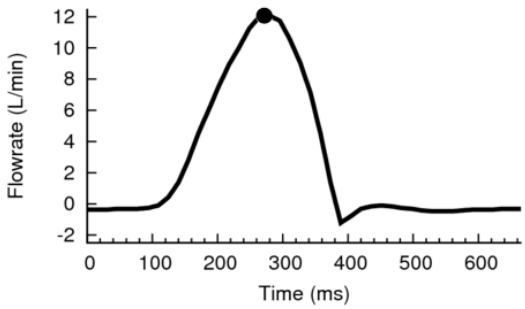

(c) Flowrate time point

Figure 7-6: (a) BDI contour plot, (b) corresponding 2D vorticity plot, and (c) flowrate curve at peak flow (Re = 4418), 3300 platelets

Blanking all regions with damage accumulation average lower than 0.5 dynes•s/cm^2 shows potential danger regions at this peak flowrate. High damage regions

are found primarily in the sinus expansion and aortic downstream chamber (figure 7-7). High damage regions are also observed in the valve region. At peak flow of the adult flow case, no damage regions exist with average damage higher than 0.5 dynes•s/cm^2.

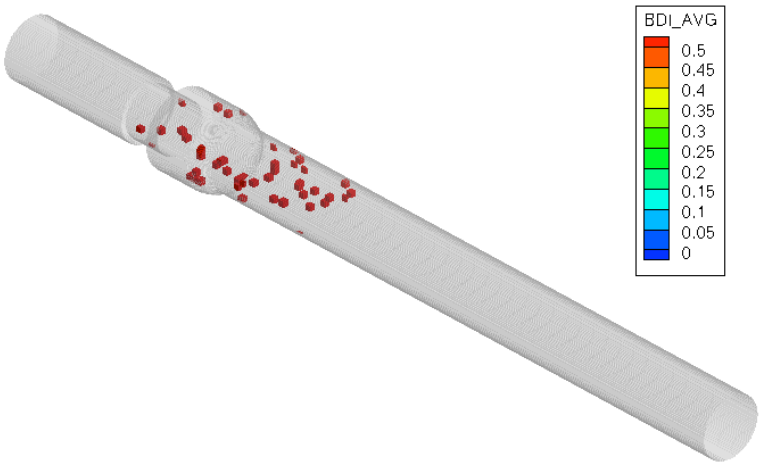

Figure 7-7: BDI contour plot at peak flow (Re = 4418), 3300 platelets. Contours blanked if damage less than 0.5 dynes•s/cm^2

At leaflet closing (Re = 0) at the end of systole, all 5400 platelets have been released in the domain. The BDI contour plot (figure 7-8) shows high damage regions throughout the entire sinus expansion region and the downstream aortic chamber. Some moderate damage regions are also observed in the upstream ventricular chamber.

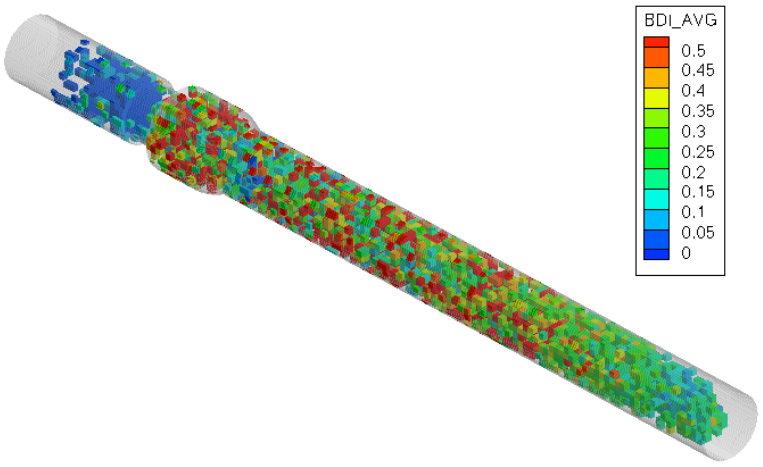

(a) BDI contour plot

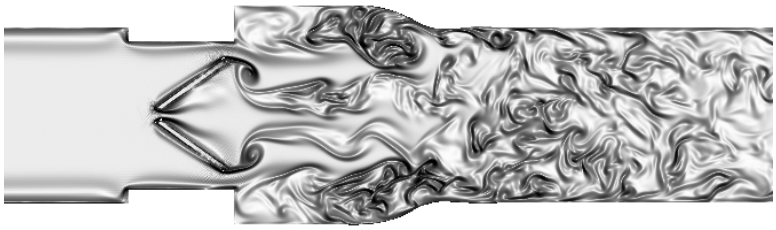

(b) 2D vorticity

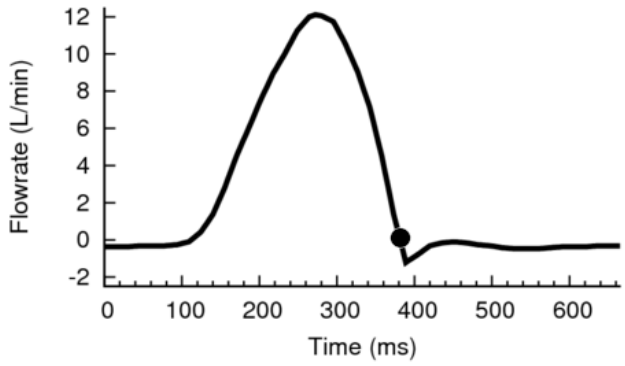

(c) Flowrate time point

Figure 7-8: (a) BDI contour plot, (b) corresponding fluid vorticity plot, and (c) flowrate curve at leaflet closing flow (Re = 0), 5400 platelets

Figure 7-9a shows leaflet closing with threshold blanking at 0.5 dynes•s/cm^2, and demonstrates a large number of damage regions filling the entire sinus expansion region as well as along the length of the aortic downstream region. No high damage regions are observed within the valve.

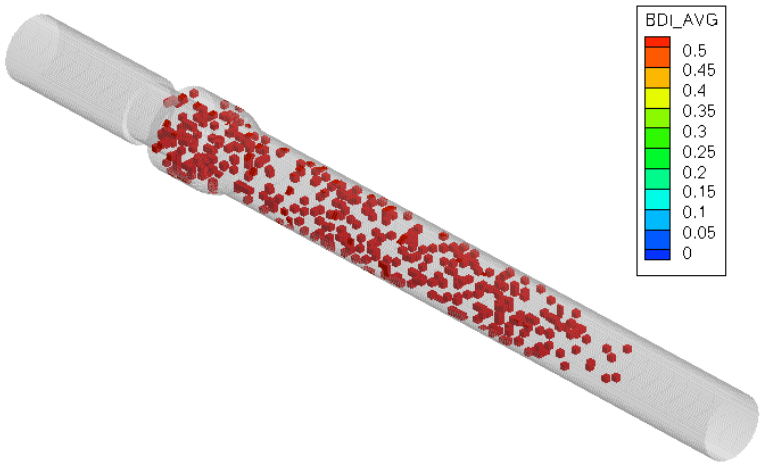

(a) Contour blanking at 0.5 dynes•s/cm^2

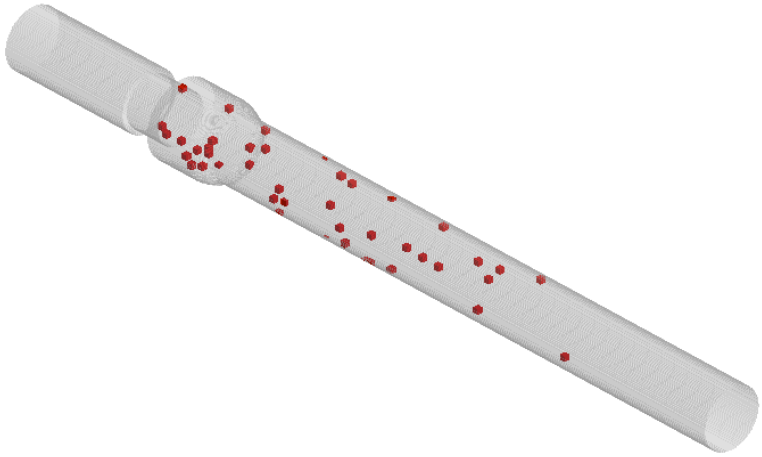

(a) Contour blanking at 1.0 dynes•s/cm^2

Figure 7-9: BDI contour plot at leaflet closing flow (Re = 0), 5400 platelets. Contours blanked if damage less than (a) 0.5 dynes•s/cm^2 (b) 1.0 dynes•s/cm^2

Higher blanking at 1.0 dynes•s/cm^2 is shown in figure 7-9b. This figure shows high damage regions occurring throughout the sinus expansion region and in the aortic downstream chamber. This figure demonstrates that for the child case, high damage regions are not restricted to the sinus expansion region but can occur for platelets that have been advected beyond the sinus.

The simulation ends after 360ms of modeling, representing full leaflet closure and the early-to-mid diastolic phase (Re = 75 in reverse flow). Figure 7-10 shows the platelet damage distribution throughout the domain, again demonstrating high damage regions existing throughout the sinus expansion and downstream aortic regions, as well as in the valve region. The corresponding flow field shows most of the vortical structures have dissipated at this stage.

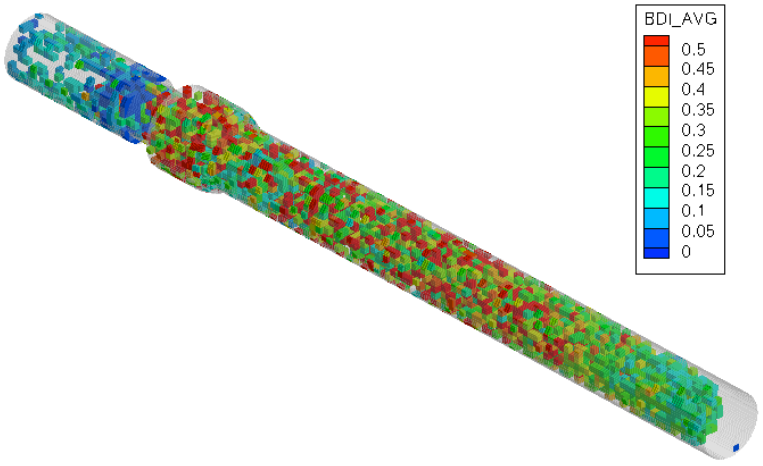

(a) BDI contour plot

(b) 2D vorticity

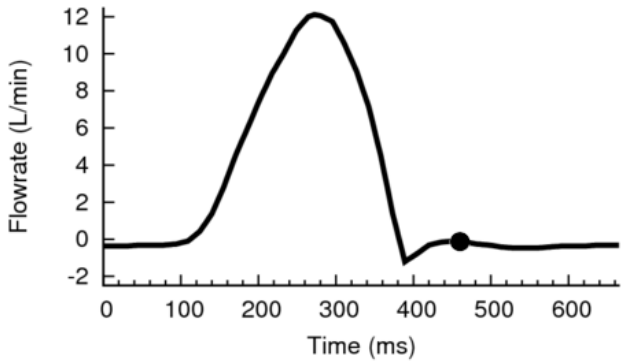

(c) Flowrate time point

Figure 7-10: (a) BDI contour plot, (b) corresponding fluid vorticity plot, and (c) flowrate curve at early-to-mid diastolic flow (Re = 75 in reverse flow), 5400 released platelets

Blanking plots are shown at the end time point of the simulation (figure 7-11) after 360ms of simulation. This again demonstrates a larger number of high damage regions throughout the domain with many located in the aortic chamber. The ventricular upstream region also contains some higher damage regions in this BDI threshold plot, even greater than 1.0 dynes•s/cm^2. It is important to emphasize that this large number of high accumulated damage regions occur for the child case with a shorter exposure time of platelets when compared to the adult case (360ms vs. 460ms).

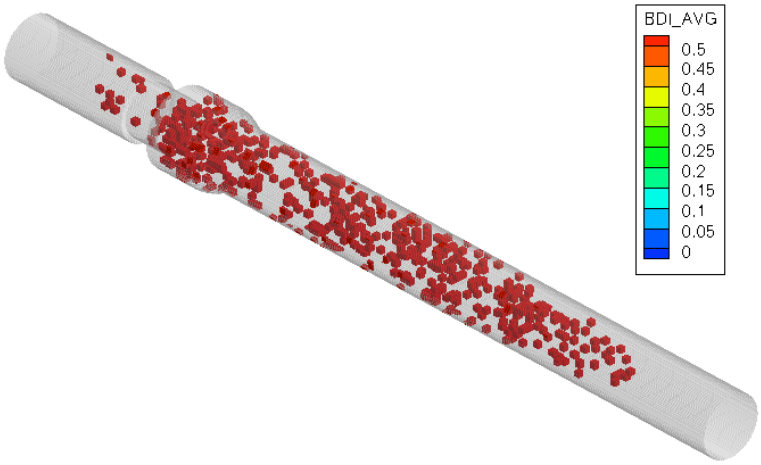

(a) Contour blanking at 0.5 dynes•s/cm^2

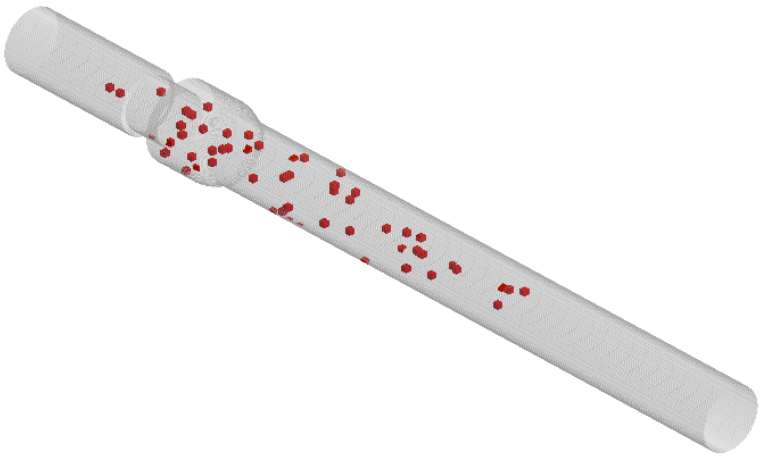

(b) Contour blanking at 1.0 dynes•s/cm^2

Figure 7-11: BDI contour plot at end simulation time point (Re = 75 in reverse flow), 5400 platelets. Contours blanked if damage less than (a) 0.5 dynes•s/cm^2 (b) 1.0 dynes•s/cm^2

7.1.5 Lagrangian view

At the end simulation time point (early diastole), the twenty platelets with highest accumulated damage are determined along with their final location. For the 5-year old child, 10 of 20 are located in the aortic downstream chamber, 9 of 20 are located in the

sinus expansion, and 1 is located in the valve. A major difference with the adult flow case is the location of the highest damaged platelets in the aortic downstream chamber for the child flow case. Four of the top 10 most damaged platelets, including the most damaged platelet overall, are located in the downstream aortic chamber for the 5-year old child simulation. For the adult case, none of the top 12 most damaged platelets are located in the aortic downstream chamber.

The most damaged platelet is tracked to observe its damage patterns as it flows through the domain. A platelet flowing through the valve, but traveling with low velocity close to the valve housing walls is shown in Figure 7-12. Here the platelet incurs moderate levels of damage (8 – 10 dynes/cm^2), but continuously, as it travels very close to the valve walls. The corresponding vorticity field shows the near-wall shear region that the platelet is caught within. The viscous shear stress field also shows this near-wall shear region. As there is no flow separation, the platelet is not swept away from the wall but instead travels slowly along this wall shear region with high levels of platelet damage.

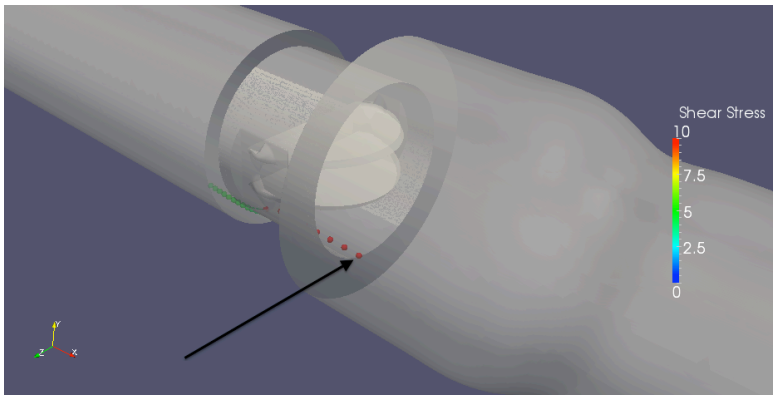

(a) Angled view

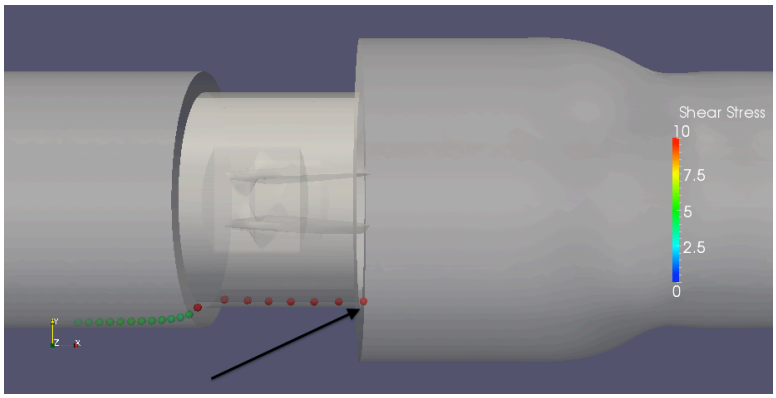

(b) Perpendicular view

(c) 2D vorticity

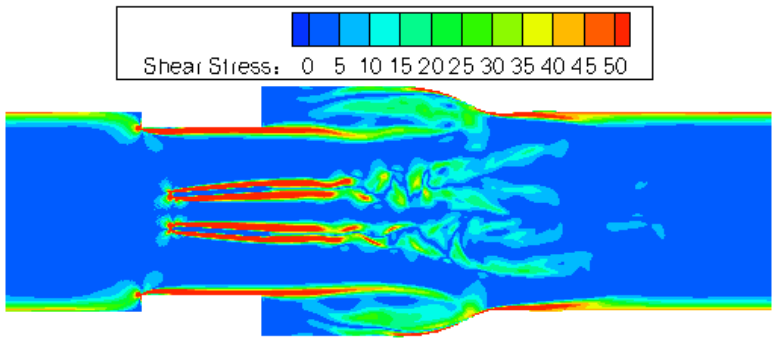

(d) Shear stress field

Figure 7-12: Platelet trail close to the valve housing wall with high levels of damage (a) 3D angled view, (b) perpendicular viewpoint, (c) corresponding vorticity field, (d) shear stress field (dynes/cm^2)

Figure 7-13 shows a time point just 25ms later, as the platelet is quickly swept into the sinus expansion region. Though only a short time later, the strong flow through

the valve explains the quick axial translation of the platelet, as seen by the wider spacing of the particle trail. The corresponding vorticity and shear stress fields show the high shear region caused by vortex shedding past the sinus expansion step. This leads to the moderate levels of platelet damage (8 – 12 dynes/cm^2) that is continuously incurred by this platelet. However, it is interesting to note that unlike the adult flow case, the platelet does not continue to recirculate in the sinus expansion. Instead, it is quickly swept out of the expansion region and into the aortic downstream region. This could be due to the weaker recirculation region for this child flow case as compared to the strong recirculation region of the adult flow case.

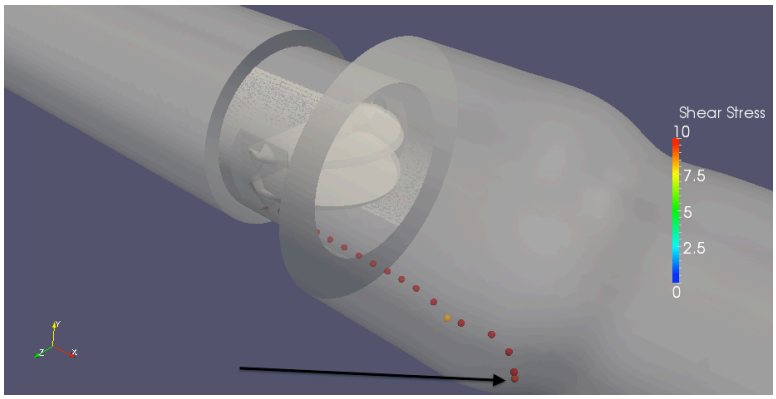

(a) Angled view

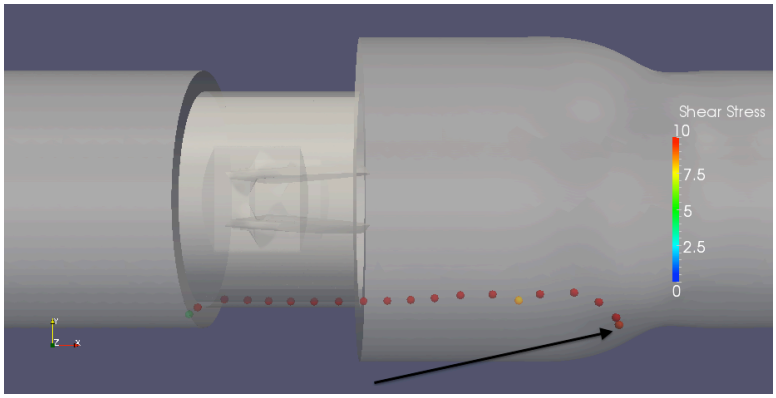

(b) Perpendicular view

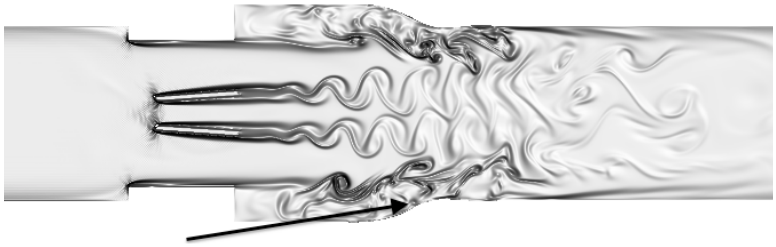

(c) 2D vorticity

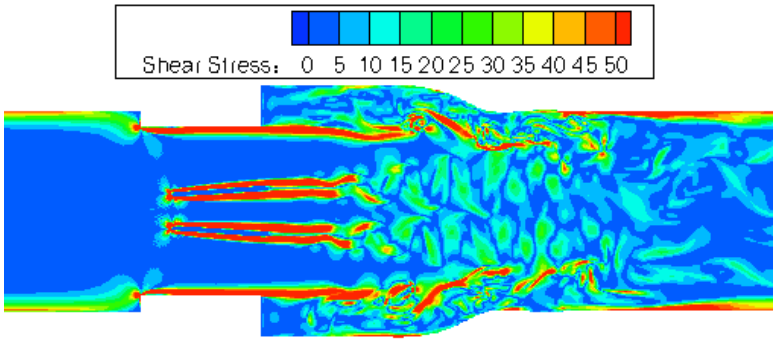

(d) Shear stress field

Figure 7-13: Platelet trail with high levels of damage while sweeping through sinus region (a) 3D angled view, (b) perpendicular viewpoint, (c) corresponding vorticity field, (d) shear stress field (dynes/cm^2)

After being swept into the aortic downstream chamber, the platelet travels slowly along the aortic chamber wall as shown in figure 7-14. This time point is taken 62ms later and shows a trail of high platelet damage. The corresponding flow and shear stress fields also show near-wall shear regions, which are caused by the vortex shedding in the sinus expansion region traversing into the aortic downstream chamber. This shear region causes high platelet damage but does not sweep the platelet away from the walls, as this region is kept close to the wall. At this time period, the platelet experiences higher levels of instantaneous damage (12 – 22 dynes/cm^2).

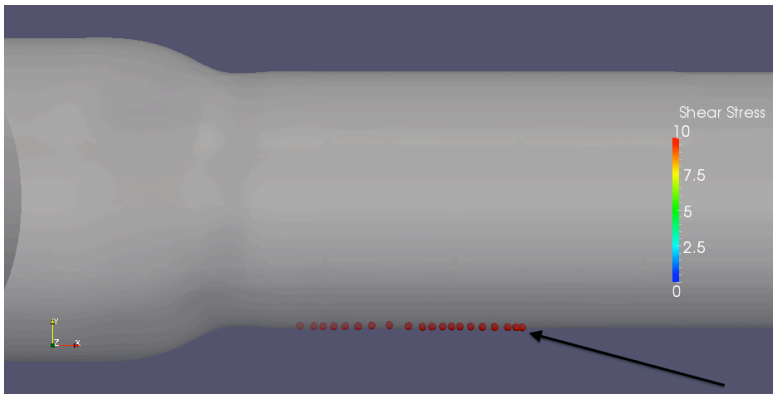

(a) Angled view

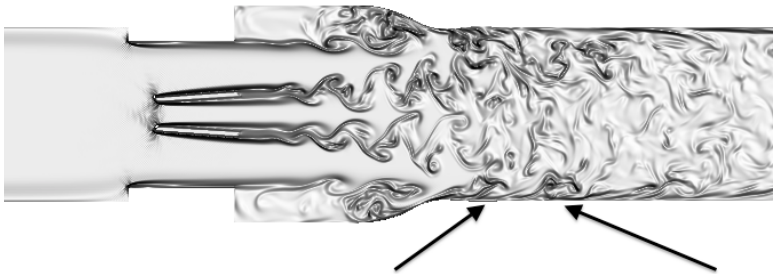

(b) 2D vorticity

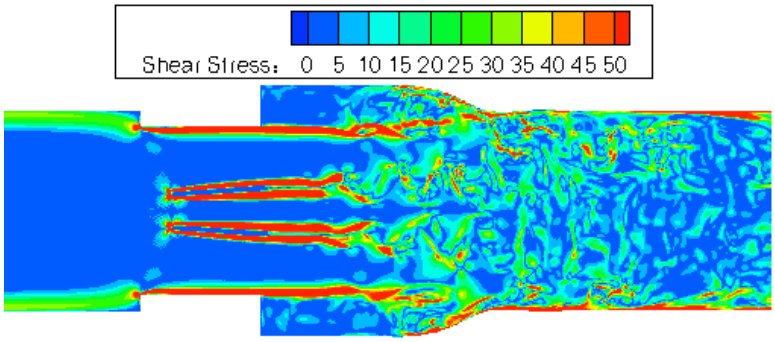

(c) Shear stress fields

Figure 7-14: Platelet trail with high levels of damage while traveling along aortic downstream wall (a) perpendicular viewpoint, (b) corresponding vorticity field, (c) shear stress field (dynes/cm^2)

Figure 7-15 shows the time history of damage accumulation for this most damaged platelet for the child flow case. This figure shows a gradual increase in damage accumulation throughout the simulation, representing the three different highlighted time periods of moderate to high levels of platelet damage. No instantaneous levels of damage are experienced by the platelet greater than 22 dynes/cm^2, but the continuous damage throughout this platelet trail leads to high overall accumulated damage.

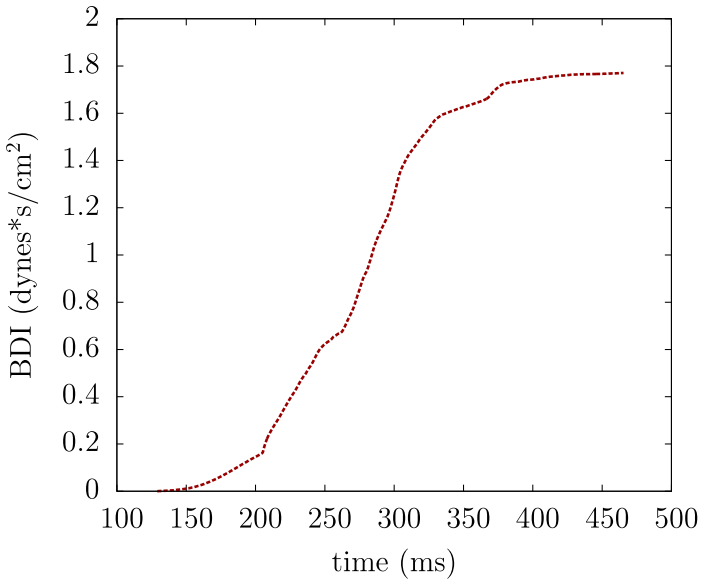

Figure 7-15: Platelet damage accumulation versus time for most damaged platelet for 5-year old child flow case

7.2 Pediatric Case #2 - Infant

Flow conditions for the infant subpopulation are taken from literature [106, 109-113] and consultation with clinicians, similar to the data taken for the child subpopulation. Infants are defined clinically as 1 month to 1 year of age [106], during which there is a large period of growth. The age of 6-months is chosen for modeling, though prosthetic valve implantation at this age is not common. However, as this flow

case is very different from a physiologic adult case, it is chosen to demonstrate a more "extreme" scenario. The overall flow conditions are listed in table 7-3.

Table 7-3: Flow conditions for 6-month old infant with comparisons to adult conditions

Age	Valve Size (mm)	Systolic %	Heart rate (bpm)	Cardiac output (L/min)	Left side MAP (mmHg)	Right side MAP (mmHg)
18+ years	21.4	40%	70	5.0	93	20
6 months	9	50%	120	1.25	55	20

7.2.1 Flow conditions and numerical setup

A 500ms cardiac cycle with an average flowrate of 1.25 L/min is modeled to match heart rate and cardiac output. Systolic flow duration of 250ms is modeled to match the 50% systolic flow duration for an infant. All platelets are modeled exactly as in the other two cases (adult, child) with the same shape (3D ellipsoid) and size (3μm major axis diameter) and with the same surface mesh (292 triangular elements).

As with the modeling of the 5-year old child, the exact geometry is taken from the physiologic adult case, but scaled down to fit the appropriate sizing of a 6-month infant. The spatiotemporal resolution of the child case simulation is 33.6μm and 1.08μs per numerical timestep.

The systolic duration is 50% for the infant case, as compared to 40% for the child and adult flow cases. Modifications are again made from physiologic adult conditions. First, the flowrate and leaflet motion time periods are scaled to a 500ms cardiac cycle compared to the 860ms adult cardiac cycle time period. The flowrate curve during systole is stretched to fit 50% systolic duration (250ms total systolic flow time). The

flowrate curve is then scaled in magnitude until the desired cardiac output of 1.25 L/min is reached. The leaflet motion curve is also stretched to fit the increased systolic duration. These curves are shown in figure 7-16. A peak flowrate of 4.8 L/min is determined after flow curve scaling, which corresponds to a peak Reynolds number of 2725 for infant flow.

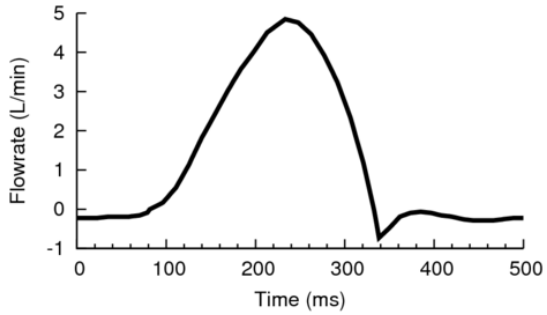

(a) Flowrate variation

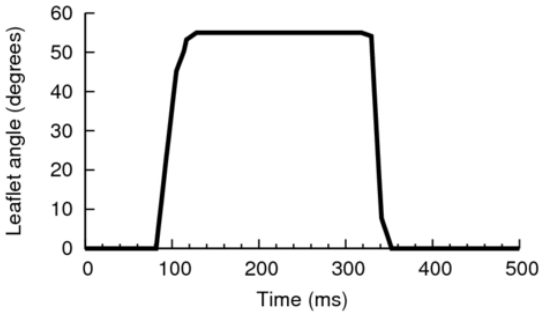

(b) Leaflet angle variation

Figure 7-16: Flowrate and leaflet variation for one cardiac cycle for a 6-month old infant

As with the adult and child cases, 5400 platelets are released during the systolic flow phase. 300 platelets are released every 11.6ms in order to reach the same 5400 number of platelets in the suspension as with adult flow modeling. These platelets are seeded 300 at a time with randomized cross-sectional position and angular orientation, with platelet seeding ending as the leaflet closure phase begins. The simulation covers all

of systole, leaflet closure, and early diastole with a total simulation time of 317ms out of the 500ms cardiac cycle. Again, this is the same fraction of the cardiac cycle simulated as the child and adult flow cases.

For the infant case, the domain is significantly smaller in size and the bulk flow velocities are higher. Platelets are released 1.25D upstream of the valve, as in the child flow case. However, as the domain is smaller, some platelets exit the domain during the simulation. These platelets do not continue to accumulate damage, but retain their final accumulated damage value upon leaving the flow domain. Figure 7-17 demonstrates the initial seed position of 300 platelets, followed by the distribution of 3997 platelets at the end of the simulation that have not exited the domain. Future simulations may be performed with a new geometry to extend the aortic chamber length so that platelets do not exit the domain.

(a) Initial seed of 300 platelets

(b) Final distribution of 3997 platelets

Figure 7-17: (a) 300 platelets seeded 1.25 diameters upstream of valve at start of simulations, (b) 3997 remaining platelets at end of simulation of 317ms.

7.2.2 Flow physics

The peak flow Reynolds number of the infant case (Re = 2725) is less than half of the adult flow case (Re = 5780), and thus very different flow fields are observed. Once again, for leaflet opening and acceleration, the flow fields are relatively similar due to the low Reynolds numbers of leaflet opening in both cases. At peak flow, the infant case does not demonstrate coherent vortex wakes past the leaflet tips, but rather a triple jet-like flow (figure 7-18b). The vorticity field does not show any small-scale structures, but a strong and coherent forward flow past the valve. The sinus region also shows very little mixing or recirculation zones, which is in stark contrast to the adult flow case. The flow past solid surfaces such as the leaflets and valve housing do not result in oscillating vortices as in the adult and child cases, but rather thin and confined fluid layers that extend far downstream of the valve. The vorticity animation is given in animation 7-3.

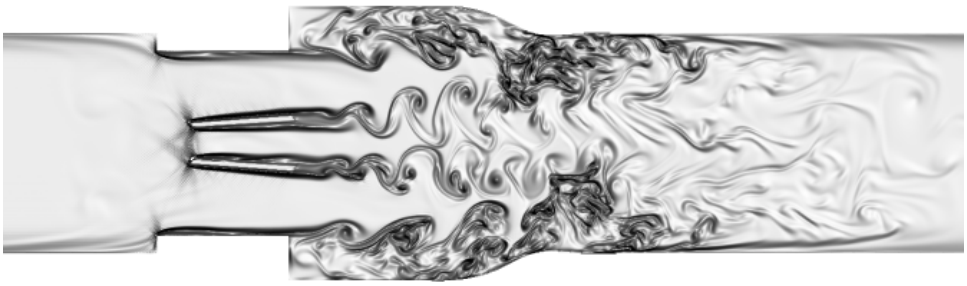

(a) Adult

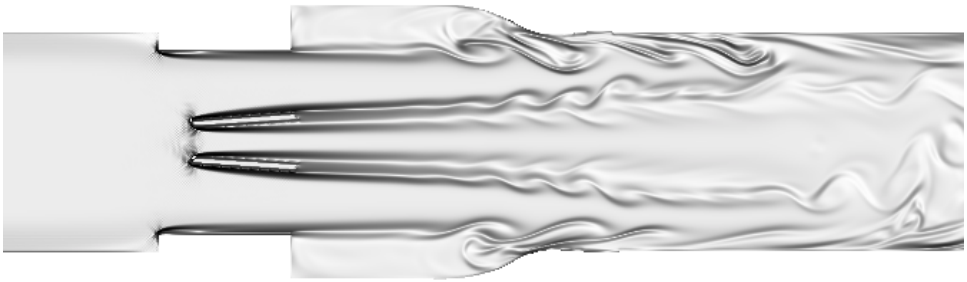

(b) Infant

Figure 7-18: 2D vorticity magnitude plots of peak flow for (a) adult flow, (b) infant flow

Observing the viscous shear stress fields (animation 7-4), the infant case shows much higher shear stress magnitudes in the flow field downstream of the valves. For flow past the leaflet tips and sinus step expansion, the coherent forward jets are associated with high shear stress magnitudes (figure 7-19). Again, though the adult case (figure 7-19a) is associated with many disorganized and small-scale structures, the shear stresses of these smaller eddies is much lower than the peak shear stresses in the infant flow case. The thin fluid shear layers for flow past solid surfaces for the infant case show very high viscous shear stress magnitudes. These layers spread in width downstream of the valve and eventually encompass the aortic chamber. It is noted that for the infant flow case, the peak inlet flow velocity (based on peak flowrate and chamber diameter) is 41% higher for the infant case. These flow field comparisons are explored in section 7.3.2.

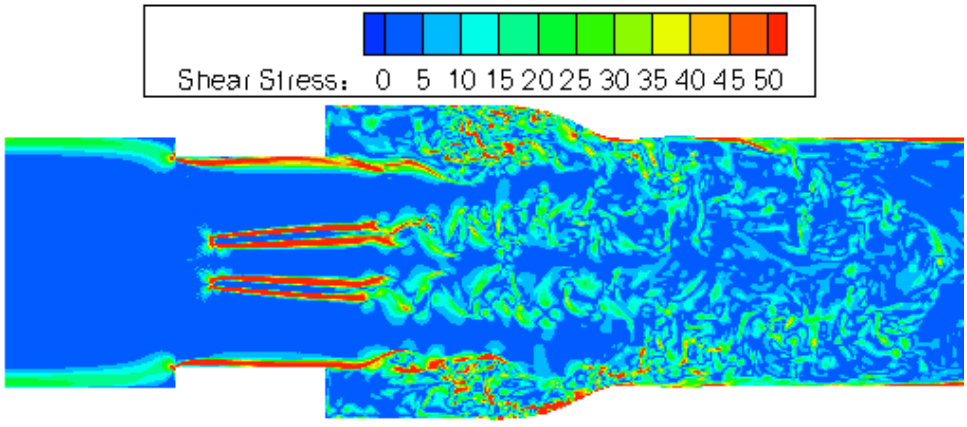

(a) Adult

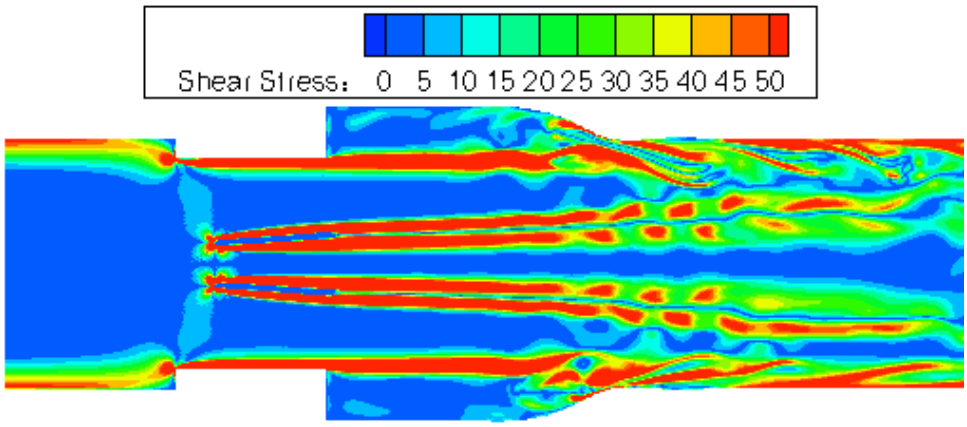

(b) Infant

Figure 7-19: Viscous shear stress fields at peak flow for (a) adult flows, (b) infant flows

At leaflet closing, the sudden impact with the valve housing shows stronger closing leakage jets for the infant case (figure 7-20). As the flow is more disorganized for the adult flow case, there are many vortical structures still present downstream of the valve at leaflet closing, which are not observed for the infant flow case. The vorticity magnitude of the impact jets is high for the infant case, both for the central b-datum jet and for the leaflet-valve impact jets.

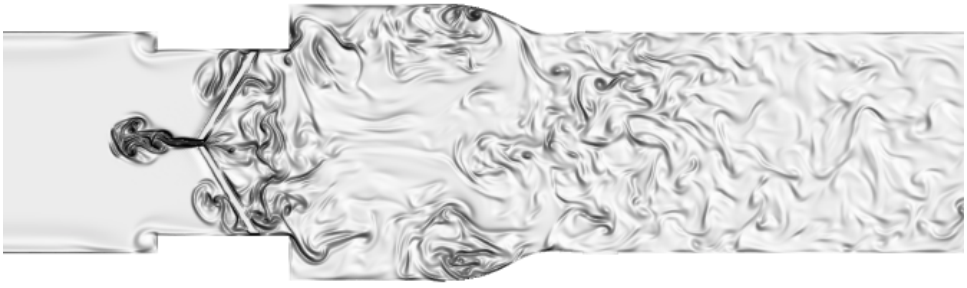

(a) Adult

(b) Infant

Figure 7-20: 2D vorticity magnitude plots of leaflet closing flow for (a) adult flow, (b) infant flow

For the shear stress fields at leaflet closing (figure 7-21), it is also observed that the infant case shows high shear stress magnitudes upon impact. This may be associated with the overall higher velocities in the infant flows as compared to the adult flows. However, it is important to note that leaflet closing is prescribed from modified adult flow data. It is quite possible that the dynamics of leaflet closing are different for the infant flow case, particularly as the leaflet size may not be scaled linearly for pediatric valves. This warrants further investigation in order to accurately model leaflet closing and leaflet impact jets in pediatric flows. For modeling modified curves from adult flows, however, the infant case shows markedly higher shear stresses at leaflet closing throughout the entire flow field.

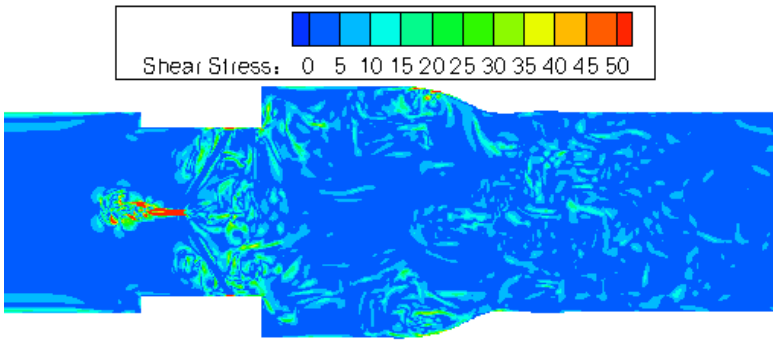

(a) Adult

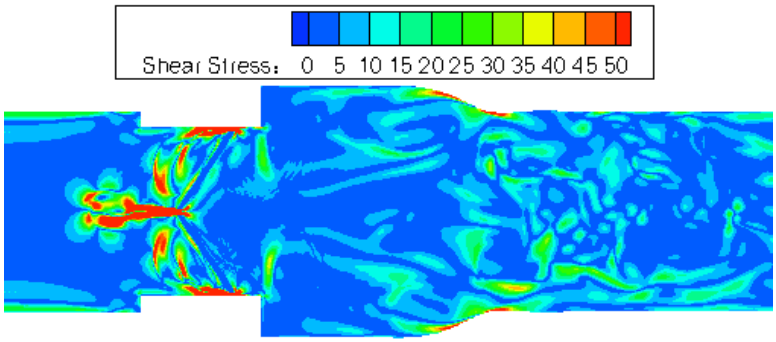

(b) Infant

Figure 7-21: Viscous shear stress fields at leaflet closing for (a) adult, (b) infant flows

7.2.3 Bulk blood damage

After 317ms of simulation, only 3997 (74%) of the seeded platelets remain in the flow domain (figure 7-17). The average BDI for all 5400 platelets is 0.4186 dynes•s/cm^2 with a standard deviation of 0.287 dynes•s/cm^2. This average damage value is higher than both the adult and child flows. It is important to note this higher average damage occurs with shorter overall exposure time for platelets. In addition, many platelets (26%) do not continue to accumulate damage upon exiting the flow domain. Figure 7-22 shows a histogram of BDI for all 5400 platelets after 317ms of simulation, representing all of systolic flow and early diastole, with interval spacing of 0.05 dynes•s/cm^2 and a

comparison to the adult damage distribution. The overall damage distribution is still skewed towards lesser damage but less than for the adult or child scenarios.

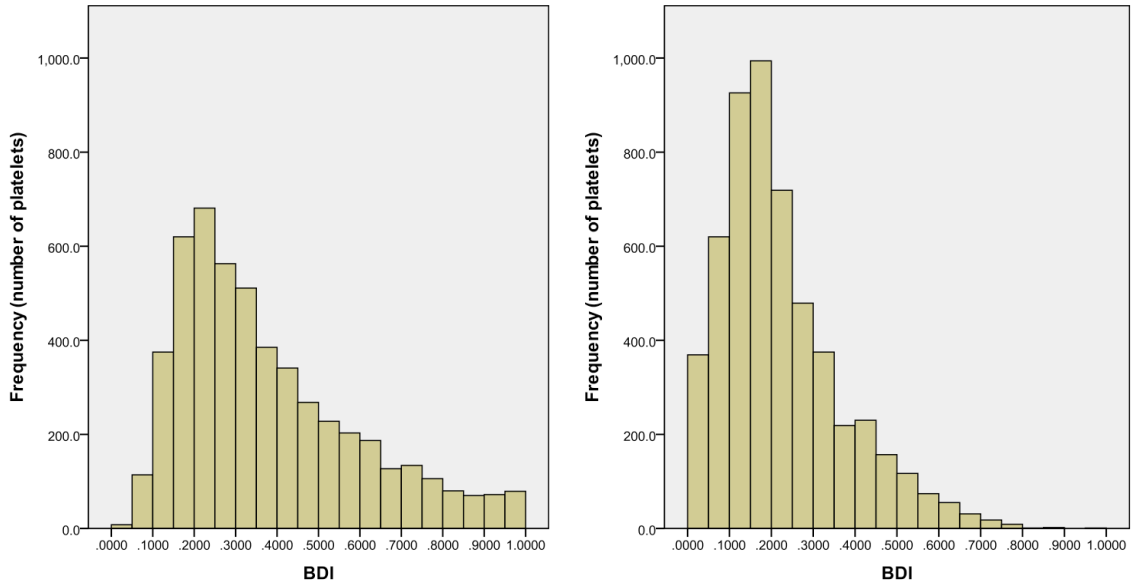

(a) Infant flow case (b) Adult flow case

Figure 7-22: BDI histogram for 5400 platelets after (a) 317ms of damage accumulation for 6-month old infant, (b) 460ms of damage accumulation for adult. Interval 0.05 dynes•s/cm^2

The maximum platelet damage for the infant case is 2.29 dynes•s/cm^2, which is lower than the maximum for the adult case at 3.60 dynes•s/cm^2 but higher than the maximum value for a child (1.77 dynes•s/cm^2). For the infant case, 248 of 5400 platelets (4.6%) have damage higher than 1.0 dynes•s/cm^2, more than both the child and adult flows. However, these values are below the minimum activation threshold of 10.0 – 35.0 dynes•s/cm^2 and are again not in danger of activation for one pass through a BMHV.

For the platelet distribution by region (table 7-4), 4380 of the 5400 platelets (81.1%) advect downstream of the sinus expansion to the aortic chamber. The sinus

region has the highest average damage, but contains only 10.5% of the released platelets. Although the aortic chamber has the second highest average damage by region, it contains significantly more platelets than the sinus region.

Table 7-4: Platelet and BDI distribution by region – 6-month old infant

	Overall		Top 10%		Top 1%	
Region	# platelets	BDI average (dynes s / cm^2)	# platelets	BDI average (dynes s / cm^2)	# platelets	BDI average (dynes s / cm^2)
Overall	5400	0.4186	540	1.070	54	1.698
Ventricular side	278	0.2239	8	1.059	1	1.479
Valve	174	0.3363	13	1.078	1	1.435
Sinus expansion	568	0.5059	81	1.034	6	1.739
Aortic side	4380	0.4229	438	1.076	46	1.703

The top 1% and 10% of damaged platelets for the infant flow case is also shown in table 7-4. Here, 81.1% of the top 10% most damaged platelets are located in the aortic chamber. For the top 1% of most damaged platelets, 85.2% are located in the aortic chamber. Although there are more highly damaged platelets in the infant flow, they are again located far from the valve where they may be less likely to form thrombi. This warrants further detail beyond a one-pass simulation, to be performed in future studies.

7.2.4 Eulerian view

The flow domain for the infant case is discretized into small cubic regions of size 1.05mm x 1.05mm x 1.05mm. The same methodology for creating the BDI contour plot is employed as in the adult and child flow cases, with a 3D contour maximum of 0.5

dynes•s/cm^2. As the seeding position is the same as the child flow case and the final BDI distribution is of interest, only the final timepoint of the Eulerian view is visualized.

The simulation ends after 317ms of modeling, representing full leaflet closure and the early-to-mid diastolic phase (Re = 115 in reverse flow). Figure 7-23a shows the platelet damage distribution throughout the domain, demonstrating high damage regions existing throughout the sinus expansion and downstream aortic regions. This is qualitatively very similar to the adult and child flow cases.

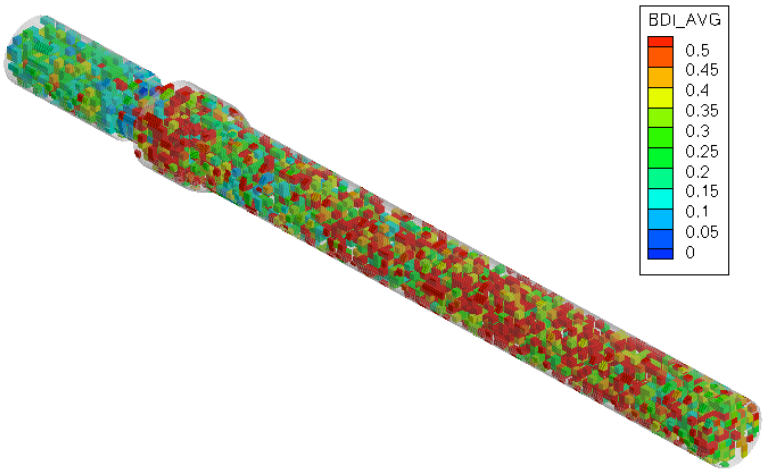

(a) BDI contour plot

(b) Contour blanking at 0.5 dynes•s/cm^2

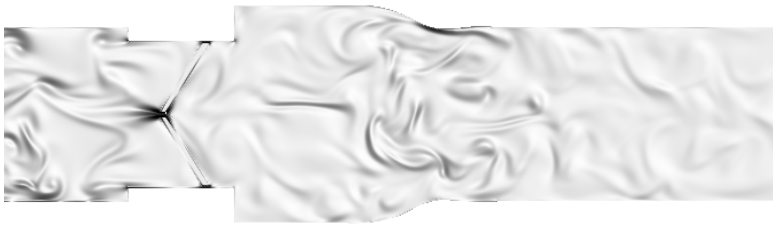

(c) 2D vorticity

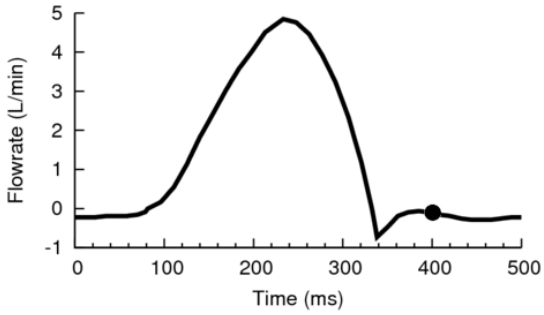

(d) Flowrate time point

Figure 7-23: (a) BDI contour plot, (b) regions blanked if damage less than 0.5 dynes•s/cm^2, (c) corresponding fluid vorticity plot, and (d) flowrate curve at early-to-mid diastolic flow (Re = 115 in reverse flow), 5400 released platelets

For the blanking plots (figure 7-23b), however, a larger number of high damage regions are observed throughout the entire domain. High damage regions fill the entire aortic chamber, extending to the computational outlet boundary. These high damage regions occur for the infant flow with a shorter exposure time of platelets when compared to the adult and child cases (317ms vs. 360ms child / 460ms adult). Although qualitatively similar to the child BDI contour plot, the infant case has a higher maximum damage value (2.29 vs. 1.77 dynes•s/cm^2) as well as a higher number of platelets with damage accumulation greater than 1.0 dynes•s/cm^2 (248 platelets vs. 99 platelets for child case).

7.2.5 Lagrangian view

The ten platelets with highest accumulated damage are determined for the 6-month old infant, with 9 of the 10 platelets located in the aortic downstream chamber. None of the most damaged platelets in the infant flow are observed to recirculate in time. The most damaged platelet for the infant case is caught in leaflet closing, and though this is not a common damage pathline, it is highlighted as a case of interest.

As the platelet flows in systole in the ventricular chamber, it travels with low velocity close to the walls (figure 7-24). This near-wall position is made clearer in the cross-sectional diagram. Here the platelet incurs moderate levels of damage (10 – 12 dynes/cm^2), but continuously for 60ms. Even though the flow in the ventricular chamber is upstream of the valve and not complex, the location of the platelet near the walls causes a high level of damage.

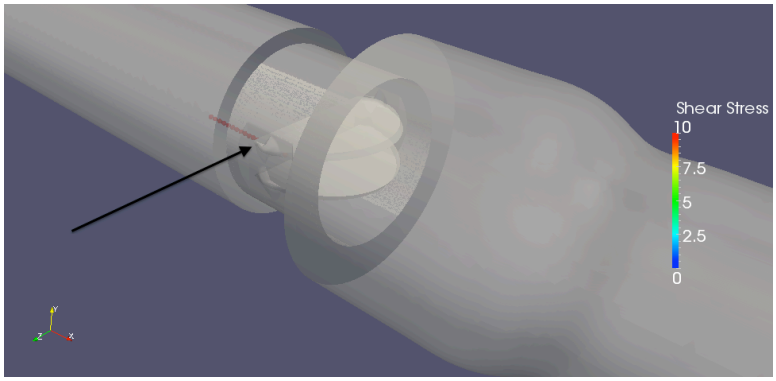

(a) Angled view

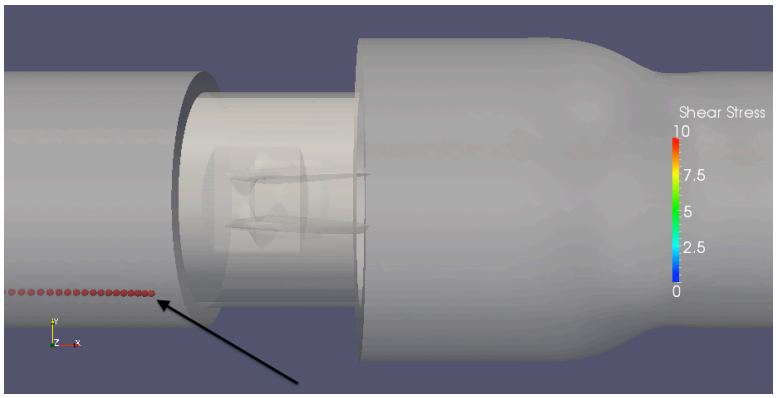

(b) Perpendicular view

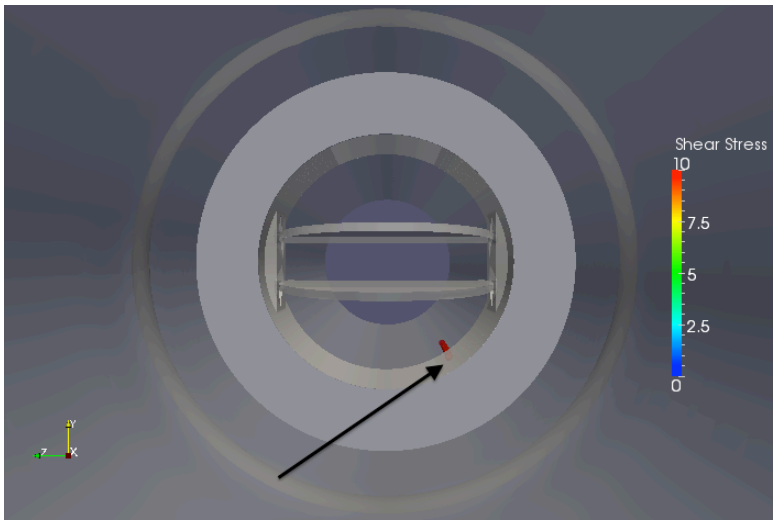

(c) Cross-sectional view

Figure 7-24: Platelet trail near ventricular wall with high levels of damage (a) 3D view, (b) perpendicular view, (c) cross-sectional view

At a time point 60ms later, the platelet travels very close to the valve housing wall, as clearly shown in the cross-sectional view (Figure 7-25). During this time period the platelet moves slowly along the valve housing wall and incurs high levels of instantaneous damage (10 – 60 dynes/cm^2) for a period of 27ms. This again highlights

the danger of platelets moving near the walls, as they can be caught in slow-moving shear regions as shown in the vorticity and viscous shear stress fields of figure 7-25.

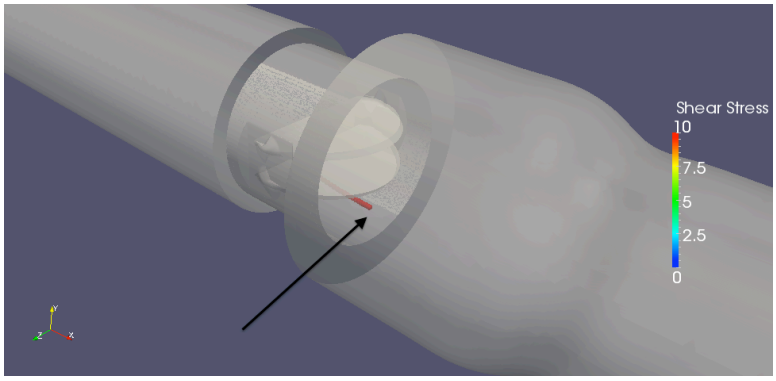

(a) Angled view

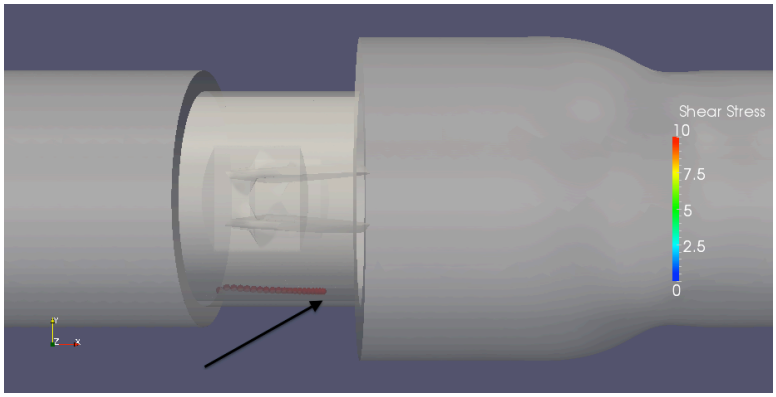

(b) Perpendicular view

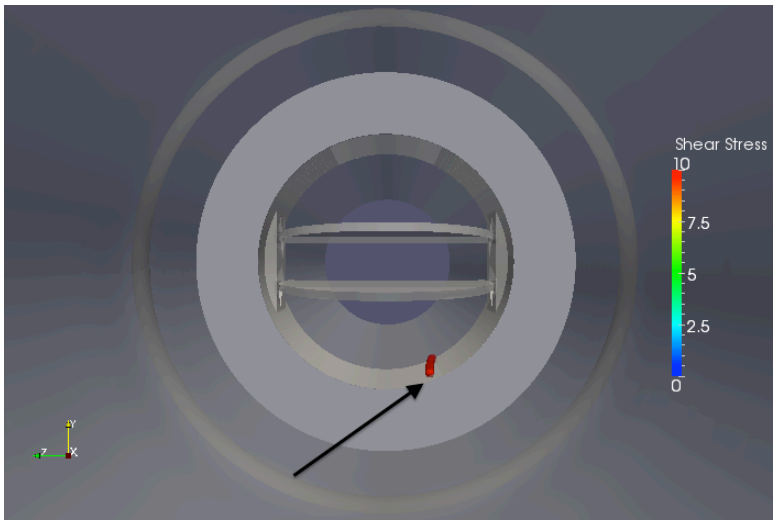

(c) Cross-sectional view

(d) 2D vorticity

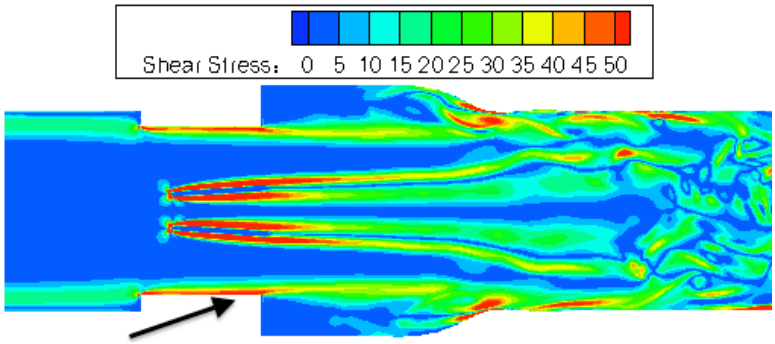

(e) Shear stress field

Figure 7-25: Platelet trail near valve housing wall with high levels of damage (a) 3D view, (b) perpendicular view, (c) cross-sectional view, (d) corresponding vorticity field, (e) corresponding shear stress field (dynes•s/cm^2)

This platelet experiences a last time period of high damage when the leaflets close. Figure 7-26 shows the platelet near the valve housing wall with the leaflets rapidly closing. The corresponding vorticity field shows a fast leaflet closing motion very close to the platelet. At this time point, the platelet is only experiencing a mild level of damage (2 – 3 dynes/cm^2).

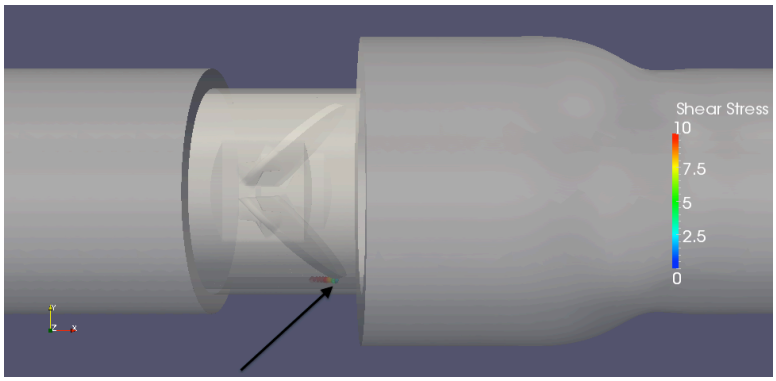

(a) Perpendicular view

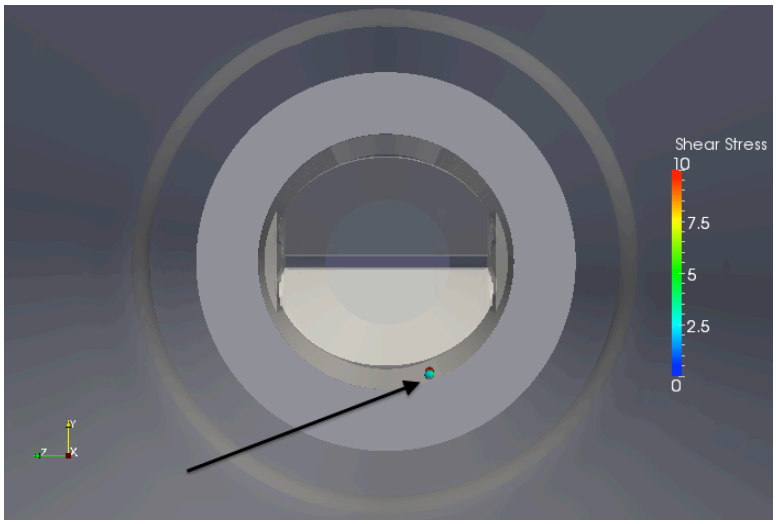

(b) Cross-sectional view

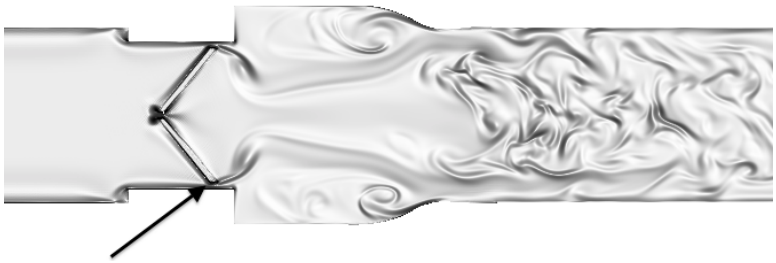

(c) 2D vorticity

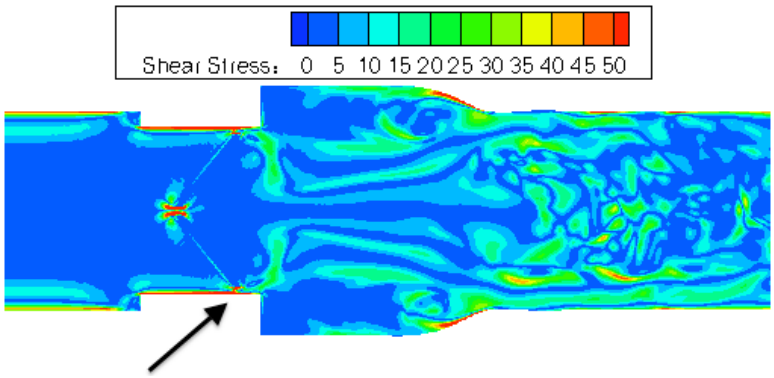

(d) Shear stress field

Figure 7-26: Platelet trail immediately before impact with closing leaflets (a) perpendicular view, (b) cross-sectional view, (c) corresponding vorticity field, (d) shear stress field

Only 5ms afterwards, the leaflets have impacted the valve housing and the platelet experiences a very high level of instantaneous damage (20 – 40 dynes/cm^2) as shown in figure 7-27. The platelet rapidly traverses upstream and is shown to be drifting along with the leaflet-valve impact jet towards the center of the valve. This is also shown in the corresponding vorticity and shear stress field.

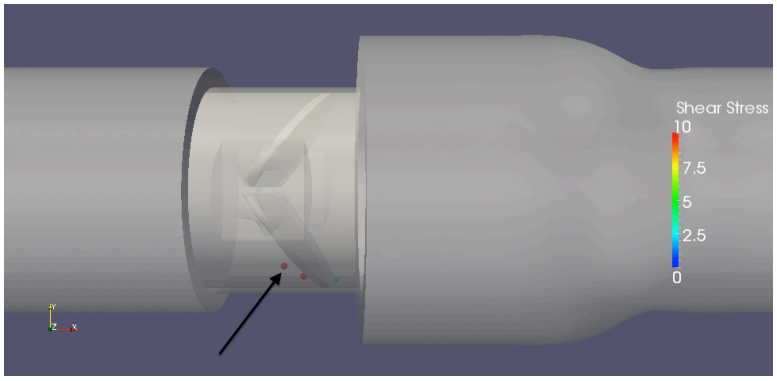

(a) Perpendicular view

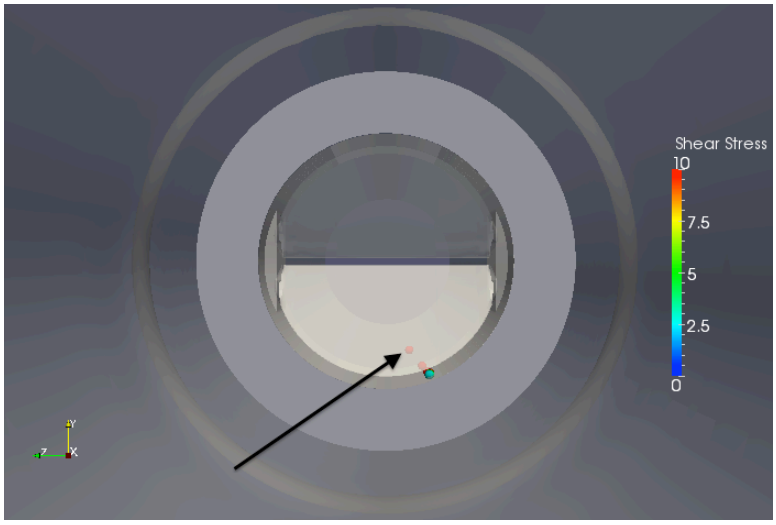

(b) Cross-sectional view

(c) 2D vorticity

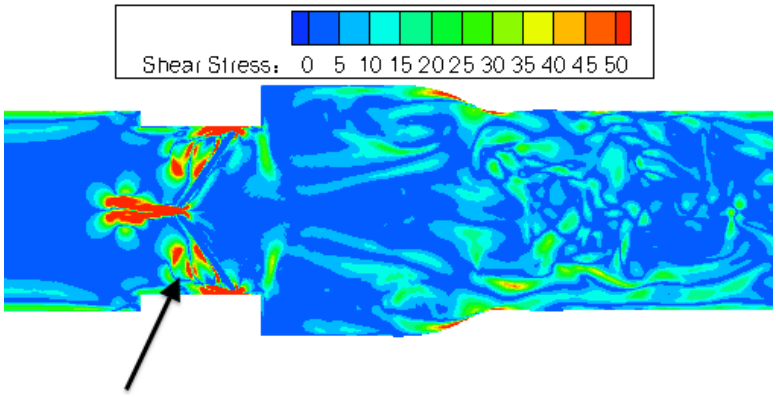

(d) Shear stress field

Figure 7-27: Platelet trail immediately after impact with closing leaflets (a) perpendicular view, (b) cross-sectional view, (c) corresponding vorticity field, (d) shear stress field

For a time point 8ms later, the platelet continues to follow the path of the leaflet-valve closing leakage jet (Figure 7-28). At this time point, the platelet is still experiencing high levels of instantaneous damage (15 – 25 dynes/cm^2). The corresponding vorticity field shows the leaflet-valve leakage jets beginning to mix with the b-datum central leakage jet as well.

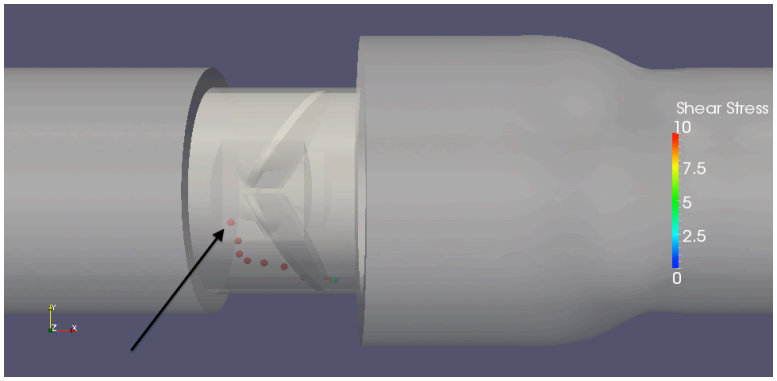

(a) Perpendicular view

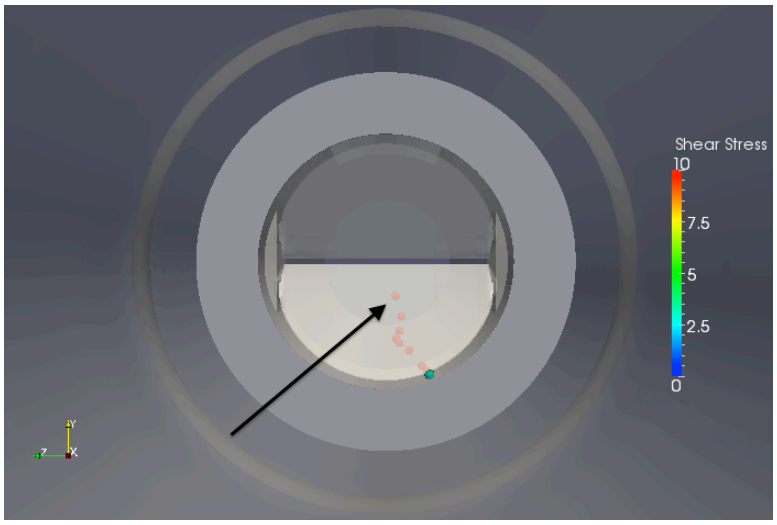

(b) Cross-sectional view

(c) 2D vorticity

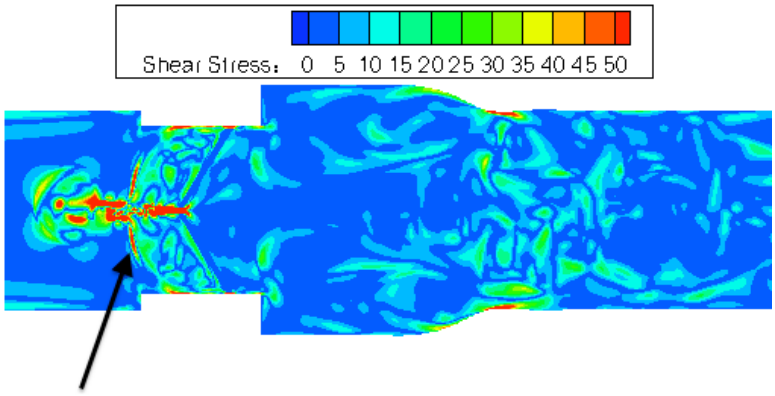

(d) Shear stress field

Figure 7-28: Platelet trail from motion with leaflet-valve closing leakage jet (a) perpendicular view, (b) cross-sectional view, (c) corresponding vorticity field, (d) shear stress field

An additional 9ms afterwards, the platelet is caught in the b-datum leakage jet as the leaflet-valve leakage jets mix with the central leakage. This causes additional high levels of damage (10 – 20 dynes/cm^2), and also pushes the platelet further upstream into the ventricular region. After being caught in the central b-datum jet, the platelet is quickly advected upstream towards the ventricular side and continues to recirculate in larger vortical structures until the simulation ends.

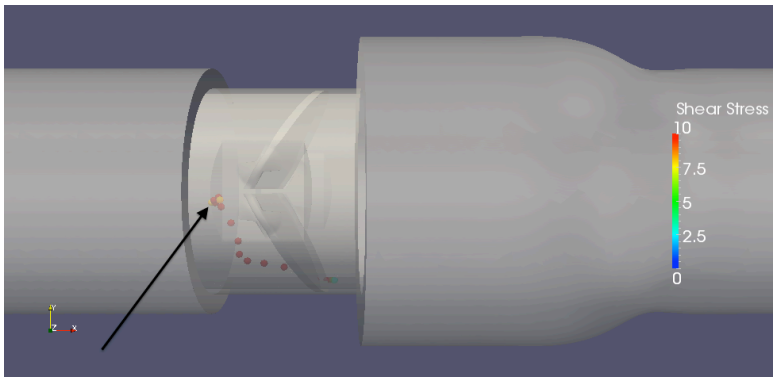

(a) Perpendicular view

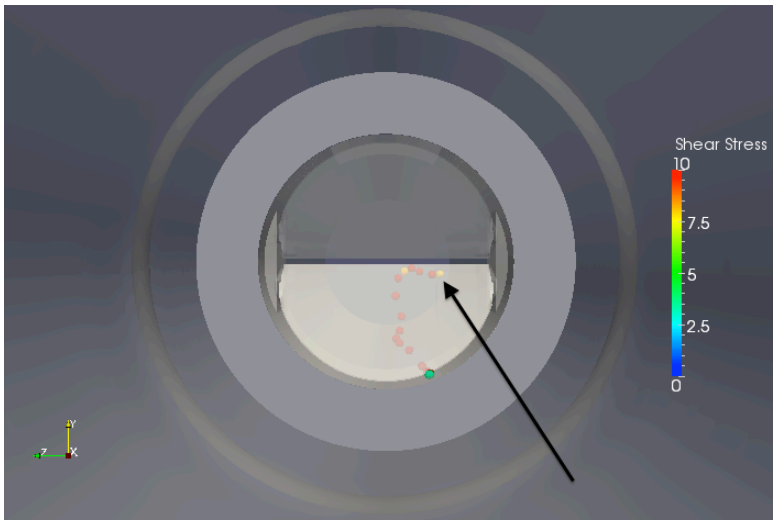

(b) Cross-sectional view

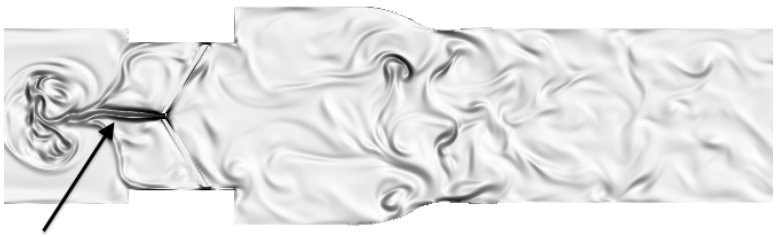

(c) 2D vorticity

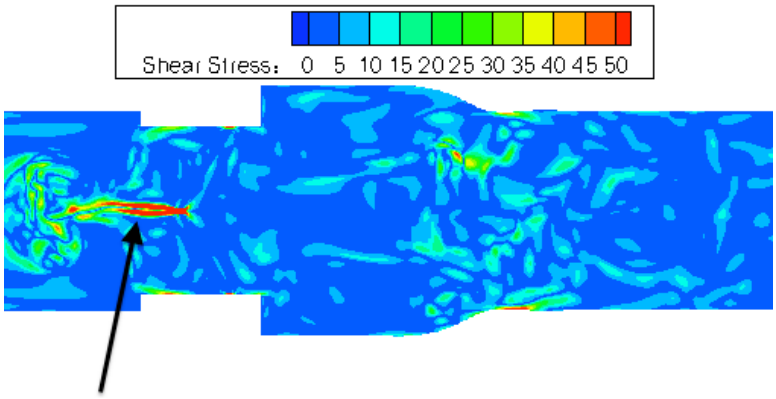

(d) Shear stress field

Figure 7-29: Platelet trail near b-datum leakage jet (a) perpendicular view, (b) cross-sectional view, (c) corresponding vorticity field, (d) shear stress field

The time history of damage accumulation for the most damaged platelet for the infant flow case is shown in figure 7-30. This shows a gradual increase in damage accumulation throughout the simulation, with three jumps in damage representing the three different highlighted time periods of high instantaneous platelet damage. These include the near-wall damage time periods of slow axial motion, as well as the damage incurred from the sudden leaflet closing. The damage accumulation slows as the platelet remains in the ventricular side for the final simulation time period and slowly recirculates after being pushed upstream by the b-datum jet. Even with a low exposure time of 250ms, the platelet experiences an accumulated damage of 2.29 dynes•s/cm^2.

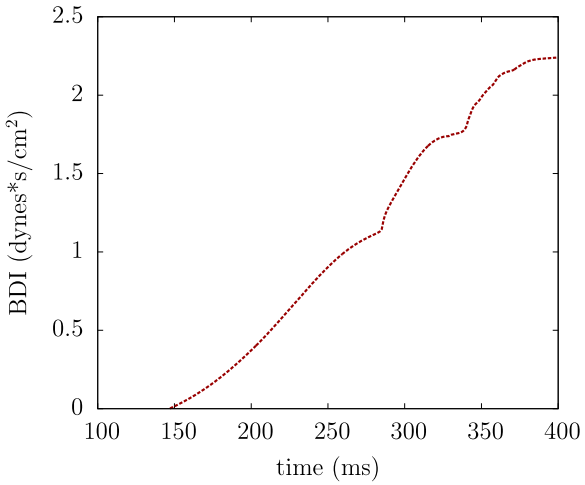

Figure 7-30: Platelet damage accumulation versus time for most damaged platelet for 6-month old infant flow case

7.3 Analysis of pediatric valve flows

7.3.1 Comments on pediatric flow simulation setup

In all three cases of suspended platelet flow, 5400 platelets are released with 300 platelets for each seed. In both the child and infant flow cases, the valve sizes scale differently than the cardiac outputs from the adult flow conditions, resulting in higher bulk flow velocities. The simulations of pediatric flows are focused on predictive assessment of valve sizes that are not FDA approved. Though it is more likely for an adolescent (12 – 18 years of age) to have an implanted prosthetic valve than a 6-month old infant, adolescent flow cases have similar Reynolds numbers as an adult case. Thus, there would be Reynolds number similarity in flow simulations and difficulties to determine differences among adolescent and adult cases. It is determined that the 5-year old child and 6-month old infant cases are of higher interest due to larger flow differences

from adult flows. Future simulations may be performed of an adolescent case to determine differences with the adult flow blood damage.

The flow and leaflet motion profiles for these cases are modified from adult flow data. In determining this flow and leaflet motion variation for the pediatric cases, simple scaling is performed of adult flow data with the objective to match all general parameters for the pediatric cases (valve size, systolic duration %, cardiac output, heart rate). Future numerical simulations may take data directly from experimental studies to model more accurate flowrate and leaflet motion curves.

7.3.2 Flow fields

The three flow scenarios (adult, child, infant) have similar flow features for leaflet opening and diastolic leakage flows. This is due to the overall low Reynolds number of these flow regimes. However, for peak flow (figure 7-31), the three flow cases produce very different flow fields. All three cases have strong forward flow past the leaflet tips and the sinus step expansion. In the adult and child cases, vortex wakes are formed for flow past the two leaflets of the BMHV.

It is observed that the adult case is characterized by a large number of small-scale eddies for leaflet vortex wakes (discussed in chapter 5). Each vortex that is shed from the leaflet tips immediately breaks apart into smaller eddies for adult flows, which spread out into the entire sinus region. For the sinus step expansion, the adult case shows a very strong and large recirculation region in the sinus, which frequently mixes with the smaller eddies of the leaflet vortex wakes. This leads to a very unstable and disorganized flow

field with small flow structures and high velocity fluctuations filling the entire sinus (figure 7-31a).

The child case (figure 7-31b) shows some formation of small eddies but not in large quantities and not immediately downstream of the leaflets. Instead, the vortices shed from the leaflets are large and coherent, resembling more traditional von Karman vortex wakes. Platelets caught in these coherent vortices simply advect downstream to the aortic chamber with high velocity. A smaller and weaker recirculation region exists in the child case in the sinus expansion. There is also less mixing between the leaflet wakes and the sinus recirculation regions for the child case. The flow fields are disorganized but more coherent than peak flow for the adult case.

For infant flow (figure 7-31c), vortex shedding is not apparent at this lower peak Reynolds number. Instead, flow past the valve is more jet-like for the three orifices with no recirculation of flow and very little mixing. Instead of an oscillating vortex wake formation, flow separation past the leaflet tips results in a confined and thin fluid layer extending from the leaflet tips. This fluid shear layer eventually expands in width into the aortic chamber. It is the lower Reynolds number of infant peak flow that leads to this thin fluid layer development instead of the formation of vortex wakes that are observed in adult and child flows.

These vorticity fields may explain why more of the highly damaged platelets for the pediatric cases are found in the aortic chamber. Platelets that experience high levels of damage in the sinus region for pediatric flows have a higher likelihood of being swept out of the sinus due to lower recirculation, which is due to the lower peak Reynolds numbers. In adult flows, however, highly damaged platelets caught in the sinus region do

not get swept out of the recirculation zone and remain in the sinus at the end of the simulation. This is particularly dangerous, as highly damaged platelets would remain near the valve, where thrombi are clinically observed to form.

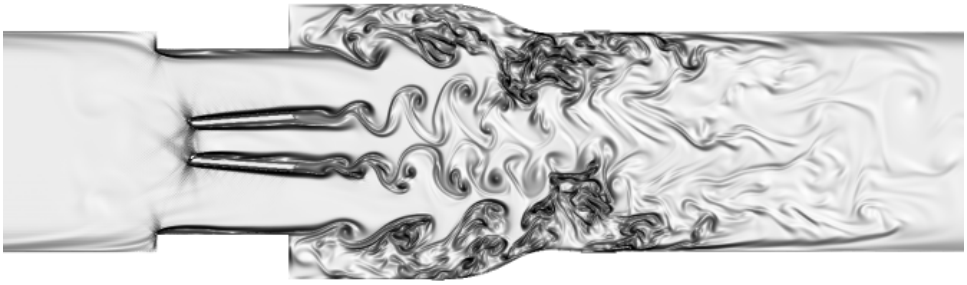

(a) Adult

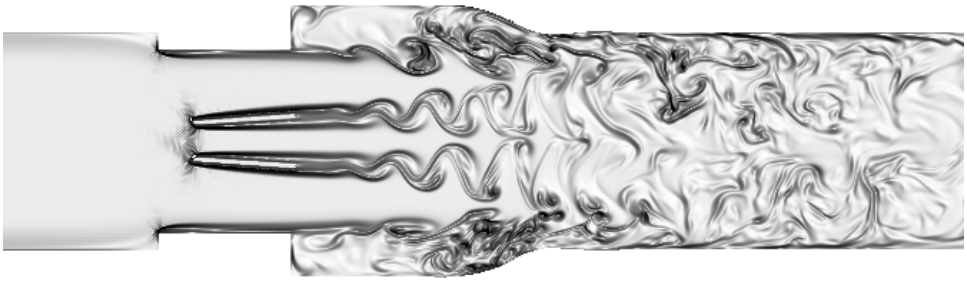

(b) Child

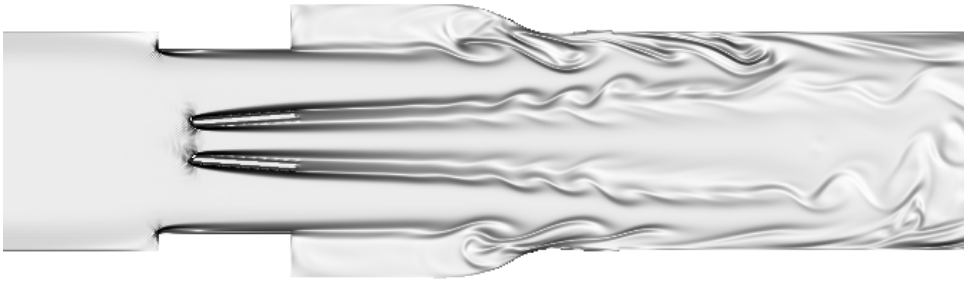

(c) Infant

Figure 7-31: Peak flow vorticity visualizations for (a) adult – Re = 5780, (b) child – Re = 4418, (c) infant – Re = 2725.

Viscous shear stress fields are also plotted at peak flow for each of the three flow cases (figure 7-32). This comparison shows the relatively moderate shear stresses in leaflet shedding vortices for the adult and child flow cases. Though the flow fields are most unstable and disorganized in adult flows (figure 7-31a), the shear stress magnitudes of adult peak flow (figure 7-32a) are actually the lowest. Similar to the conclusions of chapter 6, this indicates that observing unstable flow structures for the assessment of potential platelet damage may be misleading.

Both the adult and child flow cases show elevated shear stress regions in the sinus expansion, with recirculating flow. The child flow shear stress field is qualitatively similar to adult flow, but with higher shear stress magnitudes immediately downstream of the leaflet tips and sinus step expansion. The shear stress field of child flow (figure 7-32b) also is more coherent than in adult flow, just as the vorticity fields show more coherent flow structures in the lower Reynolds number child case.

The infant flow case (figure 7-32c) shows very high shear stresses in flow past the valve in thin shear layers. These thin shear layers are formed very close to solid surfaces of the valve, such as the leaflets and valve housing. There is no flow separation until the end of the valve, at which point the flow separates from the leaflet tips and valve housing. The thin shear layers then extend into the sinus expansion and aortic chamber while gradually expanding in width. These shear layers are associated with very high shear stress magnitudes, but not with recirculation or mixing of flow as observed in figure 7-31c. As the shear layers expand in width in the aortic chamber, shear stress magnitudes are lowered and a wider region of flow is encompassed. However, these reduced shear

stresses within the aortic chamber of infant flow are still higher than the shear stresses of the unstable flow field in the sinus expansion of adult flows.

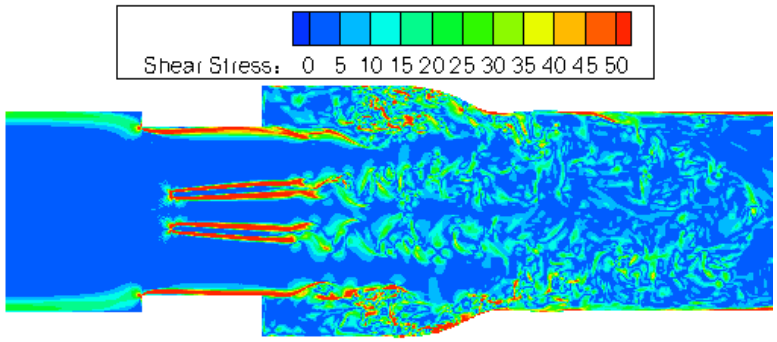

(a) Adult

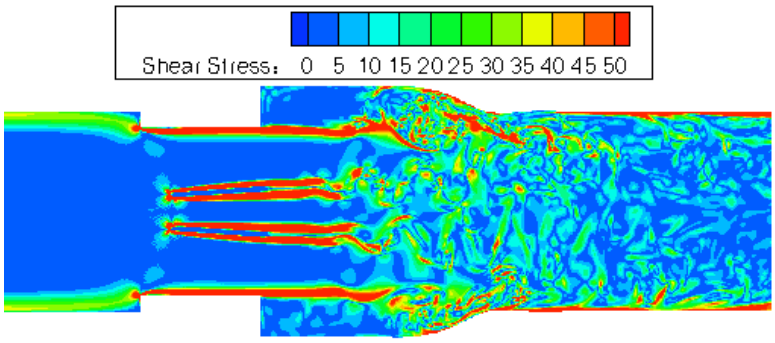

(b) Child

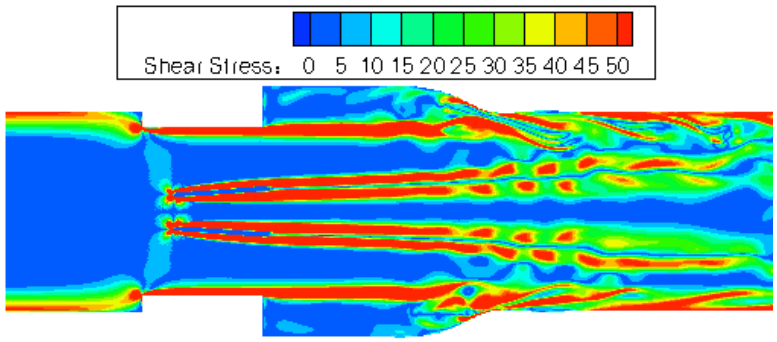

(c) Infant

Figure 7-32: Peak flow shear stress visualizations for (a) adult – Re = 5780, (b) child – Re = 4418, (c) infant – Re = 2725.

It is important to note that although the peak Reynolds number for pediatric flows are lower, the bulk average velocities are higher for the pediatric cases. Bulk flow Reynolds number can be written in terms of flowrate as

$$\mathrm{Re} = \frac{U_{avg} D}{\nu} = \frac{4Q}{\pi D \nu} \qquad \text{Equation 7-1}$$

where Q is inlet flowrate and D is inlet diameter. As the patient age becomes younger, the cardiac output (directly related to flowrate) scales down by a smaller factor than valve sizing scales down. This results in lower peak Reynolds numbers for the pediatric cases, which explains the more coherent and stable flows for younger patients. However, average inlet velocity ratio across simulation cases can be expressed as

$$\frac{U_{2,avg}}{U_{1,avg}} = \frac{Q_2}{Q_1} \bullet \frac{D_1^2}{D_2^2} \qquad \text{Equation 7-2}$$

This demonstrates how the bulk average velocities of the pediatric cases are higher than the adult case. Though the Reynolds numbers and cardiac outputs decrease for pediatric cases, the relative valve size scaling results in higher flow velocities for younger patients.

In addition, the more laminar nature of the pediatric flows may result in higher velocity gradients for flow past the valve. These higher velocity gradients extend to the more coherent flows past the valve and into the sinus in the pediatric cases. As velocity gradient is directly related to viscous shear stresses, this also means that viscous shear stresses are higher in more laminar flow past the valve. This is observed in the infant flow case, where high shear stress magnitudes are observed close to the leaflet and valve housing surfaces as well as in the jets downstream of the valve, in the form of thin shear layers. The aortic sinus is characterized by high shear stresses in thin shear layers

downstream of the leaflet and valve housing surfaces, but lower shear stress values in the middle of each orifice flow and within the sinus expansion. This is in contrast to the adult and child flow cases, where shear stress magnitudes are lower but the entire sinus region is filled with moderate levels of shear stress from the more disorganized and mixing flow fields.

It is emphasized that the thin shear layers in the infant flow are not associated with any recirculation in the flow. This may explain why platelet damage is highest in infant flows, but highly damaged platelets are primarily found far downstream of the valve. The overall higher shear stresses in the shear layers of infant flow may damage a larger number of platelets flowing through the valve, but the lack of recirculation zones means they are quickly advected downstream into the aortic chamber after experiencing high damage.

The more laminar nature of pediatric flows would result in higher velocity gradients for both healthy individuals and pediatric patients with implanted BMHVs. Thus, viscous shear stresses would generally be elevated for pediatric cases due to the nature of the flow conditions. However, for BMHVs, the two mechanical leaflets act as 'obstructions' of the normally one-orifice native valve flows. This leads to a triple orifice flow for BMHVs and generates additional shear layers in the flow that have high fluid shear stresses for pediatric cases (figure 7-32c). These shear layers grow in width and eventually encompass the aortic chamber. Native leaflets, alternatively, would limit these shear layers to the outer orifice walls where they may not affect as many platelets flowing through the aortic valve. Thus, the combination of the BMHV design and the more laminar nature of pediatric flows may lead to increased platelet damage.

Though adult flows show lower shear stress magnitudes than pediatric flows, the higher Reynolds number adult flows are characterized by more unstable and disorganized flows with high velocity fluctuations. The higher velocity fluctuations of peak flow at higher Reynolds numbers are demonstrated in section 5.3.1, where peak flow (Re = 5780) rms velocities are higher than rms velocity values at high accelerating flow (Re = 4700). These velocity fluctuations in peak adult flows may also lead to dynamic shear stress loading on platelets. Previous experimental studies have shown dynamic shear stress loading causes elevated platelet activation compared to steady shear stress loading, even if the final shear stress-exposure time load is the same [114]. The BDI model employed in this study does not factor fluctuating shear stresses or dynamic stress loading, instead using a simple linear shear stress-exposure time damage accumulation model that was found suitable in previous LBM-EBF blood damage studies [65]. However, adult flows may have elevated platelet damage *in vivo* due to high velocity fluctuations and subsequent dynamic shear stress loading on platelets, which cannot be captured with the simple BDI model of this study. Thus, although the results of these simulations demonstrate higher platelet damage for pediatric cases, the adult case may actually have comparable platelet damage due to the highly fluctuating velocities fields of higher Reynolds number adult flows. This requires further investigation in the form of dual computational-experimental studies, to be performed in future research.

7.3.3 Bulk blood damage

Although the adult case has the highest maximum damage for an individual platelet, the average blood damage was lower for adult flows than pediatric flows. The

BDI distribution at the end simulation time point for the adult, child, and infant flow cases with intervals of 0.05 dynes•s/cm^2 is plotted in Figure 7-33. In all three cases, platelet damage was skewed towards lesser degrees of damage, likely due to the low exposure time of platelets that are seeded later in the simulations. However, with decreasing patient age, the distribution became less skewed towards the lower damage values. For the infant case in particular, a high number of platelets experienced damage values greater than 1.0 dynes•s/cm^2. Very few cases in any of the simulations exhibited damage above 2.0 dynes•s/cm^2 and none were above 4.0 dynes•s/cm^2.

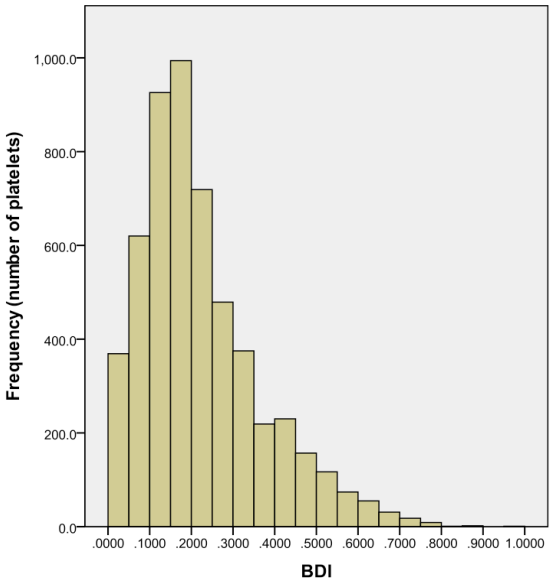

(a) Adult

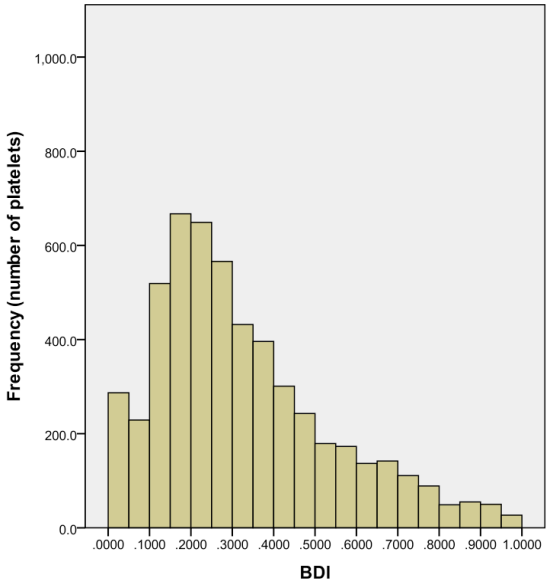

(b) Child flow

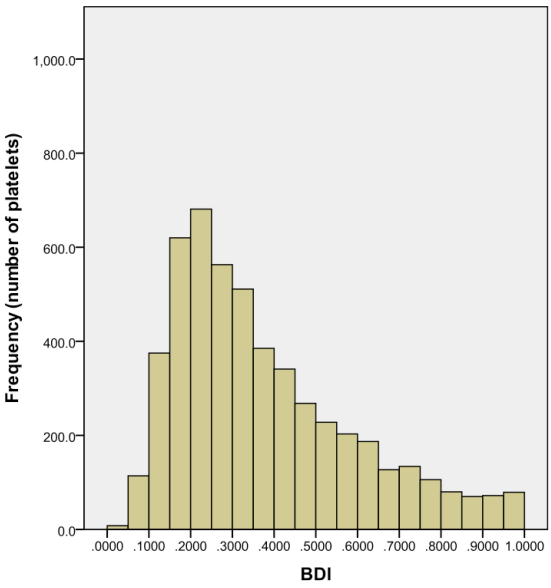

(c) Infant flow

Figure 7-33: BDI distribution for (a) adult, (b) child, (c) infant cases at simulation end time point with interval spacing 0.5 dynes•s/cm^2, with BDI values over 1.0 dynes•s/cm^2 not shown.

For these one pass simulations, no platelets are in danger of reaching the activation threshold of 10.0 – 35.0 dynes•s/cm^2 [25, 115]. However, the infant case does have 248 (4.6%) platelets that have exceeded a damage value of 1.0 dynes•s/cm^2. This is in comparison to 4 platelets (.07%) for the adult case and 99 platelets (1.8%) for the child case. Thus, although platelet activation is not a danger for one pass through the valve for an infant case, blood damage values are elevated on average and a larger number of high damage platelets exist.

Table 7-5: Average BDI values for all platelets, top 10%, and top 1% of damaged platelets for adult, child, and infant flow simulations.

Case	BDI average (dynes s / cm^2)	Top 10% - BDI average (dynes s / cm^2)	Top 1% - BDI average (dynes s / cm^2)
Adult	0.2248	0.5509	0.8355
Child	0.3416	0.8662	1.286
Infant	0.4186	1.0698	1.6976

For average blood damage values and top 1% and 10% damage values across flow conditions (table 7-5), the infant flow simulation has the highest average damage for all platelets that are modeled. For the top 1% of damaged platelets, the infant flow has an average damage value 103.2% higher than the adult flow. This again shows the overall higher platelet damage for valves sized for the pediatric population, particularly for younger patients. However, as the patient age decreased, more platelets overall were found in the aortic chamber due to lower recirculation. The top damaged platelets were also found with increasing frequency in the aortic chamber and less in the ventricular

chamber and valve regions for pediatric cases. The potential clinical significance of these differences is unknown.

7.3.4 Eulerian view

The Eulerian view comparison amongst all three cases is shown in figure 7-34 with blanking performed at 0.5 dynes•s/cm^2. These plots clearly show the larger number of high damage regions that exist in the child and infant cases as compared to the adult flow case. It is observed that the pediatric cases also have many high damage regions located within the valve and in the sinus expansion. As thrombus formation is primarily found near or within the valve region clinically, this elevated damage for pediatric flows could be of concern. Though there is clustering in the sinus region for the child and infant cases, a significant number of high damage regions exist in the aortic chamber. The infant case shows many high damage regions in the aortic chamber extending to the computational outlet boundary. These platelets, all of which do not approach the platelet activation thresholds, would likely advect downstream at the next systolic phase. Although higher damage regions exist with more frequency in the pediatric cases, the platelets that experience high damage but advect downstream may not be of highest concern for eventual thrombus formation.

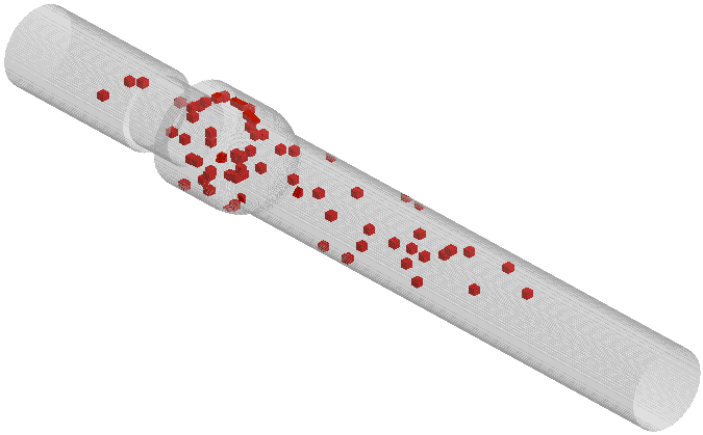

(a) Adult

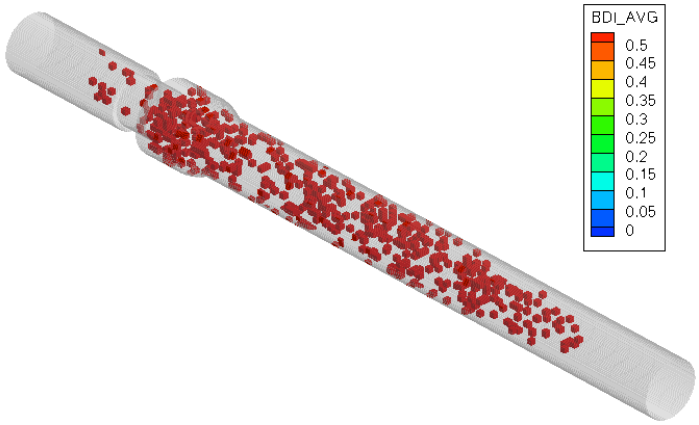

(b) Child

(c) Infant

Figure 7-34: BDI contour plot at end simulation time point, 5400 platelets. Contours blanked if damage less than 0.5 dynes•s/cm^2 for (a) adult, (b) child, (c) infant cases.

7.3.5 Lagrangian view

For the adult flow case, none of the most damaged platelets exist in the aortic chamber. However, for the child case, 4 of the top 10 most damaged platelets exist in the aortic chamber. This includes the most damaged platelet at 1.77 dynes•s/cm^2. It is noted that all four of these platelets do not traverse immediately into the aortic chamber. Instead, they first mix with the sinus recirculation region before being swept downstream. These platelets are thus influenced by the sinus recirculation region, though they do not remain in recirculation for the entire simulation.

For the infant case, 9 of the top 10 most damaged platelets reside in the aortic chamber. Although the most damaged platelet is highlighted by impact with leaflet closing, this is the only platelet in all 3 cases to be "hit" by the leaflets. This does result in an accumulated damage of 2.29 dynes•s/cm^2. However, it should be noted from the BDI evolution by time for this platelet, the leaflet closing impact does not cause a drastic increase in overall accumulated damage. Instead, the increase in damage is gradual, caused by near wall shear regions.

Although a significant number of higher damaged platelets exist for the pediatric cases, none of the platelets are found to recirculate in time as is commonly found in highly damaged platelets for the adult case. This reinforces the idea that the higher number of damaged platelets in the pediatric cases is of concern, but is of lesser concern if they get swept downstream through the aorta. These platelets that do not recirculate may be less likely to cause potential platelet aggregation if they do not continuously recirculate near the valve as in adult flows. Instead, they are widely dispersed

downstream in the aorta with elevated, but not platelet activation level, accumulated damage values.

It is important to note that these simulations employ rigid vessels, whereas anatomic aortas are distensible. Thus, platelets that are shown to traverse very closely to the wall in the simulations may not experience the same behavior for *in vivo* conditions with moving walls. This should be explored in detail in a future study employing moving wall domains.

7.3.6 Thromboembolic potential

Flow fields of vorticity appear qualitatively more unstable and disorganized for higher Reynolds number adult flows, but this does not translate directly to higher damage values for platelets in this study. This implies that observing instantaneous flow fields for chaotic, disorganized flow alone is not sufficient to make conclusions about the thromboembolic potential of a valve. However, the simulations conducted in this study are unable to account for dynamic shear stress loading on platelet damage, which may be an important factor in the development of thromboembolic complications, and thus future investigations are warranted.

Pediatric flows may have a higher average platelet damage index and higher number of highly damaged platelets. However, these platelets are not close to the activation threshold of 10.0 – 35.0 dynes•s/cm^2, and are easily advected into the aortic chamber. After traversing downstream, damaged platelets are widely dispersed and would flow through the aorta in the next systolic phase. This may be of lower concern for potential platelet activation and thrombus formation at the valve, the most important

type of thrombotic complication for prosthetic valves. Adult flows have larger recirculation regions due to higher Reynolds number at peak flow, which leads to the highest damaged platelets remaining near the valve, where they could potentially become activated and initiate the coagulation cascade. Although the elevated damage values of pediatric flows through BMHVs is of concern and should be examined in more detail in future studies, these results cannot conclusively determine the thromboembolic potential of pediatric sized valves due to the final location of highly damaged platelets.

The more laminar nature of pediatric flows is simply a product of the lower Reynolds number flow conditions for the pediatric population, and thus higher platelet damage in these flows may be unavoidable. However, the presence of the two BMHV leaflets leads to the generation of more shear layers than in native valve flows. These shear layers are associated with higher shear stresses and platelet damage indices. The simulations of chapter 6 also demonstrated the danger of recirculation zones for inducing platelet damage, and thus potential pediatric BMHV designs may focus on reducing recirculation zones for pediatric valve flows. This would ensure that already elevated platelet damage values for pediatric BMHV flows are not exacerbated by the formation of dangerous recirculation zones near the valves. This could potentially be accomplished by creating smoother geometries throughout the design, such as the leaflets and valve housing, though further investigation is warranted.

While higher levels of platelet damage in pediatric cases can be interpreted as disappointing, it may be inevitable, and does not necessarily suggest clinically important differences in thromboembolic potential. While the clinical importance of these findings is uncertain, the extent of the differences between the pediatric and adult cases is such

that it should not hinder/obstruct the development of pediatric sized valves. Further studies are clearly needed to determine the validity and potential thrombotic and clinical implications of these findings.

CHAPTER 8

DISCUSSION

8.1 Numerical Methodology

8.1.1 Suspension flow solver

The LBM-EBF method has previously been validated as a suspension flow solver with a variety of cases in the original methodology paper by Wu and Aidun [66]. Subgrid resolution modeling using the LBM-EBF method has also been validated in a previous study [91] and applied for BMHV hinge flows [63]. The implementation and validation of the FSI method for this work focuses on motion of ellipsoidal particles, as platelets are modeled as 3D ellipsoid "flat discoid" shapes. Though pulsatile BMHV flows are modeled at higher bulk Reynolds number, validation is first performed for LBM-EBF as a general suspension flow solver that can accurately capture suspended particle dynamics.

The validation cases performed with one-way FSI show excellent matching between simulation and Jeffery's orbit theory. This good matching for one-way platelet motion makes LBM-EBF highly suitable for the modeling of suspended platelets in this study. Although two-way FSI is not modeled for the platelets of this study, the general performance of the EBF method is tested with two-way FSI cases. Some drift with Jeffery's orbit is shown for two-way FSI; however, it is important to note that this modeling is performed with non-zero Reynolds number and thus some drift from theory is expected. The results show good matching at higher particle Reynolds numbers as well, particularly for capturing the diverging orbital period at critical Reynolds number that has been observed in previous studies [69, 90, 92]. The test cases also show

matching trends for diverging orbital period with variation of shear rate and variation of particle aspect ratio. Thus, the EBF method is able to capture the correct particle dynamics at higher particle Reynolds number using 2-way FSI. These test cases, in addition to the previous validations performed by Wu and Aidun [66, 91] show that the LBM-EBF method is a suitable suspension flow FSI method.

The EBF method possesses an important feature that is crucial for this work: subgrid modeling capabilities. The SBB method for fluid-solid interaction requires the solid grid to be on the same order of magnitude as the fluid grid. This would require a simulation with sub-micron fluid spatial resolution for BMHV suspension flows, which is not possible given current resources. The EBF method, however, allows for subgrid modeling due to the nature of its Lagrangian particle frame and fluid velocity interpolation using a Dirac delta function. As this research models suspended platelets of small size (3μm), subgrid EBF modeling is necessary. The validation case with representative platelet shape using subgrid modeling shows excellent matching with theory for motion of the ellipsoid. In addition, the subgrid modeling of platelets shows calculation of platelet maximum shear stresses within 30% of well-resolved particles, which is a reasonable error for subgrid modeling. This demonstrates the general applicability of EBF to model fluid-solid interaction with subgrid capabilities, which was also shown in previous studies [63, 91]. This also justifies the use of EBF to model subgrid suspended platelets for calculation of blood damage in a variety of biomedical flows, even at subgrid resolution.

Another question exists as to whether suspended platelet modeling is even necessary for these flow problems. Platelets will advect with the general flow due to

their small size, which is considerably smaller than the smallest Kolmogorov scales. The motion of platelets *in vivo* is likely affected by the presence of RBCs, but as RBCs cannot be modeled in such large flows, dilute platelet suspension modeling is performed. Point particle tracking methods, which assume platelets to be massless points, may be able to estimate platelet motion with good accuracy. This again would be due to the small size of platelets, which would passively advect with the flow. However, as blood damage is of interest in this research, it is unknown whether particle-tracking methods can estimate platelet shear stresses and damage accurately. Single-phase flow simulations that employ particle-tracking estimate the platelet shear stress using fluid viscous shear stresses or Reynolds stresses [10, 56, 62]. It is not clear how to best compute platelet shear stresses from viscous or Reynolds stress tensors, which of the two tensors should be used, and if this is accurate with blood damage experiments. The LBM-EBF method, alternatively, has been validated against whole human blood damage experiments of BMHV flows [65]. Figure 8-1 demonstrates the platelet surface shear stress variation that occurs when using a suspended platelet to track damage as performed in this study.

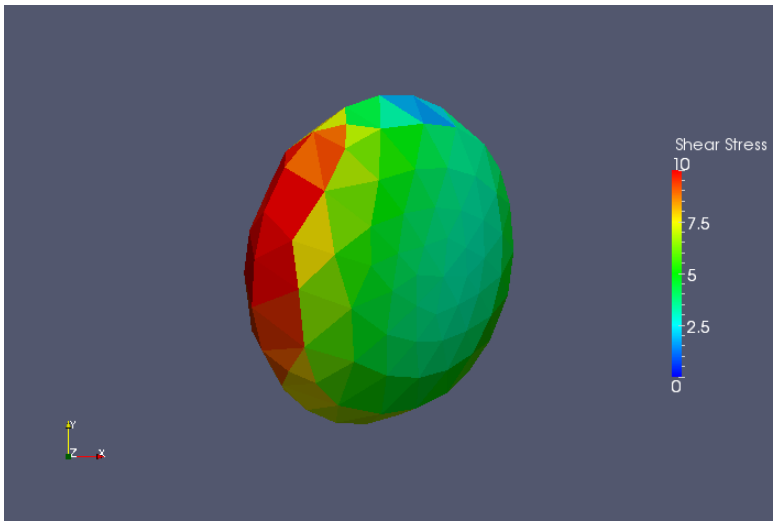

Figure 8-1: Platelet model with shear stress variation across meshed surface

The simple ellipsoidal orbit test case performed in chapter 4 shows the variation in shear stress calculation depending on platelet orientation. Point particle methods employing the viscous shear stress tensor would underestimate the maximum platelet shear stress in magnitude, and also be unable to account for orientation variation. The demonstrated underestimation of platelet stresses by point particle methods shows the appeal of modeling platelets as suspended elements with meshed surfaces, as performed with LBM-EBF in this study.

8.1.2 Parallelization

The parallelization methodology for the LBM-EBF method is described in detail in Appendix A.8. The results of parallelization scaling efficiency demonstrate that even with added computational and memory costs of entropic lattice-Boltzmann, External Boundary Force, and suspended platelet particles, the numerical methodology still scales very well for thousands of processors. This again demonstrates the appeal of LBM to model cardiovascular flow problems, as these simulations generally require very high spatiotemporal resolution. The ability of LBM to scale very well to thousands of processors is important, as these complex flow problems can be modeled in short simulation times while capturing fine scale features of the flow.

It is also important to note the good scaling efficiency of the numerical method with the presence of suspended platelets. Dense suspension flows are known for a quick reduction in scaling efficiency when employing thousands of processors [94]. However, when testing a suspension flow with particle concentration level similar to those

employed in the BMHV flow simulations, the LBM-EBF method shows very good scaling up to 4096 processors. This again justifies the use of LBM-EBF to perform parallel simulations of suspension flow through cardiovascular devices and flows.

8.2 Single-phase BMHV Flows

The LBM has been shown in chapter 5 to be validated for modeling pulsatile, high Reynolds number BMHV flows with extensive comparisons to experimental data. Although previous numerical methods have also claimed similar experimental BMHV flow validation [52, 55, 56], the numerical method of this study provides some advantages and higher insight into these flows compared to alternative methods.

8.2.1 Higher resolution modeling and lattice-Boltzmann advantages

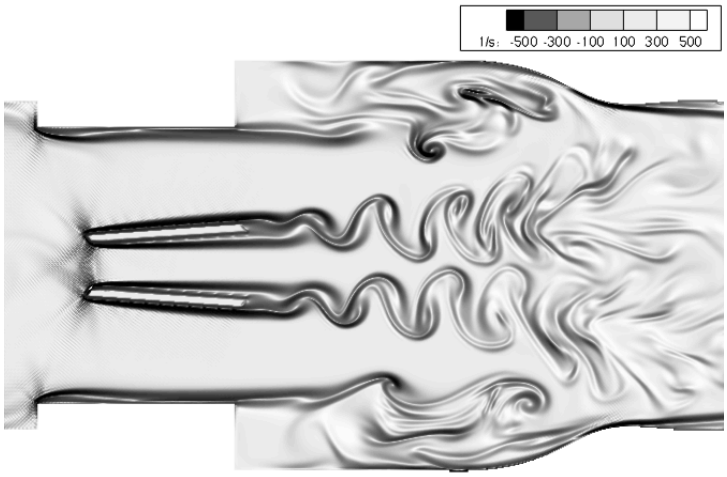

(a) Mid-acceleration phase (Re = 2070)

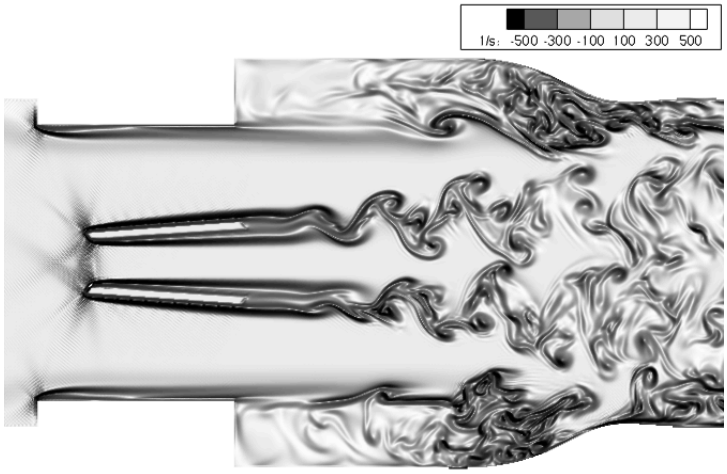

(b) Peak flow (Re = 5780)

Figure 8-2: 2D vorticity - pulsatile flow visualization of (a) mid-acceleration and (b) peak flow.

Figure 8-2 shows out-of-plane vorticity contours for two time points of systolic flow: mid-acceleration (Re = 2070) and peak flow (Re = 5780). These detailed plots show the ability of high spatiotemporal LBM simulations to capture important flow features, particularly for higher Reynolds number flows. At mid-acceleration, vortex shedding occurs past the open leaflet tips that is coherent and results in two distinct von Karman vortex streets. For peak flow, it is observed that coherent vortex streets immediately break down into smaller, chaotic eddies. These incredibly detailed fine-scale vortices are not captured in coarser resolution simulations, instead appearing as a blurred mixing of flow. Similar blurred flow results for high Reynolds number BMHV flow are demonstrated in other coarse resolution experimental and CFD studies of pulsatile BMHV flows [52, 56]. The small eddies in peak flow continue to form and disperse

throughout the domain, eventually mixing with each other as well as with vortex shedding in the sinus expansion.

It is important to note that these small eddies form downstream of the valve, and persist well beyond the sinus expansion region. Thus, it is important to maintain high spatial resolution for the entire BMHV domain and not just focus on the valve region. For future simulations, these fine scale features should be resolved to fully capture and understand complex pulsatile BMHV flow physics. In addition, for simulations involving blood elements, accurate modeling of these small eddies could play a very important role in quantifying damage to blood elements such as red blood cells and platelets. It has been proposed that capturing these fine scale features and high velocity fluctuations is crucial to the accurate determination of damage to blood elements [116].

Simulations modeling these problems at high resolution are very expensive, as the domain length scale is on the order of tens of millimeters, and the Kolmogorov length scales are on the order of tens of micrometers. Thus, numerical flow domains would lie in the range of hundreds of millions to billions of fluid grid points. For these simulations, efficient parallel algorithms are necessary. Though the high-resolution simulations of this study are expensive, they are performed with optimal parallelization and excellent efficiency using LBM, and take less than 20 hours to model a cardiac cycle with 2592 processors. Future simulations can be performed using this numerical method that can capture the finest details of similar, but different biomedical flows, with optimal parallel processing to obtain results in very short times. This can be performed to observe flow physics associated with novel cardiovascular devices, as well as accurate modeling of blood damage complications in various cardiovascular flows.

8.2.2 Turbulence in BMHV flows

Turbulence is of high interest for BMHV flows, as turbulent flows and Reynolds stresses are often correlated to high levels of blood damage [26, 117]. The smallest Kolmogorov scales for BMHV flows have been estimated on the order of tens of microns, which is several times larger than the size of suspended blood elements such as red blood cells and platelets. However, it has been proposed by Antiga and Steinman [116] that turbulent velocity fluctuations could relate to increased viscous shear stresses, due to energy dissipation that is caused by cell-cell interaction. Thus, turbulence that is caused by BMHVs may be related to the increased potential for blood damage.

To the author's knowledge, this study is the first quantification of turbulent energy mean dissipation rates, ε, and generation of energy spectra for computational simulations of BMHV flow. The results of this analysis have shown the Kolmogorov scales to be on the order of 40-60μm. These small scales are shown to exist downstream of the valve, again highlighting the need for high spatiotemporal resolution simulations throughout a large portion of the flow domain to capture intricate flow features.

The calculation of mean dissipation rates also demonstrates that the local isotropy approximation of mean dissipation rate, ε_{iso}, is a good approximation for BMHV flows with high goodness-of-fit R^2 values throughout the flow domain. This has implications for future experimental studies that are limited to the local isotropy approximation, as mean dissipation rates and Kolmogorov scales can be closely estimated with 2D plane data. The calculation of dissipation rates can also be used to determine the approximate location of small scale eddies in this flow. The high fluctuations associated with these

small eddies may be linked to an increased potential for blood damage in these flow regions.

Although dissipation rates confirm that small features of BMHV flow are located in the leaflet wakes and sinus recirculation regions, they do not capture how the turbulent energy is distributed in various length scales. This study is the first quantification of turbulence for numerical simulations with a delineation of inertial and dissipative spatial scales for BMHV flow. The energy spectrum demonstrates the development of an inertial range, but only for a small range of wavenumber modes and thus not a clear demonstration of turbulence. The inertial range is approximated for length scales on the order of 3mm to 12mm, which encompasses less than a decade of wavenumbers ($\kappa_1\eta$ = 0.004 to 0.015). It should be noted that the highest scale of this inertial range of 12mm is close to the pipe radius of 12.7mm. It is also interesting to note that the length scale where the spectra breaks off from the -5/3rd slope is roughly 3mm, which is about 60 times the Kolmogorov scale. This is remarkably consistent to the demarcation length scale defined as $L_{DL} = 60\eta$ by Pope [98] as a convenient measure that separates the inertial and dissipative scales.

Turbulence has implications for aortic valve flows, particularly for flows through prosthetic valves. The presence of a mechanical valve may lead to the onset of turbulence, though energy spectra have not been performed for native valve flows in this study and thus a direct comparison cannot be performed. Turbulent flows are generally characterized by unsteady shear stresses and increased mixing, and have been previously associated in literature with increased blood damage [26, 117]. A comparison with

turbulence in native valve flows may help provide a link between turbulence and blood damage complications associated with prosthetic valves.

Blood damage is thought to occur due to shear stresses and exposure time on suspended elements. The unsteady fluid velocities that are present in turbulent flows may be tied to both increased and unsteady shear stresses on suspended red blood cells and platelets. Unsteady shear stress loading on platelets have been tied to increased platelet activation in experimental studies [114], which may explain how turbulent flows are associated with higher blood damage. The velocity fluctuations present in turbulence may also lead to energy dissipation in cell-cell interactions, thus increasing viscous stresses and blood damage experienced by suspended elements. In addition, the increased mixing caused by turbulent flows can lead to recirculation paths for suspended elements, thus increasing their exposure time to unsteady and high shear stresses and causing high accumulated damage.

This combination of unsteady and increased shear stresses and higher mixing in turbulent flows can be tied to the thromboembolic complications that are clinically observed to form in BMHV flows. DNS simulations could clarify the link between blood damage and turbulence with spatial resolution on the order of suspended blood elements and with dense suspension modeling. However, current computational resources prohibit such simulations on as large a scale as BMHV flows. A smaller scale and simplified future study with dense suspension flow at varying Reynolds numbers could provide this link between turbulence and blood damage with reasonable computational expenses.

The unsteady shear stresses and mixing of turbulent flows may lead to other physiological complications for aortic valve flows, such as calcification of native leaflets.

Though the mechanical leaflets of this study are thromboresistant, future studies examining biological leaflets in other artificial valve flows (such as bioprosthetic valves) may quantify turbulence to link the presence of turbulence with leaflet calcification and stiffening complications. The presence of turbulence in aortic flows can also be linked to irreversible pressure loss in prosthetic valve flows [118] due to kinetic energy dissipation. This irreversible pressure loss leads to the left ventricle responding with increased work, which leads to increased stress on the myocardium.

The link between turbulence and various complications of BMHV flow are yet unclear. This study demonstrates the presence of turbulence in BMHV flows but cannot directly associate this with blood damage complications, as this is outside the scope of this study. If such a connection between turbulence and prosthetic device complications is made in future studies, prosthetic device development can be aimed to avoid turbulent flows in order to prevent serious complications.

8.3 Blood damage - Physiologic adult conditions

This study is not the first to quantify platelet damage in bulk BMHV flows for physiologic adult conditions, as this matter has been explored in several previous studies [10, 56, 64, 115, 119]. However, this is the first study to employ realistic shape and size platelets with meshed surfaces, and with flow field resolution able to capture the smallest scales of flow. This increased accuracy may help to understand blood damage as it relates to the complex flow field, instead of evaluating just the valve design.

8.3.1 Systolic flow

The Eulerian viewpoint has not been performed previously in literature, and represents a higher resolution analytical method of observing damage in the BMHV flow domain. This can highlight general regions of the valve that are known to cause high damage throughout the cardiac cycle. The results of this Eulerian view have highlighted the sinus expansion as an elevated platelet damage region. The sinus region shows high damage throughout the expansion, as demonstrated in section 6.3.1 and again in figure 8-3. The sinus region also has lower total volume compared to the aortic downstream chamber, resulting in clustering of high damage regions in the sinus and near the valve. This clustering of damage regions is of potential concern, as thrombosis complications are known to develop near the valve. The sudden step expansion is the likely cause of higher recirculation regions in the sinus flow field. This result highlights the potential of sharp solid geometries to lead to high recirculation regions and high damage levels for platelets, but requires further studies.

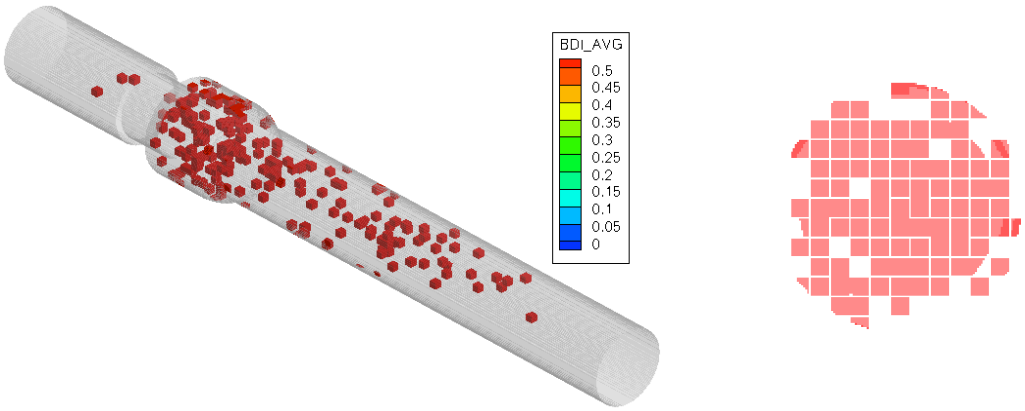

Figure 8-3: BDI contour plot at early-to-mid diastolic flow (Re = 75 in reverse flow) for angled and cross-sectional viewpoints, 5400 platelets. Contours blanked if damage less than 0.5 dynes•s/cm^2. Cross-sectional slice taken within sinus expansion.

The Lagrangian analysis also highlights the dangers of recirculation regions, as most of the highest damaged platelets are caught in recirculation zones. It is found that these platelets with high accumulated damage often experience moderate levels of instantaneous shear stress, but for extended periods of time. The damage accumulation over time, as demonstrated in section 6.4, shows that the highest damaged platelets have a pattern of gradual damage accumulation during the simulation.

An important conclusion of these simulations is the relevance of flow mixing regions in causing platelet damage. The characterization of flow fields in instantaneous time points is shown to be misleading, as they are not directly linked to final accumulated platelet damage. This suggests that future single-phase flow simulations may wish to shift analysis to both high fluid shear regions and regions of increased flow mixing to create a more complete analysis of blood damage potential. As turbulent flows are linked to high flow mixing and generally elevated platelet damage, future prosthetic device design may wish to avoid designs that induce turbulent flows or high mixing regions.

8.3.2 Diastolic flow

Though diastolic BMHV flows are linked to thromboembolic potential, simulations of diastolic flow through BMHVs are not common. The simulations of this study are at sufficient resolution to capture leakage through the b-datum jet and valve housing. Though hinge leakage is not captured in these simulations, previous studies have already explored hinge leakage flows and blood damage [62, 63, 65]. The platelets that flow through the b-datum leakage jet are shown to experience higher instantaneous

damage for a longer period of time. This is due to interaction between the b-datum leakage jet and large-scale vortices in the upstream ventricular chamber, as observed in section 5.4.3. This confirms that the b-datum leakage jets and the large-scale vortices associated with them are linked to higher platelet damage. Thus, breakup of the large vortices in b-datum leakage flows may help to reduce overall platelet damage, as has been proposed by previous experimental blood damage studies [54]. Vortex generators have been proposed to break up coherent b-datum leakage vortices to reduce blood damage, and other design modifications may aim for the same goals. Alternatively, it is shown that valve housing leakage jets are of lower concern for causing platelet damage.

8.4 Pediatric flow cases

The pediatric flow simulations of this study cannot clearly assess thromboembolic potential of valves resized for the pediatric population. This is due to the nature of one-pass simulations, and the assumptions in pediatric flow conditions and sizing that are made for the predictive numerical simulations. However, the simulations of this study can show the relative performance of valves in adult, child, and infant flows. These may complement future numerical or experimental studies to push for FDA approval of pediatric valves.

The flow fields of pediatric flows show qualitative and quantitative differences compared to adult flows. The infant flows of lower peak Reynolds number show more jet-like flows with no recirculation, but are also associated with significantly higher shear stresses in the flow field. This is primarily due to the more laminar nature of pediatric flows, which results in the generation of shear layers that lead to higher viscous fluid

shear stresses. These shear layers grow in size and eventually encompass the entire flow cross-section in the aortic chamber. Thus, the high shear stress fluid layers in pediatric flows would affect many platelets as they flow through the valve. This is caused by a combination of the BMHV design, in which the two leaflets act as obstructions in the flow and generate additional shear layers, and the more laminar nature of pediatric flow conditions. The flows for pediatric patients show a clear trend of higher platelet damage values, for bulk averages as well as top damaged platelets.

The Eulerian views show that many high damage regions exist throughout the pediatric flow domains compared to the adult geometry. These regions are located throughout the entire domain, but are clustered highly in the sinus region and aortic chamber. In combination with bulk blood damage values, these results demonstrate that pediatric BMHV flows show much higher overall platelet damage relative to adult flows. The increased clustering of high damage regions near or within the valve is again of high concern, as damaged platelets may form thrombi in these regions.

However, these results cannot clearly demonstrate a significantly higher potential for thrombus formation. The Lagrangian views highlight platelet damage paths with little to no recirculation. Instead, highly damaged platelets advect downstream to the aortic chamber where they may be less likely to cluster and form thrombi. The platelet damage values are elevated, but still do not come close to activation thresholds for one pass. The Eulerian views may show a large number of high damage regions throughout the domain, but again with damage values far from activation thresholds.

In combination with the observed dangers of recirculation and mixing flow as shown in chapter 6, these results demonstrate mixed conclusions for pediatric BMHV

flows. The higher bulk damage values are of concern, but may be an inescapable result due to the nature of pediatric flow conditions. Thus, every prosthetic device may unavoidably be associated with higher blood damage values, regardless of optimization of design. In addition, adult flows have higher velocity fluctuations, which may elevate the potential for platelet activation due to dynamic shear stress loading on platelets. The results also show maximum platelet damage values for pediatric flows of similar magnitude as adult flows. Thus, these simulations have shown a concern for pediatric blood damage complications with resized prosthetic valves, but no indication of drastically poorer performance. As prosthetic valves in adults perform well in combination with anticoagulation therapy, and as these results show elevated but similar performance for pediatric valves, this study demonstrates that BMHVs sized for the pediatric population may have blood damage performance that is not untenable. However, further computational, experimental, and clinical studies should be performed to complement this study and to further explore the general performance of pediatric re-sized valves.

8.5 Limitations and Recommendations

This research work covers the development of a suspension flow methodology capable of efficient parallel simulations of problems at very high spatiotemporal resolution. This is applied in a novel manner for BMHV flows, allowing for the modeling of realistic suspended platelets for tracking blood damage at the highest spatiotemporal resolution to date. This method is then applied as a predictive tool for pediatric flow conditions. Although this represents a strong step forward in modeling

blood damage through prosthetic devices, several limitations still exist for the present study, which can be addressed in future work.

8.5.1 Solid geometry

The solid domain for the simulations of this research is recreated from an *in vitro* bench top setup using microCT imaging. This is employed to model flows through a BMHV in the aortic valve position, and for best comparison against experimental PIV data. However, this geometry is highly simplified based on an idealized model.

For an anatomic geometry, the upstream region is actually the left ventricle, which has a conical shape. The modeling of the ventricular upstream as a long tube is not anatomically realistic. However, ventricular dynamics are not of interest in this study, and thus this geometry simplification is not of high concern. In addition, the anatomic aorta has a tortuous geometry that connects the aortic valve to the aortic sinus, the ascending aorta, aortic arch, and finally the descending aorta. In the computational and *in vitro* model, this is simplified as an axisymmetric expansion followed by a straight pipe. The aortic sinus is typically a triple dilation of the ascending aorta, and not an axisymmetric expansion. The modeling of the aortic side as a straight tube is a simplification from the curved and tortuous geometry of the aortic arch and descending aorta. This more complex anatomic geometry may affect the flow dynamics through aortic valves, and would likely result in different flow fields and blood damage values in modeling. Future simulations may employ a more anatomically realistic geometry that could contain bends in the domain and tortuosity.

Another limitation is the modeling of the solid domain as rigid, which is also a simplification used by the experiments. *In vivo* conditions include a contracting and dilating left ventricle, and distensible aorta. This natural wall motion is not taken into account in the simulations, and could also affect the flow dynamics and resulting calculations of platelet damage. This is of particular interest as near wall motions are shown to be associated with high instantaneous platelet damage in section 6.4. However, this modeling of wall motion is not straightforward and involves significant computational expense. Wall motion can be computed using knowledge of the wall material properties throughout the domain or by prescribing the complex wall motion. This wall motion modeling is a challenge even for single-phase flow simulations of this problem, even when the problem is localized to just the left ventricle or the aorta. Future simulations can, however, combine single-phase flow modeling with wall motion capabilities with the suspended particle methodology of this work.

The modeling of pediatric flow cases involves the scaling of the solid domain to match appropriate pediatric valve sizing. This may not accurately represent how pediatric sized valves would be manufactured, as a linear scaling may not be performed for all components of the valve. However, for ease of comparison amongst flow cases, the assumption of linear scaling of the entire geometry is used for these predictive pediatric flow simulations.

8.5.2 Boundary conditions

The boundary conditions for the solid domain are no-slip for the walls and leaflet, implemented by the standard bounce-back method. This method is standard for the

LBM, and is well validated as a standard FSI methodology. However, this method interprets the fluid-solid interface as a sharper interface that always lies halfway between lattice domain nodes (Appendix A.3). This may lead to a jagged interaction boundary for some lower resolution studies. It is determined that for the high-resolution simulations of this study, the spatial resolution is high enough that the pipe domain boundaries appear smooth. This is also confirmed by the good matching between simulations and experiments, where boundary walls do not appear to be an issue. Finally, the flow past the leaflets shows no flow separation, and thus any sharp interaction boundary does not seem to be an issue for high-resolution simulations. Future simulations may employ the EBF method or interpolated bounce-back methods (Appendix A.4 and A.5) to resolve a smoother fluid-solid interaction boundary. These methods are numerically expensive and the results using the less expensive SBB method already show very good matching with experimental flow data.

For the simulations of this study, flowrate inlet and stress-free outlet boundary conditions are employed. These are standard boundary conditions used by other CFD methodologies for BMHV flow problems [52, 56, 64], with flowrate data taken from experiments upstream of the valve. However, as leaflet motion and flow through BMHVs is primarily driven by pressure differential across the valve, pressure boundary conditions are optimal for these flow simulations. The use of the flowrate inlet condition may lead to a slight synchronization offset in the simulations as compared to boundary conditions based on pressure values.

Although pressure boundary conditions are not used in these simulations, it should be noted that in LBM, pressure boundary conditions and velocity boundary

conditions are similar in that they have the same effect of generating a fluid distribution function difference in the flow. Thus, the prescribed flowrate inlet and stress-free outlet boundary conditions act similar to pressure boundary conditions when used in lattice-Boltzmann methods. For details on pressure and velocity boundary condition implementation in LBM, refer to Zou *et al.* [120].

In addition, there is a concern of accuracy of synchronization between the prescribed flowrate and leaflet motion due to the explicit time-marching nature of LBM. However, the simulations employ uniform and very high temporal resolution (2.4μs), which reduce the effect of the synchronization concerns. Even for leaflet closing, where the leaflet motion is very rapid, the simulations employ 25,000 numerical timesteps during the leaflet motion period. This is such high temporal resolution that the leaflets do not have to be moved every numerical timestep, but instead only every 5 to 10 timesteps. With such high temporal resolution, any offset from "synchronization" is deemed minor.

There is also the concern of the accuracy of the flow and leaflet curves from experiments. These, and corresponding pressure curves, were taken from averaged data from experiments [52]. This is a typical practice for most CFD methods attempting to mimic experimental conditions, and these data were taken reliably and with repeatability.

8.5.3 Leaflet motion

For BMHVs implanted *in vivo* or for *in vitro* experiments, the leaflets are free to translate and rotate. The primary leaflet motion is rotational about the hinge fulcrum axis, and is driven by the pressure differential on either side of the valve. The simulations of this study restrict leaflet motion to rotational motion only about the hinge

fulcrum axis. In addition, this rotation is prescribed from average experimental data of leaflet motion for pulsatile flow. It has been shown in experiments that the leaflets also have varying motion from cycle-to-cycle [52].

The translational motion of the leaflets is due to small leaflet ear-hinge gap tolerances, and allows for the leaflets to shift slightly in all three Cartesian directions. However, this translational shifting is very small and is thought to have minimal effects on the flow field and thus the inclusion of leaflet translation is not important for this study. Though there is leaflet motion variability from cycle-to-cycle, simulations are performed in section 5.6.1 for asymmetric leaflet motion prescribed from experimental data, showing minimal lasting effects on the flow field. Thus, the use of average leaflet motion from experiments is suitable for the current study.

A simulation is performed at 160μm spatial resolution employing two-way FSI of the leaflets in section 5.7. No hinge friction modeling is employed for this simulation, as this information is not known. Although two-way FSI with lattice-Boltzmann methods are possible and can even be employed in these BMHV flow simulations, the computational flow and blood damage results of this study use only one-way FSI with prescribed leaflet motion. For best comparison of the flow fields, the conditions of the experiments must be matched as closely as possible. One-way FSI with prescribed leaflet motion ensures the best matching of conditions between simulations and experiments and is more reliable than using two-way FSI modeling. The good matching of simulations and experiments in the pulsatile flow qualitative comparisons reinforces this concept.

The lack of two-way FSI for the blood damage simulations may be problematic for the pediatric simulations. Flowrate and leaflet motion curves are modified from

physiologic adult flow data to match the general flow parameters of pediatric patients (systolic duration %, cardiac output, heart rate). In reality, flowrate variation and leaflet dynamics may be very different from adult to pediatric conditions. This adult flow scaling may not be completely accurate for pediatric flows, but is necessary due to lack of experimental pressure/flow data for these pediatric-sized valves in this specific flow domain. Thus, the predictive simulations employ modified flowrate and leaflet curves from adult conditions. Future simulations can use flowrate/pressure/leaflet motion curves taken from experimental data of pediatric sized valves.

8.5.4 Spatiotemporal resolution

The Kolmogorov scales for this *in vitro* setup for pulsatile BMHV flow have been estimated at approximately 40 - 60μm. The high-resolution simulations of this study employ 80μm spatial resolution, which is under-resolving the calculated Kolmogorov scales. However, the calculation of the Kolmogorov scale may be a conservative estimate. The Kolmogorov scale is also an order of magnitude calculation and not a strict threshold. In addition, previous DNS studies have shown the ability to capture lower order moments of turbulent flow at twice the calculated Kolmogorov scales [98, 99]. The pulsatile flow visualization at high resolution in this study have also shown coherent small eddies, which are not captured by other numerical studies. Finally, it is again noted that the simulations of this study employ the highest spatiotemporal resolution of any computational or experimental study to date. Future simulations can employ spatial resolution at 40μm to ensure that the Kolmogorov small-scale eddies are captured, with given computational resources.

The spatial resolution also does not allow for the hinge regions to be resolved. The microCT scan does include the hinge region, but the fluid spatial resolution is not high enough to capture hinge flow fields. These flows are important to capture, as significant blood damage is known to occur in the hinge regions [14, 62, 63]. However, it is not the objective of this research to study hinge flows, but rather bulk pulsatile flow through a BMHV. In addition, previous studies using this numerical method have already been performed to study BMHV hinges and hinge-like regions to assess their thromboembolic potential [63, 65].

8.5.5 Blood modeling and suspended particles

Blood is a non-Newtonian fluid, but is modeled in these simulations and in experiments as a Newtonian fluid. Although this is a simplification, blood viscosity approaches an asymptotic value of 3.5 cSt at higher shear rates. This assumption of constant blood kinematic viscosity at high shear rates is used to justify the Newtonian fluid modeling of blood for the simulations, which is suitable due to the nature of flow through the aortic valve. Future research may employ non-Newtonian fluid modeling for blood flow simulations.

The blood damage simulations of this study employ a dilute suspension of 5400 platelets in pulsatile BMHV flow. Real blood includes a dense suspension of red blood cells (~45% by volume) and platelets (~1 to 2% by volume) with suspended particle interaction. However, this would involve the modeling of billions of RBCs and platelets for a domain of this size. Thus, computational resources restrict the modeling of a dense

suspension of RBCs. It is also noted that hemolysis is a minor issue with BMHV flows, and thus it is more important to model platelet flow than RBCs.

The presence of RBCs may affect the damage experienced by platelets in BMHV flows. This may be due to the particle-particle interactions caused by RBC-platelet collision, as well as the altered platelet motion due to the properties of a dense RBC-platelet suspension. Future simulations may look at a small-scale study of dense suspension blood flow to quantify how RBC presence may affect platelet motion and damage. This influence can then be extrapolated to large-scale simulation results where modeling of RBCs at a realistic hematocrit may not be possible with limited resources.

Although 5400 suspended platelets is several orders of magnitude lower than a realistic volume fraction of platelets, it is shown in section 6.2.1 that this random sampling of platelets shows similar blood damage distribution across two simulations of random platelet seeding. Thus, the 300 platelets per seed are determined as a representative sample of platelets that pass through a cross-section of BMHV flow. For improved sampling of platelet flow, future simulations can employ more frequent seeding of platelets, particularly to resolve the suspension flow during higher flowrate regimes. In addition, multiple cardiac cycles can be simulated to improve upon the one-pass simulations that are employed in this research.

For the blood damage simulations in this study, platelet motion and damage are calculated from 1-way FSI. The platelets do not exert a force back to the flow field as is typically performed for suspension flow modeling. This simplification is justified, however, due to the relatively small size of the platelets (3μm) compared to the smallest scale eddies of the flow field (~40μm) and the fluid grid spatial resolution (80μm). Thus

it is assumed that platelets only need 1-way FSI as they passively advect with the flow. Section 6.6 also shows the very similar results between 1-way and 2-way FSI for the platelet modeling in the BMHV blood damage simulations. The demonstration of subgrid accuracy of quantifying shear stresses (section 4.1.2.6) further shows that the 1-way FSI modeling of platelets is reasonably accurate in determining platelet damage for this BMHV flow.

Although platelets are modeled with finite size and meshed surfaces, platelets are modeled as rigid 3D ellipsoids. Particle deformation capabilities exist with the numerical method, but are very costly to model. This particle deformation is necessary for RBC modeling, which are flexible membranes surrounding an interior fluid, but platelets are essentially rigid particles. Though platelets do change shape when activated, this activation/aggregation aspect of platelet modeling is not included in this study. Thus, rigid platelet modeling is a suitable assumption for the simulations of this study.

This research investigates blood damage in pulsatile flows through BMHVs, in order to determine potential for platelet activation, aggregation, and thromboembolic complications. However, no platelet adhesion or activation models are employed in this study. Though platelet damage potential is examined in this study, only accumulated damage values are calculated and no platelet aggregation is modeled. This modeling is important for future platelet damage simulations, but platelet adhesion models are relatively new in development and not yet appropriate for bulk blood flows. The simulations of this study also employ dilute platelet suspensions, and thus collisions and platelet-platelet interaction do not occur. In addition, no platelets in any of the blood

damage simulations have accumulated damage values over platelet activation thresholds, and thus platelet aggregation models are not required for these one-pass flow simulations.

8.5.6 Other Notes

In this study, BMHV flow is modeled for a 23mm St. Jude Medical Regents valve. Only this design is used, although previous studies have shown that difference in BMHV design can affect platelet damage values [62, 63, 65]. Although multiple designs should be simulated in the future, it is important to note that BMHVs are generally similar in design with fine detail differences mostly limited to the hinge regions. As hinge flows are not resolved in this work, this use of a 23mm SJM design is suitable as a representative BMHV geometry. In addition, the use of the same BMHV model helps to better delineate relative flow fields and blood damage performance of adult vs. pediatric flows.

Although this research quantifies platelet damage in pulsatile BMHV flows, the use of an experimental corollary can strengthen this study for validation and comparison purposes. Flow field visualization has been performed and used for validation purposes for this study, but platelet damage comparison has not been performed for bulk BMHV flows. An experimental setup could use whole human blood in pulsatile BMHV flows to assess damage potential using blood assays. Comparison of numerical simulations with this experimental blood damage could further validate the numerical method as appropriate for quantifying damage potential. This stronger validation would then allow for the use of the numerical method as a predictive method in other devices and biomedical flows with more confidence due to experimental blood damage validation.

8.5.7 Flow analysis - future

One of the conclusions of this study is that instantaneous flow field visualization may not have a strong connection with overall accumulated damage for suspended blood elements. Studies have previously attempted to connect flow analysis of vorticity, viscous laminar shear stress, or turbulent Reynolds stress plots at instantaneous time points with blood damage potential. However, the platelet damage modeling of this study has shown that recirculation and mixing regions for long-term exposure to damage are of higher importance than instantaneous high damage regions. Even vorticity fields only demonstrate instantaneous flow fields qualitatively and do not represent long term propensity for recirculation or mixing. Thus, a more appropriate flow analysis may be performed in the future in order to connect flow fields with blood damage, which may highlight the propensity of flow mixing to occur.

8.5.8 Future applications

This numerical method can be applied to existing BMHV designs for further optimization in order to reduce thromboembolic complications. Bioprosthetic valves with deformable leaflets may also be modeled, to determine the differences between the two valve types on platelet damage performance. However, as mechanical and bioprosthetic designs are well evolved, the numerical method is best suited for application to newer cardiovascular devices. Percutaneous valves may be modeled, as the effect of the implanted stent design on the flow fields and platelet damage is yet unknown. Other devices, such as left ventricular assist devices, can be modeled to determine

hemodynamic performance and blood damage potential. This would be an application of the numerical method for a generic cardiovascular flow and device, as the methodology is a general tool for blood damage modeling and prediction.

Long term use of this tool could involve the use of the numerical method for surgical planning. This would involve the use of patient-specific data to model pre and post-operative conditions and evaluate surgical options for patients. Although computationally expensive, this would allow for a broad assessment of post-surgical performance of cardiovascular devices for bulk flow hemodynamics as well as potential long-term blood damage complications.

CHAPTER 9

CONCLUSIONS

The present study demonstrates the potential of the numerical method to assess the hemodynamic and blood damage performance of BMHVs in details not possible with experimental or alternative computational methods. This numerical method can be applied to a wide variety of cardiovascular flows and prosthetic devices and can be used to assess and optimize current medical device designs, evaluate devices undergoing pre-clinical trials, or even predict the performance of novel designs. This study highlights the potential of computational tools for prosthetic device assessment, the complexity of pulsatile flow through a BMHV, the importance of suspension modeling for assessing platelet damage, and the potential application of BMHVs for the pediatric population.

The results of this study are:

- Validation of the numerical method as a suspension flow solver
- Demonstration of high performance parallel computing with the numerical method for efficient use on computational clusters
- Validation of the numerical method for modeling high Reynolds number, pulsatile BMHV flows
- Quantification of turbulence in BMHV peak flow
- Demonstration of complex flow dynamics in leaflet closing and mid-diastolic leakage in BMHV flows

- Leaflet malfunction in BMHVs may lead to very undesirable flows through the valve with thromboembolic implications
- Sinus recirculation regions in BMHV flows are of particular concern for platelet activation
- Flow mixing and recirculation may be more important to thromboembolic potential than instantaneous, unstable flow fields/structures
- Sharp geometries in BMHV design may cause recirculation regions that lead to high platelet damage, and should be avoided
- Central b-datum leakage flows cause high platelet damage due to strong, coherent leakage jet vortices
- Pediatric sized valves result in more coherent, laminar flows, but higher fluid shear stresses
- Pediatric sized valves have higher platelet damage values than adult sized valves
- Less recirculation in pediatric flows leads to highly damaged platelets advecting far from the valve, which is of lower concern for thromboembolic complications
- Re-sized valves may be a viable option for pediatric patients that require them, and more studies should explore their suitability
- The LBM-EBF numerical method can be used for future evaluation of medical devices and cardiovascular flows

These results of the numerical study are summarized in detail in the following subsections.

9.1 Numerical method

Though the LBM-EBF method has been well validated as a suspension flow solver [66], it is important to demonstrate the applicability of the method for parallel computations of suspension flows with accurate fluid-solid interaction, accurate platelet damage quantification, and good parallel performance for use in computationally expensive simulations.

In this work, the LBM-EBF method is shown as accurate for modeling suspended particles by comparison to theory. This is particularly important for a 3D ellipsoid that is the platelet model used for blood damage simulations. In addition, the subgrid modeling capabilities of LBM-EBF are tested, showing the continued accuracy of the LBM-EBF method when employing subgrid solid modeling. This is important for this and future research, which is limited by the computational expenses of large-scale cardiovascular flows, and thus must employ subgrid solid modeling. The importance of suspended platelet modeling is also highlighted, as it is shown that point particle methods assumed by other computational studies are not as accurate in the assessment of platelet damage.

The parallel computation performance of the numerical method is also demonstrated. This is important as high resolution simulations of BMHV flows require distributed memory computing in order to obtain results in reasonable simulation times. For the high 80μm and 2.4μs resolution, one full cardiac cycle can be simulated in parallel with 2592 processors with a run time of less than 20 hours. On a 16-core local workstation, this would translate to 4.5 months of simulation time. This parallel efficiency is made possible with the good scaling potential of lattice-Boltzmann methods, which can provide highly accurate results with the inclusion of many suspended particles

and with very short simulation run times. With a large enough computational resource, future simulations can be performed for a wide variety of cardiovascular flows and devices with high computational efficiency.

9.2 Flow fields

The mesh grid for the flow domain at this resolution is 4824 x 408 x 408, or approximately 800 million grid nodes. However, this corresponds to approximately 50,000 computational resource hours, and thus multiple cardiac cycles of simulation become very expensive. Thus, the pulsatile flow simulations of this study employ only one or two cardiac cycles for the highest spatiotemporal resolution due to computational resource constraints.

Despite computational expenses, it is noted that the results of this study are at the highest spatiotemporal resolution for this problem to date. From previous literature and coarser simulations, some of the small-scale features are lost in lower resolution simulations that are captured in the high-resolution simulations of this study. The results of this study demonstrate the importance of capturing the high-resolution complexity of cardiovascular flows through prosthetic devices, and have also quantified turbulence in BMHV flows. Other numerical studies may resolve the valve with high resolution, but not the entire flow domain [52, 56]. Without resolution of the finer scales of pulsatile aortic valve flow for the entire domain, the 3D flow fields are not accurately determined and this may alter an accurate determination of suspended platelet motion and damage quantification.

This work could also be considered a test case or reference point for future LB methods to model and accurately capture complicated biomedical flows. LBM is generally associated with lower Reynolds number flows, but the validation with experiments and speed of simulation of this work demonstrate that LBM is an appealing method for research in biomedical, specifically cardiovascular, flows with high resolution, efficiency, accuracy, and parallel performance.

These simulations also highlight the complicated aspects of pulsatile flow through a BMHV, including diastolic leakage jets and asymmetric leaflet motion. For diastole, it is observed that even with idealized computational conditions, asymmetric b-datum leakage jets form during mid-diastole. This shows the complex interaction of vortical structures throughout diastole, which leads to the oscillating and drifting jets. This has potential implications with blood damage incurred in these flows, as the b-datum jets and their interaction with large vortices are associated with higher damage in section 6.5.

Asymmetric leaflet motion is also modeled for single-phase flows but not for suspension flows. However, these cases demonstrate the effects of experimental asymmetry in leaflet motion as well as cases of severe leaflet dysfunction. It is shown that cycle-to-cycle asymmetry, which also occurs *in vitro*, has very little effect on the flow field and thus is not a high concern. Cases where one or both leaflets do not function properly, however, result in drastic differences in the flow fields with strong flows and recirculation regions. This is not explored with platelet damage as it is outside the scope of this study, but is an interesting subject that can be modeled in future work.

Two-way FSI simulations are also performed with the leaflets in order to show the applicability of LBM-EBF to capture accurate dynamic leaflet motion in complex,

pulsatile, high Reynolds number flows through BMHVs. This two-way FSI modeling is not performed in any of the suspension flow simulations, but is an important highlight to demonstrate for future work. This 2-way FSI modeling may be used for the predictive assessment of pre-clinical trial devices or novel designs that do not have experimental data available in order to prescribe motion of the solid geometry.

9.3 Blood damage

The blood damage simulations for the physiologic adult case are performed with 5400 suspended platelets and a variety of analytical viewpoints. The comparison of seeding methodologies demonstrates that the use of 300 platelet seeds with randomized positions is a representative sample of the many platelets that flow through a cross-section at one time point. This is important to give validity to the use of a dilute suspension model, as a realistic volume fraction of platelets cannot be modeled.

The bulk damage distribution highlights the sinus expansion region for highest average damage, even though most platelets advect downstream into the aortic chamber. Though high damage values exist, no platelet approaches an accumulated damage value near the threshold for platelet activation of 10.0 - 35.0 dynes•s/cm^2. However, as this is for one pass through the BMHV only, it is possible that recirculating platelets may accumulate more damage and become activated. The overall distribution of blood damage demonstrates that for the adult case, most platelets experience very low levels of accumulated damage.

The novel Eulerian viewpoint of blood damage evolution is used to highlight the evolution of damage in fine regions of the domain over time. This demonstrates that for

the physiologic adult case, higher damage regions develop with higher frequency within the sinus expansion. This again underlines the recirculation in the sinus as a danger region for platelet damage.

The Lagrangian viewpoint is employed to highlight individual platelet paths that cause very high levels of damage, and to connect this with the pulsatile flow fields. The near surface platelet path highlights the danger of platelets traveling very close to solid surfaces with no flow separation, as these platelets incur high levels of damage without being swept away from the boundary. The platelet path with high damage caused by leaflet closing wakes show the danger of instantaneous damage in these wakes, but very few platelets are caught in this damage path. The sinus recirculation paths are of particular interest as they occur most frequently of the highest damage platelets. These are particularly dangerous as they not only lead to high levels of accumulated damage, but also result in many damaged platelets recirculating for a significant time period. This may have complications if platelets become activated, as the platelet recirculation would lead to a higher likelihood of platelet aggregation.

The conclusion of the physiologic adult cases is that although high platelet damage can occur in a variety of ways, it is of particular concern to avoid high recirculation regions. These regions cause both high levels of instantaneous damage and also high-accumulated damage, with a clustering of platelets in recirculation zones. These dangerous combinations may lead to thromboembolic complications, more than platelets that are highly damaged and simply advect downstream into the aorta. Platelets that advect through the aorta to the rest of the body may take significant time to return to the heart, if at all. It is also found that platelets caught in the leaflet tip vortex wakes do

not have high levels of damage, despite the flow past these leaflets being unstable and disorganized. Thus, it is recommended that future single-phase flow simulations concentrate more on long-term recirculation or mixing flow regions than regions that show unstable flow features at instantaneous times.

A diastolic flow simulation is also performed as significant platelet damage occurs in these flows. Hinge gap flow cannot be resolved in these simulations, but the spatial resolution is high enough to resolve valve housing gaps. These simulations show that b-datum leakage jets may cause high damage to platelets, even after they have quickly advected to the ventricular side. This is caused by the platelets being trapped in the larger recirculation vortices on the ventricular side after flowing through the b-datum leakage jet. This can be connected to the asymmetric b-datum leakage jet, which interacts with large vortical structures on the ventricular side. Platelets going through the valve housing gaps experience higher damage than platelets that remain on the aortic side, but lower levels of damage than platelets going through the b-datum jet.

Pediatric simulations are also performed in order to show the predictive assessment potential of the numerical method. The cases of a child and infant are chosen to highlight patient conditions that are highly different from a physiologic adult case. The flow physics are shown to be very different for the pediatric cases, with more coherent and laminar flows compared to the adult flows. However, these flows are also associated with higher shear stress magnitudes and the formation of dangerous shear layers in the flow past the valve. Though there are higher shear stresses in pediatric flows, very few recirculation regions exist in the flow fields.

Both pediatric conditions show higher average damage values than the adult flow case, with infant flows consistently showing the highest platelet damage values. However, no platelets approach the threshold of 10.0 – 35.0 dynes•s/cm^2 for either of the pediatric flow simulations. The Eulerian view for the pediatric cases show that many of the high damage regions exist throughout the aortic downstream chamber due to low recirculation. Though more high damage regions exist in pediatric flows, this may not be of high concern, as many of the damaged platelets would advect through the aorta in the next systolic phase.

The Lagrangian viewpoint also reinforces the idea that many damaged platelets are simply advected downstream into the aorta. The sinus region still plays a role in damage, however, as many of the highly damaged platelets recirculate briefly in the sinus before being swept downstream. Unlike the physiologic adult case, the recirculation regions in the pediatric cases are not as strong. Many highly damaged platelets do not get trapped in recirculation zones and are quickly swept downstream, lowering the risk of aggregation and clustering near the valve. Thus, although average damage values are higher and more highly damaged platelets exist for pediatric flows, pediatric sized valves may not have significantly more thromboembolic potential than physiologic adult flows.

It is the conclusion of these pediatric cases that pediatric sized valves have slightly elevated risk for developing blood damage complications, but this may be due to the unavoidable nature of pediatric flows. However, the pediatric cases do not indicate severe blood damage risks that are much higher than for adult flows. These simulations indicate that design changes in prosthetic valves for adults or pediatric populations should avoid any sharp geometries in order to avoid high recirculation zones.

9.4 Potential for future

This research has demonstrated the LBM-EBF numerical method as a powerful computational tool for general use in cardiovascular flows through prosthetic devices. Although it is specifically applied to one BMHV design, it has demonstrated the capabilities of efficient, parallel assessment of blood damage performance for a prosthetic device with varying flow conditions and multiple analytic viewpoints. The numerical method has demonstrated its ability for complex flow modeling, and the importance of capturing fine-scaled details of fluid flow through cardiovascular devices. This study provides novel insight into how blood damage should be connected to flow fields, and the potential for design improvement in the well-known bileaflet mechanical heart valve. Ultimately, this study is important for its future potential, and can be a starting point for this computational method for future assessment of a wide variety of biomedical flows and medical devices.

APPENDIX A – NUMERICAL METHODS

A.1 Lattice-Boltzmann Method

In the lattice-Boltzmann method, the incompressible fluid is modeled as a distribution of fictitious fluid particles that exist on a fixed Eulerian regular lattice grid. This method discretizes 3D velocity space, and each node on this 3D grid is linked to neighboring nodes through lattice velocity vectors, $\mathbf{e}_i$ (i = 0 – 18 in the 3D, 19 lattice velocity model of this study). As all fluid particle interaction is performed with only neighboring nodes connected by lattice velocity links, the LBM is local in nature.

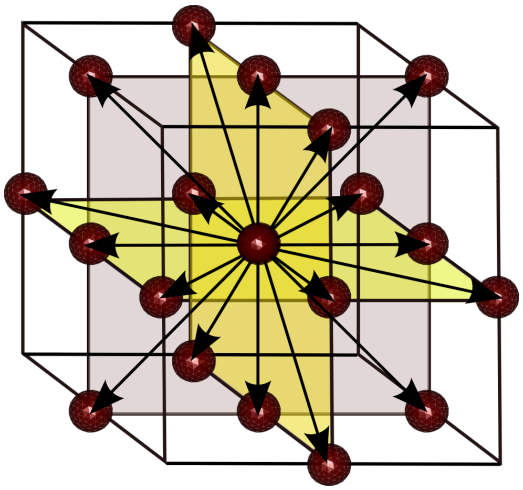

Figure A-1: Three-dimensional, 19 lattice velocity diagram for a LBM fluid grid

The fluid particle distribution function, f_i, describes a statistical distribution of microscopic fluid particles at a node and can be used to extract important macroscopic fluid properties such as density and velocity. Thus, solving for the fluid particle distributions on the 3D fluid grid determines the 3D flow field. In the simulations of this study, the lattice velocity vectors $\mathbf{e}_i$ denote a three-dimensional, 19-vector Cartesian

velocity set. The subscript i denotes a particular 3D Cartesian direction (i = 0 – 18).

Table A-1: List of lattice velocity vectors for 3D, 19-vector Cartesian set

i	$\mathbf{e}_i$	i	$\mathbf{e}_i$
0	(0,0,0)	9	(1,0,1)
1	(1,0,0)	10	(0,1,1)
2	(1,1,0)	11	(-1,0,1)
3	(0,1,0)	12	(0,-1,1)
4	(-1,1,0)	13	(0,0,1)
5	(-1,0,0)	14	(-1,0,-1)
6	(-1,-1,0)	15	(0,-1,-1)
7	(0,-1,0)	16	(1,0,-1)
8	(1,-1,0)	17	(0,1,-1)
		18	(0,0,-1)

The LBM employs an explicit time-advancement scheme to solve its equations. The fluid particle distribution changes with time through processes known as ‘streaming’ and ‘collision’. In streaming, fluid particles move to neighboring grid nodes that are connected by lattice velocity links. In collision, fluid particles arriving at a node at the same time collide with each other and change the fluid particle distribution at that node. These two processes dictate the time evolution of the fluid particle distribution at each node and only require knowledge of f_i at neighboring nodes, making all calculations localized in space.

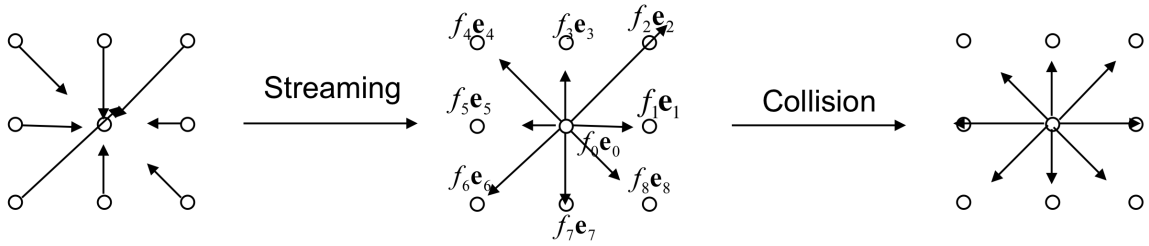

Figure A-2: General overview of streaming and collision processes

The lattice-Boltzmann equation with a single relaxation time is given by

$$f_i(\mathbf{r}+\mathbf{e}_i,t+1)-f_i(\mathbf{r},t)=-\frac{1}{\tau}\left(f_i(\mathbf{r},t)-f_i^{(0)}(\mathbf{r},t)\right) \quad \text{Equation A-1}$$

where the right hand side is the single-relaxation-time Bhatnagar-Gross-Krook (BGK) collision operator. In the lattice-Boltzmann equation, f_i is the fluid particle distribution function, $f^{(0)}$ is the equilibrium distribution function, $\mathbf{r}$ is the 3D spatial location, and t is the time. The lattice-Boltzmann method converges to solve the Navier-Stokes equations when the lattice spacing is much smaller than a characteristic simulation length scale.

The single-relaxation time scale used in the lattice-Boltzmann method is related to the macroscopic fluid kinematic viscosity ν by

$$\nu=\frac{2\tau-1}{6} \quad \text{Equation A-2}$$

The macroscopic fluid properties at each node are given by the moments of the distribution function and are determined as

$$\rho(\mathbf{r},t)=\sum_i f_i(\mathbf{r},t) \quad \text{Equation A-3}$$

$$\rho(\mathbf{r},t)\mathbf{u}(\mathbf{r},t)=\sum_i f_i(\mathbf{r},t)\mathbf{e}_i \quad \text{Equation A-4}$$

$$c_s^2 \rho \mathbf{I} + \rho \mathbf{u}\mathbf{u} = \sum_i f_i(\mathbf{r},t)\mathbf{e}_i\mathbf{e}_i$$

Equation A-5

Mass and momentum are conserved by relaxing the nodal distribution f_i to the equilibrium distribution function $f^{(0)}$. The general form of the equilibrium distribution function for incompressible flow is described as

$$f_i^{(0)}(\mathbf{r},t) = \rho(\mathbf{r},t)w_i\left[1+\frac{(\mathbf{e}_i\cdot\mathbf{u})}{c_s^2}+\frac{(\mathbf{e}_i\cdot\mathbf{u})^2}{2c_s^4}-\frac{u^2}{2c_s^2}+\frac{(\mathbf{e}_i\cdot\mathbf{u})^4}{2c_s^6}-\frac{(\mathbf{e}_i\cdot\mathbf{u})u^2}{2c_s^4}\right]+O(u^4)$$

Equation A-6

where $c_s = 1/\sqrt{3}$ is the speed of sound. The weighting coefficients w_i are based on different discrete velocity sets for LBM. These are referred to as D2Q9, D3Q15, etc., where DX refers to the number of dimensions and QXX refers to the number of lattice velocity vectors. The methodology of this study is referred to as a D3Q19 LBM method.

Table A-2: List of weighting coefficients for LBM velocity sets [70]

w_i	No. (2D)	$\lvert\mathbf{e}_i\rvert$	D2Q9	D3Q15	D3Q19	D3Q27
w_0	1	0	4/9	2/9	1/3	8/27
w_1	6 (4)	1	1/9	1/9	1/18	2/27
$w_{\sqrt{2}}$	12 (4)	$\sqrt{2}$	1/36	0	1/36	1/54
$w_{\sqrt{3}}$	8 (0)	$\sqrt{3}$	0	1/72	0	1/216

It should be noted that macroscopic fluid properties such as density, velocity, and kinematic viscosity that are determined by solving LBM are non-dimensional. The relation between non-dimensional LBM fluid properties and actual physical values are determined based on the spatial resolution and the single-relaxation time parameter τ of the simulation. Nondimensionalization can be accomplished by introducing the reference scales to build the bridge between physical units and lattice Boltzmann units [70].

A.2 Entropic Lattice-Boltzmann

Entropic Lattice-Boltzmann (ELB) methods are employed to allow for simulation of higher Reynolds number flows. By examining the BGK collision operator (re-printed below), the updated fluid distributions (left-hand side) rely on a term modified by the inverse of the relaxation parameter τ (right-hand side, second term, denoted *RHS2*). As τ is positively correlated with the kinematic viscosity ν as given in Equation A-2, this *RHS2* term is inversely proportional to ν.

$$f_i(\mathbf{r}+\mathbf{e}_i,t+1) = f_i(\mathbf{r},t) - \frac{1}{\tau}\left(f_i(\mathbf{r},t) - f_i^{(0)}(\mathbf{r},t)\right) \qquad \text{Equation A-7}$$

In LBM, compressibility issues arise when non-dimensional velocity grows too large. The general limitation is $u < 0.10$. The Reynolds number in a given simulation is thus increased by decreasing the non-dimensional kinematic viscosity ν. For simulations of higher Reynolds number flows, this means that the term $1/\tau$ grows in magnitude. This will magnify the effect of the difference between the current fluid distribution f_i and the equilibrium distribution $f_i^{(0)}$ for the *RHS2* term. At higher Reynolds number flows, instabilities form as *RHS2* grows in magnitude and the updated fluid distributions are computed as negative values. This results in the unphysical calculation of negative density values.

A solution to these instabilities is the use of the entropic lattice-Boltzmann (ELB) method. The recently developed ELB method by Keating *et al*. [72] is used in this research. The ELB method uses a discrete *H*-theorem constraint that enforces positive definiteness on the distribution function values, thus removing the instabilities at higher Reynolds number flows. The *H* function is defined as

$$H[\mathbf{f}] = \sum_i f_i \ln\left(\frac{f_i}{w_i}\right)$$ Equation A-8

where w_i is the weighting coefficient for LBM and

$$\sum_i w_i = 1$$ Equation A-9

The ELB method modifies the single-relaxation collision operator τ to form a two-parameter collision operator as follows

$$f_i(\mathbf{r} + \mathbf{e}_i, t+1) = f_i(\mathbf{r}, t) - \frac{\gamma(\mathbf{x}, t)}{2\tau}\left(f_i(\mathbf{r}, t) - f_i^{(0)}(\mathbf{r}, t)\right)$$ Equation A-10

where the function $\gamma(\mathbf{x},t)$ is the nontrivial root of

$$H[\mathbf{f}] = H[\mathbf{f} - \gamma(\mathbf{f} - \mathbf{f}^{(0)})]$$ Equation A-11

which is employed so that the collision operator does not violate entropy. When $\gamma = 2$, the entropic LB collision operator reduces to the standard BGK collision operator. The γ value is determined by using a rapidly converging Newton-Raphson procedure at each time iteration for fluid grid points that are becoming unstable. These unstable grid points are identified by checking if the difference between the sum of fluid distributions f_i and the sum of equilibrium distributions $f^{(0)}$ is above a threshold level. This is equivalent to determining the difference in fluid density calculation by using f_i compared to $f^{(0)}$. The threshold level chosen for this study is 6% difference in fluid density values (after tuning simulations), which is considered optimal for correctly identifying unstable nodes while also reducing computational costs associated with applying the entropic LBM.

In some instances, such as for artificial outflow boundary conditions, the Newton-Raphson procedure for determining γ fails. In this scenario, a slower, but universally

convergent bisection method is employed. The details of these scenarios are given in the Appendix B.3.1. The ELB method leads to universally stable explicit algorithms at small viscosities and high Reynolds numbers. Details on the ELB method can be found in the paper by Keating *et al*. [72].

The standard representation of the kinematic viscosity in single-relaxation lattice-Boltzmann methods is defined as

$$\nu = \frac{1}{6}(2\tau - 1)$$

Equation A-12

However, by using ELB at unstable grid nodes, the value of the relaxation parameter τ is locally modified. The effective viscosity at nodes that employ ELB then becomes

$$\nu_{eff} = \frac{1}{6}\left(\frac{4\tau}{\gamma} - 1\right)$$

Equation A-13

Thus, the ELB method can be thought of as locally increasing the viscosity at unstable nodes in order to enforce positive definiteness to fluid distribution values. This local increase in viscosity is only performed for unstable nodes at the timestep of instability. After the ELB method stabilizes the node, the viscosity returns to the original single-relaxation LB definition.

A.3 Standard Bounce Back Method

The standard boundary condition employed for wall surfaces for LBM is the standard bounce-back (SBB) condition [74, 81, 82]. This method evolved from the boundary conditions of lattice gas methods, from which the lattice-Boltzmann method was derived. The SBB method resolves the fluid-solid interaction boundary via links that connect fluid nodes and nodes within the solid. These lattice velocity links that cross the

solid boundary are identified as 'bounce-back' boundary links. Fluid distributions that stream across solid boundary links are bounced back, reversing direction. In the case of a stationary boundary, the fluid distribution is bounced back with the same magnitude but opposite direction with which it was originally streamed. In the case of a moving solid boundary, the bounced back fluid distribution is adjusted appropriately based on the moving solid boundary momentum by

$$f_i(\mathbf{r}, t+1) = f_{i'}(\mathbf{r}, t^+) + 2\frac{\rho w_i}{c_s^2} u_b \cdot \mathbf{e}_i \qquad \text{Equation A-14}$$

where t^+ refers to the distribution post-collision but pre-streaming, i' is the link with direction opposite to i, and $\boldsymbol{u_b}$ is the local solid boundary velocity.

In the case of two-way fluid-solid interaction using SBB methods, the fluid distributions that bounce off the solid boundary impart momentum onto the solid surface, thus providing a fluid-to-solid interaction force. This can be interpreted as a momentum transfer between the fluid and solid. This fluid-to-solid interaction force is defined as

$$\boldsymbol{F}_{i'}^{(b)}(\mathbf{r}_b, t) = -2\mathbf{e}_i \left[f_{i'}(\mathbf{r}, t^+) + \frac{\rho w_i}{c_s^2} u_b \cdot \mathbf{e}_i \right] \qquad \text{Equation A-15}$$

where $\mathbf{r_b}$ is the boundary location along the link. The SBB method assumes the fluid-solid interface exists exactly midway between fluid and solid nodes. For cases where the wall does exist halfway between fluid and solid nodes, e.g. parallel plates, the SBB method is second-order accurate [82]. However, the halfway position assumption does not hold for curved surfaces, and the accuracy devolves to first-order [81, 121].

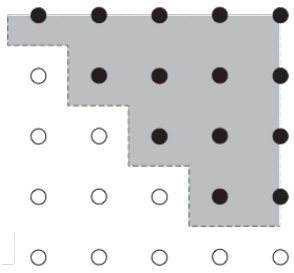

Figure A-3: Standard bounce-back (SBB) fluid-solid interaction boundary [66]

For large solid surfaces, such as curved surfaces or large obstructions, the standard bounce-back method is suitable for fluid-solid interaction modeling. If the fluid grid resolution is sufficiently high, the SBB method can adequately interpolate the location of the 3D curved solid surface. Though the SBB method interpolates the fluid-solid interface as halfway between fluid nodes, this becomes a minor issue for cases of high fluid grid resolution, large solid surfaces with a regular boundary (ex. circular walls), and non-moving or slow-moving surfaces. This is the case for the large 3D curved solid domain of the simulations in this study, and thus the SBB method is used for these large curved surface domains.

A.4 External Boundary Force Method

For small particles that have irregular and/or deforming shape, the standard bounce-back method is insufficient. For these small particles, the ratio of the solid particle grid to the fluid grid becomes significant, and the jagged FSI boundary from SBB methods leads to higher inaccuracies. These problems become compounded by particles that can move rapidly through the fluid domain, as instabilities arise when particles traverse more than one nodal link per simulation timestep. Particles that can deform in shape also lead

to changes in the FSI boundary, which can cause additional issues. With solid phase modeling, the inaccurate boundary interpolation leads to fluid-to-solid interaction forces that are inaccurate. This can heavily affect the modeling of solid particle motion and deformation, as well as the determination of shear or normal stresses on the particle. Finally, the SBB method requires a solid mesh resolution that is equal to or larger than the fluid grid resolution, due to the nature of bounce-back links that must be determined [69-71]. Thus, any sub-grid modeling of solid particles is not possible.

To avoid these problems, a novel method is employed that determines a more accurate fluid-solid interaction boundary. Instead of the traditional standard bounce-back method for fluid-solid coupling, a novel external boundary force (EBF) method developed by Wu and Aidun [66] is used. The small solid particles in the suspension use Lagrangian reference frames that move continuously through the fixed Eulerian fluid domain. The solid particle surface is mapped on the Lagrangian frame by boundary nodes, creating a mesh of surface elements. This Lagrangian frame for the solid is then mapped onto the 3D fluid domain.

In the EBF method, the moving Lagrangian frame for the solid particle allows for the exact position of the solid boundary surface nodes to be determined within the fixed fluid domain. The two frames of reference used in the EBF method allow for a smoother and more accurate interpolation of the fluid-solid interaction boundary. A Dirac delta function, first described in the work by Peskin [122] for the Immersed Boundary method, is used in the EBF method to interpolate the location of the solid boundary nodes. This interpolation of the solid surface location is also used in Peskin's Immersed Boundary (IB) method, with which the external boundary force method has many similarities.

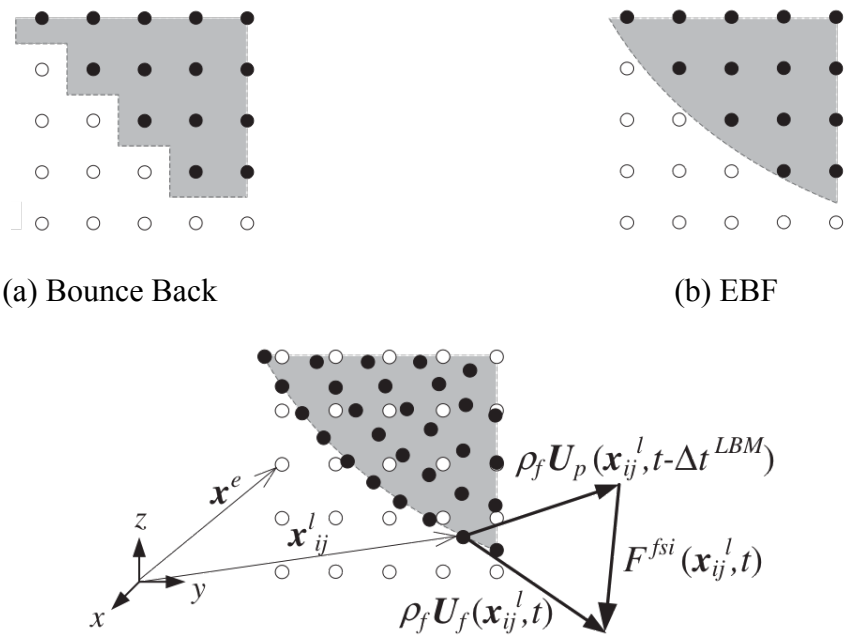

(a) Bounce Back (b) EBF

(c) EBF: No-slip enforcement at fluid-solid boundary

Figure A-4: Fluid-solid coupling at solid boundary, SBB vs. EBF method [66]

The principle of the standard bounce-back method is momentum transfer between the fluid and solid phases in the form of fluid particles that 'bounce' off the interaction boundary. The external boundary force (EBF) method works instead by enforcing the no-slip boundary condition at all solid boundary nodes. The external boundary force is the calculated fluid-solid interaction force required to impose the no-slip boundary condition at each node in the fluid-solid boundary interface.

Let Π_s and Π_f represent the solid and fluid domains, respectively. Let Γ represent the fluid-solid interaction boundary, with Γ_s and Γ_f as the sets of solid and fluid boundary nodes, respectively. The force per unit volume experienced by the solid from the fluid will be referred to as $\mathbf{F}^{\text{fsi}}$. In order to calculate the external boundary force, the fluid

velocity and density at the solid boundary node are first determined by

$$\mathbf{U}_f(\mathbf{x}^i_j,t) = \int_{\Pi_f} \mathbf{u}(\mathbf{x}^e,t)D(\mathbf{x}^e - \mathbf{x}^i_j)d\mathbf{x}^e, \quad \mathbf{x}^i_j \in \Gamma_s$$

$$\rho_f(\mathbf{x}^i_j,t) = \int_{\Pi_f} \rho(\mathbf{x}^e,t)D(\mathbf{x}^e - \mathbf{x}^i_j)d\mathbf{x}^e, \quad \mathbf{x}^i_j \in \Gamma_s \qquad \text{Equation A-16}$$

where $\mathbf{U}_f$ is the interpolated fluid velocity at the solid boundary node, ρ_f is the interpolated fluid density at the solid boundary node, $\mathbf{u}$ is the fluid velocity at a lattice node, ρ is the fluid density at a lattice node, $\mathbf{x}^i_j$ is the position vector of the j^{th} solid boundary node on particle i, and $\mathbf{x}^e$ is the fluid node position vector. $D(\mathbf{x}^e - \mathbf{x}^i_j)$ is a Dirac delta function used in this work for interpolation of fluid velocities and densities at a fluid-solid interface. The Dirac delta function is originally described and used in the Immersed Boundary work by Peskin [122].

First, the location of the solid node is determined within the 3D fluid grid. Then, the fluid velocity is interpolated at the solid node using the Dirac delta function and information from nearby fluid nodes. The fluid density at the solid boundary node is similarly interpolated using the Dirac delta function and nearby fluid nodes. The total value of the Dirac delta function, $D(\mathbf{x})$, can be broken down into individual Cartesian components by

$$D(\mathbf{x}) = D(\mathrm{x})D(\mathrm{y})D(\mathrm{z}) \qquad \text{Equation A-17}$$

The individual component of the Dirac delta function $D(x)$ is then defined as

$$D(x) = \begin{cases} 0, & x \le -2 \\ \frac{1}{8}\left(5 + 2x - \sqrt{-7 - 12x - 4x^2}\right), & -2 \le x \le -1 \\ \frac{1}{8}\left(3 + 2x + \sqrt{1 - 4x - 4x^2}\right), & -1 \le x \le 0 \\ \frac{1}{8}\left(3 - 2x + \sqrt{1 + 4x - 4x}\right), & 0 \le x \le 1 \\ \frac{1}{8}(5 - 2x - \sqrt{-7 + 12x - 4x^2}, & 1 \le x \le 2 \\ 0, & 2 \le x \end{cases}$$ Equation A-18

Assuming that the solid particle moves at the velocity of the previous time step, the fluid-solid interaction force needed to enforce the no-slip condition is then given by

$$\mathbf{F}^{fsi}(\mathbf{x}_j^i, t) = \rho_f(\mathbf{U}_f(\mathbf{x}_j^i, t) - \mathbf{U}_p(\mathbf{x}_j^i, t - \Delta t^{LBM}))/\Delta t^{LBM}, \quad \mathbf{x}_j^i \in \Gamma_s$$ Equation A-19

where the LBM time step $\Delta t^{LBM} = 1$, the term $\mathbf{U}_p(\mathbf{x}^i_j, t-\Delta t^{LBM})$ is the particle velocity at solid boundary node $\mathbf{x}^i_j$ at the previous time step, and ρ_f is the fluid density at the solid node. This step can be explained as first determining the discrepancy in fluid linear momentum using the values of fluid and solid velocity at the solid boundary node. This difference in fluid linear momentum over one time step is corrected by applying the external boundary force, thus enforcing no-slip at the boundary. It is critical to note that this $\mathbf{F}^{fsi}$ value is a force density at the solid boundary node, and thus must be multiplied by a volume in order to obtain a true fluid-solid interaction force value. The volume is equal to the local volume that is "owned" by the solid boundary node. This local volume determination is critical and can vary depending on the solid modeling methodology. For this research, the suspended solid particles are meshed at their surface only, and a conal local volume methodology is determined as most accurate. This local volume methodology will be discussed in further detail in the Appendix A.6 and Appendix B.2.

By Newton's third law, there is an equal and opposite force of the solid acting on the fluid. This two-way fluid solid interaction for the EBF method is enforced by first determining the solid-to-fluid external boundary force $\mathbf{g}(\mathbf{x}^e,t)$, and then adding it to the BGK collision operator as an external body force by

$$\mathbf{g}(\mathbf{x}^e,t) = -\int_{\Gamma_s} \mathbf{F}^{fsi}(\mathbf{x}^i_j,t) D(\mathbf{x}^e - \mathbf{x}^i_j) d\mathbf{x}^i_j, \qquad \mathbf{x}^e \in \Gamma_f$$

$$f_i(\mathbf{r}+\mathbf{e}_i,t+1) = f_i(\mathbf{r},t) - \frac{1}{\tau}\left(f_i(\mathbf{r},t) - f_i^{(0)}(\mathbf{r},t)\right) + 3w_i \mathbf{g}(\mathbf{x}^e,t)\cdot \mathbf{e}_i \qquad \text{Equation A-20}$$

As demonstrated, the solid-to-fluid external boundary force $\mathbf{g}(\mathbf{x}^e,t)$ is added directly as an additional force term to the lattice-Boltzmann BGK collision operator to complete two-way fluid-solid interaction. The Dirac delta function is again employed, thus fluid nodes within a radius of two grid spacing are affected by the presence of a solid node.

The EBF method has been validated as second-order accurate in space and has been described in detail by Wu and Aidun [66]. A variety of rigid and deformable suspension flow validation cases have been simulated using the EBF method and are described in the methodology paper [66].

A.5 Interpolated Bounce-back Methods

An alternative FSI method for large surfaces, the interpolated bounce-back (IBB) method, is also implemented for possible use in future research. This is a higher order method than the SBB method, but encounters problems when used in combination with the entropic LBM. The problems with this method will be discussed in detail in Appendix B.3.3, but the IBB methodology is first described here.

For standard bounce-back wall conditions, flow through parallel plates is 2nd order accurate in velocity, and 1st order accurate in pressure. This is due to the walls being located exactly halfway between fluid nodes, thus making the SBB boundary perfectly coincide with the actual wall boundary. For curved surfaces where the wall position is not halfway between fluid nodes, the SBB method reduces to 1st order accurate in velocity and 0th order accurate in pressure.

For cases with sufficiently high spatial resolution, the 1st order velocity accuracy of SBB methods is adequate. Lower spatial resolution cases can be significantly improved in accuracy by a modification to SBB methods that better interpret the wall location. These methods are known as interpolated bounce back (IBB) boundary conditions, and improve velocity to 2nd order accurate and pressure to 1st order accurate [79]. The IBB boundary conditions require additional fluid distribution values at nodes that neighbor the wall boundary node.

The IBB conditions also require the determination of q, the fraction of fluid grid spacing at which the wall is located. For SBB methods, as the wall is assumed to be located halfway between fluid nodes, the value of q is ½. If the wall is located closer to the fluid node, q is less than ½. If the wall is located further away, q is greater than ½. Note that this q value is different from the q-criterion described in section 3.9 for 3D flow visualization.

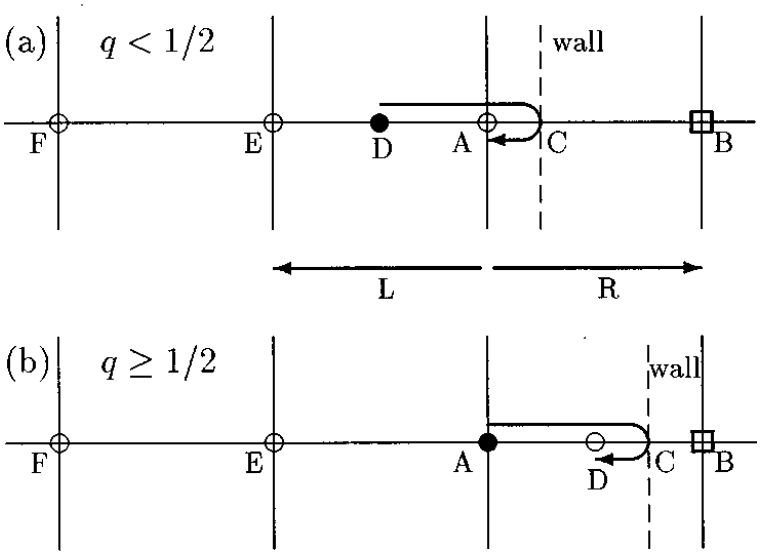

Figure A-5: Interpolated bounce-back conditions for determining wall position [79]

The linear interpolated bounce back condition requires fluid distributions at one neighboring node to the bounce-back fluid node. Linear IBB is applied for different cases of q by

$$\begin{aligned} f_{i'}(\mathbf{r},t+1) = &\quad 2qf_i^c(\mathbf{r},t) + (1-2q)f_i^c(\mathbf{r}-\mathbf{c}_i,t), \quad q < \frac{1}{2} \\ f_{i'}(\mathbf{r},t+1) = &\quad \frac{1}{2q}f_i^c(\mathbf{r},t) + \frac{(2q-1)}{2q}f_{i'}^c(\mathbf{r},t), \quad q \geq \frac{1}{2} \end{aligned} \qquad \text{Equation A-21}$$

where $\mathbf{c}_i$ is the lattice velocity link direction that hits the solid wall, and f^c is the fluid distribution function, post-BGK collision but pre-streaming. The linear IBB method has shown to be 2nd order accurate in velocity in comparisons to theoretical flow cases and against SBB methods.

The quadratic interpolated bounce back condition is even more accurate than linear IBB methods, but requires fluid distributions at two neighboring nodes. Quadratic IBB is applied for different cases of q by

$$f_{i'}(\mathbf{r},t+1) = q(2q+1)f_i^c(\mathbf{r},t) + (1+2q)\times(1-2q)f_i^c(\mathbf{r}-\mathbf{c}_i,t) - q(1-2q)\times f_i^c(\mathbf{r}-2\mathbf{c}_i,t), \qquad q < \frac{1}{2}$$ Equation A-22

$$f_{i'}(\mathbf{r},t+1) = \frac{1}{q(2q+1)}f_i^c(\mathbf{r},t) + \frac{(2q-1)}{2q}f_{i'}^c(\mathbf{r},t) + \frac{(1-2q)}{(1+2q)}f_{i'}^c(\mathbf{r}-\mathbf{c}_i,t), \qquad q \geq \frac{1}{2}$$ Equation A-23

The quadratic IBB method is also 2nd order accurate in velocity and 1st order accurate in pressure, and has been shown to be more accurate than linear IBB methods in direct comparison cases. For both linear and quadratic IBB methods, a value of q = ½ results in the original standard bounce-back formulation for wall boundaries.

A.6 Local volume definition

The fluid-to-solid interaction term $\mathbf{F_{fsi}}$ in the EBF method is given in the form of force density, or force divided by volume. Each calculation of $\mathbf{F_{fsi}}$ at a solid node determines only the force density at that solid node. Thus, in order to determine appropriate FSI forces at each solid node, the term $\mathbf{F_{fsi}}$ must be multiplied by a volume. These would be local volumes that are "owned" or associated with each solid node. The calculation of these local volumes depends on the solid modeling methodology.

In the original methodology paper by Wu and Aidun, a lattice-spring method is employed to simulate the suspended solid particles [66]. In this method, the entire particle volume is initially discretized into finite volumes. Thus, this methodology can easily determine the local volumes associated with solid boundary nodes, as the volume discretization is handled inherently by the lattice-spring method.

For the new implementation of the EBF method for this study, the solid phase modeling is performed differently. The surface mesh is discretized into triangular elements using meshing software, but the particle volume is not discretized into finite volumes. Thus, the local volumes associated with solid nodes are not inherently handled by the solid modeling method of this study. An alternative method must be determined to associate local volumes with solid boundary nodes, which has not been performed prior to this study.

A.6.1 Mesh element area calculation

Mesh element areas must be calculated at every timestep for deformable particles, and once for rigid particles. A demonstration of this is given in figure A-6 for one triangular element.

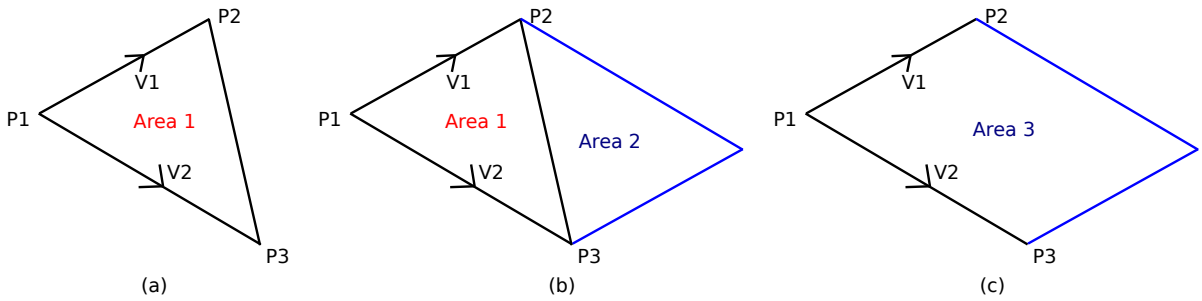

Figure A-6: (a) triangular element with 3 nodal points P1, P2, P3, and two vectors **V1**, **V2** formed from nodal points. (b) Mirrored element with equal area. (c) Parallelogram formed by two vectors

The nodal points P1-P3 of one triangle element are known at all times for rigid and deformable particles. These points can be used to determine two vectors **V1** and **V2**

on the element plane (Figure A-6a). Mirroring this element on the same 2D plane creates a second virtual element with equal area (Figure A-6b). It is noted that the magnitude of the cross product V1 x V2 is equal to the area of the parallelogram formed by V1 and V2 (Figure A-6c). The area of this parallelogram is also equal to the sum of the areas of the two mirrored elements. Thus, one can determine the element area at any time by

$$\text{Area} = \frac{\|\text{V1} \times \text{V2}\|}{2}$$

Equation A-24

For rigid particles, as these elements do not change in shape throughout the simulation, areas need only to be calculated once. For deformable particles, this calculation must occur at every timestep.

A.6.2 Various local volume calculation methods

Suspended particles in LBM-EBF simulations can be modeled as fluid-filled capsules with shell membranes or completely solid particles. For fluid-filled capsules, the calculation of local volumes is straightforward. As the thickness of the shell membrane is known, the local volume can be simply calculated as

$$\text{Volume}_{shell} = \text{Area}_{element} \times \text{thickness}_{shell}$$

Equation A-25

However, for completely solid particles like platelets, the volume extends from the triangular surface elements to the center of the particle. Thus, the local volume "owned" by the solid node/element can be thought of as a pyramidal volume with a base triangular element and an apex point at the particle center.

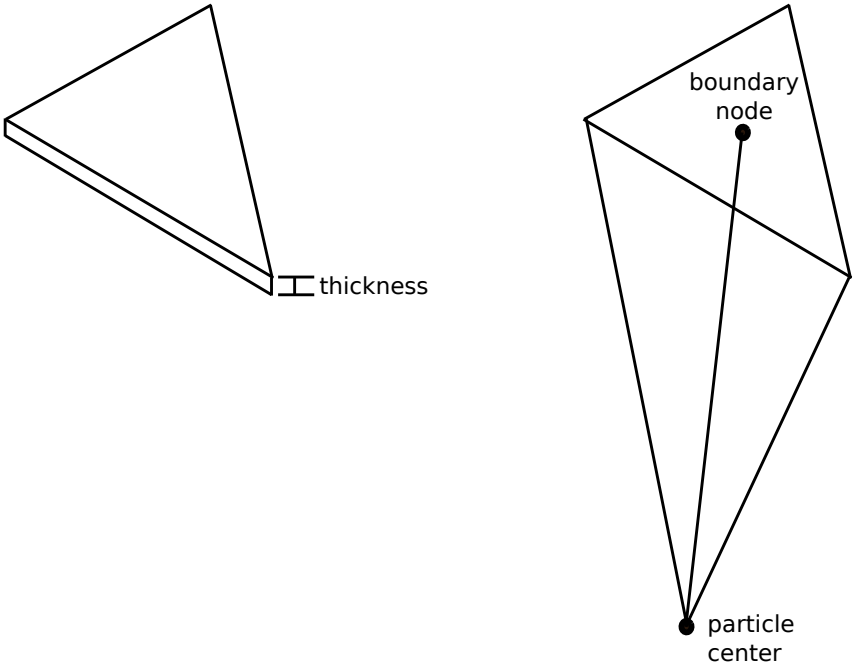

Figure A-7: Difference in local volumes for a mesh element for: shell particle (left) vs. completely solid particle (right)

One method for determining the local volumes for a completely solid particle is to calculate them as all equivalent, regardless of solid node position. A similar method is employed by the lattice spring method of the original EBF methodology, as the entire particle volume is discretized into equal finite volumes.

Another method of local volume calculation is to assume that the proportion of one element area to the total surface area is equivalent to the proportion of one local volume to the total particle volume. This can be defined as

$$\frac{\text{Volume}_{\text{local}}}{\text{Volume}_{\text{total}}} = \frac{\text{Area}_{\text{local}}}{\text{Area}_{\text{total}}} \qquad \text{Equation A-26}$$

Additional local volume methodologies are also defined, including the estimation of the local volume as the local element area to the power of 3/2. This is derived from

the principle that surface element areas are two-dimensional, and volumes are three-dimensional. Thus, an appropriate power scaling is required to translate from element area to local volume.

The inaccuracies of these local volume calculation methods for use with EBF are described in Appendix B.2.

A.6.3 Local Volume Calculation by Conal Volume Method

A local volume methodology is employed that accounts for the distance from the particle center to the solid boundary node. This method models the local volume for a solid boundary node as the conal volume created by the surface triangle element and the apex point at the particle center. More specifically, this is a pyramidal volume for each surface boundary node.

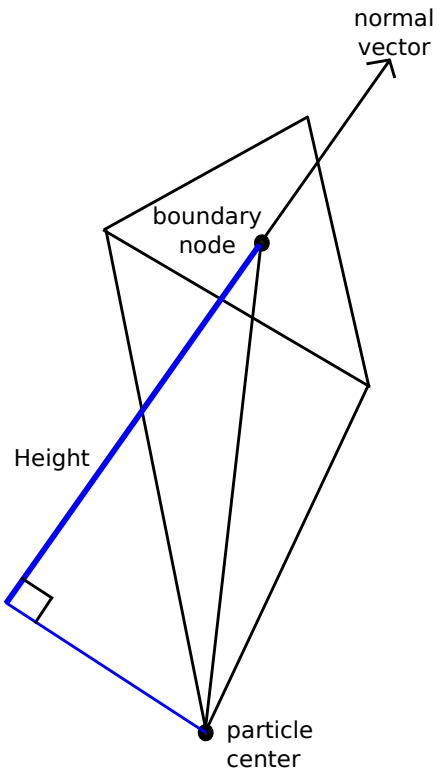

Figure A-8: Conal local volume method. Determine height value in local volume calculation by dot product of node-to-center distance and the normal vector to surface element

The local volume is thus defined from conal volume theory as

$$\text{Volume}_{\text{local}} = \frac{1}{3}\text{Area}_{\text{element}} \times \text{H}$$

Equation A-27

where the area is equivalent to the surface triangle element, and the height *H* is the normal height to the particle center. This is defined as the dot product of the vector from the surface node to the particle center with the unit normal vector at the surface element.

This method is tested for accuracy by computing local volumes for each solid element and accumulating them to determine a total volume. A variety of ellipsoidal

particles are tested and compared with theoretical volume values. Each particle surface is meshed with the same resolution of 0.1 for triangular element length. The total volumes are then compared to the theoretical volume of an ellipsoid, defined as

$$\text{Volume}_{\text{ellipsoid}} = \frac{4}{3}\pi \, a \times b \times c$$

Equation A-28

Table A-3: Comparison of ellipsoid theoretical vs. simulated volumes

Particle dimensions	Volume (Theory)	Volume (Simulation)	% difference
12x9x9	4071.50	4011.68	1.47
12x6x6	1809.55	1778.67	1.71
12x3x3	452.39	436.49	3.51
10x10x10	4188.79	4124.05	1.55
7x7x3.1	636.28	634.12	0.34

From Table A-3, the estimation of local volumes is shown to be accurate for a variety of ellipsoid geometries. The worst estimation is for an ellipsoid of aspect ratio 4, with a difference from theory of 3.51%. The 7x7x3.1 ellipsoid particle is the platelet particle used in the simulations of this study. This platelet is scaled appropriately based on the spatial resolution of each simulation. For this particle, the difference with theory is only 0.34%, showing the excellent ability to approximate mesh local volumes.

The difference in volume estimation from simulation to theoretical values can be explained by the meshing of the particle surface. The theoretical values are taken from a perfectly smooth ellipsoid geometry, but the meshing of the particle surface creates discrete triangle elements. Though the mesh resolution is high for these particles, it cannot perfectly capture a theoretical ellipsoid geometry due to finite discretization.

Thus, some difference with theoretical values is expected. However, the excellent matching for the platelet particle is very promising for the simulations of this study.

A.7. Outflow boundary conditions

A.7.1 Stress-free outlet and prescribed flow inlet

The stress-free and prescribed inlet flow boundary conditions for the lattice-Boltzmann method is described in detail by Aidun *et al.* [69] and is resolved as follows. Consider the inlet nodes to be located at $x = 0$, and the outlet nodes to be located at $x = x_{max} = L$. This gives an axial length of L+1 lattice units for the fluid domain.

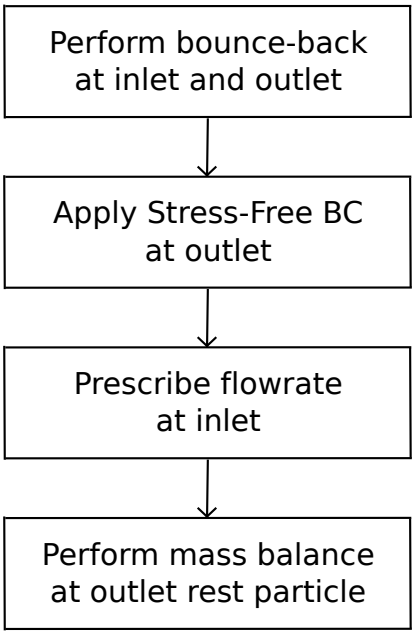

Figure A-9: Flowchart of methodology for imposing prescribed flow inlet, stress-free outlet boundary conditions

First, a pre-conditional bounce-back operator is employed at both the inlet and outlet, treating them as solid walls. Next, at the outlet fluid nodes, the fluid distributions

with lattice velocity links facing into the interior fluid domain (at x = L) are copied from the distribution values with the same lattice velocity link directions from x = L – 1. This completes the stress-free theory of $\partial u_x / \partial x = 0$ at $x = x_{max}$. As the copying of distribution values from x = L – 1 to x = L involves writing over previously existing distribution values, the difference between the old and newly written distribution values is stored and accumulated per fluid node as a mass balance term δ.

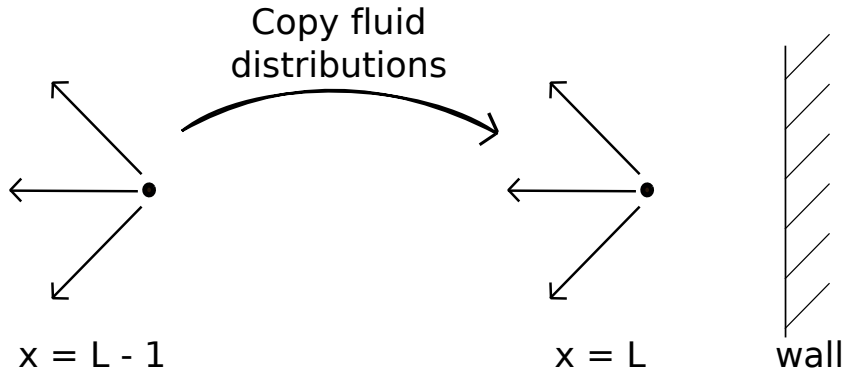

Figure A-10: Implementation of stress-free outlet boundary condition for lattice-Boltzmann methods

The prescribed flowrate condition is then implemented by adding flow momentum at the inlet. Based on the flow profile (plug, Poiseuille), the appropriate axial velocity value u_{inlet} is determined for each inlet fluid node. Next, the flow momentum is added to the system by distributing ρu_{inlet} among the lattice velocity links that are streaming into the flow domain at the inlet. This added flow momentum is added onto the pre-existing fluid distribution values. As this introduces mass into the system, the value of ρu_{inlet} is added to the mass balance term δ.

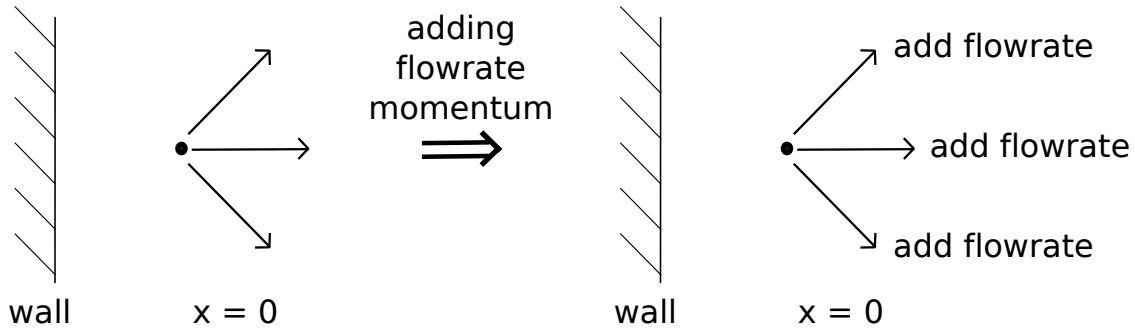

Figure A-11: Implementation of prescribed inlet flow boundary condition for lattice-Boltzmann methods

Finally, in order to maintain mass balance throughout the system, the mass balance term δ is subtracted from the rest particle f_0 at the outlet fluid node. This concludes the necessary steps for modeling prescribed inlet flow and stress-free outlet boundary conditions. Further details on the theory and implementation into lattice-Boltzmann methods can be found in the methodology paper by Aidun *et al.* [69].

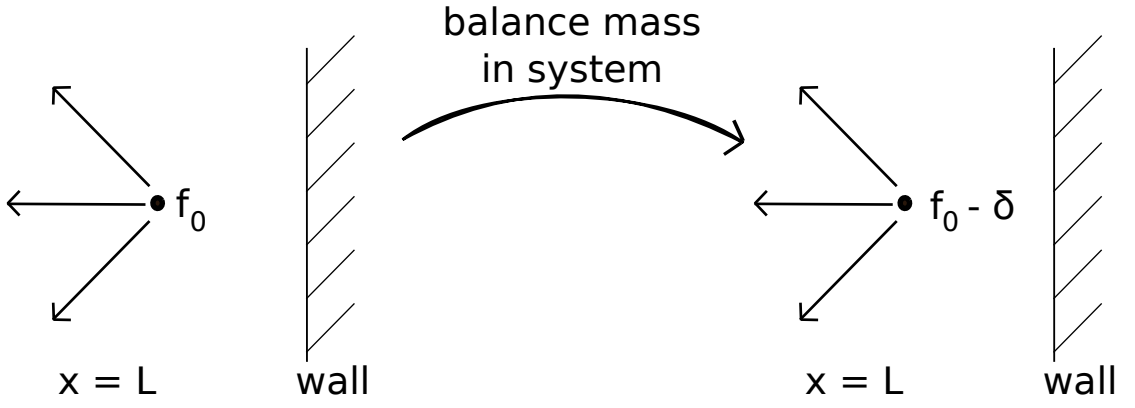

Figure A-12: Balancing mass of system after imposing prescribed flow inlet, stress-free outlet boundary conditions for lattice-Boltzmann methods

A.7.2 Alternative outflow boundary conditions

Additional outflow boundary conditions are implemented as alternative methods for possible use in future research. These include the Do Nothing (DNT) Condition and the Zero Normal Shear Stress (ZNS) Condition, which are both artificial outflow conditions similar to the stress-free condition. However, these alternative conditions do not work well with entropic LBM for higher Reynolds number flows. These problems will be discussed in detail in Appendix B.3.2, but the alternative methods are first described here.

A.7.2.1 Do Nothing Condition

The Do Nothing (DNT) boundary condition is an artificial outflow condition that is used in a variety of computational fluid dynamics methodologies. The general form of the DNT boundary condition is

$$-p + \nu \frac{\partial u_{k_0}}{\partial x_{k_0}} = 0; \qquad \nu \frac{\partial u_k}{\partial x_{k_0}} = 0, \quad k \neq k_0 \qquad \text{Equation A-29}$$

where p is the pressure, ν is the kinematic viscosity, k are the three Cartesian directions, and k_0 is orthogonal to the outflow boundary. The DNT condition has been used for lattice-Boltzmann methods with a formulation created by Junk and Yang [123] that approximates DNT conditions with at least first order accuracy. At the outflow boundary, the one fluid distribution in the direction k_0 normal to the boundary and pointing into the interior flow field is prescribed as

$$f_{k_0}(\mathbf{r}, t+1) = F_{k_0}^{(0)}\left(1, \mathbf{u}(\mathbf{r}, t)\right) - \left(\frac{\nu}{\tau} - 1\right)\left(f_i(\mathbf{r}, t) - f_i^{(0)}(\mathbf{r}, t)\right)_{k_{0^*}} \qquad \text{Equation A-30}$$

where k_{0*} is opposite in direction to k_0, and the function $F^{(0)}{}_{k0}$ is defined as

$$F_i^{(0)}\left(\rho,\mathbf{u}(\mathbf{r},t)\right) = w_i\left(\rho + 3\mathbf{u}\bullet\mathbf{e}_i + \frac{9}{2}\left((\mathbf{u}\bullet\mathbf{e}_i)^2 - \frac{1}{3}|\mathbf{u}|^2\right)\right) \qquad \text{Equation A-31}$$

where w_i are the LBM weights as previously defined, and ρ and $\boldsymbol{u}$ are the density and velocity at the fluid node, respectively. The remaining distributions with velocity link directions pointing into the interior flow field are prescribed by the formulation

$$f_i(\mathbf{r},t+1) = f_{i^*}^c(\mathbf{r}+\mathbf{e}_i,t) + 6w_i\mathbf{u}(\mathbf{r},t)\bullet\mathbf{e}_i, \quad \mathbf{e}_i \neq \hat{n} \qquad \text{Equation A-32}$$

where f^c is the post-collision distribution, and *i** is opposite in direction to *i*. The other fluid distributions that do not point into the interior flow field follow simple BGK operations and are streamed appropriately.

A.7.2.2 Zero Normal Shear Stress Condition

The Zero Normal Shear Stress (ZNS) boundary condition is another artificial outflow condition that has been translated for use in LBM by Junk and Yang [123]. The general form of the ZNS boundary condition is

$$-p + 2\nu\frac{\partial u_{k_0}}{\partial x_{k_0}} = 0; \qquad 2\nu S[\mathbf{u}]:\mathbf{e}_k\otimes\mathbf{e}_{k_0} = 0, \quad k \neq k_0 \qquad \text{Equation A-33}$$

with the same variable definitions as the DNT condition. At the outflow boundary, the fluid distribution in the one direction k_0 normal to the boundary and pointing into the interior flow field is prescribed as

$$f_{k_0}(\mathbf{r},t+1) = F_{k_0}^{(0)}\left(1,\mathbf{u}(\mathbf{r},t)\right) - \left(\frac{2\nu}{\tau} - 1\right)\left(f(\mathbf{r},t) - f_i^{(0)}(\mathbf{r},t)\right)_{k_{0^*}} \qquad \text{Equation A-34}$$

The remaining distributions with velocity link directions pointing into the interior flow field are prescribed by the formulation

$$f_i(\mathbf{r},t+1) = f_i^{(0)}(\mathbf{r},t) + \sum_{k=1}^{d}(c_{ik}^2 - 1)\frac{w_i}{w_{m_k}\left\|\boldsymbol{c}_{m_k}\right\|^2} \times \left(f_{m_k}(\mathbf{r},t) - f_{m_k}^{(0)}(\mathbf{r},t)\right)$$

$$\boldsymbol{c}_{m_k} = \left\|\boldsymbol{c}_{m_k}\right\|\boldsymbol{e}_k \qquad \text{Equation A-35}$$

where m_k points in the Cartesian coordinate directions. The other fluid distributions that do not point into the interior flow field follow simple BGK operations and are streamed appropriately.

A.8 Parallelization of Computational Methodology

Though subgrid resolution modeling is possible with the LBM-EBF method, the fluid spatial resolution must still be high enough to capture the bulk fluid flow field as well as Kolmogorov eddy scales. The spatial resolution that is required is discussed in section 5.5. The general range for spatial resolution for BMHV flows is on the order of 10μm – 100μm. With an inlet diameter of 0.0254m and a long aspect ratio due to artificial outflow conditions, these simulations require 100 million to 1 billion fluid grid points. Thus, parallel computing is a requirement for these BMHV flow studies.

For parallel processing applications, the two most common modes of parallelization are: shared memory and distributed memory computing. Shared memory parallelization methods, such as OpenMP protocol, are very easy to implement and have excellent scaling performance. However, limitations exist on the number of processors possible for parallel computing, as computer memory must be a shared resource. Alternatively, distributed memory parallelization methods, such as Message Passing Interface (MPI) protocol, allow for large cluster computing as computer memory can be distributed across multiple computational nodes.

Although MPI protocol is optimal for simulations of BMHV flow, the implementation is quite difficult, as all communicated data must be exactly specified by both the source and the receiving location. This becomes even more difficult with suspension flow simulations due to the large data communication necessary for parallel processing. However, due to the parallel computing capabilities of LBM with MPI protocol, 1000-3000 processor cores are used in parallel for simulations of this study with excellent scaling efficiency.

A.8.1 Lattice-Boltzmann Parallelization

A legacy LBM in-house solver is used as a starting point for the code development of this study. This legacy code employs parallel processing for the lattice-Boltzmann method with standard bounce-back suspension flow modeling. The parallel performance for this legacy code was analyzed in the work by Clausen *et al.* [94].

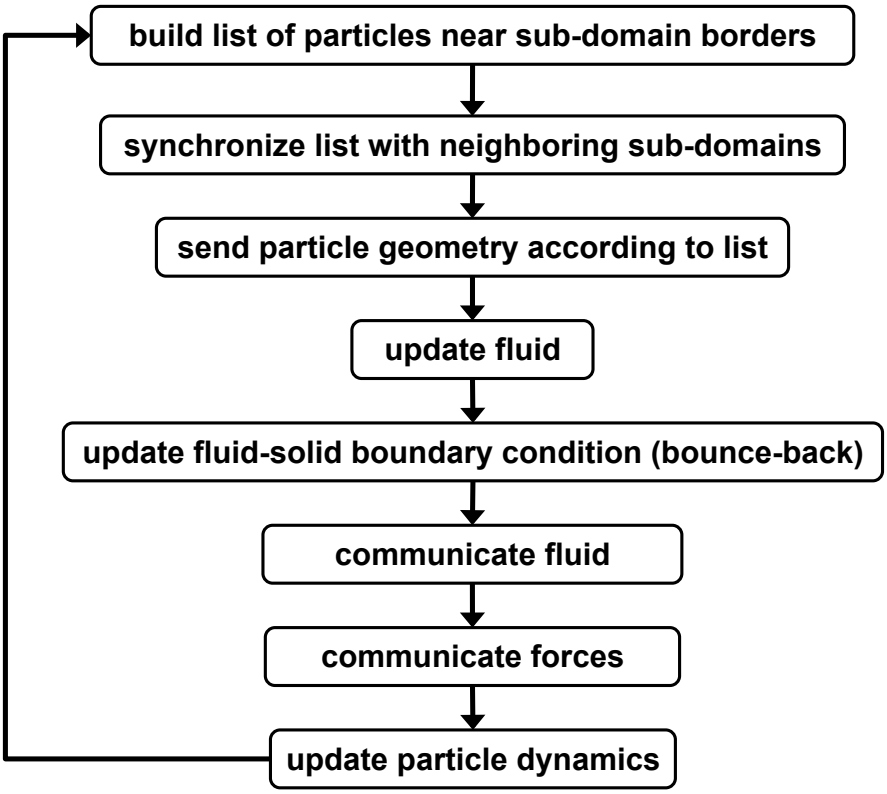

Figure A-13: Flowchart demonstrating LBM parallel computing for each timestep [94]

The high applicability of LBM to parallelization lies in the local nature of all flow calculations. The single-relaxation BGK operator for updating fluid particle distributions requires only neighboring nodes. Thus, the required flow modeling parallelization is straightforward. Large 3D flow domains are broken into smaller 3D subdomains that neighbor each other at subdomain boundary surfaces. Fluid data transfer is required across boundaries of subdomains. Since this must occur at every timestep and at unchanging locations, this parallelization implementation is very easy and efficient.

For each subdomain, a surrounding layer of "ghost nodes" is created at the surface boundaries. This ghost node layer, depicted on figure A-14, contains fluid node

information from neighboring subdomains that is necessary for flow calculations for the subdomain nodes at the boundary. Each subdomain also sends its boundary fluid node data to its neighbors. This sent data becomes the neighboring subdomain's ghost node layer for use in its flow field calculations. As this fluid data communication occurs every timestep and for known fluid nodes, an MPI_Sendrecv command is used for optimal data transfer. This command is one of the most efficient data communication commands in MPI protocol.

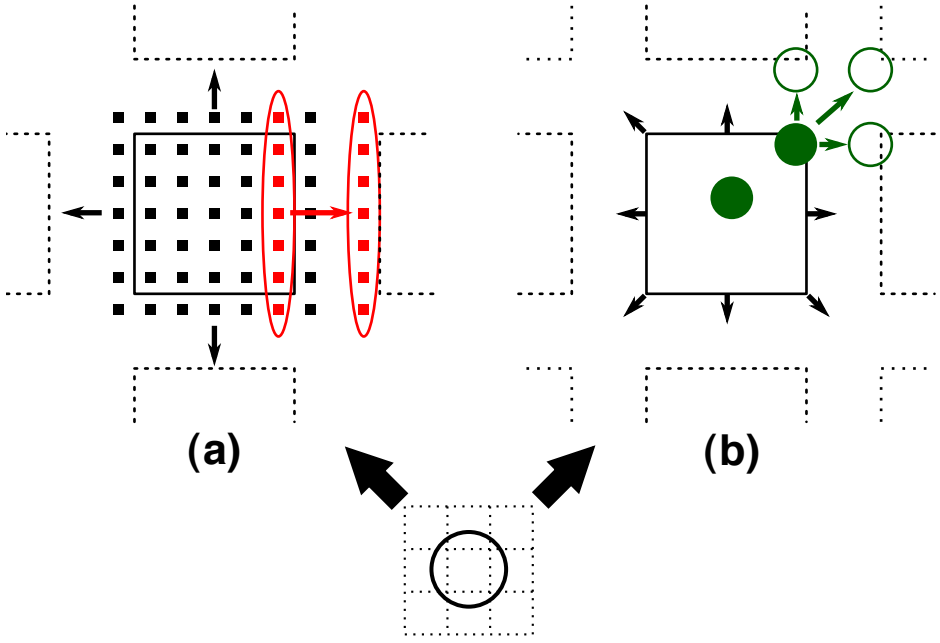

Figure A-14: (a) Ghost node fluid data communication across subdomain borders, and (b) Particle data communication to multiple subdomains [94]

Communication of suspended particle data is more complicated for LBM. As the suspended particles move throughout the domain, they can overlap across several 3D subdomains. This is demonstrated in figure A-14 where the particle overlaps four subdomains. The primary calculations for particle forces and torques and particle

dynamics occur at the subdomain that "owns" the particle. This is the subdomain at which the particle center is located. When a particle overlaps several subdomains, it first computes fluid-solid interaction modeling for all surface nodes, wherever those nodes are located. Next, the particle forces and torques are all sent to the subdomain that "owns" the particle and accumulated. Particle dynamics are then computed with the updated forces and torques on the particle, and particle motion and orientation are updated. Finally, the updated particle motion and orientation data is sent back to all subdomains that are overlapped by the particle for computing fluid-solid interaction for the next timestep. If the particle center moves to a different subdomain, this subdomain becomes the new "owner" of the particle.

In the legacy code, non-moving large surfaces (such as pipe walls or large obstructions) do not require data communication. Their position is fixed and the bounce-back links off these surfaces do not change, and thus no data needs to be communicated. However, this does become an issue for moving large surfaces, such as the moving leaflets of the BMHV, and will be covered below.

Table A-4: Single-phase flow scaling efficiency for 1024^3 LBM domain in shear flow [94].

Cores	Total time (s)	Efficiency (%)	Subdomain	$\mathcal{T}$	SU/s
2048	612.0	100.0	$128 \times 64 \times 64$	1.634	1.754×10^9
4096	306.4	99.87	$64 \times 64 \times 64$	3.268	3.509×10^9
8192	144.0	106.2	$64 \times 64 \times 32$	6.944	7.456×10^9
16,384	79.19	96.60	$64 \times 32 \times 32$	12.66	1.359×10^{10}
32,768	43.96	87.00	$32 \times 32 \times 32$	22.73	2.441×10^{10}
65,536	25.83	74.05	$32 \times 32 \times 16$	38.46	4.129×10^{10}

The fluid flow parallelization is extremely efficient for LBM and can be characterized as "embarrassingly parallel". Table A-4 shows scaling for single-phase simulations of simple shear flow and demonstrates that even for 16,384 processor cores, the LBM scales with almost 97% efficiency. For the table, T = LB timesteps per second, SU/s = site (node) updates per second, efficiency = % scaling compared to ideal 1:1 scaling. Efficiency is based on increasing the number of cores starting from 2048 cores.

Table A-5: Multi-phase flow scaling efficiency for 512^3 LBM domain with 13,824 deformable particles in shear flow [94]

Cores	Total time (s)	Efficiency (%)	Subdomain	$\mathcal{T}$
512	458.9	100.0	$64 \times 64 \times 64$	0.218
2048	215.7	53.19	$64 \times 32 \times 32$	0.464
4096	126.7	45.26	$32 \times 32 \times 32$	0.789
8192	94.52	30.34	$32 \times 32 \times 16$	1.058

Table A-5 shows how the presence of suspended deformable particles reduces the efficiency of the LBM code. This test simulation is of a dense suspension (40% by volume fraction) of 13,824 particles with a large number of particle-particle interactions and with deformation modeling. The scaling efficiency drops to 53% when increasing the number of cores by a factor of 4, due to the large amount of particle data communication that is required, and the increased calculations for deformation modeling and particle-particle interaction.

It should be noted that though the presence of suspended particles reduces the efficiency of the LBM code, the simulations of this study employ only rigid particles with no particle-particle interaction and very dilute suspensions only. Thus, the scaling

efficiency is expected to remain high and the simulations are closer to single-phase flow than the dense suspension flow tests of Clausen *et al.* [94].

A.8.2 External Boundary Force Parallelization

For the LBM-EBF method, parallelization is similar in concept to that developed for the legacy LBM-SBB solver and described by Clausen *et al.* [94]. However, the use of the External Boundary Force (EBF) method requires a modified parallelization strategy. Even though the LBM is not changed for either methodology, the EBF method affects the necessary fluid flow data transfer as well as solid particle data transfer.

A.8.2.1 Fluid Flow Parallelization

The SBB method for modeling small particles determines bounce-back links at the fluid-solid interface. These links only extend to the fluid node at the fluid-solid interface, and so even bounce-back links at fluid subdomain boundaries do not require any extra fluid data. The single ghost node layer is sufficient for SBB methods of modeling suspension flow.

The EBF method works differently by requiring fluid data interpolation within a radius of two fluid nodes. This is necessary to determine fluid density and velocities at the FSI solid boundary node, and requires the use of the Dirac delta function for interpolation [122]. Thus, the single ghost node layer is not sufficient and a double ghost node layer is required to permit EBF modeling.

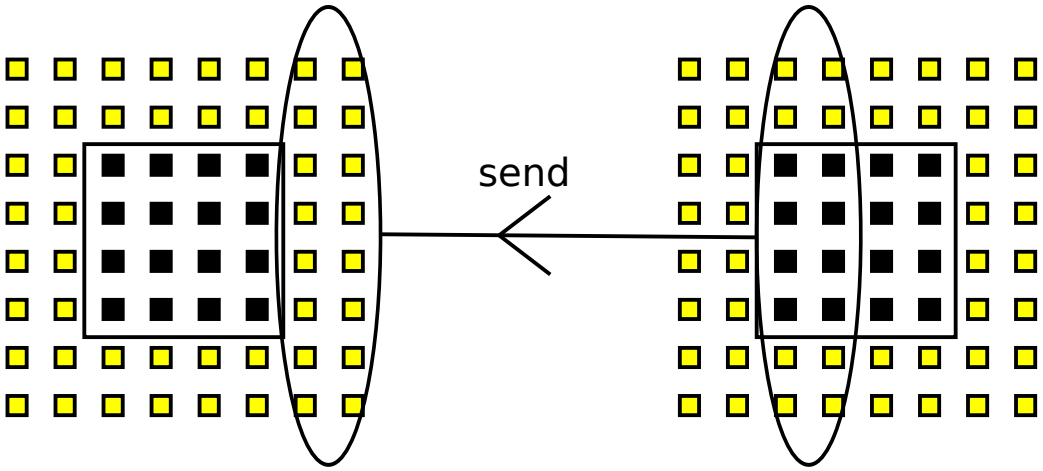

Figure A-15: Sending of fluid nodal data at fluid subdomain (black squares) to function as double ghost node layer (yellow squares) at neighboring fluid subdomain

Though a second layer of ghost nodes is required for EBF modeling, this fluid data communication is again known at every timestep and thus efficient MPI_Sendrecv commands can still be employed for optimal parallel processing. The second ghost node layer increases the amount of fluid data that must be communicated, but some modifications are made for efficiency. The EBF method only requires fluid data in the form of densities and velocities, and thus only this data needs to be sent for both double ghost node layers. Though the SBB method requires only one ghost node layer, the bounce-back links require all fluid distribution f_i values for completing FSI. This amounts to 19 floating-point values for the 3DQ19 method for SBB, whereas the EBF method only requires 4 floating-point values (one density, three velocity directions) for fluid data communication.

A.8.2.2 Particle Force Parallelization

The accumulation of forces and torques and calculation of particle dynamics is performed identically to that described in Section A.8.1. For 1-way FSI with the EBF method, the Dirac delta function must be employed to interpolate fluid node data in order to determine forces from the fluid onto the solid particle surface. For 2-way FSI, the forces on the solid particle node must be re-interpolated back onto the fluid flow field. This is performed to enforce equal and opposite forces at the solid boundary, in accordance with Newton's third law. This solid-to-fluid interaction also employs the Dirac delta function with a radius of two fluid nodes.

This solid-to-fluid interaction becomes an issue when the solid node lies near the boundary between fluid subdomains. In this case, the solid node force values influence fluid nodes across multiple subdomains. Two of these scenarios are depicted in figure A-16, with the solid nodes depicted as circles with an X.

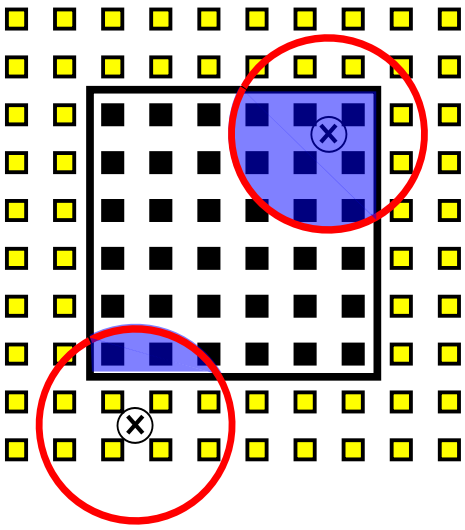

Figure A-16: Example of two cases of solid nodes (circles with X) lying near fluid subdomain boundaries. Red circles show the radius of influence of the solid node, and the blue shaded areas show the affected area of the current fluid subdomain

In the first case, the solid node lies within the fluid subdomain (top right circle with X in Figure A-16) but influences fluid nodes lying in the ghost node layers. In the second case, the solid node lies within the ghost node layers (bottom left circle with X in Figure A-16) but influences fluid nodes within the current fluid subdomain. In the first scenario, the solid node is "owned" by the current fluid subdomain because it resides within the subdomain. The red circle shows the radius of influence of the solid node, which extends to the ghost node layers. The solid-to-fluid force interpolation is first performed for fluid nodes that lie within the fluid subdomain (black squares within blue shaded area) within a radius of 2 nodes.

Next, the solid nodal force data is sent via MPI communication to neighboring subdomains. At the neighboring subdomains, this solid node data that is received is seen to reside within the ghost node layers. This is identical to the second case scenario (bottom left circle with X). Here, the solid-to-fluid force interpolation is performed for fluid nodes that lie within the fluid subdomain (black squares within blue shaded area) within a radius of 2 nodes. This completes all solid-to-fluid force interpolation and two-way FSI for the parallelized EBF method.

A.8.3 Boundary Condition Parallelization

For a periodic domain, fluid data communication needs only to be performed between neighboring subdomains as described in Sections A.8.1 and A.8.2.1. For the simulations of this study, prescribed flow inlet and stress-free outlet boundary conditions are required. Though this inlet and outlet are physically separated, the implementation of

these boundary conditions with LBM requires a mass balance operation (Section A.7.1). This mass balance term is applied at the outlet nodes, but includes contributions from the added flowrate at the inlet. Thus, the inlet conditions affect the mass balance operations at the outlet.

However, it is noted that although multiple subdomains separate the inlet and outlet, no actual fluid data communication is required between the inlet and outlet. The prescribed flow conditions are known for every processor used in the simulations because it is read from an input file. Thus, the added flowrate at every timestep is known by all subdomains, including the outlet subdomains. Since LBM models an incompressible flow, the added momentum ρu_{inlet} is also exactly known. This term is used in the mass balance operation, and thus no fluid data communication is required to parallelize the prescribed flow and stress-free outlet boundary conditions.

A.8.4 Leaflet motion Parallelization

Leaflet motion must also be parallelized for the simulations of this study. As the leaflet surface is large, it can span across multiple subdomains. Though particles such as platelets can technically overlap multiple subdomains, their size is relatively small compared to the fluid subdomains. Thus they are considered "small" particles and data communication is only performed across neighboring subdomain boundaries. Leaflet surfaces are considered "large" surfaces as they can span across subdomains that do not neighbor each other. Thus a different strategy for leaflet motion parallelization is required.

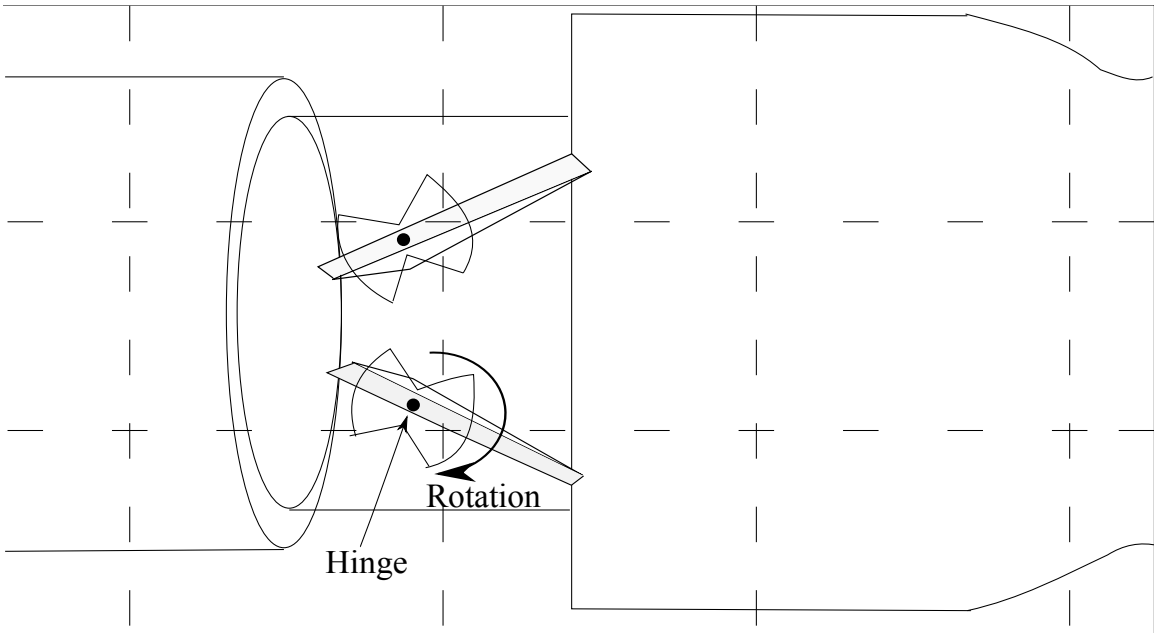

Figure A-17: Leaflet surface split among multiple subdomains. In this case, the dashed lines mark subdomain boundaries. Leaflets span four subdomains in this 2D view.

Though leaflet rotation results in different fluid subdomains containing the leaflets at different times, the leaflets are known to only reside within a specific region throughout their entire angle sweep. This region is the valve housing, as well as a small part of the entrance of the sinus aortic expansion when the leaflets are fully open. Thus, leaflet motion modeling and parallelization is only performed for fluid subdomains in this region, reducing the number of total calculations.

For prescribed leaflet motion, the leaflet motion and position is known by reading angle variation data from an input file. The leaflet begins in an initialized position, and then the new angular position is prescribed from the input data. After the leaflet motion is prescribed and the new position is set, the fluid subdomains loop through all leaflet surface elements to determine which elements reside within the given subdomain. The

new leaflet position is thus re-partitioned among these fluid subdomains by this process. After determining which leaflet surface nodes are "owned" by the subdomain, bounce-back links are determined to allow for updated fluid-solid interaction modeling. For the next leaflet motion, these links are cleared and a new leaflet position is determined.

Dynamic leaflet motion from two-way fluid solid interaction employs a combination of the methods for small particle modeling and prescribed leaflet motion modeling. First, for a given leaflet position, forces and torques are computed at every solid surface node via the SBB method. Next, as with small particles such as platelets, these forces and torques are accumulated onto one central processor that "owns" the leaflet. A subdomain that contains the hinge fulcrum is chosen as the "owner", as this position does not change throughout leaflet rotation. Leaflet dynamics are then updated via Newtonian dynamics equations using the accumulated torque about the hinge fulcrum line. The leaflet position is then updated and the leaflet surface is re-partitioned across multiple subdomains, as performed with prescribed leaflet motion modeling.

A.8.5 Other notes on Parallelization

Modifications are made to the fluid flow solver to include the Entropic LB method for capturing higher Reynolds number flows. Though this is a modification to LBM, the calculations performed for entropic LB are completely localized to individual fluid nodes. Thus, no extra fluid node-to-node communication is performed, and no special parallelization methods are required.

Interpolated bounce-back methods employ data from neighboring fluid nodes to the nodes that border the solid surfaces. Linear interpolation requires one neighboring

fluid node, and quadratic interpolation requires two neighboring fluid nodes. Though double ghost node layer fluid communication is already in place, the interpolated bounce-back methods require fluid distribution data from a second layer (linear and quadratic interpolation) or even a third layer (quadratic interpolation). The second ghost node layer may exist for EBF parallelization, but this layer only sends fluid density and velocity data, not the required 19 fluid distribution values. Thus, significant extra data communication is required in order to perform linear and quadratic interpolated bounce-back modeling.

APPENDIX B – NUMERICAL METHODS AND ISSUES

B.1 Additional BMHV flow modeling notes

In the closing phase, the leaflet coming into contact with the valve causes the formation of impact pressure waves. These waves can bounce back from the artificial outflow condition and affect the interior fluid flow. Thus, the ventricular pipe length is variably increased from 3 diameters in length to 13 diameters in length to prevent the interior flow from being significantly affected by the imposed stress-free boundary condition. For prescribed leaflet motion cases, this ventricular inlet is optimized at 4 diameters in length to eliminate the effect of pressure waves on the total flow field. However, for two-way leaflet FSI modeling, the ventricular inlet requires a length of at least 13 diameters.

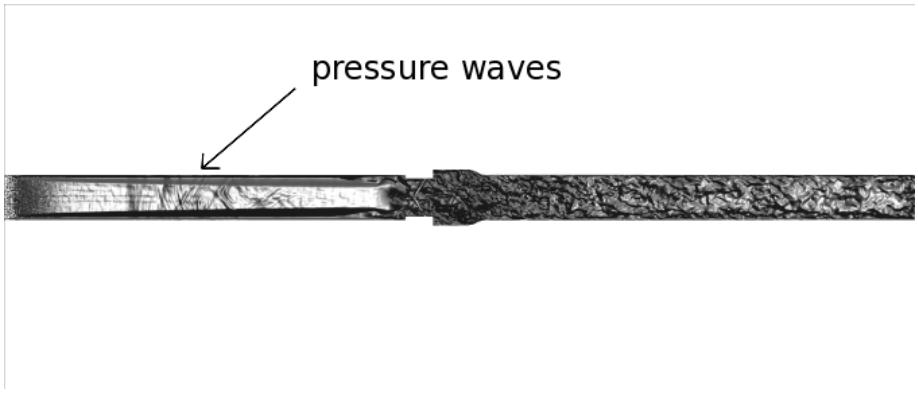

Figure B-1: Pressure wave formation caused by leaflet closing impact with valve housing

The lattice-Boltzmann method uses a 3D rectangular prism fluid grid domain for modeling flow. This fluid grid domain is large enough to enclose the entire flow chamber and valve. The solid domain is thus imposed onto this 3D flow grid. As the BMHV flow

domain is a complicated geometry, this results in many fluid nodes in the 3D fluid domain to be located outside of the BMHV geometry. Thus, customized coding is employed to only model flow within the BMHV and the experimental flow chamber. This is performed by "flagging" outside fluid nodes and ignoring flow modeling at these outside nodes.

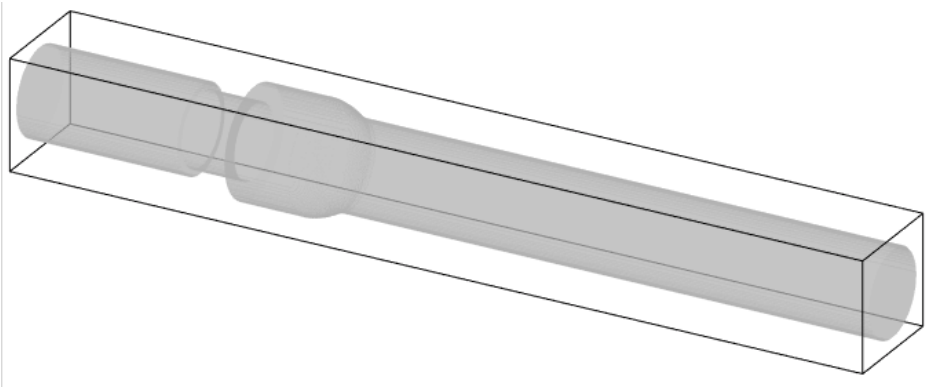

Figure B-2: Solid domain (gray) imposed within 3D box fluid domain

B.2 Failed Local Volume Methods for EBF Method

The local volume test simulations in this section are all performed for a flow domain of 120x120x60, with a shear rate of $G = 1/6000$, wall velocity of $U_w/2 = +/- 0.01$ in LB units, and relaxation parameter $\tau = 5.0$.

One local volume calculation method is to define all local volumes as equivalent, regardless of solid node position. A similar method is employed by the lattice spring method to discretize the particle volume into equal finite volumes [66].

This method is employed for Jeffery's orbit for a solid sphere particle of radius 10 (in LB units), corresponding to a Reynolds number of $Re_p = 0.044$. The results for the orientation angle and the rate of rotation match perfectly for multiple periods of rotation for this solid spherical case.

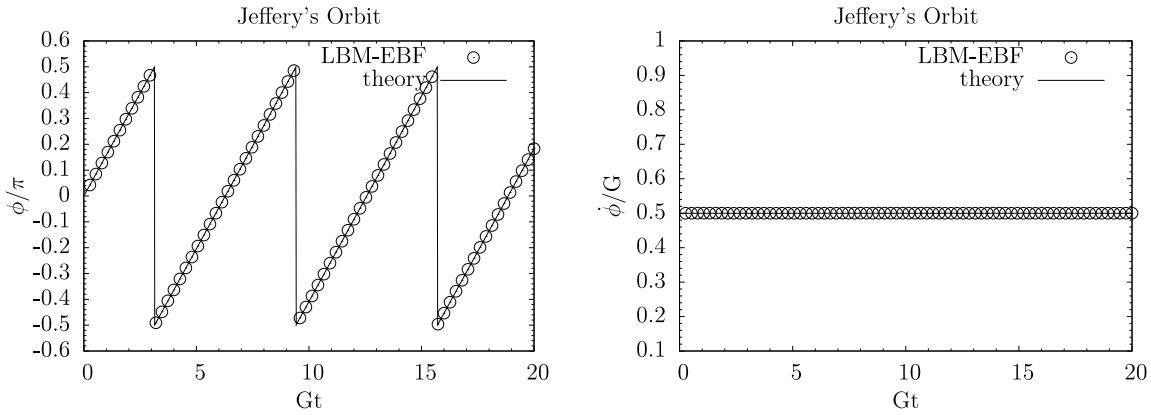

Figure B-3: Jeffery's orbit for sphere radius 10, Re_p = 0.044, G=1/6000. Local volume method of equivalent volumes for all mesh elements

For the same flow conditions but with a 12x9x9 solid ellipsoid (Re_p = 0.064), the simulations do not match well with theory. Within one orbit period there is a large drift of the ellipsoid from theory that subsequently grows larger as more simulation time elapses. This inaccuracy in simulation results also shows in the results of the rate of rotation. Some drift can be expected over time due to the modeling of non-zero Reynolds number. However, this should occur gradually over time and large drifts should not be seen within one orbital period. The Jeffery's orbit validation cases of the SBB method and EBF original implementation also do not see a significant drift for multiple periods of rotation [66, 69].

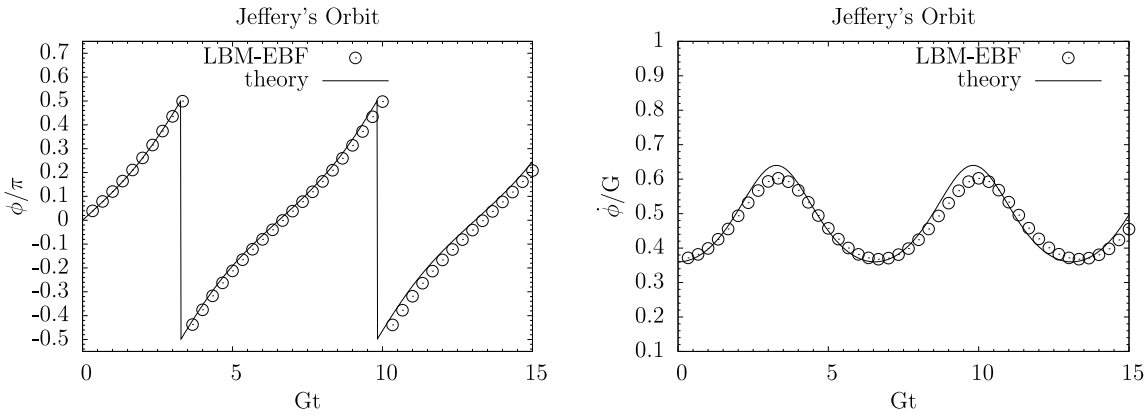

Figure B-4: Jeffery's orbit for ellipsoid 12x9x9 radius, $Re_p = 0.064$, G=1/6000. Local volume method of equivalent volumes for all mesh elements

The orbital period drift for the ellipsoid can be attributed to assuming equal volumes for all solid surface elements. Even if the mesh elements are equal in area, the distance from the surface node to the particle center would not be equal. Thus, it is incorrect to assume that the local volumes are equal for all surface nodes. The spherical particle has equal distance from surface nodes to the particle center due to perfect symmetry, and thus the local volumes are equal and accurate results are seen for the sphere case.

Another test is performed for the local volume calculation method that assumes that the proportion of one element area to the total surface area is equivalent to the proportion of one local volume to the total particle volume. For a solid sphere of radius 10, this again results in highly accurate matching between simulations and theory (not shown). However, for the 12x9x9 ellipsoid case, the orbital period drift from theory is again observed. Although the drift is less significant than for the previous local volume calculation method, it still occurs within the first two periods of rotation.

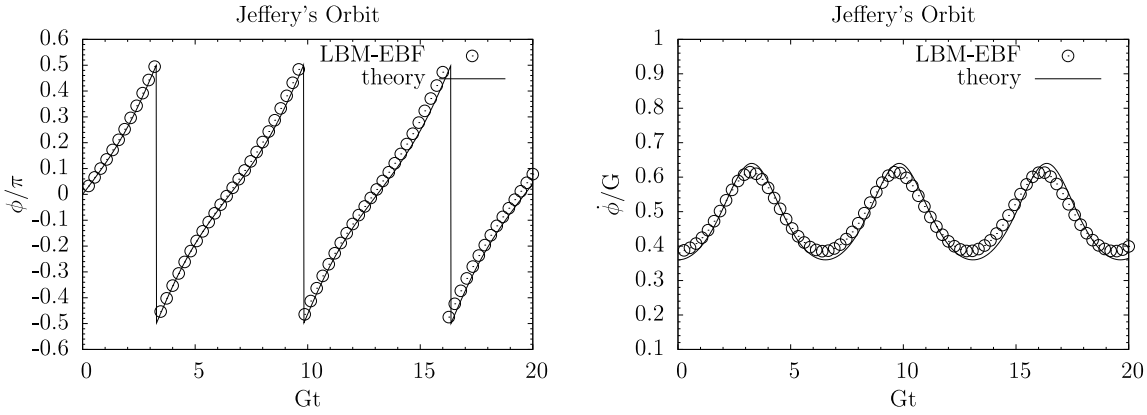

Figure B-5: Jeffery's orbit for ellipsoid 12x9x9 radius, Re_p = 0.064, G=1/6000. Local volume method of proportional volumes based on mesh element area proportion.

This orbital period drift can again be attributed to the distance from the surface node to the particle center. Though there may be a difference in element areas due to different curvatures for an ellipsoid, this methodology does not take into account the difference in node-to-center lengths. Thus, this local volume estimation method is also inaccurate. The spherical particle again has equal distance from surface nodes to the particle center, and accurate results are seen once more for the sphere case.

Additional local volume methodologies are also attempted, including the estimation of the local volume as the local element area to the power of 3/2. However, it is found that the results are once again inaccurate for this local volume methodology (results not shown).

B.3 Flow solver issues

In developing the numerical methodology for this study, a variety of new features are implemented into the legacy LBM-SBB code. Though these features are successfully implemented individually, some difficulties are found in combining the features.

Important notes are made on this subject, as a combination of methodologies has not been performed for these various features.

B.3.1 Entropic Lattice-Boltzmann issues

The entropic lattice-Boltzmann (ELB) method has already been shown in multiple previous studies to lead to universally stable flow simulations and to be able to capture turbulent flows at Reynolds numbers of up to 25,000 [72, 76-78]. This same method is implemented into the LBM code of this study and tested for stability. It is determined that for a periodic domain, pressure-driven flow, the ELB method is capable of running simulations of flow at Reynolds number 20,000 - 25,000 with universal stability. Tests of higher Reynolds number flows are not performed, as the peak Reynolds number of BMHV aortic flow is 6000, and thus the stability tests at Reynolds number 20,000 – 25,000 are sufficient. The ability of the ELB method to accurately capture higher Reynolds number flows is demonstrated with comparison to BMHV experimental data at high Reynolds number, and is shown in the Chapter 5.

For the ELB method, the modification to the relaxation parameter τ in the BGK collision operator is determined by calculating for a variable, γ, that enforces positive definiteness to the collision operator. The ELB methodology papers recommend the use of the fast and efficient Newton-Raphson method for determining γ. For the stability tests with periodic flow, it is found that the Newton-Raphson method efficiently determines this value. However, instabilities arise when applying ELB in combination with artificial outflow conditions, namely the stress-free boundary condition.

At high Reynolds number flows, enforcing a stress-free boundary condition at an artificial outlet is unphysical as the flow is still highly fluctuating. Extending the flow domain can reduce the influence on the interior flow field, but the enforcement of an unphysical outlet condition still creates a large number of instabilities at the outlet. Thus, the ELB method must be employed very frequently at outlet fluid nodes to enforce positive definiteness. The value of γ must be determined at these outlet nodes using a root-finding method (see Methods section for entropic LB details).

The Newton-Raphson method, though a quadratic convergent root-finding method, is not universally convergent. If there is a near-zero slope for the root-finding curve at the current "guess" value, then the Newton-Raphson method guesses a new root value that shoots to infinity. For highly fluctuating solutions, this can occur multiple times and a correct root value may never be found. These "infinity guess" issues are discovered when using the Newton-Raphson method to determine γ at the stress-free outlet nodes for high Reynolds number.

An alternative solution is to employ a universally convergent bisection method for determining γ. The limits for γ are known (between 0 and 2) for high Reynolds number flows, and thus a bisection method will universally find the appropriate root value γ. This method is slower (linear convergent) than Newton-Raphson, but is discovered to work with high Reynolds number flows, ELB methods, and stress-free outlet conditions. Mixed root-finding methods exist as well, but the bisection method is chosen for this thesis due to its universal convergence properties, ease of implementation, and minimal extra computations.

Thus, for the simulations of this study, a Newton-Raphson method is first employed for applying ELB at unstable fluid nodes. If an abnormally large γ guess is made by the Newton-Raphson method, then it is known that Newton-Raphson is failing and will not converge to find the appropriate root value. In this case, a bisection method is instead employed to appropriately determine γ. This method combination is shown to work well with ELB methods and stress-free outlets, in particular for the BMHV flow simulations of this study at high Reynolds number.

B.3.2 Additional artificial outflow conditions

The Do Nothing (DNT) and Zero Normal Shear Stress (ZNS) boundary conditions are both implemented successfully with the LBM code [123]. However, it is observed that the results using DNT and ZNS boundary conditions are not significantly more accurate than the stress-free condition. The DNT and ZNS conditions also produce results that are very similar with each other. Thus, only the ZNS condition results are shown. A sample case of Poiseuille flow is run for prescribed inlet flow and stress-free (SPP), ZNS, and DNT outlet conditions.

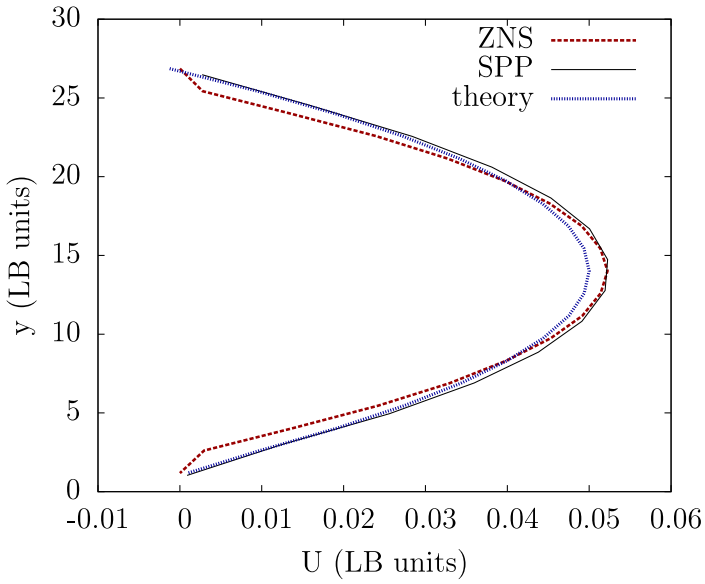

Figure B-6: Poiseuille flow velocity comparison with stress-free (SPP) and zero normal shear stress (ZNS) outlet conditions vs. theoretical Poiseuille flow profile

This very simple test shows that the stress-free outlet condition actually matches better than the ZNS condition, though both overshoot the theoretical peak flow velocity. Other sample flow cases yield similar results, with stress-free outlets consistently leading to more accurate results than DNT or ZNS boundary conditions.

In addition, problems are discovered with DNT and ZNS artificial outflow conditions when used at higher Reynolds number flows. When entropic lattice-Boltzmann (ELB) methods are used at high Reynolds number, stress-free outlet conditions are universally stable but DNT and ZNS conditions fail due to numerical instabilities. For the stress-free outlet condition (see Methods chapter for details), fluid distribution values are copied from x = L – 1 to x = L, where x = L is the outlet and x = L – 1 is the neighboring interior fluid node. The pre-conditioner bounce-back operation at the walls only reverses direction of fluid distributions at the outlet, but does not change

their magnitude. These are both performed after an entropic LB stability algorithm is already enforced. The copying of fluid distributions and enforcement of bounce-back operators do not change fluid distribution values after they have been stabilized, but only move their location. Thus, no issues are found with the stress-free outlet condition in combination with entropic LB.

However, DNT and ZNS conditions require fluid distribution values from neighboring nodes in their calculations. These calculations cause the entropic LB method to fail, as ELB methods only enforce positive definiteness locally at the fluid node. Entropic LB methods do not account for collision calculations that involve fluid distributions at other neighboring fluid nodes, and do not ensure positive definiteness for these types of calculations. Thus, it is observed that at high Reynolds number, DNT and ZNS conditions lead to instabilities and simulation failure.

B.3.3 Interpolated Bounce Back Conditions

Interpolated bounce back (IBB) conditions are implemented to improve on the accuracy of standard bounce-back (SBB) to determine fluid-solid interaction boundaries. Both linear and quadratic interpolation methods are implemented, but only linear interpolation results are shown here. A periodic flow through a circular pipe is simulated for a flow domain of 160x29x29 in LB units with a pipe of radius 12 LB units.

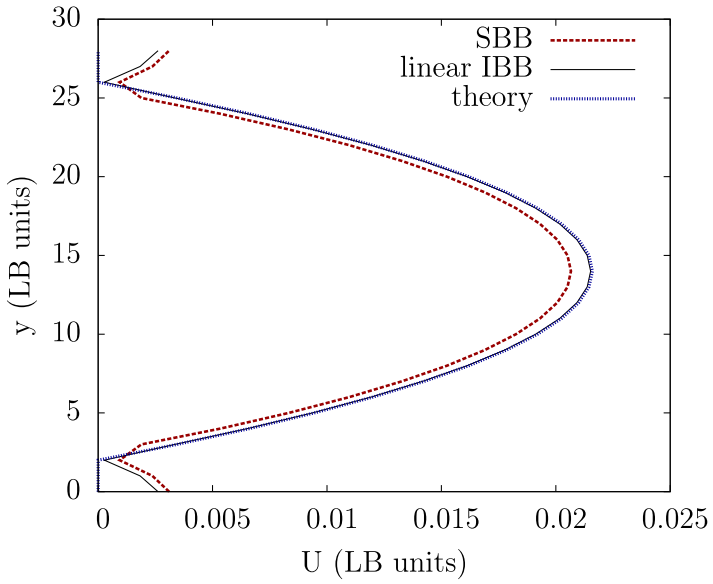

Figure B-7: Poiseuille flow velocity comparison with standard bounce-back and linear interpolated bounce back conditions vs. theoretical values, pipe radius 12 LB units

The linear interpolated bounce-back conditions shows excellent matching with theory in this low-resolution pipe flow case. The standard bounce back method clearly under predicts theoretical values of axial velocity at all radial positions.

A larger case is also simulated with a flow domain of 400x58x58 in LB units and a circular pipe of radius 26 LB units.

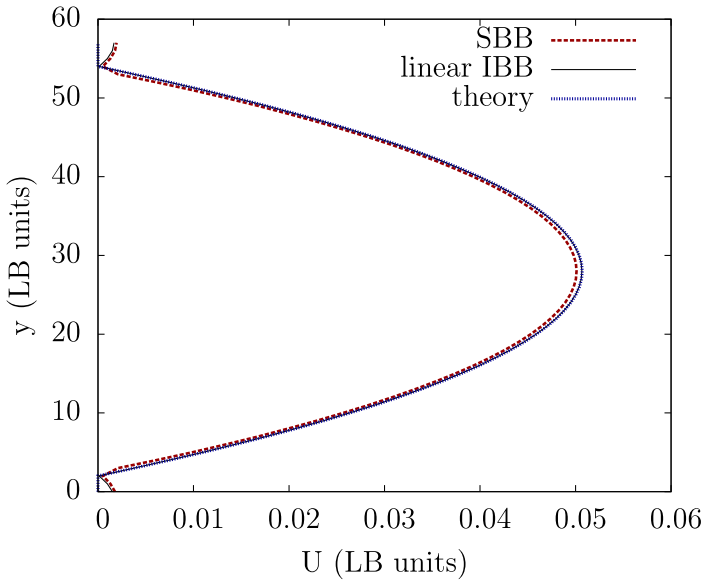

Figure B-8: Poiseuille flow velocity comparison with standard bounce-back and linear interpolated bounce back conditions vs. theoretical values, pipe radius 26 LB units

In this case with a higher fluid spatial grid resolution, the SBB method performs very well. Although the SBB method still under predicts the axial velocity values, the error is much smaller and the simulation is very close to theory. The linear IBB method is more accurate than the SBB method but not significantly. Just increasing the pipe radius to 26 LB units shows significant accuracy improvement using the SBB method.

It should be noted that for the simulations of this study, the flow chamber radii are calculated between 80 to 160 LB units depending on the fluid spatial resolution. Thus, it can be expected that the SBB method will be even more accurate with theory due to a much higher grid resolution. The linear IBB method, though technically more accurate than SBB methods, does not provide significant improved accuracy at high fluid spatial resolution to justify the increased cost of computational resources.

In addition, interpolated bounce-back conditions also encounter problems in combination with entropic LB methods, similar to the problems of the alternative artificial outflow conditions (Appendix B.3.2). Interpolated bounce-back methods also use neighboring nodes in their calculations, thus removing the positive-definiteness that is enforced by entropic LB methods. It is found that at higher Reynolds numbers, the IBB methods fail due to numerical instabilities, as entropic LB methods cannot enforce stability when combined with IBB methods. Thus, the sufficient solution accuracy, universal stability, and cheaper cost of the SBB method justify its use for the simulations of this study.

B.4 Problems with Dynamic Leaflet Motion

Though two-way FSI modeling of leaflet motion is simple in theory, several issues arise that can cause inaccuracies with the leaflet motion modeling. The primary issues are odd-even numerical instabilities from two-way FSI modeling, and pressure waves formed upon leaflet-valve contact.

B.4.1 Numerical Instabilities

Several instabilities are discovered in which the leaflet is too sensitive to the fluid forces acting upon it. The first instabilities are found immediately when two-way FSI modeling of leaflet motion is activated. Despite a 4^{th}-order accurate Runge-Kutta method for updating leaflet position, the leaflet moves too rapidly within one timestep. The fluid then reacts strongly to this rapid leaflet motion, and pushes the leaflet in the opposite

direction with an even stronger interaction force. This cycle repeats and leads to leaflet "fluttering", which crashes the simulation due to shockwaves that are formed in the flow.

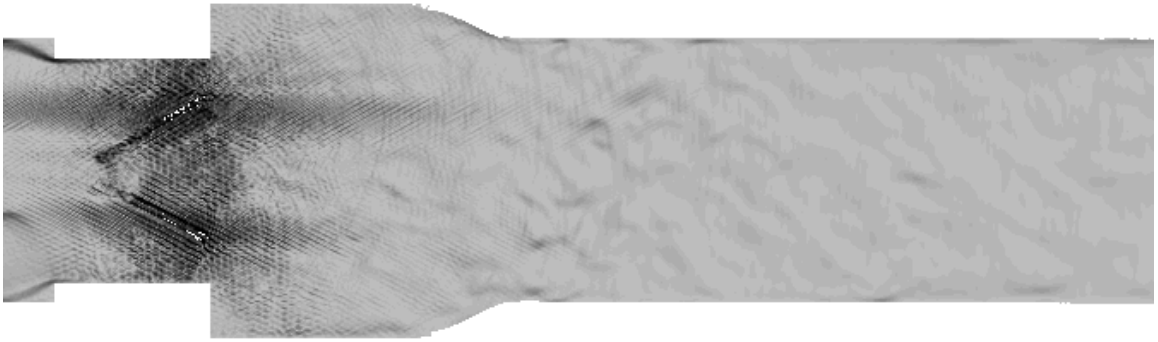

Figure B-9: Shockwaves in flow caused by leaflet "fluttering" from two-way FSI instabilities

These problems are solved by the use of torque averaging from the two most recent numerical timesteps. The instabilities are referred to as "odd-even" instabilities in which the forces or torques on a solid surface (in this case, a leaflet) switch signs from timestep to timestep, causing unstable motion and failure of the simulation. The modeling of small, suspended particles using the SBB method also encountered these problems, and a similar force averaging method was employed in previous works to stabilize the simulations [71, 85, 86]. This odd-even force and torque averaging method is similarly applied for dynamic leaflet motion modeling, and succeeds in stabilizing the simulations.

Further problems are encountered in which the leaflets do not flutter, but experience progressively higher torque values that cause an overly rapid leaflet motion.

Though the leaflet motion is in the correct direction, the movement is too rapid and also results in shockwaves that crash the simulation.

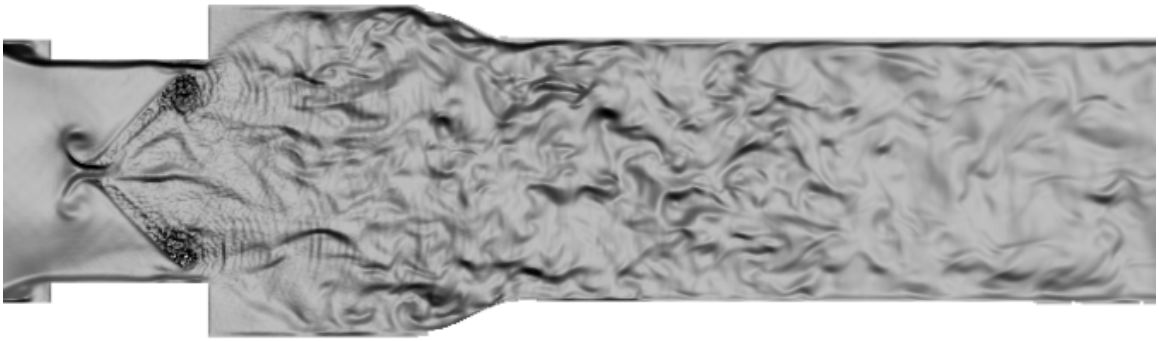

Figure B-10: Instability in flow field caused by overly rapid leaflet motion in one direction

Leaflet motion in BMHVs includes some friction forces due to leaflet ear contact with the hinge recess region. This friction modeling is not included in the two-way FSI modeling. Instead, cap limits are employed to zero the angular acceleration of the leaflets if torque values become too high. These cap limits succeed in stabilizing the simulation and work to prevent overly rapid leaflet motion. LBM simulations with solid motion are generally unstable when solid nodes traverse several fluid lattice nodes within one numerical timestep. Thus, cap limit values are calculated by determining what torque value would violate this guideline. These limits are enforced to prevent the solid from traversing more than two fluid lattice nodes per timestep. These cap limit values are not universal for all LBM simulations, but must be calculated based on varying spatiotemporal resolutions and simulation parameters.

B.4.2 Pressure Wave Problems

As previously noted, the simulations of this study employ a stress-free outlet boundary condition. The stress-free boundary condition is an artificial outflow condition that is used in numerical models to reduce the required domain size. The pre-conditional operator for this boundary condition is to employ bounce-back conditions at the outlet, which reflects the fluid motion at the artificial outlet. For the majority of the cardiac cycle, this does not affect the interior flow field. However, upon leaflet-valve closing impact, pressure waves are observed to form, which rapidly traverse the flow domain. These waves are reflected at the stress-free outlet, and eventually return to hit the leaflets. The simulations remain stable, as the fluid viscosity diminishes the effect of the pressure waves due to the traveled length. However, the pressure waves still affect the leaflet motion from 2-way FSI, causing the leaflets to rapidly open and close. This leads to a "swaying" motion for the leaflets, which does not crash the simulation but is highly inaccurate. Alternative artificial outflow methods are employed, such as the Do Nothing (DNT) and Zero Normal Shear Stress (ZNS) conditions (section A.7.2). However, these alternative methods also failed to resolve pressure wave issues of dynamic leaflet motion.

The solution to this problem is very simple, and only requires the extension of the domain length. This increases the length that the pressure waves must traverse, thus diminishing their effect. For prescribed leaflet motion, as the rotation of the leaflets is prescribed, the ventricular inlet length is fixed at three to four diameters. For dynamic leaflet motion, a ventricular inlet length of 13 diameters is determined as suitable for capturing accurate two-way FSI motion of the leaflets. The flow results, shown in the

next subsection, employ this 13 diameter ventricular inlet length. An inlet length of 9 diameters is deemed insufficient, as pressure waves still cause a “swaying” motion of the leaflets in this case.

APPENDIX C – ANIMATIONS

Animation 5-1: Out-of-plane vorticity magnitude animation for physiological adult flow, spanning two cardiac cycles and starting from peak flow (5_1_vorticity_adult.avi, 10.8MB)

Animation 5-2: Viscous fluid shear stress magnitude animation for physiological adult flow, for one cardiac cycle and starting from late diastole (5_2_shearStress_adult.avi, 6.8MB)

Animation 5-3: Isosurfaces of coherent 3D vortical structures based on the q-criterion for physiological adult flow, for one cardiac cycle and starting from leaflet opening (5_3_q_criterion.avi, 38MB)

Animation 6-1: Platelet seeding and release of 5400 total platelets, with 300 platelets released 1 diameter upstream of the valve every 20ms during systole (6_1_seeding.avi, 2.4MB)

Animation 6-2: Eulerian view of blood damage evolution for physiological adult case

(6_2_eulerian.avi, 2.6MB)

Animation 6-3: Lagrangian particle tracking view of highly damaged platelet undergoing near sinus expansion wall recirculation path (6_3_lagrangian.avi, 1.1MB)

Animation 6-4: Release of 2000 suspended platelets on aortic edge of BMHV for mid-diastole showing platelet leakage (6_4_diastole.avi, 1.9MB)

Animation 7-1: Out-of-plane vorticity magnitude animation for 5-year old child flow, for one cardiac cycle and starting from late diastole (7_1_vorticity_child.avi, 4.3MB)

Animation 7-2: Viscous fluid shear stress magnitude animation for 5-year old child flow, for one cardiac cycle and starting from late diastole (7_2_shearStress_child.avi, 6.9MB)

Animation 7-3: Out-of-plane vorticity magnitude animation for 6-month old infant flow, for one cardiac cycle and starting from late diastole (7_3_vorticity_infant.avi, 2.2MB)

Animation 7-4: Viscous fluid shear stress magnitude animation for 6-month old infant flow, for one cardiac cycle and starting from late diastole (7_4_shearStress_infant.avi, 5MB)

APPENDIX D – DATA GUIDE

The data used in this thesis can be found in the following directories, arranged by thesis specific aims. This data is available in backup sources (external hard drives, cloud servers) in the CFM lab.

- /7_Projects_DATA
  - /7_Projects_DATA/0_SETUP_GEOMETRIES
    - /7_Projects_DATA/0_SETUP_GEOMETRIES/BMHV Mesh
    - /7_Projects_DATA/0_SETUP_GEOMETRIES/FEA_INFO FILES
    - /7_Projects_DATA/0_SETUP_GEOMETRIES/initial_tests
  - /7_Projects_DATA/1_SpecificAim1
    - /7_Projects_DATA/1_SpecificAim1/EBF_InitialValidation
    - /7_Projects_DATA/1_SpecificAim1/Ellipsoid Orbit
    - /7_Projects_DATA/1_SpecificAim1/FEA_INFO
    - /7_Projects_DATA/1_SpecificAim1/Jingshu_code
    - /7_Projects_DATA/1_SpecificAim1/subgrid_shearStress
  - /7_Projects_DATA/2_SpecificAim2
    - /7_Projects_DATA/2_SpecificAim2/3D_viz
    - /7_Projects_DATA/2_SpecificAim2/Asymmetric_leaflet
    - /7_Projects_DATA/2_SpecificAim2/JFM1_validation
    - /7_Projects_DATA/2_SpecificAim2/JFM2_newFlows
    - /7_Projects_DATA/2_SpecificAim2/random
  - /7_Projects_DATA/3_SpecificAim3
    - /7_Projects_DATA/3_SpecificAim3/angle_BDI_variation
    - /7_Projects_DATA/3_SpecificAim3/BDI_Final_data
    - /7_Projects_DATA/3_SpecificAim3/initial test runs
    - /7_Projects_DATA/3_SpecificAim3/Lagrangian_movies
    - /7_Projects_DATA/3_SpecificAim3/mid_diastole_simulation
    - /7_Projects_DATA/3_SpecificAim3/movies_samples
    - /7_Projects_DATA/3_SpecificAim3/randomSeed_simulation
    - /7_Projects_DATA/3_SpecificAim3/SIMULATIONS
  - /7_Projects_DATA/4_SpecificAim4
    - /7_Projects_DATA/4_SpecificAim4/adult
    - /7_Projects_DATA/4_SpecificAim4/BDI
    - /7_Projects_DATA/4_SpecificAim4/child
    - /7_Projects_DATA/4_SpecificAim4/infant
    - /7_Projects_DATA/4_SpecificAim4/infant2
    - /7_Projects_DATA/4_SpecificAim4/pediatric_conditions

- /7_Projects_DATA/5_OtherWork
  - /7_Projects_DATA/5_OtherWork/1_DynamicLeafletMotion
  - /7_Projects_DATA/5_OtherWork/2_InterpolatedBounceBack
  - /7_Projects_DATA/5_OtherWork/3_OutletBCs
  - /7_Projects_DATA/5_OtherWork/4_AnnaFallonWork
- /7_Projects_DATA/6_OtherPeoplesWork
  - /7_Projects_DATA/6_OtherPeoplesWork/BDI Movies

REFERENCES

1. Yoganathan, A.P., Lemmon, J., and Ellis, J.T., *Heart Valve Dynamics*. 2 ed. Biomedical Engineering Handbook. 1995.
2. Black, M.M., and Drury, P.J., *Mechanical and Other Problems of Artificial Valves.* Current Topic in Pathology, 1994. **86**: p. 127-159.
3. Rosamond, W., Flegal, K., Furie, K., et al., *Heart Disease and Stroke Statistics.* Circulation, 2008. **117**(e): p. 25-146.
4. Chan, V., Malas, T., Lapierre, H., Boodhwani, M., Lam, B., Rubens, F.D., Hendry, P., Masters, R., Goldstein, W., Mesana, T., et al., *Reoperation of left heart valve bioprostheses according to age at implantation.* Circulation, 2011. **124**(11): p. S75--S80.
5. Daebritz, S., Sachweh, J., Hermanns, B., Fausten, B., Franke, A., Groetzner, J., Klosterhalfen, B., and Messmer, B., *Introduction of a flexible polymeric heart valve prosthesis with special design for mitral position.* Circulation, 2003. **108**(10): p. II--134.
6. Hyde, J.A., Chinn, J.A., and Phillips Jr, R.E., *Polymer heart valves.* Journal of Heart Valve Disease, 1999. **8**(3): p. 331.
7. Yoganathan, A., Leo, H., Travis, B., and Teoh, S., *Heart Valve Bioengineering.* Encyclopedia of Comprehensive Structural Integrity, 2003: p. 795–796.
8. Simon, H.A., *Numerical Simulations of the Micro Flow Field in the Hinge Region of Bileaflet Mechanical Heart Valves*, in *School of Chemical and Biomolecular Engineering*. 2009, Georgia Institute of Technology: Atlanta.
9. Grunkemeier, G.L.a.A., W.N.J., *Clinical Evaluation and Analysis of Heart Valve Substitutes.* Journal of Heart Valve Disease, 1998. **7**(2): p. 163-169.
10. Dumont, K., Vierendeels, J., Kaminsky, R., Van Nooten, G., Verdonck, P., and Bluestein, D., *Comparison of the Hemodynamic and Thrombogenic Performance of Two Bileaflet Mechanical Heart Valves Using a CFD/FSI Model.* Journal of Biomechanical Engineering, 2007. **129**: p. 558-565.
11. Giersiepen, M., Wurzinger, L.J., Opitz, R., and Reul, H., *Estimation of Shear Stress-Related Blood Damage in Heart Valve Prostheses- in Vitro Comparison of 25 Aortic Valves.* International Journal Of Artificial Organs, 1990. **13**(5): p. 300-306.
12. Danziger, J., *Vitamin K-dependent proteins, warfarin, and vascular calcification.* Clinical Journal of the American Society of Nephrology, 2008. **3**(5): p. 1504-1510.
13. Walker, P.a.Y., A.P., *In Vitro Pulsatile Flow Hemodynamics of Five Mechanical Aortic Heart Valve Prostheses.* European Journal of Cardiothoracic Surgery, 1992. **6**: p. S113-S123.
14. Ellis, J., Healy, T.M., Fontaine, A.A., Saxena, R., and Yoganathan, A., *Velocity measurements and flow patterns within the hinge region of a medtronic parallel bileaflet mechanical heart valvewith clear housing.* Journal of Heart Valve Disease, 1996. **5**(6): p. 591-599.

15. Ellis, J., and Yoganathan, A., *A comparison of the hinge and near-hinge flow fields of the St. Jude medical hemo- dynamic plus and regent bileaflet mechanical heart valves.* J. Thorac. Cardiovasc. Surg., 2000. **119**: p. 83-93.
16. Lu, P.C., Lai, H.C., and Liu, J.S., *A reevaluation and discussion on the threshold limit for hemolysis in a turbulent shear flow.* Journal of Biomechanics, 2001. **34**(10): p. 1361--1364.
17. Skoularigis, J., Essop, M., Skudicky, D., et al., *Frequency and Severity of Intravascular Hemolysis after Left-Sided Cardiac Valve Replacement with Medtronic Hall and St. Jude Medical Prostheses, and Influence of Prosthetic Type, Position, Size, and Number.* American Journal of Cardiology, 1993. **71**: p. 587-591.
18. Vallana, F., Rinaldi, S., Galletti, P.M., Nguyen, A., and Piwnica, A., *Pivot design in bileaflet valves.* ASAIO, 1992. **38**(3): p. M600.
19. Chien, S., *Red Cell Membrane and Hemolysis, in Cardiovascular Flow Dynamics and Measurements*. 1977, Baltimore: University Park Press.
20. Chandran, K.B., Rittgers, S.E., and Yoganathan, A.P., *Biofluid mechanics: the human circulation*. 2012: CRC Press.
21. Martini, F.H., *Blood*. 5 ed. Fundamentals: Anatomy and Physiology: Prentice Hall.
22. Nevaril, C.G., Lynch, E.C., Alfrey, C.P., et al., *Erythrocyte Damage and Destruction Induced by Shearing Stress.* Journal of Laboratory and Clinical Medicine, 1968. **71**: p. 784.
23. Leverett, L.B., Hellums, J.D., Alfrey, C.P., et al., *Red Blood Cell Damage by Shear Stress*. Biophysical Journal, 1972. **12**: p. 257-273.
24. Blackshear, P.L., *Mechanical Hemolysis in Flowing Blood*. Biomechanics: Its Foundation and Objectives by Fung Y.C., Perrone N., Anliker. 1972: Prentice Hall.
25. Hellums, J.D.a.B., C.H.I., *Blood Cell Damage by Mechanical Forces*. Cardiovascular Flow Dynamics and Measurements. 1977: University Park Press.
26. Sallam, A.M.a.H., N.H.C., *Human Red Blood Cell Hemolysis in a Turbulent Shear Flow: Contribution of Reynolds Shear Stresses.* Biorheology, 1984. **21**: p. 783-797.
27. Lu, P.C., Lai, H.C., and Liu, J.S., *A Reevaluation and Discussion on the Threshold Limit for Hemolysis in a Turbulent Shear Flow.* Journal of Biomechanics, 2001. **34**: p. 1361-1364.
28. Born, G.V.R., *Aggregation of Blood Platelets by Adenosine Diphosphate and Its Reversal.* Nature, 1962. **194**: p. 927-929.
29. Born, G.V.R.a.C., M.J., *The Aggregation of Blood Platelets.* Journal of Physiology, 1963. **168**: p. 178-195.
30. Brown, C.H., Leverett, L.B., Lewis, C.W., et al., *Morphological, Biochemical, and Functional Changes in Human Platelets Subjected to Shear Stress.* J. Lab. Clin. Med., 1975. **3**: p. 462-474.
31. Bernstein, E.F., Marzec, U., and Johnston, G.G., *Structural Correlates of Platelets Functional Damage by Physical Forces.* Trans. Am. Soc. Artif. Intern. Organs, 1977. **23**: p. 617-625.

32. Anderson, G.H., Hellums, J.D., Moake, J.L., et al., *Platelet Lysis and Aggregation in Shear Fields.* Blood Cells, 1978. **4**(3): p. 499-511.
33. Sheriff, J.a.B., D. and Girdhar, G. and Jesty, J., *High-shear stress sensitizes platelets to subsequent low-shear conditions.* Annals of Biomedical Engineering, 2010. **38**(4): p. 1442-1450.
34. Bellhouse, B.J., and Talbot, L., *The fluid mechanics of the aortic valve.* Journal of Fluid Mechanics, 1969. **35**(4): p. 721-735.
35. Lee, C.S.F., and Talbot, L., *A fluid-mechanical study of the closure of heart valves.* Journal of Fluid Mechanics, 1979. **91**(1): p. 41-63.
36. Wippermann, F.K., *On the fluid dynamics of the aortic valve.* Journal of Fluid Mechanics, 1985. **159**: p. 487-501.
37. Ku, D.N., *Blood flow in arteries.* Annual Review of Fluid Mechanics, 1997. **29**(1): p. 399-434.
38. Peskin, C.S., *The fluid dynamics of heart valves: experimental, theoretical, and computational methods.* Annual Review of Fluid Mechanics, 1982. **14**(1): p. 235-259.
39. Yoganathan, A., Z. He, and S.C. Jones, *Fluid Mechanics of Heart Valves.* Annual Review of Biomedical Engineering, 2004. **6**: p. 331-362.
40. Shipkowitz, T., Ambrus, J., Kurk, J., et al., *Evaluation Technique for Bileaflet Mechanical Valves.* Journal of Heart Valve Disease, 2002. **11**(2): p. 275-282.
41. Akins, C.W., *Results with mechanical cardiac valvular prostheses.* Annals of Thoracic Surgery, 1995. **60**(6): p. 1836-44.
42. Ellis, J.T., Travis, B.R., and Yoganathan, A.P., *An In Vitro Study of the Hinge and Near-Field Forward Flow Dynamics of the St. Jude Medical® Regent™ Bileaflet Mechanical Heart Valve.* Annals of Biomedical Engineering, 2000. **28**(5): p. 524-532.
43. Simon, H.A., Leo, H.L., Carberry, J., and Yoganathan, A., *Comparison of the Hinge Flow Fields of Two Bileaflet Mechanical Heart Valves under Aortic and Mitral Conditions.* Annals of Biomedical Engineering, 2004. **32**(12): p. 1607-1617.
44. Lim, W.L., Chew, Y.T., Chew, T.C., and Low, H.T., *Particle image velocimetry in the investigation of flow past artificial heart valves.* Journal of Biomechanics, 1994. **22**(3): p. 307-318.
45. Lim, W.L., Chew, Y.T., Chew, T.C., and Low, H.T., *Steady flow dynamics of prosthetic aortic heart valves: a comparative evaluation with PIV techniques.* Journal of Biomechanics, 1998. **31**(5): p. 411-421.
46. Lim, W.L., Chew, Y.T., Chew, T.C., and Low, H.T., *Pulsatile flow studies of a porcine bioprosthetic aortic valve in vitro: PIV measurements and shear-induced blood damage.* Journal of Biomechanics, 2001. **34**(11): p. 1417-1427.
47. Brucker, C., Steinseifer, U., Schroder, W., and Reul, H., *Unsteady flow through a new mechanical heart valve prosthesis analysed by digital particle image velocimetry.* Measurement Science and Technology, 2002. **13**: p. 1043.
48. Manning, K.B., Kini, V., Fontaine, A.A., Deutsch, S., and Tarbell, J.M., *Regurgitant flow field characteristics of the St. Jude bileaflet mechanical heart valve under physiologic pulsatile flow using particle image velocimetry.* Artificial Organs, 2003. **27**(9): p. 840-846.

49. Herbertson, L.H., Deutsch, S., and Manning, K.B., *Near Valve Flows and Potential Blood Damage During Closure of a Bileaflet Mechanical Heart Valve.* Journal of Biomechanical Engineering, 2011. **133**: p. 094507.
50. Lamson, T.C., Rosenberg, G., Geselowitz, D.B., Deutsch, S., Stinebring, D.R., Frangos, J.A., and Tarbell, J.M., *Relative blood damage in the three phases of a prosthetic heart valve flow cycle.* ASAIO, 1993. **39**(3): p. M626.
51. Leo, H.L., Dasi, L.P., Carberry, J., Simon, H.A., Yoganathan, A.P., *Fluid dynamic assessment of three polymeric heart valves using particle image velocimetry.* Annals of Biomedical Engineering, 2006. **34**(6): p. 936-952.
52. Dasi, L.P., Ge, L., Simon, H.A., Sotiropoulos, F., and Yoganathan, A., *Vorticity dynamics of a bileaflet mechanical heart valve in an axisymmetric aorta.* Physics of Fluids, 2007. **19**: p. 067105–067117.
53. Dasi, L.P., and Murphy, D.W., and Glezer, A., and Yoganathan, A.P., *Passive flow control of bileaflet mechanical heart valve leakage flow.* Journal of Biomechanics, 2008. **41**(6): p. 1166-1173.
54. Murphy, D.W., L.P. Dasi, J. Vukasinovic, A. Glezer, and A.P. Yoganathan, *Reduction of Procoagulant Potential of b-Datum Leakage Jet Flow in Bileaflet Mechanical Heart Valves via Application of Vortex Generator Arrays.* Journal of Biomechanical Engineering, 2010. **132**: p. 071011.
55. Ge, L., Leo, H.L., Sotiropoulos, F., and Yoganathan, A., *Flow in a mechanical bileaflet heart valve at laminar and near-peak systole flow rates: CFD simulations and experiments.* Journal of Biomechanical Engineering, 2005. **127**: p. 782-797.
56. De Tullio, M.D., Cristallo, A., Balaras, E., and Verzicco, R., *Direct numerical simulation of the pulsatile flow through an aortic bileaflet mechanical heart valve.* Journal of Fluid Mechanics, 2010. **622**: p. 259.
57. Nobili, M., Morbiducci, U., Ponzini, R., Del Gaudio, C., Balducci, A., Grigioni, M., Maria Montevecchi, F., Redaelli, A., *Numerical simulation of the dynamics of a bileaflet prosthetic heart valve using a fluid-structure interaction approach.* Journal of Biomechanics, 2008. **41**(11): p. 2539-2550.
58. Borazjani, I., Ge, L., and Sotiropoulos, F., *Curvilinear immersed boundary method for simulating fluid structure interaction with complex 3D rigid bodies.* Journal of Computational Physics, 2008. **227**(16): p. 7587-7620.
59. Borazjani, I., and Sotiropoulos, F., *The effect of implantation orientation of a bileaflet mechanical heart valve on kinematics and hemodynamics in an anatomic aorta.* Journal of Biomechanical Engineering, 2010. **132**: p. 111005.
60. Xenos, M., Girdhar, G., Alemu, Y., Jesty, J., Slepian, M., Einav, S., and Bluestein, D., *Device Thrombogenicity Emulator (DTE)-Design optimization methodology for cardiovascular devices: A study in two bileaflet MHV designs.* Journal of Biomechanics, 2010. **43**(12): p. 2400-2409.
61. Simon, H.A., Ge, L., Sotiropoulos, F., Yoganathan, A.P., *Simulation of the Three-Dimensional Hinge Flow Fields of a Bileaflet Mechanical Heart Valve Under Aortic Conditions.* Annals of Biomedical Engineering, 2009: p. DOI: 10.1007/s10439-009-9857-0.

62. Simon, H.A., Ge, L., Sotiropoulos, F., and Yoganathan, A., *Numerical Investigation of the Performance of Three Hinge Designs of Bileaflet Mechanical Heart Valves.* Annals of Biomedical Engineering, 2010. **38**(11): p. 3295--3310.
63. Yun, B.M., Wu, J., Simon, H.A., Arjunon, S., Sotiropoulos, F., Aidun, C.K., and Yoganathan, A., *A Numerical Investigation of Blood Damage in the Hinge Area of Aortic Bileaflet Mechanical Heart Valves During the Leakage Phase.* Annals of Biomedical Engineering, 2012.
64. Shahriari, S.a.M., H. and Hassan, I. and Kadem, L., *Evaluation of shear stress accumulation on blood components in normal and dysfunctional bileaflet mechanical heart valves using smoothed particle hydrodynamics.* Journal of Biomechanics, 2012.
65. Wu, J., Yun, B.M., Fallon, A.M., Hanson, S.R., Aidun, C.K., and Yoganathan, A., *Numerical Investigation of the Effects of Channel Geometry on Platelet Activation and Blood Damage.* Annals of Biomedical Engineering, 2011: p. 897-910.
66. Wu, J. and C.K. Aidun, *Simulating 3D deformable particle suspensions using lattice Boltzmann method with discrete external boundary force.* International Journal for Numerical Method in Fluids, 2010. **62**(7): p. 765-783.
67. Fallon, A.M., L.P. Dasi, U.M. Marzec, S.R. Hanson, and A.P. Yoganathan, *Procoagulant properties of flow fields in stenotic and expansive orifices.* Annals of Biomedical Engineering, 2008. **36**(1): p. 1-13.
68. Aidun, C.K., and Lu, Y., *Lattice Boltzmann simulation of solid particles suspended in fluid.* Journal of Statistical Physics, 1995. **81**(1): p. 49-61.
69. Aidun, C.K., Lu, Y., and Ding, E., *Direct analysis of particulate suspensions with inertia using the discrete Boltzmann equation.* Journal of Fluid Mechanics, 1998. **373**: p. 287.
70. Aidun, C.K., and Clausen, J.R., *Lattice Boltzmann Method for Complex Flows.* Annual Review of Fluid Mechanics, 2010. **42**: p. 439-472.
71. Macmeccan, R.M., Clausen, J.R., Neitzel, G.P., and Aidun, C.K., *Simulating deformable particle suspensions using a coupled lattice-Boltzmann and finite-element method.* Journal of Fluid Mechanics, 2008. **618**: p. 13-58.
72. Keating, B., Vahala, G., Yepez, J., Soe, M., and Vahala, L., *Entropic lattice Boltzmann representations required to recover Navier-Stokes flows.* Physical Review E, 2007. **75**(3): p. 36712.
73. Ding, E.J., and Aidun, C.K., *Extension of the lattice-Boltzmann method for direct simulation of suspended particles near contact.* Journal of Statistical Physics, 2003. **112**(3): p. 685-708.
74. Ladd, A.J.C., *Numerical simulations of particulate suspensions via a discretized Boltzmann equation. Part 1. Theoretical foundation.* Journal of Fluid Mechanics, 1994. **271**: p. 285-309.
75. Ladd, A.J.C., and Verberg, R., *Lattice-Boltzmann simulations of particle-fluid suspensions.* Journal of Statistical Physics, 2001. **104**(5): p. 1191-1251.
76. Chikatamarla, S.S., and Frouzakis, C.E., and Karlin, I.V., and Tomboulides, A.G., and Boulouchos, K.B., *Lattice Boltzmann method for direct numerical simulation of turbulent flows.* Journal of Fluid Mechanics, 2010. **656**: p. 298-308.

77. Vahala, G., Keating, B., Soe, M., Yepez, J., Vahala, L., Carter, J., and Ziegeler, S., *MHD turbulence studies using lattice Boltzmann algorithms.* Commun Comput Phys, 2008. **4**: p. 624-646.
78. Vahala, G., Keating, B., Soe, M., Yepez, J., Vahala, L., and Ziegeler, S., *Entropic, LES and boundary conditions in lattice Boltzmann simulations of turbulence.* The European Physical Journal - Special Topics, 2009. **171**(1): p. 167-171.
79. Bouzidi, M., Firdaouss, M., and Lallemand, P., *Momentum transfer of a Boltzmann-lattice fluid with boundaries.* Physics of Fluids, 2001. **13**: p. 3452.
80. Feng, Z.G., and Michaelides, E.E., *The immersed boundary-lattice Boltzmann method for solving fluid-particles interaction problems.* Journal of Computational Physics, 2004. **195**(2): p. 602-628.
81. Ginzbourg, I., and Adler, P.M., *Boundary flow condition analysis for the three-dimensional lattice-Boltzmann model.* J. Phys. II, 1994. **4**: p. 191-214.
82. Ziegler, D.P., *Boundary conditions for lattice-Boltzmann simulations.* Journal of Statistical Physics, 1993. **71**: p. 1171-1177.
83. Reasor Jr, D.A., Clausen, J.R., and Aidun, C.K., *Coupling the lattice-Boltzmann and spectrin-link methods for the direct numerical simulation of cellular blood flow.* International Journal for Numerical Methods in Fluids, 2012. **68**(6): p. 767-781.
84. Senis, Y., et al., *Platelet Proteomics: Principles, Analysis, and Applications*. 2011: Wiley.
85. Clausen, J.R., and Aidun, C.K., *Capsule dynamics and rheology in shear flow: Particle pressure and normal stress.* Physics of Fluids, 2010. **22**: p. 123302.
86. Clausen, J.R., Reasor, D.A., and Aidun, C.K., *The rheology and microstructure of concentrated non-colloidal suspensions of deformable capsules.* Journal of Fluid Mechanics, 2011. **685**(1): p. 202-234.
87. Jeffery, G.B., *The motion of ellipsoidal particles immersed in a viscous fluid.* Proceedings of the Royal Society of London, Series A, 1922. **102**: p. 161.
88. Hunt, J.C.R., Wray, A.A., and Moin, P., *Eddies, streams, and convergence zones in turbulent flows.* Studying Turbulence Using Numerical Simulation Databases, 1988. **1**(2): p. 193-208.
89. Jeong, J., and Hussain, F., *On the identification of a vortex.* Journal of Fluid Mechanics, 1995. **285**: p. 69-94.
90. Ding, E.J., and Aidun, C.K., *The dynamics and scaling law for particles suspended in shear flow with inertia.* Journal of Fluid Mechanics, 2000. **423**: p. 317-344.
91. Wu, J. and C.K. Aidun, *A method for direct simulation of flexible fiber suspensions using lattice--Boltzmann equation with external boundary force.* International Journal of Multiphase Flow, 2010. **36**: p. 202-209.
92. Rosen, T., Lundell, F., and Aidun, C.K., *Effect of fluid inertia on the dynamics and scaling of neutrally buoyant particles in shear flow.* Journal of Fluid Mechanics, 2013.
93. Reasor Jr, D.A., *Numerical Simulation of Cellular Blood Flow*, in *Mechanical Engineering*. 2011, Georgia Institute of Technology: Atlanta. p. 164.
94. Clausen, J.R., and Reasor Jr, D.A., and Aidun, C.K., *Parallel performance of a lattice-Boltzmann/finite element cellular blood flow solver on the IBM Blue*

Gene/P architecture. Computer Physics Communications, 2010. **181**(6): p. 1013-1020.
95. Ellis, J.T., *An in vitro investigation of the leakage and hinge flow fields through bileaflet mechanical heart valves and their relevance to thrombogenesis* in *Mechanical Engineering*. 1999, Georgia Institute of Technology: Atlanta.
96. Brown, M.L., Parsheh, M., and Aidun, C.K., *Turbulent flow in a converging channel: effect of contraction and return to isotropy.* Journal of Fluid Mechanics, 2006. **560**: p. 437-448.
97. Ge, L., Dasi, L.P., Sotiropoulos, F., and Yoganathan, A.P., *Characterization of hemodynamic forces induced by mechanical heart valves: Reynolds vs. viscous stresses.* Annals of Biomedical Engineering, 2008. **36**(2): p. 276-297.
98. Pope, S.B., *Turbulent Flows*. 2000: Cambridge University Press.
99. Yeung, P.K., and Pope, S.B., *Lagrangian statistics from direct numerical simulations of isotropic turbulence.* Journal of Fluid Mechanics, 1989. **207**(1): p. 531-586.
100. Kim, J., Moin, P., and Moser, R., *Turbulence statistics in fully developed channel flow at low Reynolds number.* Journal of Fluid Mechanics, 1987. **177**(1): p. 133-166.
101. Yun, B.M., Dasi, L.P., Aidun, C.K., and Yoganathan, A.P., *Computational modeling of flow through bileaflet mechanical heart valves using the lattice-Boltzmann method.* Journal of Fluid Mechanics (under review), 2013.
102. Yun, B.M., Dasi, L.P., Aidun, C.K., and Yoganathan, A.P., *Highly resolved pulsatile flows through bileaflet mechanical heart valves using the lattice-Boltzmann method.* Journal of Fluid Mechanics (under review), 2013.
103. Fox, S.I., *Human Physiology*. 9 ed. 2006: McGraw-Hill.
104. Weisstein, E.W. *Disk Point Picking*. Available from: http://mathworld.wolfram.com/DiskPointPicking.html.
105. Ge, L., Jones, S.C., Sotiropoulos, F., Healy, T.M., and Yoganathan, A.P., *Numerical simulation of flow in mechanical heart valves: grid resolution and the assumption of flow symmetry.* Journal of Biomechanical Engineering, 2003. **125**: p. 709.
106. Yoganathan, A.P., Fogel, M., Gamble, S., Morton, M., Schmidt, P., Secunda, J., Vidmar, S., and Nido, P., *A new paradigm for obtaining marketing approval for pediatric-sized prosthetic heart valves.* The Journal of Thoracic and Cardiovascular Surgery, 2013.
107. Karamlou, T., Jang, K., Williams, W.G., Caldarone, C.A., Van Arsdell, G., Coles, J.G., and McCrindle, B.W., *Outcomes and Associated Risk Factors for Aortic Valve Replacement in 160 Children A Competing-Risks Analysis.* Circulation, 2005. **112**(22): p. 3462-3469.
108. Raghuveer, G., Caldarone, C.A., Hills, C.B., Atkins, D.L., Belmont, J.M., and Moller, J.H., *Predictors of prosthesis survival, growth, and functional status following mechanical mitral valve replacement in children aged< 5 years, a multi-institutional study.* Circulation, 2003. **108**: p. 174-179.
109. Kaldararova, M., Balazova, E., Stankovicova, I ., Brucknerova, I .,and Masura, J., *Echocardiographic measurements of the aorta in normal children and young adults.* Bratislavske lekarske listy, 2006. **108**(437-441).

110. Pees, C., Glagau, E., Hauser, J., and Michel-Behnke, I., *Reference Values of Aortic Flow Velocity Integral in 1193 Healthy Infants, Children, and Adolescents to Quickly Estimate Cardiac Stroke Volume.* Pediatric cardiology, 2013: p. 1-7.
111. Pettersen, M.D., Du, W., Skeens, M.E., and Humes, R.A., *Regression Equations for Calculation of Z Scores of Cardiac Structures in a Large Cohort of Healthy Infants, Children, and Adolescents: An Echocardiographic Study.* Journal of the American Society of Echocardiography, 2008. **21**(8): p. 922-934.
112. Sluysmans, T., and Colan, S.D., *Theoretical and empirical derivation of cardiovascular allometric relationships in children.* Journal of Applied Physiology, 2005. **99**(2): p. 445-457.
113. Zilberman, M.V., Khoury, P.R., and Kimball, R.T., *Two-dimensional echocardiographic valve measurements in healthy children: gender-specific differences.* Pediatric cardiology, 2005. **26**(4): p. 356-360.
114. Sheriff, J., Soares, J.S., Xenos, M., Jesty, J., and Bluestein, D., *Evaluation of Shear-Induced Platelet Activation Models Under Constant and Dynamic Shear Stress Loading Conditions Relevant to Devices.* Annals of Biomedical Engineering, 2013: p. 1-18.
115. Alemu, Y., and Bluestein, D., *Flow-induced platelet activation and damage accumulation in a mechanical heart valve: Numerical studies.* Artificial Organs, 2007. **31**(9): p. 677--688.
116. Antiga, L., and D.A. Steinman, *Rethinking turbulence in blood.* Biorheology, 2009. **46**(2): p. 77-81.
117. Kameneva, M.V., Burgreen, G.W., Kono, K., Repko, B., Antaki, J.F., and Umezu, M., *Effects of turbulent stresses upon mechanical hemolysis: experimental and computational analysis.* ASAIO Journal, 2004. **50**(5): p. 418-423.
118. Dyverfeldt, P., Hope, M.D., Tseng, E.E., and Saloner, D., *Magnetic Resonance Measurement of Turbulent Kinetic Energy for the Estimation of Irreversible Pressure Loss in Aortic Stenosis.* JACC: Cardiovascular Imaging, 2013. **6**(1): p. 64-71.
119. Alemu, Y., Girdhar, G.,Xenos, M.,Sheriff, J.,Jesty, J.,Einav, S. and Bluestein, D., *Design Optimization of a Mechanical Heart Valve for Reducing Valve Thrombogenicity-A Case Study with ATS Valve.* ASAIO, 2010. **56**(5): p. 389.
120. Zou, Q., and He, X., *On pressure and velocity flow boundary conditions and bounceback for the lattice Boltzmann BGK model.* Physics of Fluids, 1996. **9**(6): p. 1591 - 1598.
121. Noble, D.R., Chen, S., Georgiadis, J.G., and Buckius, R.O., *A consistent hydrodynamic boundary condition for the lattice Boltzmann method.* Physics of Fluids, 1995: p. 203-209.
122. Peskin, C.S., *The immersed boundary method.* Acta Numerica, 2002. **11**: p. 479.
123. Junk, M., and Yang, Z., *Outflow boundary conditions for the lattice Boltzmann method.* Progress in Computational Fluid Dynamics, an International Journal, 2008. **8**(1): p. 38-48.